Experimental study of fast electron transport in dense plasmas

Xavier Vaisseau

To cite this version:

Xavier Vaisseau. Experimental study of fast electron transport in dense plasmas. Plasma Physics [physics.plasm-ph]. Université de Bordeaux, 2014. English. NNT : 2014BORD0432 . tel-01198927

HAL Id: tel-01198927

https://theses.hal.science/tel-01198927

Submitted on 14 Sep 2015

HAL is a multi-disciplinary open access archive for the deposit and dissemination of scientific research documents, whether they are published or not. The documents may come from teaching and research institutions in France or abroad, or from public or private research centers.

L'archive ouverte pluridisciplinaire **HAL**, est destinée au dépôt et à la diffusion de documents scientifiques de niveau recherche, publiés ou non, émanant des établissements d'enseignement et de recherche français ou étrangers, des laboratoires publics ou privés.

THÈSE

présentée à

L'UNIVERSITÉ DE BORDEAUX

ÉCOLE DOCTORALE DES SCIENCES PHYSIQUES ET DE L'INGÉNIEUR

par **Xavier Vaisseau**

pour obtenir le grade de

DOCTEUR

SPÉCIALITÉ : ASTROPHYSIQUE, PLASMAS, NUCLÉAIRE

Experimental study of fast electron transport in dense plasmas

---

Soutenue le 19 décembre 2014

Devant la commission d'examen formée de :

M. CASNER, Alexis	Ingénieur Chercheur, CEA	Président
Mme. HANNACHI, Fazia	Directrice de recherche, CENBG	Examinatrice
M. MALKA, Victor	Directeur de recherche, École Polytechnique	Rapporteur
M. MIQUEL, Jean-Luc	Ingénieur Chercheur, CEA	Examinateur
M. ROTH, Markus	Professeur, Technische Universität Darmstadt	Rapporteur
M. SANTOS, João	Maître de Conférence, Université de Bordeaux	Co-directeur de thèse
M. TIKHONCHUK, Vladimir	Professeur, Université de Bordeaux	Directeur de thèse

Remerciements

Cette thèse a été préparée au laboratoire CELIA. Je voudrais d'abord remercier son directeur, Philippe Balcou, de m'y avoir accueilli pendant ces trois années.

Je tiens ensuite à remercier Vladimir Tikhonchuk d'avoir accepté d'être mon directeur de thèse. J'ai énormément apprécié ses qualités scientifiques et relationnelles en temps que directeur du M2 fusion, puis en temps que directeur de thèse. Merci d'avoir relu si attentivement mon manuscrit dans des délais si courts.

Merci à toi João pour ces trois années. Merci de m'avoir fait confiance pour ce stage de M1, vrai baptême du feu au LULI où j'ai découvert l'univers des manip' sur lasers de puissance, qui a conditionné toute la suite. J'ai énormément apprécié tes qualités scientifiques et pédagogiques. Tu m'as non seulement appris toutes les bases de la préparation et de l'exécution d'une manip' sur les grandes installations laser, mais tu m'as aussi poussé vers les simulations numériques pour que je puisse toucher aux différents aspects du travail de recherche. Je te remercie de m'avoir fait voyager tout au long de ma thèse et de m'avoir permis de rencontrer toutes ces personnes à travers le monde. J'ai énormément apprécié ta personnalité et ton amitié en dehors des manip'. Merci pour ces soirées inoubliables à San Francisco et à Osaka ! Je te remercie infiniment de m'avoir donné toute cette autonomie et de m'avoir poussé à donner le meilleur de moi-même.

Un grand merci à toi Sébastien, mon correspondant CEA, de t'être aussi grandement impliqué dans mon encadrement pendant les manip' mais aussi pour la déconvolution des données. J'ai pu grâce à toi découvrir le monde des expériences sur les chaînes laser à haute cadence (c'est sûr, ça change tout d'avoir plus qu'un tir toutes les 2 heures) et développer des aptitudes pour le bricolage (oui, je sais, je partais de loin !). Je te remercie aussi pour toutes ces heures passées à assister à mes répèt' et pour tes suggestions, toujours très intéressantes et pertinentes.

Je tiens aussi à remercier les membres de mon jury de thèse, en particulier Victor Malka et à Markus Roth, pour avoir accepté la lourde tâche de rapporteur malgré des délais un peu courts. Merci à Jean-Luc Miquel d'avoir accepté d'être examinateur, et à Fazia Hannachi qui n'a malheureusement pas pu assister à la soutenance. Merci à Alexis Casner d'avoir accepté d'être président du jury et pour toutes nos discussions pendant ces trois dernières années.

Je remercie particulièrement Laurent et Thierry pour leur soutien et leur implication personnelle dans la réussite de mon parcours.

Le CELIA offre vraiment d'excellentes conditions de travail. Je voudrais remercier toutes les personnes que j'y ai rencontrées. Merci à Dimitri, Claude, Fabien et à tous mes collègues du groupe PETRUX. Merci à Philippe, Xavier, Jean-Luc, Jérôme, Dominique, Bernard, Hervé, Xavier, Marina, Frédéric (mon premier co-bureau !), Emmanuel. Merci à Rachel de m'avoir initié aux simulations PIC et d'avoir passé autant de temps à répondre à mes questions. Merci à Céline, Emmanuelle, Sophie, Loïc et Elodie.

Je voudrais particulièrement remercier tous les doctorants et post-docs du CELIA que j'ai pu côtoyer pendant ces trois ans. Merci à Mathieu, Nesrine et François, d'avoir partagé ce bureau avec moi. Merci pour toutes nos discussions et pour ces moments partagés, que ce soit en manip' ou en conf'. Merci à Amélie, Mathieu et Pierre, mes anciens collègues de M1, Lorenzo, Benjamin, Mathieu, Pierre-Marie, Basil, Takaya, Dario, François, Arnaud, Ludovic,

Claudio, Gabrielle, Guillaume, Gabriel, Mokrane, Emma, Alexandra, qui a la particularité étrange d'avoir les mêmes goûts musicaux que moi, Rémi, Jessy, Igor, Julien, Luca, Bart et Mickael, mes collègues du M2 fusion. Merci à Luca d'avoir passé autant de temps à m'expliquer le fonctionnement des simulations Monte-Carlo. Merci à toi Witold de nous avoir servi de guide à Darmstadt pendant cette école d'hiver au GSI. Merci aux personnes que j'ai rencontrées pendant les différentes écoles d'été et les conférences, en particulier à Lena, Anna et Sergei, mes amis russes.

J'ai eu la chance pendant les deux premières années de pouvoir enseigner à l'IUT, et pour cela je remercie Medhi et Claire. Merci à Eric et Vincent pour toutes ces heures passées à co-encadrer les TP de thermo.

Une partie importante de ma thèse a consisté à faire des manip' sur les grandes installations laser internationales, qui impliquaient à chaque fois un nombre important de personnes. J'adresse mes remerciements les plus sincères à tous ceux que j'ai pu y côtoyer. Merci à Shaun, Mianzhen, Jaebum, Jonathan, Anna, Robert, Yongjoo, Hiroshi, Ross, Elijah, Kun, Drew, Mingsheng, Prav, Hui et Sugreev. Merci à toi Alessio pour tous ces bons moments passés, et pour ces soirées à San Francisco, Osaka et Paris. Je remercie toutes les personnes rencontrées lors des manip' au LULI, en particulier Motoaki, Luca, Arthur, Charlie, Sophie, Emilie, Fabien et Mathieu.

Merci à Javier Honrubia de m'avoir initié aux simu' de transport hybrides et pour son accueil à Madrid. Un grand merci à toi Arnaud d'avoir passé autant de temps à m'aider à interpréter les résultats de simu', mais aussi de m'avoir fait découvrir la vie nocturne madrilène.

Un très grand merci à mes amis, qui ont toujours été là pour me supporter dans les meilleurs moments comme dans les pires. Merci à vous, Nicolas (ça doit faire pas loin de 20 ans qu'on se connaît maintenant !) et Vincent, vivement la prochaine repèt' ! Merci à Marion et Alex, mes amis motards passionnés de cuisine. Merci à Marion, Alex et Julien, mes amis doctorants du LOMA et de l'I2M, pour ces soirées à partager nos doutes, nos angoisses sur notre présent et notre avenir. Merci à Justine, Nono, Maxime et Yon.

Pour terminer, je voudrais adresser un immense remerciement à ma famille pour leur présence essentielle. Merci à mes parents de m'avoir permis d'arriver jusque-là et d'avoir assuré un soutien si indéfectible. Merci à Sylvie et à toi Eddy pour ces conseils, ces moments partagés, et ce fameux Roadtrip moto jusqu'en Autriche (vivement le prochain !). Un grand merci à toi Lou de m'avoir fait découvrir le monde des chevaux, un univers si riche qui s'est avéré être un échappatoire essentiel dans les pires moments de rédaction. Et finalement, merci à toi Sarah de partager ma vie. Je ne pense pas que j'aurai pu arriver à tout ça sans ton soutien. Je te remercie d'avoir assumé la lourde tâche de relecture de ma thèse, en anglais en plus, mais promis je ferai pareil pour la tienne !

Résumé

Cette thèse se place dans le contexte de la fusion thermonucléaire pour la production d'énergie, dans le cadre de l'allumage rapide par faisceaux d'électrons chauds. Le travail présenté a pour but de caractériser la source de faisceaux d'électrons rapides, accélérés par lasers intenses ($10^{19} - 10^{20}$ W/cm^2), et leur propagation dans des plasmas denses aussi bien à l'état solide que comprimé.

La première étude présentée avait pour but d'étudier la propagation d'électrons rapides, caractérisés par une densité de courant $> 10^{11}$ A/cm^2, dans des cibles d'aluminium chauffées à la température de Fermi par un choc plan contra-propagatif, qui les comprimait à deux fois la densité du solide. La géométrie de compression plane nous a permis de dissocier les pertes d'énergie dues aux effets résistifs et collisionnels, en comparant des cibles solides et comprimées de masses surfaciques identiques. Nous avons observé pour la première fois une augmentation des pertes d'énergie d'origine résistive dans les échantillons chauffés. La confrontation des données expérimentales avec les simulations, incluant une caractérisation complète de la source électronique, de l'état de compression des cibles et du transport d'électrons, a permis d'étudier l'évolution temporelle de la résistivité du matériau. Elle a notamment permis d'estimer que le pouvoir d'arrêt résistif dans les cibles tièdes et denses est d'amplitude comparable au pouvoir d'arrêt collisionnel.

Dans la deuxième étude, nous avons analysé l'accélération et le transport d'électrons rapides produits lors de l'interaction d'un laser à haut contraste avec un cône de cuivre, enchâssé dans un bloc de carbone, et comprimé par un choc plan contra-propagatif. Un système d'imagerie X a permis de visualiser le couplage entre le faisceau laser intense et le cône à différents instants de la compression. Ce diagnostic, donnant accès à la distribution spatiale du faisceau d'électrons chauds, a montré une génération d'électrons dans tout le volume du cône pour des temps supérieurs au temps de débouché de choc au niveau de la pointe. Pour des temps antérieurs, l'interaction se produit à haut contraste, la source est restreinte au niveau de la pointe du cône, et la propagation collimatée des électrons vers l'intérieur de la cible est assurée par les champs magnétiques auto-générés. Ces conclusions ont été obtenues en confrontant les données expérimentales aux simulations.

Une caractérisation hydrodynamique de la compression par choc de la cible a été effectuée à l'aide d'une technique de radiographie X, permettant de visualiser la propagation du front de choc dans la cible, sa collision avec la pointe du cône et son glissement le long des parois. Les mesures sont en accord avec des simulations hydrodynamiques.

Mot clés : Fusion par confinement inertiel; Allumage rapide; Transport d'électrons relativistes créés par laser; Diagnostics X; Codes hybrides; Codes PIC; Codes hydrodynamiques; Effets résistifs; Effets collisionnels.

Summary

The framework of this PhD thesis is the inertial confinement fusion for energy production, in the context of the electron fast ignition scheme. The work consists in a characterization of the transport mechanisms of fast electrons, driven by intense laser pulses ($10^{19} - 10^{20}$ W/cm^2) in both cold-solid and warm-dense matter.

The first goal was to study the propagation of a fast electron beam, characterized by a current density $> 10^{11}$ A/cm^2, in aluminum targets initially heated close to the Fermi temperature by a counter-propagative planar shock. The planar compression geometry allowed us to discriminate the energy losses due to the resistive mechanisms from collisional ones by comparing solid and compressed targets of the same initial areal densities. We observed for the first time a significant increase of resistive energy losses in heated aluminum samples. The confrontation of the experimental data with the simulations, including a complete characterization of the electron source, of the target compression and of the fast electron transport, allowed us to study the time-evolution of the material resistivity. The estimated resistive electron stopping power in a warm-compressed target is of the same order as the collisional one.

We studied the transport of the fast electrons generated in the interaction of a high-contrast laser pulse with a hollow copper cone, buried into a carbon layer, compressed by a counter-propagative planar shock. A X-ray imaging system allowed us to visualize the coupling of the laser pulse with the cone at different moments of the compression. This diagnostic, giving access to the fast electron spatial distribution, showed a fast electron generation in the entire volume of the cone for late times of compression, after shock breakout from the inner cone tip. For earlier times, the interaction at a high-contrast ensured that the source was contained within the cone tip, and the fast electron beam was collimated into the target depth by self-generated magnetic fields. These conclusions were obtained by a confrontation of experimental data to simulation results.

The hydrodynamic characterization of the shock-induced target compression was performed using a X-ray point projection radiography technique, allowing to visualize a propagation of the shock front into the target, its collision with the cone tip and its subsequent sliding along the cone walls. The measurements are in agreement with hydrodynamic simulations.

Keywords: Inertial confinement fusion; Fast ignition; Laser-driven fast electron transport; X-ray diagnostics; Hybrid codes; PIC codes, Hydrodynamic codes; Resistive effects; Collisional effects.

Contents

Chapter 1

Introduction

According to the latest report of the Intergovernmental Panel on Climate Change (IPCC) the global warming related to the accumulation of anthropic greenhouse gazes will be responsible for the rise of the global mean temperature up to 4.8°, under the most pessimistic scenario, in the years 2081-2100 compared to the mean value of the 1986-2005 period [IPC, 2014]. This global temperature rise could be responsible for an increased occurrence of extreme climate events such as droughts, heavy rainfalls, intense heat waves and a current sea level rise up to 0.8 m leading to millions of environmental migrants. Agriculture would also be first in line to be affected by the impact of climate change with a decrease of production yields of 2% per decade if not any considerable adaptation effort is made, whereas the global demand would require an increase of 14%.

The development of a low carbon energy system is a major challenge of the next decade. Fossil fuel, including oil, coal and natural gas, currently represents nearly 82% of the global energy supply (Fig. 1.1). While the proportion of fossil fuel in the global energy mix did not vary much during the last 30 years, the global energy consumption has more than doubled in the 1971-2011 period and keeps rising [IEA, 2013].

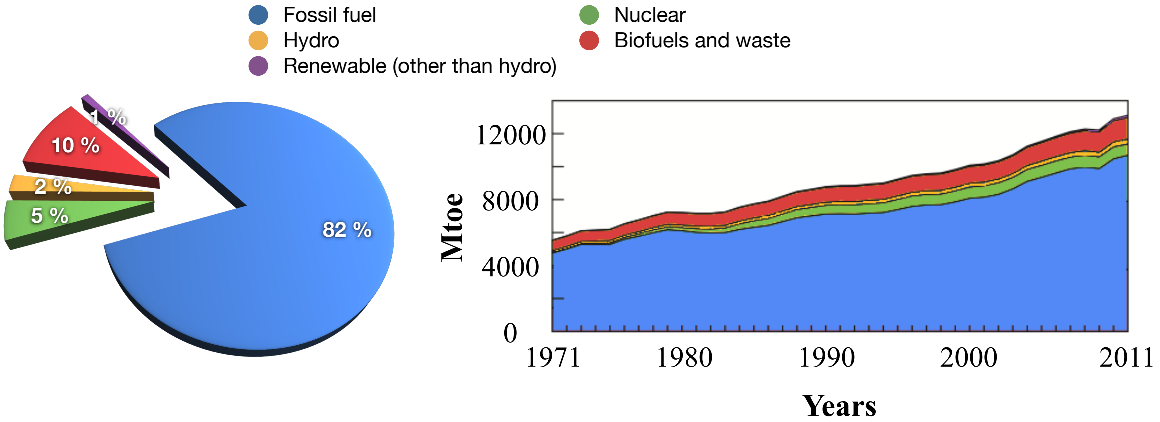

Figure 1.1: (Left) World total primary energy supply repartition in 2011. The total is estimated to 13113 Million Tons of oil equivalent (Mtoe), or 5.49×10^{20} J. (Right) World primary energy supply in the 1971-2011 period

In 2012 the International Energy Agency (IEA) proposed the so called 2DS scenario giving the world a 80% chance of keeping the global temperature rise below 2°C compared to pre-industrial levels. One of the main constraints is to reduce the fraction of fossil fuel from 82% down to 20% by 2050. In OECD[1] countries this leads to halving the fossil-fuel energy used

---

[1] The *Organisation for Economic Co-operation and Development* (OECD) regroups more than 30 countries

in electricity generation and transport compared to the 2011 level. This dramatic reduction cannot be triggered by a single cleaner technology but rather by the increase of both renewable and nuclear energy in the total mix, the latter having to reach 18% by 2050 [IEA, 2012].

Electricity production based on nuclear fission, releasing an important amount of energy by splitting a heavy nucleus into smaller parts, stands out by its important capacity of energy production characterized by low CO_2 emission. 437 nuclear reactors are currently in operation in the world [IAE, 2014]. Nuclear energy production has been in steady expansion since the early 1970s until the recent Fukushima Daiichi nuclear disaster on March 2011, leading to a sudden drop of the global nuclear electricity production of 10% between 2010 and 2012, and to a growing awareness of the population of the potential dramatic ecological impacts of nuclear fission. At the end of year 2013, 72 nuclear reactors were in construction, most of which belonging the the so-called generation III reactors, designed to reduce the consequences of major accidents. However, the estimated resources of the 235 isotope of uranium, labeled as ^{235}U, used as fissile fuel in current nuclear reactors, would only allow to ensure electricity production during 100 years by burning uranium at the same rate as today. Generation IV (Gen IV) reactors currently under study would offer an important extension of nuclear fission life, up to several thousand years, while offering the possibility to transmute minor actinide nuclei, constituting the most radioactive category of nuclear wastes . Based on the use of a fast neutron spectrum, Gen IV reactors use as fuel, in the so-called Sodium cooled Fast Reactors (SFR), a combination of ^{239}Pu and of ^{238}U, constituting more than 99% of uranium ore resources. Fast neutron reactors also offer the possibility to produce more fissile fuel (^{239}Pu) than they consume (breeder reactors). This fairly interesting characteristic is achieved by successive neutron capture of ^{238}U fertile nuclei followed by several beta decays. A major inconvenient of SFR arises from the use of liquid sodium as coolant, due to the extremely high chemical reactivity of sodium and water.

An alternative to conventional nuclear energy production technologies could arise from nuclear fusion, that could provide a safer, cleaner and nearly inexhaustible source of energy. The basic principle relies on the important amount of energy released during the fusion process of two light nuclei, lighter than the stable iron nucleus. This fusion process taking place when the two nuclei overcome the Coulomb potential requires to heat the fuel up to several million degrees. Nuclear fusion constitutes the engine of stars in the so-called proton-proton chain reaction converting hydrogen into helium. In order to be energetically efficient, this reaction, characterized by a dramatically low cross-section, requires a huge amount of matter to be confined during a sufficient duration. This requirement achieved in stars by gravitational confinement cannot be considered as a sustainable way of producing energy on earth. Several other exothermic nuclear fusion reactions are currently examined for energy production perspectives in laboratory, the most interesting ones being the following:

$$\begin{aligned} \mathrm{D} + \mathrm{D} &\underset{50\%}{\longrightarrow} \mathrm{T}(1.01\ \mathrm{MeV}) + \mathrm{p}(3.02\ \mathrm{MeV}) \\ &\underset{50\%}{\longrightarrow} {}^{3}\mathrm{H_e}(0.82\ \mathrm{MeV}) + \mathrm{n}(2.45\ \mathrm{MeV}) \qquad (1.1) \\ \mathrm{D} + \mathrm{T} &\longrightarrow {}^{4}\mathrm{H_e}(3.5\ \mathrm{MeV}) + \mathrm{n}(14.1\ \mathrm{MeV}) \qquad (1.2) \\ \mathrm{D} + {}^{3}\mathrm{H_e} &\longrightarrow {}^{4}\mathrm{H_e}(3.6\ \mathrm{MeV}) + \mathrm{p}(14.7\ \mathrm{MeV}) \qquad (1.3) \end{aligned}$$

with D, T, $^{3}\mathrm{H_e}$ and $^{4}\mathrm{H_e}$ the nuclei of deuterium, tritium, helium 3 and helium 4 (alpha particle), respectively. The evolution of the total probability of fusion reactions, or cross sections σ, are

---

including all Western Europe, North American, Japan, Australia, New-Zeland, South Korea, Czech Republic, Hungary, Poland, Chili, Slovenia, Israel and Estonia.

represented in Fig. 1.2 as a function of the incident particle energy (the first ion on the left-hand side of the previous equations, the second one being at rest). The number of fusion reactions

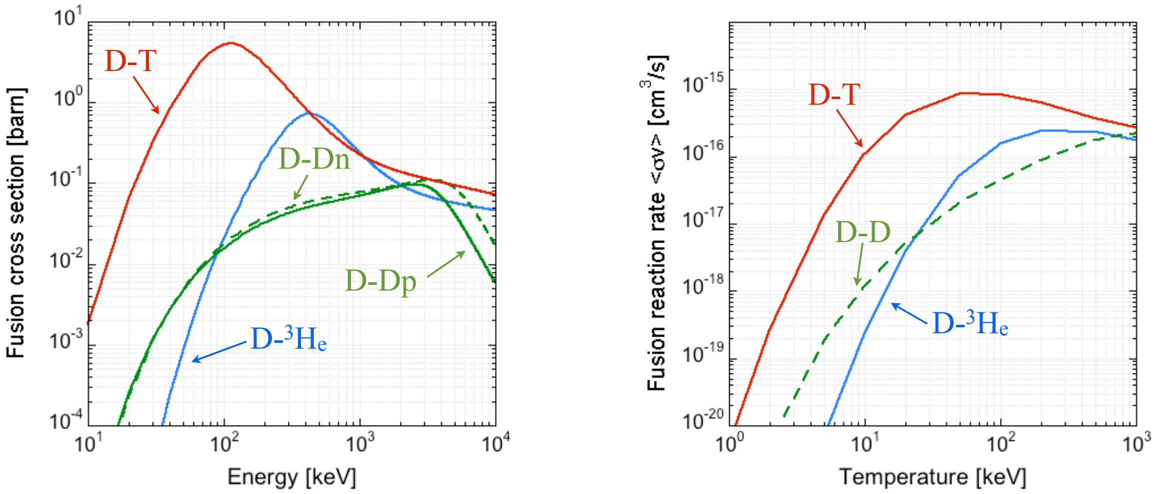

Figure 1.2: (Left) Evolution of fusion reaction cross sections for D−Dn (green dashed line), D−Dp (green solid line), D−T (red solid line) and D + H_e^3 (blue solid line) as a function of the incident particle, the first ion of each pair, the other particle being considered at rest. (Right) Evolution of the fusion reaction rate as a function of the ion temperature. All data are taken from [Huba, 2009].

per unit of time and volume, or reaction rate $\langle \sigma v \rangle$, can be calculated by the following:

$$\langle \sigma v \rangle = \int_0^\infty \sigma(v) f(\boldsymbol{v}) v d\boldsymbol{v} \tag{1.4}$$

with v the relative velocity of the particle and $f(\boldsymbol{v})$ the velocity distribution among the plasma. The evolution of the reaction rate as a function of the temperature is presented in Fig. 1.2 when considering a plasma at thermal equilibrium characterized by a Maxwellian distribution function. One can clearly note that the D-T reaction has the highest cross section obtained at the lowest temperature, of the order of tens of keV. This reaction, releasing 17.6 MeV of energy, has consequently been chosen for energy production purposes, despite its important drawbacks. The fusion energy is indeed split between an alpha particle and a neutron, this latter carrying 80% of the released energy due to its lower mass, being electrically neutral. This energetic neutron can consequently only be collected outside the reactor, triggering major technical collection and safety radiation issues. Tritium is also a radioactive element with a 12.32 years half-life. The D-D fusion reaction appears to be more interesting in an energy production purpose since it is characterized by a double disintegration channel among which only one of them creates a neutron. The reaction rate of the D-D fusion reaction is however way lower than for D-T reaction. The most interesting reaction for energy production purposes would be given by Eq. 1.3. It releases even more energy than a D-T reaction while creating only charged particles that could be easily collected inside the reactor, dramatically decreasing the amount of generated radioactive wastes. However the $^3\mathrm{H}_\mathrm{e}$ helium isotope does not exist on Earth and has consequently to be created by fairly expensive nuclear reactions. It is worth mentioning that all the described fusion reactions are characterized by a fairly low maximum cross sections, lower than 5 barns. This last figure has to be compared with the 300 barns obtained for nuclear fission of a ^{235}U nucleus by thermal neutrons. Yet, the energy yield of the complete fusion of 1 g of D-T is equivalent to the energy released by the fission of $\sim$ 4.2 g of ^{235}U, or the burn of $\sim$ 8 T of oil. Another major advantage of nuclear fusion is the absence of chain reactions, at the very basis of nuclear fission reactor operation, avoiding potential runaway reactions and thus considerable safety issues.

As previously mentioned a key issue in nuclear fusion energy production is to confine a sufficient amount of extremely hot matter during a sufficient duration in order to recover more fusion energy than what was injected to heat the plasma and start fusion reactions. This physical constraint can be summarized by the so called *Lawson criterion* obtained by balancing energy losses by thermal conduction and radiation, and the fusion energy power, proportional to the reaction rate $\langle \sigma v \rangle$. The Lawson criterion writes in the D-T case:

$$n.\tau_E \geq 10^{15}\ \mathrm{cm}^{-3}.\mathrm{s} \tag{1.5}$$

with n the density of the considered plasma and τ_E the confinement time. It is worth mentioning that this inequality is obtained assuming a temperature of 1 keV. Two different confinement approaches are currently under study.

Magnetic confinement fusion (MCF) has been studied since the end of the 1950s and is currently the most advanced approach. It consists in confining a low density plasma ($n \sim 10^{12} - 10^{14}\ \mathrm{cm}^{-3}$) during a fairly long duration ($\tau_E \sim 100\,\mathrm{s}$) by intense magnetic fields. The most studied magnetic confinement device, called *tokamak* (Fig. 1.3), that could be transliterated from the russian acronym into "toroidal chamber with magnetic coils", consists in confining the plasma in a toroidal chamber by a combination of both toroidal and poloidal magnetic fields, created by magnetic induction into the plasma and by external magnets, respectively. The ITER tokamak, an international project currently in construction in France, aims at recovering a fusion power of 500 MW, 10 times higher than the injected 50 MW input power. Another magnetic confinement device currently under study is called *stellarator* (Fig. 1.3), such as the Wendelstein 7-X machine currently in construction in Germany. The helically shaped magnetic field is in this case produced by a single coil system that has in return to be twisted in a rather complicated shape, and consequently rather challenging to build. A major advantage of the

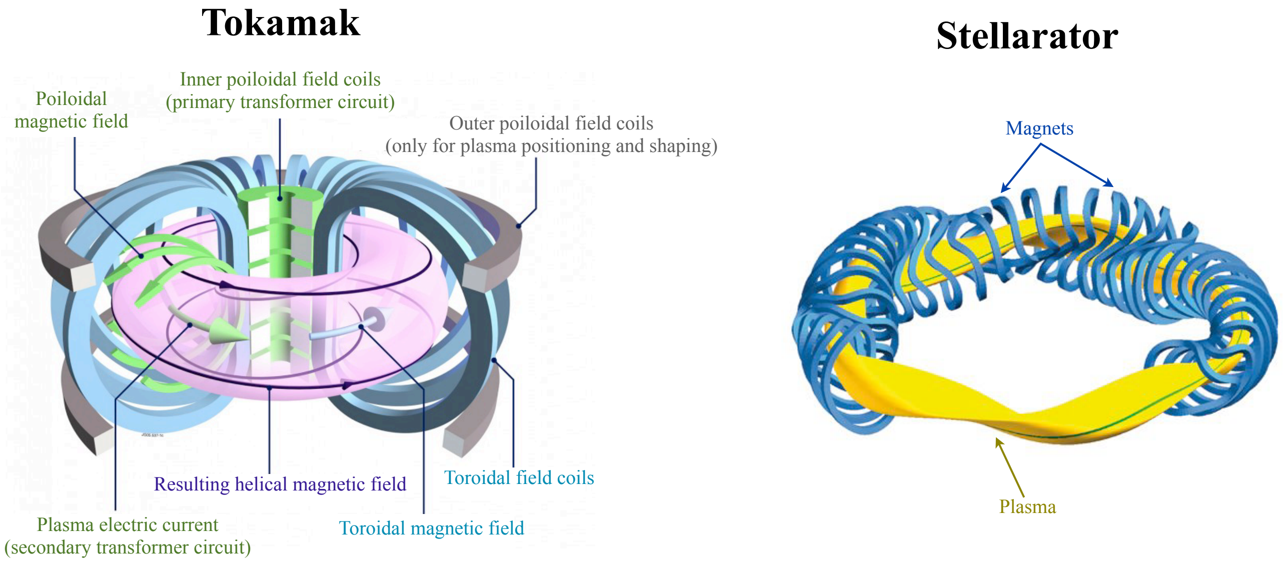

Figure 1.3: (Left) Example of a tokamak fusion device. The helical magnetic field is generated by a combination of a toroidal field, created by external magnets, and by a poloidal field, created by magnetic induction into the plasma. The external poloidal field coils are only used for plasma positioning and shape control (image taken from [efda, 2014]. (Right) Illustration of the magnet geometry and of the confined plasma in a stellarator device (image taken from [ipp, 2014]).

stellarator is to offer the best possibility for steady-state operation due to the quasi-absence of so-called disruptions, arising from fast growing instabilities and characterized by a violent release of the plasma energy, resulting in potential severe damages of the confinement chamber. Inertial confinement fusion (ICF), constituting the main framework of this thesis, consists in confining a millimeter scale initial radius D-T capsule, compressed by a factor ~ 1000, by its own inertia. The obtained high density plasma ($n \sim 10^{26}$ cm^{-3}) is confined during a extremely short duration, of the order of a few ps. This important compression is achieved by intense electromagnetic radiations, either laser light or X-ray radiation, acting on the target during a few ns. An important effort is actually made on *National Ignition Facility* (NIF) in the United-States in order to reach the so-called ignition, where the fusion nuclear reactions should become self-sustained. A similar installation, the *Laser MégaJoule* (LMJ), is currently under construction in France.

1.1 Concept of inertial confinement fusion

1.1.1 Direct and indirect drive schemes

The first ICF scheme that was historically introduced is called *direct drive*. The mm-scale D-T capsule is firstly irradiated by a large number of laser pulses, of a few tens of nanosecond duration. The external layer of the capsule, usually made of plastic, is heated and rapidly ablated. Due to coronal plasma expansion and momentum conservation the D-T shell, initially in a cryogenic state, is consequently accelerated inward. At the end of compression, the imploding fuel is suddenly stopped by the high pressure, forming at the center of the target a so-called hot spot which lasts a so-called stagnation time of $\approx 100-300$ ps. The target assembly is isobaric, the pressure of the shell being equilibrated by the hot spot pressure during the stagnation time. If the areal density of the hot spot, being the product of its density ρ_{HS} by its radius R_{HS}, is sufficiently high so that $\rho_{HS}R_{HS} > 0.3$ g.cm^{-2}, and providing that its ion temperature $T_i > 4$ keV, the alpha particles produced by the D-T nuclear fusion reactions are stopped inside the hot spot, deposit their energy and increase the hot spot temperature: the hot spot is ignited, producing even more energy due to self-sustaining fusion reactions. The nuclear burn wave propagates into the rest of the target, releasing a much more important amount of energy than the energy absorbed into the capsule if the areal density of the capsule is high enough so that $\rho_{CF}R_{CF} > 1$ g.cm^{-2}. This direct drive scheme exhibits however major drawbacks. Both the inherent target surface roughness and the non-uniformity of laser irradiation can seed a non-uniform shell acceleration that can be exponentially amplified over a few hundreds of ps by hydrodynamic instabilities. Three main kinds of hydrodynamic instabilities can degrade the compression on an ICF target:

- The Rayleigh-Taylor Instability (RTI) takes place when a higher density fluid is accelerated towards a lower density fluid, or in other words when density and pressure gradients are in opposition. It is responsible for the mix of the two fluids, the lighter one creating bubbles and the heavier one falling into the lighter one as spikes. RTI grows during the ablation phase, when the low density ablated plasma accelerates the higher density fuel inside the target, and also at the end of the implosion when the dense fuel is suddenly slowed down by the high pressure hot spot, resulting in a mix between hot and cold fuels that can prevent ignition.

- The Richtmeyer-Meshkov Instability (RMI) develops when a shock crosses a non planar interface between two fluids of unequal densities. The shock induces a distortion of the interface which is accelerated with a non-uniform speed, causing the instability to grow.

It is worth noting that the RMI instability is developing at the initial stage of target irradiation and then further amplified by the RTI instability when the shell is accelerated.

- The Kelvin-Helmholtz Instability (KHI) grows when two fluids are in motion with different speeds. The change in tangential fluid speed at the interface causes a growth of any initial perturbation. KHI grows in an ICF target when RTI has already grown, structuring spikes. It is worth mentioning that any technique used to minimize the growth of RTI automatically acts on KHI.

An improvement of the direct drive scheme, called *indirect drive*, has been introduced in order to release the different constraints associated with hydrodynamic instabilities [Lindl, 1995]. This scheme consists in focusing the laser pulses on the inner walls of a cylindrical, or rugby-shaped, gold cavity, called *hohlraum*, containing the D-T capsule (Fig. 1.4). The laser light is converted into a nearly Planckian intense X-ray emission, with a radiation temperature $T_r \sim 300$ eV, ablating the outer shell of the capsule, causing its implosion. It is worth noting that the choice of a gold-made hohlraum is dictated by the increased X-ray conversion efficiency with increasing Z number. The major advantage of indirect drive is the dramatically increased irradiation uniformity compared to direct drive. The target fabrication process and the target implosion, including the physics of laser-to-X-rays conversion, are in return much more complex. The indirect drive scheme is currently under study on the NIF, and has also been chosen on the LMJ. Results of the National Ignition Campaign (NIC) show that hydrodynamic instabilities need to be better controlled in order to reach ignition [Goldstein, 2012]. In 2013, a NIF shot resulted for the first time in an output fusion energy, of a few kJ, greater than the energy deposited into the fuel [Hurricane et al., 2014]. This important experimental result must however not be confused with the breakeven, where the output fusion energy exceeds the 1.9 MJ energy delivered by laser beams, which has not been demonstrated yet. The 2013 result was obtained using the so-called high-foot implosion design [Dittrich et al., 2014; Park et al., 2014], which was introduced to decrease the RTI at the ablation front. This is achieved

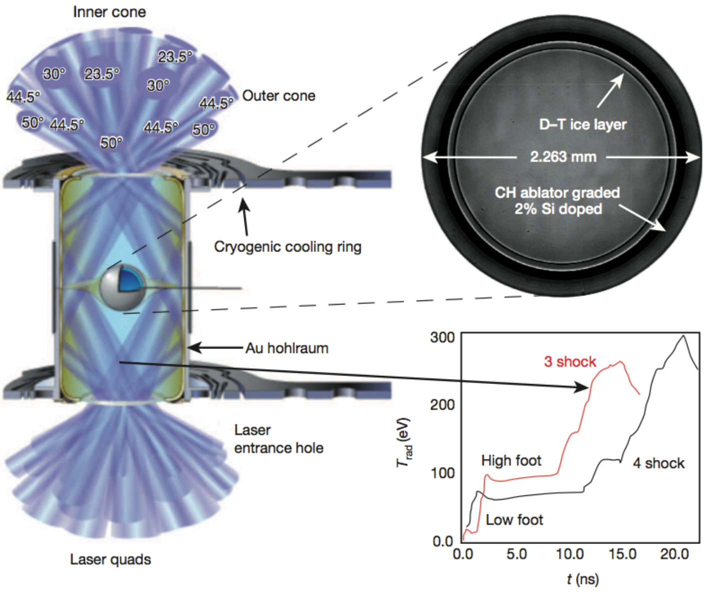

Figure 1.4: Illustration of the indirect drive scheme. The presented geometry is currently used on the National Ignition Facility. The evolution of the holhraum radiation temperature as a function of time illustrates the difference between the low-foot and the high-foot implosion designs (Image taken from [Hurricane et al., 2014]).

by increasing the hohlraum radiation temperature produced by the foot of the laser pulse, as illustrated on Fig. 1.4, leading to an increase of the ablation velocity and a subsequent decrease of the RTI growth rate (Fig. 1.5). It is worth mentioning that the shape of the laser pulse is tuned in order to reach high pressure gradually, avoiding as much as possible any important pre-heating of the target. The main drawback of the high-foot design is to increase the adiabat α of the capsule, defined as the ratio of its pressure over the Fermi pressure, making the fuel less compressible for a given amount of absorbed energy. Future efforts on the NIF could consist in maintaining a sufficient control of the RTI on the ablation front while coming back to lower adiabat implosions, which are highly required to reach ignition.

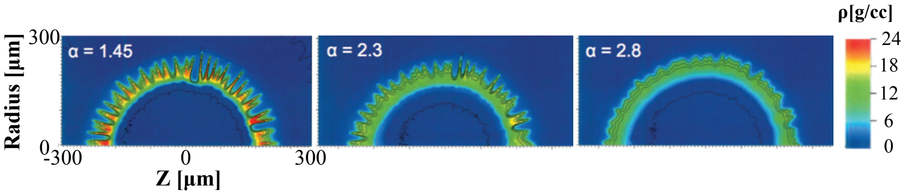

Figure 1.5: Illustration of the RTI stabilizing effect of the high-foot implosion design. As the adiabat α grows the amplitude of spikes and bubbles are clearly reduced (Image taken from [Dittrich et al., 2014]).

1.1.2 Fast ignition

Electron fast ignition

In 1994, Tabak et al. [1994] proposed an alternative ignition scheme, called *fast ignition*, where the compression and the ignition stages are completely separated. This technique allows to dramatically release the constraints on symmetry implosion compared to conventional schemes, lowering the required implosion velocity and the subsequent RTI growth rate. After a smaller compression of the D-T capsule, the hot spot is in this case heated by a high energetic beam of particles. The expected energy gain is also more important (> 100) than with conventional schemes while decreasing the required laser energy. The pioneering fast ignition scheme stands as follows. The D-T capsule is initially compressed with ns-scale laser beams, with $I_L \sim 10^{15}$ W.cm^{-2}, in order to reach a fuel assembly of a homogeneous density core of $\rho \sim 300$ g.cm^{-3} and with $\rho R > 1$ g.cm^{-2} (isochorical fuel assembly). At the very end of compression, during the stagnation time, a first intense laser pulse with $I_L > 10^{18}$ W.cm^{-2} is sent on the target to bore a hole through the ablated plasma. This low density plasma channel is then used as a guide for a second intense laser pulse with $I_L > 10^{19}$ W.cm^{-2} that is absorbed at the critical density surface, now near the compressed core, into a relativistic electron beam, also referred as fast electrons. These fast electrons propagate into the dense plasma and finally deposit their energy into a small part of the core, thus creating an off-center hot spot and triggering the ignition of the target (Fig. 1.6). The fast ignition scheme constitutes the main framework of this thesis.

2D hydrodynamic numerical simulations of a dense spherical core performed by Atzeni [1999] considering an electron beam of circular section and constant power over time provide

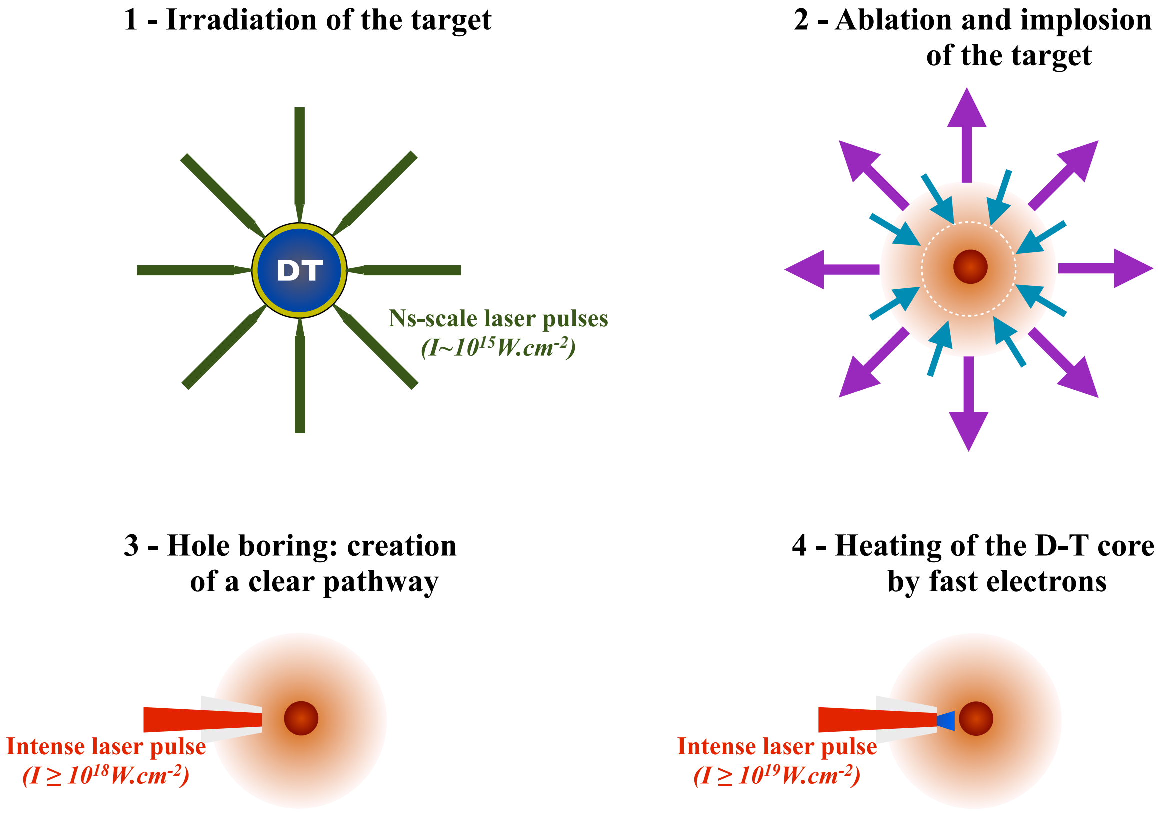

Figure 1.6: Illustration of the different steps of the pioneering fast ignition scheme.

the optimal parameters of the electron source minimizing the required ignitor energy:

$$E_{\mathrm{ign}} = 140\rho_{100}^{-1.85}\ \mathrm{kJ} \tag{1.6}$$

$$\tau_{\mathrm{ign}} = 54\rho_{100}^{-0.85}\ \mathrm{ps} \tag{1.7}$$

$$I_{\mathrm{ign}} = 2.4\times10^{19}\rho_{100}^{0.95}\ \mathrm{W/cm^{-2}} \tag{1.8}$$

$$r_{\mathrm{HS}} = 60\rho_{100}^{-0.97}\ \mu\mathrm{m} \tag{1.9}$$

$$\tag{1.10}$$

with ρ_{100} the compressed fuel density in units of 100 g/cc. If one considers a compressed core with $\rho = 300$ g/cc, the fast electron beam of intensity $I_{\mathrm{ign}} \simeq 6.8\times10^{19}$ W.cm^{-2} should deposit $E_{\mathrm{ign}} \simeq 18$ kJ into the dense core over a $\tau_{\mathrm{ign}} \simeq 20$ ps duration and in a hot-spot radius $r_{\mathrm{HS}} \simeq 20\ \mu$m. The electron source should also be characterized by a mean energy $\langle E\rangle \sim 1-2$ MeV, high enough to propagate from the source to the dense core through the high-density plasma, but not too high in order to increase fast electron energy absorption into the core [Honrubia & ter Vehn, 2006]. The fast ignition scheme initially aims at decreasing the required laser energy used to reach ignition in order to increase the fusion energy gain. The fuel assembly should ideally require 300 kJ of the laser energy while the ignitor laser pulse should not carry more than 100 kJ. Considering the scaling laws presented before, this energy requirement assumes that at least 18% of the ignitor pulse energy is coupled to the dense core. Many issues currently need to be solved in order to assess the feasibility of the fast ignition scheme. The fast electron generation processes with high-intensity and highly energetic laser pulses, more specifically the characterization of the fast electron energy and angular distributions and of the laser-to-fast electrons conversion efficiency, is still an open research field. The fast electron transport across a large panel of plasmas, differing by both their density ($\rho = 1-400$ g/cc) and temperature ($T = 1 - 300$ eV), that can be encountered in a fast ignition target, still needs to be characterized. The fast electron beam propagation is indeed highly affected by different mechanisms, producing energy losses and acting on its divergence, as described further in this thesis.

An alternative to the hole boring process has been introduced a few years ago. It consists in building a FI target with a re-entrant hollow cone, its tip being located fairly close from the D-T capsule center, eventually close to the D-T core at stagnation time, providing a clear pathway for the ignitor laser pulse (Fig. 1.7). In 2001, Kodama et al. [2001] demonstrated an enhancement of D-D fusion neutron production by using a spherical target with a re-entrant gold cone compressed by 9 laser beams of the Gekko laser facility (Institue for Laser Engineering, Osaka, Japan). The use of a 0.5 PW short pulse laser beam focused on the cone tip resulted in an enhancement of the neutron yield by a factor 10 compared to the case without any heating laser pulse.

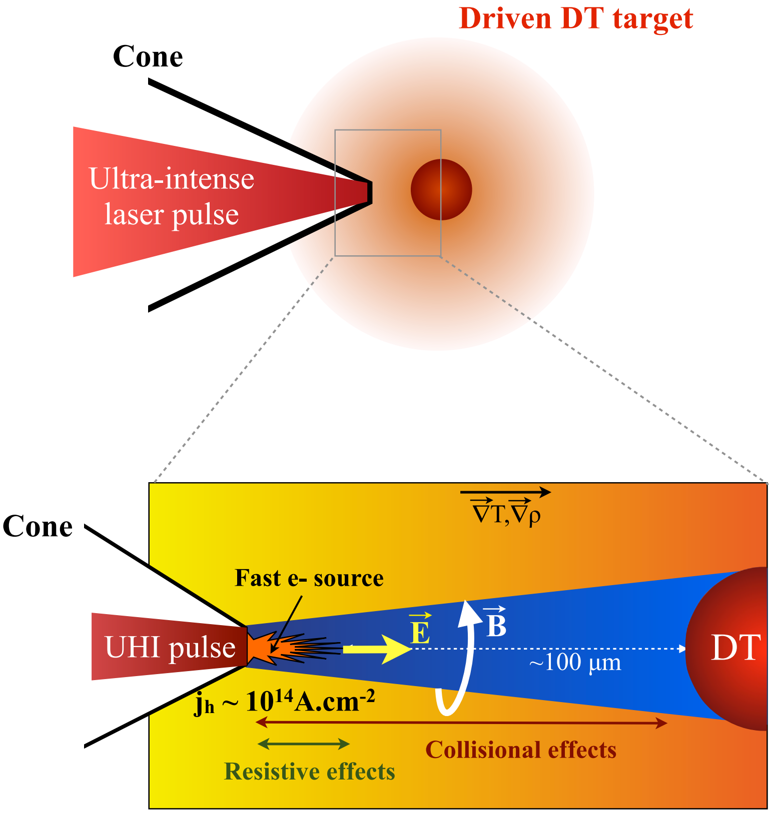

Figure 1.7: Illustration of the cone target design (top). The schematic representation of fast electron transport through a fast ignition target is also given (bottom).

The introduction of a cone into a FI target however rises some important issues. The cone must indeed survive the high pressure arising from the compression. Moreover, the asymmetric implosion of the target drives a strong shock in the cone walls, resulting in a plasma jet along the cone axis that moves the fast electron generation region further away from the dense core. Finally, the generation of an electron source, sufficiently collimated and with an adapted mean energy for an efficient coupling with the D-T core, arising from the interaction between the cone tip and the cone walls, is still under study. Indeed MeV electrons, required for a efficient coupling with the fuel core, are partly stopped into the cone walls. It is worth mentioning that no laser installation is currently able to perform full scale fast ignition experiments with the required laser energies (Fig. 1.8).

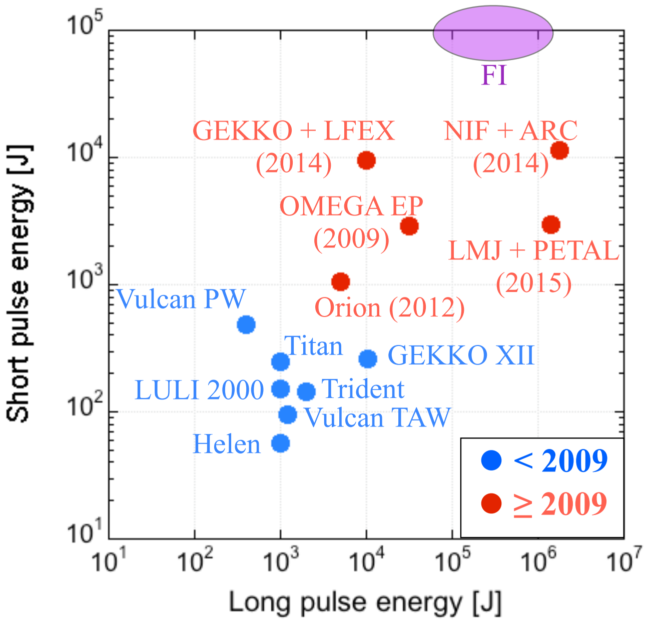

Figure 1.8: Presentation of laser facilities built before (blue circles) and after (red circles) 2009 as a function of their short pulse and long pulse energy capabilities. No laser system currently reaches the laser parameters required for the fast ignition scheme (purple oval area) (Inspired from [Patel, 2013]).

Ion fast ignition

An alternative to fast electrons consists in using an ion source as a driver. The main advantages of ions are their typical peaked energy deposition profile at the end of the ion range (Bragg peak), allowing a fairly localized energy deposition and a weaker sensibility to nonlinear effects. The ignition requirements, similarly to the electron fast ignition, consist in producing the energy deposition rate of 10^{22} W.cm^{-3}, by the deposition of 10 kJ over 20 ps within a volume of a linear dimension of 20 μm, to the cold D-T fuel initially compressed at 400 g.cm^{-3} and with an areal density $\rho.R = 2$ g.cm^{-2}. Even though many ion species could be used for ion FI, protons and carbon ions are mostly studied since they constitute "technologically convenient" species. It is worth noting that the optimum energy for carbon ion fast ignition is much more important, of the order of $\sim$ 450 MeV, due to the more important energy per nucleon required for heavy ions to penetrate the compressed D-T core [Fernandez et al., 2008]. The pioneering concept of ion fast ignition consists in using a high-intensity $> 10^{20}$ W.cm^{-2} laser pulse to irradiate a foil, distinct from the fuel, to generate a proton beam by the process of target normal sheath acceleration (TNSA) described in section 1.5.1 [Roth et al., 2001; Atzeni et al., 2002]. This initial design uses the $15 - 28$ MeV portion of the Maxwellian proton distribution from TNSA driven by a 10 PW, 100 kJ laser pulse. The proton beam is generated 3 mm away from the D-T capsule and focused ballistically into the core (Fig. 1.9).

Another advantage of protons over other particles is their range lengthening with increasing plasma temperature, which can be explained as follows. When a broad proton energy distribution spectrum is generated, the fast protons penetrate in the cold fuel, preheating the material and leading to a deeper penetration of the slower protons that arrive later. A larger fraction of particles can consequently contribute to ignition. However, the Maxwellian distribution from TNSA represents a net drawback compared to a monoenergetic distribution which would require less proton beam energy to ignite the target, of the order of 9 kJ, $\sim$ 25% less than for TNSA distributions [Atzeni et al., 2002].

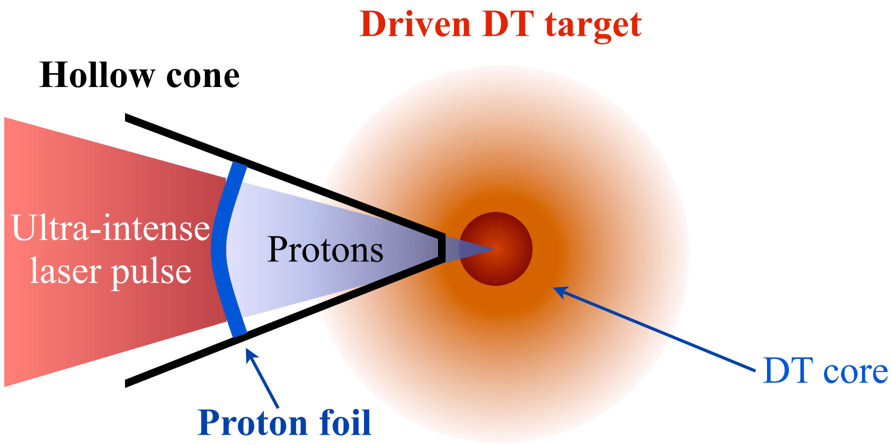

Figure 1.9: Illustration of the pioneering concept of ion fast ignition (inspired from [Key et al., 2006]).

Some other acceleration mechanisms can provide an alternative to the proton FI if the TNSA mechanisms proves unfeasible. The Break-Out Afterburner (BOA) mechanism observed experimentally on the Trident laser facility (Los Alamos National Laboratory, USA) is a promising mechanism for producing carbon ion beams suitable for FI, with a quasi-monoenergetic ~ 0.5 GeV beam generated with a reasonable efficiency [Henig et al., 2009; Hegelich et al., 2011; Jung et al., 2013a; Roth et al., 2013]. The BOA mechanism can be briefly explained as follows. In a first phase, a relatively thin target, characterized by a thickness of a few hundreds of nanometers, is volumetrically heated by an intense laser pulse, accelerating all the target electrons. In a second phase, a strong longitudinal electrostatic field driven by plasma waves accelerate an important population of quasi-monoenergetic ions. This acceleration process ceases rapidly due to the hydrodynamic expansion of the target. Recent experimental results showed a maximum energy of accelerated carbon ions of ~ 1 GeV using 225 nm thick targets [Jung et al., 2013b], already well above the required energy for FI. Even if the BOA mechanism intrinsically generates monoenergetic ions, laser pulses currently available produce broad ion spectra. This issue is related to the non-optimal Gaussian pulse shape that is either too long (> 0.5 ps) in the case of Nd:glass lasers, generating a too important hydrodynamic expansion, or too short when using Ti:Sapphir laser systems. The optimization of ion sources by the BOA mechanism is currently under study. It is worth mentioning that a detailed summary on the current status of the ion fast ignition scheme has been recently published by Fernandez et al. [2014].

1.1.3 Shock ignition

Another alternative ignition scheme, called *shock ignition* (SI), was introduced by Betti et al. [2007]. The idea is here again to implode the target at a low speed in order to generate higher fusion gains. A low speed implosion indeed allows to assemble more fuel for the same amount of kinetic energy in the shell, allowing either to obtain higher fusion gains with the same amount of initial laser energy compared to the classical ignition scheme, or to obtain acceptable gains at a lower laser energy. However a low speed implosion leads to low hot spot pressures, preventing from igniting the target. The basic idea of the SI scheme is to dramatically increase the hot spot pressure by launching a strong shock at stagnation. The D-T capsule is firstly symmetrically imploded at low velocity, and on a low adiabat, with both moderate laser peak power and total energy. At the end of compression, when the fuel approaches stagnation, a high intensity ($\sim 3 \times 10^{15} - 10^{16}$ W.cm^{-2}) laser spike with the same spherical symmetry as the compression beams is sent on the target (see Fig. 1.10), driving a converging shock that is amplified by collision with the diverging shock, leading to a sudden increase of the hot spot pressure up to $500-1000$ Gbar and of its temperature, and hence to the ignition of the target. The main advantage of the SI scheme compared to the FI scheme is to use a single laser driver. The required highly shaped laser pulse time-profiles are in within the capability of the NIF and of the LMJ facilities. However, as every central high temperature hot spot design, SI is fairly sensitive to symmetry and stability constraints. Parametric instabilities, such as stimulated Brillouin scattering, stimulated Raman scattering or two plasmon decay, detailed further in this thesis, may be responsible for an increase of the reflection of the incoming laser light and a consequent decrease of the energy coupling. Experiments performed on the OMEGA laser facility (Rochester, USA) in the spherical geometry have shown that 35% of the incident laser light was indeed backscattered [Theobald et al., 2013]. Fast electrons generated by parametric instabilities could also be a source of preheating of the fuel, reducing the core compression efficiency. However, providing that their mean energy is not too high, fast electrons could be stopped in the outer layer of the imploding target, significantly contributing to the ablation shock pressure [Ribeyre et al., 2013].

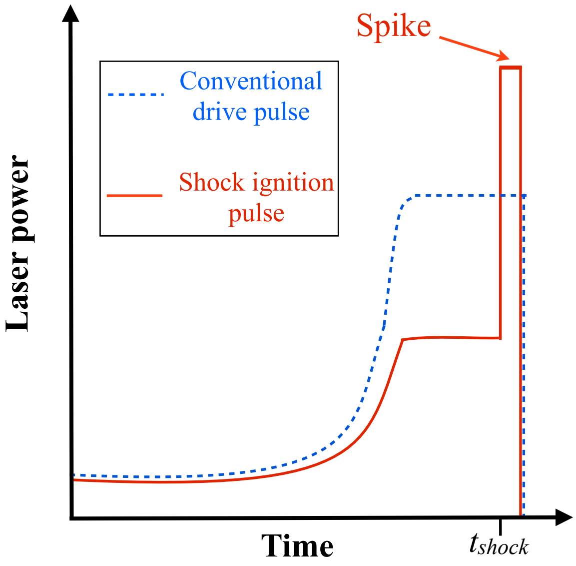

Figure 1.10: Schematic of a simplified laser pulse shape used for shock ignition (red solid line). The conventional pulse shape is plotted for comparison (blue dashed line) (Inspired from [Perkins et al., 2009]).

1.1.4 Impact ignition

Impact ignition is the third alternative ignition design that was proposed in 2005 by Murakami & Nagatomo [2005]. The compression and heating steps are here again separated in order to allow a low velocity implosion of the fuel. Impact ignition targets consist of a D-T shell with a hollow cone inserted in it. The cone is caped by a thin fragment of a spherical shell, called impact shell, made of a D-T layer coated with a low-Z ablator (Fig. 1.11). In a first step the target is symmetrically compressed at a low speed by either ns-scale laser pulses or X-ray radiations. At the stagnation phase, when the target is fully driven, a moderate intensity $\sim 10^{15}$ W.cm^{-2} laser pulse is focused on the impact shell. This latter is consequently accelerated to a very high speed, of the order of $1000-1500$ km.s^{-1}, and finally collides with the compressed fuel. The conversion of kinetic energy into thermal energy increases both the pressure and the temperature of the hot spot, leading to ignition of the target. The ignitor laser

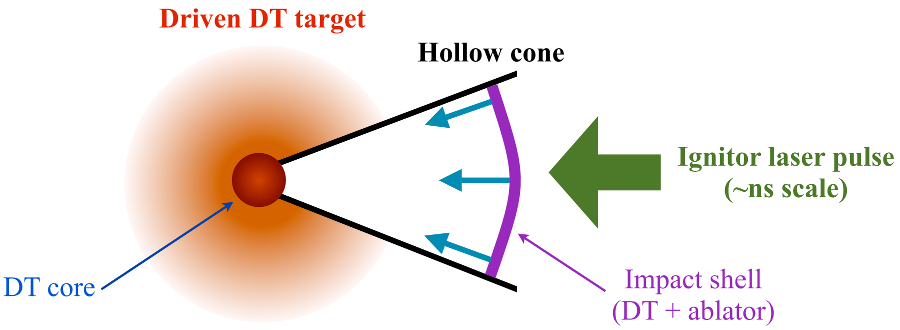

Figure 1.11: Illustration of the impact ignition scheme configuration.

pulse is here again similar to the main laser pulses used to drive the target. The main challenge of this scheme consists in accelerating the impact shell at such high velocities. An experiment performed on the Nike facility (Naval Research laboratory, USA), using a $\lambda_L = 248$ nm krypton fluoride (KrF) laser system, demonstrated a high speed acceleration of a thin low Z foil up to ~ 1000 km.s^{-1} [Karasik et al., 2010]. It is worth mentioning that the use of a so short wavelength laser results in an ablation process at higher densities, leading to higher pressures at a given intensity compared to longer wavelength lasers. A series of integrated experiments have been performed in 2009 on the Gekko XII laser facility. Nine laser pulses, carrying a total energy of 3 kJ, were used to compress a spherical target, and a 0.41 kJ, 700 TW laser pulse was used to accelerate the impact shell. A sharp increase of the measured neutron yield created by D-D fusion reactions was obtained when optimizing the ignition shock timing, demonstrating that the neutron yield enhancement was actually driven by the collision between the impactor and the compressed fuel [Azechi et al., 2009]. The measured coupling efficiency between the ignitor laser pulse and the impact shell was $\sim 3\%$. 2D numerical simulations estimated that a fusion energy gain could be obtained from the impact ignition scheme assuming an implosion velocity of $1000 - 1500$ km.s^{-1} and a coupling efficiency of $3 - 10\%$ achieved by a $200 - 300$ kJ ignitor laser pulse [Murakami et al., 2014].

1.2 Intense laser beams

The fast ignition scheme requires to accelerate a relativistic electron beam with a high energy (kJ scale), high intensity ($\geq 10^{20}$ W.cm^{-2}) and short duration ($\sim$ 10 ps) laser pulse. The generation of such short laser pulses have been made possible in 1967 by the development of the mode locking technique [DeMaria et al., 1967]. The achievable intensity was however too small due to the limitation of the laser pulse energy to a few mJ to avoid any damages of the laser optics due to the development of non-linear effects (Kerr lens effect). A novel amplification technique called Chirped Pulse Amplification (CPA), described in section 2.2, was introduced in 1985 [Strickland & Mourou, 1985]. CPA is currently used on the whole majority of high intensity laser systems. It indeed allows the generation of PW peak power laser pulses, with peak intensity $\geq 10^{21}$ W.cm^{-2} on some laser facilities, enough to produce fast electron beams that could be used to trigger nuclear fusion reactions in a fast ignition target.

1.3 Fast electron beams: state of the art

In order to understand the underlying physics of fast ignition, the generation and transport processes of fast electron beams into a large panel of plasmas, of various densities and temperatures, have been significantly studied for the last 20 years, both theoretically and experimentally. We present in this section a non exhaustive list of the obtained experimental results with relativistic laser pulses ($I > 10^{18}$ W.cm^{-2}).

1.3.1 Laser-to-electrons conversion efficiency

The characterization of the quantity of laser energy converted into fast electrons, or conversion efficiency, has been extensively measured in various experiments. In 2000, Hatchett et al. [2000] used a set of fast electron transport simulations to reproduce the bremsstrahlung emission measured during the experiment, inferring a 40% value for an intensity on target of 3×10^{20} W.cm^{-2}. By using the same technique but measuring a line emission, called K$_\alpha$, Wharton et al. [1998] calculated a conversion efficiency of 25% for a lower intensity of 3×10^{19} W.cm^{-2}. Following this result, Yasuike et al. [2001] varied the laser intensity from 10^{18} W.cm^{-2} up to 3×10^{20} W.cm^{-2} and measured a conversion efficiency increasing from 10% to 50%, respectively. These rather high conversion efficiencies have however to be reconsidered since an important physical phenomenon, called refluxing, has not been taken into account. This physical process, described in detail in this thesis, is characterized by a recirculation of fast electrons into the target, generating an additional X-ray emission responsible for an increased but false measurement of the conversion efficiency. A recent experiment performed by Theobald et al. [2006] estimated a constant conversion efficiency of 10% by measuring K$_\alpha$ emission generated by focusing a $10^{19}-10^{21}$ W.cm^{-2} laser pluse on a thin copper foil. By measuring bremsstrahlung emission, another recent study [Nilson et al., 2008; Chen et al., 2009a] calculated a conversion efficiency of (30 ± 10)%, with 10% of the laser energy converted into $1-3$ MeV electrons, constituting the most favorable energy range for fast ignition. A rather different study performed by Westover et al. [2011] presents a measure of the conversion efficiency as a function of the fast electron beam divergence angle. In the limit cases, corresponding to divergence angles of 0° and of 65°, the author calculated conversion efficiencies of 25% and 60%, respectively. By using a high contrast and very short ($\sim$ 25 fs) laser pulse free of any pedestal, Santos et al. [2013] measured a conversion efficiency of 10%. Finally, a recent experiment performed by Vauzour et al. [2012] calculated a conversion efficiency of 40%, by measuring K$_\alpha$ emission of different tracer layers embedded into a multilayer target.

In summary, the uncertainty on the conversion efficiency is still rather significant due to the lack of adapted experiments and of the difficulty of the process. The inherent indirect nature of the measurement indeed requires an important numerical work to reproduce the measured X-ray emissions. It is worth mentioning that the laser intensity is not the only parameter fully determining the conversion efficiency value, since the hydrodynamic state, the pre-plasma scale length, the laser pulse duration, the focal spot diameter and the laser beam incidence angle also play an important role [Davies, 2009]. The lack of experimental data with $\sim$ 10 ps laser pulses of different wavelengths also rises some concerns about the feasibility of the fast ignition scheme, related the conversion efficiency into $1-3$ MeV electrons.

1.3.2 Fast electron mean energy

The measurement of the energy distribution of fast electron beams is not a trivial process. Indeed, the only direct measurement currently available consists in fielding an electron spectrometer into the target chamber. This diagnostic only allows to measure an energy spectrum representative of the fast electron population which escaped the target (> MeV). However, due to the presence of a strong electric field at the rear side of the target, most of the electron population is actually re-injected into the target and cannot escape [Cottrill et al., 2010]. Indirect measurements of the fast electron spectrum are usually performed by characterizing the X-ray

emission, either bremsstrahlung or K_α photons, generated during fast electron transport and by comparing the emission to simulation results.
One of the most commonly used energy distribution is the 3D relativistic Maxwell-Jüttner distribution given by:

$$f(E) \propto \beta\gamma^2 \exp\left[-\frac{E}{T_h}\right] \tag{1.11}$$

with $\beta = v/c$, v the fast electron speed, $E = (\gamma-1)m_e c^2$ the electron energy and $\gamma = (1-\beta^2)^{-0.5}$ the Lorentz factor. The parameter T_h is usually referred as the temperature of the fast electron beam. It is worth mentioning that this denomination is clearly not related to a temperature in the thermodynamics sense, but rather to a convenient parameter characterizing the mean energy $\langle E\rangle \simeq aT_h$, where a varies from 1.5 from $T_h < m_e c^2$ to 3 in the relativistic limit. A large number of experimental measurements [Sawada et al., 2014; Key et al., 1998; Chen et al., 2008a] and of numerical simulations [Chrisman et al., 2007] revealed a two-temperatures behavior of the fast electron distribution:

$$f(E) \propto \exp\left[-\frac{E}{T_{h_1}}\right] + R\exp\left[-\frac{E}{T_{h_2}}\right] \tag{1.12}$$

with T_{h_1} and T_{h_2} the coldest and hottest temperature components of the fast electron beam, respectively, and R a scale factor for the hottest energy component. Some recent numerical simulations pointed out a more complex distribution function characterized by a power law $f(E) \propto E^{-n}$, with $n > 0$, at rather low energies, up to a few MeV, while exhibiting a high energy tail described by a classical Maxwellian distribution [Ren et al., 2004; Micheau et al., 2010]. This trend, observed in our experiments described in chapters 4 and 5, was recently reported in two other papers [Vauzour et al., 2012; Santos et al., 2013].

The scaling of the fast electron temperature T_h with the intensity of the laser pulse, or more precisely with the $I\lambda_L^2$ parameter [Gitomer et al., 1986; Gibbon & Forster, 1996], has been extensively studied. By measuring the bremsstrahlung emission of fast electrons generated at laser intensities of $I \leq 10^{19}$ W.cm^{-2}, Beg et al. [1997] proposed the following empirical law:

$$T_h^{\text{Beg}}[\text{keV}] = 215(I_{18}\lambda_{\mu\text{m}}^2)^{1/3} \tag{1.13}$$

with I_{18} the laser intensity in units of 10^{18} W.cm^{-2} and $\lambda_{\mu\text{m}}$ the laser wavelength in micrometers. The recent experiment performed with the laser intensity up to $I \leq 10^{21}$ W.cm^{-2} [Chen et al., 2009a] and the relativistic model developed by Haines et al. [2009] seem to be in agreement with the Beg's law extendeed to such higher $I\lambda_L^2$ values. A different scaling law was introduced by Wilks et al. [1992] from numerical simulations, and confirmed by measurements [Malka & Miquel, 1996; Yasuike et al., 2001; Davies, 2002] of electron and ion spectra at the rear side of the target. Here the electron temperature scales as the ponderomotive potential:

$$T_h^{\text{Wilks}}[\text{keV}] = 511[\sqrt{1 + 0.73 I_{18}\lambda_{\mu\text{m}}^2} - 1] \tag{1.14}$$

It is important to point out that experiments are most often based on the characterization of bremsstrahlung spectra, as already mentioned. These measurements are however most sensitive to the electron energies smaller than 5 MeV. The high energy part of the electron beam being not so well known, the measured temperature could be rather underestimated. But in principle there are not so many electrons at such > 5 MeV energies. Moreover, all these measurements do not take into account the pre-plasma effects, which determine the dominant laser energy absorption mechanism and consequently dramatically affect the fast electron temperature [Nuter et al., 2008]. In summary, a large controversy still exists on the characterization of the fast electron energy distribution.

1.3.3 Fast electron divergence

The characterization of the fast electron beam divergence is of primary importance for the fast ignition scheme. This parameter is in fact mainly determined by the laser-plasma interaction, and fairly less by elastic electron-ion collisions in the target depth during its transport [Debayle et al., 2010]. Indeed, the dispersion is mainly conditioned by fast electrons scattering in magnetic fields driven by the so-called Weibel instability described further in section 2.5.6.
Different methods are currently used to measure the electron beam divergence:

- K_α emission: one of the most commonly used diagnostic consists in imaging the K_α line emission during the interaction between fast electrons and a fluorescent tracer buried into a multilayer target. By varying the depth of the fluorescent layer, one can easily infer the shape of the electron beam. This diagnostic was used in our experiments presented in chapters 4 and 5.

- Shadowgraphy: this method consists in sending a low energy probe laser beam perpendicular to the target. The laser pulse then interacts with the expanding rear surface of the target and is absorbed in the high density regions ($> 10^{19}$ cm^{-3}) before being measured by a CCD camera. The divergence of the electron beam is finally characterized by measuring, on the obtained shadowgram, the extent of the darker region.

- Optical emission: when fast electrons reach the rear surface of a solid target, an intense optical self-emission contains both coherent or incoherent parts. The coherent part, called optical transition radiation (OTR), is emitted when a charged particle crosses boundaries between two media with different dielectric properties. The incoherent part comes from the synchrotron radiation emitted by fast electrons in strong laser field. These emissions are imaged, and the electron beam divergence is calculated by varying the target depth, just as for K_α emission. The incoherent thermal emission is produced from a plasma heated due to the fast electron energy deposition. It is produced over a several 100 ps time-scale.

A compilation of different experimental results is presented on Fig. 1.12 [Green et al., 2008]. The electron beam divergence increases logarithmically with the laser intensity. However, the influence of the preformed plasma, which can dramatically affect the electron divergence due to the deformation of the laser-plasma interaction region [Debayle et al., 2010], is not taken into account here. Moreover, the characterization of the divergence by the described methods requires several laser shots, one for each target depth, potentially changing the initial laser conditions due to laser-energy fluctuations.

1.3.4 Fast electron transport

Fast electron beam transport in solid materials is affected by several mechanisms, differing by their collisional or collective nature. They are described by theoretical models [Bethe, 1953; Moliere, 1948; Davies et al., 1997; Bell et al., 1997].
Close to the source, the fast electron beam can carry a current exceeding a MA level. Such a high current cannot propagate in a free space [Alfvén, 1939] and is actually neutralized by a return current formed by background thermal electrons propagating in the opposite way. This return current $\mathbf{j_b}$ is driven by an axial electromotive field generated, via the Lenz's law, by the azimuthal magnetic field created by the fast electron beam itself. These thermal electrons propagating at fairly low speed are highly collisional and induce, via the Ohm's law, an electric

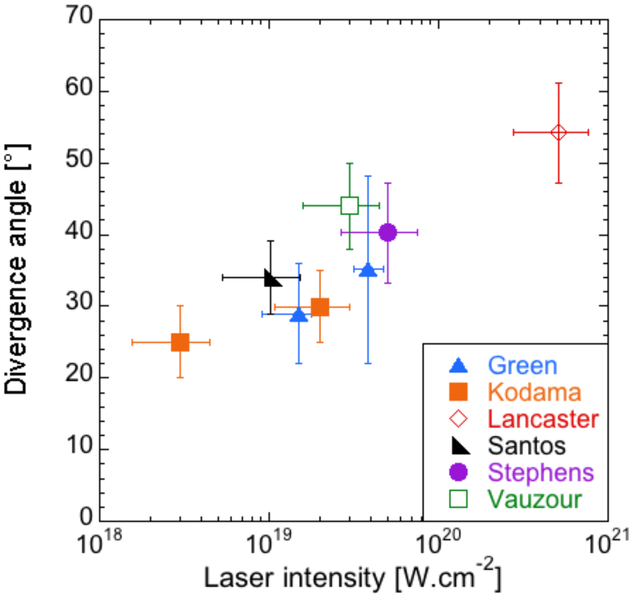

Figure 1.12: Fast electron beam divergence as a function a the laser pulse intensity. The data were compiled from different publications (Green et al. [2008]; Kodama et al. [2001, 2004]; Santos et al. [2002]; Stephens et al. [2005]; Lancaster et al. [2007]; Vauzour et al. [2014]).

field $\mathbf{E} = \eta \mathbf{j_b}$ that contributes to the slowing down of the intense fast electron beam. Collisional processes also play an important role in the fast electron propagation. While electron-ion collisions are mainly responsible for their angular deflection, electron-electron collisions induce important energy losses.

The characterization of fast electron energy losses per unit of length, or stopping power, by both collisional and collective mechanism is a key parameter for the fast ignition scheme. While most of the fast electron transport experiments were performed in cold-solid materials, there is a strong need to characterize collisional and collective stopping powers in compressed targets, more representative of fast ignition conditions.

1.4 Current status of the fast ignition scheme

An important amount of theoretical and numerical works have been performed within the last years to optimize the fast electron source parameters required to obtain fusion energy gain in a fast ignition target. The intrinsic limits of coupling efficiency of fast electrons with the D-T core were found to require an unreasonable amount of laser energy to ignite targets. It was therefore possible to artificially modify the fast electron transport conditions in order to increase the fraction of fast electrons coupling to the target core. This section, inspired by the paper of Robinson et al. [2014], presents a non-exhaustive summary of the ignition calculations together with a recall of fast electron divergence controlling techniques.

1.4.1 Ignition scale calculations

Let us assume a spherical D-T target of 0.5 mg already assembled by a 300 kJ ns-scale laser pulse close to the time of peak compression, reaching a peak density of 500 g/cc. When considering a collimated 20 μm radius, monoenergetic fast electron beam of 10 ps duration, it was found that the lowest electron ignition energy $E_{ig} = 16.2$ kJ is attained for the electron energy of 2 MeV [Solodov et al., 2007]. By considering a more realistic Maxwellian distribution, the

ignition energy increases to $E_{ig} = 21.5$ kJ for a mean electron energy of $\langle E \rangle = 1.25$ MeV. These results stress the fact that even for an ideal case, the required ignition energy is already of the order of several tens of kJ. Numerical simulations performed by Atzeni showed in addition that the introduction of fast electron scattering effects increases the ignition energy by 20% [Atzeni et al., 2009].
A series of more realistic integrated simulations has been performed using a fast electron source distribution calculated by Particle-In-Cell (PIC) simulations, accounting for the physics of the laser-plasma interaction. Strozzi et al. [2012] found an electron energy distribution described by a two temperature profile, and an angular distribution characterized by a fourth order super-Gaussian function. By choosing an artificially collimated electron beam, the minimum laser ignition energy is $E_{ig} = 132$ kJ, independently of the beam radius. By assuming a laser-to-electrons conversion efficiency of 52%, obtained in the PIC simulations, the corresponding laser mean intensity is $I_L = 1.4 \times 10^{21}$ W.cm^{-2}, with a duration of 18.5 ps and a radius of 18 μm, yielding a fast electron beam mean energy $\langle E \rangle = 8.2$ MeV. This fairly high required ignition energy can be explained by the 6.8 g.cm^{-2} range of $\langle E \rangle = 8.2$ MeV electrons which is higher that the fuel areal density (6 g.cm^{-2}). In other words, the electrons are too energetic to be stopped in the D-T core and deposit only a fraction of there energy over this region. If the fast electron divergence is included into simulations, this laser ignition energy skyrockets to 1 MJ [Strozzi et al., 2012], dooming the fast ignition scheme. It is however worth mentioning that these simulations are limited to the first 0.36 ps of interaction, while the fast ignitor laser pulse duration is ~ 10 ps. Moreover, there is a clear lack of experimental data in a regime close to the fast ignition regime. A recent calculation performed by Bellei et al. [2013] using a fast electron source extracted from improved PIC simulations showed that the fast electron mean energy could be decreased by increasing the electron source spot size. For a 25 μm distance between the optimal electron source chosen in their study and the D-T core, a minimum ignition energy of $E_{ig} = 250$ kJ is required, which is still too high.

The conclusion of these ignition scale calculations is the absolute necessity to reduce the fast electron beam divergence before its propagation into the fast ignition target, and over its propagation before it reaches the D-T core [Bellei et al., 2013].

1.4.2 Controlling fast electron transport

Several physical processes that could allow to control the divergence of fast electron beams are currently studied.

Self collimation

As detailed in section 2.5.2 of this thesis an inhomogenous fast electron current density is responsible for the generation of the return current and a resistive magnetic field. This self-generated field could be sufficiently strong to collimate the fast electron beam, lowering the required ignition energy. A set of numerical simulations showed that for a 30° half angle divergence beam, the magnetic field could still improve the coupling efficiency. However, the expected divergence in a fast ignition target being in excess of 50° the self-collimation effect would only play a minor role in improving the coupling efficiency [Debayle et al., 2010; Kemp & Divol, 2012].

Resistive guiding

Resistivity gradients are also responsible for the generation of intense magnetic fields, and could consequently be used to confine fast electrons toward higher resistivity regions. Resistive guiding is based on the fact that at sufficiently high temperatures, the plasma resistivity of any material is described by the so-called Spitzer resistivity (see section 2.5.3), scaling with the material atomic number as $\eta \propto Z$. By using a target structured with different materials one may force the resistive guiding process to take place. In a fast ignition target, two conditions are mandatory to obtain an efficient guiding. First, the collimated magnetic field needs to persist during the entire ignitor laser pulse. Second, the high resistivity path must survive the compression of the spherical shell, this latter condition being far from a trivial issue. A first advanced concept using wire-like structures have been proposed [Solodov et al., 2010]. The basic idea is to build a mid-Z wire, made for example from copper, connecting the cone tip to a region close to the D-T core (see Fig. 1.13). Fast electrons are in this case guided by the generated resistive magnetic field at the interface of the 40 μm diameter, 75 μm length copper wire with the D-T background plasma. Numerical results obtained by injecting a Maxwellian electron beam, with a $\langle E \rangle = 1.6$ MeV mean energy (corresponding to $T_h = 0.65$ MeV), into the wire showed that the electron beam was collimated during the whole 10 ps injection. Moreover the coupling efficiency with the D-T core was estimated to 45%, much higher than the 7% obtained with no wire. The survivability of such a thin wire until peak compression of the target, and the subsequent maintenance of a clean resistivity path is however still an open issue.

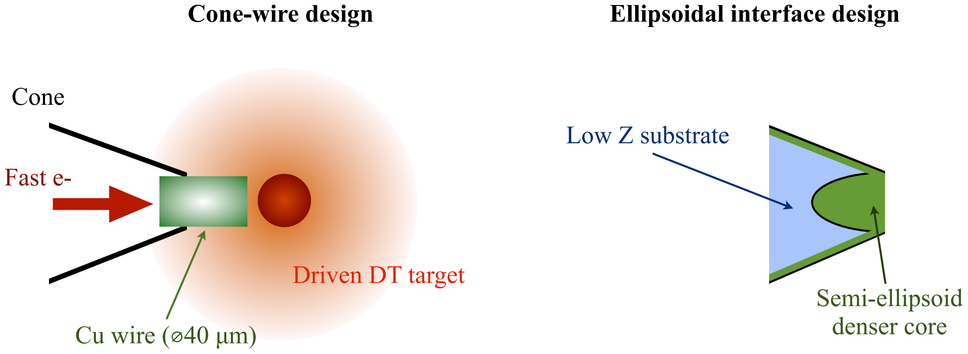

Figure 1.13: (Left) Illustration of the cone wire target design. (Right) Illustration of the ellipsoidal cone tip shape. The denser core is surrounded by a lower Z material.

Another concept of resistive guiding consists in structuring the cone itself. A cone design proposed by Schmitz [Schmitz et al., 2012] consists in replacing the cone tip by an ellipsoidal structure producing an azimuthal magnetic field deflecting the electrons specularly at the interface (Fig. 1.13), reducing the electron initial angular spray. This cone tip shape is the analogous of an elliptical mirror used in optics. Numerical simulations have shown an improvement by a factor $2-3$ in the coupling efficiency with the core compared to the unguided case [Robinson & Schmitz, 2013]. A different approach proposed by Campbell et al. [2003] consists in using two concentric cones, their respective walls being separated by a vacuum gap. This structure is able to confine fast electrons by the electric field generated inside the vacuum gap, and consequently guide them to the cone tip. Numerical simulations showed that this double cone structure was able to confine fast electrons on a ps-scale time duration, resulting in a 1/3 decrease of energy losses by the cone walls compared to a single cone structure [Cai et al., 2009]. A so-called extended double cone configuration proposed by Johzaki et al. [2011] consists in extending the vacuum gap and the cone tip (Fig. 1.14). In order to reduce collisional effects, the inner cone is made of a high density but low Z material, such as Diamond-Like Carbon (DLC). Numerical simulations showed an enhancement of the core heating by fast electrons by a factor 4 compared to a single cone configuration. Integrated experiments are however required to prove this guiding performance.

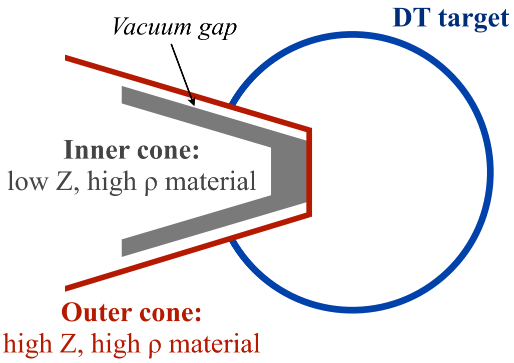

Figure 1.14: Illustration of the extended double cone design.

Imposed magnetic fields

An alternative to the magnetic fields self-generated by the fast electron current itself consists in imposing an axial external magnetic field. The basic idea of this process is here again to confine electrons into a small radius, increasing their flux in the D-T fuel. A set of numerical simulations of fast ignition cone target implosions, with an artificially imposed 5 kT axial magnetic field, and using a fast electron source energy and angular distributions based on PIC simulation results, resulted in a fast electron ignition energy of 130 kJ. A decrease of the imposed field down to 3 kT resulted in doubling the required ignition energy [Strozzi et al., 2012].

Two different approaches of high intensity magnetic field generation are currently studied. The first one relies on the flux compression. In a good conductor, characterized by a magnetic diffusion time much longer than the capsule implosion time, an enclosed magnetic flux $\Phi \propto \int B.dA$ in an area A remains constant. As a consequence, as the area of the conductor decreases with implosion, the magnetic field strength rises. Experimental results obtained by imploding cylindrical and spherical capsules on the Omega laser system showed an increase of a seed magnetic field of ≤ 10 T up to $2-4$ kT [Knauer et al., 2010; Chang et al., 2011; Hohenberger et al., 2012]. A set of preliminary numerical simulations of fast ignition cone target implosion, with an initial seed magnetic field, showed however that the magnetic field does not diffuse into the gold cone. In other words, fast electrons are generated far from the high magnetic field region. This result has two main consequences. First, the increase of magnetic axial field encountered by fast electrons generates a so-called magnetic mirror, reflecting particles backward. Second, one has to decrease the stand-off distance between the fast electron source and a high enough magnetic field region required to confine them.

A second high intensity magnetic field generation method uses laser driven intense currents in coil targets. In the scheme proposed by Daido et al. [1986], a coil connects two metal plates (Fig. 1.15). A ∼kJ, ns-scale laser pulse is focused on one of the plates, generating a ∼ 10 keV fast electron population that eventually reaches the other plate, resulting in a charged capacitor configuration. A high ns-scale transient current flows through the coil, generating a ∼kT magnetic field, as obtained by Fujioka et al. [2012] on the Gekko laser facility and more recently by Santos et al. on the LULI pico2000 facility. The capacitor is short-circuited after a few ns, when the thermal plasma expanding from the irradiated plate reaches the other plate. The main advantage of this technique is to allow to create a magnetic field on the short laser pulse side of a fast ignition cone only, allowing the magnetic mirror effect to push fast electrons toward the compressed fuel. The short duration of the flowing current also prevents the magnetic field from being too much modified by the implosion.

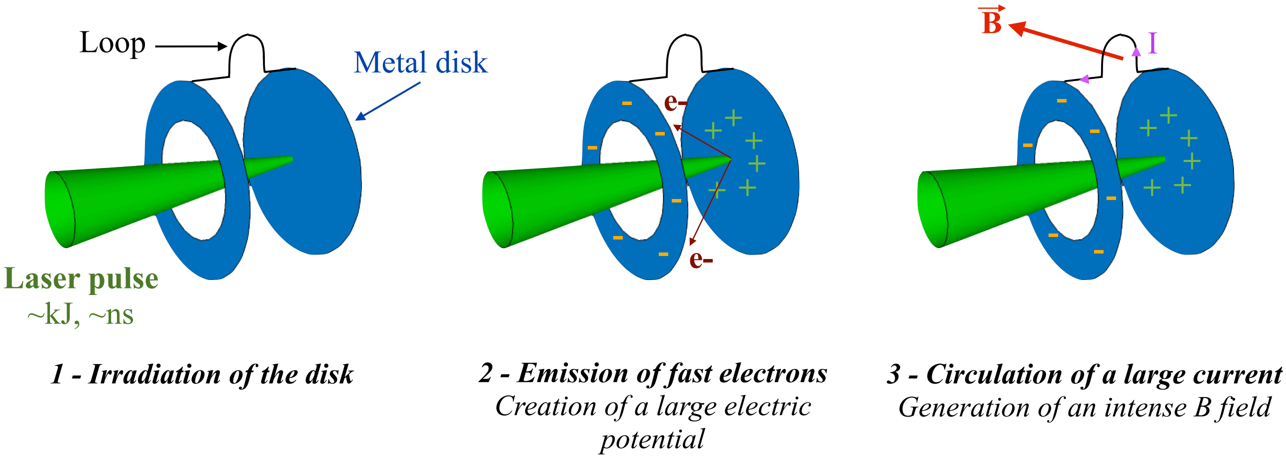

Figure 1.15: Illustration of the capacitor coil target design.

1.5 Applications of laser-generated fast electron beams

In addition to the fast ignition scheme, several other applications may use such fast electron beams. We provide in this section a non-exhaustive list of potential applications.

1.5.1 Ion beam production

Fast electrons can be responsible for the creation of intense ion beams. This process, called Target Normal Sheath Acceleration mechanism (TNSA), firstly described by Snavely et al. [2000] and Wilks et al. [2001], can be described as follows. A fast electron beam accelerated by an intense laser pulse propagates into a thin solid target. When the beam reaches the rear surface, a hot electron cloud is created, resulting in the formation of an intense electric sheath field that accelerates ions present on the surface. The generated ion beam can carry $2\% - 7\%$ of the laser pulse energy and reach a maximum energy of ~ 68 MeV [Gaillard et al., 2011].

1.5.2 High-energy gamma-ray source

The deceleration of fast electrons propagating into a solid target generates an intense broad-spectrum bremsstrahlung emission in the keV−MeV range. The MeV photon source (gamma-rays) is characterized by a sub-millimetric extent and a short duration, comparable to the laser pulse duration, those values being much shorter than what can be obtained with conventional accelerators. Such gamma-ray sources are of great interest for non-destructive control of dense matter, in particular in the aircraft and automobile industries [Glinec et al., 2005].

1.5.3 Electron-positron pairs creation

The generation of intense beams of positrons are of great interest to study astrophysical processes, such as gamma-ray bursts, or for general antimatter researches. Laser-generated fast electrons can be used to generate positrons via two physical processes. The first one, called the Bethe-Heitler process, corresponds to the electron-positron pair production in the interaction of high-energy photons with a high Z nucleus in a solid target. In the second process (Trident process), electron-positron pairs are generated in a direct interaction of a fast electron with a nucleus. It is worth mentioning that the Bethe-Heitler process dominates over the Trident process in a thick high-Z solid target while this trend is reversed in a thin target $< 30\ \mu$m [Chen et al., 2009b]. The laser-generated positron source is characterized by a density $\sim 10^{13}$ cm^{-3}, an intensity $\sim 10^{12}$ W.cm^{-2} and a broad energy spectrum ($4-20$ MeV) [Chen et al., 2010]. It has also recently been shown, using a 8 T magnetic field, that the divergence of positron beams could be reduced from 20° down to 4° [Chen et al., 2014].

1.5.4 Radiotherapy

Radiation therapy is the treatment of a cancer tumor with a beam of intense ionizing radiation. Most treatments currently use high energy X-rays generated by compact electron accelerators. However an important drawback of this techniques relies on the fact that the X-rays dose deposition is maximum at shallow depth and decreases slowly right after, which does not spare the normal tissues surrounding the tumor. High energy electrons created by laser beams offer the advantage of increasing the dose deposition deep into the tissues compared to photons, enhancing the quality of the treatment [Malka et al., 2008]. The laser-generated electron source could be also much narrower compared to the classical radiotherapy. In addition to X-ray and electron radiotherapy, hadrons[2] are also used for the cancer treatment but to much narrower extent. Protons and light ions, such as carbons, are currently used in the medical practice. The main advantage of ions relies on their unique dose deposition property: the maximum of the energy deposition per unit length is at the end of their trajectory (Bragg peak), allowing a fairly precise treatment of the tumor. The cost of hadron therapy is however currently too important since it requires large and extremely expensive particle accelerators (synchrotrons) and complicated systems of beam guiding. The use of laser generated fast electrons to produce ion beams could make the hadron therapy more accessible.

1.6 Goal and contents of the thesis

Many aspects of fast electron generation and transport processes have been studied during the last 15 years. Experimental campaigns benefited from the increase in laser capabilities, with an increasing achievable peak intensity, and an important development of plasma diagnostics. Numerical simulations performed with increasing computational resources allowed a better understanding of fast electron beam generation processes, of fast electron energy loss mechanisms and of fast electron beam divergence, by reproducing with a fairly good agreement experimental results.

Yet, many aspects of fast electron transport still need to be characterized, such as the fast electron stopping power modifications in a warm and compressed matter, compared to a cold-solid medium. The peculiar role of collective energy losses, highly modified with the heating of the target due to the modification of its resistivity, has been so far poorly experimentally studied. As suggested by several numerical studies, collective effects could however be responsible for important energy losses close to the fast electron source in a fast ignition target, where the current density is the highest. The generation of fast electrons obtained by coupling a high-intensity laser pulse with a cone tip also needs to be systematically characterized. The modification of the fast electron source position being pushed far away into the cone due to the inherent plasma jet generated during the compression stage could indeed severely decrease the coupling efficiency, and dramatically affect the fast electron transport.

The goal of this thesis is to perform an experimental characterization of fast electron transport in dense plasmas. We mainly focused on studying the fundamental physical processes in experimental campaigns of smaller scale compared to the fast ignition scheme. All presented

---

[2] A hadron is composed of quark and anti-quark particles. This category includes protons and neutrons

experiments have in common a dual laser beam geometry, with a ns-scale laser pulse used to compress the target up to twice the solid density, and heating it up to a few eV, and a ps-scale laser pulse generating a fast electron beam. The 1D compression geometry was mainly chosen due to its simplicity compared to a spherical compression.

The thesis is structured as follows:

Second chapter provides a summary of the fast electron beam generation and transport theories. The role of both collisional and collective processes is detailed.

Third chapter details the functioning of the diagnostics used in our experiments. Most of them were sensitive to the X-ray emissions. A special attention is devoted to the description of the emission processes.

Fourth chapter is dedicated to the studies of fast electron energy losses in a compressed and heated material. We present the results of an experimental campaign dedicated to the comparative characterization of the fast electron beam transport in cold-solid and warm-compressed materials. The geometry of the experiment was adapted to discriminate the influence of collisional and of resistive processes into the electron beam energy losses. The results are interpreted by comparison with the theoretical models and extensive numerical simulations.

Fifth chapter is dedicated to the characterization of the fast electron energy source. We describe experimental results obtained in two experimental campaigns dedicated to the study of the generation and transport of fast electrons in a cone target embedded into a thick carbon layer, and compressed by a 1D planar shock. A complete hydrodynamic characterization of the target was performed by X-ray point-projection radiography. The experiment is interpreted with a series of hydrodynamic and kinetic simulations.

Sixth chapter provides a summary of the obtained experimental results and their interpretation in the framework of fast ignition studies, and in the more general fast electron transport context.

Part I

Theoretical aspects

Chapter 2

Theory of fast electron generation and transport

In the fast ignition scheme for inertially confined fusion targets, a fast electron beam with a mean energy, and a divergence, adapted for an efficient coupling with the D-T core must be generated. The fast electron population is accelerated at relativistic energies using ultra-intense laser pulses, of the order of several petawatts. Reaching such high intensities is not a trivial process. Since the end of the 1960s the increase in laser intensity has been made progressively following an improvement of the optics technology to create high-energy short duration pulses.

The description of the propagation of fast electron into dense matter requires to take into account several physical effects. Collisional processes, playing an important role in fast electrons diffusion, involve short range binary interactions between fast electrons, ions and background plasma electrons. Collective effects are produced in a larger scale macroscopic electromagnetic fields, involving a large number of particles, and directly depending on the fast electron beam current intensity and current density. Collective effects play an important role in fast electron angular diffusion, both by enhancing or lowering the electron spreading depending on the target conditions.

This chapter is dedicated to briefly summarizing the fast electron transport theory, as a basis for the interpretation of the original experimental results presented in chapters 4 and 5, as well as for the conception of diagnostic hardware, presented in chapter 3. A basic description of plasmas and plasma parameters that are used throughout this thesis is firstly given. The physical principles of generation of intense laser pulses are then exposed, before providing a description of fast electron acceleration mechanisms. Fast electron transport theory, describing both collisional and collective mechanisms of energy loss and scattering, is finally presented.

2.1 Theoretical concepts of plasma physics

2.1.1 General properties of plasmas

A plasma is defined as a state of matter where atoms are at least partially ionized. This fundamental property implies that the motion of particles is importantly influenced by the electromagnetic fields generated by the propagation of particles themselves, which reveals the complexity of plasma physics. This dichotomy between charged particles and electromagnetic fields is responsible for the collective behavior of plasmas: the coherent movement of charged particles is responsible for the generation of oscillations also called plasma waves. The term plasma actually includes a large variety of systems ranging from weakly ionized plasmas where a small fraction of free electrons and ions interact with neutral atoms and molecules, such as what can be found in the Earth ionosphere, to highly ionized and hot plasmas that can be found in stars or in the laboratory fusion devices. A major property of plasmas called *quasi-neutrality* is directly linked to their ability to react to any perturbation and consequently to neutralize a local electrical perturbation: in a plasma, the electric field created by a charged particle is screened by opposite charges beyond a certain distance, making the plasma globally neutral. This quasi-neutrality condition is mathematically given by:

$$-en_e + \sum_i Z^* en_i = 0 \tag{2.1}$$

with n_e the electron density, e the elementary charge, Z^* the ionization degree and n_i the density of the ionic species of index i.

2.1.2 Landau length

The Landau length is defined as the minimum approach distance between two electrons of the considered plasma. In other words, this distance corresponds to the situation where the mean kinetic energy of an electron is exactly equal to the potential energy of interaction between two electrons. The average Landau length r_0 can consequently be calculated by the following:

$$\frac{1}{2}m_e v_e^2 = k_B T_e = \frac{e^2}{4\pi\epsilon_0 r_0} \tag{2.2}$$

with m_e the mass of an electron, T_e the electron temperature, $k_B \simeq 1.3807 \times 10^{-23}$ J.K^{-1} the Boltzmann constant and $\epsilon_0 \simeq 8.8542 \times 10^{-12}$ F.m^{-1} the vacuum permittivity. The Landau length is finally given by:

$$r_0 = \frac{e^2}{4\pi\epsilon_0 k_B T_e} \tag{2.3}$$

For a plasma electron temperature $T_e = 1$ keV the Landau length is $r_0 \simeq 1.4 \times 10^{-12}$ m. This characteristic length can be generalized to two arbitrary particles a and b, characterized by their charge Z_a and Z_b, respectively. Their relative speed is given by $v_{\text{rel}} = |v_a - v_b|$, and the reduced mass of the system is $\mu = (m_a m_b)/(m_a + m_b)$. The generalized Landau length r_{ab} is then given by:

$$r_{ab} = \frac{Z_a Z_b e^2}{4\pi\epsilon_0 \mu v_{\text{rel}}^2} \tag{2.4}$$

2.1.3 Debye length

The quasi-neutrality property of plasmas implies that local fields created by charged particles are screened beyond a certain distance from the source. This length, called the Debye length, plays a major role in collisions between two charged projectiles since it defines the maximum distance where a collision can occur. In order to calculate its value, let us consider a fixed ion with a charge q_i in a plasma characterized by an uniform electron temperature T_e. The electric potential Φ created by this ion is different from the Coulomb potential, $\Phi_{\text{vac}} = q_i/4\pi\epsilon_0 r$, since electrons are attracted by the ion and consequently screen its electric field. At a high enough distance from the ion the electron density is equal to $n_{e,0}$, the unperturbed electron density. In order to evaluate this potential one can consider that an elementary volume of electrons around the ion is affected by both the electric attraction force $\mathbf{f_e} = n_e e\mathbf{E} = -n_e e\boldsymbol{\nabla}\Phi(\mathbf{r})$ and the repulsive pressure force $\mathbf{f_{pe}} = -k_B T_e \boldsymbol{\nabla} n_e$ due to the electron accumulation around the fixed ion. Considering an equilibrium between those forces one can write:

$$\mathbf{f_e} + \mathbf{f_{pe}} = 0 \Rightarrow -n_e e \boldsymbol{\nabla}\Phi(\mathbf{r}) - k_B T_e \boldsymbol{\nabla} n_e = 0 \Rightarrow \frac{1}{n_e}\frac{dn_e}{dr} = -\frac{e}{k_B T_e}\frac{d\Phi}{dr} \tag{2.5}$$

The last equation was obtained considering a spherical symmetry problem due to purely radial forces. This equation can easily be integrated, giving the Boltzmann distribution of electrons in the electrostatic potential:

$$n_e(r) = n_{e,0} \exp\left(-\frac{e\Phi(r)}{k_B T_e}\right) \simeq n_{e,0}\left(1 - \frac{e\Phi(r)}{k_B T_e}\right) \tag{2.6}$$

The last equation was obtained considering that the kinetic energy $k_B T_e$ is higher than the potential energy $e\Phi$. The ion potential Φ can finally be evaluated by using the Maxwell-Poisson equation:

$$\nabla.\mathbf{E} = -\Delta\Phi = \frac{\rho}{\epsilon_0} = \frac{-en_e + q_i n_{i,0}}{\epsilon_0} = -\frac{n_e - n_{e,0}}{\epsilon_0}e \tag{2.7}$$

By injection the expression of the density n_e from Eq. 2.6 into Eq. 2.7, and by expressing the Laplacian operator in spherical coordinates one finds:

$$\Delta\Phi = \frac{n_e e^2}{\epsilon_0 k_B T_e}\Phi \Rightarrow \Phi = \frac{q_i}{4\pi\epsilon_0 r}\exp\left(-\frac{r}{\lambda_D}\right) \tag{2.8}$$

with $\lambda_D = \sqrt{\epsilon_0 k_B T_e / n_e e^2}$ the Debye screening length. It is worth mentioning that the Debye screening effect can only be defined if the number of electrons in the sphere of radius equal to the Debye length is higher than unity. The number of electrons in the Debye sphere is given by:

$$N_D = \frac{4}{3}\pi n_e \lambda_D^3. \tag{2.9}$$

2.1.4 Collective oscillations: the plasma frequency

As already mentioned a plasma tends to suppress any local electric perturbation. These perturbations indeed generate a collective movement of charged particles called plasma wave. Therefore, another important parameter in plasma physics is the oscillation frequency of these waves, called *plasma frequency*, which can be understood as the inverse of the plasma response time to an electric perturbation. In order to calculate the plasma frequency ω_{pe}, let us consider a slab of neutral plasma characterized by a length L along the x-axis direction. At a certain time electrons are dragged along the x positive direction from a distance equal to x and released. This situation is the equivalent of a charged parallel plate capacitor characterized by an electric field between the two plates given by $E = -\sigma_s/\epsilon_0$, $\sigma_s = -en_e x$ being the surface charge density. By inserting the electric field expression into the equation of motion of electrons one finds:

$$\frac{d^2x}{dt^2} = -\frac{n_e e^2 x}{m_e \epsilon_0} = -\omega_{pe}^2 x \tag{2.10}$$

This last equation describes a harmonic oscillator with a frequency equal to the electron plasma frequency $\omega_{pe} = \sqrt{n_e e^2 / m_e \epsilon_0}$. The contribution of ions can be neglected since $m_e << m_i$. The Debye length and the electron plasma frequency are linked with the electron thermal speed $v_{Te} = \sqrt{k_B T_e / m_e}$ through the relation $v_{Te} = \lambda_D \omega_{pe}$. If considering a movement of electron close to relativistic speeds, which is the case during an interaction with a high-intensity laser pulse, as discussed in the next sections, the plasma frequency must take into account the rising of the electron mass from a factor $\gamma = [1 - (v_e/c)^2]^{-0.5}$, called the Lorentz factor, with

$c = 3 \times 10^8$ m.s^{-2} the speed of light in vacuum. In the relativistic case the plasma frequency simply writes $\omega'_{pe} = \gamma\omega_{pe}$.

2.1.5 Propagation of electromagnetic waves: the critical density

We derive in this section the condition of propagation of electromagnetic waves in plasmas. Let us consider an incident planar electromagnetic wave characterized by electric **E** and magnetic **B** fields given by:

$$\mathbf{E} = \mathrm{Re}(\mathbf{E_0})\exp\left(i\mathbf{k}.\mathbf{r} - i\omega_L t\right) \quad ; \quad \mathbf{B} = \mathrm{Re}(\mathbf{B_0})\exp\left(i\mathbf{k}.\mathbf{r} - i\omega_L t\right) \tag{2.11}$$

with k the wave number and ω_L the laser pulsation. Electromagnetic waves are characterized by a transverse polarization in such a way that $\mathbf{k}.\mathbf{E} = 0$. The evolution of the electric and magnetic components are ruled by the four Maxwell equations which can be re-written in the Fourier space:

$$\begin{aligned}
\nabla.\mathbf{E} &= \frac{\rho}{\epsilon_0} \Rightarrow i\mathbf{k}.\mathbf{E} = \frac{\rho}{\epsilon_0} \\
\nabla.\mathbf{B} &= 0 \Rightarrow i\mathbf{k}.\mathbf{B} = 0 \\
\nabla \times \mathbf{E} &= -\frac{\partial \mathbf{B}}{\partial t} \Rightarrow \mathbf{k} \times \mathbf{E} = \omega_L \mathbf{B} \\
\nabla \times \mathbf{B} &= \mu_0 \mathbf{j} + \frac{1}{c^2}\frac{\partial \mathbf{E}}{\partial t} \Rightarrow -\frac{\omega_L}{c^2}\mathbf{E} = i\mu_0\mathbf{j} + \mathbf{k} \times \mathbf{B}
\end{aligned} \tag{2.12}$$

with $\mu_0 = 4\pi \times 10^{-7}$ H.m^{-2} the vacuum permeability and $\mathbf{j} = -en_e\mathbf{v_e}$ the electron current density. The electron velocity $\mathbf{v_e}$ can be deduced from the electron equation of movement in the Fourrier space and by neglecting the magnetic field effects assuming that $v_e/c << 1$:

$$\frac{d\mathbf{v_e}}{dt} = -\frac{e}{m_e}\mathbf{E} \Rightarrow \mathbf{v_e} = -\frac{ie}{m_e\omega_L}\mathbf{E} \tag{2.13}$$

By replacing the expression of the current density and of the magnetic field in Maxwell-Faraday equation one finds:

$$-\frac{\omega_L}{c^2}\mathbf{E} = -\frac{\omega_{pe}^2}{c^2\omega_L}\mathbf{E} + \frac{1}{\omega_L}\mathbf{k} \times \mathbf{k} \times \mathbf{E} \tag{2.14}$$

By using the vectorial identity $\mathbf{k} \times \mathbf{k} \times \mathbf{E} = \mathbf{k}.(\mathbf{k}.\mathbf{E}) - k^2\mathbf{E}$ and since $\mathbf{k}.\mathbf{E} = 0$ for an electromagnetic wave the equation of propagation for the electric field writes:

$$\left(-\omega_{pe}^2 - k^2c^2 + \omega_L^2\right)\mathbf{E} = 0 \tag{2.15}$$

The dispersion relation of a pure electromagnetic wave in a non-collisional plasma finally writes:

$$k^2c^2 = \omega_L^2 - \omega_{pe}^2 \tag{2.16}$$

This relation implies a strong condition on the electromagnetic wave propagation. Indeed, in order to exist in plasmas, electromagnetic waves must be characterized by a frequency ω_L greater than the electron plasma frequency ω_{pe}. In other words a laser pulse cannot propagate into a plasma beyond a certain density, called *critical density*. This critical density n_c can be calculated as a function of the laser wavelength λ_L from the limiting case $\omega_L = \omega_{pe}$, corresponding to the plasma resonance:

$$n_c = \frac{4\pi\epsilon_0 c^2 m_e}{e^2}\frac{1}{\lambda_L^2} \sim \frac{1.116 \times 10^{21}}{\lambda_{L,\mu\mathrm{m}}^2}[\mathrm{cm}^{-3}] \tag{2.17}$$

with $\lambda_{L,\mu\text{m}}$ the laser wavelength in microns. When reaching n_c the laser pulse is mostly reflected. A part of the laser field however penetrates into the plasma within a thin depth $\sim c/\omega_{pe}$, called the *skin depth*, as an evanescent wave. A laser pulse with an incident direction characterized by an angle θ from the target normal penetrates the plasma to a lower density $n_e = n_c \cos^2\theta$. A possible way to increase the penetration range of laser pulses according to Eq. 2.17 consists in decreasing the laser wavelength, which can be done by the frequency doubling method described in the next section. The decrease of the plasma frequency in the relativistic case can be accounted for by the critical density increase by a factor $n'_c = \gamma n_c$. Thus the ultra-high intensity laser pulses are able to penetrate deeper into the plasma.

2.1.6 Coulomb logarithm

Collisions between charged particles are characterized by the impact parameter, which is defined as the perpendicular distance between the incident particle trajectory and the target. The Coulomb logarithm accounts for the ratio between the maximum and minimum impact parameters. The maximum impact parameter $b_{\max}$ is equal to the Debye screening length. The minimum impact parameter is usually chosen either as the Landau length r_{ei} defined as the minimum approach distance involving a scattering of the incident electron at $\pi/2$, or as the De Broglie length $\lambdabar_r = \hbar/\mu v_r$ if quantum effects are important. The Coulomb logarithm can be written as:

$$\ln\Lambda = \ln\left(\frac{b_{\max}}{b_{\min}}\right) = \max\left[\ln\left(\frac{\lambda_D}{\max(r_{ei}, \lambdabar_r)}\right), 2\right] \tag{2.18}$$

The minimum impact parameter can also be taken as the geometric mean value of r_{ei} and of the De Broglie length:

$$b_{\min} = \sqrt{r_{ei}^2 + \lambdabar_r^2} = \sqrt{\left(\frac{Z^* e^2}{4\pi\epsilon_0 k_B T_e}\right)^2 + \left(\frac{\hbar}{\sqrt{(m_e k_b T_e)}}\right)^2} \tag{2.19}$$

In ideal plasmas characterized by a kinetic energy of electrons fairly higher than their potential energy, and consequently by a high number of electrons in the Debye sphere, the Coulomb logarithm can reach values close to 10. Collisions at high impact parameters are in this case dominant over low impact parameter collisions, which means that an incident particle undergoes several collisions before its trajectory significantly changes. In a strongly non-ideal plasma, where close collisions are dominant, the Coulomb logarithm is close to 2. This value is also often chosen as the minimum Coulomb logarithm value. As discussed in the next section this Coulomb logarithm is of primary importance for characterizing collisional laser energy absorption in a plasma through the electron-ion frequency.

2.1.7 Plasma statistics: Saha ionization equation and Thomas-Fermi model

The ionization state of a plasma is a key parameter for the determination of its physical properties, such as the plasma resistivity, as discussed in section 2.4. Two ionization models are widely used: the Saha-Boltzmann (SB) and the Thomas-Fermi (TF) model.

Let us consider a plasma characterized by a population of electrons described by the Maxwell-Botlzmann statistics. Assuming that the local thermodynamic equilibrium (LTE) conditions are reached, the ratio between the ionic densities of two successive ionization states, n_Z and

n_{Z+1}, is given by the Saha-Boltzmann equation:

$$\frac{n_{Z+1}}{n_Z} = \frac{G_{Z+1}(T_e)}{G_Z(T_e)}\frac{2}{n_e}\left(\frac{\pi m_e k_B T_e}{h^2}\right)^{3/2} \exp\left(-\frac{I_Z}{k_B T_e}\right) \tag{2.20}$$

with G_Z and I_Z the statistical partition function and the ionization potential, respectively, of the ion population characterized by the charge state Z. The mean ionization degree writes:

$$\overline{Z^*} = \frac{n_e}{n_i} = \frac{\sum Z n_Z}{\sum n_Z} \tag{2.21}$$

It is worth mentioning that the Saha theory is not so well adapted for high density plasmas, with a large number of Coulomb collisions. The Saha-Boltzman equation is indeed calculated from Boltzmann distribution law when neglecting Coulomb interactions between free electrons, and between ions and free electrons. Harrach & Rogers [1981] have shown by comparing results obtained with the SB model and with the ACTEX code taking into account ion and electron correlations [Rogers, 1981] that the SB model provides fairly accurate results for plasma densities ≤ 1 g.cm^{-3} and for temperatures from a few eV up to several hundred eV.

For higher plasma densities the Thomas-Fermi model provides a convenient description of the matter. This semi-classical statistical model was independently developed by Llewellyn H. Thomas and Enrico Fermi in 1926. Unlike the SB model, the TF model does not contain any energy level concept. Atoms are described as spheres characterized by a radius $r_0 = (3/4\pi n_i)^{1/3}$ containing a nucleus of charge Z and a certain density of uniformly distributed independent electrons moving into an effective potential V. The two hypothesis of the TF model are the following:

- The chemical potential μ is constant within the atom so that $\mu(\mathbf{r}) = \mu$.
- Electrons are characterized by their classical energy $E = p^2/2m_e + V$.

The chemical potential can be determined by imposing a neutral atomic sphere condition:

$$\int n_e(\mathbf{r}) d\mathbf{r} = Z \tag{2.22}$$

where the integration is made over the whole atomic sphere. The electron density $n_e(\mathbf{r})$ is calculated considering that each atomic state is characterized by an occupation probability given by the Fermi-Dirac statistics yielding:

$$n_e(\mathbf{r}) = \frac{2}{h^3}\int \frac{d\mathbf{p}}{1 + \exp\left[(E-\mu)/k_B T\right]} \tag{2.23}$$

The effective potential V can be simply derived considering that it must contain a "nuclear part" being dominant when the radius r tends towards 0, and an "electron-electron" part taking into account the contribution of all other electrons:

$$V(\mathbf{r}) \propto \underbrace{-\frac{Z}{r}}_{\text{nucleus}} + \underbrace{\int_0^{r_0} \frac{n_e(\mathbf{r}')d\mathbf{r}'}{|\mathbf{r}-\mathbf{r}'|}}_{\text{other e-}} \tag{2.24}$$

where the potential is given in atomic units. The electron density can be re-written as:

$$n_e(\mathbf{r}) = \frac{4\pi}{h^3}(2m_e k_B T)^{3/2} F_{1/2}(\frac{\mu - V}{k_B T}) \tag{2.25}$$

with the Fermi integral $F_i(\mu/k_BT_e)$ given by:

$$F_i(\mu/k_BT_e) = \int_0^\infty dt \frac{t^i}{1+\exp\left(t-\mu/k_BT_e\right)} \tag{2.26}$$

The ionization degree Z^* given by the TF model can be derived by considering the number of electrons located at the border of the atomic sphere, defined by $r = r_0$, and free to switch immediately to another atom:

$$Z^* = \frac{4}{3} r_0^3 n_e(r_0) \tag{2.27}$$

A fairly useful analytical expression derived by More [More, 1981, 1985] provides a convenient way to calculate the ionization degree as a function of the plasma density and temperature within a precision of a few percents. The evolution of the the ionization degree in aluminum targets as a function of the electron temperature calculated with the More's expression is plotted in Fig. 2.1. It is worth mentioning that More's expression is used throughout this thesis when a calculation of ionization degree is required.

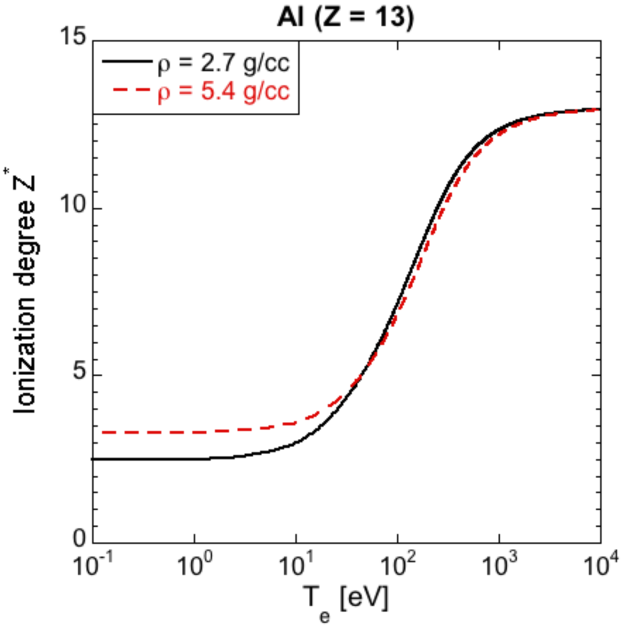

Figure 2.1: Evolution of the ionization degree as a function of the electron temperature for aluminum at solid density, $\rho_0 = 2.7$ g.cm^{-3} (black solid line), and at $\rho = 5.4$ g.cm^{-3}, calculated using More's expression [More, 1985].

One can note that an important property of TF model is its capacity to predict the free electron density for $T_e = 0$, making this model of great interest for the description of electric conductors.

2.2 Short laser pulses

2.2.1 Generation of intense laser pulses

Q-switching

The first short-pulse generation mechanism that was historically introduced is called Q-switching. It was first experimentally demonstrated by McClung & Hellwarth [1962]. Q-switching consists in inserting into the laser cavity an attenuator that introduces strong losses in the gain medium, preventing any laser effect from occurring. The quality factor of the optical cavity, defined as the fraction of stored energy to dissipated energy and labeled with the Q letter, is initially fairly low. When the population inversion reaches its maximum value, spontaneous emission losses preventing any increase of this value, the energy stored in the gain medium peaks at a maximum level. At this precise time the Q factor is suddenly increased, allowing the laser effect to take place. The stored energy is consequently quickly released into an intense pulse of a few nanoseconds duration and up to a few gigawatts peak power. Two kinds of Q-switches currently exist. Passive Q-switches use saturable absorbers whose transmission dramatically increase when the intensity in the cavity reaches a certain threshold, which directly depends on the nature of the absorbing material. Active Q-switches use externally controlled devices such as fast shutters or Pockels cells, providing an enhanced control of the pulse repetition rate.

Mode locking

Another high-intensity pulse generation mechanism, called *mode locking*, appeared in the 1970s. The basic principle of this technique was demonstrated in 1964 by Hargrove et al. [1964]. Mode-locking allows to produce temporally short laser pulses down to a few femtoseconds. A laser cavity is constituted, in its simplest form, of a gain medium surrounded by two mirrors, separated by a distance L. This mirror configuration is similar to a Fabry-Perot interferometer. The resulting constructive or destructive light interferences allow consequently only a specific range of wavelengths, called cavity modes, to propagate. These modes are characterized by a frequency separation $\Delta\nu = c/(2L)$. The number of modes allowed to propagate in the cavity is also determined by the gain medium itself. Indeed, the medium amplifies frequencies only within a certain range, called gain bandwidth. Without any further constraint all modes in the cavity oscillate with completely random phases. The introduction of a certain phase relationship between those modes forces them to periodically constructively interfere, creating an output beam characterized by a train of laser pulses of extremely short duration. The maximum focused intensity that can be reached by the the mode locking technique is close to 10^{15} W.cm^{-2}.

CPA: chirped pulse amplification

The increase of laser intensity I_L provokes non-linear effects potentially hazardous for laser cavities. A laser pulse propagating in a medium is indeed characterized by a higher intensity on the center than on its wings (Gaussian pulse). When the power of the pulse reaches the so-called critical power $P_{\mathrm{crit}} \propto \lambda_L^2/4\pi n_0 n_2$, with λ_L the laser wavelength and $n = n_0 + n_2 I_L$ the refractive index of the material characterized by the linear and non-linear indices n_0 and n_2, respectively, a so-called Kerr lens forms into the material resulting in the focusing of the pulse overcoming its natural diffraction. When the intensity of the focused pulse exceeds the material ionization threshold, a plasma is created. The higher electron density in the central part of the beam generates a transverse negative index gradient, away from the center, that acts like a defocusing lens. The refractive index N of a plasma is easily deduced from Eq. 2.16 [Gibbon, 2005]:

$$N(r) = \sqrt{\left(1 - \frac{n_e(r)}{n_c}\right)} \tag{2.28}$$

with $n_e(r)$ the local electron density and n_c the critical density when $\omega = \omega_{pe}$. The laser beam splits into several beamlets called filaments [Garmire et al., 1966], considerably damaging the amplifying medium and mirrors of the laser cavity, and consequently limiting the maximum output power achievable. A schematic of the filamentation process is plotted on Fig.2.2. The distortions of the laser beam wavefront accumulated during its propagation can be characterized by the so called B-integral given by $B = (2\pi/\lambda_L)\int n_2 I_L(z)dz$, that must be minimized. Generating high intensity laser pulses however means working at high fluences in the amplifying medium yielding to prohibitive values of the B-integral.

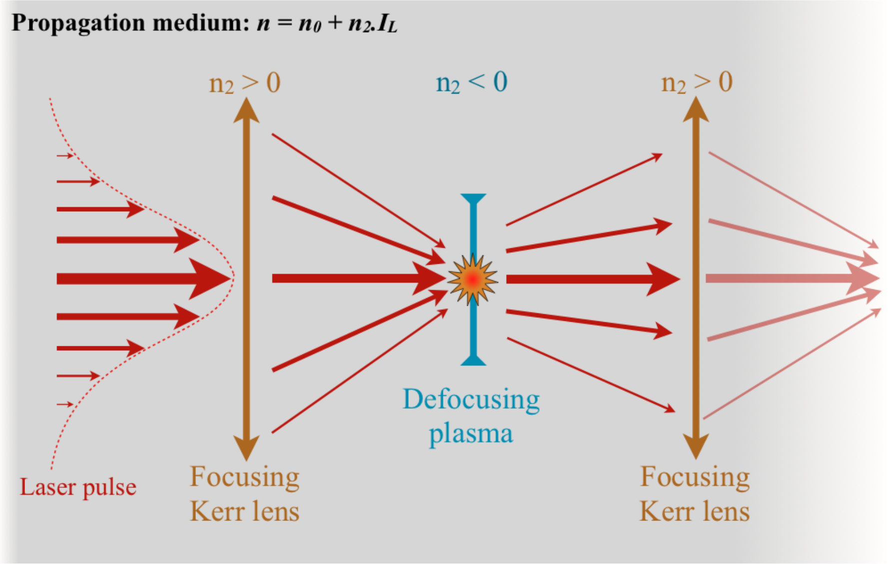

Figure 2.2: Illustration of the filamentation process. Due to the inherent larger intensity in the center of the spot the laser pulse is focused in the medium by the created Kerr lens, creating a plasma. A defocusing lens is then generated by the negative electron density gradient (towards the center of the pulse). The pulse undergoes several focusing-defocusing cycles which could severely damage the amplifying medium.

In 1985 Donna Strickland and Gérard Mourou introduced a new concept of pulse amplification allowing to overcome the 10^{15} W.cm^{-2} limit. This technique, called chirped pulse amplification (CPA) [Strickland & Mourou, 1985], was firstly introduced by Brookner [1985] in for the radars. Indeed, radar pulse generation faced a similar challenge since the generation of short and energetic pulses required huge peak powers that cannot whithstand by electrical circuits. The optical CPA technique is nowadays a part of every ultra-intense laser system in the world. It can be described as follows. A low intensity and low energy (∼nJ) laser pulse is emitted from an oscillator, constituting the first element of a laser system. This pulse is then stretched by temporally separating its different wavelengths. The duration of the pulse is stretched up to 10^6 times of its initial duration. A commonly used stretcher is made of two diffracting gratings disposed in an antiparallel configuration, introducing a positive dispersion of the different wavelengths [Martinez, 1987]. This system indeed ensures that the different frequencies run over paths of different lengths: the higher frequencies travel more than the lower frequencies, the pulse is temporally chirped. A mirror forces the pulse to make a double-pass in the stretcher. This double-pass configuration ensures that the beam is not spatially stretched, or in other words that its different frequency components are not transversally separated in space with respect to their propagation direction. Another advantage of this configuration is to increase the temporal chirp by a factor two compared to a single pass configuration. A telescope must be located between the two gratings to ensure that the dispersion of the different components is inverted [Martinez et al., 1984]. This telescope can either be composed of a pair of lenses [Martinez et al., 1984] or a pair of prisms [Fork et al., 1984]. The second grating is mounted with its surface parallel to the image of the first grating made by the telescope. At this point, the peak intensity of the pulse is fairly low. The stretched pulsed is then amplified up to 10^9 times of its initial intensity without triggering any non linear effect. The pulse finally goes through a compressor made of a pair of gratings in a parallel configuration exactly compensating all stretching effects, and thus introducing a negative dispersion between the different wavelengths. The duration of the pulse is shorten down to its initial value, when emitted by the oscillator. A double-pass configuration prevents here again any spatial chirp on the impulsion. Fig. 2.3 illustrates the basic principle of CPA. The CPA technique allows to reach pulse durations shorter than a picosecond with focused laser intensities up to 10^{21} W.cm^{-2} containing up to hundreds of joules, such as on the pico2000 laser system (LULI, France), the OMEGA EP laser system (Rochester, USA) or the PETAL laser system (Le Barp, France) currently in phase of operational validation.

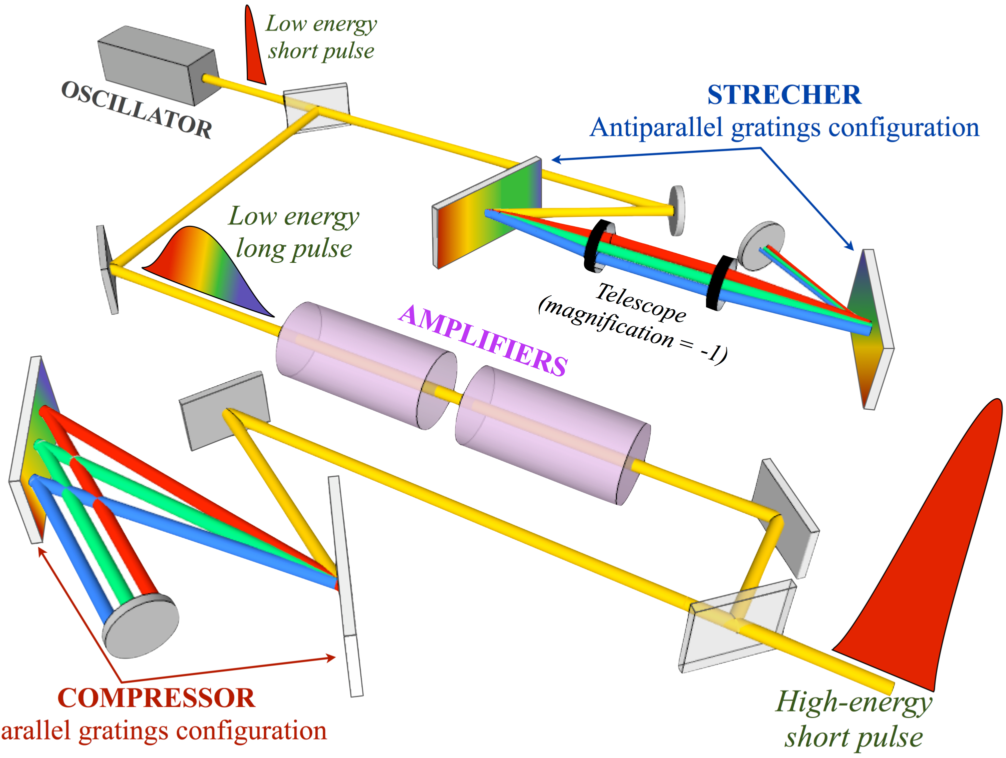

Figure 2.3: Illustration of the CPA technique.

OPCPA: Optical Parametric Chirped-Pulse Amplification

The CPA technique presents some major drawbacks. The limited number of amplifying media which are currently available, such as the classical Ng:glass medium, does not provide large enough bandwidths to generate shorter pulse durations. In addition, CPA pulses are characterized by a ∼ns scale pedestal preceding the main short pulse coming from the amplified spontaneous emission (ASE) of the laser system. This pedestal strongly affects any laser-solid experiment since it creates an expanding plasma, called pre-plasma, profoundly modifying the interaction processes between the main pulse and the target. The detailed effects of ASE are discussed in section 2.2.2. Finally the necessary cooling of the amplifying medium between each shot, that can last up to 2 h, does not currently allow any high repetition rate of the more energetic short pulse laser systems. The inversion population is indeed obtained using electromagnetic radiation from flash lamps, with an important part of the emitted energy inducing undesirable non linear thermal effects in the amplifying medium.

An alternative to the CPA pulse amplification technique is called Optical Parametric Chirped-Pulse Amplification (OPCPA), which basic principle can be described as follows. In a first step a low intensity pulse of a mean frequency ω_s emitted by an oscillator is stretched, just like in the CPA technique. The core of the OPCPA technique relies on the amplification of the stretched pulse. The laser beam propagates through a nonlinear crystal, such as a Beta Barium Borate (BBO) crystal, that is pumped by another laser beam of frequency ω_p, of a few ns duration and carrying a large amount of energy. A parametric amplification can occur: a large amount of pump photons are instantly converted into photons of the incident laser pulse. In other words the energy of the pump pulse is efficiently transferred to the incident laser pulse. The leftover energy is carried away by an idler laser beam of frequency ω_i so that the matching condition $\omega_p = \omega_s + \omega_i$ is satisfied. This process is called Optical Parametric Amplification (OPA). Finally the amplified pulse is compressed, just like in the CPA technique. A schematic of the OPCPA technique is presented on Fig.2.4. The advantages of OPCPA over classical CPA are that the inherent prepulse level is lower, the high gain amplification is reached in a shorter distance leading to more compact systems and the thermal effects due to the heating of the crystal are much weaker. The petawatt JLF-Titan (LLNL, USA) laser system uses such an OPCPA preamplifier, amplifying the laser beam up to 5 J before passing through a classical amplifier.

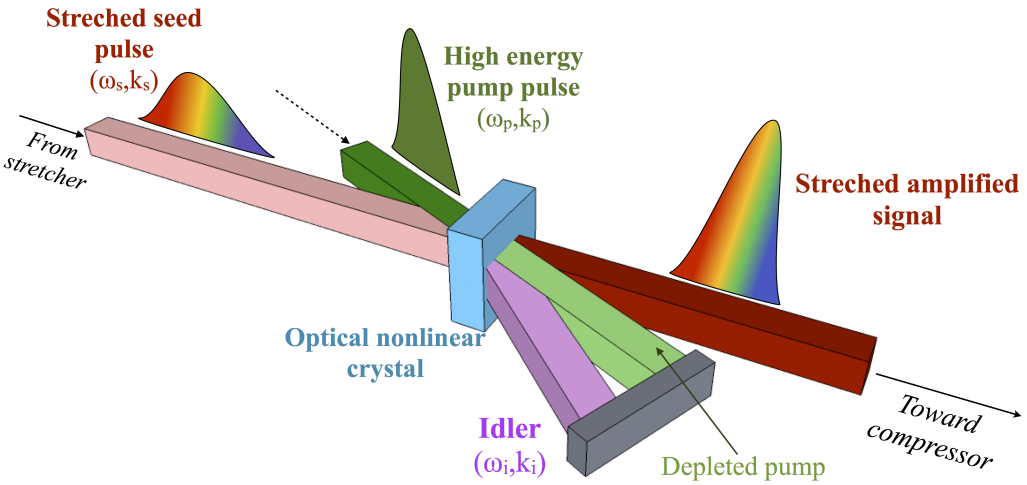

Figure 2.4: Illustration of the OPCPA technique.

2.2.2 Pulse contrast

Ultra-intense laser systems do not only emit short-duration pulses. They are indeed generated together with a nanosecond scale component, called pedestal, preceding the main pulse. The emission of a parasitic pedestal is inherent to the laser system itself. This phenomenon corresponds to the unavoidable amplification of the spontaneous emission (ASE) in the amplifying medium that can possibly limit the achievable gain. The ratio between the main pulse maximum intensity to the ASE-pedestal intensity is referred as the pulse *contrast*, which is usually of the order of $\sim 10^6 - 10^7$. This value which may seem to be fairly weak at first glance has to be compared to the $10^{19} - 10^{20}$ W.cm^{-2} peak focused intensity that is commonly achieved in current laser systems. The pedestal intensity is indeed of the order of $10^{12} - 10^{13}$ W.cm^{-2} which is high enough to ionize a solid density target. The main pulse consequently interacts with a plasma expanding at the thermal sound velocity $C_s = \sqrt{Z k_B T / m_i}$, dramatically changing the conditions of interaction and the laser absorption, and thus the spectrum and total energy of generated fast electrons. This important modification of the target density gradient has to be taken into account in numerical simulations in order to reproduce experimental results. However in some cases one may want to dramatically reduce, or even to suppress this pedestal. Indeed some experiments may require an interaction between the main laser pulse and a steep density gradient, such as in particle acceleration experiments [Dong et al., 2003; d'Humières et al., 2005; Henig et al., 2009]. In the experiment described in chapter 5, which uses cone targets, a high contrast pulse was required. In addition the increase of peak intensities that can be reached by laser pulses requires drastic measures to maximize pulse contrast. A possible solution is to double the pulse frequency, going from ω_L to $2\omega_L$. For example a typical infrared laser pulse characterized by a wavelength $\lambda_{L,\omega_L} = 1.06$ μm can be converted into a "green" visible pulse with a wavelength $\lambda_{L,2\omega_L} = 0.53$ μm. This frequency doubling process is achieved by sending the laser pulse into a non-linear crystal. The anharmonic vibrations of the crystal electrons around their nuclei generate the second order harmonic of the incident wave that propagates in the same direction. The conversion efficiency being proportional to the intensity squared, the main pulse is more efficiently converted than the pedestal. The generated target pre-plasma is characterized by a smaller gradient length than without any frequency doubling process. This process may however not be sufficient to obtain perfectly cleaned pulses. Another advantage of conversion frequency is that the 2ω pulse is also able to propagate further deep into the target since the critical density value $n_c \propto \omega_L^2$ given by Eq. 2.17 is multiplied by a factor four.

2.2.3 Plasma mirrors

Another technique used to clean laser pulses consists in finding an optical switch that would only allow the main pulse to go through. Considering the extremely short duration of laser pulses one has to find a fast enough device that would react in the sub-picosecond time scale. Ionization of dielectric materials is a strongly non-linear process that matches this criterion. Indeed, when irradiated by an intensity below the ionization threshold, the incoming light partly goes through the material. A small proportion of the pulse is also reflected by the surface. When reaching the ionization threshold a large proportion of electrons are injected into the conduction band: the dielectric behaves like a dramatically efficient metal-like reflective surface. The so-called plasma mirror technique is base on this phenomena [Kapteyn & Murnane, 1991]. A dielectric material, such as silicate, is set-up in such a way that the pedestal intensity is too low to ionize the material whereas the main pulse intensity is high enough so that its rising front creates a highly reflective plasma above critical density. The basic principle of plasma mirrors is presented in Fig. 2.5.

When using a single plasma mirror the contrast of the pulse can be enhanced up to ~ 500 [Gold, 1994] even if in most cases the contrast enhancement is closer to 100 [Doumy et al., 2004]. The set-up of a double plasma mirror configuration can enhance this contrast up to a factor 10^4 [Doumy, 2006]. For short pulse durations from the sub-picosecond level to several picoseconds the gradient scale length of the expanding plasma mirror surface is lower than the pulse wavelength. The main pulse is consequently specularly reflected. The plasma mirror effect stays active during several picoseconds until this plasma gradient scale length becomes comparable to the pulse wavelength. The post-pulse part of the beam is then reflected within broader angle values. As a consequence plasma mirrors can be used to clean laser pulses up to 5 ps maximum duration. Crossing this limit would indeed result in important distortions of the reflected wavefront due to the plasma expansion [Doumy et al., 2004]. Finally, another practical advantage of plasma mirrors is to act as a protective layer for extremely expensive final optics that could be severely damaged by the target debris.

A major limitation in the use of plasma mirrors arises from the irreversible destruction of the

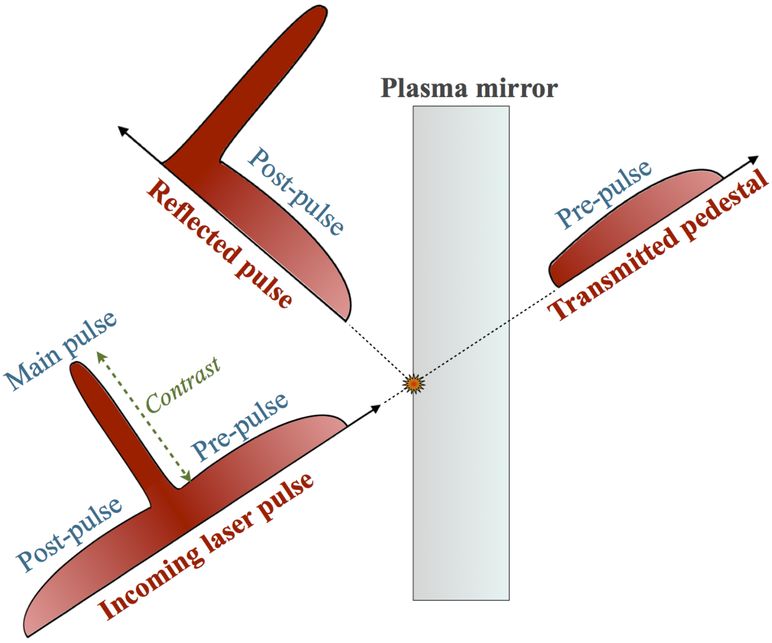

Figure 2.5: Plasma mirror concept. The major part of the pre-pulse of the incoming pulse is transmitted through the dielectric material. The main pulse intensity is high enough to instantly ionize the material and is consequently specularly reflected by the created plasma. In a more realistic case, even if the pre-pulse is not totally suppressed after reflection on the plasma mirror, its level is decreased by two orders of magnitude.

dielectric surface after each laser shot. The mirror has consequently to be replaced after each shot which makes this technique not suitable for high repetition rate laser systems. A possible solution has been studied by Backus et al. [1993]. The solid plasma mirror is replaced by a stable liquid jet of ethylene glycol that regenerates itself in less than a millisecond, making it suitable for kilohertz-repetition-rate laser systems. The authors obtained a pulse contrast close to 400. Another drawback of the use of plasma mirrors, either in a solid or a liquid state, comes from the fact that the creation of the reflective surface by the main pulse itself unavoidably decreases the pulse energy by a factor ~ 2.

2.3 Fast electron acceleration mechanisms

2.3.1 Interaction between an intense laser pulse and a single isolated electron

Let us consider an incident laser pulse characterized by the electromagnetic fields $(\mathbf{E}, \mathbf{B})$ incident on an isolated electron initially at rest in the laboratory frame. The motion of this particle is ruled by the action of the associated Lorentz force:

$$\frac{d\mathbf{p}}{dt} = -e\left(\mathbf{E} + \mathbf{v} \times \mathbf{B}\right) \tag{2.29}$$

with $\mathbf{v}$ the speed of the electron and $\mathbf{p} = \gamma m \mathbf{v}$ its momentum depending on the relativistic Lorentz factor $\gamma = (1 + p^2/m^2c^2)^{0.5}$. The position $\mathbf{r}$ of the electron is linked to its speed by:

$$\frac{d\mathbf{r}}{dt} = \mathbf{v} \tag{2.30}$$

The electric $\mathbf{E}$ and magnetic $\mathbf{B}$ fields can be re-written as a function of the vector potential $\mathbf{A}$. In the Coulomb gauge conditions, $\nabla.\mathbf{A} = 0$, and provided that there is no electromagnetic sources, the fields are given by:

$$\mathbf{E} = -\frac{\partial \mathbf{A}}{\partial t} \tag{2.31}$$

$$\mathbf{B} = \nabla \times \mathbf{A} \tag{2.32}$$

Let us consider a purely transverse incident electromagnetic wave, which is always the case in our experiments, polarized in the y-axis direction and propagating in the x-axis direction. This wave is characterized by the vector potential $\mathbf{A} = \mathbf{A}_\perp = A\cos(\Phi)\mathbf{e_y}$, with the phase $\Phi = \omega_L t - kx$, and $k = \omega_L/c$ is the wave number. In this situation the transverse component of the electron impulsion is given by:

$$\mathbf{p}_\perp = e\mathbf{A}_\perp \tag{2.33}$$

The transverse component of the electron momentum, directly depending on the vector potential, is consequently conserved throughout the interaction. At fairly low laser intensities the movement of the electron will be purely transverse. Indeed the effect of the magnetic field will be negligible since its amplitude is given by $B = E/c$ in vacuum. The electron maximum oscillation velocity is given by:

$$\frac{v_\perp}{c} = a = \frac{eE}{m_e w_L c} = 0.85 \times \sqrt{I_{18}\lambda_{\mu\mathrm{m}}^2} \tag{2.34}$$

with a the normalized laser field, I_{18} the laser intensity in units of 10^{18} W.cm^{-2}, $w_L = 2\pi c/\lambda_L$ the laser pulsation and $\lambda_{\mu\mathrm{m}}$ the laser wavelength in microns. In other words, the previous approach is valid for $a < 1$ that is for $I < 10^{18}$ W.cm^{-2}. For $a > 1$ the motion of the electron has to be considered as relativistic. The effects of the magnetic field are no longer negligible. The electron consequently acquires also a movement in the laser incident direction. The conservation of the electron momentum in this parallel direction yields:

$$p_\parallel = m_e c(\gamma - 1) \tag{2.35}$$

Considering that the relativistic γ factor can be written as $\gamma^2 = 1 + p_\perp^2/m_e^2c^2 + p_\parallel^2/m_e^2c^2$, the parallel and perpendicular components are linked by:

$$p_\parallel = \frac{p_{\perp^2}}{2m_e c} \tag{2.36}$$

The parallel momentum is consequently always positive: the electron is dragged along the laser propagation axis. Using the two previous equations on can find the angle of electron ejection from the laser pulse. The ejection angle θ of the electron writes

$$\tan\theta = \frac{p_\perp}{p_\parallel} = \sqrt{\frac{2}{\gamma - 1}} \tag{2.37}$$

The ejection angle narrows when the energy of the electron increases: non-relativistic electrons are ejected along the incident wave polarization while relativistic particles are ejected along the laser pulse propagation direction. The components of the electron momentum in the laboratory frame write:

$$\begin{aligned} p_x &= \frac{a}{4}\left[1+\cos 2\Phi\right] \\ p_y &= a\cos\Phi \\ p_z &= 0 \end{aligned} \tag{2.38}$$

The electron trajectory in the laboratory frame is finally given by [Gibbon, 2005]:

$$\begin{aligned} x &= \frac{1}{4}a^2\left[\Phi + \frac{1}{2}\sin 2\Phi\right] \\ y &= a\sin\Phi \\ z &= 0 \end{aligned} \tag{2.39}$$

Figure 2.6 presents those trajectories for different values of the normalized laser amplitude a. The shape of the trajectories depends on the laser amplitude. Trajectories are stretched by a factor a^2 in the transverse direction and by a factor a in the parallel direction. The drift velocity of the electron in the laser propagation axis averaged over a laser cycle writes:

$$v_D = \frac{\langle p_x\rangle}{\langle\gamma\rangle mc} = \frac{a^2 c}{4+a^2} \tag{2.40}$$

The movement of electron directly depends on the laser intensity. When considering a more realistic case with a finite pulse duration one can show that the electron is accelerated by the rising edge of the laser pulse, but it is immediately slowed down during the decreasing part until it completely stops when the laser pulse ends [Gibbon, 2005]. The fact that the electron does not gain any energy from the laser is the consequence of its adiabatic motion. This is the case if the field amplitude changes slowly during a laser period. However even if the electron comes back to its initial position in the perpendicular direction, it is still moved along the laser propagation axis over a distance $\Delta_x = \int v_D(t)dt$. The orbits of the electron can be calculated in its own rest frame, where the drift velocity is zero. Electron trajectories in this rest frame are given by [Gibbon, 2005]:

$$\begin{aligned} x &= \frac{1}{2}q^2\sin 2\Phi \\ y &= 2q\sin\Phi \\ z &= 0 \end{aligned} \tag{2.41}$$

with $q = a/(1+a^2/2)$. These equations correspond to the figure eight orbit shape that is compressed in the transverse direction when increasing the laser intensity. Figure 2.6 presents the electron trajectories in its rest frame for different amplitudes. In a more realistic case the interaction between an electron and an incident short laser pulse takes place in a plasma. There are processes which are responsible for the breaking of the adiabaticity of the electron motion, such as collisions with the background ions, strong density gradients or electric fields. A substantial fraction of the laser energy can consequently be transferred to plasma electrons. The next section describes the acceleration mechanisms of electrons in solid materials.

2.3.2 Linear absorption mechanisms

Let us consider a short laser pulse ($\sim$ fs) incident on an overdense plasma. Due to a short duration of the pulse the plasma does not expand during the interaction. This situation can consequently be modeled by an incident laser pulse on a semi-infinite overdense plasma charac-

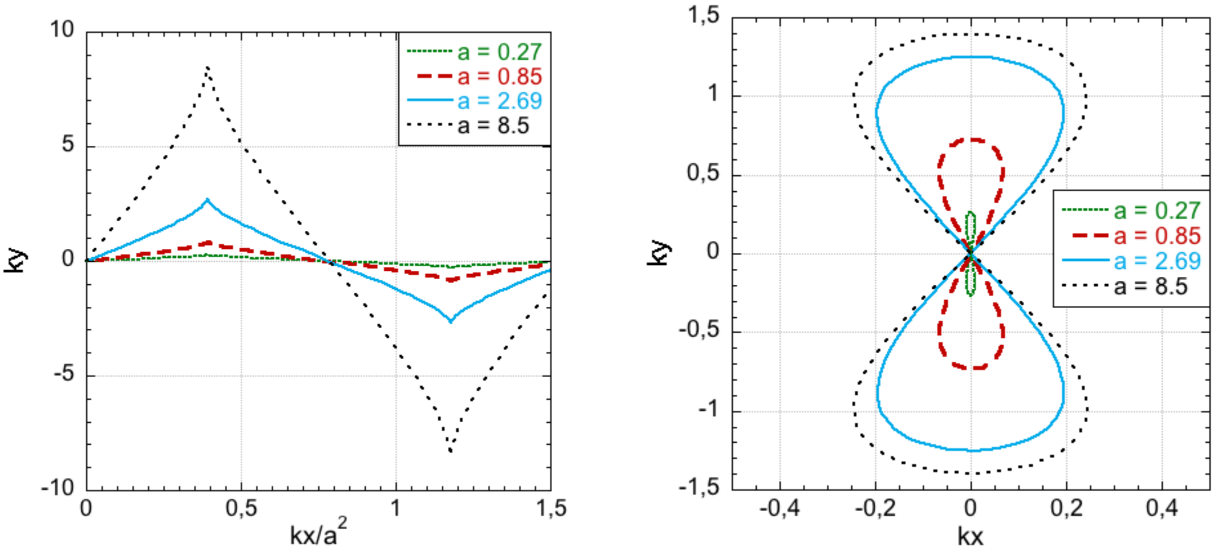

Figure 2.6: Electron orbits in the laboratory frame (left-hand side) and in its own rest frame (right-hand side) for different values of the normalized laser amplitude a: $a = 0.27$ (dotted line), $a = 0.85$ (dashed line), $a = 2.69$ (solid line) and $a = 8.5$ (dash-dotted line). Considering an incident laser pulse with a wavelength $\lambda_L = 1$ μm these values corresponds to laser intensities $I = 10^{17}$ W.cm^{-2}, $I = 10^{18}$ W.cm^{-2}, $I = 10^{19}$ W.cm^{-2} and $I = 10^{20}$ W.cm^{-2}, respectively.

terized by a steep vacuum-matter interface. The medium is completely opaque to the incident laser pulse. In a more detailed approach, the component oscillating in the incidence plane of the laser field penetrates into the plasma and is attenuated within the skin-depth, equal to c/ω_{pe}. The longitudinal component is attenuated within the Debye scale length λ_D being equal to v_{Te}/ω_{pe}.
At intensities $I < 10^{16}$ W.cm^{-2} the absorption of laser energy is ruled by linear processes depending on the laser frequency and on the electron-ion collision frequency ν_{ei}.

Collisional absorption

At low intensities $I < 10^{15}$ W.cm^{-2} collisions between the accelerated electrons and the plasma ions is the dominant absorption mechanism: a photon is absorbed by an electron scattering on an ion. This process is also called *inverse bremsstrahlung* since it is exactly the opposite of the bremsstrahlung process. By considering a Maxwellian plasma the collision frequency is given by the Landau-Spitzer theory [Landau, 1936; Spitzer, 1956]:

$$\nu_{ei}[\mathrm{s}^{-1}] = 2.91 \times 10^{-6} Z^* n_e T_e^{-3/2} \ln \Lambda \tag{2.42}$$

with T_e the electron temperature, Z^* the plasma ionization degree and $\ln \Lambda$ the Coulomb logarithm. At low plasma temperature and for a low frequency laser pulse the electron-ion collision frequency can be higher than the laser frequency in such a way that $\omega_L << \nu_{ei} << \omega_{pe}$. In this regime the dominant collisional absorption mechanism is called *normal skin effect*. The laser field penetrates into the plasma within a thickness $l_{NSE} \simeq (c/\omega_{pe})\sqrt{\nu_{ei}/\omega_L}$. The corresponding absorption coefficient efficiency calculated by Rozmus et al. [1996] is given by:

$$f_{NSE} = \frac{\omega_L}{\omega_{pe}} \left(\sqrt{\frac{8\nu_{ei}}{\omega_L}} \right) \tag{2.43}$$

When considering a higher laser frequency $\nu_{ei} < \omega_L$ and if the accelerated electron mean free path is shorter than the skin depth, the dominant absorption mechanism is called *collisional absorption*. The absorption coefficient efficiency is given by [Rozmus et al., 1996]:

$$f_{CA} \simeq \frac{2\nu_{ei}}{\omega_{pe}} \tag{2.44}$$

When increasing further the laser intensity the plasma temperature rises in such a way that the collision frequency $\nu_{ei} \propto T_e^{-3/2}$ decreases dramatically. Moreover the quiver velocity v_{osc} of the electron in the laser field becomes comparable to its thermal velocity which reduces further more the collision frequency [Pert, 1995]:

$$\nu'_{ei} \simeq \nu_{ei} \frac{v_{Te}^3}{(v_{\text{osc}}^2 + v_{Te}^2)^{3/2}} \tag{2.45}$$

Collisional absorption mechanisms becoming rapidly negligible when exceeding laser intensities $I > 10^{17}$ W.cm^{-2} leave other mechanisms responsible for an efficient electron acceleration.

Non-collisional mechanisms

When rising the plasma electron temperature, the mean free path of accelerated electrons can become larger than the skin depth. The absorption of the laser field consequently becomes non-local, the energy being transported deeper into the plasma. When considering a laser frequency just above the electron-ion collision frequency, $\nu_{ei} < \omega_L < \omega_{pe} v_{Te}/c$ the laser energy is absorbed over an anomalous skin depth $l_{ASE} \simeq (c^2 v_{TE}/\omega_{pe}^2 \omega_L)^{1/3}$. This mechanism is called *anomalous skin effect* (AS) [Weibel, 1967]. The absorption coefficient calculated by Rozmus & Tikhonchuk [1990] considering a moderate laser field $a < 0.1$ is given by:

$$f_{AS} \simeq 1.5 \left(\frac{\omega_L}{\omega_{pe}}\right)^{2/3} \left(\frac{v_{Te}}{c}\right)^{1/3} \tag{2.46}$$

The absorption does not depend on the collision frequency anymore even though the electrons are depositing the absorbed laser energy beyond the anomalous skin-depth in electron-electron collisions. When considering a higher laser frequency such that $\nu_{ei} < \omega_{pe} v_{Te}/c < \omega_L$ the absorption is mainly governed by the *sheath inverse bremsstrahlung* (SIB) process [Catto & More, 1977; Yang et al., 1995]. Collisions take place close to the vacuum-material interface in the skin depth since the electron transit time through this skin depth becomes longer than the laser period. The corresponding absorption efficiency is given by [Rozmus et al., 1996]:

$$f_{SIB} \sim 6.4 \left(\frac{v_{Te}}{c}\right)^3 \left(\frac{\omega_{pe}}{\omega_L}\right)^2 \tag{2.47}$$

The absorption efficiency by SIB decreases when the laser frequency increases. AS and SIB constitute in fact two complementary faces of the same physical process. The main difference is that the fastest electrons, characterized by $v_x > v_{Te}$, v_x being the electron speed along the laser incident axis, are more efficiently accelerated by SIB while the AS mechanism transfers the laser energy to the slowest electrons, characterized by $v_x < v_{Te}$.

Resonance absorption

All the physical processes previously described involve non-collective mechanisms. For laser intensities $I < 10^{16}$ W.cm^{-2} a linear collective absorption mechanism, called *resonance absorption*, takes place when an incident laser pulse enters in resonance with ω_{pe} and drives an electrostatic wave [Freidberg et al., 1972]. Resonance absorption requires two conditions. First, the laser field must have a component in the longitudinal direction, parallel to the electron density gradient ∇n_e. This criterion can be fulfilled by considering a p-polarized incident laser pulse[1] incident at the angle θ with respect to the target normal. Indeed in this situation the laser pulse is reflected from the density defined by $n_e = n_c \cos^2\theta$. The longitudinal component of the electric field then tunnels up to the critical density n_c, forcing electrons to oscillate along the plasma density gradient, driving a plasma wave. Figure 2.7 illustrates this geometry of incidence.

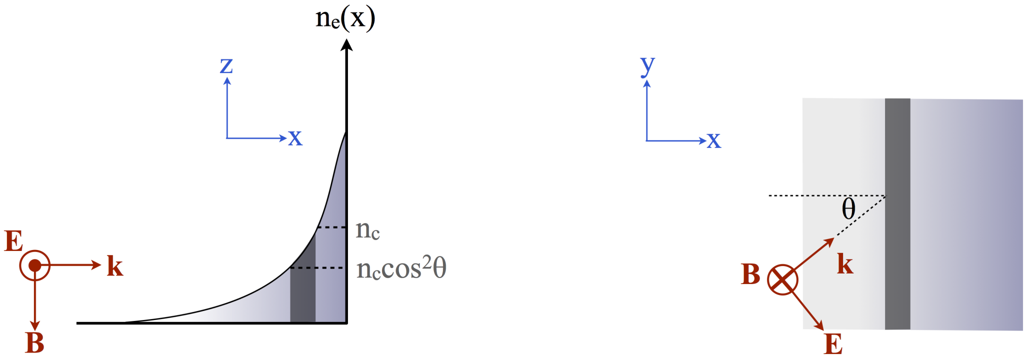

Figure 2.7: Geometry of interaction between a laser pulse and a density gradient fulfilling the resonance absorption interaction conditions. The incoming laser pulse is polarized in the $x-y$ plane of incidence. The incident wave vector makes an angle θ with respect to the target normal. The dark grey area corresponds to the region between the density $n_c \cos^2\theta$ where most of the pulse is specularly reflected and the critical density n_c. A fraction of the laser field tunnels through this region and eventually excites a plasma wave at the critical density.

Another condition required for resonance absorption to occur is that several optical cycles of the laser pulse must be able to penetrate into the underdense pre-plasma formed in front of the target. In other words, the resonance absorption requires long enough gradient scale lengths $L = (\nabla n_e/n_e)^{-1}$. Indeed, if this last condition is not fulfilled the amplitude of oscillation of electrons becomes larger than L and the plasma wave is excited and completely damped at each optical cycle. This criterion is mathematically summarized by the parameter $\xi = (kL)^{1/3}\sin\theta$, with the term kL being proportional to the number of oscillations in the pre-plasma. If one considers a long density gradient characterized by $kL >> 1$ the fraction of laser energy absorbed by resonance absorption is given by [Gibbon, 2005]:

$$f_{ra} \simeq 2.65\xi^2 \exp\left(-4\xi^3/3\right) \tag{2.48}$$

For $\theta = 0$, at normal incidence, $f_{ra} = 0$. The excited plasma wave growth is however limited by several mechanisms, the most important being the wave breaking. It is worth mentioning that unlike the linear mechanisms presented above, the resonance absorption transfers the laser energy to a small fraction of the electrons. In other words, this mechanism is responsible for the generation of a population of fast electrons. Numerical simulations confirmed by experimental results have shown that the energy distribution of accelerated fast electrons is close to a Maxwellian distribution characterized by a temperature $T_{ra}[\text{keV}] \simeq 14(I_{16}\lambda_{L,\mu\text{m}}T_e)^{1/3}$, with T_e the plasma background electron temperature in keV, I_{16} the laser pulse intensity in units of W.cm^{-2} and $\lambda_{\mu\text{m}}$ the laser wavelength in microns [Forslund et al., 1977; Estabrook & Kruer, 1978].

---

[1] A p-polarized laser pulse refers to a polarization of the electric field in the plane of incidence whereas a s-polarized laser pulse refers to a polarization perpendicular to the plane of incidence

2.3.3 Non-linear absorption mechanisms

When exceeding laser intensities of $\sim 10^{16}$ W.cm^{-2}, the amplitude of oscillation of electrons in the laser field v_{quiv}/ω_L could be higher than the skin depth c/ω_{pe}. In this situation, non-linear absorption mechanisms must be taken into account.

Vacuum heating

For sharp density gradients the resonance absorption ceases to work. Another absorption mechanism responsible for the generation of fast electron population was proposed by Brunel [1987] and is called *vacuum heating*. The Brunel mechanism takes place when a p-polarized laser pulse interacts at oblique incidence with a very steep density gradient. The oblique incidence is required in order for the laser electric field to contain a component along the density gradient direction. Unlike for the resonance absorption mechanism, the laser field cannot drive any plasma wave. However the laser electric field is sufficiently intense to drag out into vacuum a fraction of electrons initially in the target skin depth, beyond the Debye screening length, during a half-period of the pulse. The conjugate action of the reversed laser electric field during the second half-period of the pulse with the intense space charge electric field created by the lack of negative charges at the target surface accelerates the expelled electrons back into the plasma. Re-injected electrons propagate significantly beyond the skin depth, where the laser is stopped, and lose their energy in collisions. Vacuum heating is responsible for the acceleration of electrons up to energies close to the ponderomotive potential $U_p = [\sqrt{(1+a^2)} - 1]m_e c^2$, detailed in the next section. The laser absorption coefficient due to the Brunel mechanism can be estimated with a capacitor model, neglecting the effect of the magnetic field. Let us consider a p-polarized laser beam incident on a solid mirror-like target characterized by a density n_e. The incoming laser pulse, striking the target at an angle θ from target normal, is characterized by an electric field of amplitude E_L with a component along the target normal direction of amplitude $E_d = E_L \sin\theta$. A standing wave is soon created resulting from the interaction between the incident pulse and the reflected pulse of equal amplitude. The component of the laser electric field E_d is consequently equal to $E'_d = 2E_L \sin\theta$, provided that the whole pulse is reflected. In a more realistic case one has to take into account the imperfect material reflectivity through the coefficient of reflexion η_a, leading to a driving field $E''_d = [1 + (1-\eta_a)^{0.5}]E_L \sin\theta$. This field is responsible for the extraction of a thin layer of electrons up to a distance Δx from the target normal, leaving the target surface with a positive charge, and consequently creating a capacitor. The electric field between the two plates is equal to $E_{\text{cap}} = \sigma/\epsilon_0$ with $\sigma = n_e e \Delta x$. Considering that the accelerated electron mean kinetic energy is equal to the ponderomotive potential U_p one can show that the fraction of absorbed energy by the Brunel mechanism writes in a non relativistic limit[Gibbon, 2005]:

$$f_B^{\text{non-relat}} = \frac{a}{2\pi}\left[\frac{(1+8\beta_B)^{0.5}-1}{2\beta_B}\right]^3 \alpha(\theta) \tag{2.49}$$

with $\beta_B = a\alpha/2\pi$ and $\alpha = \sin^3\theta/\cos\theta$.

The angular dependence of the absorption coefficient is plotted in Fig.2.8. It is worth mentioning that the previous approach is not valid high intensity since the contribution of the magnetic field is neglected. Considering a more realistic geometry with not so steep density gradients Gibbon & Bell [1992] have shown, by performing numerical simulations, that the transition between resonance absorption and vacuum heating is more complex and fairly depends on the laser irradiance $I_L\lambda_L^2$ and on the gradient scale-length. The weakest point of the simple electrostatic model presented above is that it is rather unadapted to describe the electric current setting up along the target surface due to the oblique incident plane wave. A magnetic

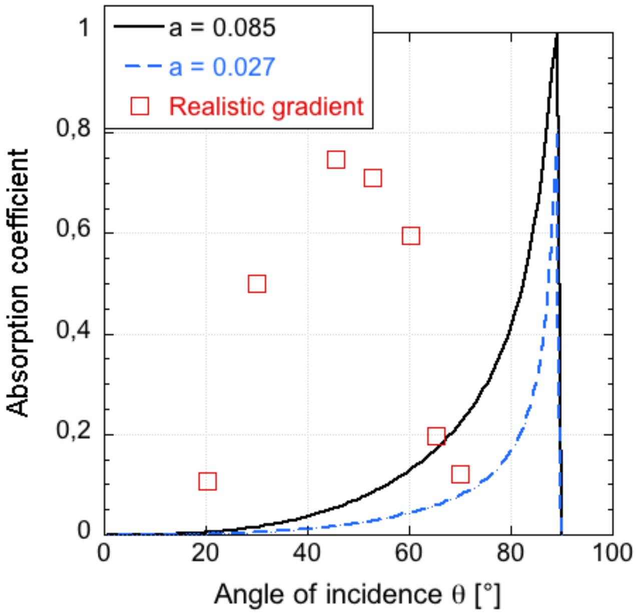

Figure 2.8: Angular dependence of the absorption coefficient by the Brunel mechanism as a function of the angle of incidence. The different curves represent the predictions in the non-relativistic cases for laser normalized intensities $a = 0.085$ (black solid line) and $a = 0.027$ (blue dotted line), corresponding to laser intensities $I = 10^{16}$ W.cm^{-2} and $I = 10^{15}$ W.cm^{-2} with $\lambda_L = 1\ \mu$m, respectively. Results of more realistic numerical simulations performed by Gibbon & Bell [1992] with a density gradient $L = 0.1\lambda_L$ and a laser irradiance $I\lambda_L^2 = 10^{16}$ W.cm^{-2}.μm^{-2} are plotted with square open symbols. The maximum absorption occurs with an angle of incidence close the 45°.

field is indeed created that could deflect fast electrons and prevent a significant fraction of them from re-entering the target. In addition some electrons keep circulating in vacuum, creating an electric field that tends to prevent further electrons from being ejected from the target. This numerical study also showed that the optimum incident angle that maximizes the laser absorption is closer to $\theta_{\max} \simeq 45°$. Finally, for small density gradients characterized by $L \sim 0.1\lambda_L$ and for laser intensities in the $[10^{16} - 10^{18}]$ W.cm^{-2} range, the vacuum heating becomes the dominant electron acceleration mechanism. The maximum absorption of the Brunel mechanism peaks at $\sim 70\%$ at moderate intensities and decreases down to $\sim 10\%$ at high irradiance.

Relativistic $\mathbf{j} \times \mathbf{B}$ heating

The Brunel mechanism neglects the influence of the magnetic field of the laser pulse. A similar effect to vacuum heating on a steep density gradient can be also driven by the $\mathbf{v} \times \mathbf{B}$ component of the Lorentz force. This so called $\mathbf{j} \times \mathbf{B}$ heating, introduced by Kruer & Estabrook [1985], becomes the dominant absorption mechanism at high laser irradiances $I_L\lambda_L^2 \geq 10^{18}$ W.cm^{-2}.μm^{-2}. In order to explain the basic principle of this heating mechanism, it is first necessary to derive the expression of the ponderomotive force acting on a single electron during a non-relativistic laser interaction. Let us consider an incident pulse linearly polarized characterized by an electric field $\mathbf{E} = \mathbf{E_0}(\mathbf{r}, \mathbf{t}) \cos(\omega_L t)$ and a magnetic field $\mathbf{B}(\mathbf{r}, t)$. The electron movement is ruled by the Lorentz force:

$$m_e \frac{d\mathbf{v}}{dt} = -e\left[\mathbf{E}(\mathbf{r}, t) + \mathbf{v} \times \mathbf{B}(\mathbf{r}, t)\right] \tag{2.50}$$

At the lowest order the electron simply oscillates around its initial position $\mathbf{r_0}$ due to the action of the electric field only. The trajectory of the electron consequently writes:

$$\mathbf{r_1} = \frac{e}{m_e\omega_L^2}\mathbf{E}(\mathbf{r_0}, t) \tag{2.51}$$

If one considers the second order the electron movement is ruled by:

$$m_e \frac{d\mathbf{v_2}}{dt} = -e\left[(\mathbf{r_1}.\nabla)\mathbf{E}(\mathbf{r_0}, t) + \mathbf{v_1} \times \mathbf{B}(\mathbf{r_0}, t)\right] \tag{2.52}$$

where the electric field has been expanded around the $\mathbf{r_0}$ position. By injecting the expression of $\mathbf{r_1}$ given by Eq. 2.51 into Eq. 2.52, and by using Maxwell-Faraday's equation, one finds:

$$m_e \frac{d\mathbf{v_2}}{dt} = -\frac{e^2}{m_e\omega_L^2}\left[(\mathbf{E_1}.\nabla)\mathbf{E_1} - \omega_L \mathbf{E_1} \times \int (\nabla \times \mathbf{E_1})\, dt\right] \tag{2.53}$$

The averaging of Eq.2.53 over a single laser period yields:

$$\langle m_e \frac{d\mathbf{v_2}}{dt}\rangle = -\frac{e^2}{m_e\omega_L^2}\langle(\mathbf{E_1}.\nabla)\mathbf{E_1}) + \mathbf{E_1} \times \nabla \times \mathbf{E_1}\rangle \tag{2.54}$$

Using the following vectorial identity

$$\nabla(\mathbf{AB}) = (\mathbf{A}.\nabla)\mathbf{B} + (\mathbf{B}.\nabla)\mathbf{A} + \mathbf{A} \times \nabla \times \mathbf{B} + \mathbf{B} \times \nabla \times \mathbf{A}$$

Equation 2.54 can be simplified:

$$\langle m_e \frac{d\mathbf{v_2}}{dt}\rangle = -\frac{1}{4}\frac{e^2}{m_2\omega_L^2}\nabla\langle\mathbf{E_1^2}\rangle = -\frac{1}{4}\frac{e^2}{m_2\omega_L^2}\langle\left[\nabla(|\mathbf{E_0^2}|) + \nabla(|\mathbf{E_0^2}|)\cos(2\omega_L t)\right]\rangle \tag{2.55}$$

The slowly variable term of Eq. 2.55 compared to the laser frequency is called the *ponderomotive force* $\langle \mathbf{F_p} \rangle$:

$$\langle \mathbf{F_p} \rangle = -\frac{e^2}{4 m_e \omega_L^2} \nabla(|\mathbf{E_0^2}|) = -\frac{e^2}{4 m_e \omega_L^2} \frac{1}{2c} \nabla I \tag{2.56}$$

If we consider now an incident laser pulse on a solid target, all charged particles, independently of their charge, are consequently pushed away from high intensity laser regions, both radially and inside the target. However this force being proportional to the inverse of the particle mass, its direct effect on ion trajectories is fairly small. The charge separation electric field created by the efficient ejection of electrons drives ions at higher time scales, of the order of several ps. This effect is directly involved in the hole boring mechanisms were the laser pulse is responsible for the inward movement of the target surface [Wilks et al., 1992].

The second term in Eq.2.55 exhibits a high frequency component, oscillating at twice the laser frequency, and which is due to the magnetic component of the Lorentz force. Electrons oscillate along the laser propagation axis at the vacuum-solid interface. The inherent inhomogeneties of the laser pulse allow non-adiabatic coupling between the pulse and those particles: bunches of electrons accelerated up to several MeV are injected into the target at each half laser period. This effect is more efficient at normal incidence angle of the laser pulse, and with increasing laser intensity.

The expression of the ponderomotive force has been generalized for relativistic intensities [Quesnel & Mora, 1998; McKinstrie & Dubois, 1988]. Its expression is given by:

$$\mathbf{F_p} = -m_e c^2 \nabla \langle \gamma \rangle \tag{2.57}$$

with $\langle \gamma \rangle = \sqrt{1 + \langle \mathbf{p^2} \rangle / m_e^2 c^2 + e^2 \langle \mathbf{A^2} \rangle / m_e^2 c^2}$, $\langle p \rangle$ the mean momentum of the electron and $\mathbf{p}_{\text{osc}} = e\mathbf{A}/m_e c$ the quiver impulsion. This nonlinear force can be derived from the ponderomotive potential:

$$U_p = m_e c^2 \left(\langle \gamma \rangle - 1 \right) \tag{2.58}$$

A set of numerical simulations performed by Wilks et al. [1992] have shown that the temperature of accelerated electrons is close to the ponderomotive potential:

$$T_{\mathbf{j}\times\mathbf{B}} \simeq m_e c^2 \left[\sqrt{1 + a^2} - 1 \right] = m_e c^2 \left[\sqrt{1 + 0.73 I_{18} \lambda_{L,\mu\text{m}}^2} - 1 \right] \tag{2.59}$$

Parametric instabilities

When considering fairly long density gradients, characterized by long underdense pre-plasmas generated by the ASE pedestal, other nonlinear mechanisms can be responsible for the acceleration of electrons. The incident laser pump $(\omega_0, \mathbf{k_0})$ wave propagating in this underdense region can decay into two daughter waves, called *parametric instabilities* [Drake, 1974]. The nature of the excited waves can be rather different: ion acoustic wave ω_{ia}, electron plasma wave ω_{pe} and electromagnetic wave ω_{EM}. In all cases the three-wave interaction processes are ruled by the phase matching conditions:

$$\omega_0 = \omega_1 + \omega_2 \tag{2.60}$$

$$\mathbf{k_0} = \mathbf{k_1} + \mathbf{k_2} \tag{2.61}$$

with $1, 2$ referring to the daughter waves. Four different mechanism of wave decay can be found, depending on their location (Fig. 2.9):

- Stimulated Raman scattering: the incident wave decays into an electron plasma wave and into a diffused electromagnetic wave $(\omega_L = \omega_{\text{pe}} + \omega_{\text{EM,diff}})$

- Stimulated Brillouin scattering: the incident wave decays into a diffused electromagnetic wave and into an ion acoustic wave ($\omega_L = \omega_{\text{EM,diff}} + \omega_{\text{ia}}$)
- Two plasmon decay: as the name of this instability suggests the incident wave decays into two electron plasma waves ($\omega_L = \omega_{\text{pe}} + \omega'_{\text{pe}}$)
- Ion-acoustic decay: the incident waves decays into an electron plasma wave and into an ion acoustic wave $\omega_L = \omega_{\text{pe}} + \omega_{\text{ia}}$

In the case of short laser pulses like those involved in our experiments the motion of ions during this small amount of time can be neglected so that stimulated Brillouin scattering and ion-acoustic decay can be neglected. Stimulated Raman scattering and two plasmon decay are for instance responsible for the acceleration of fast electrons up to several MeV, until wave breaking.

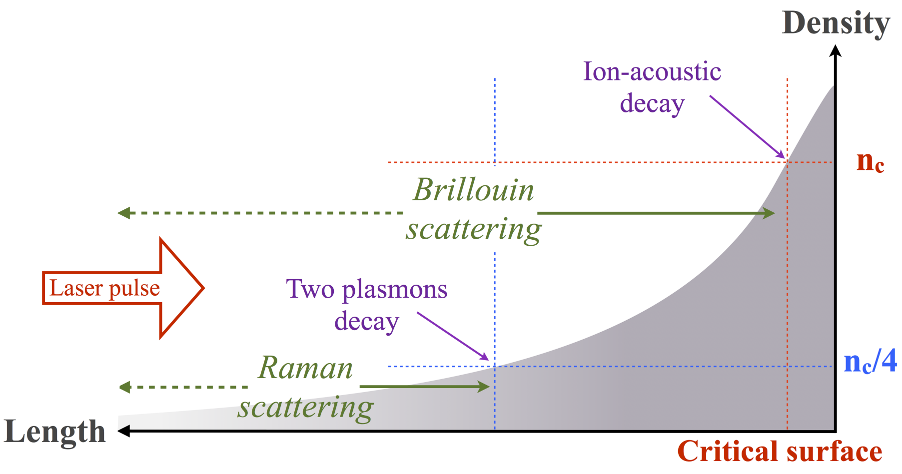

Figure 2.9: Schematic of the possible location creation for the parametric instabilities. The stimulated Raman scattering can grow below the quarter of the critical density. The stimulated Brillouin scattering grows below the critical density. The two plasmon decay and ion-acoustic decays occur near a quarter of the critical density and near the critical density, respectively.

2.3.4 Conclusion on acceleration mechanisms

As described in this section there exist a large number of electron acceleration mechanisms which mainly depend on the laser intensity regime and the plasma density gradient length. In fact an even more complicated situation could be considered since the different processes can act together. For weakly relativistic intensities $I < 10^{18}$ W.cm^{-2} and for steep density gradients $L\lambda_L \leq 0.1$ the dominant mechanism is vacuum heating, provided that the laser pulse arrives at the target at oblique incidence, injecting bunches of fast electrons into the target at each laser period. For smaller density gradients lengths the resonance absorption is the dominant absorption mechanism. In our experiments characterized by relativistic interactions ($I \in [10^{19}, 10^{20}]$ W.cm^{-2}), $\mathbf{j} \times \mathbf{B}$ heating becomes the dominant mechanism, injecting electron bunches up to several MeV at each half laser period. In addition, fast electrons are injected closer to the laser pulse incident direction for highly-relativistic intensities. This mechanism, whose efficiency increases with the laser intensity, is also responsible, via the ponderomotive force, for the steepening of the density gradient.
To conclude this chapter, Fig. 2.10 present a typical spectrum obtained by coupling a $I > 10^{20}$ W.cm^{-2}, 0.7 ps duration short pulse with an aluminum solid target. This spectrum was

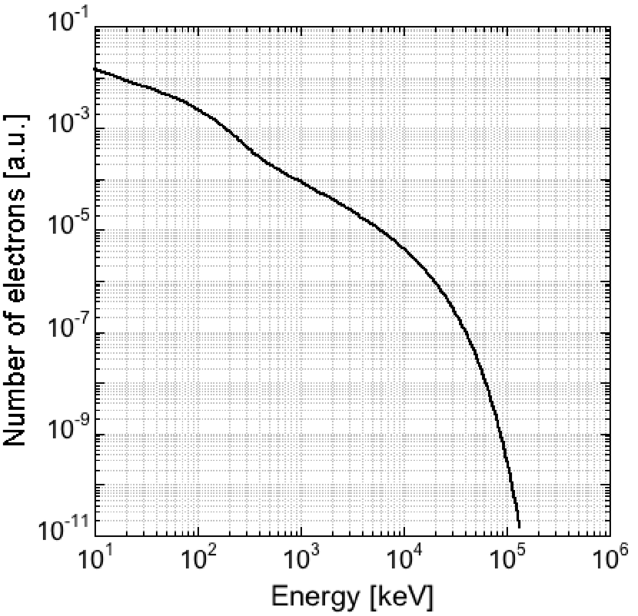

Figure 2.10: Fast electrum spectrum generated by coupling the $I > 10^{20}$ W.cm^{-2}, 0.7 ps Titan short pulse beam with an aluminum target.

generated on the JLF-Titan laser system during an experimental campaign presented in chapter 4. One can note that the different absorption mechanisms are responsible for the acceleration of a broad spectrum of fast electrons in the $\sim$ 10 keV - 100 MeV energy range. The current lack of unified theory that could quantitatively describe the laser absorption and the generated fast electron spectrum for a wide range of parameters would necessitate to experimentally assess the role of the different acceleration mechanisms. This characterization is however beyond the scope of this thesis

2.4 Fast electron beam collisional transport

2.4.1 Angular diffusion

Let us begin this chapter by a description of elastic collisions, which are of a primary importance for the fast electron transport. Elastic collisions originate from the interaction between a fast electron and a point-like ion, fairly heavier than the incoming particle, with a mass considered as infinite. During the collision the ion only gains a small fraction of the incident particle energy. The electron is consequently angularly scattered: its trajectory slightly changes while its energy remains approximately constant. Considering the collision of an incident fast electron with a non-relativistic energy with an immobile ion with no internal structure, generating a Coulombian potential, the differential cross section derived by Rutherford is given by:

$$\frac{d\sigma_{\text{Ruth}}}{d\Omega} = 4r_e^2 \frac{Z^2c^4}{v_e^4} \left(\frac{1}{4\sin^2\left(\frac{\theta}{2}\right)} \right)^2 \tag{2.62}$$

with $r_e = e^2/(4\pi\epsilon_0 m_e c^2)$ the electron classical radius, v_e the incident electron speed and θ the electron diffusion angle. Small angle deviations are consequently dominating over large angle deviations. A singularity at $\theta \to 0$ is due to the long range character of the Coulomb potential. It is corrected by taking into account the screening effects either by the atomic electrons in a neutral atom or by the Debye screening by free electrons in a plasma. The screened potential chosen in a non-ionized media is the Wentzel-Yukawa-like potential, $V(r) \sim (Ze/r)\exp-(r/a)$, with a the screening length equal to the Thomas-Fermi radius $a_{TF} = 0.885(\hbar^2/m_e e^2)Z^{-1/3}$. This potential decreases faster than the Coulomb potential beyond the screening length. Using a quantum approach based on the first Born approximation which considers a small angle deviation and a moderate Z target, the Rutherford cross section corrected by Nigam et al. [1959] is given by:

$$\frac{d\sigma}{d\Omega} = 4r_e^2 \frac{Z^2}{\beta^4\gamma^2}\left(\frac{1}{4\sin^2\left(\frac{\theta}{2}\right)+\theta_0^2}\right)^2 \tag{2.63}$$

where relativistic effects are taken into account in the Lorentz factor γ. This corrected expression introduces the screening angle $\theta_0 = \alpha Z^{1/3}/(0.885\gamma\beta)$, with $\alpha = e^2/(4\pi\epsilon_0\hbar c)$ the fine structure constant. The screening angle similarly to the Coulomb logarithm in a plasma removes the divergence of Rutherford's cross section at small deviation angles.

The cross sections are describing the probability of a single collision of an electron with an isolate ion. A more realistic situation of an entire fast electron beam scattering over a large number of ions are described by the scattering theories which are using statistical approaches. We present in this section the principal results of the multiple scattering theory [Moliere, 1948], completed by Bethe [1953], which has the advantage of being fully analytic even if restricted to the small angle approximation. It is worth mentioning that a more complex multiple diffusion theory, valid for all angles of scattering, has been developed by Goudsmit & Saunderson [1940].

Molière's multiple diffusion theory consists in solving the transport equation of the angular distribution function $f_M(\mathbf{\Omega}, s)$, with s the thickness of the crossed material, given by:

$$\frac{\partial f(\mathbf{\Omega}, s)}{\partial s} = n_i \int \left[f(\mathbf{\Omega}-\mathbf{\Omega}', s) - f(\mathbf{\Omega}, s)\right]\frac{d\sigma}{d\theta'}d\mathbf{\Omega}' \tag{2.64}$$

with $\mathbf{\Omega}-\mathbf{\Omega}'$ the direction of the electron velocity before the last scattering event and $d\mathbf{\Omega}' \simeq \theta' d\theta' d\phi$. Assuming a cylindrical symmetry of the fast electron beam the distribution function $f_M(\theta, s)$ can be developed on a Bessel function basis $J_0(x)$:

$$f_M(\theta, s)\theta d\theta = \Theta d\Theta \sum_{n=0}^{\infty} \frac{f^{(n)}}{B^n} \tag{2.65}$$

with

$$f^{(n)}(\Theta) = \frac{1}{n!}\int_0^\infty u J_0(u\Theta)\left[\frac{u^2}{4}\ln\left(\frac{u^4}{4}\right)\right]^n \tag{2.66}$$

This formula introduces the reduced angle $\Theta = \theta/(\theta_c\sqrt{B})$, with B a parameter introduced by Molière as the solution of the equation given by $B - \ln B = b$. The angle θ_c, first introduced by Williams [58] and re-used by Molière, is defined as the probability equal one of a single scattering event at angle $> \theta_c$ takes place over the length s. The angle θ_c is given by:

$$\theta_c = 4\pi n_i s Z(Z+1)\left(\frac{r_e}{\gamma\beta^2}\right)^2 \tag{2.67}$$

with n_i the atomic density of the material. The parameter b is given by $b = \ln(\theta_c^2/\theta_M^2) - 0.154$, with θ_M the screening angle exactly calculated by Molière and given by:

$$\theta_M = \theta_0^2 \left[1.13 + 3.76 \left(\frac{Z\alpha}{\beta} \right)^2 \right] \tag{2.68}$$

This screening angle replaces the angle θ_0 calculated in the Born approximation in the previous section. In its first development, Molière considered that its theory is valid when the number of collisions given by $\exp(b)$ is sufficiently large (≥ 20). Gremillet [2001] showed however by a set of Monte-Carlo simulations that this figure can be decreased down to 5 collisions.
Bethe showed that the three first terms in Eq. 2.66, $f^{(1)}$, $f^{(2)}$ and $f^{(3)}$, are sufficient to fully calculate the angular distribution function within a 1% precision for all angles. When considering small scattering angles so that $\Theta \leq 2$ the first order of Molière's angular distribution function $f^{(0)}$ dominates over the correction given by $f^{(1)}$. The first order is given by:

$$f^{(0)}(\theta, s) = 2 \exp \left(-\frac{\theta^2}{\theta_c^2 B} \right) \tag{2.69}$$

In other words, assuming a large number of collisions and small angles of deviation, or a small thickness s, the angular distribution function after crossing a material can be approximated by a Gaussian function. This result is a direct consequence of the central limit theorem stating that a sufficiently large number of selections of a random variable tends to the normal distribution. For small angles of deviation this first Gaussian term is dominant over the higher orders of $f^{(n)}$. The mean quadratic diffusion angle given by the full width at half-maximum (FWHM) of the previous function finally writes:

$$\sqrt{\langle \theta^2 \rangle} = \theta_c \sqrt{\ln 2 \ln \left(\frac{\theta_c^2}{1.167 \theta_M^2} \right)} \tag{2.70}$$

where a large number of collisions was considered in such a way that $B \sim b$.

This theory is only valid when considering the propagation of electrons in a cold non-ionized medium. In our experiments, targets were often heated up to several eV leading to an ionization of the material to a degree Z^*. In this case, the free-electrons also contribute to the screening of the Coulomb potential. The angle of scattering calculated in Eq. 2.70 remains however valid provided the new screening angle θ_M is corrected. To do so, the Coulomb potential is modified as [Gremillet, 2001]:

$$V(r) = \frac{Ze}{4\pi\epsilon_0 r} \left[\underbrace{\left(1 - \frac{Z^*}{Z} \right) \exp(-r/a_M)}_{\text{bound electrons}} + \underbrace{\left(\frac{Z^*}{Z} \right) \exp(-r/\lambda_{DH})}_{\text{free electrons}} \right] \tag{2.71}$$

with $a_M = \hbar/p\theta_M$ Molière's screening parameter and λ_{DH} the Debye-Huckel length given by [Lampe, 1970]:

$$\lambda_{DH} = \sqrt{\left(\frac{\epsilon_0 k_B T_e}{e^2 n_i Z^* (Z^* + 1)} \right)} \tag{2.72}$$

This potential is inspired by Nardi & Zinamon [1978]. The screening angle, calculated by [Gremillet, 2001] is given by:

$$\theta_p = \theta_D^{\xi_1} \theta_M^{\xi_2} \exp\left[-q(1-q) \right] \tag{2.73}$$

with $q = Z^*/Z$, $\theta_D = \hbar/(p\lambda_{DH})$ and the parameters ξ_1 and ξ_2 defined as:

$$\xi_1 = q^2 - \frac{2q(1-q)}{\frac{\theta_M^2}{\theta_D^2} - 1} \tag{2.74}$$

$$\xi_2 = (1-q)^2 + \frac{2q(1-q)}{1 - \frac{\theta_D^2}{\theta_M^2}} \tag{2.75}$$

The scattering angle is finally obtained by replacing the screening angle θ_M in Eq. 2.70 by θ_p, taking into account the ionization degree of the plasma depending on its temperature. The dependence of the scattering angle in function of the incident electron energy and of the penetration range for different materials is presented on Fig. 2.11. The mean deviation angle increases with the penetration range s and with the background electron temperature T_e, but decreases when the energy of the incident electron increases. The propagation of high energy electrons ($\gtrsim$ 500 keV) is not so much influenced by elastic collisions. In compressed targets however, which is the case in our experiments, the increase of material density is responsible for an enhanced diffusion, even for high energy particles.

2.4.2 Collisional stopping power

During its propagation in a dense matter an electron is slowed-down in collisions with other particles. As mentioned in the previous section, collisions with ions do not contribute to the slowing down of the electron because of a large mass difference: in such an elastic collision the electron is scattered while keeping its initial energy. Collisions with other electrons are responsible for a substantial amount of energy losses. The electron collisional stopping power, defined as the amount of lost energy per unit length due to collisions with the background electrons, can be written as the following:

$$\frac{dE}{ds} = -ZEn_i \int_0^{1/2} \epsilon \frac{d\sigma}{d\epsilon} d\epsilon \tag{2.76}$$

with n_i the density of atoms, $E = (\gamma - 1)m_e c^2$ the energy of the incident electron, $\epsilon = \Delta E/E$ the fraction of transferred energy and $d\sigma/d\epsilon$ the energy transfer differential cross section. The integration interval can be split into two intervals $0 \leq \epsilon \leq \epsilon_1$ and $\epsilon_1 \leq \epsilon \leq 1/2$. The energy fraction ϵ_1 accounts for electron average binding energy in the atomic potential: the incident electron losses $\epsilon < \epsilon_1$ correspond to the atom excitation. The upper limit equal to 1/2 accounts for the indiscernability of two scattered electrons, thus considering that the fastest electron is the incident one. The determination of the electron stopping power mostly consists in evaluating the energy transfer cross section.

Cold-solid material

Let us begin by considering the first energy interval, where the incident electron propagating in cold matter transfers a part of its energy to an atomic bound electron. This collision is responsible from the atomic excitation - the jump of the bound electron from an atomic level to another one. If one takes into account the binding energies of the bound electrons and all the contributions of the excited quantum states, the stopping power is given by [Bethe, 1933]:

$$\left(\frac{dE}{ds}\right)_{\text{bound}}^{\text{cold}} = -ZEn_i \int_0^{\epsilon_1} \epsilon \frac{d\sigma}{d\epsilon} d\epsilon = -En_i Z\sigma_e \left[\ln\left(\frac{2\epsilon_1(\gamma^2-1)(\gamma-1)}{(I_0/m_e c^2)^2}\right) - \beta^2\right] \tag{2.77}$$

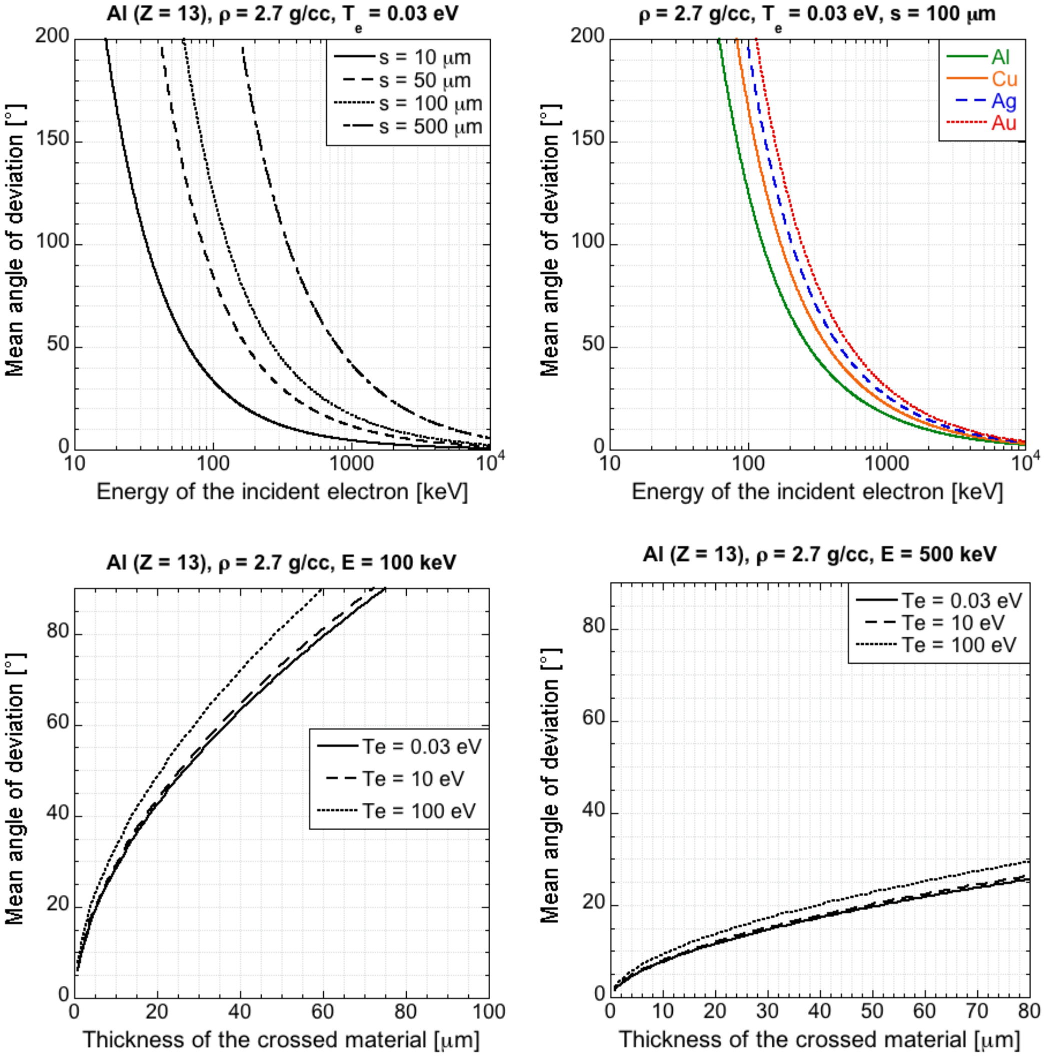

Figure 2.11: (Top left) Mean angle of deviation induced by elastic scattering as a function of penetration depth in a cold aluminum, $s = 10$ μm (solid line), $s = 50$ μm (dashed line), $s = 100$ μm (dotted line) and $s = 500$ μm (dashed-dotted line) and as a function of the incident electron energy. (Top right) Dependence of the mean angle of deviation as a function of the incident electron energy in different cold-solid materials: Al (green solid line), Cu (orange solid line), Ag (blue dashed line) and Au (red dotted line). (Bottom) Mean angle of deviation in aluminum targets for 100 keV (left) and 500 keV (right) electrons as a function of the penetration depth s for the background temperature: 0.03 eV (solid line), 10 eV (dashed line) and 100 eV (dotted line).

with $\sigma_e = 2\pi r_e^2/\beta^2(\gamma-1)$ the electron characteristic cross section, $r_e = e^2/4\pi\epsilon_0 m_e c^2$ the electron classical radius and I_0 the mean ionization potential defined as:

$$\ln I_0 = \sum_n f_n \ln E_n \tag{2.78}$$

where the excitation energy E_n is weighted by the oscillator strengths f_n. Since the oscillator strengths for high binding energies are not so well known, there is a convenient semi-empirical formula calibrated by experimental results introduced by Sternheimer [1966] for $Z \geq 13$:

$$I_0[\text{eV}] \simeq 9.76Z + 58.9Z^{-0.19} \tag{2.79}$$

The binding energy of atomic electrons in the domain $\epsilon > \epsilon_1$ is small compared with the energy of the incident electron. Thus the scattering can be considered as an interaction with a free electron. The corresponding stopping power is given by [Möller, 1932]:

$$\left(\frac{dE}{ds}\right)^{\text{cold}}_{\text{free}} = -ZEn_i \int_{\epsilon_1}^{1/2} \epsilon \frac{d\sigma}{d\epsilon} d\epsilon = -En_i\sigma_e Z \left[\ln \frac{1}{4\epsilon_1} + 1 - \frac{2\gamma - 1}{\gamma^2} \ln 2 + \frac{1}{8}\left(\frac{\gamma - 1}{\gamma}\right)^2\right] \tag{2.80}$$

The total collisional stopping power in a cold matter is finally given by the sum of Eqs. 2.77 and 2.80, which does not depend on ϵ_1 [Rohrlich & Carlson, 1954; Seltzer, 1974]:

$$\left(\frac{dE}{ds}\right)^{\text{cold}}_{\text{total}} = -En_i\gamma_e Z \left[\ln\left(\frac{(\gamma^2-1)(\gamma-1)}{2(I_0/m_ec^2)^2}\right) 1 - \beta^2 - \frac{2\gamma-1}{\gamma^2}\ln 2 + \frac{1}{8}\left(\frac{\gamma-1}{\gamma}\right)^2 - \delta\right] \tag{2.81}$$

An additional parameter δ has been introduced in Eq. 2.112. The electron stopping power model detailed in this section considers a sum of pair collisions. However the propagation of an electron in a dense medium indeed generates a polarization electric field, depending on the material dielectric properties, that screens the incident electron field itself. This so-called *density effect*, introduced by Fermi [1940], is responsible for a decrease of the electron stopping power. The electric field screening effect is enhanced for high energy electrons propagating approximately at the same speed as the polarization cloud given by $c/\sqrt{\epsilon_c}$, with ϵ_c the dielectric permittivity of the crossed material. A further detailed study of density effects performed by Sternheimer et al. [1982] provides an approximate analytical expression for δ:

$$\delta = \begin{cases} 0 & \text{if} \quad X \leq X_0 \\ 4.606X + C + a(X_1 - X)^m & \text{if} \quad X_0 < X < X_1 \\ 4.606X + C & \text{if} \quad X \geq X_1 \end{cases} \tag{2.82}$$

with the different parameters $X = \log(p/m_eC)$, $C = -2\ln(I_0/\hbar\omega_{pe}) - 1$, $a = -(C + 4.606X_0)/(X_1 - X_0)^m$ and $m = 3$. The parameters X_0 and X_1 are defined as:

$$X_0|_{I_0<100\text{eV}} = \begin{cases} 0.2 & \text{if} \quad -C < 3.681 \\ -0.326C - 1 & \text{if} \quad -C \geq 3.681 \end{cases} \tag{2.83}$$

$$X_0|_{I_0>100\text{eV}} = \begin{cases} 0.2 & \text{if} \quad -C < 5.215 \\ -0.326C - 1.5 & \text{if} \quad -C \geq 5.215 \end{cases} \tag{2.84}$$

$$X_1 = \begin{cases} 2 & \text{if} \quad I_0 < 100 \text{ eV} \\ 3 & \text{if} \quad I_0 > 100 \text{ eV} \end{cases} \tag{2.85}$$

As plotted in Fig. 2.12 the density effects via the term δ significatively decreases the electron stopping power at energies of incidence above a few MeV. The evolution of the stopping power for different elements is also presented on Fig. 2.12

Hot-solid material

A hot-enough material is partially ionized, and the stopping power must be modified to account for the collisions with free electrons along with the contribution of bound electrons. The

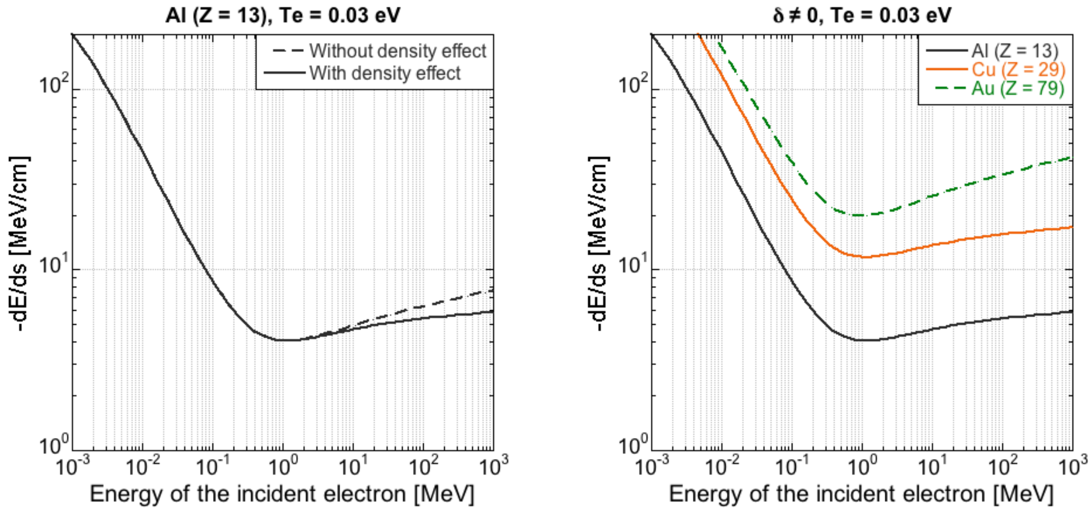

Figure 2.12: (Left) Dependence of the stopping power of an incident electron in a cold aluminum with (black full line) and without (black dotted line) density effect. Density effects become important for $E > 1$ MeV. (Right) Comparison of the stopping power of an incident electron in aluminum (black solid line), copper (orange solid line) and gold (green dotted line) materials taking into account density effect.

corresponding stopping power can be written in a form similar to Eq. 2.112:

$$\left(\frac{dE}{ds}\right)^{\text{hot}}_{\text{bound}} = -En_i\sigma_e(Z - Z^*)\left[\ln\left(\frac{(\gamma^2-1)(\gamma-1)}{2(I_p/m_ec^2)^2}\right) + 1 - \beta^2 - \frac{2\gamma-1}{\gamma^2}\ln 2 + \frac{1}{8}\left(\frac{\gamma-1}{\gamma}\right)^2\right] \tag{2.86}$$

This equation contains the parameter in Z^* the ionization degree, characterizing the number of electrons which actually remain bound to the nucleus. The modified ionization potential I_p takes into account the ionization degree of the atom. Due to the lack of experimental data characterizing the electron collisional stopping power in an ionized medium, the expression of I_p cannot be derived from measurements. A simple analytical formula based on the Thomas-Fermi model was proposed by Hooper [1985] for any element and any charge state:

$$I_p[\text{eV}] = 10Z\frac{\exp\left(1.29q^{0.72-0.18q}\right)}{\sqrt{1-q}} \tag{2.87}$$

with $q = Z^*/Z$ the ionization rate introduced in Eq. 2.73. One can note that the ionization potential increases with increasing values of Z^* due to the weaker screening effect of the nucleus field. A convenient analytical formula based on Thomas-Fermi model and calculating the ionization degree Z^* for any density and any electron temperature can be found in More [1985]. Energy losses due to collisions with the Z^* free electrons write as in Eq. 2.80, with minor modifications:

$$\left(\frac{dE}{ds}\right)^{\text{hot}}_{\text{free}} = -En_i\sigma_eZ^*\left[\ln\frac{1}{4\epsilon_{\min}} + 1 - \frac{2\gamma-1}{\gamma^2}\ln 2 + \frac{1}{8}\left(\frac{\gamma-1}{\gamma}\right)^2\right] \tag{2.88}$$

where the atomic number Z has been replaced by the ionization degree Z^* and the energy transfer ϵ_1 has been replaced by the quantity ϵ_{min} given by [Nardi & Zinamon, 1978]:

$$\epsilon_{\text{min}} = \left(\frac{\lambdabar_r}{D}\right)^2 \tag{2.89}$$

with $\lambdabar_r$ the De Broglie wavelength calculated in the center of mass frame [Solodov & Betti, 2008]:

$$\lambdabar_r = \frac{\hbar}{m_e c\sqrt{2(\gamma - 1)}} \tag{2.90}$$

The distance D is the effective Debye length given by $D = \max(\lambda_{DH}, r_i)$. In the case of a non-degenerated plasma the distance D is given by the Debye-Hückel distance λ_{DH}. In a degenerated dense plasma, the effective Debye length is given by the inter-atomic distance $r_i = [3/(4\pi n_i)]^{(1/3)}$.

Another contribution to the stopping power of electrons in plasmas is due to the electron driven plasma waves. The corresponding contribution to the stopping power writes [Pines & Bohm, 1952]:

$$\left(\frac{dE}{ds}\right)^{\text{hot}}_{\text{plas}} = -E n_i \sigma_e Z^* \ln\left[1 + \left(\frac{v_e}{\omega_{pe}\lambda_D\sqrt{3/2}}\right)^2\right] \tag{2.91}$$

with v_e the incident electron speed and ω_{pe} the electron plasma frequency.
The total collisional stopping power in hot matter finally writes as a sum of the three contributions:

$$\left(\frac{dE}{ds}\right)^{\text{hot}}_{\text{total}} = \left(\frac{dE}{ds}\right)^{\text{hot}}_{\text{bound}} + \left(\frac{dE}{ds}\right)^{\text{hot}}_{\text{free}} + \left(\frac{dE}{ds}\right)^{\text{hot}}_{\text{plas}} \tag{2.92}$$

The dependence of the stopping power in an aluminum at solid density on the temperatures is presented in Fig. 2.13. Plasma waves play an important role in electron stopping power at moderate temperature $T_e > 100$ eV. The associated stopping power becomes comparable to the free electron stopping power at high temperatures $T_e > 1000$ eV. One can also note that the total stopping power in a warm matter depends weakly on the temperature.

2.4.3 Radiative stopping power: bremsstrahlung emission

The Coulomb collision of an incident charged projectile with a charged target particle generates a continuous photon emission, called *bremsstrahlung*, which can be responsible for a significant fraction of the total energy losses. The photon emission is increasing with Z^2 and becomes the dominant energy loss mechanism for highly relativistic electrons. The derivation of the radiative stopping power cross section is not trivial. Many cross sections, exhibiting different validity domains, have been published in the literature. An exhaustive synthesis can be found in [Koch & Motz, 1959]. We derive in this section a qualitative cross section based on an analytical formula providing the essence of the bremsstrahlung emission process. We then describe a more realistic cross section based on the Bethe-Heitler model [Bethe & Heitler, 1934] and modified by Salvat et al. [2006].

Semi-classical model of bremsstrahlung emission

Let us consider an incident particle carrying a charge q and a mass M propagating with the speed $\mathbf{v}$. This situation is illustrated in Fig. 2.14. At the time t' the particle emits an

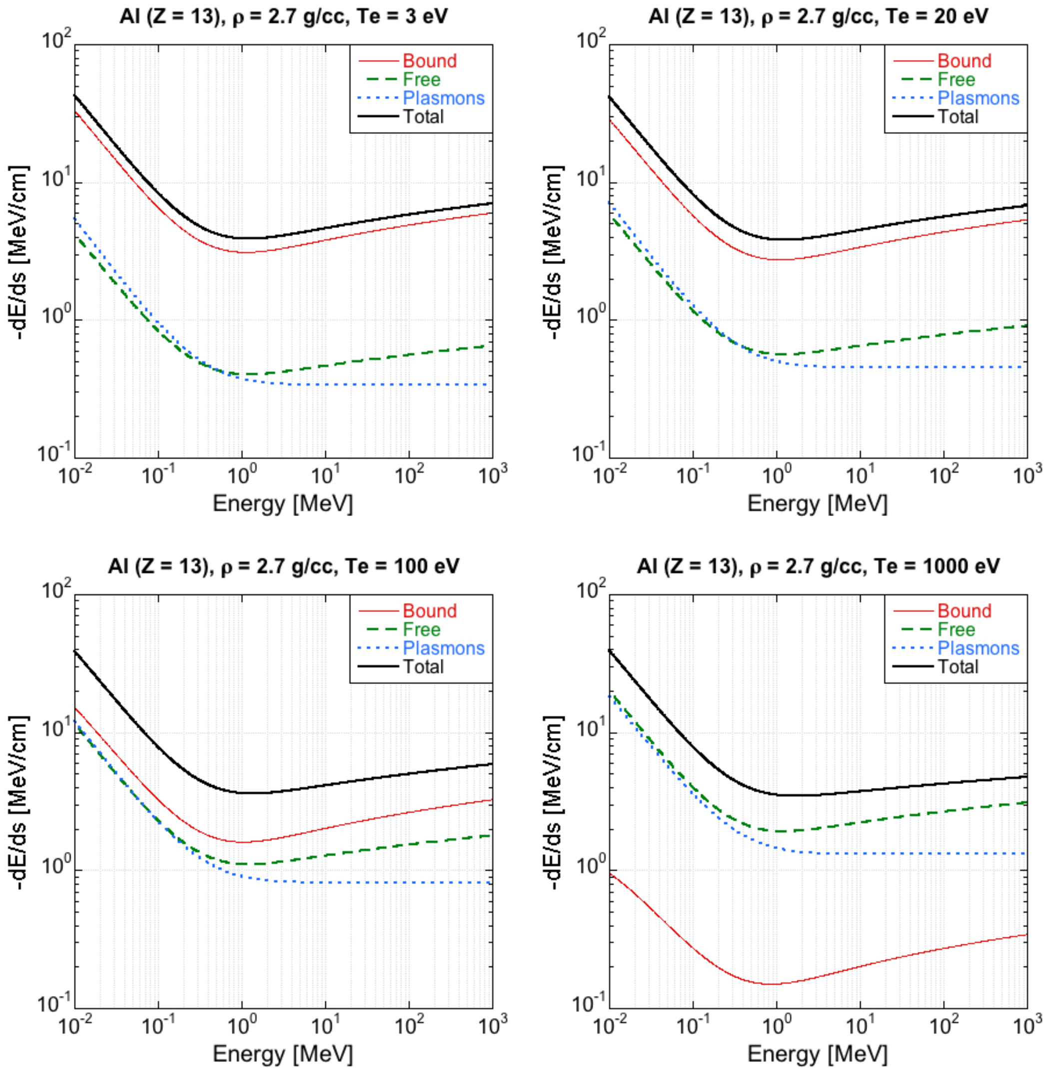

Figure 2.13: Dependence of the stopping power in the aluminum at solid density characterized by an electron temperature $T_e = 3$ eV (top left), $T_e = 20$ eV (top right), $T_e = 100$ eV (bottom left), $T_e = 1000$ eV (bottom right). The contribution of the different processes to the total stopping power (black solid line) is presented: bound electrons (red thin solid line), free electrons (green dashed line) and plasmons (blue dotted line).

electromagnetic field which arrives to the detector at $t > t'$ at a distance $\mathbf{R}(\mathbf{t}')$ from the particle, so that $t = t' + R(t')/c$, where the propagation medium index of refraction is equaled to one for the sake of simplicity. The corresponding electromagnetic potentials, called the Lienard-Wiechert potentials, are given by [Jackson, 1975]:

$$\Phi(\mathbf{r}, t) = \frac{1}{4\pi\epsilon_0} \frac{q}{R - \mathbf{R}.\mathbf{v}/c}\bigg|_{t'} \tag{2.93}$$

$$\mathbf{A}(\mathbf{r}, t) = \frac{\mu_0}{4\pi} \frac{q\mathbf{v}}{R - \mathbf{R}.\mathbf{v}/c}\bigg|_{t'} \tag{2.94}$$

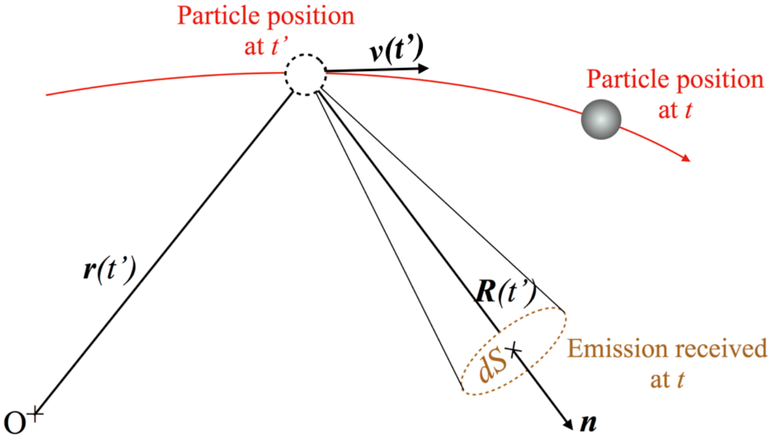

Figure 2.14: Particle position and emission at t' and $t > t'$.

The corresponding electromagnetic fields write:

$$\mathbf{E} = \frac{q}{4\pi\epsilon_0}\left[\underbrace{\frac{(1-v^2/c^2)(\mathbf{n}-\mathbf{v}/c)}{(1-\mathbf{n}.\mathbf{v}/c)^3R^2}}_{\text{Coulomb field}} + \underbrace{\frac{\mathbf{n}\times(\mathbf{n}-\mathbf{v}/c)\times\dot{\mathbf{v}}}{c^2(1-\mathbf{n}.\mathbf{v}/c)^3R}}_{\text{Radiated field}}\right] \tag{2.95}$$

$$\mathbf{B} = \frac{1}{c}\mathbf{n}\times\mathbf{E} \tag{2.96}$$

Both the electric and magnetic fields can be written as the sum of two different contributions. The first one decreasing as R^{-2}, and being negligible far from the particle, is the Coulomb field of the particle. The second term is fundamental for bremsstrahlung emission. It decreases as R^{-1} and depends on the acceleration $\dot{\mathbf{v}}$ of the particle. This second term corresponds to the radiated field by the charged particle.

The quantity of energy dW radiated by the particle during the time interval dt and received by the surface element dS characterized by the solid angle $d\Omega = dS/R^2$ can be calculated by evaluating the module of the Poynting vector $\mathbf{S} = \mathbf{E}\times\mathbf{B}/\mu_0$.

$$\frac{d^2W}{dtdS} = R^2\frac{dP}{d\Omega} = R^2|\mathbf{S}| = R^2\epsilon_0 c|\mathbf{E}_\perp|^2 \tag{2.97}$$

with P the radiated power and $\mathbf{E}_\perp$ the component of the electric field perpendicular to the vector $\mathbf{n}$. By injecting the expression of the electric field given by Eq. 2.96 into the previous equation, the power radiated by unit of solid angle is:

$$\frac{dP}{d\Omega} = \frac{\mu_0 q^2}{16\pi^2 c}\frac{|\mathbf{n}\times(\mathbf{n}-\mathbf{v}/c)\times\dot{\mathbf{v}}|^2}{(1-\mathbf{n}.\mathbf{v}/c)^6} \tag{2.98}$$

The spectral distribution of radiated energy $d^2W/dSd\omega$ can finally be given by operating a Fourier transformation on the previous equation [Jackson, 1975]:

$$\frac{d^2W}{dSd\omega} = \frac{\mu_0 q^2}{16\pi^3 c}\left|\int_{-\infty}^{\infty} dt' e^{-i\omega(t'-\mathbf{n}.\mathbf{r}(t')/c)}\frac{\mathbf{n}\times(\mathbf{n}-\mathbf{v}/c)\times\dot{\mathbf{v}}}{(1-\mathbf{n}.\mathbf{v}/c)^2}\right|^2 \tag{2.99}$$

This expression can be re-written as:

$$\frac{d^2W}{dSd\omega} = \frac{\mu_0 q^2}{16\pi^3 c}\left| \int_{-\infty}^{\infty} dt' e^{-i\omega(t'-\mathbf{n}.\mathbf{r}(t')/c)} \frac{d}{dt'}\left[\frac{\mathbf{n}\times(\mathbf{n}\times\beta)}{1-\beta.\mathbf{n}}\right]\right|^2 \tag{2.100}$$

In order to evaluate this integral we consider the low frequency limit $\omega \rightarrow 0$ so that the exponential term tends to 1. In this particular case the integrand is an exact differential. The spectral density of emission writes:

$$\lim_{\omega\to 0}\frac{d^2W}{dSd\omega} = \frac{\mu_0 z^2 e^2}{16\pi^3 c}\left|\epsilon^*\left(\frac{\beta_{\mathbf{f}}}{1-\mathbf{n}.\beta_{\mathbf{f}}} - \frac{\beta_{\mathbf{i}}}{1-\mathbf{n}.\beta_{\mathbf{i}}}\right)\right|^2 \tag{2.101}$$

with $c\beta_{\mathbf{i}}$ and $c\beta_{\mathbf{f}}$ being the initial and final velocity of the incoming particle, respectively, and ϵ the polarization of the emission. In the relativistic limit $\gamma >> 1$ and by considering a small variation of the module of the speed difference $\Delta\beta = \beta_{\mathbf{f}} - \beta_{\mathbf{i}}$ [2] one can show that the spectral density of emissions writes [Jackson, 1975]:

$$\lim_{\omega\to 0}\frac{d^2W}{dSd\omega} \simeq \frac{\mu_0 q^2}{4\pi^3 c}\gamma^2|\Delta\beta|^2\frac{1+\gamma^4\theta^4}{(1+\gamma^2\theta^2)^4} \tag{2.102}$$

The evolution of the spectral density of emission is plotted in Fig. 2.15. In the relativistic case the photons are radiated into a cone characterized by an angle of aperture $\theta \sim 1/\gamma$. In other words the faster the particle is, the more collimated is the emission. The total intensity of radiated energy per frequency unit in the relativistic limit writes:

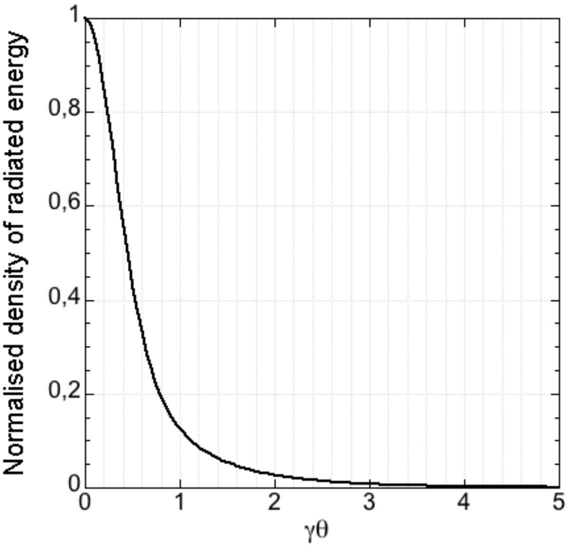

Figure 2.15: Evolution of the normalized density of radiated energy as a function of $\gamma\theta$ in the relativistic limit.

$$\lim_{\omega\to 0}\frac{dW}{dS} = \frac{\mu_0 q^2}{3\pi c}\gamma^2|\Delta\beta|^2 \tag{2.103}$$

---

[2] This condition is equivalent to a small angle of diffusion θ approximation.

In the non-relativistic limit ($\beta << 1$), Eq. 2.103 writes:

$$\lim_{\omega \to 0} \frac{dW}{dS} = \frac{\mu_0 q^2}{3\pi M^2 c^3} Q^2 \tag{2.104}$$

with $Q = |\mathbf{p_f} - \mathbf{p_i}|$ the modulus of the transferred momentum during the collision.
Let us consider now the collision of an incident fast particle with the Coulomb field produced by a fixed atom characterized by a charge Ze. This general scheme of collision is responsible for the bremsstrahlung emission generated during our experiments. The spectral density of emission per unit of momentum dQ, with $Q = 2p^2(1-\cos\theta)$ when considering an elastic collision, writes:

$$\frac{d^2\chi}{d\omega dQ} = \frac{dW(\omega, Q)}{d\omega}.\frac{d\sigma_d(Q)}{dQ} = \frac{dW(\omega, Q)}{d\omega} 8\pi \left(\frac{qZe}{4\pi\epsilon_0 \beta c}\right)^2 \frac{1}{Q^3} \tag{2.105}$$

with $d\sigma_d/dQ$ the Rutherford elastic scattering differential cross section. By integrating over all transferred momentum the emission cross section writes:

$$\frac{d\chi}{d\omega} \simeq \frac{16}{3} \frac{Z^2 e^2}{4\pi\epsilon_0 c} \left(\frac{q^2}{4\pi\epsilon_0 M c^2}\right)^2 \frac{1}{\beta^2} \ln\left(\frac{Q_{\min}}{Q_{\max}}\right) \tag{2.106}$$

It is important to note that this expression is valid for small momentum transfers so that $Q < 2Mc$. The determination of the minimum and maximum values of Q can be done separately in the non-relativistic and in the relativistic limits. We however limit our description to the latter case. The maximum momentum transfer is dictated by the condition of validity of Eq. 2.106 leading to $Q_{\max} \simeq 2Mc$. The minimum transfer of impulsion occurs when the incident particle, the scattered particle and the emitted photon all have the parallel moments so that $Q_{\min} = p_i - p_f - k_p$, with k_p the momentum of the photon. If the incident and scattered particles travel at relativistic speeds the minimum transfer of impulsion writes:

$$Q_{\min} \simeq \frac{M^2 c^3 \hbar\omega}{2E_i E_f} \tag{2.107}$$

By re-injecting $Q_{\min}$ and $Q_{\max}$ into Eq. 2.106 one finds [Jackson, 1975]:

$$\frac{d\chi_{\mathrm{re}}}{d\omega} \simeq \frac{16}{3} \left(\frac{Z^2 e^2}{4\pi\epsilon_0 c}\right)^2 \left(\frac{q^2}{4\pi\epsilon_0 M c^2}\right)^2 \ln\left(\frac{\lambda'' E_i E_f}{Mc2\hbar\omega}\right) \tag{2.108}$$

with λ'' a parameter close to unity. Note that this latter equation obtained in a semi-classical approximation is very similar to what can be found with the quantum formulation using Born's approximation [Jackson, 1975].

Energy distribution of bremsstrahlung emission

A more realistic cross section of bremsstrahlung emission of an electron based on the Bethe-Heitler model was proposed by Salvat et al. [2006]. This model based on Born's approximation requires for the kinetic energy of both the incident and the scattered electrons to be much larger than $m_e c^2$, meaning that the particles must be relativistic. The screening of the nucleus electric field is chosen as an exponential attenuation form, derived from Wentzel's model [Wentzel, 1927], corresponding to the following electron density:

$$\rho_e(r) = \frac{Z}{4\pi R^2} \frac{1}{r} \exp\left(-r/R\right) \tag{2.109}$$

with $R = 0.885 a_B Z^{-1/3}$ the screening radius equal to the Thomas-Fermi radius and $a_B = 4\pi\epsilon_0\hbar^2/m_e e^2$ the Bohr radius. The bremsstrahlung emission cross section is given by:

$$\frac{d\sigma}{dW} = r_e^2 \alpha Z^2 \frac{1}{W}\left[\epsilon^2\phi_1(b) + \frac{4}{3}(1-\epsilon)\phi_2(b)\right] \tag{2.110}$$

with $\alpha = 1/137.036$ the fine structure constant, r_e the classical electron radius, W the emitted photon energy $(0 < W < E)$ and the parameters ϵ, ϕ_1, ϕ_2, b given by:

$$\begin{aligned}
\epsilon &= \frac{W}{\gamma m_e c^2} \\
b &= \frac{R m_e c}{\hbar}\frac{1}{2\gamma}\frac{\epsilon}{1-\epsilon} \\
\phi_1(b) &= 4\ln\left(R m_e c/\hbar\right) + 2 - 2\ln\left(1+b^2\right) - 4b\arctan\left(1/b\right) \\
\phi_2(b) &= 4\ln\left(R m_e c/\hbar\right) + 7/3 - 2\ln\left(1+b^2\right) - 6b\arctan\left(1/b\right) \\
&\quad - b^2\left[4 - 4b\arctan\left(1/b\right) - 3\ln\left(1+b^{-2}\right)\right]
\end{aligned} \tag{2.111}$$

The scaled bremsstrahlung energy spectrum $\xi = \frac{\beta^2}{Z^2} W \frac{d\sigma}{dW}$ is plotted in Fig. 2.16 for several incident electron energies for the aluminum and gold targets. A summary of more complex but more accurate radiative cross sections was made by Seltzer & Berger [1986] in the 1 keV − 10 GeV energy interval. Results from this study are also plotted in Fig. 2.16 in the aluminum target case. One can note that the difference with the Bethe-Heitler model increases with the incident electron energy.

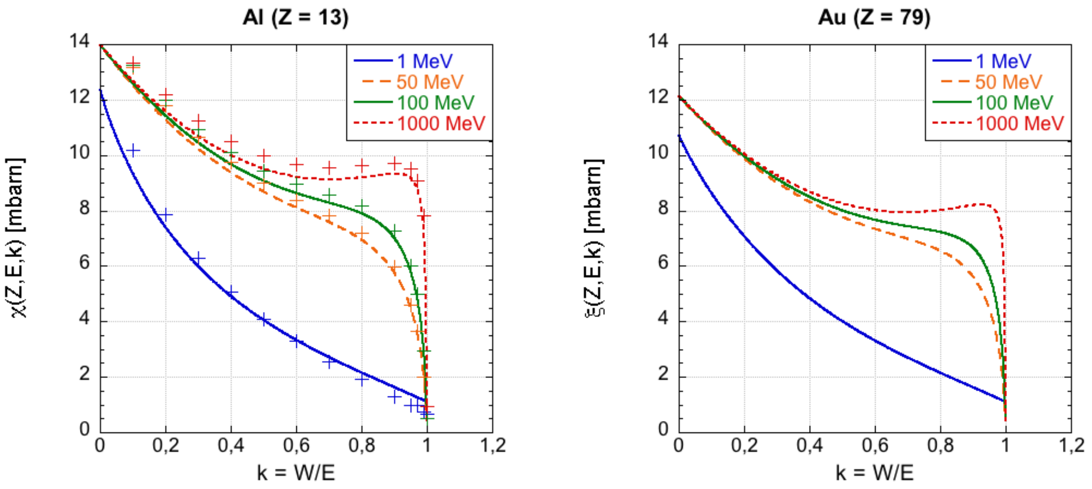

Figure 2.16: Dependence of the scaled bremsstrahlung energy spectrum on the $k = W/E$ ratio for different electron energies $E = 1$ MeV (blue solid line), $E = 50$ MeV (orange dashed line), $E = 100$ MeV (green solid line) and $E = 1000$ MeV (red dotted line). The incident electron propagates through an aluminum (left-hand side) and a gold target (right-hand side). Numerical calculations given by Seltzer are plotted with cross symbols.

Angular distribution of bremsstrhalung emission

The bremsstrahlung emission generated by a high energy charged particle is strongly peaked in the forward direction into a cone characterized by an aperture $\theta \sim 1/\gamma$. Several analytical formula for the angular dependence of the bremsstrahlung cross sections were summarized by

Koch and Motz. We present in this section the simplest cross section which was derived by Schiff [1951], corresponding to the 2BS expression in Koch and Motz article.

$$\frac{\partial \sigma^2_{\text{schiff}}}{\partial W \partial \theta} = 4Z^2 \alpha r_e^2 \frac{\gamma}{W/m_e c^2} y \left[\frac{16 y^2 \gamma_p}{(y^2+1)^4 \gamma} - \frac{(\gamma+\gamma_p)^2}{(y^2+1)^2 \gamma^2} + \left(\frac{\gamma^2+\gamma_p^2}{(y^2+1)^2\gamma^2} - \frac{4y^2\gamma_p}{(y^2+1)^4\gamma} \right) \ln M(y) \right] \quad (2.112)$$

with the parameters γ_p (scattered electron energy), y (reduced angle) and $M(y)$ given by:

$$\gamma_p = \gamma - W/m_e c^2 \quad ; \quad y = \gamma\theta \quad ; \quad M(y) = \left[\left(\frac{(k/m_e c^2)^2}{2\gamma\gamma_p} \right)^2 + \left(\frac{Z^{1/3}}{111(y^2+1)} \right)^2 \right]^{-1} \quad (2.113)$$

This expression was obtained considering an exponential attenuation form of the screened field (Yukawa type potential). The cross section, calculated here using Born's approximation, is in principle valid in the ultra-relativistic regime $\gamma >> 1$, $\theta << 1$. However a comparison with the experimental data showed that the expression remains valid even in the moderate-relativistic regime Koch & Motz [1959].

Radiative stopping power

The radiative stopping power can be calculated by the following expression:

$$\left(\frac{dE}{ds} \right)_{\text{brem}} = -n_i \int_0^E W \frac{d\sigma}{dW} dW \quad (2.114)$$

The integral is calculated over all energies of an emitted photon, the maximum energy being the incident electron energy. The dependence of the radiative and total stopping powers in aluminum and gold targets on the electron energy are plotted in Fig. 2.17. The radiative stopping power increases monotonically with the electron energy, compared to the logarithmic dependence of the collisional stopping power. The contribution of the radiative stopping power becomes non-negligible at relativistic energies, above ∼ 10 MeV for aluminum targets and ∼ 1 MeV for gold. Radiative energy losses become the dominant energy loss mechanism for fast electrons above 50 MeV and 10 MeV in aluminum and gold, respectively. A useful formula derived by Berger & Seltzer [1964] allows to quickly estimate these so-called critical energies beyond which the radiative energy losses become the dominant mechanism:

$$E_c[\text{MeV}] \simeq \frac{800}{Z+1.2} \quad (2.115)$$

In our experiment the fraction of fast electrons carrying an energy greater than a few MeV is fairly weak. This allows us to neglect the contribution of radiative energy losses without making a too important error.

2.4.4 Collisional range

The calculation of the stopping powers of fast electrons in the dense matter allows to deduce a more practical physical parameter called *range*. This parameter is the maximum distance over which an electron of a given initial energy E can propagate in a target before being stopped.

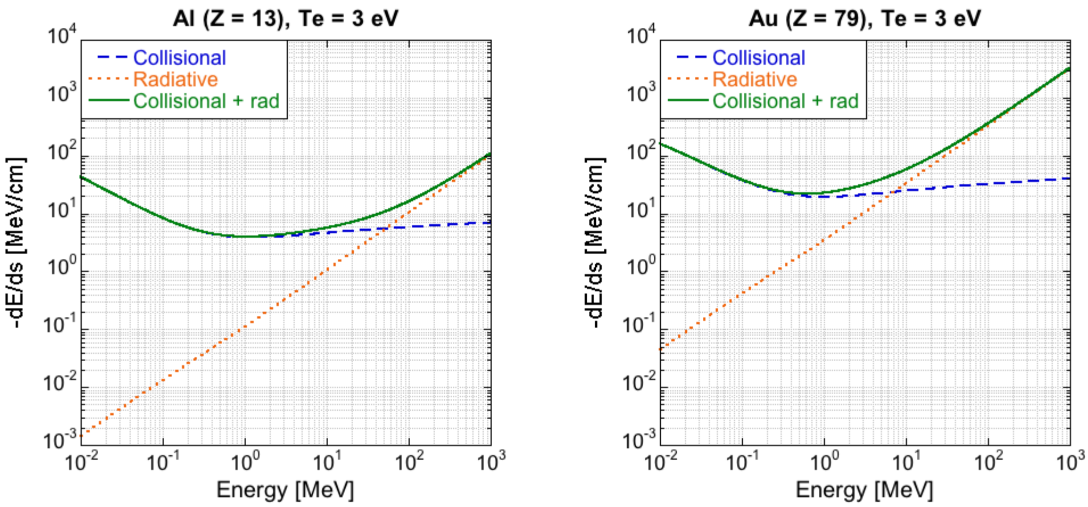

Figure 2.17: Dependence of the radiative stopping power (orange dotted line) and of the collisional stopping power with (green solid line) and without (blue dashed line) taking into account radiative effects on the incident electron energy for the aluminum (left) and gold (right) targets at the temperature 10 eV.

The range is given by:

$$R = -\int_0^E \left(\frac{dE}{ds}\right)^{-1} dE \tag{2.116}$$

with dE/ds the total stopping power derived in the previous section. The dependence of the electron range for different initial energies in aluminum and gold targets at solid density is presented in Fig. 2.18. Incident electrons with energies $E < 40$ keV are stopped within less than 10 μm of aluminum. The range given by Eq. 2.116 was calculated considering a propagation of fast electrons along a straight line. In reality, as mentioned in the previous section, fast electrons are deviated from their initial trajectories by multiple collisions with the

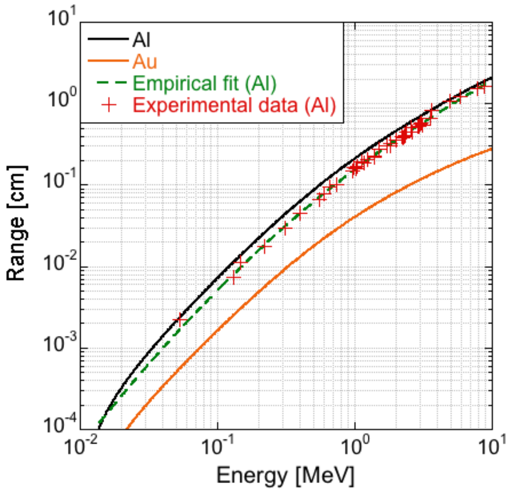

Figure 2.18: Evolution of the maximum range of fast electrons as a function of their incident energy estimated by Eq. 2.116 in aluminum (black solid line) and in gold (orange full line) targets. The range in aluminum targets is compared to the empirical range of Katz (green dashed line) based on experimental measurements (red crosses).

background atoms. The actual range is in fact slightly smaller than the predicted range. A convenient empirical law determined by Katz & Penfold [1952] on the basis of experimental measurements allows to calculate the actual range in aluminum targets:

$$R[\mathrm{cm}] = \begin{cases} \frac{0.412}{\rho[\mathrm{g/cc}]} E^{1.265-0.0954\ln E} & \text{for } 0.01 < E < 2.5 \text{ MeV} \\ \frac{1}{\rho[\mathrm{g/cc}]}(0.53E - 0.106) & \text{for } E \geq 2.5 \text{ MeV} \end{cases} \tag{2.117}$$

The empirical law and the experimental measurements are presented in Fig. 2.18. To conclude, it is worth mentioning that an accurate description of the fast electron collisional range in dense targets requires the use of numerical transport simulations, using Monte-Carlo or Fokker-Planck codes.

2.5 Fast electron beam collective transport

The propagation of fast electrons in dense matter cannot be only described as a sum of physical phenomena associated with each particle. In addition to the energy losses of each electron separately the collective processes provide a contribution proportional to the fast electron current. This chapter briefly introduces the main ideas of collective transport into dense plasmas. For the sake of simplicity we assume that the fast electron density is much lower than the background electron density, which is always the case in our experiments, except in the pre-plasma regions, or inside the hollow cone target presented in chapter 5. A presentation of a more detailed study of the complex collective transport theory can be found in the PhD thesis of Gremillet [2001] or Debayle [2008].

2.5.1 Neutralization of the fast electron current: Alvén limit and return current

Let us consider a fast electron beam propagating in a dense plasma. This situation involves a large number of physical processes related to the accumulation of negative charges brought with the fast electrons. This generates an electrostatic field that expels background thermal electrons out of the incident beam. This charge neutralization is performed within the time $\tau_{neut} \sim \max\left[1/\nu_{ei}, 1/\omega_{pe}\right]$, with ν_{ei} the electron-ion collision frequency and ω_{pe} the plasma frequency. This neutralization time is close to a few femtoseconds in our experimental conditions, which is much shorter than the electron beam duration. The beam charge neutralization is consequently considered as an instantaneous process. The organized flux of a large number of fast electrons generates an intense current, $I_b \simeq N_b e/\tau_{las} \sim 1$ MA in our experimental conditions, with N_b the number of fast electrons and τ_{las} the laser pulse duration. This current is responsible for the creation of a magnetic field pinching the electron beam itself. In 1939 Alfvén demonstrated that this pinching magnetic field is able, when strong enough, to deviate fast electrons towards the reverse direction, and thus preventing the beam propagation [Alfvén, 1939]. Let us consider a fast electron beam of radius R and of uniform density across its propagation direction, characterized by an intensity I. This current generates a magnetic field B_I at the edge of the beam given by:

$$B_I = \frac{\mu_0 I}{2\pi R} \tag{2.118}$$

The Larmor radius of a single electron propagating with a momentum $p = \gamma m_e v_e$ into this field is given by:

$$r_L = \frac{\gamma m_e v_e}{e B_I} \tag{2.119}$$

The Alfvén limit current can be derived by considering that the Larmor radius is equal to half the radius of the electron beam [Hammer & Rostoker, 1970], so that $r_L = R/2$. This derivation yields a limit current I_A given by:

$$I_A[kA] = \frac{4\pi m_e c}{\mu_0 e}\gamma_b\beta_b \simeq 17\gamma_b\beta_b \tag{2.120}$$

Considering a maximum fast electron energy of 120 MeV, which corresponds to the upper limit in our experiments, the upper bound of the current limit is $I_A \sim 4$ kA, fairly lower than the current carried by the generated fast electron beam I_b. In fact the dynamic azimuthal magnetic field also generates, via the Lenz's law, an axial electromotive field that accelerates background electrons in the opposite direction, creating a return current I_{ret} that partially neutralizes the incident current. The total current, or net current, that has to be taken into account in Alvén's limit is therefore $I_{tot} = I_b + I_{ret}$. A perfect current neutralization that would implie the equality $\mathbf{j}_b = -\mathbf{j}_{ret}$ is in fact never fully satisfied. The conditions required for an efficient current neutralization can be derived from the analytical calculations performed by Lee [1971] considering a cylindrical incident beam. When the radius of the beam r_b is higher than the magnetic skin depth $\lambda_e = c/\omega_{pe}$ the return current is actually able to match the incident beam shape: the incident current is confined within the magnetic field region and the neutralization is fairly efficient. In the limit case, the radius of the beam is smaller than the magnetic skin depth, and the return current spreads too far from the incident beam region: the incident current is poorly neutralized. In our experimental conditions the radius of the beam $r_b \sim 5$ μm, given by the focal spot size in a first approximation, is larger than the magnetic skin depth $\lambda_e \sim 10^{-2}$ μm, yielding an efficient neutralization.

The neutralization of the incident beam decays in time. Indeed the finite conductivity of the crossed material triggers a diffusion of the magnetic field by the collisional return current. The effective neutralization time scale is given by the magnetic diffusion time:

$$\tau_D = \frac{\mu_0 r_b^2}{\eta} \tag{2.121}$$

where η is the resistivity of the material. In our experimental condition the neutralization of the incident beam is maintained during ~ 10 ps, which is longer than the beam duration: the neutralization is considered as fairly efficient. This problem is however not so trivial in the fast ignition scheme since the duration of the beam is comparable with the value given by Eq. 2.121 [Davies, 2004].

2.5.2 Induced electromagnetic fields

The intense electromagnetic fields generated by the propagating fast electron beam can greatly affect the beam propagation itself. In order to describe these effects and to estimate the intensity of the created fields we consider in this section the model developed by Davies et al. [1997]. The electric field can be calculated via the generalized Ohm's law and Maxwell-Faradays's law, respectively:

$$\mathbf{E} = -\eta\mathbf{j_b} + \frac{\eta c}{4\pi}\boldsymbol{\nabla}\times\mathbf{B} + \frac{1}{n_e e}\boldsymbol{\nabla}(n_e T_e)$$

$$\frac{1}{c}\frac{\partial\mathbf{B}}{\partial t} = -\boldsymbol{\nabla}\times\mathbf{E} \tag{2.122}$$

where the ideal gas expression for the plasma pressure has been considered. This expression for the electric field remains valid assuming that the fast electron beam duration is longer than the charge neutralization time, and shorter than the magnetic diffusion time (Eq. 2.121). By injecting the first equation into the second, the temporal evolution of the magnetic field is given by:

$$\frac{1}{c}\frac{\partial \boldsymbol{B}}{\partial t} + \frac{\partial}{\partial \boldsymbol{r}} \times \left[\frac{\eta c}{4\pi}\boldsymbol{\nabla} \times \boldsymbol{B}\right] = \underbrace{\eta \boldsymbol{\nabla} \times \boldsymbol{j_b}}_{current} + \underbrace{\boldsymbol{\nabla}(\eta) \times \boldsymbol{j_b}}_{resistivity} + \underbrace{\frac{1}{n_e e}\boldsymbol{\nabla}(n_e) \times \boldsymbol{\nabla}(T_e)}_{crossed\ gradients} \tag{2.123}$$

A magnetic field generation is due to three main effects. The first one mathematically described by $\eta\nabla \times \mathbf{j}_b$, and labeled *current*, states that the curl of the current is responsible for the collimation of fast electrons. The second effect, given by $(\nabla\eta) \times \mathbf{j}_b$, and labeled *resistivity*, describes the generation of magnetic field by resistivity gradients, which can be produced due to inhomogeneous compression and/or heating of the medium. The possible collimation or deflection of the electron beam directly depends on the sign of resistivity gradients. Pérez et al. observed a collimation of fast electron beam injected into a foam target cylindrically compressed presenting a resistivity gradient towards the target center (Fig. 2.19) [Pérez, 2010; Pérez et al., 2011]. In that experiment the plasma was in the strongly coupled state as the target material was heated up to only a few eV. In that case, the resistivity depends on the plasma density, which was lower in the center due to the fact that the fast electrons were injected before convergence of the compression shock.

Resistivity gradients can also be directly imposed by the target composition. Kar et al. [2009] observed a magnetic collimation of fast electrons propagating into a highly resistive tin layer surrounded by a less resistive aluminum. A similar experiment was performed by Ramakrishna et al. [2010] using aluminum cylinders containing, or not, an iron core. The authors observed a collimation of fast electrons in the presence of the Fe core. The three experimental setups are presented in Fig. 2.19.

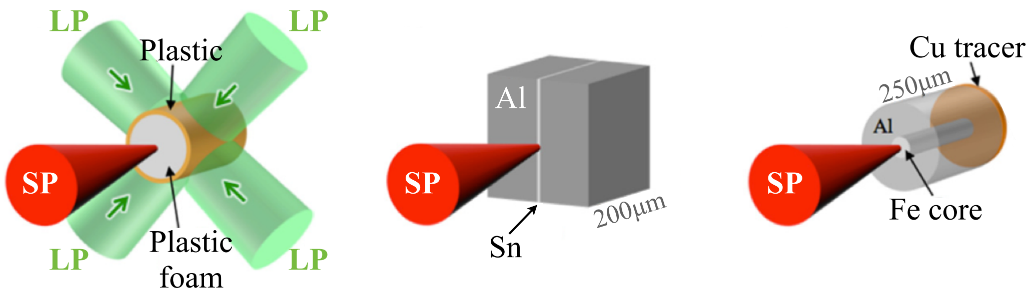

Figure 2.19: Experimental setups designed to observe fast electron magnetic collimation due to induced resistivity gradients (left hand side plot) or target built-in resistivity gradients consisting in an Al-Sn-Al sandwich (middle plot) or in a Fe core surrounded by Al material (right hand side plot). The image is taken from [Norreys et al., 2014]

Assuming a Gaussian (both in time and space) laser pulse, the maximum electric and magnetic field amplitudes can be estimated in function of the laser intensity I_0, pulse duration τ_L, plasma resistivity η, the fast electron beam radius R_b and of the laser-to-fast electrons conversion efficiency $\eta_{L\rightarrow e}$ [Davies et al., 1997]:

$$E_{max}[\mathrm{V.m^{-1}}] \simeq 6 \times 10^9 \left(\frac{\eta}{2 \times 10^{-6}\ \Omega.\mathrm{m}}\right)\left(\frac{\eta_{L\rightarrow e}}{0.3}\right)\left(\frac{I_L}{10^{17}\ \mathrm{W.cm^{-2}}}\right)\left(\frac{1\ \mu\mathrm{m}}{\lambda}\right)^{2/3} \tag{2.124}$$

$$B_{max}[\mathrm{T}] \simeq 230 \left(\frac{\eta}{2\times 10^{-6}\ \Omega.\mathrm{m}}\right)\left(\frac{2\ \tau_L}{1\ \mathrm{ps}}\right)\left(\frac{10\ \mu\mathrm{m}}{R_b}\right)\left(\frac{\eta_{L\to e}}{0.3}\right)\left(\frac{I_L}{10^{17}\ \mathrm{W.cm^{-2}}}\right)\left(\frac{1\ \mu\mathrm{m}}{\lambda}\right)^{2/3} \tag{2.125}$$

According to these equations the electromagnetic effects are expected to dominate over the collisional effects for the laser intensities $I_L \geq 10^{18} - 10^{19}$ W.cm^{-2}.

2.5.3 Plasma resistivity

As mentioned above collective mechanisms acting on fast electron propagation in plasmas directly depend on the plasma DC resistivity. This parameter plays a major role in fast electron energy losses as we will see in the next section. It is therefore important to characterize the plasma resistivity over a wide range of electron temperatures that can be reached in a target during an experimental campaign. The key parameter describing the resistivity, and its inverse value, the plasma conductivity, is the electron collision frequency, as it can be shown using the Drude model. Several models have been proposed to infer the collision frequency as a function of the electron temperature. We describe in this section the Eidmann-Chimier model [Eidmann et al., 2000; Chimier, 2008].

Drude model

The resistivity of metals and plasmas is described by the Drude model. Valence electrons are considered as free to move into the material, colliding with fixed ions. The Drude model is based on four fundamental hypothesis:

- between two collisions electrons are completely free of interacting with other particles. Their trajectory is dictated by the force exerted by an external field, if any.
- collisions are instantaneous, electrons do not conserve the history of previous collisions.
- between two collisions electrons travel during a mean characteristic time τ. The collision frequency is defined as $\nu_e = 1/\tau$. The effect of collisions on the average electron motion can be described by a drag force $\mathbf{F_d} = -(m/\tau)\mathbf{v_e}$, with $\mathbf{v_e}$ the electron speed.
- the electron collisions are leading to heating of the background plasma.

The fundamental principle of dynamics applied to a free electron in a metal under the influence of an constant external electric field yields:

$$m_e\frac{d\mathbf{v_e}}{dt} = -e\mathbf{E} - \frac{m_e}{\tau}\mathbf{v_e} \tag{2.126}$$

When solving the previous equation one finds for $t >> \tau$:

$$\mathbf{v_e} = -\frac{e\tau}{m_e}\mathbf{E} = -\frac{e}{m\nu_e}\mathbf{E} \tag{2.127}$$

The current density $\mathbf{j_e} = -en_e\mathbf{v_e}$ consequently writes:

$$\mathbf{j_e} = \frac{e^2 n_e}{m_e\nu_e(T_e)}\mathbf{E} = \sigma_{DC}(T_e)\mathbf{E} \tag{2.128}$$

with $\sigma_{DC} = 1/\eta$ the DC electric conductivity for a metal. If one considers a more general situation with an oscillating electric field at the frequency ω the AC conductivity is given by:

$$\sigma_{AC}(\omega) = \frac{\sigma_{DC}}{1 + i\omega/\nu_e} \tag{2.129}$$

The plasma conductivity is thus directly related to the electron collision frequency ν_e which depends on the electron temperature T_e. The Eidmann-Chimier model provides an expression of the collision frequency over a large range of electron temperatures, from a few tenths of eV up to several keV.

Collision frequency and plasma resistivity

At a very low electron temperature $T_e << T_F$, well below the Fermi temperature T_F, the collision frequency in a cold-solid material is dominated by electron-phonon collisions. Its expression has been calculated by Yakovlev & Urpin [1980] in the case of the degenerate matter of white dwarfs and neutron stars:

$$\nu_{e-ph} \simeq \frac{k_s}{2\pi\epsilon_0}\frac{e^2 k_B T_i}{\hbar^2 v_F} \tag{2.130}$$

with T_i the ion temperature, $v_F = \hbar(3\pi^2 n_e)^{1/3}$ the Fermi velocity and k_s a tabulated constant depending on the considered material and used to adapt the previous expression to measured values of cold metals. For aluminum one finds $k_s \sim 1.25$. One can note that the expression of ν_{e-ph} is obtained for the thermal equilibrium conditions, $T_e = T_i$. It is also worth mentioning that Eq. 2.130 is only valid below the material melting point.

When increasing T_e, and for $T_e >> T_i$, ionization takes place into the material. Electron-electron collisions become the dominant process in the $0.1T_F < T_e < T_F$ temperature range. The electron-electron collision frequency writes:

$$\nu_{e-e} = A_\nu \frac{k_B T_e^2}{\hbar T_F} \tag{2.131}$$

with A_ν a fitting parameter ranging from 1 to 100. For aluminum $A_\nu = 1$ [Chimier, 2008]. The electron-electron collision frequency depends on the square of the electron temperature.

In the upper limit, when considering high electron temperatures $T_e >> T_F$, the collision frequency is described by the Spitzer model, which considers a Maxwellian background electron distribution [Spitzer, 1956]:

$$\nu_{sp} = \frac{4}{3}(2\pi)^{1/2} k_{sp} \frac{Z^* e^4 m_e n_e}{(4\pi\epsilon_0)^2 (m_e k_B T_e)^{3/2}} \ln\Lambda \tag{2.132}$$

with k_{sp} a dimensionless parameter equal to $3\pi/32$ and $\ln\Lambda$ the Coulomb logarithm defined in Eq. 2.18. The Spitzer collision frequency decreases rapidly with the electron temperature at the power 3/2. It is important to note that the Spitzer model is not valid at low electron temperatures, close to the Fermi temperature, where the considered material is in a degenerate state: both the electron degeneracy effects and ion correlations have to be taken into account. Considering the behavior of the collision frequency expressions below ($\propto T_e^2$) and well beyond ($\propto T_e^{-3/2}$) the Fermi temperature, it is reasonable to assume that ν_e reaches a maximum value close to the Fermi temperature. In order to find the expression of ν_e in this range one can note that the mean free path λ_e of an electron around the maximum value of ν_e cannot be lower than the atomic inter-distance r_i. Therefore, one can require that λ_e should not be smaller than the atomic sphere of radius r_i. This condition is directly equivalent to the following:

$$\nu < \frac{v_{ch}}{r_i} \tag{2.133}$$

with v_{ch} an electron characteristic velocity chosen as $v_{ch} = \sqrt{v_F^2 + v_{Te}^2}$, with v_{Te} the electron thermal speed. The corresponding cut-off frequency introduced by Eidmann et al. [2000] writes:

$$\nu_c = \frac{\sqrt{v_F^2 + v_{Te}^2}}{r_i} \tag{2.134}$$

The interpolation expression for the collision frequency given by Eidmann and modified by Chimier [2008] is finally given by the harmonic mean value of the various collision frequencies:

$$\nu_e^{-2} = (\nu_{e-ph} + \nu_{e-e})^{-2} + \nu_c^{-2} + \nu_{sp}^{-2} \tag{2.135}$$

The dependence of the collision frequency and separate contributions on the electron temperature is plotted in Fig. 2.20 (top left) considering an ion temperature $T_i = 0.03$ eV. The corresponding resistivity calculated by Eq. 2.128 is plotted on Fig. 2.20 (top right) together with the Spitzer resistivity.

Measurements of the aluminum resistivity have been performed by Milchberg et al. [1988]. The basic idea of their experimental set up was to measure the reflection of a $\sim$ mJ, $\tau = 400$ fs laser pulse incident on aluminum targets as a function of the laser intensity. The index of refraction of the material is indeed directly linked to the AC conductivity by the following relation given by the Drude model:

$$n^2 = \frac{\epsilon}{\epsilon_0} = \frac{1}{\epsilon_0}\left(1 - \frac{i\sigma_{AC}}{\omega\epsilon_0}\right) \tag{2.136}$$

with ϵ being the material permittivity. If one considers a sharp vacuum-material boundary, the Fresnel coefficients link the index of refraction and the reflectivity. In the experiment however the laser ASE pedestal triggered an expansion of the material characterized by moderate gradient scale-length values ($\sim \lambda_L/15$). The Helmholtz wave equation had to be solved for each expansion scale length in order to calculate the target conductivity and the collision frequency. The electron temperature and the ionization degree were inferred from Doppler shifted reflected spectrum of the laser pulse. These two parameters are indeed linked to the interface expansion velocity by the following:

$$v_0^2 = \left(\frac{2}{\gamma_{al} - 1}\right)^2 \frac{Z^* k_B T_e}{m_i} \tag{2.137}$$

with $\gamma_{al} = C_{p_e}/C_{v_e} = 1.7$ the ratio between the aluminum heat capacity at constant pressure and at constant volume. The resistivity was finally calculated with the Drude DC resistivity given by Eq. 2.128. The electron density n_e was modeled considering a local thermodynamic equilibrium (LTE). Considering the extremely short pulse duration this last assumption is not completely valid. However, according to the authors, any time-dependent calculation would not yield higher electron density values. The experimental measurements of aluminum resistivity are in fairly good agreement with the Eidmann-Chimier model. In particular the saturation region can be clearly seen.

Another model of electric conductivity widely used in numerical simulations is called the LMD model. It was firstly proposed by Lee & More [1984] and corrected by Desjarlais [2001]. It consists of a linearization of the Boltzmann equation considering a weak electric field and small density and temperature gradients. The collision frequency is presented as a function of Fermi-Dirac integrals of $\mu/k_B T_e$, with μ the chemical potential:

$$\nu = \frac{n_e e^2 \tau_{ei}}{m_e} A\left(\mu/k_B T_e\right) \tag{2.138}$$

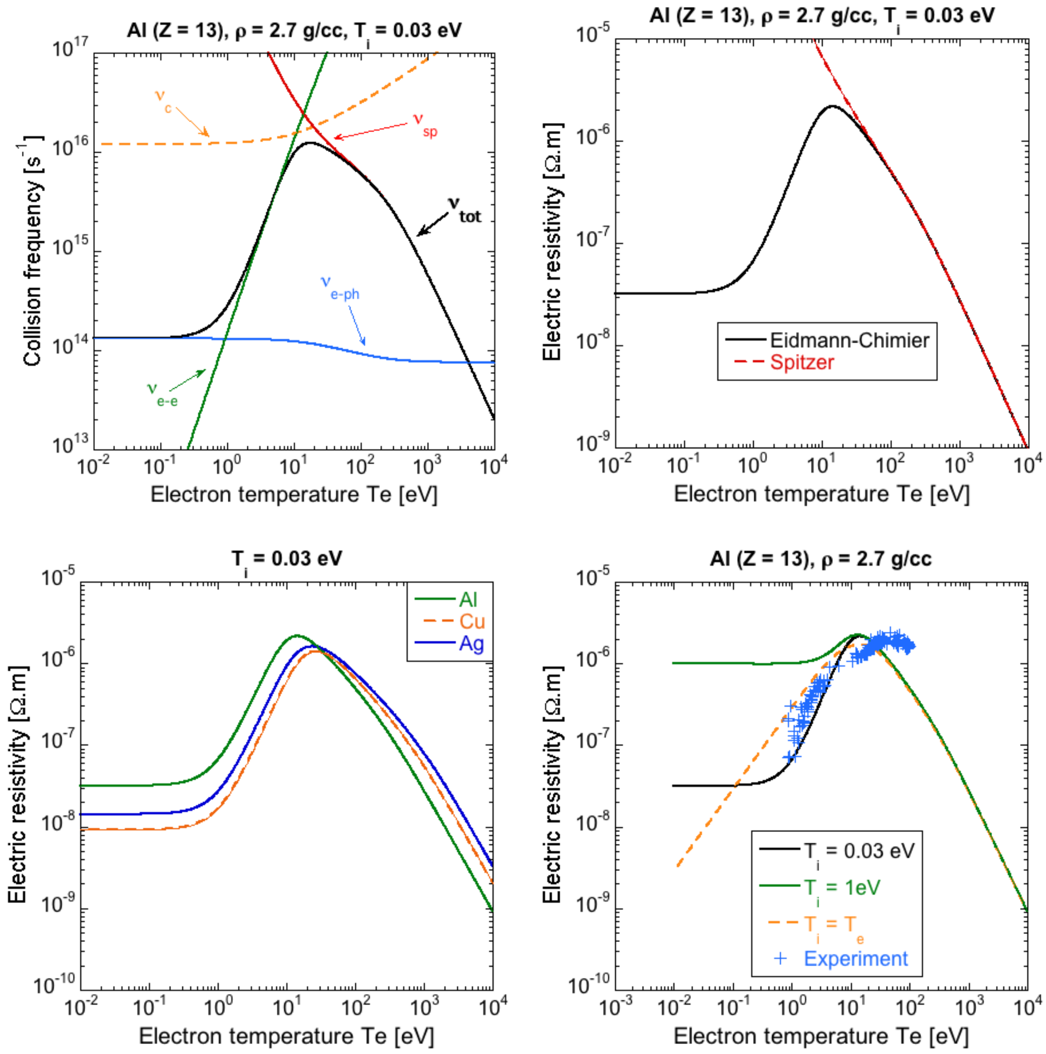

Figure 2.20: (Top left) Dependence of the collision frequency ν_e and its different components ν_{e-ph}, ν_{e-e}, ν_c and ν_{sp} as a function of the electron temperature and considering an ion temperature $T_i = 0.03$ eV. (Top right) Aluminum resistivity is given by both the Eidmann-Chimier model and by the Spitzer model for $T_i = 0.03$ eV. (Bottom left) Resistivity of aluminum (green solid line), copper (orange dashed line) and silver (blue solid line). (Bottom right) Comparison of the resistivity of aluminum for different ion temperatures $T_i = 0.03$ eV (black solid line), $T_i = 1$ eV (green solid line) and considering the electron-ion equilibrium $T_i = T_e$ (orange dashed line). Experimental measurements of aluminum resistivity performed by Milchberg are plotted with blue crosses.

with the Fermi integrals defined as:

$$\begin{aligned} A\left(\mu/k_BT_e\right) &= \frac{4}{3}\frac{F_2(\mu/k_BT_e)}{\left[1+\exp\left(-\mu/k_BT_e\right)\right]F_{1/2}(\mu/k_BT_e)^2} \\ F_i(\mu/k_BT_e) &= \int_0^\infty dt\frac{t^i}{1+\exp\left[t-\mu/k_BT_e\right]} \end{aligned} \tag{2.139}$$

The electron relaxation time τ_{ei} is given in the case of Coulomb collisions by:

$$\tau_{ei} = \frac{3\sqrt{m_e}(k_BT_e)^{3/2}}{2\sqrt{2}\pi(Z^*)^2n_ie^4\ln\Lambda}\left[1+\exp\left(-\mu/k_BT_e\right)\right]F_{1/2}(\mu/k_BT_e) \tag{2.140}$$

It is worth mentioning that the Eidmann-Chimier and LMD models provide slightly different results for the electric conductivity as illustrated in Fig. 2.20.

2.5.4 Collective stopping power: resistive heating

Fast electrons propagating in dense matter loose their energy in collisional processes and consequently heat the target. Resistive processes are also contributing to the electron energy losses. Indeed, as already mentioned in the beginning of this section, a fast electron beam propagating into a dense medium partially transfers its energy to a resistive electric field $\mathbf{E}_{\mathrm{ret}} = \eta \mathbf{j}_{\mathrm{ret}}$ maintaing a return current j_{ret}. This return current mainly composed of thermal electrons is highly collisional and participate in the heating of the target. These resistive processes are far from being negligible when compared to collisional processes if the incident current $\mathbf{j_b} \sim \mathbf{j_h}$ is high enough ($\geq 10^{10} - 10^{11}$ A.cm^{-2}). As we will show in this section resistive heating can take place in a very short time scale, and the subsequent fast electron resistive stopping power may overcome the collisional stopping power. We use in this section the rigid beam approximation which implies a fixed current density. This strong assumption, which does not allow to model the dynamic of fast electron beams, is sufficient to derive rough estimations on fast electron beam energy losses.

The amount of energy lost by fast electrons per unity of length dE_h/ds can be calculated using a simple model developed by Lovelace & Sudan [1971] and modified by Gremillet [2001]. This model is based on the solution of the energy conservation equation separately for the contribution to the magnetic field of the beam ($\mathbf{B_b}$) and of the plasma ($\mathbf{B_p}$) linked by $\mathbf{B_b} = -f\mathbf{B_p}$, with f the neutralization rate. The energy conservation equation given by the Poynting theorem writes:

$$\frac{\partial E_{b,p}}{\partial s \partial t} = \int \mathbf{j_{b,p}}.\mathbf{E}.dS \tag{2.141}$$

By assuming a Gaussian shaped (in the transverse plan) fast electron beam with a constant current density (rigid beam approximation), the amount of lost energy per unit of length in the electromotive field writes:

$$\frac{dE_b}{ds}(t) = \frac{I_b^2}{4\pi\epsilon_0 c^2} \ln\left(1 + 2\frac{t}{\tau_D}\right) \tag{2.142}$$

with $I_b = e\pi r_b^2 n_b \beta_b c$ the fast electron current. For the sake of simplicity we consider a monoenergetic electron beam propagating at the speed $\beta_b c$. The evolution of W_b as a function of time is presented on Fig. 2.21 for different fast electron populations. In less than a picosecond fast electrons lose a non-negligible fraction of energy. The resistive energy transferred to the plasma via Joule's effect writes:

$$\frac{dE_p}{ds}(t) = \frac{1}{2}\frac{I_b^2}{4\pi\epsilon_0 c^2} \ln\left(1 + 4\frac{t}{\tau_D}\right) \tag{2.143}$$

This model also provides an estimate for the electron temperature of the plasma, considered as an ideal gas, due to Joule's effect, according to:

$$\frac{3}{2} n_p k_B T_e = \frac{dE_p}{ds} \tag{2.144}$$

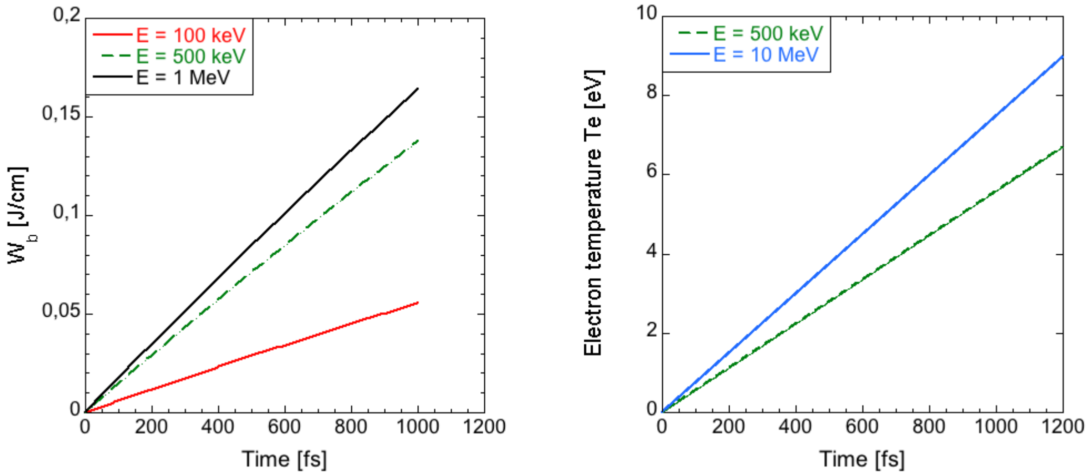

Figure 2.21: (Left)Evolution of resistive energy losses per unit of length for three fast electron populations characterized by $E = 100$ keV (red solid line), $E = 500$ keV (green dashed line) and $E = 1$ MeV (black solid line). This plot was obtained for $r_b = 5\ \mu$m, $\eta = 2.2 \times 10^{-6}\ \Omega$.m (close to cold aluminum maximum resistivity), and a beam density $n_b = 1.0 \times 10^{25}$ cm^{-3}. (Right) Evolution of the resistive heating in an aluminum plasma for two fast electron energies $E = 500$ keV (green dashed line) and $E = 10$ MeV (blue solid line) and considering the same parameters as for the left-hand side plot.

The evolution of the temperature as a function of time is then given by:

$$T_e[\text{eV}] \simeq 400\beta_b^2 \left(\frac{Z^* n_i}{6.0 \times 10^{22}\ \text{cm}^{-3}}\right)^{-1} \left(\frac{n_b}{1.0 \times 10^{20}\ \text{cm}^{-3}}\right)^2 \left(\frac{\eta}{1.0 \times 10^{-6}\ \Omega.m}\right) \left(\frac{\Delta t}{500\ \text{fs}}\right) \quad (2.145)$$

The evolution of the plasma temperature due to resistive heating is plotted in Fig. 2.21. In less than a picosecond this qualitative model shows that the plasma can already be heated up to a few eV, which illustrates the efficiency and the importance of resistive mechanisms in conditions similar to those found in our experiments.

In order to compare the contribution of resistive heating and collisional heating, the resistive heating of the material can be described by the model proposed by Davies [2003]. By assuming a perfect neutralization of the beam ($\mathbf{j}_b = -\mathbf{j}_{ret}$) the energy conservation equation gives:

$$C_e \left.\frac{\partial T_e}{\partial t}\right|_{\text{res}} = -n_b \beta_b u_b \left(\frac{dE}{ds}\right)_{\text{res}} = \mathbf{j}_{ret}.\mathbf{E}_{\text{ret}} = \eta j_b^2 \quad (2.146)$$

with C_e the heat capacity of the plasma electrons at constant volume, $u_b \lesssim c$ the fast electron speed and $(dE/ds)_{\text{res}} = -e\eta j_{\text{ret}}$ the resistive stopping power. This equation was obtained by neglecting heat conduction which is justified by the extremely short duration of the electron beam propagation. Ionization processes were also neglected. Even if this last hypothesis is not completely valid, the general tendency is conserved [Vauzour et al., 2014]. The resistive stopping power as a function of the background electron temperature is plotted in Fig. 2.22. It rises with the electron temperature, peaks at about 10 eV close to the Fermi temperature due to the resistivity saturation, and decreases rapidly at high temperature in the Spitzer resistivity regime.

The energy conservation equation to both collisional and resistive processes yields the total energy deposition:

$$C_e \left.\frac{\partial T_e}{\partial t}\right|_{\text{total}} = -n_b\beta_b u_b \left(\frac{dE}{ds}\right)_{\text{res}} - n_b\beta_b u_b \left(\frac{dE}{ds}\right)_{\text{coll}} = \eta j_h^2 + \frac{j_b}{e}\left|\frac{dE}{ds}\right|_{\text{coll}} \tag{2.147}$$

with $(dE/ds)_{\text{coll}}$ given by Eq. 2.112 in the case of a cold material. When considering only the logarithmic term and by neglecting corrective terms in the collisional stopping power, the energy deposition by collisional processes writes:

$$C_e \left.\frac{\partial T_e}{\partial t}\right|_{\text{coll}} = -n_b\beta_b c \left(\frac{dE}{ds}\right)_{\text{coll}} = -\frac{j_b}{e}\left(\frac{dE}{ds}\right)_{\text{coll}} = \frac{2\pi r_e^2 Z m_e c^3 n_i n_b}{\beta_b(\gamma_b - 1)} \ln\left[\frac{(\gamma_b^2-1)(\gamma_b-1)}{2(I_0/m_e c^2)^2}\right] \tag{2.148}$$

By looking at Eq. 2.147 one can note that the collisional heating scales as j_b whereas resistive heating scale as j_h^2. As a consequence, the Ohmic heating can be the dominant heating term at the front side of a target, where the current density is the highest. The rapid drop of j_b due to the inherent fast electron energy losses and the beam divergence may invert this trend, making collisional heating the dominant heating mechanism deeper into the target. That behavior can be quantified by calculating the ratio between collisional to resistive losses:

$$R_{\text{coll-res}} = \frac{\partial_t T_e|_{\text{coll}}}{\partial_t T_e|_{\text{res}}} = \frac{2\pi r_e^2 Z m_e c^2 n_i}{\beta_b^2(\gamma_b-1)e\eta j_b} \ln\left[\frac{(\gamma_b^2-1)(\gamma_b-1)}{2(I_0/m_e c^2)^2}\right] \tag{2.149}$$

The ratio $R_{\text{coll-res}}$ is plotted on Fig. 2.147 as a function of fast electron current density for an electron energy $E = 500$ keV. Two different resistivities are considered, $\eta_{max} = 2.3 \times 10^{-6}$ Ω.m and $\eta_{min} = 3.3 \times 10^{-8}$ Ω.m, corresponding to the extreme values that can be found in our experiments, provided that the electron temperature does not exceed a few hundreds of eV. The

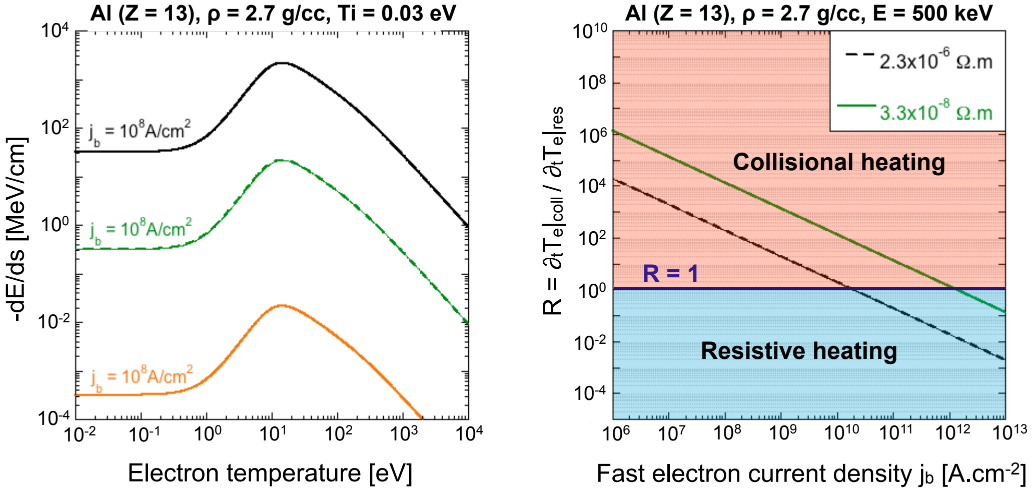

Figure 2.22: (Left) Dependence of the resistive stopping power on the electron temperature for three different electron current densities $j_b = 10^8$ A.cm^{-2} (orange solid line), $j_b = 10^{11}$ A.cm^{-2} (green dashed line) and $j_b = 10^{13}$ A.cm^{-2} (black solid line). The ion temperature is set at $T_i = 0.03$ eV. The resistivity was calculated with the Eidmann-Chimier model. (Right) Ratio between collisional to resistive energy losses in aluminum targets for two resistivities $\eta = 2.3 \times 10^{-6}$ Ω (black dashed line) and $\eta = 3.3 \times 10^{-8}$ (green solid line).

horizontal line $R = 1$ splits the plot into two areas where collisional heating is dominant (upper part) and where resistive heating is dominant (lower part). When considering a current density greater than $j_b = 10^{10}$ A.cm^{-2} (for the highest η considered here) resistive effects can be more important than collisional effects. In our experiments, current densities $> 10^{11}$ A.cm^{-2} were reached in aluminum layers (see chapter 4). One can consequently expect that resistive heating is in this case the dominant heating mechanism. In fact Eq. 2.149 considers that fast electrons propagate along straight lines, neglected the electron scattering. This qualitative model can only provide the estimates of the order of magnitude. Indeed, as discussed in section 2.4.1, the electron scattering may rapidly decrease the current density and the subsequent resistive heating effects. In addition, the target resistivity evolves with time as shown in Fig. 2.20. In particular, the material resistivity rises from low temperature up to the Fermi temperature T_F, of the order a few eV, and decreases for higher temperatures. This mechanism is a key point in the experimental study presented in chapter 4. In [Santos et al., 2007, 2013] by Santos and collaborators it has been shown that resistive heating is the dominant mechanism in a thin front side of the target, within the first 10 to 20 microns.

2.5.5 Fast electron refluxing

When reaching the rear interface of the target, fast electrons escape. An intense electric field $E_s \sim k_B T_b / e\lambda_{De}$ of the order of several MV per micron is created in the charge separation layer over a distance comparable to the Debye length λ_{De} [Hatchett et al., 2000]. This electric field is responsible for the creation of a force which tends to re-injected electrons into the target. This phenomenon, called fast electron refluxing, is illustrated in Fig. 2.23. It is rather efficient: only a small fraction of the electrons with a sufficient energy $\gtrsim$ MeV, carrying a charge of a few nC, are able to escape the intense charge separation field and to propagate into vacuum Tikhonchuk [2002]. The measurement of the escaped electron spectrum, even if fairly different from spectrum inside the target, can provide a useful information on the fast electron beam.

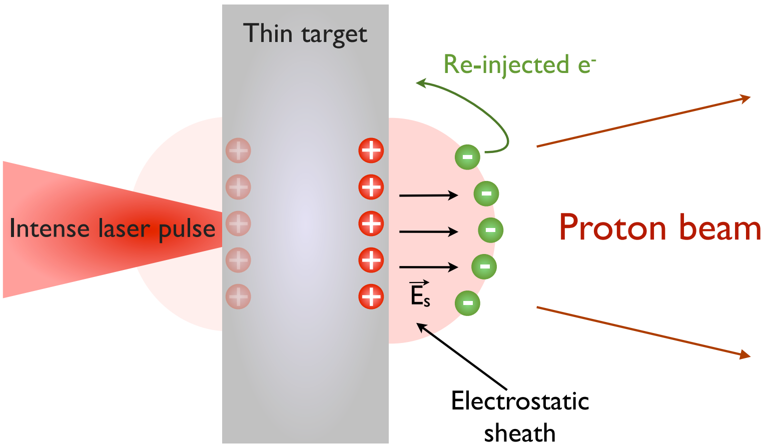

Figure 2.23: Illustration of the refluxing mechanism. Fast electrons leaving the target create an intense charge separation field that re-inject a large fraction of them into the target. If the propagation medium is thin enough this mechanism can also take place at the front side of the target, making fast electrons going through the target several times. The charge separation electric field is also responsible for the acceleration of proton beams by the TNSA mechanism.

The fraction of re-injected electrons can be evaluated considering a simple capacitor model. It is given by $\zeta_r = 1 - \exp(-\Phi)$, with $\Phi = eV/T_h$, V the electrostatic potential and T_h the fast electron temperature. This value, highly depending on experimental conditions, is often $> 90\%$

[Myatt et al., 2007] provided their energy is high enough. Re-injected fast electrons can cross the target, bounce on the other edge, and so on, performing several round trips.
Fast electron refluxing in thin targets is responsible for an efficient enhancement of the target heating [Martinolli et al., 2006; Pérez, 2010]. It was also shown both experimentally and numerically that fast electron refluxing is responsible for an artificial increase of tracer emission (mostly K_α emission, see section 3.1) [Quinn et al., 2011; Sawada et al., 2014; Theobald et al., 2006], which has to be taken into account in numerical simulations to avoid an overestimate of the fast electron population from the experimental K_α yield data. Refluxing can also be suppressed by increasing the target size or by creating a *get lost layer* at the rear side of a target. This last process can be performed by shooting a long pulse laser beam on an ablator layer, creating an expanding plasma [Sawada et al., 2014; Vauzour et al., 2014]. Quinn et al. [2011] and Sawada et al. [2014] also observed that the radial extension of the K_α emission is mostly dictated by the first pass of fast electrons through the target. This can be explained by the following. After several round trips into the target, the fast electron beam radial extension is fairly more important than during its first pass. The generated K_α signal is consequently weaker and weaker, leading a measured K_α spot size mostly dictated by the first pass.
Finally, the intense charge separation field created by fast electrons escaping the target is responsible for an efficient ion acceleration called *Target Normal Sheath Acceleration* (TNSA). This TNSA mechanism, firstly observed by Snavely et al. [2000] and modeled by Wilks et al. [2001], can accelerate ions up to a several 10s of MeV. The electron refluxing phenomenon is also responsible for an enhancement of the maximum accelerated ion energy provided that the target is thin enough [Mackinnon et al., 2002; Sentoku et al., 2003]. This can be explained by the following. When considering a target thickness L_T greater than a half of the laser pulse length $L_p/2$ fast electrons propagating into the target overlap only locally, near the target edge. If the target is thin enough so that $L_T < L_p/2$ the efficient superposition of electrons leaving the target and entering the target increases the effective electron density. Since the charge separation electric field directly depends on the electron density, the TNSA mechanism is in this thin target case more efficient.

2.5.6 Beam instabilities

In the previous section we assumed that the propagation of electron beams was unperturbed. However the stability of an electron beam can be affected by a perturbation of the self-generated electromagnetic field. Initial be am density perturbations can give rise to a large variety of beam instabilities that dramatically affect the propagation of electron beams.

Microscopic instabilities

Microscopic instabilities generate local electrostatic or electromagnetic fields on a micrometer scale size. They are characterized by the growth rates that can reach the plasma frequency time scale. One of the firstly studied instability is called the *two stream instability* [Buneman, 1959]. It develops when two beams of charged particles cross each other in opposite directions, such as the incident and the return currents. In this situation longitudinal density perturbations can give rise to the development of longitudinal electrostatic waves. When considering a fairly low density fast electron beam compared to the plasma electron density such as $n_b << n_p$ the driven wave frequency is close to the plasma frequency ω_{pe} while its phase velocity is slightly lower than the fast electron beam velocity v_b. The two stream instability can strongly affect the propagation of fast electrons that are slowed down until their average speed gets close to the wave speed itself, and that their initial energy distribution is completely modified. The growth of this instability is fortunately easily inhibited in a highly collisional plasma when the plasma electron collision frequency ν_{ei} is higher than the instability growth rate. This condition yields a fast electron beam density threshold, given by [Gremillet, 2001]:

$$n_b > \min\left[n_p, \frac{16 n_p \gamma_b^3}{3^{3/2}(\omega_{pe}/\nu_{ei})^3}\right] \tag{2.150}$$

In our experiment, since $n_b << n_p$, the two-stream instability amplitude can be considered as negligible.

Perturbations of beam density in the transverse direction compared to the beam propagation direction are responsible for another instability first described by Weibel [1959]. Current density perturbation in the transverse direction triggers a fluctuation of magnetic fields that amplify the initial current fluctuations. This phenomenon is amplified by the presence of a return current. The Weibel instability is responsible for the creation of micro-currents with opposite signs spatially separated by the skin-depth c/ω_{pe} scale, which strongly deteriorates the current neutrality. As the instability grows these magnetic filaments merge into larger filaments. The Weibel instability strongly affects the beam propagation in the target. It is responsible for the beam initial angular dispersion due to fast electron randomly scattering in the thin intense filamented magnetic layer located in the vicinity of the laser-plasma interaction region [Adam et al., 2006; Debayle et al., 2010]. It is worth mentioning that the Weibel instability can be extended to collisional plasmas, which is called resistive filamentation. The two-stream and Weibel instabilities constitute two limits of a more general instability characterized by an arbitrary perturbation direction with respect to the beam propagation axis [Bret et al., 2004].

Macroscopic instabilities

Macroscopic instabilities develop on the fast electron beam radius size scale. Their growth rate, comparable to the magnetic diffusion time $\tau_D >> \omega_{pe}^{-1}$, is fairly lower than the microscopic instabilities growth rate. Macroscopic instabilities are a direct consequence of the finite conductivity of the propagation medium. For example the so-called *hollowing* instability is due to a focusing magnetic field created by the imperfect neutralization of the incident beam. A current over-density is consequently created on the beam propagation axis. The subsequent Ohmic heating of the material being more important on the beam center than on its edge, the resistivity of the crossed material $\eta \propto T_e^{-3/2}$ (Spitzer regime) becomes lower on the beam axis. Since fast electrons propagate towards higher resistivity regions this situation results in the hollowing on the incident beam. If the heating is strong enough the incident beam shape is transformed in an annular shape. Davies [2003] estimated that the required intensity to observe such a phenomenon should be greater than 10^{19} W.cm^{-2}.

Another macroscopic instability called the *hosing* instability is driven by a lateral displacement of the beam [Hum, 1983]. The background plasma trying to conserve the total current generates a magnetic field that exerts a retracting force, pulling fast electrons toward the beam propagation axis. The diffusion of the magnetic field due to the finite resistivity of the plasma induces a phase shift between the beam oscillations and the retracting force which consequently amplifies the unstable oscillations.

2.6 Conclusion on the theory of fast electron transport

When a fast electron beam is generated in a dense plasma, a neutralization in both charge and current takes place within a time close to $1/\nu_{ei}$, of the order of a few femtoseconds. This current neutralization allows to overcome Alfvén's limit and the subsequent transport of large currents over long distances, on the time scale of the magnetic diffusion time τ_D, of the order of a few tens of ps. Magnetic fields generated by density or current gradients dramatically affect

the fast electron beam propagation, producing focusing or defocusing effects.
Collisional effects dramatically affect fast electron beam propagation. While elastic electron-ion collisions are responsible for the angular scattering of the beam and its subsequent isotropisation, electron-electron collisions result in the slowing down of the incident beam, transferring its energy to the background electrons, efficiently heating the plasma. The progressive diffusion of electrons is responsible for a decrease of the current density. As a consequence, the collective energy losses, scaling as $\propto j_h^2$, decrease. They represent the dominant energy loss mechanism for current densities $> 10^{11}$ A.cm^{-2} that can be typically encountered close to the fast electron source. They represent an important contribution to the total energy losses.
Current perturbations acting on self-generated electromagnetic fields are responsible for the development of beam instabilities, on microscopic or macroscopic scales. These latter being characterized by a growth rate comparable to the magnetic diffusion time, they can be neglected in our experiments. Microscopic instabilities developing on the micron size scale and on the collision frequency time scale play however a significant role in the fast electron beam propagation, in particular they are likely to determine the initial beam divergence.

Chapter 3

Fast electron beam diagnostics

The characterization of the fast electron source created by intense laser pulses is of primary importance in our study. It is however a non-trivial issue since fast electron beam exist only for a few ps and mostly propagate in overdense targets. During their propagation fast electrons emit photons in the eV-MeV range. This electromagnetic emission, generated by a multitude of atomic or nuclear processes, may escape from the target, provided its energy is high enough. Unlike charged particles, photons have the advantage of being neutral and weakly perturbed by intense electromagnetic fields generated in the interaction. In our experiments we focused on the detection of X-ray emissions in the keV-MeV range. This energy range has the advantages that the photons are mainly produced by fast electrons, not by the thermal electrons, and also to be energetic enough to escape the target without being too much absorbed. Other diagnostics are also used to characterize the fast electron beam propagation. One of them consists in directly collecting fast electrons escaped from the target. The drawback of this diagnostic is to detect only the population of fast electrons with a sufficient kinetic energy to escape the charge separation field created at the rear side of the target [Cottrill et al., 2010]. In addition, the detected electron spectrum greatly depends on the initial fast electron distribution, and on the target shape and composition. The optical emission can also be used to extract an information about the high energy part of the fast electron spectrum (CTR), and on the temperature of the background plasma (thermal emission).

We present in this chapter the physical mechanisms of photon emission, which were used in our experiments for the fast electron diagnostics. We begin with a description of the X-ray emission, mainly focusing on the K_α spectroscopy as well as on bremsstrahlung emission, which were of primary importance in our experiments. The detectors used to characterize these emissions, such as K_α spectrometers, K_α imagers or bremsstrahlung spectrometers, called bremsstrahlung *cannons*, are then be described. To conclude this chapter the scheme of an electron-positiron spectrometer is presented.

3.1 X-ray emission

3.1.1 K-shell emission

As mentioned in the previous section, fast electrons propagating in a dense matter transfer their energy in collisional processes with the surrounding atoms. An incident electron can cause an atomic transition from the ground level i to an excited level j if its energy is larger than the atomic transition energy $E > E_{ij}$. If one is interested to discriminate fast electrons from the thermal ones, this transition energy should be the highest possible. One of these particular transitions is the ionization of an electron belonging to the most inner shell of the atom, characterized by the quantum number $n = 1$, corresponding to the K-shell, or $1s$ orbital.

This ionization can only take place if the incident electron has an energy higher than the binding energy of this K-shell B_K, given as a function of the atomic number Z < 92, with a 4% maximum error, by [Casnati et al., 1982]:

$$\frac{B_K}{R_y} = 0.424 Z^{2.1822} \tag{3.1}$$

with $R_y = m_e.e^3/8.\epsilon_0^2.h^2 \sim 13.606$ eV the Rydberg energy. When such an ionization process occurs, the ion can decay down to a more stable state by filling-in the inner shell gap with an electron coming from an outer shell (L or M shells). The released energy can be either transferred to another atomic electron (Auger effect), or to be emitted as an X-ray photon characterized by a very specific energy. This latter X-ray fluorescence is called K_α emission in the case of a $2p \rightarrow 1s$ transition (L-shell to K-shell). The whole process leading to K_α emission is summarized in Fig.3.1. Unlike bremsstrahlung emission, which will be described in the next section, K_α transition leads to an isotropic emission: the fluorescence photons are emitted in 4π sr.

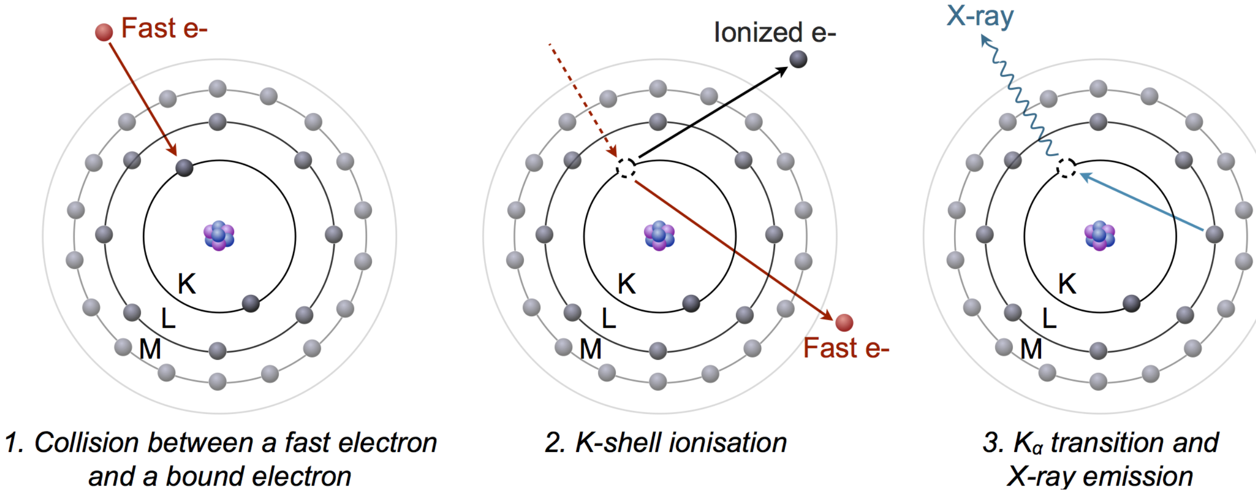

Figure 3.1: K_α radiative deexcitation after fast electron ionization of the K-shell.

K_α transitions are in fact split into two possible transitions called $K_{\alpha 1}$ and $K_{\alpha 2}$ and corresponding to $2p_{1/2} \rightarrow 1s$ and $2p_{3/2} \rightarrow 1s$ transitions, respectively. Due to the quantum selection rules allowing atomic transitions between two energy levels only if $\Delta l = \pm 1$ and $\Delta j = 0, \pm 1$, with l the orbital quantum number and j the total angular quantum number, the $2s_{1/2} \rightarrow 1s$ transition is forbidden. K_β emission corresponding to a $3p \rightarrow 1s$ transition (M-shell to K-shell) can also occur, even if it is less probable than the K_α emission. Besides, because of the successive ionization of the outer shells for increasing temperature, the probability of K_β emission relative to that of K_α emission decreases with the temperature. All these radiative transitions are summarized in Fig. 3.2, for the case of copper atoms.

The K_α energy transitions can be estimated with the Moseley empirical law as a function of the atomic number Z for $3 < Z < 60$. Moseley's model assumes that there is no distinction between $K_{\alpha 1}$ and $K_{\alpha 2}$ emissions and provides an estimation with a 5% error [Moseley, 1913] given by

$$E_{K\alpha}[\text{eV}] = 10.206\,(Z-1)^2 \tag{3.2}$$

The K_α emission was widely used in our experiments as a signature of fast electron propagation, acting like a fast electron counter. For the copper, a material used in our experiment as

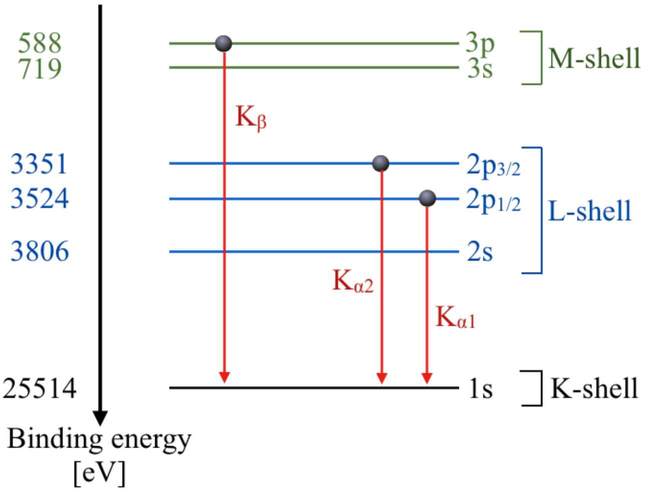

Figure 3.2: Position of the first energy levels in copper atoms. The radiative transitions after inner-shell ionization of the atom are represented with red arrows.

a fast electron tracer, this K_α transition is characterized by $E_{K\alpha} \sim 8002$ eV. It can only occur for incoming electrons with the energy higher than $B_K = 8996$ eV, well above the background electron thermal energy. The K_α fluorescence can also provide a bright quasi-monochromatic source of X-rays that can be used for radiography purposes, as discussed in chapter 5.

K-shell emission cross section

The K-shell emission cross section σ_K can be expressed by the following:

$$\sigma_K = f_K.\sigma_{\text{ion}} \tag{3.3}$$

with σ_{ion} the K-shell ionization cross section and f_K the fluorescence yield. This latter term accounts for the fact that there is another relaxation mechanisms, the Auger electron emission. K-shell ionization cross sections have been wildly studied both theoretically and experimentally. The theoretical description for any element requires complex quantum calculations. As a consequence very few theoretical expressions succeeded in describing K-shell ionization cross sections over a wide range of incident electron energy. Numerical calculations also lack of convenient expressions that could be used directly. A large number of empirical laws based on fitting the experimental results have been published. We describe in this part the empirical model of Hombourger, which is one of the most widely used in experiments and numerical simulations. The ionization cross section can be written as follows [Hombourger, 1998]:

$$\sigma_{\text{ion}} = N_K.\pi.a_B^2.G_r.\left(\frac{R_y}{B_K}\right)^{C_U}.D_U \tag{3.4}$$

with $N_K = 2$ the number of K-shell electrons and $a_B = \epsilon_0.h^2/\pi.m_e.e^2 \sim 0.53$ Å the Bohr radius. C_U and D_U are two dimensionless factors given by:

$$\begin{aligned} C_U &= 2.305 - \frac{0.316}{U} + \frac{0.1545}{U^2} \\ D_U &= \left(3.125 - \frac{4.172}{U} + \frac{1.877}{U^2}\right).\frac{\ln(U)}{U} \end{aligned} \tag{3.5}$$

Those factors depend on the dimensionless parameter $U = E/B_K$, called overpotential, defined as the ratio between the incident electron energy and the K-shell binding energy. The term G_r in Eq. 3.4, is the Grysinski's factor, which accounts for the relativistic corrections [Gryzinski, 1965; Quarles, 1976]:

$$G_r = \left(\frac{1+2J}{U+2J}\right) \cdot \left(\frac{U+J}{1+J}\right)^2 \cdot \left(\frac{(1+U).(U+2J).(1+J^2)}{J^2.(1+2J)+U.(U+2J).(1+J^2)}\right) \tag{3.6}$$

with $J = m_e.c^2/B_k$. It is worth mentioning that the behavior of the ionization cross section at high U values is described by the $\ln(U)/U$ factor in the D_U term.

Ionization cross sections are shown in Fig. 3.3 for the materials commonly used in our experiments as fast electron tracers. Experimental measurements of Cu-K-shell ionization cross sections from Llovet et al. [2000]; Liu et al. [2000]; Zhou et al. [2000] are also plotted for copper. The ionization cross section is zero below the K-shell binding energy, also called K-edge. It rises rapidly just above this threshold and peaks at approximately 3 times the binding energy. The position and the shape of this peak has been confirmed by several experimental measurements. For some materials such as copper, silver or tin, the cross sections then decrease until ∼ 1 MeV and start again to increase gradually. The position of this minimum is roughly the same for all

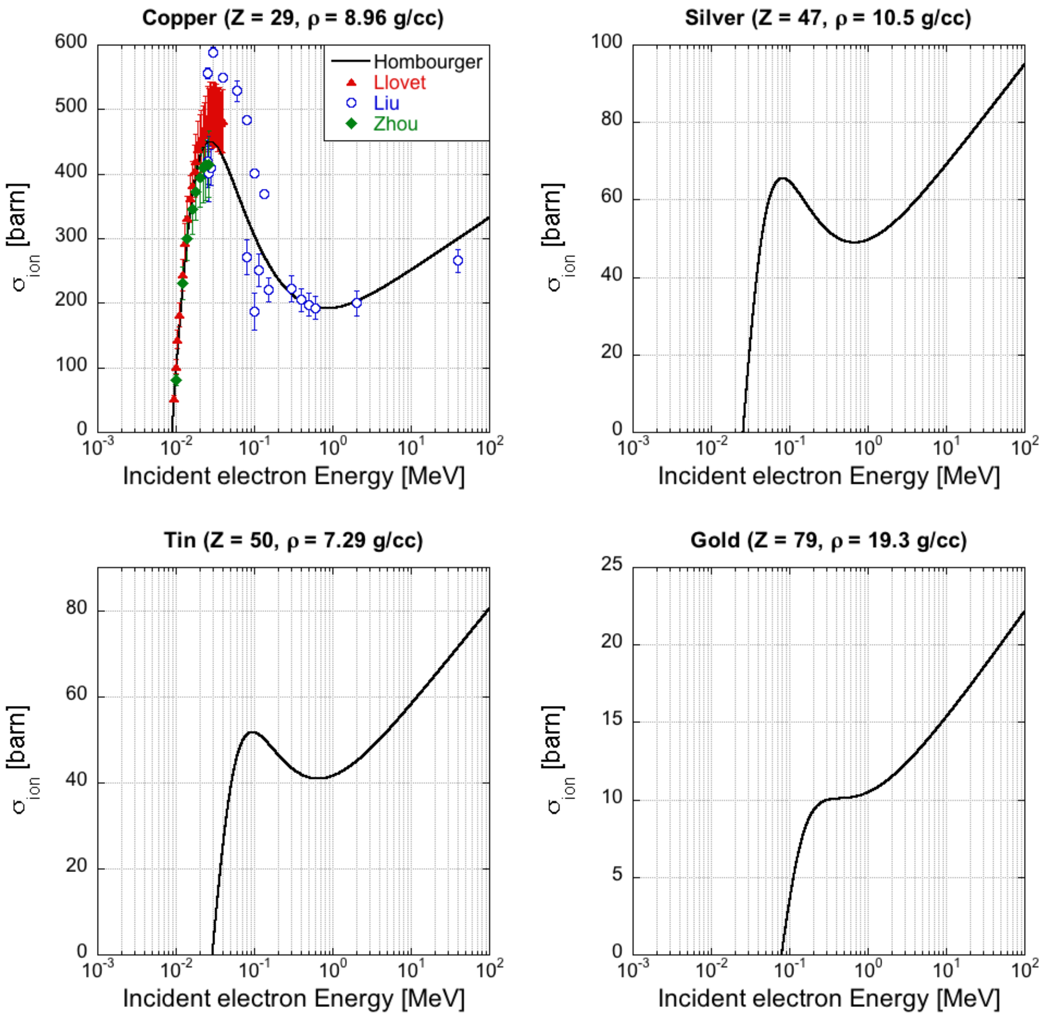

Figure 3.3: K-shell ionization cross sections by the electron impact as a function of the incident electron energy for the copper (top left), silver (top right), tin (bottom left) and gold (bottom right). Gold was not used in our experiments as a fast electron tracer. Its ionization cross section is plotted here as an illustration of high Z material behavior.

materials and its depth decreases for increasing Z atomic number. For high-Z materials such as gold this local minimum does not exist.

One can also note the lack of experimental measurements of K-shell ionization cross sections at relativistic energies greater than a few MeV. This could affect experimental data interpretation since relativistic effects are not so well included in the ionization cross sections that can be found in the literature. The recent paper by Davies et al. [2013] points out that none of the existing ionization cross section include density corrections. As mentioned in the previous sections, this effect, important for high energy electrons, triggers a decrease of the electron stopping power, and thus a decrease of the ionization cross section, due to the screening of the incident electron charge by the polarization field of the propagation medium. This correction is more important for high Z number atoms. In our study however most of the fast electrons have energies lower than 1 MeV, as shown on Fig. 2.10. As a consequence the density-effect should not lead to a significant error in the interpretation of our experimental results (see chapters 4 and 5).

K_α fluorescence efficiency

The radiative emission is not the only process which is involved in atomic deexcitation. It competes with the emission of an Auger electron. The probability of deexcitation by K_α emission depending on the atomic number Z is called the fluorescence yield f_K. This yield can be estimated by an empirical formula proposed by Kahoul et al. [2011], based on experimental results in the $6 \leq Z \leq 99$ range:

$$f_K = 0.985.\frac{(Z/30.896)^{3.847}}{1+(Z/30.896)^{3.847}} \tag{3.7}$$

The fluorescence yield as a function of the atomic number Z is plotted in Fig. 3.4 both for experimental results and the fit given by Eq. (3.7). References of experimental values can be found in [Kahoul et al., 2011].

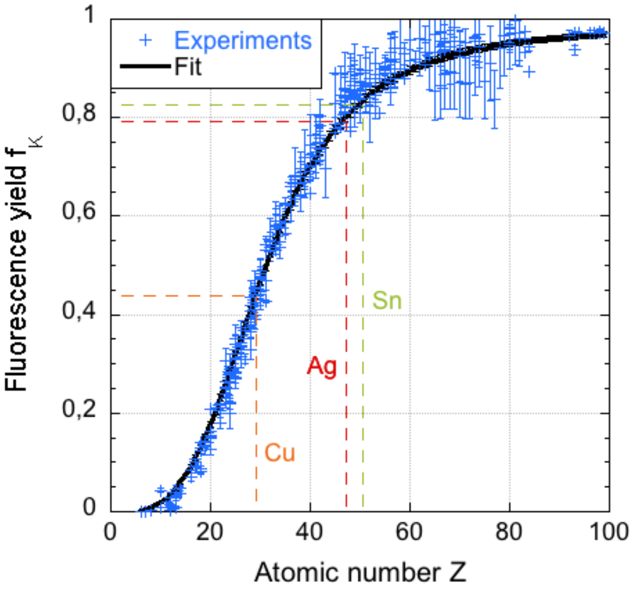

Figure 3.4: Radiative deexcitation probability as a function of the atomic number from experimental data (blue crosses) and a fit given by Eq. (3.7) (black curve). The highlighted values are corresponding to the copper (orange), silver (red) and tin (green) used in experiments presented in the next section.

The fluorescence yield f_K increases monotonously with the atomic number Z. For low Z

elements, the Auger rate is larger than the K-shell emission. This trend is inverted for elements above $Z \sim 30$.

K_α photon number

Let us consider a fast electron population described by an energy distribution function $f(E)$ propagating in a dense, thick medium with an ion density n_i. The number of emitted K_α photons can be written as follows:

$$N_\alpha = n_i \int_0^\infty f(E_0) \left(\int_{Eo}^0 f_K \sigma_K \left(\frac{dE}{ds} \right)^{-1} dE \right) dE_0 \tag{3.8}$$

with $N_e = \int_0^\infty f(E)dE$ the number of fast electrons and dE/ds the stopping power detailed in the previous chapter. Eq. 3.8 is valid only if one makes an assumption of a thick medium so that all electrons are stopped in. In other words, the range of fast electrons must be shorter than the target thickness. In our experiments, the K_α fast electron tracers buried into the targets were not thick enough ($\sim 10\ \mu$m) to justify such an assumption, except for the lowest energy electrons. In such a situation the number of photons emitted per unit length is given by:

$$\frac{dN_\alpha}{ds} = n_i f_K \int \sigma(v) f(v) dv \tag{3.9}$$

with v the relativistic electron speed. Even if the K_α radiation is completely isotropic so that photons are emitted with an equal probability in 4π steradian, K_α diagnostics must be located as close as possible from the target axis due to the re-absorption of the generated line emissions during their propagation.

Attenuation of the emission

The number of K_α photons arriving on the different detector is smaller than the number of initially emitted photons. Some of them are absorbed in the matter along the propagation path. The transmitted part T of the signal depends on the nature and the thickness s of the medium, as well as on the energy of the considered photon. This transmission factor can be written as:

$$T = \exp \left[-\frac{\mu_X}{\rho} \rho s \right] \tag{3.10}$$

with ρ the density of the medium, ρs its areal mass and μ_X/ρ its mass-attenuation coefficient given by

$$\frac{\mu_X}{\rho} = \frac{\sigma_{tot}}{uA} \tag{3.11}$$

with $u \sim 1.66 \times 10^{-24}$ g the atomic mass unit, A the mass number and σ_{tot} the total cross section of the photon scattering and absorption. This latter term takes into account all the processes involved in photon-matter interaction: photoelectric effect, coherent (Rayleigh) and incoherent (Compton) scattering and electron-positron pair creation. The values of mass-attenuation coefficients for different elements or mixtures as a function of the photon energy can be found in the NIST database [Hubbel & Seltzer, 2014]. These coefficients are plotted in Fig. 3.5 for the tracers used in our experiments. Mass-attenuation coefficients decrease when the photon energy increases. This can be understood as a better transmission of more energetic photons. The discontinuities correspond to the K-edges and L-edges of the atomic shells. Those

edges, located right after the binding energy of an electron in the K-shell or the L-shell, and corresponding to a sudden decrease of the transmission, are due to the photoelectric effect. The contribution of the different physical processes involved in attenuation of photons are plotted for the case of silver. One can note that the pair production mechanism appears for a photon of energy $E_X = 2m_ec^2 = 1.022$ MeV.
Experimental measurements are inevitably affected by the transmission of the materials that are on the photon's path. In particular this may create an anisotropy of the K_α emission. The position of the different photon detectors must be carefully chosen, and the deconvolution of the obtained result must take into account this attenuation.

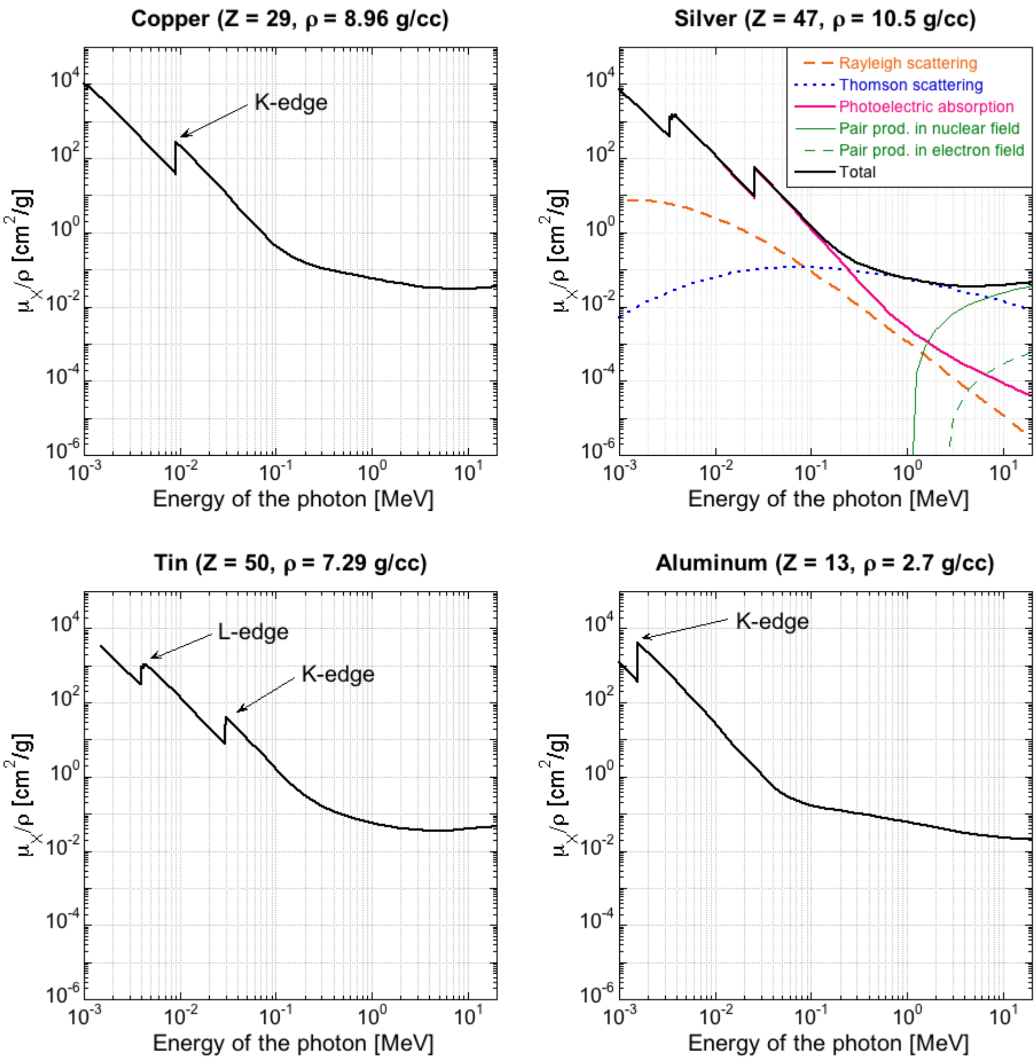

Figure 3.5: Mass attenuation coefficients as a function of the incident photon energy for aluminum (top left), copper (top right), silver (bottom left) and tin (bottom right) materials. The discontinuities leading to a sudden decrease of the transmission correspond to K-edges and L-edges. The contributions of different processes to the mass attenuation coefficient are given for the silver.

K-shell spectroscopy

As mentioned in the beginning of this section, the transition of an electron from the L-shell to the K-shell is split into two contributions called $K_{\alpha1}$ and $K_{\alpha2}$, corresponding to $2p_{1/2} \rightarrow 1s$ and

$2p_{3/2} \rightarrow 1s$ transitions, respectively. The probability of $K_{\alpha 2}$ emission in the thermal equilibrium is however twice smaller than $K_{\alpha 1}$, leading to a lower number of emitted $K_{\alpha 2}$ photons. This ratio remains approximately constant when increasing the electron temperature T_e. However the increase of electron temperature leads to a broadening of the emission lines due to the following mechanisms:

- The increase of microscopic fields with the ionization level. This so-called Stark effect removes the degeneracy of atomic sub-levels.
- The increase of the thermal speed of background electrons. This is called the Doppler effect.
- The increase of electron collision frequency.

All these broadening mechanisms can be used to estimate the background electron temperature of the medium. The increase of the electron temperature above $50 - 100$ eV produces also a noticeable energy shift of the emission lines. In our experiments this shift was too weak to be detected with our spectrometers. The set up of a high resolution spectrometer in an experiment must however be carefully studied in order to be sure that this energy shift matches with the detector bandwidth.

The K_β emission corresponding, to a M-shell → K-shell transition, is less intense than K_α emission, by a factor 10 at a low temperature. The K_β emission, also subject to emission line broadening. It is more affected by the increase of the electron temperature and the resulting ionization of the M-shell. The plasma temperature can be directly estimated from the K_β emission line, or, in a more common way, by the ratio between the K_α and the K_β emissions [Myatt et al., 2007; Nilson et al., 2008].

Limitations of K_α emission as a fast electron counter

In the laser-solid interaction, in addition to fast electrons, other particles are produced such as photons or ions. Those particles can also lead to the K_α emission when propagating in a dense matter. In order to use K_α emission as a fast electron counter one has to make sure that fast electrons are the main contributor to this radiation. We discuss in this section the possible contribution of photons to the production of K_α emission and compare it with electron based K_α production. Let us consider an isotropic photon source with photons propagating on straight-line trajectories in a copper tracer layer of a thickness s. For the sake of simplicity we consider that the upper limit of photon energy is lower than the pair creation threshold (1.022 MeV). The number of K_α photons emitted per incident photon, called the photon yield Y_{ph}, can be written as [Davies et al., 2013]:

$$Y_{ph} = 0.396 \left[1 - \exp(-X) + X \int_X^\infty \frac{\exp(-t)}{t} \, \mathrm{d}t \right] \tag{3.12}$$

with $X = s/l_{ph}$ the ratio between the copper tracer thickness s and the photon attenuation length l_{ph} . If we consider an electron beam propagating at a constant velocity in the same copper layer, the yield from electrons can be written as:

$$Y_{e^-} = n_a \sigma_K s \tag{3.13}$$

with $n_a = 8.49 \times 10^{22}$ m^{-3} the atomic number density of cold-solid copper. The ratios of Y_{ph} and Y_{e^-} are plotted in Fig. 3.6. The yield for photons is maximum at the threshold and then decreases gradually with the increasing energy. The yield for electrons however has the same trend as the K-shell ionization cross section plotted in Fig.3.3 . One can also note that the photons with energies lower than 70 keV produce more K-shell emissions than electrons. This trend is inverted for higher energies.

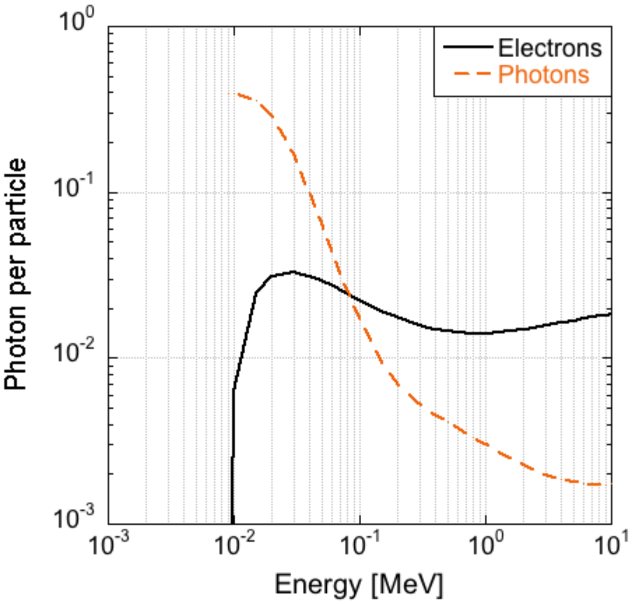

Figure 3.6: K-shell yield per incident particle for an isotropic distribution of electrons (black-solid line) and of photons (orange-dashed line) propagating in a $s = 20$ μm copper layer.

In order to study more carefully the contribution of photons in the K-shell emission it is important to discuss their potential sources. Photons can be produced by bremsstrahlung emission as discussed in section 3.1.2. The number of bremsstrahlung photons produced by electrons becomes important for the energy above > 1 MeV. The photon yield Y_{ph} is lower than the electron yield at these relativistic energies. As a consequence, in most cases, the bremsstrahlung emission is not contributing to a noticeable K-shell emission. Another photons source is the line emissions of target elements with a higher Z than the K-shell emitting tracer. This source can make a non negligible contribution of the higher Z material in K-shell production. It should consequently be evaluated for each target design. This effect may have an importance in one of our experiments where the K$_\alpha$ emission of a tin tracer layer can produce secondary K$_\alpha$ photons in a copper tracer layer located immediately after the tin layer. In order to estimate this contribution, let us consider that the tin emission comes from a point-like source and the photons propagates through $\Delta x = 10$ μm of copper, corresponding to the initial thickness of our copper tracer layer. The number of photo-induced copper K$_\alpha$ photons $n_{Cu,Sn}$ emitted per steradian in the detector direction is given by [Martinolli, 2003] :

$$n_{Cu,sr} = \frac{f_K}{4\pi} n_{Sn,sr} \int_0^{2\pi} d\phi \int_0^{\pi/2} \int_0^{\Delta x} \exp\left[-\frac{\mu_{Cu,Sn} x}{\cos\theta}\right] \frac{\mu_{Cu,Sn} x}{\cos\alpha} \exp\left[-\frac{\mu_{Cu,Cu}(\Delta x - x)}{\cos\theta}\right] \sin\theta d\theta dx \quad (3.14)$$

with $n_{Sn,sr}$ the number of tin K$_\alpha$ photons emitted per steradian, $\mu_{Cu,Cu} = (21.5)^{-1}$ μm the linear absorption coefficient of copper K$_\alpha$ photons in the copper layer [Hubbel & Seltzer, 2014] and $\alpha = 30°$ the angle between the electron propagation axis and the detector direction. The factor $\mu_{Cu,Sn} = (71.98)^{-1}$ μm can be inferred from the partial ionization cross section of the copper K-shell by tin K$_\alpha$ photons calculated using Verner's fit [Verner & Yakovlev, 1995]. For photon with an energy $E < 100$ keV interacting with an ion characterized by the quantum numbers n, l and by its ionization degree, the photon-ionization cross section is given by the following empirical law:

$$\sigma_{nl} = \sigma_0 \left\{ \left[\left(\frac{E}{E_0} - 1 \right)^2 + y_w^2 \right]^{-Q} \left(1 + \sqrt{\frac{E}{E_0} \frac{1}{y_A}} \right)^{-P} \right\} \tag{3.15}$$

with σ_0, E_0, y_w, y_A and P fitting parameters depending on the considered element. The Q factor is given by $Q = E/E_0 + l - 0.5P$.
Considering a number of tin photons $n_{Sn,sr} = 1.0 \times 10^{11}$ ph/sr, which is close to the highest yield value measured in our experiments, the number of photo-induced Cu-K$_\alpha$ photons in the $\Delta x = 10$ μm copper layer is given by $n_{Cu,sr} \sim 7 \times 10^9$ ph/sr, which represents in fact only a few percent of the total emission of the copper layer, and can consequently be neglected in our analysis.

Another source of secondary K$_\alpha$ emission are the fast ions, especially the protons. Indeed, the cross section for the protons with the energy larger than 3.4 MeV exceeds that for electrons. A detailed discussion of this problem can be found in [Davies et al., 2013]. Considering that the number of protons crossing the targets is very weak in our experimental conditions, their contribution to the K$_\alpha$ emission is also negligible on the results described in the following chapters.

3.1.2 Bremsstrahlung emission

Bremsstrahlung emission is produced in a collision between two charged particles of different species. In our experiments, most of the emitted radiations comes from the interaction between fast electrons and the background plasma ions. The collisions between an incident electron and ions, which can be considered at rest, produce a continuous emission on a broad spectral range. The intensity of this emission, lower than the intensity of K$_\alpha$ emission, decreases exponentially for increasing photon energy. As mentioned in section 2.4.3, the bremsstrahlung emission cross section is proportional to Z^2: this process is more important for high Z materials. The bremsstrahlung radiation is also more important for high energy electrons ($>$ 1 MeV) which emit a larger amount of photons. Moreover, unlike the K$_\alpha$ emission, the bremsstrahlung emission is not isotropic. Photons are emitted in a cone centered on the incident electron direction and described by an opening angle $\sim 1/\gamma$: the more energetic is the incident electron, the more collimated is the bremsstrahlung emission around the electron propagation direction. As a consequence, the analysis of bremsstrahlung emission is a powerful tool to characterize the fast electron beam energy distribution propagating in the target. As discussed in chapter 4, such a study requires however a support from the numerical simulations.

3.2 X-ray diagnostics

Most of the diagnostics used in our experiment to detect line emissions, such as the K$_\alpha$ emission, use crystals of different shapes. Such X-ray detection is based on the Bragg's diffraction law. This law, illustrated in Fig. 3.7, states that only a certain reflected wavelength λ can interfere constructively for a given grazing angle θ on a crystal. The Bragg's law is given by:

$$n\lambda = 2d \sin\theta \tag{3.16}$$

with $n \in \mathbb{N}^*$ and d the spacing length between two crystal planes. Bragg's law allows to reflect any photon with the energy $E_\nu = hc/\lambda$, provided that one chooses carefully the incidence angle, the diffraction order and the crystal (defined by its $2d$ spacing parameter). However the reflected signal decreases dramatically when increasing both the incidence angle or the diffraction order. These parameters are usually limited to $n < 5$ and to grazing angles $\theta > 10°$. The accessible photon energy bandwidth of crystals allowed us to detect photons from a few keV to ~ 100 keV.

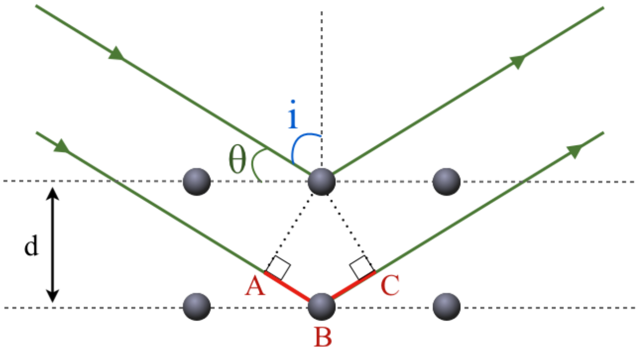

Figure 3.7: Illustration of the Bragg's law for photon beam incident at the grazing angle θ defined as $\theta = \pi/2 - i$, with i the angle of incidence. The bottom beam has to travel an extra distance given by $AB + BC = 2d \sin\theta$ compared to the upper beam. This extra distance must be an integer multiple of the photon wavelength so that the two represented beams propagate in phase.

3.2.1 X-ray spectroscopy

The spectrometers described in this section allowed us to characterize the K_α and K_β radiations emitted in the interaction of the studied fast electrons with the different tracer layers buried into the targets. Those spectrometers use Bragg crystals which differ by their shape and by their inter-atomic plane spacing, leading to substantial differences in terms of reflectivity, spectral resolution or signal-to-noise ratio. All the spectrometers described in this section are commonly used in laser-plasma experiments worldwide.

Flat crystal spectrometer

Let us begin by the simplest configuration of a flat crystal. In this configuration all the atomic planes are parallel to the surface of the crystal. Such a flat crystal consequently acts as a X-ray mirror which would in addition select the reflected wavelengths. In order to be reflected by the crystal, an incident photon with an energy $E_\nu = hc/\lambda$ should have an angle of incidence θ satisfying the Bragg's law. In other words, for a X-ray source at a given location, each part of the crystal reflects a very specific wavelength, which leads to a spatial dispersion of the incoming wavelengths on the detector. Let us calculate the spectral dispersion function $E_\nu = f(x)$, with x being the position of the reflected ray of an energy E_ν on the detector. Using the notations of Fig. 3.8, the grazing angle θ is given by:

$$\sin\theta = \frac{a}{\sqrt{a^2 + \frac{x^2}{4}}} \tag{3.17}$$

Combining this equation with the Bragg's law given by Eq. 3.16, one finds the dispersion function of a flat crystal:

	Crystal type	**n**	**2d**	**$\Delta\alpha$**	**Dimensions**	**a**	**E$_{\text{centered}}$**	**Spectral line**
Configuration 1	ZYA	1	6.714 Å	0.4°	7.62 × 1.27 cm	4.64 cm	8.59 keV	Cu-K$_\alpha$, Cu-K$_\beta$
Configuration 2	ZYA	1	6.714 Å	0.4°	7.62 × 1.27 cm	4.78 cm	8.18 keV	Ni-K$_\alpha$, Cu-K$_\alpha$, Cu-K$_\beta$

Table 3.1: Characteristics of the HOPG crystal used in our experiments in the low energy channel to detect the Cu-K$_\alpha$, Cu-K$_\beta$ and Ni-K$_\alpha$ emissions. E$_{centered}$ corresponds to the energy of the X-rays reflected at the center of the crystal. The configuration number one corresponds to the standard DC-HOPG configuration while the number two was obtained by removing three spacers under the crystal.

$$E_\nu = \frac{nhc}{2da}\sqrt{a^2 + \frac{x^2}{4}} \tag{3.18}$$

For a parameter $a << x$ this dispersion function is linear. The spectral resolution of the detector $\Delta E_\nu / E_\nu$ can be calculated by differentiating Eq. 3.18 :

$$\frac{\Delta E_\nu}{E_\nu} = \frac{x}{4a^2 + x^2}\Delta x \tag{3.19}$$

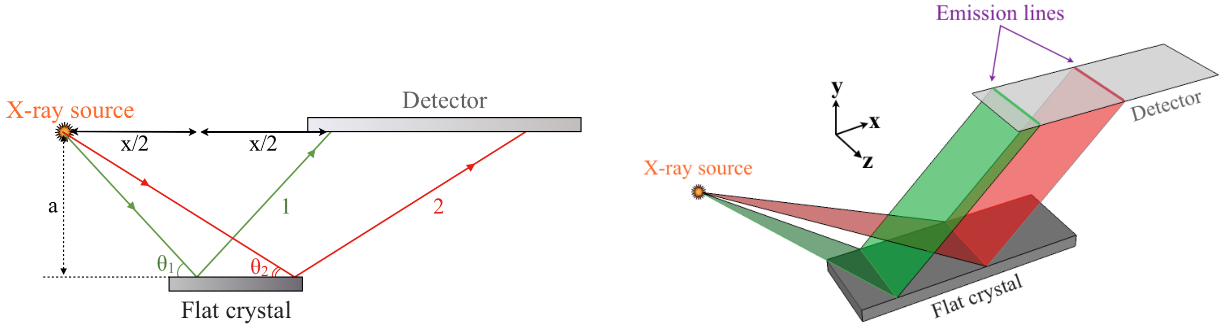

Figure 3.8: Flat-crystal geometry for two incident X-rays at different energies.

The 3D view of the flat crystal geometry presented in Fig. 3.8 allows to notice that each wavelength is reflected from the crystal along a line in the z direction. The X-ray signal on the detector consequently appears like a series of parallel lines along the z direction, stretched along the x direction due to the spectral width of the emission. This spread in the z direction produces a strong decrease of the detected signal, leading to a poor signal-to-noise ratio.

In order to increase the signal intensity, a special flat crystal called Highly Oriented Pyrolitic Graphite, or HOPG, was developed [Pak et al., 2004]. The HOPG crystal is made of a mosaic of microscopic crystals oriented approximately along the crystal plane direction, like a conventional flat crystal, but with a spread in angle $\Delta\alpha$ of a few degrees. This spread increases the reflectivity of the crystal. Indeed X-rays of a given wavelength can now be reflected by a wider region than a narrow line. However the detected line emissions are also artificially broadened. We used in our experiments a double channel spectrometer (DC-HOPG), developed by Akli et al. [2010], with two absolutely calibrated HOPG crystals optimized to detect copper K$_\alpha$ emission and silver K$_\alpha$ emission. A schematic of this spectrometer is presented in Fig. 3.9.

In our experiments we only used the low energy channel. Its characteristics are presented in Tab. 3.1 for two used configurations. The first one is the standard configuration and the second one was obtained by removing three spacers under the crystal to shift the spectral bandwidth to the lower energies in order to detect the nickel K$_\alpha$ emission line (7.461 keV).

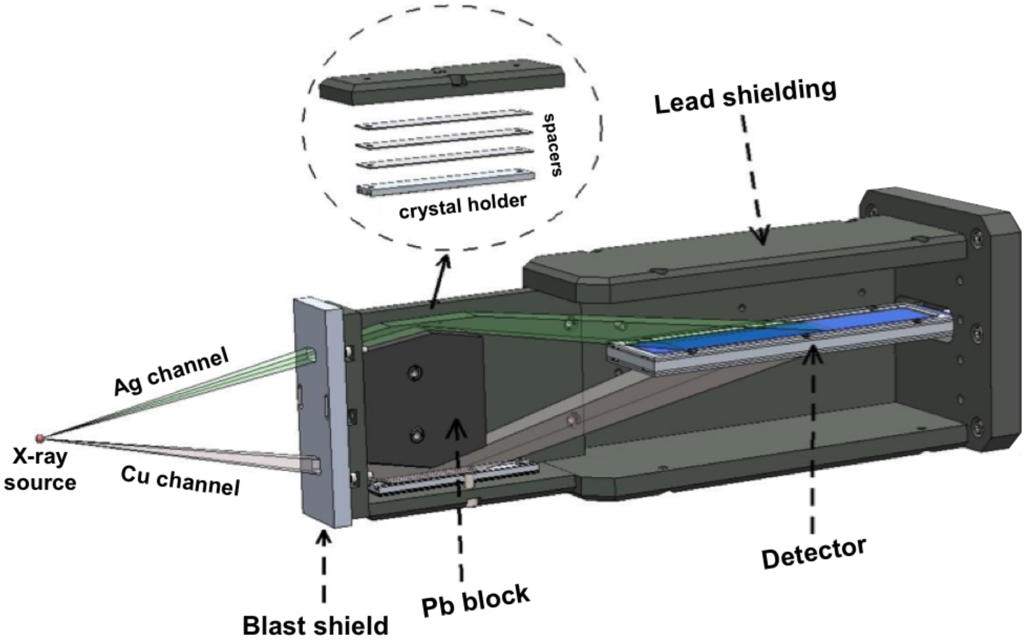

Figure 3.9: Dual channel spectrometer using two HOPG crystals. The front side lead block, as well as the global lead shielding of the spectrometer, avoid any direct irradiation of the detectors. Crystal height can by adjusted by inserting some spacers between the crystal back surface and its holder. This allows a slight tuning of the accessible bandwidth. The image was taken from [Akli et al., 2010].

The limitations in terms of both crystal length and height allowed us to detect signals in the $7.5 - 10.5$ keV energy interval. The resolution power $\Delta E/E$ of the spectrometer was calculated by Akli et al. [2010] where the DC-HOPG was used to measure the photon spectrum from laser irradiated copper targets. The resolution power was modeled using ray tracing by the following:

$$\left(\frac{\Delta E_\nu}{E_\nu}\right)^2 = \left(\frac{\Delta E_\nu}{E_\nu}\right)^2_{\text{nat}} + \left(\frac{\Delta E_\nu}{E_\nu}\right)^2_{\text{src}} + \left(\frac{\Delta E_\nu}{E_\nu}\right)^2_{\text{pls}} + \left(\frac{\Delta E_\nu}{E_\nu}\right)^2_{\text{crys}} + \left(\frac{\Delta E_\nu}{E_\nu}\right)^2_{\text{det}} \tag{3.20}$$

The first term corresponds to the broadening of the ray due to its natural width, leading to a spectral broadening of 2 eV. The second term directly depends on the effective source size giving a spectral broadening of 20 eV. The third term is linked to the spectral broadening of the plasma. The spectral width of the emission line depends on the local plasma characteristics, such as the Doppler effect, the plasma self-absorption or the ionization degree. In the experiment, this term led to a spectral broadening of 2.5 eV. The fourth term is due to the intrinsic characteristics of the crystal such as its depth, its mosaicity or it roughness, leading to spectral broadenings of 4.5 eV, 7 eV and 8 eV respectively. The last term is due to the detector resolution, leading to a spectral broadening of 4 eV. The total resolution for the copper K_α line is finally estimated to ~ 50 eV, which does not allow to resolve the $K_{\alpha 1}$ and $K_{\alpha 2}$ emissions, which are spectrally separated by 20 eV. The contribution of the crystal to the broadening of the emission line also includes the fact that actual crystals reflect wavelengths with incident angles $\theta_B \pm \Delta\theta$ around the Bragg's angle. The variation of the crystal reflectivity with the incidence angle, called *rocking curve*, is calculated by measuring the reflectivity of the crystal as a function of the angle of incidence of a monochromatic X-ray source. The deviation $\Delta\theta$ corresponding to the width of the rocking curve is around 10^{-3} degrees for the quartz crystals and it is closer to 10^{-1} degrees for HOPG crystals.

In summary, conventional flat crystals do not allow to obtain a good enough signal-to-noise ratio. The use of HOPG crystals increases the signal intensity, with however a loss of spectral resolution. Such a crystal can thus be used to measure the intensity of K_α signals and, when absolutely calibrated, to measure the number of photons emitted by the target. In order to increase the spectral resolution, the crystal geometry must be modified.

Cylindrical and conical spectrometers

A possible way to increase the signal-to-noise ratio is to focus the emission lines on the detector. This can be done by changing the geometry of the crystal. The simplest technical way to achieve this is to bend the crystal in a cylindrical shape. In this geometry the diffracted X-rays are focused on a line which is parallel to the cylinder axis. In order to avoid any astigmatism, the distance between the detector and the crystal should be equal to the radius of curvature R_c of the crystal, as illustrated in Fig. 3.10 (left).

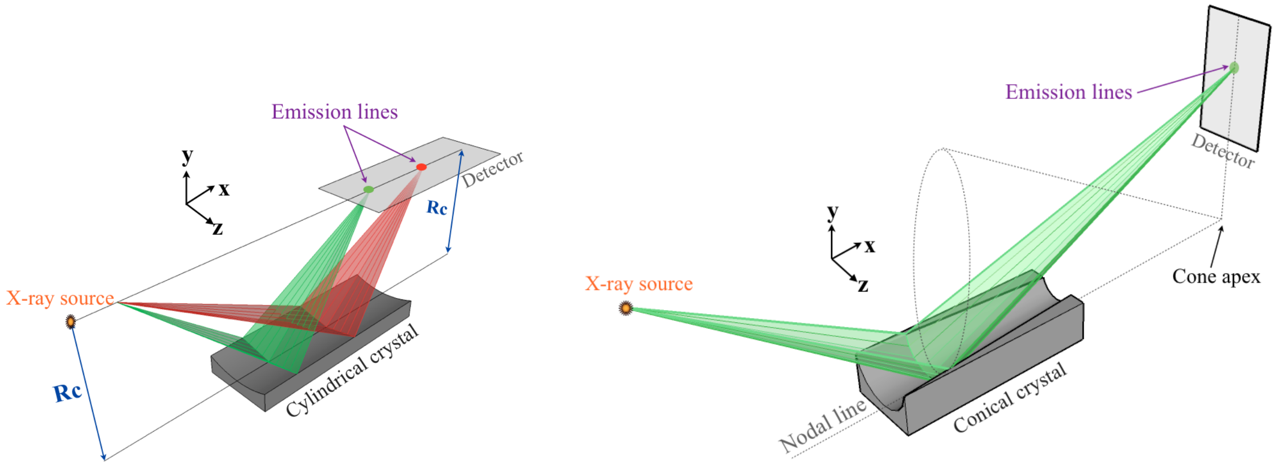

Figure 3.10: (Left) Cylindrical crystal in the *Von Hamos* configuration. The distance between the detector and the crystal is equal to the radius of curvature of the crystal. (Right) Conical crystal configuration. The detector lies on the image plane going through the cone apex. The radius of curvature of the crystal decreases when approaching the image plane.

This configuration in called *Von Hamos* configuration [Hamos, 1939]. The signal collected with such a spectrometer has usually a lower intensity than with a HOPG flat crystal, but with a much lower noise. The achieved spectral resolution allows to fully separate copper $K_{\alpha 1}$ and $K_{\alpha 2}$ emissions [Vauzour, 2012; Pérez, 2010]. A possible drawback of the *Von Hamos* geometry is that it is not compatible with the voluminous detectors such as streak cameras, presented in the next section. Indeed, in this case, the bulk of the camera must be perpendicular to the cylinder axis, which can severely complicate the design of an experiment, and especially the diagnostic set-up in the interaction chamber.

An improvement of this geometry was proposed by Hall [1984]. It consists in using a crystal of a conical shape, with the cone apex being in the image plane. The cone is tilted so that the crystal surface occupies a similar position to that of the equivalent cylindrical crystal. This geometry, illustrated in Fig. 3.10, leads to a focus of the emission on a line perpendicular to the cone axis and going through the cone apex (nodal line). The focusing is similar to that of a cylindrical crystal, but with a radius of curvature decreasing when approaching the image plane. As a consequence, two rays spectrally separated by an energy interval E_{int} are diffracted

Crystal type	**n**	**2d**	**α**	**Dimensions**	**L**	**Spectral lines**
KAP	5	26.64 Å	17.48°	5×4 cm^2	62 cm	Cu-K$_{\alpha 1}$, Cu-K$_{\alpha 2}$

Table 3.2: Characteristics of the conical potassium-acid-phtalate (KAP) crystal used in our experiments.

on the detector with a spatial interval depending on their energy. A spectrometer using such a conical crystal can be fully described by two parameters, being the cone half-angle α and the distance between the source and the image plane L. By using a geometrical optics approach, one can find in a first approximation that the conical spectrometer can be characterized by the cylindrical mirror equation:

$$\frac{1}{p} + \frac{1}{q} = \frac{2\sin\theta_c}{R} \tag{3.21}$$

The radius of curvature R of the conical crystal can be written as:

$$R(x_c) = -2\frac{y_c}{L}(L - x_c) \tag{3.22}$$

with x_c and y_c the coordinates of the intersection between the incoming ray and the crystal. The image position on the focus line y_i is then given by:

$$y_i = \frac{y_c}{x_c}(L - 2x_c) \tag{3.23}$$

Using the Bragg's law, the dispersion relation between the image position and the incoming wavelength can be finally derived:

$$\frac{dy_i}{d\lambda} = \frac{L}{2d}\left[1 + \left(\frac{y_i + 2y_c}{L}\right)^2\right]^{3/2} \tag{3.24}$$

This geometric approach has however a number of faults. It supposes that the radius of curvature R is equal to the actual radius of the crystal r. This statement is not true since R actually represents the radius of the crystal taken perpendicularly to the cone surface. Another complication arises from the oblique incidence of X-rays, also propagating in the z axis direction. Those rays, reflecting at different x_c positions on the crystal, are focused on the image plan at different positions. This geometrical effect reduces the spectral resolution of the spectrometer. It remains however negligible provided that the crystal width in the y direction is not too big. The conical spectrometer used in our experiment was developed by Martinolli [2003]. The characteristics of the conical crystal are presented in Table 3.2.

In order to detect the copper K$_\alpha$ emission lines we used the 5th order of diffraction of the crystal, leading to a significant decrease of the detected signal compared to a use of the crystal at the first order. The reflectivity of the crystal is however sufficiently high to detect an intense enough signal. The spectral bandwidths accessible are plotted in Fig. 3.11 in function of the diffraction order.

In summary, the stigmatic cylindrical crystals allow to increase dramatically the signal-to-noise ratio compared to the flat HOPG crystals. They are also characterized by a fair enough intrinsic resolution allowing to spectrally resolve copper K$_{\alpha 1}$ and K$_{\alpha 2}$ emissions. Based on the cylindrical geometry, conical crystals have the advantage of reducing the required space in an experimental chamber. The astigmatism is however not achieved, leading to a non-optimal focus of X-ray emission.

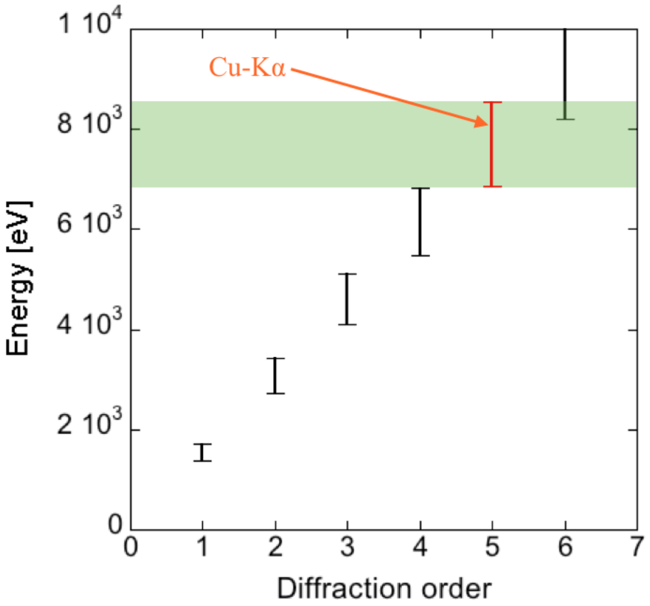

Figure 3.11: Dependence of the accessible energy bandwidth as a function of the diffraction order. The fifth order used in our experiments to detect copper K_α emission is highlighted in the green zone.

Other geometries of reflecting crystals are sometimes used, such as spherical crystals. They are more often used as imagers, as described in section. 3.2.2. Another less commonly used geometry is the toroidal one, allowing a better spectral resolution [Hauer et al., 1985; Pisani et al., 1999]. Such crystal shapes are however much more expensive due to the technical difficulty of fabrication. Each toroidal shape is moreover only adapted to a very specific experimental configuration.

Transmission spectrometer

The detection of more energetic X-rays, above 20 keV, would be quite challenging with the crystals presented in the previous sections. Indeed the Bragg angles associated with such high energies are so small ($< 10°$) that the reflectivity of the crystal is too weak. These high energy X-rays are however quite interesting for the diagnostic of fast electron population, of primary interest for the fast ignition scheme. An alternative to reflective crystals consists in using transmission crystals. In such configurations, the atomic planes are perpendicular to the surface of the crystal. The reflectivity is then increased by increasing the thickness of the crystal. Incident X-rays are refracted according to the Laue diffraction. We used in our experiment two spectrometers based on the Cauchois geometry [Cauchois, 1932] with the cylindrical transmission crystals. The configuration is presented in Fig.3.12.

The geometry of such spectrometers implies that incident X-rays with the same energy are reflected in two symmetrical zones of the crystal, leading to two emission lines on the detector, symmetric with respect to the crystal axis. The position of the emission line on the detector X_D in the positive direction is given by:

$$X_D = \frac{nhc}{2dE_\nu} R \left(1 + \frac{D}{B}\right) \tag{3.25}$$

with R the radius of curvature of the crystal, D the distance between the focal circle and the detector, and B given by:

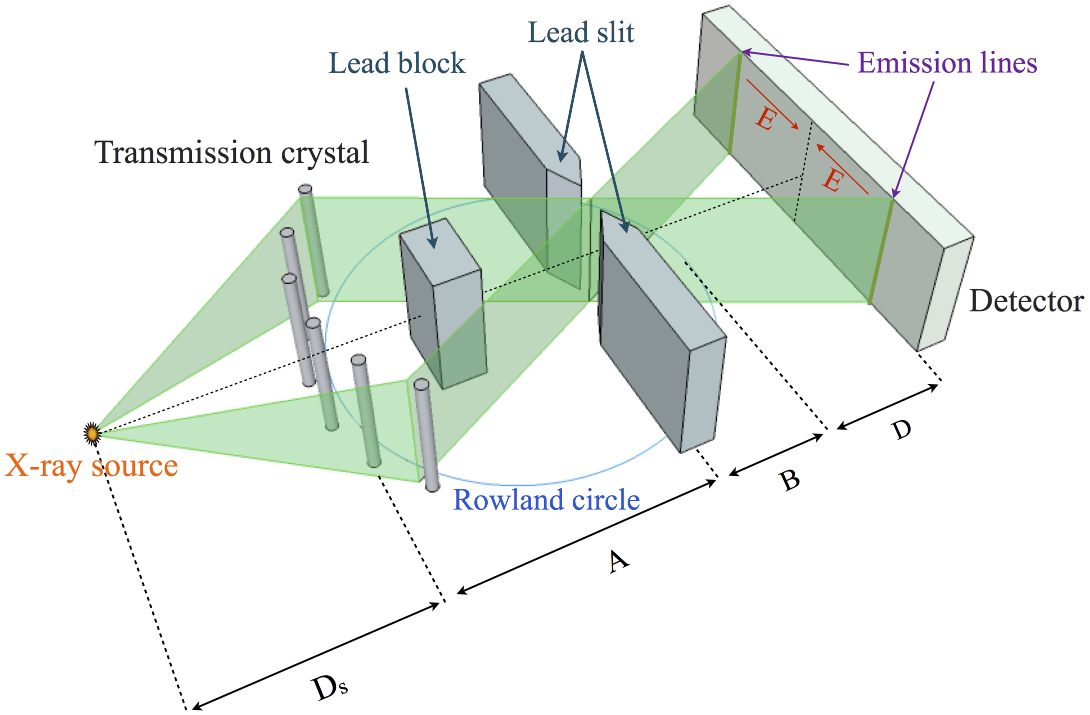

Figure 3.12: Geometry of the transmission crystal spectrometer (TCS) used in our experiments. The radius of curvature of the crystal is twice larger than the Rowland circle radius. The diffraction of the incoming signal is increasing with the decreasing energy

$$B = R\left(\frac{R + D_s}{R + 2D_s}\right) \tag{3.26}$$

with D_s the distance between the X-ray source and the crystal. These formulae are derived considering small angles of incidence on the crystal [Seely et al., 2008]. The parameter B corresponds to the distance between the focal circle and the specific zone where diffracted X-rays of different wavelength cross one another. It is important to note that this position does not depend on the X-ray energy. This implies that all diffracted X-rays satisfying the Bragg's law cross one another to this zone, which allows to integrate a lead slit in the device preventing most of the background noise to propagate through the spectrometer and to be eventually detected. When going through the full calculations, it is possible to show that the previous assumption is not completely true, leading to a crossing of the different X-rays at different locations. This effect is however negligible. A lead block located between the X-ray source and the crystal also prevents any direct light from entering the spectrometer, except from a small pinhole.

The energy resolution of the spectrometer can be calculated by differentiating Eq. 3.25:

$$\left|\frac{\Delta E_\nu}{E_\nu}\right| = \frac{2dE_\nu}{nhcR}\Delta X\left(1 + \frac{D}{B}\right) \tag{3.27}$$

with ΔX the spatial resolution of the detector, which is close to 50 μm in our experiments using Imaging Plates (IPs). As a consequence, the energy resolution increases when increasing the distance D between the focal circle and the detector. In the upper limit given by $\{D >> R, D_s >> R\}$ the resolution is increased by a factor 2. The intensity of the detected signal however decreases when increasing D. We used in our experiments two similar spectrometers named LCS (LULI Crystal Spectrometer) and TCS (Transmission Crystal Spectrometer)

Crystal type (Miller's indices)	**n**	**2d**	**R**	**D**	**A**	**D_s**
Quartz $(10\bar{1}1)$	1	6.687 Å	254 mm	0 or 200 mm	104.8 mm	600 mm

Table 3.3: Characteristics of the transmission crystal spectrometers used in our experiments.

belonging to the LULI laboratory (Palaiseau, France) and to the LLNL laboratory (Livermore, USA), respectively. Both of them were developed by the Artep company [Artep, 2014]. Their characteristics are presented in Tab. 3.3. The distance between the focal circle and the detector D can take two values, the detector being on the focal circle ($D = 0$ mm) or 254 mm behind.

The dependence of the detected energy on the position of the emission line X_D on the detector in the positive direction is plotted in Fig. 3.13 for the two configurations. The figure allows one to notice that smaller energies are diffracted at higher angles. When increasing the distance D between the focal circle and the detector the minimum accessible energy consequently increases. In our case, the minimum energies accessible are $\sim$ 7 keV and $\sim$ 16 keV for $D = 0$ mm and $D = 200$ mm, respectively, due to the limited width of the detector ($\sim$ 14 cm). For a given energy range between two emission lines, the separation of the two detected signals is also higher when increasing the distance D. This spectrometer allows with its modest spectral resolution to separate in most cases $K_{\alpha 1}$ and $K_{\alpha 2}$ emissions of high Z elements. The spectrometer resolution is mostly limited by the detector resolution.

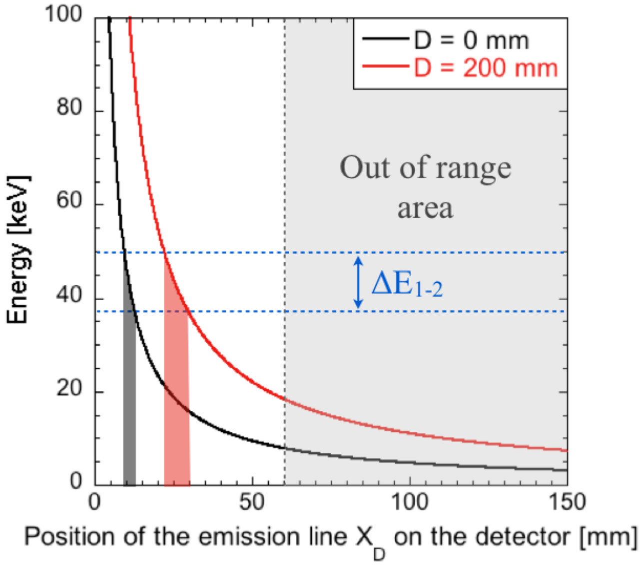

Figure 3.13: Spectral dispersion of the transmission crystal based spectrometer calculated with Eq. 3.25 for the two possible positions of the detector at $D = 0$ mm, on the focal circle (black line) and at $D = 200$ mm of the focal circle (red line). The accessible detection zone of our spectrometers due to the finite size of the detector is delimited by the grey area. The energy separation between two incident rays called 1 and 2 increases when increasing the distance to the focal circle.

This kind of spectrometer has been used in many experiments worldwide. In many cases, a significant level of background noise was detected, especially when using energetic picosecond laser beams of a few joules to hundreds of joules like on the LULI pico2000 laser system, the JLF-Titan laser system or the OMEGA-EP laser system. An experimental image obtained on the JLF-Titan laser system during an experimental campaign described in chapter 4, showing such a background noise, is plotted in Fig. 3.14. Numerical calculations using the GEANT

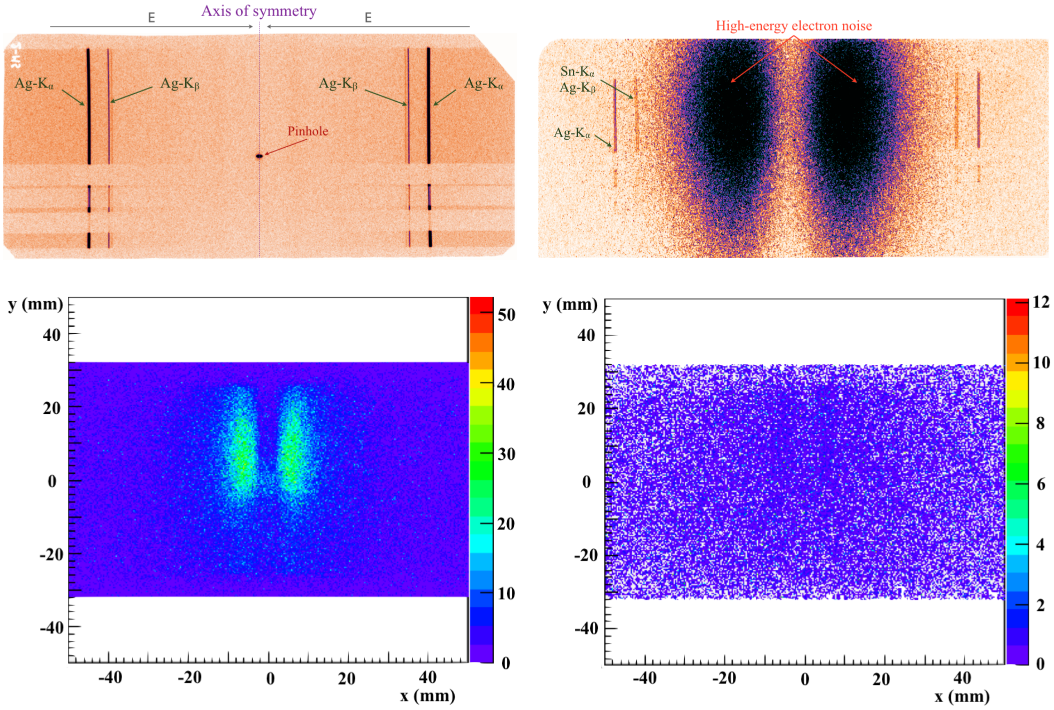

Figure 3.14: (Top left) Silver spectrum obtained in an experimental campaign on the CELIA Eclipse laser system ($E \sim 40$ mJ, $I \sim 1 \times 10^{19}$ W.cm^{-2}, 5000 shots accumulated) with a low background noise level due to the absence of high energy electrons. (Top right) Experimental spectrum obtained in an experiment on the JLF-Titan laser system described in the next section. The high background noise due to scattered high energy electrons is clearly visible. (Bottom) Results of GEANT 4 Monte-carlo simulations performed by injecting fast electrons into the spectrometer with (bottom left) and without any 0.5 T magnet (bottom right).

4 Monte-carlo code performed by Thfoin et al. [2014] have shown that this background noise can be attributed to two main contributions. The first one is due to highly energetic X-rays of several hundreds of keV going through the spectrometer and decreasing the signal-to-noise ratio uniformly over the whole detector. A possible way to reduce this contribution is to increase the lead slit thickness. The second contribution mostly affects the central part of the detector. The generated noise level is so high that it could hide the signal of interest if located in this central region. This noise is due to fast electrons generated in laser-plasma interaction, scattering into the spectrometer. This fast electron contribution can be almost totally suppressed by setting-up a moderate intensity magnet of 0.5 T in front of the spectrometer. This magnet prevents electrons with an energy < 100 MeV, characterizing most of the accelerated electron population, from going through the crystal. Examples of GEANT 4 simulation with and without magnet are presented in Fig. 3.14. These calculations were successfully confirmed in an experimental campaign performed on the pico2000 laser system presented in chapter 5 (Fig. 3.15).

In conclusion, the transmission crystal spectrometers are used to detect high energy emission lines, in the $20 - 100$ keV range, corresponding to high Z element transitions. The cylindrical shape of the crystal forces the different emissions to cross each other at the same location on the crystal axis. This geometrical aspect allows to filter most of the noise emission, which makes this spectrometer well adapted to the harsh environment that can be found in sub-kJ to kJ petawatt laser experiments. A modified version of this spectrometer, named SPECTIX (Spectromètre PETAL à Cristal en TransmIssion X), will be set-up on the LMJ-PETAL laser system. SPECTIX will use two energy channels, allowing to detect high energy X-rays in the

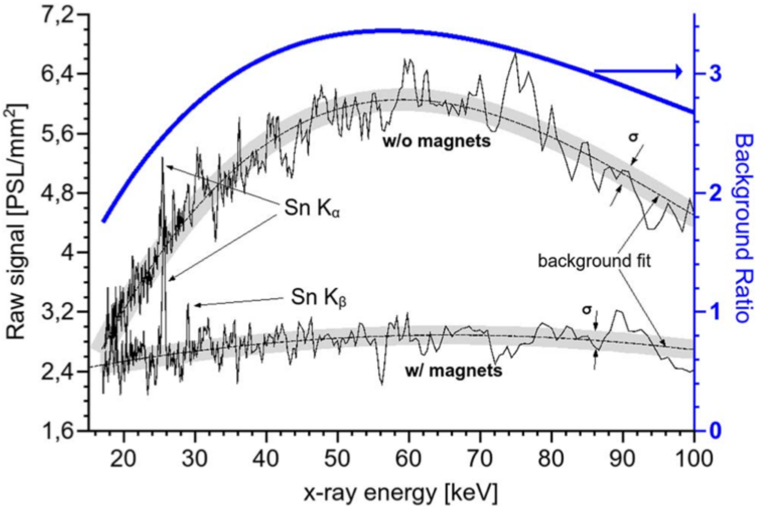

Figure 3.15: Experimental tin spectra recorded by the LCS on the LULI2000 laser facility. The short pulse beam was characterized by an intensity on target $I \sim 10^{19}$ W.cm^{-2} and a 1 ps FWHM duration. The signal without any magnet was obtained with 12.6 J on target. It is characterized by a high background noise. The signal with magnet was obtained with 10 J on target. The background ratio (blue solid line) between the two background fits illustrate the efficiency of the magnet. The light grey areas represent the noise standard deviation σ. The 50×30 mm^2 magnet was characterized by an uniform 0.5 T field.

$6 - 90$ keV energy range with a spectral resolution > 300.

3.2.2 X-ray imagers

The study of fast electron transport in dense matter often requires to image a peculiar zone of emission, generated by fast electrons propagating into the target. This technique may allow to characterize the divergence of fast electrons by imaging a tracer layer buried at different depth into a target, such as presented in the experimental section. It can also be used to fully characterize the coupling between fast electrons and a target of complex design, such as a cone target presented in chapter 5. Different imaging systems based on various physical processes can be used. We present in this section two different kinds of imagers that were used in our experiments.

Spherically bent crystal

The equivalent of spherical mirrors in the X-ray domain are the spherical crystals. Their great interest rely on their possibility, via the Bragg's law, to discriminate a narrow X-ray energy range of interest from a broad range of noise emission. By choosing an appropriate configuration, it is then possible to configure the imager in order to only image the K$_\alpha$ emission from a fluorescent layer, which is a signature of fast electron propagation, with a spectral resolution $\Delta\lambda/\lambda \sim 10^{-3} - 10^{-4}$ [Sinars et al., 2003]. As for spherical mirrors, the relation between the distance p between an object (the X-ray source) and the crystal, and the distance q between the crystal and the image is given by:

$$\frac{1}{p} + \frac{1}{q} = \frac{2}{R_c} \tag{3.28}$$

with R_c the radius of curvature of the crystal. This relation can however be written only when considering objects close to the mirror axis and for a near normal incidence X-rays to the mirror surface (paraxial approximation). The geometry of a spherical Bragg imager is presented in Fig. 3.16.

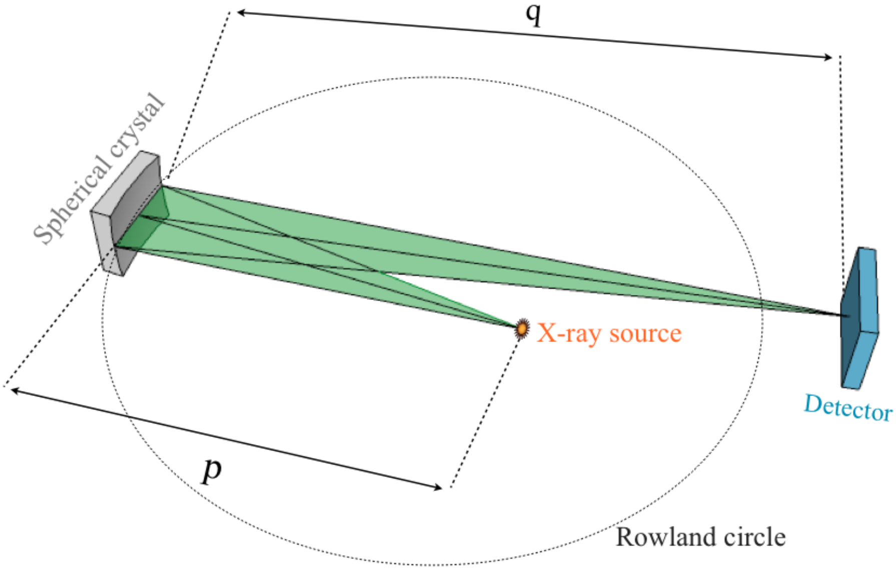

Figure 3.16: Geometry of a Bragg imager using a spherical crystal.

In a more general approach, the symmetry breaking induced by an object lying off the mirror axis leads to two perpendicular image planes, characterized by different radii of curvature of the crystal R_t and R_s, called tangential and sagittal planes, respectively. The tangential plane is contains both the mirror axis and the chief ray[1]. The sagittal plane is perpendicular to the tangential plane and contains the chief ray. Considering these two particular planes, Eq. 3.28 writes as follows:

$$\begin{aligned} \frac{1}{p}+\frac{1}{q_t}=\frac{1}{f_t}=\frac{2}{R_t\sin\theta_{\mathrm{B}}} \\ \frac{1}{p}+\frac{1}{q_s}=\frac{1}{f_s}=\frac{2\sin\theta_B}{R_s} \end{aligned} \tag{3.29}$$

with θ_{B} the Bragg angle at the center of the mirror, f_t and f_s the focal lengths in the tangential and sagittal planes of incidence, respectively. The object must be located inside the Rowland circle at a distance p satisfying $2f_t > p > f_t$. The rays contained in the tangential plane usually focus first, leading to a distortion of the final image due to the astigmatism of the focusing crystal. For toroidal mirrors, the relation $R_s = R_t\sin^2\theta_{\mathrm{B}}$ implies that such mirrors are perfectly stigmatic since $q_t = q_s$ in this case. This particular characteristic is not true for spherical mirrors because of the equality between the two radii $R_s = R_t$. A possible way to overcome this problem is to tune the Bragg angle close to $\theta_{\mathrm{B}} = 90°$ and to use spherical crystals fairly close from a paraxial geometry, which limits their astigmatism and the subsequent loss of spatial resolution. In a Bragg angle range $80° < \theta_{\mathrm{B}} < 90°$ the spherical crystal is nearly as efficient as the toroidal crystal. For smaller Bragg angles, the use of expensive toroidal crystals is however absolutely necessary to get a better spatial resolution.

We used in our experiments spherical Bragg crystals designed to detect the K_α emission

---

[1] The chief ray is defined by a ray starting from an off-axis point object and going through the center of the optical device

Crystal type (Miller's indices)	**n**	**2d**	θ_{B}	**Emission line**
Quartz ($21\bar{3}1$)	2	3.082 Å	$88.7 \pm 1°$	Cu-$K_{\alpha 1}$ @ 8047.78 ± 5 eV

Table 3.4: Characteristics of the spherical crystals used in our experiments.

lines. Their characteristics are presented in Tab. 3.4. The paraxial conditions ($\theta_{\mathrm{B}} \sim 90°$) imply constraints on the choice of the crystal. Indeed one has to find an intense enough emission line, characterizing the fast electron population of interest, which is in addition characterized by a high enough energy (> keV) to propagate with a small attenuation through the target to the detector, and with a Bragg angle matching the paraxial conditions. The copper K_α, around 8 keV, matches all the previous conditions and was imaged in our experiments.

The choice of the geometrical parameters, such as the radius of curvature of the crystal R_c or the p and q distances, is fully dictated by the required magnification and resolution. The magnification γ in fully stigmatic conditions is given by:

$$\gamma = \frac{q}{p} \tag{3.30}$$

The resolution in the sagittal plane σ_s limiting the resolution of the spherical crystal can be estimated by [Sinars et al., 2003]:

$$\sigma_s = \frac{L_s(\gamma + 1)(1 - \sin^2 \theta_{\mathrm{B}})}{\gamma} \tag{3.31}$$

with L_s the aperture of the crystal. The dependence of σ_s on the magnification γ is plotted in Fig. 3.17.

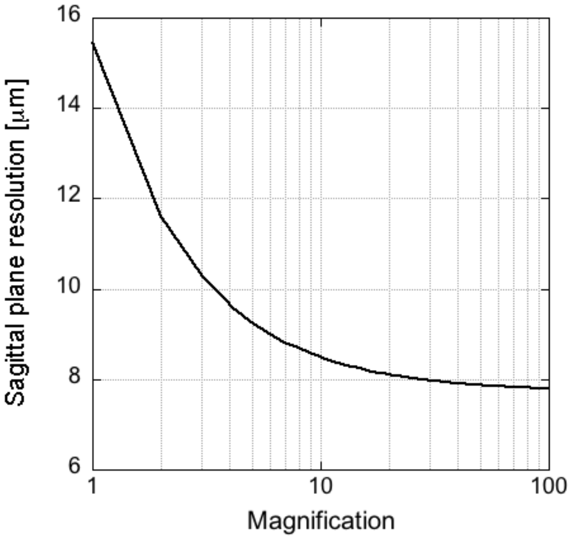

Figure 3.17: Theoretical resolution of the spherical crystal in the sagittal plane considering a crystal aperture $L_s = 15$ mm and a Bragg angle $\theta_{\mathrm{B}} = 88.7°$.

For magnifications > 10, which are typically achieved in our experiments, the resolution is fairly constant. In order to minimize the intrinsic astigmatism, the crystal aperture L_s can be decreased by putting a mask on the crystal edges, which consequently limits the active part of the crystal to its middle part. By doing so the solid angle of collection is however decreased, which also decreases the intensity of the signal diffracted to the detector. One has in fact to find a compromise between a good enough resolution and a high enough solid angle of collection

R_c [mm]	γ	L_s [mm]	p [mm]	p [mm]	σ [μm]
500	6	15	291.7	1750	~ 10
500	8.3	15	280.1	2329.7	~ 10
380	3.9	15	238.3	937.9	~ 10

Table 3.5: Set of parameters of the Cu-K$_\alpha$ imagers used in our experiments.

required to obtain a measurable signal. The resolution in the tangential plane is limited by the coma and by higher order aberrations. It is then always lower than the sagittal resolution given by Eq. 3.31. The resolution of the spherical crystal imager is then limited by the sagittal resolution. Table 3.5 presents the different set of parameters used in our experiments.

The reflectivity of Bragg's crystal directly depends on the plasma temperature [Pérez, 2010]. Indeed, the energy bandwidth accessible with such crystals is close to 10 eV. Line emissions are consequently shifted out of this bandwidth when the temperature increases significantly. This important effect has to be taken into account when setting up a spherical crystal during an experiment.
In order to get a good enough signal-to-noise ratio one has to work on the suppression of the direct irradiation of the detector by the unwanted emissions. The intense X-ray noise can be almost suppressed by inserting a thick enough lead block between the source and the detector. Some alignment precautions must however be taken in order to avoid any hiding of the reflected signal of interest. Since angles between incident rays of interest on the crystal and the reflected signal are quite small, close to 1°, the set-up of such a lead block is not so trivial. Another important source of noise emission may come from fast electrons interacting with the detector. A magnet of a moderate field located at a sufficient distance from the detector can suppress this contribution.

In conclusion, the Bragg spherical crystals are widely used to image K$_\alpha$ emissions created by fast electrons crossing a fluorescent tracer layer. Their intrinsic astigmatism limiting their resolution to ~ 10 μm can be optimized by adapting the experimental configuration to a near normal Bragg angle of incidence. They however have the advantage of being less complex and less expensive to manufacture than toroidal crystals, which completely eliminate astigmatism for low Bragg angles. Toroidal crystals have also the inconvenient of being more complex to align with their six degrees of freedom. The set up of spherical crystals must take into account the dramatic loss of reflectivity associated with the increase of plasma temperature and of the subsequent ray shifting. Another drawback of spherical crystals is the limitation of the X-ray energy. The difficulty of manufacturing high quality crystals with a small atomic spacing is quite significant. In this case, one has to use other imagers.

Kirk-Patrick Baez microscope

A dramatic intrinsic energy selectivity of Bragg's crystals can be overcome by using classical reflective mirrors, which allow to reflect a broader range of incoming wavelengths of a higher energy. The reflectivity of such mirrors is however extremely weak in the X-ray energy range. This can be explained by the following. The propagation of X-rays in a matter can be described by the complex refractive index $\tilde{n}$ given by:

$$\tilde{n} = n - i\beta = 1 - \delta - i\beta \tag{3.32}$$

with n the refractive index of the material, β its absorption coefficient and $\delta = (n_e e^2 \lambda^2 / 8\pi^2 \epsilon_0 m_e c^2)$ a small positive term, which depends on the material and on the incoming wavelength λ. If one considers an incident ray at normal incidence $\theta = 90°$ on a reflective surface, being an interface between vacuum and the reflective material, the reflectivity can be written as follows [Michette, 1986]:

$$R|_{90°} = \left[\frac{1-\widetilde{n}}{1+\widetilde{n}}\right]^2 = \frac{\delta^2+\beta^2}{(2-\delta)^2+\beta^2} \tag{3.33}$$

For a metal such as the gold tabulated values $\delta = 0.01$ and $\beta = 0.009$ for a wavelength $\lambda = 3.5$ nm yield a very small reflectivity $R|_{90°} = 4.6 \times 10^{-5}$. A possible way to enhance it would be to work at grazing angles of incidence. Let us consider a plane wave of amplitude A traveling through a medium characterized by its complex index $\widetilde{n}_2 = 1 - \delta_1 - i\beta_1$, incident at a grazing angle θ_i on a planar boundary with a second medium characterized by $\widetilde{n}-2 = 1-\delta_2-i\beta_2$, with $\delta_2 > \delta_1$. In such a situation, a fraction of the wave is reflected at an angle θ_r while the other part is transmitted into the second material with an angle θ_t. Fig. 3.18 illustrates the described situation. We consider in a first approximation that there is no absorption of the light ($\beta_1 = \beta_2 = 0$). By decomposing the incident wave into a parallel and a perpendicular components of amplitude $A_{/\!/}$ and $A_\perp$, with respect to the plane of incidence $x-z$, the reflected components of amplitude $R_{/\!/}$ and $R_\perp$ are given by the Fresnel relations:

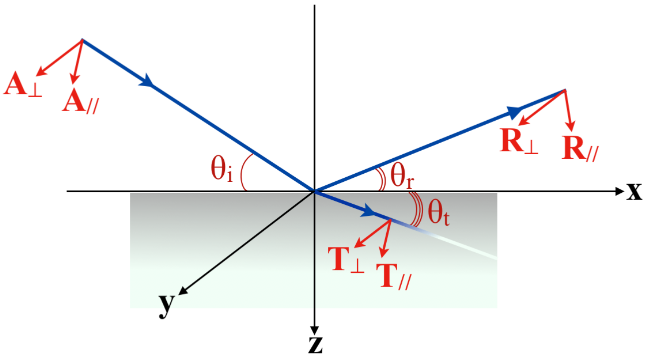

Figure 3.18: Incident electromagnetic wave in the $x-z$ plane with a grazing angle θ_i. The wave is characterized by an amplitude $A_{/\!/}$ in the parallel direction ($x-z$ plane) and an amplitude $A_\perp$ in the perpendicular direction, along the y axis direction. The reflected wave is characterized by an angle of reflection $i_r = \pi/2 - \theta_r$ and by amplitudes $R_{/\!/}$ and $R_\perp$. The transmitted wave is characterized by an angle of transmission $i_t = \pi/2 - \theta_t$ and by amplitudes $T_{/\!/}$ and $T_\perp$.

$$\begin{aligned}\frac{R_{/\!/}}{A_{/\!/}} &= \frac{(1-\delta_2)^2\sin\theta_i - (1-\delta_1)[(1-\delta_2)^2-(1-\delta_1)^2\cos^2\theta_i]^{1/2}}{(1-\delta_2)^2\sin\theta_i + (1-\delta_1)[(1-\delta_2)^2-(1-\delta_1)^2\cos^2\theta_i]^{1/2}}\\ \frac{R_\perp}{A_\perp} &= \frac{(1-\delta_1)\sin\theta_i - [(1-\delta_2)^2-(1-\delta_1)^2\cos^2\theta_i]^{1/2}}{(1-\delta_1)\sin\theta_i - [(1-\delta_2)^2-(1-\delta_1)^2\cos^2\theta_i]^{1/2}}\end{aligned} \tag{3.34}$$

For the particular value of the grazing angle θ_c, called *critical angle*, and given by:

$$\cos\theta_i = \frac{1-\delta_2}{1-\delta_1} \tag{3.35}$$

the Fresnel coefficients are:

$$\begin{aligned} \frac{R_{/\!/}}{A_{/\!/}} &= 1 \\ \frac{R_{\perp}}{A_{\perp}} &= 1 \end{aligned} \tag{3.36}$$

In other words, at this particular value of the grazing angle, $\theta_t = 0$, and the incident electromagnetic wave is totally reflected. The incident wave is consequently totally reflected for $\theta_i \leq \theta_c$. Accounting for the absorption and for the interface with vacuum ($\delta_1 = 0, \beta_1 = 0, \beta_2 = \beta \neq 0$), Eq. 3.34 can be written as:

$$\begin{aligned} \frac{R_{/\!/}}{A_{/\!/}} &= \frac{\tilde{n}^2 \sin\theta_i - (\tilde{n}^2 - \cos^2\theta_i)^{1/2}}{\tilde{n}^2 \sin\theta_i + (\tilde{n}^2 - \cos^2\theta_i)^{1/2}} \\ \frac{R_{\perp}}{A_{\perp}} &= \frac{\sin\theta_i - (\tilde{n}^2 - \cos^2\theta_i)^{1/2}}{\sin\theta_i + (\tilde{n}^2 - \cos^2\theta_i)^{1/2}} \end{aligned} \tag{3.37}$$

with $\tilde{n}^2 = (1-\delta)^2 - \beta^2 - 2i(1-\delta)\beta$. Reflectivities R_s and R_p of the parallel and perpendicular components of the incident wave, respectively, are finally given by:

$$\begin{aligned} R_p &= \left| \frac{R_{/\!/}}{A_{/\!/}} \right|^2 \\ R_s &= \left| \frac{R_{\perp}}{A_{\perp}} \right|^2 \end{aligned} \tag{3.38}$$

The dependence of R_s and R_p on the incident angle is plotted in Fig. 3.19 considering a reflective material made of platinum and for two energies, 1 keV and 8.038 keV (Cu-K$_\alpha$ transition), of the incident wave. For the lowest energy case, corresponding to higher β and δ factors, the reflectivity decreases smoothly when increasing the grazing angle. For the higher energy case, the reflectivity is relatively high at grazing angles lower than the critical angle ($\theta_c = 0.585°$) and it drops rapidly for $\theta_i > \theta_c$. The right-hand side plot allows to see the rapid decrease of reflectivity, both for parallel and perpendicular polarizations, for higher angles of incidence. One can also note that for small angles θ_i, the reflectivity of the two components is fairly similar, so that $R_p \simeq R_s$.
The angle of total reflection θ_c is associated with a wavelength λ_c calculated according to the dispersion theory. By injecting the expression of δ into Eq. 3.35 one finds:

$$\cos\theta_c = 1 - \delta = 1 - \frac{n_e e^2 \lambda_c^2}{8\pi^2 \epsilon_0 m_e c^2} \tag{3.39}$$

For a small grazing angle $\theta \gtrsim 0$, the critical wavelength is given by:

$$\lambda_c \simeq \frac{2\pi c \theta_c}{e} \sqrt{\frac{\epsilon_0 m_e}{n_e}} \tag{3.40}$$

The spectrum of reflected wavelengths is characterized by $\lambda > \lambda_c$. Eq. 3.40 also shows that the critical angle decreases with increasing the X-ray energy. In other words, for a fixed grazing angle $\theta_i < \theta_c$ the reflectivity of the material decreases when increasing the energy of the incident photon. This effect is illustrated in Fig. 3.20 for an incident wave at $\theta_i = 0.5°$ on platinum reflective surface.

The detection of emission lines of interest necessitates to focus the incident signal on the

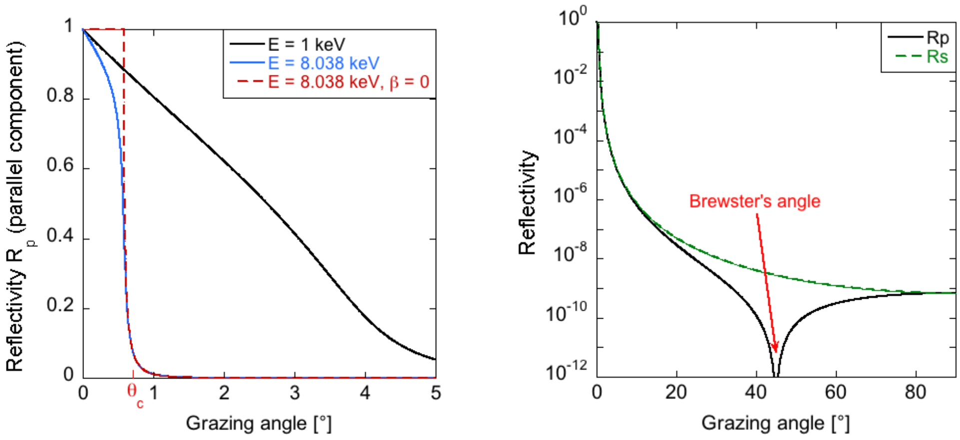

Figure 3.19: (Left) Dependence of the reflectivity R_p of the parallel component on the angle of incidence on platinum. The plots correspond to an incident energy of 1 keV (black full line) and 8.038 keV (Cu-K$_\alpha$) for $\beta = 5.12^{-6}$ (blue solid line). The reflection of the Cu-K$_\alpha$ emission on a non absorbing platinum ($\beta = 0$) is represented by the red dotted line. The corresponding critical angle is $\theta_c = 0.585°$. (Right) Dependence of R_p and R_s on the angle of incidence in the $[0 - 90°]$ range. They are similar for small grazing angles $\theta_i \leq \theta_c$ and rapidly drop afterwards. A sudden decrease of R_p around $\theta_i = 45°$ is due to the Brewster's angle where only the perpendicular component is reflected.

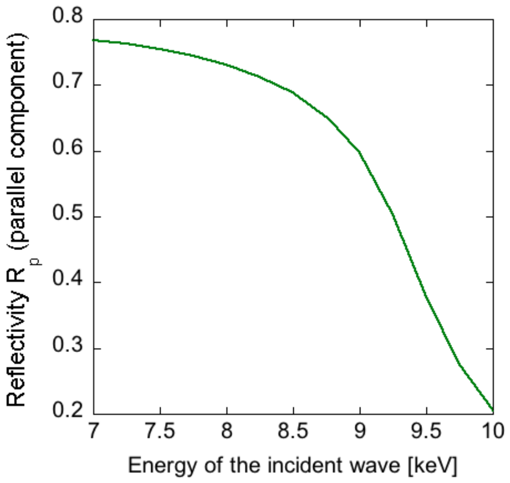

Figure 3.20: Dependence of the parallel component reflectivity R_p on the photon energy for a grazing angle $\theta_i = 0.5°$.

detector using spherical mirrors. The focal lengths of a such spherical mirror are given by Eq. 3.29. Since at low grazing angle $\sin\theta << 1$, the focal length in the sagittal plane of incidence is much bigger than the focal length in the tangential plane. As a consequence, a spherical mirror used at grazing incidence angle behaves as a cylindrical mirror. The grazing angle of incidence configuration however introduces strong optical aberrations compared to the paraxial configuration, such as the astigmatism and coma. The astigmatism has already been described in section 3.2.2. The coma aberration is due to the fact that at a grazing angle configuration, the different parts of the spherical mirror are at different distances from the source, leading to a magnification which also varies across the mirror: the magnification is higher on the edge of the mirror closer to the source than on the opposite side.

A configuration permitting to compensate strong optical aberrations induced at grazing angles of incidence was introduced by Kirkpatrick & Baez [1948]. It consists of a set of two successive perpendicular cylindrical mirrors with equal radii of curvature (Fig. 3.21).

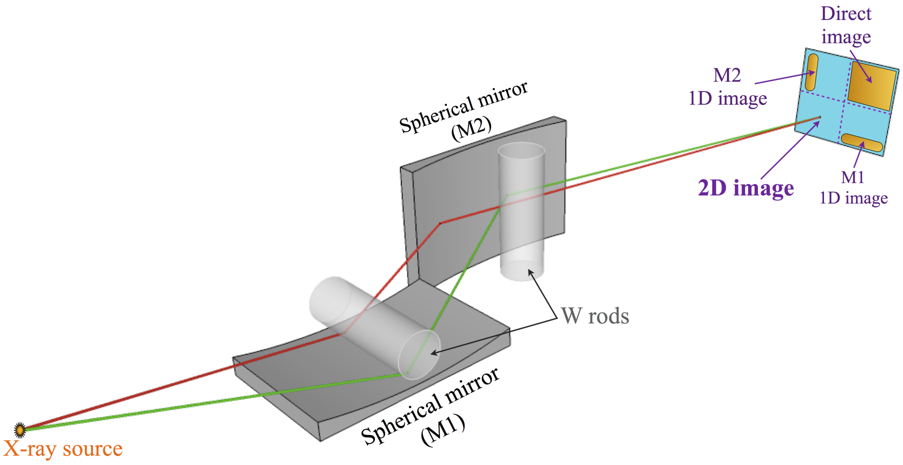

Figure 3.21: Illustration of the KB microscope configuration.

Such a system, called Kirkpatrick-Baez microscope (KB), has the focusing properties of a single lens of an axial symmetry. The astigmatism is removed compared to a single mirror configuration, in such a way that an image point is created from an objet point. It however introduces a new aberration, called anamorphotism, which is due to the fact that the two mirrors are not located at the same distance from the source. Therefore the magnifications in the two directions along mirrors axis are different. The simplest correction would require to tilt the detector is such a way that it is not perpendicular to the plane of incidence. A more complex but more efficient way would be to add a third spherical mirror, in the same plane as the first one [Michette, 1986].

The KB microscope that we used in our experiments was developed by Friesen et al. [2013], at the University of Alberta in Canada. Its general design is presented in Fig. 3.22.

It consists of a single pair of platinum coated perpendicular mirrors configured to collect an incident angle of 0.5°, close from the platinum critical angle. This microscope was firstly designed to detect the ~ 8 keV emission line of the Cu-K$_\alpha$ transition. The total reflectivity of the pair of mirrors is close to 0.5. The solid angle of collection is 3.4 μsr, which has to be compared to a typical angle of 0.25 msr for a spherical Bragg crystal [Sinars et al., 2003]. The two orders of magnitude in the solid collection angle are compensated with the high bandwidth of this KB microscope, allowing to detect emissions in the $4-9$ keV energy range compared to the ~ 5 eV bandwidth of the Bragg crystal. The potential energy shift of the Cu-K$_\alpha$ emission line with the increase of the plasma temperature is consequently not an issue when setting-up this imager. The characteristics of the KB microscope used in our experiments are presented

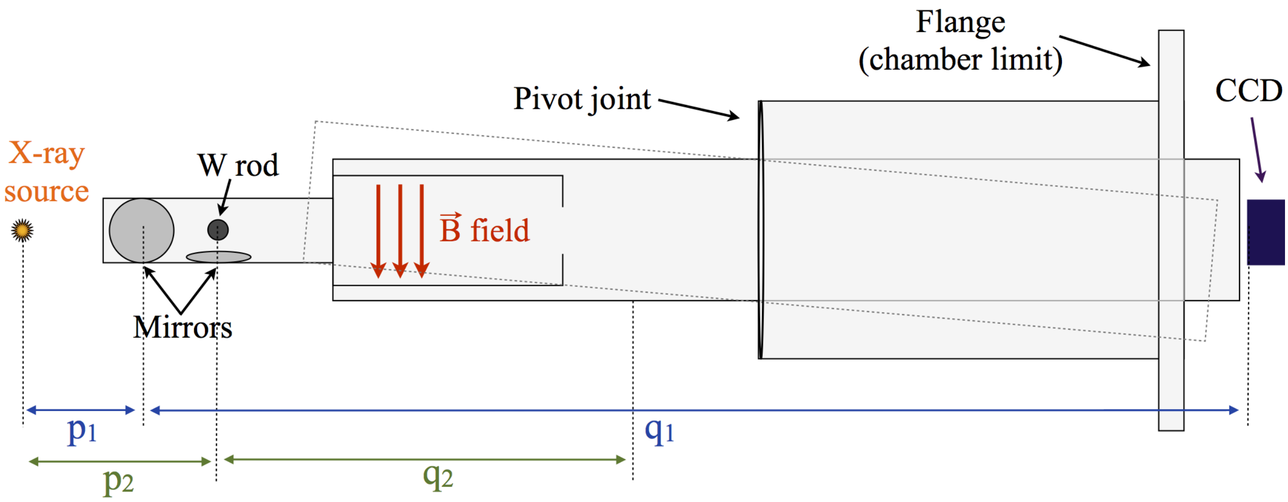

Figure 3.22: Design of the KB microscope used in our experiments. An O-ring allows a slight pivoting of the tube for adjustments. The second mirror is out of focus.

	Mirror 1	**Mirror 2**
Coating	Pt	Pt
Angle of incidence	0.5°	0.5°
Mirror diameter	25.4 mm	25.4 mm
Radius of curvature	20 m	20 m
Object distance	$p_1 = 94.6$ mm	$p_2 = 120$ mm
Image distance	$q_1 = 1232$ mm	$q_2 = 1206$ mm
Magnification	12.5	9.66
Peak resolution	8 μm	37 μm
In focus	Yes	No

Table 3.6: Characteristics of the KB microscope used in our experiments. Due to technical constraints on purchasable mirror curvatures the second mirror is out of focus.

in Tab. 3.6.

A collimator consisting of two tungsten rods mounted parallel to each mirror surface ensures that only X-rays with an incidence angle of 0.5° are collected. Two pairs of magnets generating a peak field of 0.5 T located right after the mirrors prevent most of the fast electrons escaped from the target from contributing to the detected noise. The detector consists in a Princeton Instruments CCD camera with a 20 μm pixel size and a 1340 × 1300 pixels chip area, or in an imaging plate (IP). IPs are passive devices, sensitive to ionizing emissions (photons, electrons, protons and heavier ions). They offer several advantages, including a good resolution (≥ 25 μm), a linear response, an important dynamic range (over $5-6$ decades) characterized by a low detection threshold and a high energy saturation threshold, a complete reusability and an insensitivity to electromagnetic pulses.

The camera has to be enclosed into a shielded box in order to avoid most of the disruptions that would be caused by electromagnetic pulses (EMP) generated in the interaction of an ultra-intense laser pulse with a solid target. A typical experimental image is shown in Fig. 3.23. It is split into four quarters, separated by the shadow of the crossed pair of tungsten rods. The first quarter (top left) corresponds to the direct irradiation of the detector by X-rays which did not reflected from the mirrors. The second and third quarters (bottom left and top right)

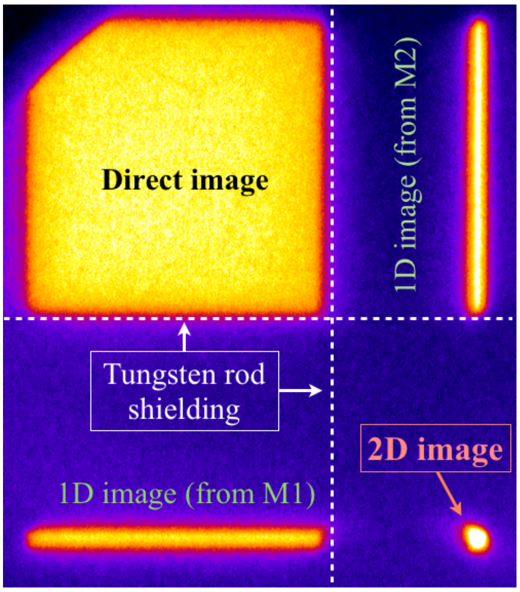

Figure 3.23: Experimental KB image obtained in a shot on a copper target. The image is split into quarters separated by the shadow of the pair of tungsten rods.

are produced by X-rays reflected from the first or second mirror only, respectively. Finally, the fourth quarter corresponds to the 2D image, for incident X-rays with an angle $\theta_i = 0.5°$ that reflected on both mirrors.

In conclusion, the KB microscopes offer the advantage of being sensitive to a broader energy range than Bragg spherical crystals. They are also less complex to build since they only use a pair of metal coated reflective surfaces. This simple configuration suffers however from an optical aberration that leads to a necessity of image processing in order to deconvolve experimental data. The peak resolution reached by the KB microscope used in our experiments is lower, at least in one direction, than the one obtained by spherical Bragg crystals.

3.2.3 Bremsstrahlung cannon

In addition to high intensity line emissions, fast electrons generate throughout their propagation an intense continuous emission of hard X-rays. This bremsstrahlung emission is characterized by a broad continuous spectrum that decreases in intensity with the increasing energy of the photon. The characterization of bremsstrahlung emission is quite interesting because the emitted photon spectrum is directly related to the fast electron distribution. Several diagnostics were developed in order to perform such measurements. A first technique uses photonuclear reactions [Hatchett et al., 2000; Stoyer et al., 2001]. There are atomic nuclei, such as isotopes of gold and of copper, that exhibit a giant resonance cross section of the reaction with emission of a proton or a neutron for photon energy of several MeV. The $(\gamma, x.n)$ nuclear reactions, with emission $x \sim [1-7]$, generate radioactive elements that emit characteristic secondary gamma rays. The quantification of these gamma rays allows to characterize the primary bremsstrahlung emission. The photonuclear cross sections are however sufficiently high for photons with energies above 5 MeV which makes this technique unsuitable in our experiments, since the the spectral range of interest extends from a few keV to a few MeV.
A second technique consists in using a differential filtering. The incident photon flux is measured after crossing several successive layers of material of different composition and thickness. We used in our experiments a bremsstrahlung spectrometer based on the differential filtering,

Filter	**Thickness [cm]**	**Density [g/cc]**
Al	1.0e-2	2.2
Ti	1.0e-2	2.7
Fe	1.0e-2	4.54
Cu	1.0e-2	8.96
Mo	1.0e-2	10.22
Ag	1.5e-2	10.5
Sn	5.0e-2	7.31
Ta	5.0e-2	16.65
Au	1.56e-2	19.3
Pb	1.0e-1	11.35
Pb	2.0e-1	11.35
Pb	3.0e-1	11.35
Pb	4.0e-1	11.35
Pb	6.35e-1	11.35
Pb	6.35e-1	11.35

Table 3.7: Characteristics of the filters composing the bremsstrahlung cannon used in our experiments.

called bremsstrahlung cannon, and developed by [Chen et al., 2008a]. It is made of fifteen 1×1 inch^2 filters with an increasing atomic number, ranging from aluminum to lead, creating fifteen energy bins. A MS-type imaging plate is located behind each filter layer. This design is adapted from Nolte et al. [1999] where thermoluminescent detectors were used instead of IPs. Since the photon absorption is well known at each step of the cannon, it is eventually possible to deconvolve the incident bremsstrahlung spectrum. The stack of filters and of IPs is enclosed into a plastic-made cartridge which avoid any deleterious exposure of IPs to the ambient light. Both the cartridge and 250 μm mylar foils surrounding each filter allow to minimize the contribution to the measured signal of secondary electrons that could be created in the stack. Table 3.7 presents the filters used in the cannon.

The cartridge is contained in a 1.8 cm thick lead box shielding against fast electrons up to 2 MeV. A 12.5 cm long lead collimator with a $\frac{1}{2}$ inch diameter centered hole is located in front of the cannon in order to suppress the fluorescence from the target, the chamber walls or all the other diagnostics. A scheme of the cannon is presented in Fig. 3.24.

In order to avoid as much as possible any contribution of fast electrons to the measured signal, a magnet is usually located in front of the collimator. The accessible bandwidth of the cannon ranges from $\sim$ 10 keV to $\sim$ 3 MeV. Above this maximum value, the composition and the number of filters do not allow any precise discrimination between the incident photon energies. A major drawback of this cannon relies on the number of IPs that have to be used. It requires from users to extract, scan and replace fifteen IPs after each shot.

Another cannon design has been proposed by Scott et al. [2013]. They developed a spectrometer also based on the differential filtering but using a single imaging plate, located under 25 lead blocks of the thickness increasing up to 6.5 cm. A scheme of the cannon is presented on Fig. 3.24. Since the parts of the IP are irradiated by different portions of the photon beam one has to make sure that the photon flux is fully uniform across the whole detector. To achieve this requirement the detector has to be located far enough from the emission source ($\sim$ 40 cm). This cannon allows to discriminate photons with energies up to 3 MeV. A 20 cm long lead collimator is located in front of the cannon to block the fluorescence emissions up to 100 MeV.

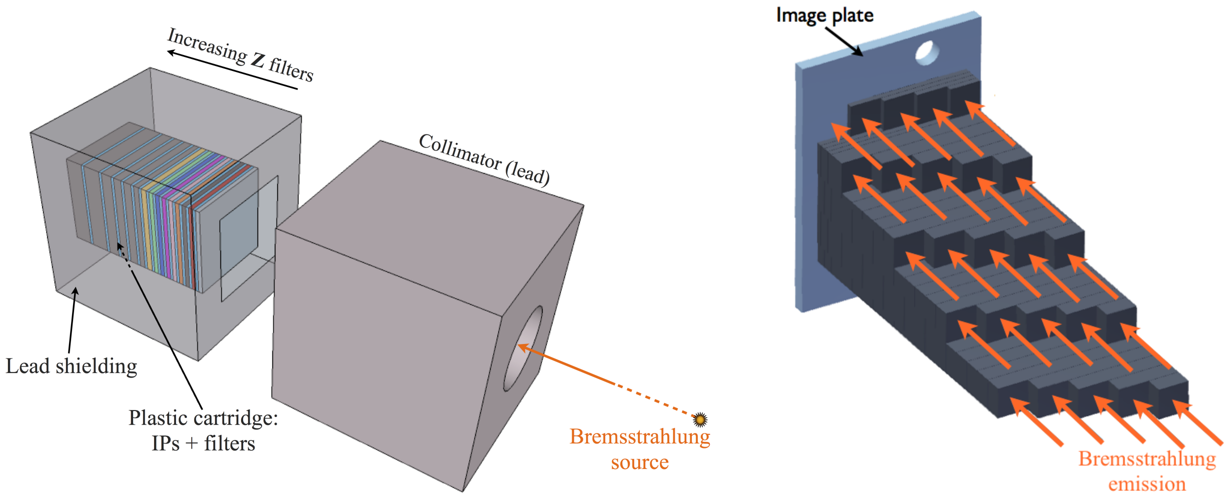

Figure 3.24: (Left) Bremsstrahlung cannon design that was used in out experiments. Fifteen IPs are used to measure the bremsstrahlung signal. They are surrounded by different thicknesses and varieties of materials, ranging from a thin layer of aluminum at the entrance of the cannon to a thick layer of lead. (Right) Alternative design of bremsstrahlung cannon. A single IP is used as detector. The filters are made of various thicknesses of lead material.

A 0.4 T magnet prevents fast electrons up to 100 MeV from entering the cannon.

The deconvolution of electron spectrum from measured bremsstrahlung spectrum is not unambiguous. Complex Monte-Carlo numerical simulations are required to do so. In order to be computationally tractable, simulations are usually subdivided into several modeling steps. First, an electron spectrum is injected into the target, creating a bremsstrahlung X-ray emission due to collisions with the target ions. In a second step the X-ray spectrum is injected into the simulated cannon. The energy deposition within the active layer of each IP is then compared to the PSL signal experimentally measured. The procedure is repeated by changing the electron source parameters until an acceptable agreement between the numerical and the experimental set of data is found. This iterative technique may however produce errors since a limited number of detectors is used: different electron spectra can generate the same measured signal. A possible way to increase the spatial resolution and to constrain the injected electron spectrum is to use several cannons inside the chamber at different angles. The deconvolution of bremsstrahlung spectra also requires a good enough accuracy of collisional atomic data implemented in Monte-Carlo numerical codes.

3.3 Electron spectrometer

A fraction of high energy fast electrons created by a laser pulse may leave the target. The resulting remaining positive charge creates an electric field that re-inject fast electrons into the target, thus creating an electron cloud with a thickness close to the Debye length. However a small fraction of electrons with a sufficiently high energy may escape the target and propagate into vacuum as explained in section 2.5.5. The detection of escaped electrons provides another method to characterize the fast electron population. Several electron spectrometers (ESPEC) have been developed. They are all based on the same detection technique. Fast electrons entering the spectrometer through a small slit are deflected in a static magnetic field created by permanent magnets. They are consequently dispersed along circular trajectories whose radius is determined by the electron energy. They end up by interacting with a detector. The general

geometry of ESPEC is shown in Fig. 3.25. The use of permanent magnets, that do not require an external power supply, ensures that the magnetic field is not affected by electromagnetic pulses generated during laser-plasma interaction. The existing ESPECs use different detectors. Malka & Miquel [1996] used a stack of six thick silicon diodes protected by small lead pieces to avoid any background generated by unwanted X-rays or by the electromagnetic noise. Each fast electron of energy E interacting with a diode generated $E_{\mathrm{eV}}/3.66$ electron-positron pairs that were finally detected. Chen et al. [2003] developed an ESPEC similar to the configuration introduced by Gahn et al. [2000], using as a detector a set of scintillating fibers. Incoming electron generates a visible light signal, propagating into the fiber coupled to a CCD camera. These detectors do not necessitate to break the chamber vacuum after each shot since they are remotely read out, which is their main advantage. But they are also sensitive to electromagnetic pulses that can freeze them out after an ultra-intense laser shot.
We used in our experiment a compact electron spectrometer developed by Chen et al. [2008b]. This ESPEC uses permanent magnets producing a 0.8 T magnetic field, with a < 10 % variation across the electron dispersion plane, well adapted to disperse escaped fast electrons in the $\sim [0.1 - 100]$ MeV energy range. The calibration curve showing the dependence of the detected electron energy on the x transverse coordinate is presented in Fig. 3.25.

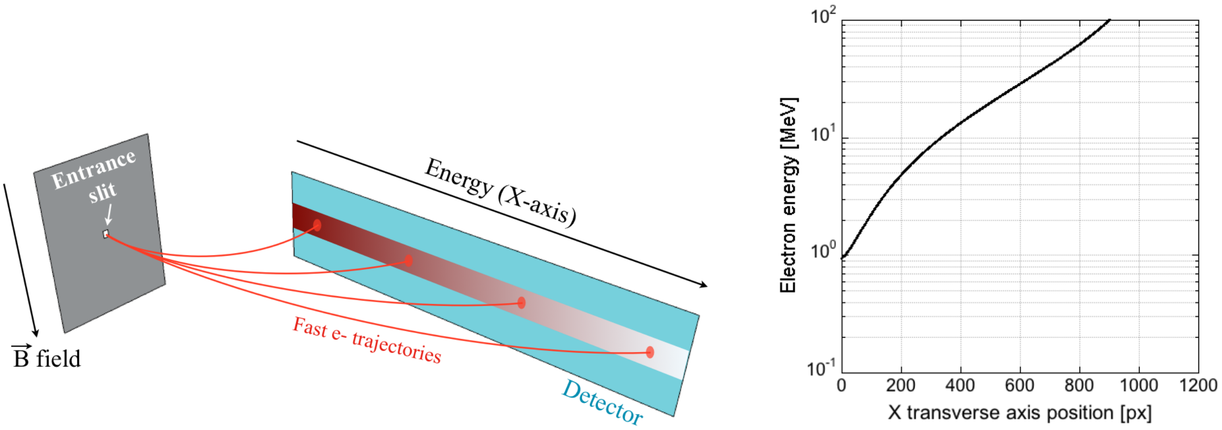

Figure 3.25: (Left) Geometry of the electron spectrometer used in our experiment. (Right) Calibration of the electron spectrometer used in our experiment. The first pixel corresponds to the edge of the imaging plate that has to be placed accurately into the spectrometer.

The detector is in this case a standard SR-type imaging plate, which implies to open the chamber after each shot in order to collect and scan it. The use of such a passive detector has several advantages compared to scintillating fibers. First it is completely insensitive to the electromagnetic pulse that can paralyze electrical devices. It also offers a better energy resolution than the scintillator array thanks to its smaller pixel size. Lastly, it does not necessitate any complex mechanical pieces, such as electrical vacuum feedthroughs required by the use of a CCD camera.

In conclusion, the electron spectrometers can be used to measure high energy fast electrons escaping from the target. These measurements provide an alternative to bremsstrahlung cannons to characterize the fast electron distribution. However, escaped electron spectra differ significantly from their distribution inside the target. Data deconvolution requires a precise understanding of the target space charge conditions. ESPECs can also be used to detect other particles such a protons [Chen et al., 2003] accelerated by a strong electric field induced by fast electrons leaving the target (TNSA mechanism) or positrons [Chen et al., 2006] generated in the interaction of fast electrons > 1.5 MeV with heavy nuclei, such as gold.

Part II

Experimental data: results and interpretation

Chapter 4

Fast electron transport in planar compressed targets: 1D geometry

The success of the fast ignition scheme requires a deep understanding of fast electron transport in a large variety of plasmas. In particular, the characterization of the stopping power of fast electrons propagating into a fast ignition target for both collisional and resistive mechanisms is of primary importance. Considering the variety of laser systems that currently exists worldwide, none of them offers the laser energy and intensity required for a full scale fast-ignition experiment. However smaller scale experiments provide a possibility to test and validate different physical models involved in the fast electron transport. This experimental work is crucial to validate numerical codes providing capabilities for the design of full-scale FI targets and on the evaluation of the feasibility of the FI scenario.

A large number of experiments performed on intermediate laser scale facilities studied the fast electron transport in solid materials, far from the hydrodynamic conditions of FI. The compression of a material allows not only to modify its density but also other physical properties such as the resistivity related to the field self-generated by the electron beam propagation, responsible for energy losses and/or beam confinement/dispersion. We describe in this chapter an experimental campaign performed at the JLF-Titan laser facility (LLNL, USA), dedicated to the study of fast electron propagation in an aluminum compressed at twice the solid density and its theoretical interpretation. The adopted 1D compression is achieved with a strong shock wave leaving behind a homogeneous heated and compressed material. The areal density ρL of the aluminum propagation layer is kept constant throughout compression, thus allowing a separation of collisional and collective energy losses when comparing with un-compressed targets of the same initial thickness. This experimental design is consequently well adapted to study the dependence of the resistive energy losses as a function of target heating due to the compression.

It is important to note that this experimental work constitutes a direct continuation of Benjamin Vauzour PhD work [Vauzour, 2012], but for a higher fast electron current density, providing an experimental validation of theoretical predictions.

4.1 Experimental setup

The experiment described in this chapter was performed on the JLF-Titan laser facility (Lawrence Livermore National Laboratory, USA). The experimental, theoretical and numerical work was conducted within a large international collaboration between the CELIA laboratory, the University Politécnica of Madrid (Spain), the University of California San-Diego (UCSD, USA), the Instituto Superior Técnico (IST, Portugal), the University of Strathclyde (UK), the Ohio State University (OSU, USA), the Lawrence Livermore National Laboratory (LLNL, USA), the KAERI (South Korea) and General Atomics (USA).

4.1.1 The JLF-Titan laser system

Before detailing the Titan laser system, we provide a brief description of the Jupiter Laser Facility (JLF). JLF currently includes four laser installations and target chambers: Janus, Titan, COMET and Europa, the two latter being completely independent from the two former. The Janus Nd:glass laser system generates two laser pulses from 200 ps to 10 ns durations containing 200 J to 1 kJ, respectively, at the wavelength $\lambda_L = 1.053\ \mu$m.

Overview of the laser system

The Titan laser system provides a combination of a ns-scale long pulse (LP) beam, generated by the Janus laser, and a petawatt-class short pulse (SP) beam. The SP beam is generated using the combination of an OPCPA preamplifier together with a classical CPA main amplifier. The $100 - 200$ fs, $\lambda_L = 1.053\ \mu$m seed pulse is generated by a commercial Time Bandwidth Products™ GLX-200 master oscillator of average power up to 400 mW with a 150 MHz repetition rate. It is then stretched up to 1.6 ns and sent through the OPCPA preamplifier made of a BBO crystal pumped by a laser pulse at 1.06 μm. The pre-amplified pulse carrying a few mJ of energy is then amplified up to 5 J going through a series of Nd:glass rods. The pulse is finally amplified to its full energy, up to 150 J, by taking a dual pass through disk amplifiers. The beam is then compressed down to 0.7 ps in the compressor, made of two 40×80 cm^2 diffracting gratings, before entering the target chamber. It is then focused by an f/3 off-axis parabola (OAP) down to a 7 μm FWHM focal spot, yielding a peak intensity $> 10^{20}$ W.cm^{-2} on target. The SP beam direction into the chamber is fixed by the conception of the installation. A scheme of the Titan short pulse laser system is shown on Fig. 4.1

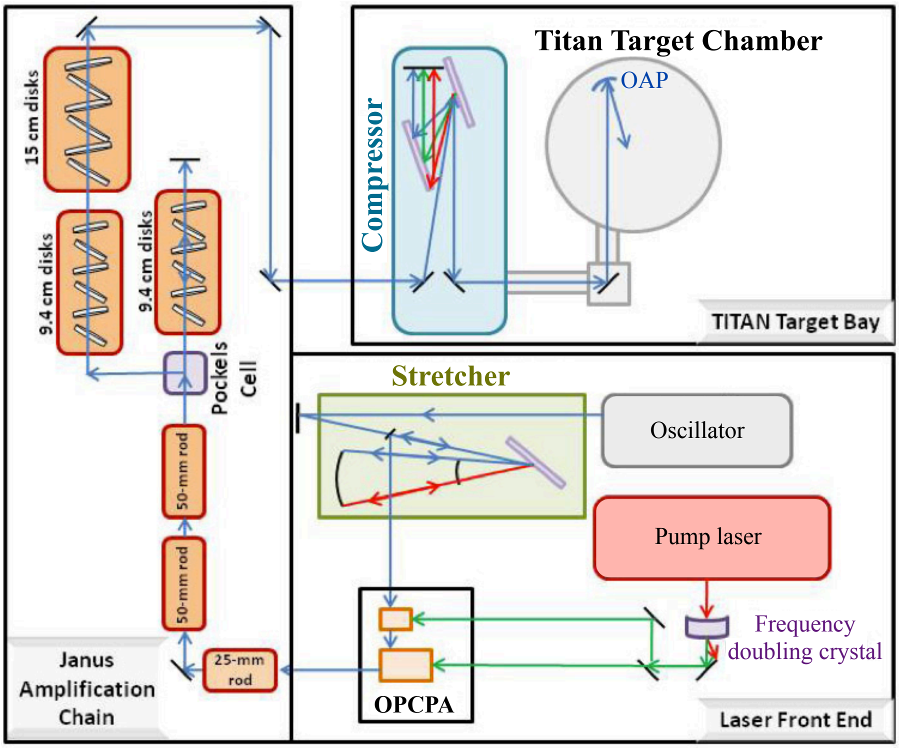

Figure 4.1: Scheme of the Titan short pulse laser chain (image inspired from [Chen, 2009]).

The LP beam taken from one of the Janus beams can be frequency doubled, as it was the case in our experiment, by going through a KDP crystal, decreasing the final pulse energy down to ∼ 400 J. The long pulse is focused by a f/5 lens with a 200 mm focal length into a 20 μm focal spot, or, if coupling the lens with a random phase plate (RPP) into a 200 μm to 400 μm focal spot. The latter configuration is used in our experiment to generate a shock on the target. A delay line allows to vary a time delay between the LP and the SP from -10 ns to $+10$ ns. Unlike the SP beam, the LP beam can enter the target by one of the multiple ports, allowing a large number of laser configurations, determined by the users needs.

Pre-pulse

As any short pulse laser system, the Titan pulse is characterized by an inherent pre-pulse affecting the interaction conditions with a dense target due to the created pre-plasma (section 2.2.2). The characterization of this pre-pulse is consequently of primary importance for the interpretation of the experimental data. In particular the pre-pulse defines the initial conditions for the numerical simulations since both the target hydrodynamics and the fast electron source strongly depend on the quality of the target surface.
The Titan pre-pulse was measured using a leakage of the beam through a mirror. The leakage was focused onto a photodiode protected by a water cell acting as a filter against the high-intensity main pulse [MacPhee et al., 2008; Le Pape et al., 2009], and coupled to an 8 GHz oscilloscope. The pre-pulse profile obtained during a 150 J, 0.7 ps shot on target is presented in Fig. 4.2.

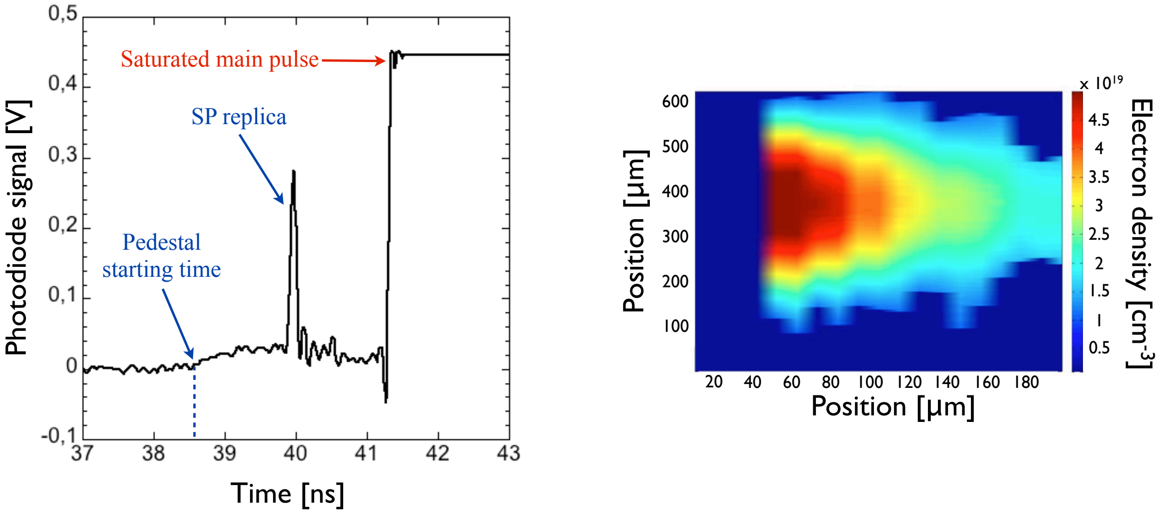

Figure 4.2: (Left) Titan pre-pulse profile measurement. (Right) Experimental 2D electron density for a pedestal of 70 mJ arriving 3 ns before the main pulse and a SP replica of 30 mJ arriving 1.4 ns before the main pulse. The zero position corresponds to the initial position of the target. Both plots were taken from [Le Pape et al., 2009].

One can note that the pre-pulse exhibits two main components. The first one is a long pedestal, arriving ∼ 3 ns before the main pulse, which originates from the OPCA pre-amplification stage of the laser chain. It is due to a parasitic phenomenon called Amplified Optical Parametric Fluorescence (AOPF) which can basically be explained by the spontaneous decay of a pump photon into and idler and a signal photon, the latter being parametrically amplified. This long pedestal carries $5 - 80$ mJ of energy and is responsible for the pulse contrast estimated to $\sim 10^{-7}$. The second component is a replica of the short pulse main component that is reflected into the laser chain, arriving 1.4 ns prior to the main pulse. The ∼ 100 ps FWHM of this replica is not representative of its actual duration-width because of the combined oscilloscope,

photodiode and cable system bandwidth. It is assumed that this replica has the same duration as the main pulse (0.7 ps). The SP replica carries $1-30$ mJ of energy.
The pre-plasma formed by the whole pre-pulse was inferred from side-on interferometric measurements probing the plasma. The phase-shift of the probe laser pulse is related the plasma electron density by the following:

$$\Phi(x) = -\frac{2\pi}{\lambda_P n_c}\int_x^{r_0}\frac{n_e(r)r}{\sqrt{r^2-x^2}}dr \tag{4.1}$$

with λ_P the wavelength of the probe beam. The electron beam is then deconvolved by applying an Abel inversion [Dasch, 1992] assuming an axial symmetry of the SP laser beam around the propagation axis. The obtained 2D electron density map is plotted in Fig. 4.2 for a pedestal of 70 mJ and a SP replica of 30 mJ. The measured pre-plasma electron density is around 10^{20} cm^{-3} at 50 μm from the target, which is the typical value used in our simulations presented in the next sections. It is worth mentioning that the pre-plasma measurements are in fairly good agreement with numerical simulations using the pre-pulse profile presented in Fig. 4.2 as an input [Le Pape et al., 2009].

Laser pulses characteristics

In the experiment described in this chapter both the Titan SP and LP beams were used. Their characteristics were the following:

The short pulse laser beam used for fast electron beam generation carried $E_{SP} = (115 \pm 30)$ J of energy, the incertitude being the standard deviation of the laser energy over all shots, highlighting the important energy fluctuations on a shot-to-shot basis. The pulse duration τ_{SP} was determined by second order autocorrelation measurements, yielding $\tau_{SP} = 0.7$ ps full width at half maximum (FWHM). The SP was focused on the target with the Titan $f/3$ OAP into a 7 μm FWHM focal spot. This spatial spot size was determined by imaging the focal spot at a low flux (Fig. 4.3). The dependence of the encircled energy on the radius is presented in Fig. 4.3. This quantity is normalized by the total energy of the laser beam. One can note that the fraction of energy contained in the spot FWHM is close to 40%. The peak intensity on target was estimated to $I_{SP} = (2 \pm 1) \times 10^{20}$ W.cm^{-2}.

The frequency doubled ($\lambda_{LP} = 0.53$ μm) long pulse laser beam used for the target compression carried $E_{LP} = (410 \pm 9)$ J of energy. It was characterized by a 5 ns square temporal profile. The LP beam was focused on the target with the $f = 200$ mm Titan lens and a phase zone plate, yielding a flat top spot size of 875 μm FWHM, much larger than the SP beam spot size, and carrying 50% of the laser energy within this radius. The peak intensity of target was estimated to 1.4×10^{13} W.cm^{-2}.

4.1.2 Experimental setup

The design of the targets used in the experiment is presented in Fig. 4.4. The goal of the campaign is to study fast electron propagation into an aluminum sample of initial thickness $L_0 = \{20, 40, 60, 80\}$ μm. The SP laser pulse used to generate the fast electron beam is focused on the front side of the target, on an aluminum generation layer of 5 μm thickness, at an angle of 16.5° with respect to target normal. The LP beam used to compress the target is focused at the rear side of the target on a 15 μm polypropylene layer at an angle of 17° with respect to target normal. The expansion of the ablated polypropylene layer creates a shock front wave propagating inside the target in an opposite direction with respect to the fast electron beam.

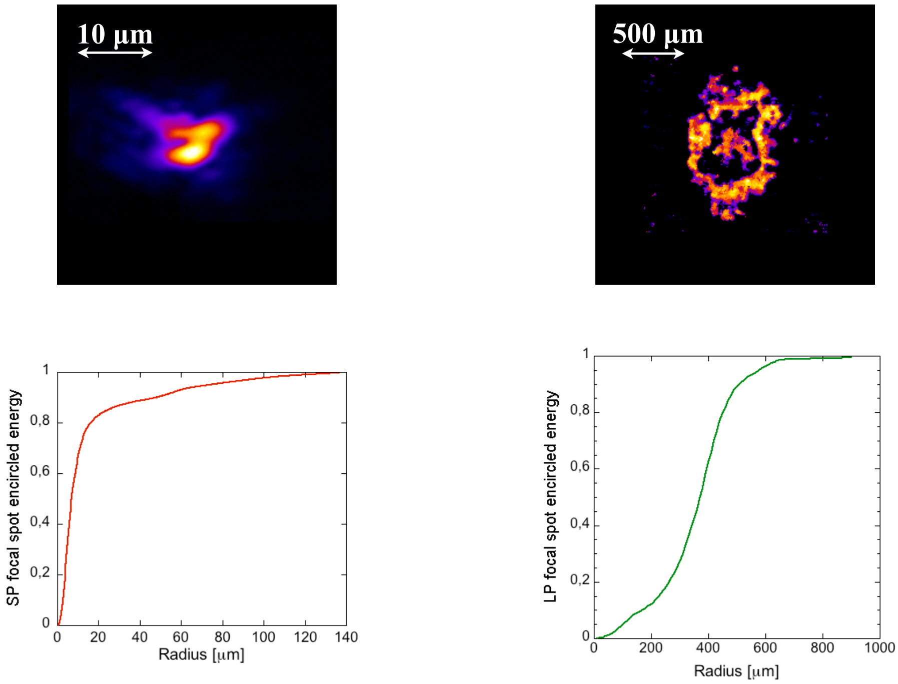

Figure 4.3: (Up) Images of Titan SP (left) and LP (right) focal spots. (Down) Corresponding encircled energies.

The dimension of the LP focal spot compared to the SP focal sport ensures wide uniform hydrodynamic conditions transverse to the fast electron propagation axis, disabling any potential 2D effects, such as density or resistivity gradients. The delay between the two laser pulses is adjustable, depending on the aluminum sample thickness. Indeed, when studying fast electron transport in compressed targets, one has to make sure that the aluminum sample is almost fully compressed, but both the aluminum generation layer and the silver tracer are still intact. The fast electron beam propagation is characterized by the K_α fluorescence emission of tracer layers surrounding the central aluminum sample: a 5 μm silver tracer layer at the front side of the target, located right after the generation layer, to characterize the fast electron beam source, and two consecutive 10 μm tin and copper layers located after the aluminum sample to characterize the fraction of electrons having crossed the central aluminum sample. One can note that another advantage of using a polypropylene ablator layer is to protect the rear side copper tracer from being damaged by any direct laser irradiation.

The following diagnostics were used to collect the emissions generated by fast electrons:

- An absolutely calibrated Cauchois-type hard X-ray spectrometer (see section 3.2.1), called TCS, located at the front side of the target is used to measure the front side Ag-K_α and the rear side Sn-K_α emissions. The ratio between those two emissions allows one to characterize the fraction of generated fast electrons having crossed the central aluminum propagation layer. The determination of the number of emitted photons is also a key parameter in our study in order to calibrate the transport simulations as detailed in the next section.

- An absolutely calibrated spectrometer using a high-reflectivity HOPG flat crystal (see section 3.8) located at the rear side of the target is used to measure the rear side Cu-K_α emission and the front side Ag-K_α emissions using two different channels.

- Two imaging systems located at the rear side of the target constituted by a spherical Bragg

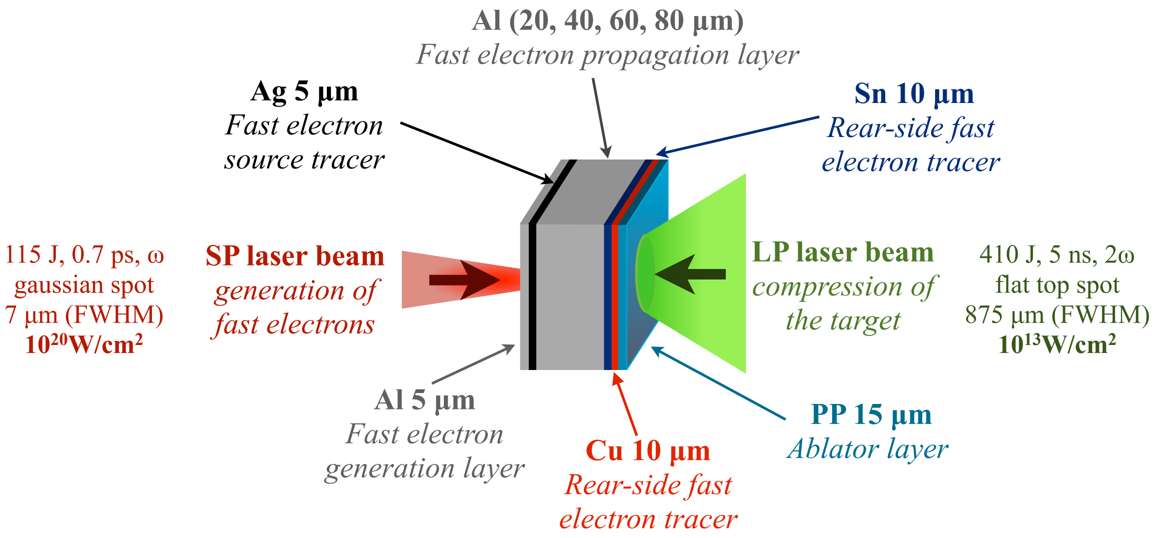

Figure 4.4: Target design used in the Titan experiment.

crystal (see section 3.2.2) looking up the target with a 40° angle with respect to its normal and a Kirkpatrick-Baez microscope (see section 3.2.2) looking down the target with a 40° angle, are used to image the Cu-K$_\alpha$ emission, allowing to determine the dependence of the fast electron beam size on the target thickness, or in other words the divergence of the electron beam. The Bragg imager signal is collected with a MS-type imaging plate whereas the KB microscope signal is collected with a Princeton Instruments CCD camera characterized by a 20 μm pixel size and a 1340 × 1300 pixels chip area.

- A permanent magnet spectrometer (see section 3.3) located at the rear side of the target, at 62° from target normal, measure the spectrum of fast electrons escaped from the target. The measurement of this distribution allows here again a comparison with the transport simulations.

- Two bremsstrahlung cannons (see section 3.2.3) located at the rear side of the target at 45° and 70° from target normal measured the bremsstrahlung spectrum emitted by fast electrons. As detailed in the next section, these measurements are of primary importance to check the validity of the fast electron source simulations.

- Streaked optical pyrometry (SOP) measurements are performed to measure the target rear-side thermal emission due to shock breakout in order to determine the delays between the two laser pulses. This synchronization process is detailed in section 4.1.3.

The experimental setup is presented on Fig. 4.5. The fast electron propagation is studied considering two different cases. The first one corresponds to the propagation of fast electrons in a cold ($T_e = 0.03$ eV) and solid ($\rho_0 = 2.7$ g/cc) aluminum sample. The second case corresponds to the propagation of fast electrons in a warm ($T_e \sim 3$ eV) and compressed ($\rho \sim 2\rho_0 = 5.4$ g/cc) aluminum plasma.

4.1.3 Synchronization of the laser pulses

As mentioned earlier in this chapter, the delay between the two laser pulses must be carefully determined for the success of the experimental campaign. The synchronization process between the two laser pulses is consequently rather critical and must be precisely done. This delay

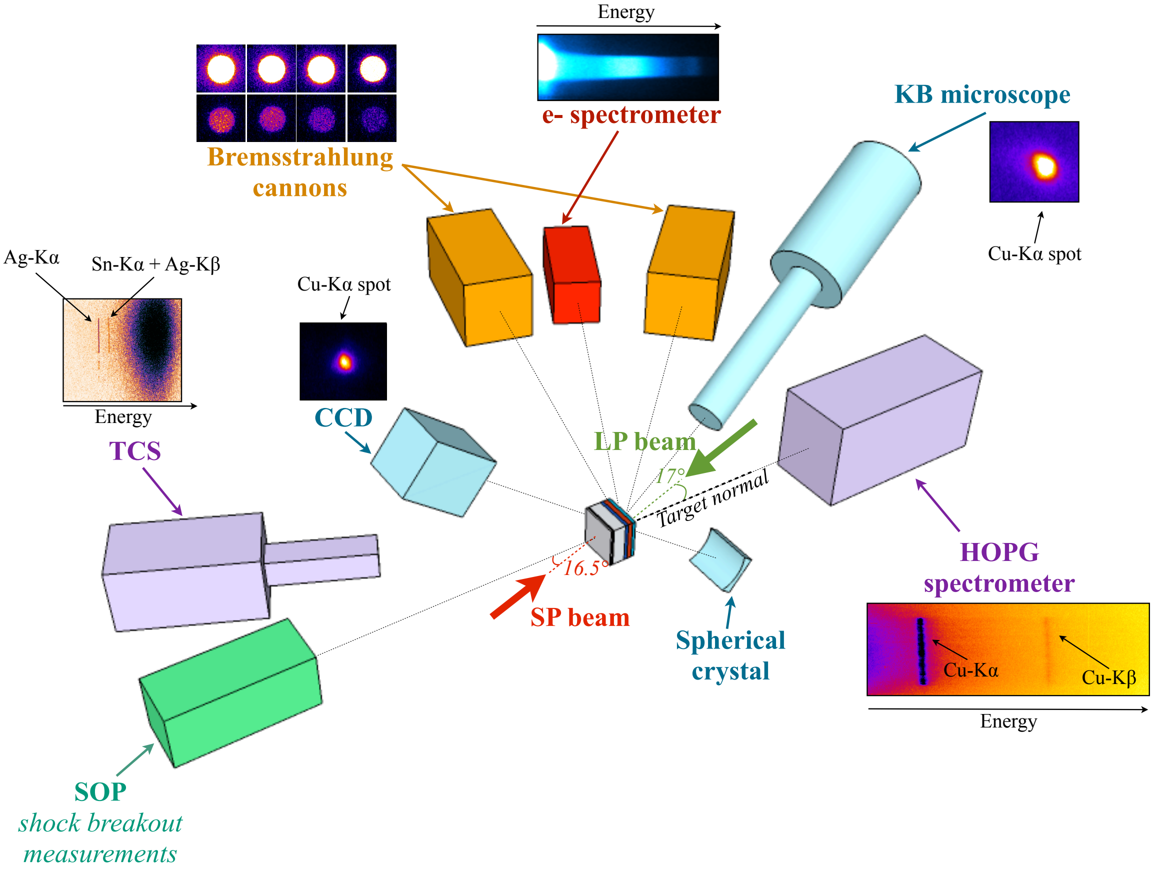

Figure 4.5: Experimental setup used in the Titan campaign.

directly depends on the thickness of the aluminum sample fully conditioning the total target thickness. Two cases can be distinguished.

Warm-compressed targets

When studying fast electron propagation in compressed aluminum samples, the SP laser beam must be fired just before full compression of the central aluminum layer, and before the shock front reaches the front side silver tracer. The first step of the experimental campaign is consequently to determine the shock speed. To do so, the streaked optical pyrometry measurement was performed using the setup presented in Fig. 4.6. A 25 μm aluminum foil set-up at the target chamber center (TCC) is irradiated by the LP laser beam. The shock breakout induced thermal emission at the read side of the foil is imaged with a series of lens and mirrors on the entrance slit of a streak camera. The optical signal is converted on a photocathode into electrons with the number proportional to the incoming optical signal intensity. These electrons are then deviated by a time-increasing electric field perpendicularly to the entrance slit. This tension ramp must be synchronized with the laser pulse. The amplitude of the field increasing linearly with time, the late coming electrons are more deviated than the earlier electrons. Deviated particles go through a micro channel plate where their number is multiplied by $\sim 10^4$ before interacting with a phosphorescent screen. The converted signal is finally collected by a CCD camera. The perpendicular dimension of the measured signal consequently corresponds to the temporal dimension. By comparing the shock breakout signal obtained by shooting the 25 μm aluminum foil with a reference taken by directly sending the LP beam at a very low flux on the streak camera, one can precisely measure the delay between the beginning of the compression and the shock breakout time, and consequently to deduce the shock speed (with a $\sim$ 100 ps precision due to the temporal jitter of the signal triggering the streak camera). An example of such a SOP measurement is presented in Fig. 4.7. A notch filter is located right in front of the streak camera slit to avoid any 2ω laser light background. A shock breakout time of 1.6 ± 0.1 ns is experimentally measured in the case of the 25 μm aluminum foil with a LP

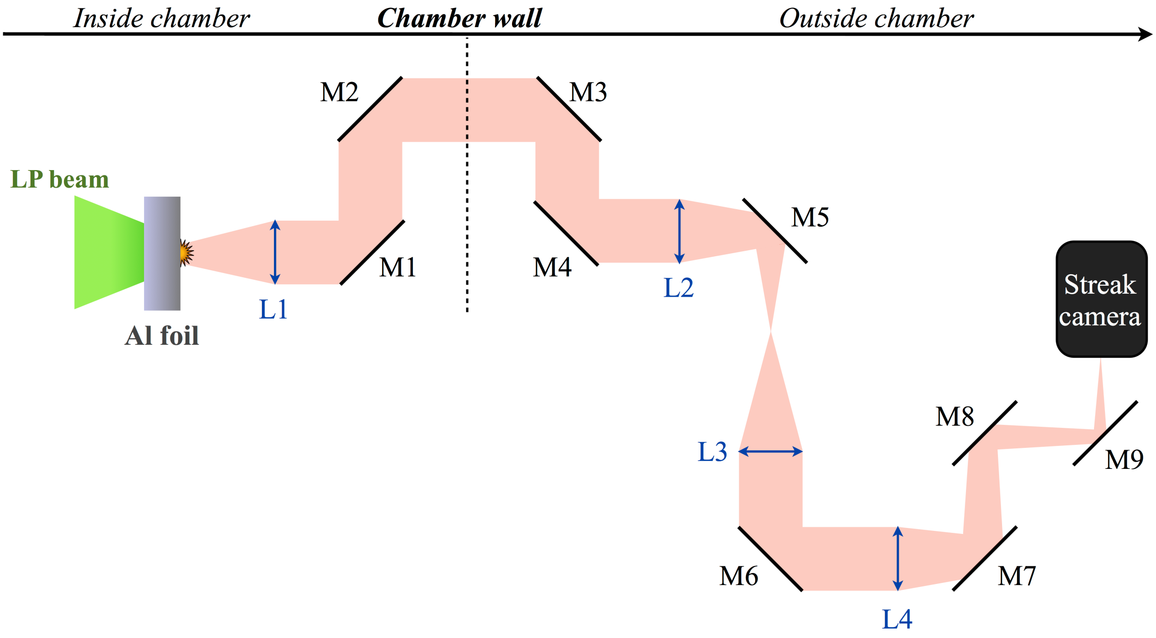

Figure 4.6: Design of the SOP diagnostic. The important number of required metallic mirrors and achromatic lenses is dictated by the experimental room configuration.

beam carrying 368 J of energy, yielding a mean shock speed of $v_{\text{shock}} = 15.6 \pm 0.9$ μm/ns. One can note that the presented LP beam temporal profile is not a square function, due to that fact the reference was measured at low energy flux. When the pulse is amplified in a real shot, the trailing edge of the pulse travels in a gain medium characterized by a lower inversion than the front side of the pulse, yielding to a square profile.

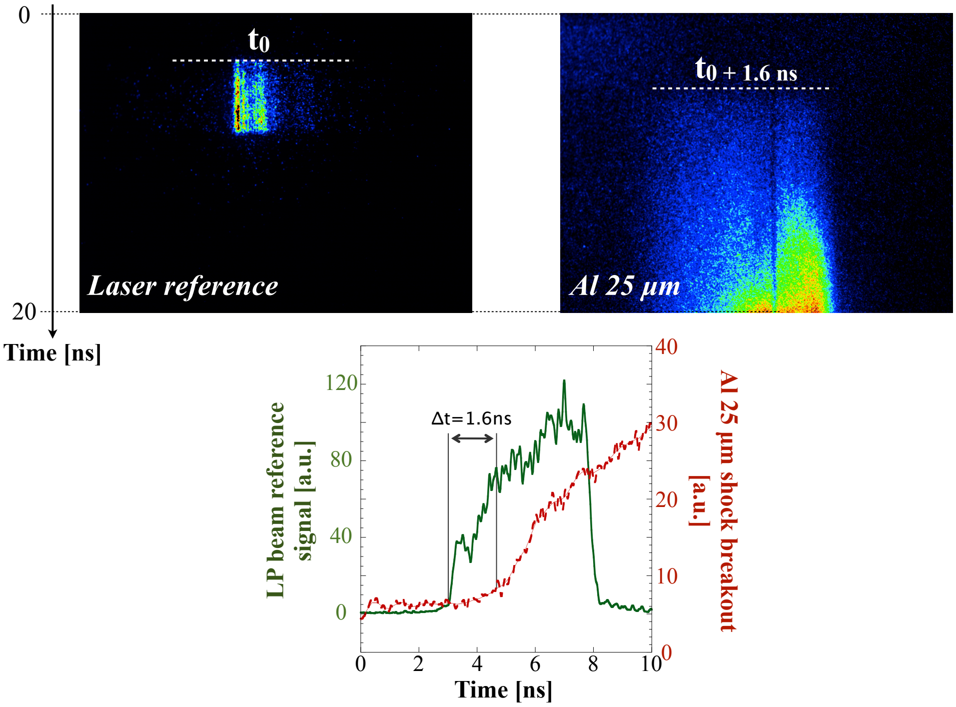

Figure 4.7: Determination of the shock front speed. A reference of the LP beam temporal profile is firstly acquired with the streak camera (left). The laser pulse is then fired on a 25 μm aluminum foil and the rear side shock breakout induced thermal emission is imaged on the streak camera (right). The determination of the shock breakout time is finally done by comparing these two signals (bottom plot).

It is worth mentioning that the SOP measurements could also be performed by shooting on the targets described in Fig. 4.4, instead of aluminum foils, but without any front side aluminum and silver layers [Vauzour, 2012]. The shock breakout time measurement is then used to calibrate 2D radiative-hydrodynamic simulations performed with the CHIC code [Maire et al., 2007] by Ph. Nicolaï. After reproducing the experimental aluminum foil shock breakout time, the CHIC code is used to determine the delay between the two laser pulses allowing to inject the fast electrons at the moment when the aluminum propagation layer is fully compressed, for all target thicknesses. The simulated 1D density and temperature profiles along the fast electron propagation axis are plotted in Fig. 4.8 e), f), g) and h). The SP beam ASE is also taken into account in hydrodynamic simulations, resulting in an expanding front side aluminum layer and a slightly compressed and heated silver tracer. One can also note that the aluminum sample thickness is approximately divided by a factor ≈ 2 in the compressed case compared to the solid case whereas its density is multiplied by the same factor, keeping the areal density constant throughout compression when comparing targets of the same initial thickness. Compressed aluminum layers are also heated up to a few eV, close to the aluminum Fermi temperature (~ 11 eV). Table 4.1 summarizes the hydrodynamic and delay parameters. One can note that the areal densities of the solid and compressed targets of the same initial thickness are indeed fairly comparable.

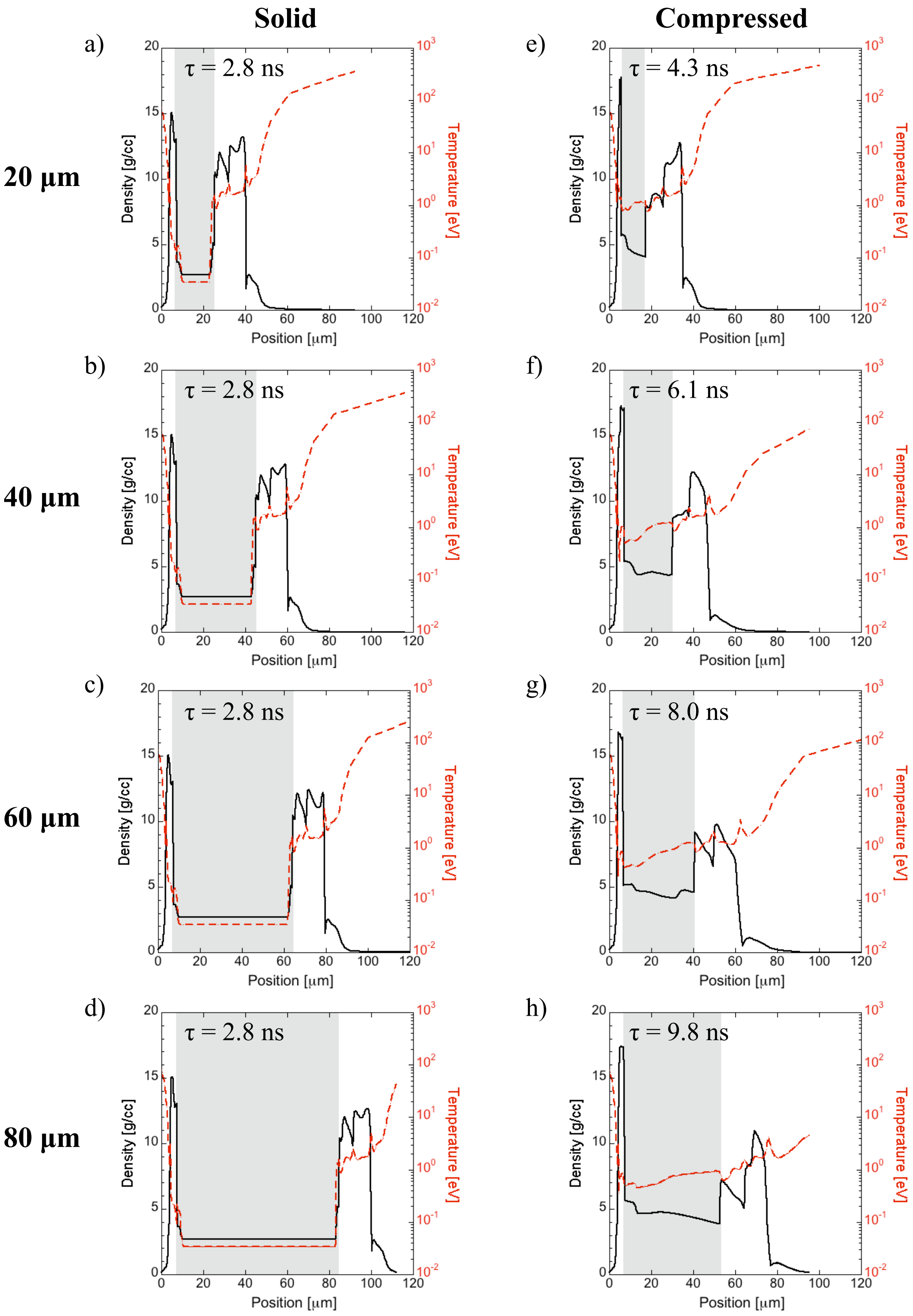

Figure 4.8: On-axis density and temperature profiles extracted for solid (a), b), c), d)) and compressed (e), f), g), h)) targets right before injection of fast electrons. The central aluminum sample is highlighted by the gray areas. The corresponding chosen delay between the two laser pulses is indicated in each plot.

Al layer initial thickness [μm]		**20**	**40**	**60**	**80**
Solid	$\tau_{\mathrm{SP/LP}}$ [ns]	2.8	2.8	2.8	2.8
	L_{Al} [μm]	17.8	37.5	56.5	77.25
	ρL_{Al} [mg.cm^{-2}]	5.27	10.6	15.70	21.40
Compressed	$\tau_{\mathrm{SP/LP}}$ [ns]	4.3	6.1	8.0	9.8
	L_{Al} [μm]	11.3	22.65	33.66	45.51
	ρL_{Al} [mg.cm^{-2}]	5.24	10.48	15.51	21.00

Table 4.1: Summary of the hydrodynamic parameters calculated for solid (top) and compressed (bottom) targets. The quantity $\tau_{\mathrm{SP/LP}}$ represents the delay between the two laser pulses adopted in the experimental campaign. L_{Al} stands for the actual thickness of the central aluminum sample and ρL_{Al} is the areal density of the aluminum sample.

Cold-solid targets

In order to study fast electron propagation in cold and solid aluminum samples it is necessary to fire the LP laser beam prior to the SP laser beam. This can be explained by two main reasons. The first one is that it is important to keep similar radiative properties of the rear side copper and tin tracers for an efficient comparison between solid and compressed samples. The second reason is due to the inherent fast electron refluxing phenomenon if the rear side of the target exhibits a steep density gradient. As mentioned is section 2.5.5, fast electrons leaving the target create an intense charge separation electric field that pulls them back into the target. Electrons traveling back and forth in the target consequently generate an additional K_α emission leading to an increase of the measured fluorescence signal in solid targets and a false estimation of the transported energy. To avoid this undesired phenomenon, the LP laser beam is also fired in solid targets to create an expanding plasma at the rear side acting as a *get lost layer*, moving the charge separation zone far away from the target, and trapping electrons inside this expanding zone. A set of numerical PIC simulations performed by Vauzour et al. [2012] with the PICLS code [Sentoku & Kemp, 2008] considering a 3.0×10^{19} W.cm^{-2} SP laser beam incident on a 10 μm aluminum layer having, or not, a rear-side get lost layer, showed a fairly efficient inhibition of the refluxing effect with a lost layer (Fig. 4.9). These 1D simulations actually overestimate the refluxing effect since transverse electron deviations are not modeled.

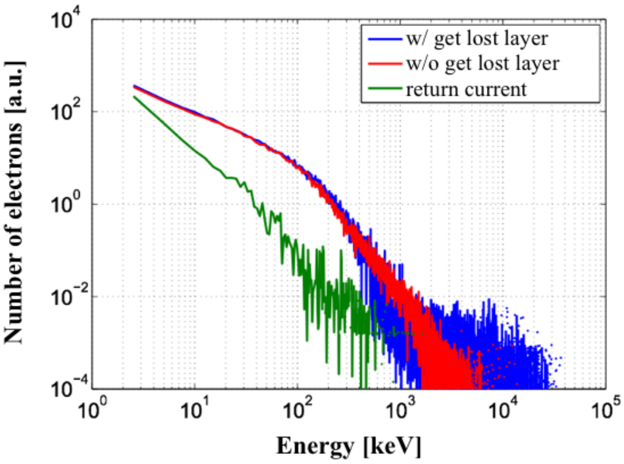

Figure 4.9: Temporally averaged fast electron spectra re-injected into the aluminum target without (blue solid line) and with (red solid line) a get lost layer. The return current contribution is also represented (green solid line).

In addition, the collisions were not taken into account, preventing them from participating to refluxing inhibition since electrons characterized by $E < 40$ keV should be stopped into the lost layer. An experimental evidence of refluxing inhibition has also been obtained in the Titan experiment described in this chapter. The TCS spectrometer possesses a pinhole, allowing to image the source. Fig. 4.10 presents two pinhole images obtained by shooting on a multilayer target with the short pulse beam only, and with both laser pulses, creating a lost layer. One can clearly see the entire 5×5 mm^2 target structure with the SP beam only due to an important fast electron refluxing. This structure disappears when creating a lost layer.

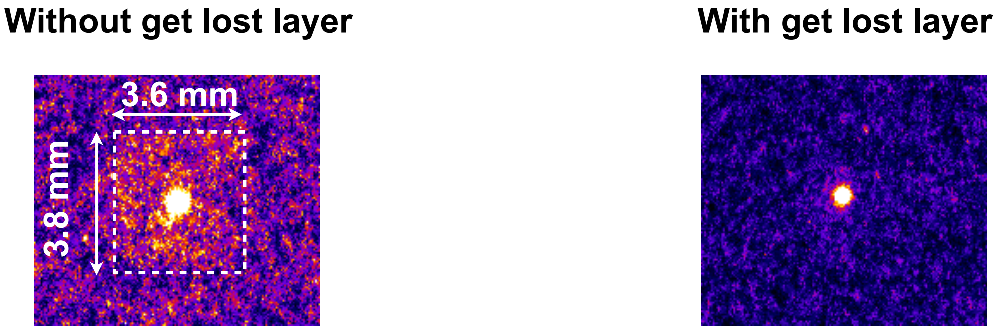
Without get lost layer

With get lost layer

Figure 4.10: Images of the target obtained with the TCS diagnostic pinhole. When shooting the SP beam only (left), the image of the target is clearly visible due to fast electron refluxing. The measured horizontal and vertical dimensions, 3.6 mm and 3.8 mm, respectively, perfectly matches the target size (5×5 mm^2) considering that the pinhole, characterized by magnification of ~ 0.76, is located on the equatorial plane and at 20° with respect to target normal.

Fast electrons are injected when the rear side of the target, composed by the polypropylene layer and by the two copper and tin tracer layers, is fully compressed, right before the shock front enters the aluminum central layer, keeping it cold and at solid density. The delay between the two laser pulses estimated with the hydrodynamic CHIC simulations is $\tau = 2.8$ ns. The hydrodynamic profiles corresponding to cold-solid targets are plotted in Fig. 4.8 a), b), c) and d). Table 4.1 summarizes the hydrodynamic conditions of cold-solid targets.

To conclude this section, a key condition in our study is the conservation of the areal density throughout the compression. As collisional losses directly depend on ρL_{Al}, they should remain constant when comparing solid and compressed targets of the same initial thickness. Any variation in terms of stopping power will consequently be attributed to a modification of resistive energy losses. This remarkable condition will be discussed again in the next sections.

4.2 Experimental results

We present in this section the experimental results obtained in the Titan campaign, with the goal to observe a modification of fast electron stopping power with the target compression.

4.2.1 Cu-K$_\alpha$ spot size

The dependence of the copper K$_\alpha$ spot size on the aluminum sample thickness provides a useful diagnostic to quantify the fast electron beam divergence. Two diagnostics are devoted to such a measurement: a Bragg imager based on a spherical crystal and a Kirkpatrick-Baez microscope using as detectors a MS-type imaging plate and a CCD camera, respectively. The KB efficient shielding ensured very few failures of the CCD camera due to intense electromagnetic pulses generated in each shot. Due to the viewing angle of the two diagnostics, the estimate of the Cu-K_α emission is not straightforward and needs to be accompanied with a similar deconvolution processes. The KB data are deconvolved as follows:

1. The image is rotated by 1.5° in order for the mirror axis to correspond to the horizontal and vertical directions.
2. The 2D spot is extracted from the rest of the signal.
3. A mean background is measured all around the spot edges and subtracted to the whole image.
4. The image is corrected for magnifications, which are different in the vertical and in the horizontal planes.
5. The viewing angles are corrected through bicubic interpolations performed with Matlab. These transformations do not conserve the detected signal, disabling any photon counting capability.
6. Two vertical and horizontal line-outs going through the spot center are taken and fitted by a Gaussian function.
7. The spot size FWHM is calculated by averaging the vertical and horizontal FWHM.

The Bragg imager spot size deconvolution goes through a fairly similar process, except for the initial 1.5° rotation. Experimental results measured by these two imagers are presented in Fig. 4.11. The spot size increases with the target thickness due to fast electron divergence. One can note that there is no obvious difference between solid and compressed samples, as already observed in several experiments [Vauzour et al., 2014]. The fast electron divergence seems consequently to be much more dictated by the generation processes rather than by the hydrodynamic conditions encountered into the target, at least for the considered energy range and the target thickness. The two diagnostics also provide fairly similar results. By extracting the slope of a linear fit going through the experimental data, a mean angle of divergence can be estimated for the spherical imager and the KB microscope, yielding $(19 \pm 3)^\circ$ and $(17 \pm 4)^\circ$ half width at half maximum (HWHM), respectively.

4.2.2 K_α spectrometers

Two K_α spectrometers are fielded into the experimental chamber to collect the rear-side copper and front-side silver emissions (DC-HOPG spectrometer) and the front side silver and rear-side tin emissions (TCS). Silver K_α emission is generated fairly close from the laser-plasma interaction region, providing a way to characterize the fast electron source. Copper and tin K_α emissions are generated right after the central aluminum propagation layer, characterizing the fraction of electrons having crossed this sample. Due to their different K_α emission cross sections (Fig. 3.3), these two rear-side tracers are sensitive to different fast electron population minimum energies, being ~ 25 keV and ~ 70 keV for copper and tin, respectively. Due to some experimental issues with the silver channel of the DC-HOPG, this spectrometer is actually only used for copper fluorescence measurements. The deconvolution of the DC-HOPG and of the TCS results relies on calibration measurements performed by D.P. Higginson and collaborators (LLNL, USA). Considering the location of these two spectrometers (see Fig. 4.5) the emitted signal must cross a non negligible quantity of matter before being detected. Measured emissions must consequently be corrected by the appropriate material transmissions presented in

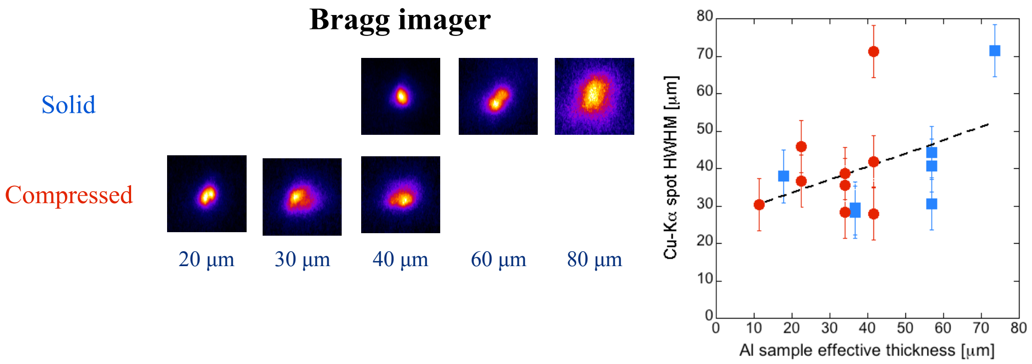

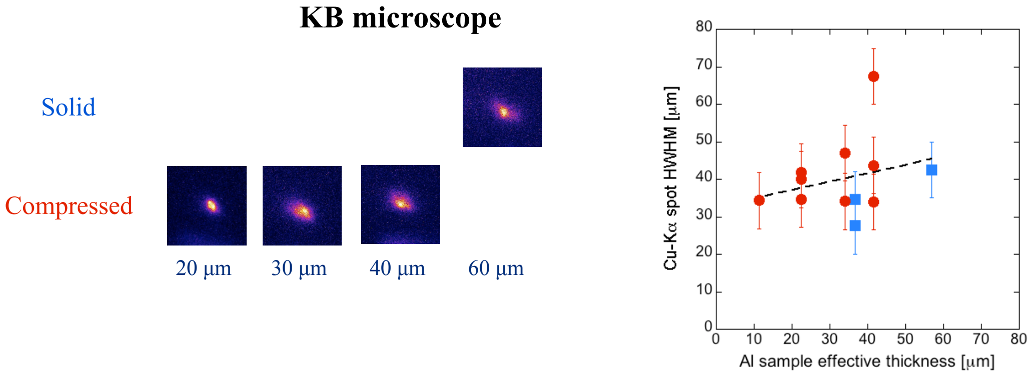

Figure 4.11: Evolution of the copper K_α spot HWHM as a function of the target effective thickness (right) calculated from experimental measurements (left) for solid (blue squares) and compressed (red circles) targets. The spot was imaged with both a Bragg spherical crystal (top) and a Kirckpatrick-Baez microscope (bottom).

Al sample thickness L_0 [μm]	**Cu-K_α [μm]**	**Ag-K_α [μm]**	**Sn-K_α [μm]**
20	0.961	0.775	0.902
40	0.961	0.775	0.893
60	0.961	0.775	0.885
80	0.961	0.775	0.877

Table 4.2: Transmission of the K_α line emissions through the materials between the emission zone and the spectrometer. The target areal density being conserved with compression, the transmission values are similar for solid and compressed targets of the same initial thickness.

Table. 4.2. The dependence of the absolute yields on the aluminum sample effective thickness is presented in Fig. 4.12. The Ag-K$_\alpha$ emission is representative of the number of fast electron generated into the front side aluminum layer. The data dispersion, within a factor 3, indicates the stability of the fast electron source, despite inherent fluctuations mainly due to the SP laser beam energy fluctuations. When looking at the Sn-K$_\alpha$ and Cu-K$_\alpha$ yields, one may expect a decreasing trend of these absolute values related to an increasing fraction of fast electrons being stopped into the increasing thickness aluminum sample. Due to the laser energy fluctuations, these trends are not obvious in these two plots. In order to get rid of any shot-to-shot fluctuations, a straightforward approach consists in normalizing Sn-K$_\alpha$ and Cu-K$_\alpha$ rear side absolute yields by the front side Ag-K$_\alpha$ yield. These ratios are shown in Fig. 4.13.

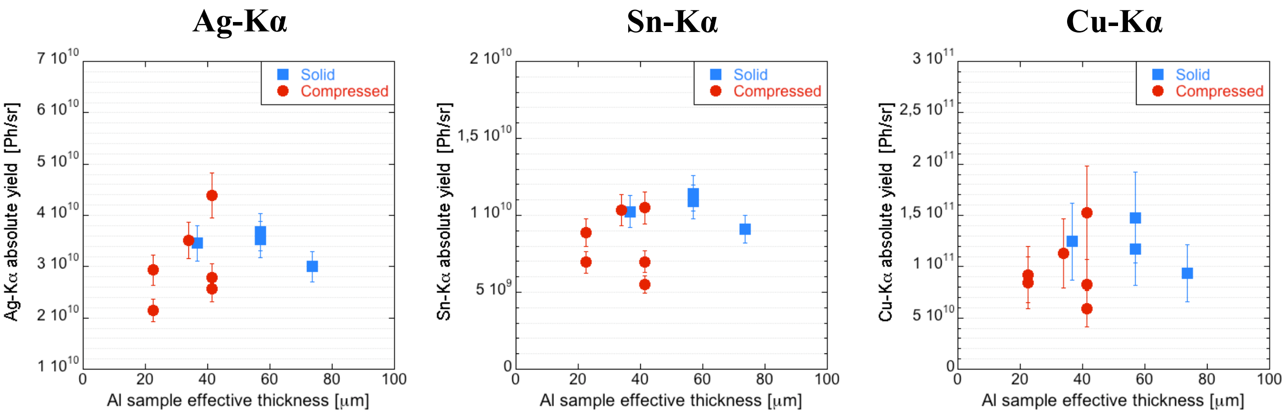

Figure 4.12: Dependence of the Ag-K$_\alpha$ (left), Sn-K$_\alpha$ (middle) and Cu-K$_\alpha$ (right) absolute yields for solid (blue squares) and compressed (red circles) on the aluminum sample effective thickness. The values are corrected by the material transmission.

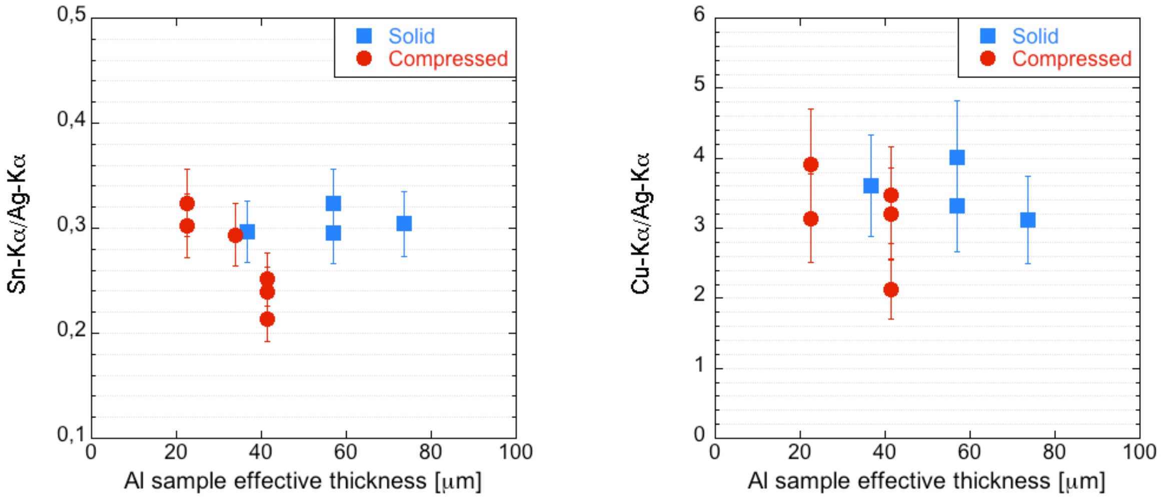

Figure 4.13: Dependence of the Sn-K$_\alpha$/Ag-K$_\alpha$ (left) and Cu-K$_\alpha$/Ag-K$_\alpha$ ratios on the aluminum propagation layer effective thickness.

As mentioned earlier in this section, the tin and copper tracers are sensitive to different fast electron energy populations. When comparing the tin and silver K$_\alpha$ ionization cross sections, one may note a fairly similar trend. The Sn-K$_\alpha$/AgK$_\alpha$ ratio is consequently directly related to the fraction of fast electrons with energies greater than 70 keV having crossed the aluminum propagation layer. The two plots presented in Fig. 4.13 exhibit a fairly similar behavior. First, the ratios seem to decrease when the aluminum sample effective thickness increases, independently of the target hydrodynamic state. This can easily be explained by an increase of total energy losses when the quantity of matter to be crossed increases. The decreasing trend of the Sn-K$_\alpha$/Ag-K$_\alpha$ ratio in solid targets is however not so obvious. A remarkable trend is also seen when comparing solid and compressed samples. The ratios indeed decrease faster in the case of compressed samples, exhibiting an increase of energy losses with compression associated to a rise of density, and probably also of temperature.

The determination of the dominant physical mechanisms, either collisional or resistive, responsible for this increase of energy losses in compressed samples, constitute one of the most important aspects in our study. According to section 2.5.4 the integrated collisional and resistive energy losses of fast electrons over the whole aluminum sample can be deduced from the corresponding scaling laws:

$$\begin{aligned} \left.\frac{dE}{dz}\right|_{\text{coll}} &\propto \rho \Rightarrow \Delta E_{\text{coll}} \propto \langle\rho\rangle L_{\text{Al}} \\ \left.\frac{dE}{dz}\right|_{\text{res}} &\simeq e\eta j_b \Rightarrow \Delta E_{\text{res}} \propto \langle\eta j_b\rangle L_{\text{Al}} \end{aligned} \tag{4.2}$$

where the symbols $\langle\rangle$ denote averaged values over L_{Al}. The collisional stopping power depending on the aluminum sample density should consequently increase with the compression. However, according to the hydrodynamic simulation results presented in Fig. 4.8 and summarized in Table 4.1, as the aluminum sample areal density ρL_{Al} remains approximately constant when comparing target of the same initial thickness, integrated collisional energy losses should be similar in these two cases. The resistive energy losses depend on the fast electron current density j_b, and on the target resistivity η depending on the electron temperature. According to the hydrodynamic simulation results, the temperature in the compressed aluminum sample is close to 3 eV, which is comparable to the Fermi temperature. As described in section 2.5.3 the Eidmann-Chimier model predicts high resistivity values in this temperature domain, ~ 20 times greater than the resistivity of a solid aluminum, as represented in Fig 4.14. Therefore, the resistive energy losses integrated over the aluminum sample thickness should increase in compressed samples. This result must however be tempered since the electron beam may, as mentioned in section 2.5.4, rapidly heat the aluminum propagation layer up to several hundreds of eV, where the resistivity described by the Spitzer model does not depend on the initial density anymore and decreases rapidly with T_e. We will come back to this remark in the next section.

By plotting the Sn-K$_\alpha$/Ag-K$_\alpha$ and Cu-K$_\alpha$/Ag-K$_\alpha$ ratios as a function of the aluminum sample areal density, one obtains a simple graphical representation allowing to discriminate the resistive energy losses from the collisional energy losses, since any modification between solid and compressed samples should be attributed to a modification of resistive energy losses. The two plots are presented in Fig. 4.15. A remarkable results can be immediately seen on the Sn-K$_\alpha$/Ag-K$_\alpha$ ratio evolution plot, representing the fraction of electrons having crossed the aluminum central propagation layer. This ratio is fairly lower for the thickest compressed targets, compared to the solid targets. Considering the underlying behavior of the collisional and resistive stopping powers, this lower ratio constitutes an experimental evidence of enhanced resistive energy losses for the thickest compressed targets in the studied interaction regime $I_L = 2 \times 10^{20}$ W.cm^{-2}. This result constitutes the major result of the experimental campaign. The Cu-K$_\alpha$/Ag-K$_\alpha$ ratio does not clearly exhibit a difference between solid and compressed samples. This is however not in contradiction with the Sn-K$_\alpha$/Ag-K$_\alpha$ ratio results considering that copper and tin tracers are sensitive to different parts of the fast electron population.

In order to study in details the underlying physical processes responsible for this behavior and

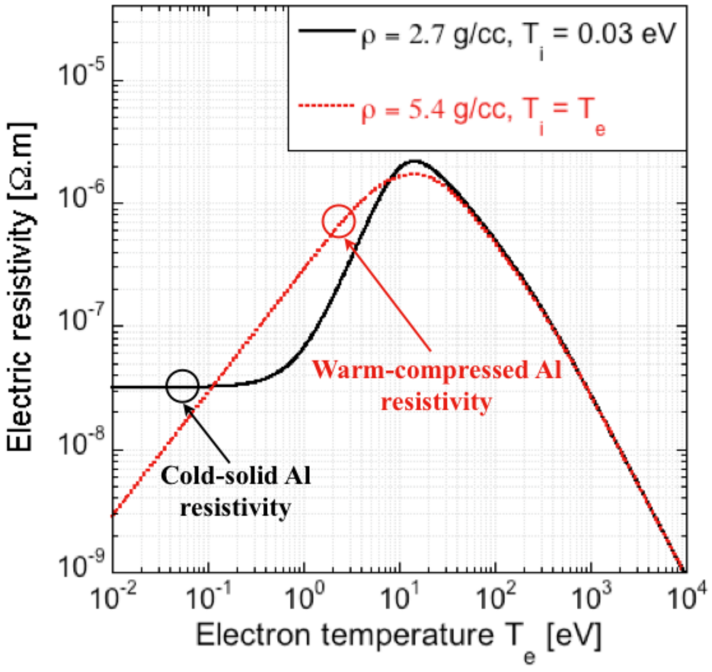

Figure 4.14: Dependence of the aluminum sample resistivity on the electron temperature in the case of cold-solid material (black solid line), with $T_i = 0.03$ eV, and warm-compressed material (red dotted line) considering the thermodynamic equilibrium $T_i = T_e$.

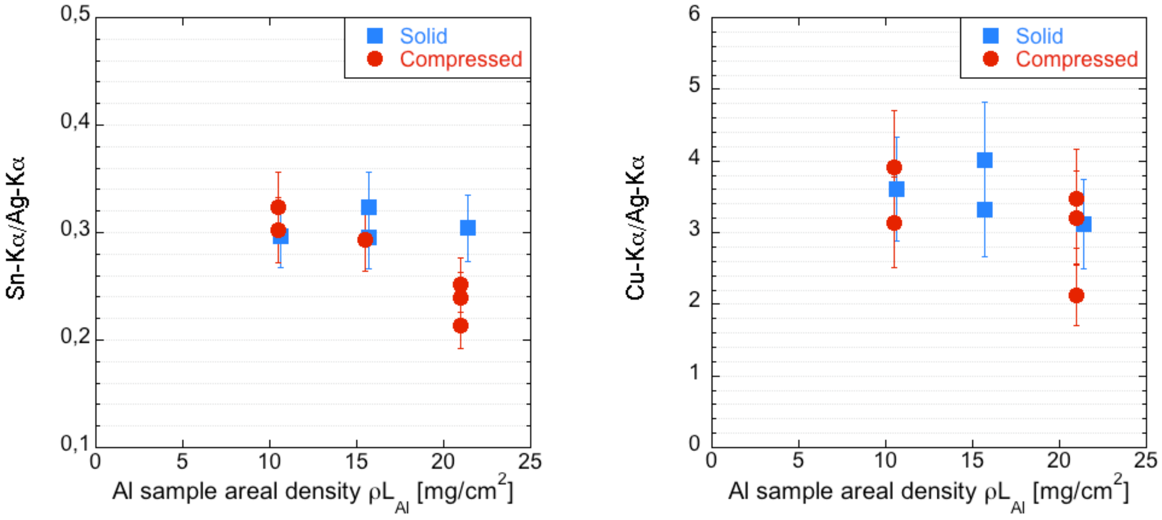

Figure 4.15: Evolution of the Sn-K$_\alpha$/Ag-K$_\alpha$ (left) and Cu-K$_\alpha$/Ag-K$_\alpha$ ratios as a function of the aluminum propagation layer areal density.

to quantify the modification of both collisional and resistive energy losses with compression, a set of transport simulations needs to be performed. This constitutes the main topic of section 4.4.

4.2.3 Bremsstrahlung cannons

The two bremsstrahlung cannons described in section 3.2.3 fielded into the experimental chamber allow a measurement of the bremsstrahlung spectrum emitted from the target. Bremsstrahlung cannon raw data consist in fifteen signals, proportional to the number of photo-stimulated luminescence (PSL) photons measured in the image plate scanning process performed 30 minutes after each shot. A typical result, representative of all shots is presented in Fig. 4.16. The determination of the initial fast electron spectrum based on these experiment data is not straightforward and needs Monte-Carlo-type numerical simulations described in section 4.4.3. A simpler Matlab program running in a few seconds was developed allowing to evaluate the bremsstrahlung spectrum after each laser shot. The basic idea of this program is that the transmission of the materials composing the cannon filters is well known and tabulated. Therefore, there is a linear relation between the spectrum of the photons and the response of the detector. The full deconvolution process is based on the following. Let us assume a photon spectrum $I(E)$ characterized by N energy bins entering the bremsstrahlung cannon. The number of PSL photons J_i obtained after scanning the ith IP is given by the following matrix equation:

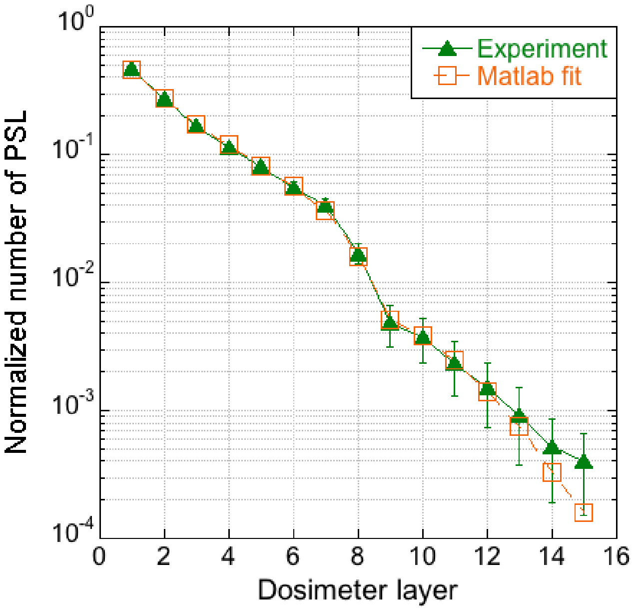

Figure 4.16: Dependence of the measured (green triangles) number of PSL photons normalized to the signal integral on the number of the IP dosimeter layer. Each data point represents an averaged value over the IP area. The fit (orange squares) obtained by injecting Eq. 4.5 into the Matlab script is in fairly good agreement with experimental data.

$$F.I = J \Rightarrow \begin{pmatrix} F^1(E_1) & F^1(E_2) & \dots & F^1(E_N) \\ F^2(E_1) & F^2(E_2) & \dots & F^2(E_N) \\ \vdots & \vdots & \ddots & \vdots \\ F^{15}(E_1) & F^{15}(E_2) & \dots & F^{15}(E_N) \end{pmatrix} \begin{pmatrix} I_1 \\ I_2 \\ \vdots \\ I_N \end{pmatrix} = \begin{pmatrix} J_1 \\ J_2 \\ \vdots \\ J_{15} \end{pmatrix} \tag{4.3}$$

with the F-matrix elements given by:

$$\begin{aligned}
F^1(E_k) &= T^1(E_k).R_{\mathrm{IP}}(E_k)\\
F^2(E_k) &= T^1(E_k).T^2(E_k).R_{\mathrm{IP}}(E_k)\\
&\vdots\\
F^i(E_k) &= T^1(E_k).T^2(E_k)...T^i(E_k).R_{\mathrm{IP}}(E_k)
\end{aligned} \tag{4.4}$$

with $T^i(E_k)$ the transmission of an incident photon of energy E_k just in front of the ith IP and $R_{\mathrm{IP}}(E_k)$ the IP sensitivity, or in other word the number of PSL photons generated by an incident bremsstrahlung photon of energy E_k. The number of rows and columns of the F matrix is fixed by the number of filters composing the bremsstrahlung cannon, which is 15 in our case. The transmission of the cannon filters taken from the NIST database [Hubbel & Seltzer, 2014] is plotted in Fig. 4.17 together with the IP sensitivity calculated by Bonnet et al. [2013]. It is worth mentioning that the F-matrix elements are also taking into account the IP transmission as well as the transmission of mylar protective layers surrounding each filter. As a consequence, the photon spectrum is deconvolved by the following process:

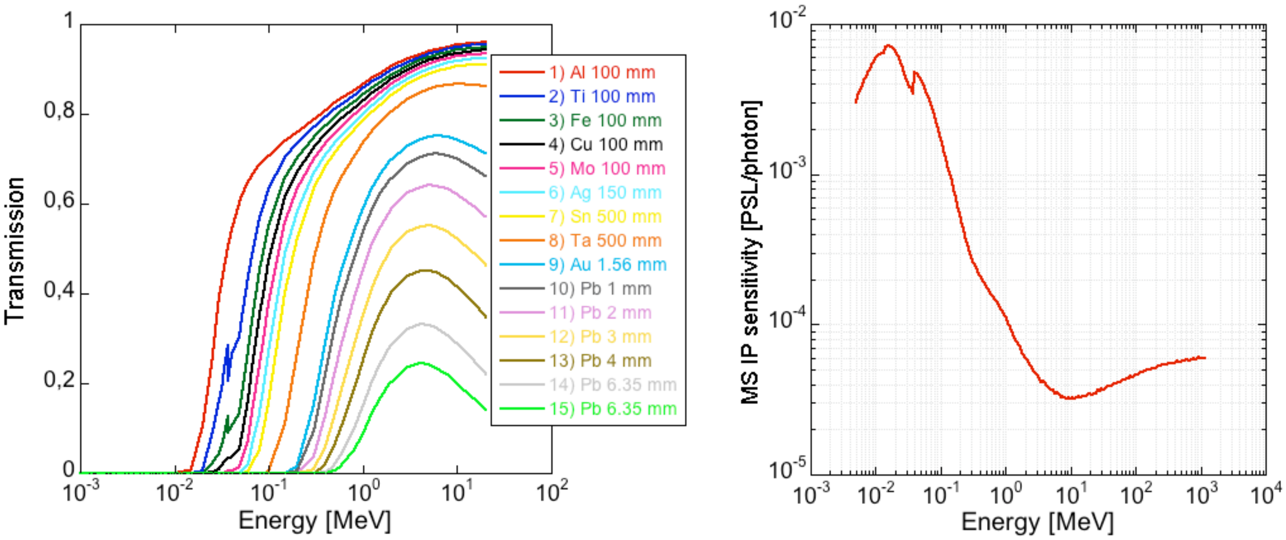

Figure 4.17: (Left) Transmission of the materials composing the bremsstrahlung cannon filters. (Right) Dependence of the sensitivity of MS-type imaging plates on the incident photon energy.

1. A photon spectrum $I(E)$ is chosen by the user who has to propose a mathematical function as well as a photon energy range.
2. The photon spectrum is injected into the program and the resulting PSL values are compared to experimental values.
3. The difference between the calculated and the experimental spectrum is evaluated and the initial photon spectrum is modified in order to reduce the difference until a good agreement is achieved with the experimental results.

Among all the mathematical functions injected into the Matlab script, the double exponential function provides the best agreement with the experimental results (Fig. 4.16):

$$I(E) = \alpha \exp\left(-\frac{E}{T_1}\right) + \beta \exp\left(-\frac{E}{T_2}\right) \tag{4.5}$$

	T_1 [MeV]	T_2 [MeV]	α [keV^{-1}]	β [keV^{-1}]	N_{ph}
Cannon 1 (45°)	0.023 ± 0.002	0.23 ± 0.04	35 ± 6	0.94 ± 0.3	$(6 \pm 2) \times 10^8$
Cannon 1 (70°)	0.050 ± 0.003	0.26 ± 0.064	11 ± 4	0.47 ± 0.2	$(3 \pm 2) \times 10^8$

Table 4.3: Summary of the temperature values, and α and β parameters, averaged over all laser shots for the two cannons. The mean number of detected photons N_{ph} is also presented.

with $E \in [20\,\mathrm{keV}, 2.8\,\mathrm{MeV}]$. The dependence of two temperatures T_1 and T_2 for the two cannons on the aluminum sample initial thickness is presented in Fig. 4.18. No significant difference can be seen comparing solid and compressed samples. Mean temperatures averaged over all shots and calculated for each cannon are summarized in table 4.2.3. Bremsstrahlung photon distributions are characterized by higher mean temperatures at higher angle from fast electron propagation axis. However, the number of photons detected closer to fast electron propagation axis, at 45°, is found to be about two times higher than at 70°.
The validity of this analysis has to be confirmed by Monte-Carlo simulations that are described in section 4.4.3, together with the deconvolution process of the fast electron spectrum.

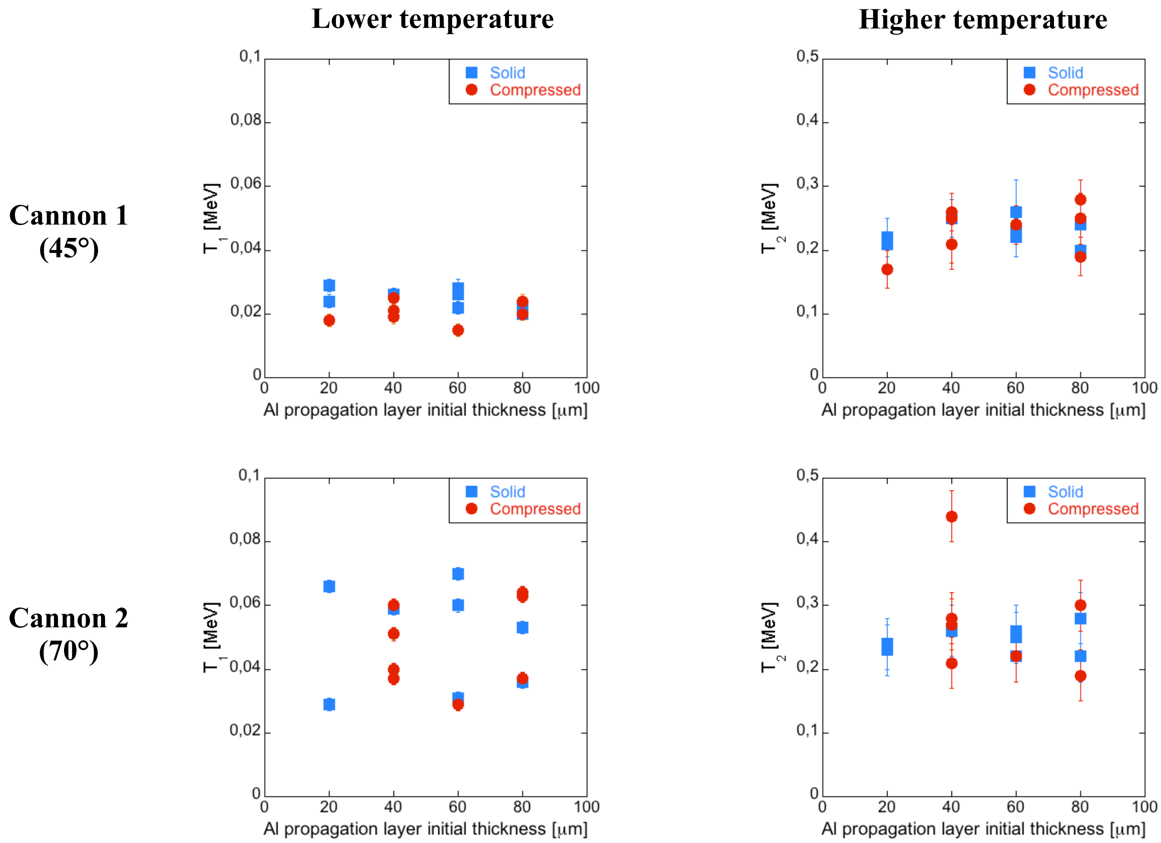

Figure 4.18: Dependence of the temperatures characterizing the colder (left) and the hotter (right) parts of the bremsstrahlung photon spectrum on the aluminum sample initial thickness for cannon 1 (top) and cannon 2 (bottom).

4.2.4 Electron spectrometer

The electron spectrometer located at 62° from target normal measured fast electron spectra leaving the rear side of the target. These escaped electrons can provide informations about the fast electron source spectrum. Due to differences between measured spectra and the source spectra inside the target, a set of transport simulation presented in section 4.4.2 was performed to fully interpret these results. A typical measured fast electron spectrum is presented in Fig. 4.19. One can note that above 10 MeV the measured electron spectrum presents important fluctuations due to limited sensibility of the detector. Experimental spectra are fitted with two exponential functions, giving the cold and hot temperatures plotted in Fig. 4.19 for all shots. The colder part is ∼ 30 times more intense than the hotter part. Similarly to the bremsstrahlung cannons, no significant difference can be seen between solid and compressed samples. Electron spectrometer results are indeed much more sensitive to the fast electron source distribution than to the transport mechanisms.

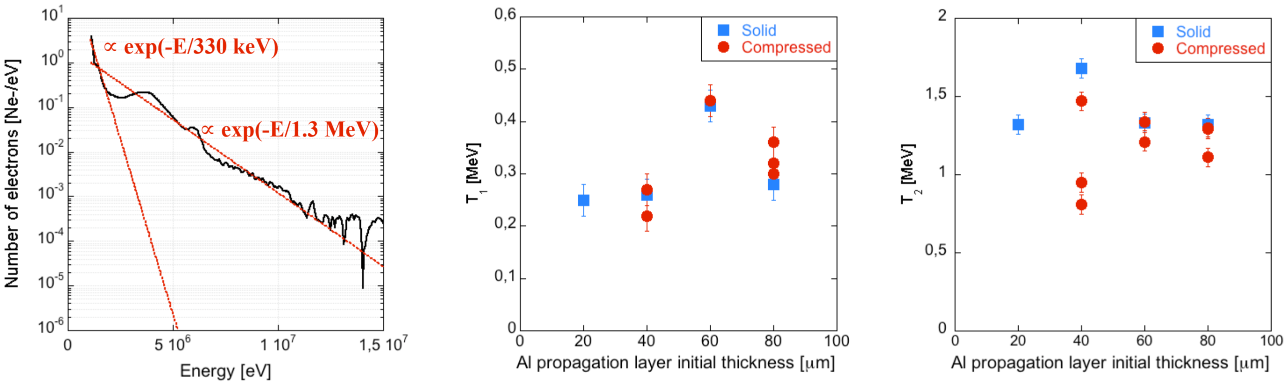

Figure 4.19: Example of measured electron spectrum at 40 cm from the target rear surface (left). The dependence of the fitting cold (middle) and hot (right) temperature, T_1 and T_2, respectively, on the aluminum sample initial thickness does not show any significant variation between the shots. No clear difference can also be seen between solid and compressed samples.

4.2.5 2D density and temperature gradients effects

The presented study relies on an important assumption about the target compression. The compressed area must indeed be much larger than the fast electron beam propagation axis to avoid any 2D compression effects, such as density and temperature lateral gradients. The comparison between solid and compressed samples can only be accomplished if this 1D planar compression condition is fully satisfied, which is the case in this study considering the 875 μm diameter of the LP beam focal spot.

In the previous experiment performed on the JLF-Titan laser system, which used the same targets and the same diagnostic tools, we experienced such 2D effects. Due to technical issues, the phase zone plate used together with the LP beam focusing lens resulted in a much smaller focal spot than expected, close to 200 μm FWHM instead of the required ∼ 800 μm.

The laser pulses characteristics were the following. The SP beam carrying ∼ 120 J of energy was focused into a ∼ 10 μm FWHM focal spot. It was characterized by a Gaussian temporal profile of 0.7 ps FWHM yielding and intensity of target of $\sim 1 \times 10^{20}$ W.cm^{-2}. The 5 ns squared LP beam carried 160 J of energy focused into a ∼ 200 μm focal spot, yielding an intensity on target $\sim 1.4 \times 10^{14}$ W.cm^{-2}.

The determination of the delay between the two laser pulses, depending on the aluminum central layer thickness, relied here again on the hydrodynamic simulations performed with the CHIC code. However, due to technical issues, no shock breakout measurements required for the calibration of the simulations could be performed. The delays were consequently chosen from the CHIC simulation results only. Since the simulations were performed considering 300 J of laser energy instead of 160 J, the following scaling law was used. The shock pressure generated by the LP beam is proportional to $I_L^{2/3}$ [Lindl, 1995]. Since the shock speed depends on the square of the shock pressure, the shock breakout time scales as:

$$t_{160\text{J}} = t_{300\text{J}} \left(\frac{300}{E_{\text{LP}}}\right)^{1/3} \tag{4.6}$$

with $t_{300\text{J}}$ the shock breakout time calculated with the CHIC code considering 300 J of laser energy, $E_{\text{LP}} = 160$ J the measured laser energy and $t_{160\text{J}}$ the scaled delay to adopt. These results are presented in Fig. 4.20.

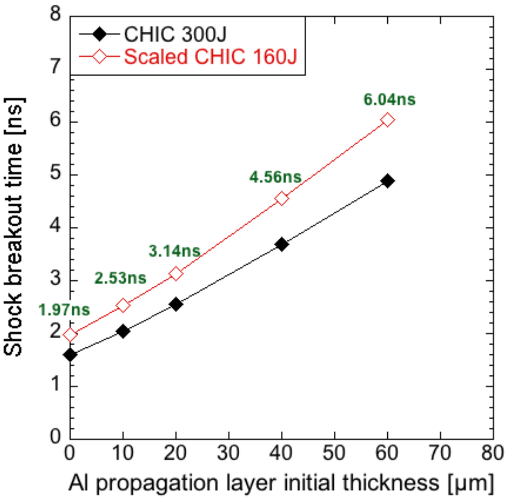

Figure 4.20: Dependence of the shock breakout time from the aluminum central layer on the aluminum layer initial thickness for simulated values considering a LP beam energy of 300 J (black full diamonds) and the corresponding scaled delays for $E_{\text{LP}} = 160$ J (red open diamonds). The 0 μm position corresponds to solid cases, where the rear side copper and tin tracers only are compressed.

This smaller LP beam focal spot produced 2D compression effects, generating density and temperature gradients across the fast electron propagation axis, as illustrated by the density profiles calculated with the CHIC code shown in Fig. 4.21.

The dependence of the Cu-K$_\alpha$ spot size on the aluminum sample thickness measured by both the Bragg spherical imager and the Kirkpatrick-Baez microscope is plotted in Fig. 4.22. For solid targets, the divergence angle of the fast electron beam is close to 20° HWHM for the two diagnostics, which is fairly close to what is found in the experiment described at the beginning of this chapter. However, in the compressed target cases, a dramatic increase of Cu-K$_\alpha$ spot sizes can be clearly seen, yielding a divergence angle $\leq 75°$ HWHM (Table 4.23). Such a divergence angle value in compressed cases, observed by two independent diagnostics, is unusually large compared to what can be found in the literature with more extended shock fronts. The dependence of the Sn-K$_\alpha$/Ag-K$_\alpha$ ratio on the aluminum propagation layer areal density plotted in Fig. 4.24 shows a similar trend to what was presented at the beginning of this chapter, despite lower values. The ratio is indeed lower in the thickest compressed cases, compared to solid cases, which strengthens the resistive inhibition hypothesis. However the 2D compression effects make it difficult to draw such a conclusion due to the apparition of resistivity and density transverse gradients in compressed targets that do not exist in solid cases.

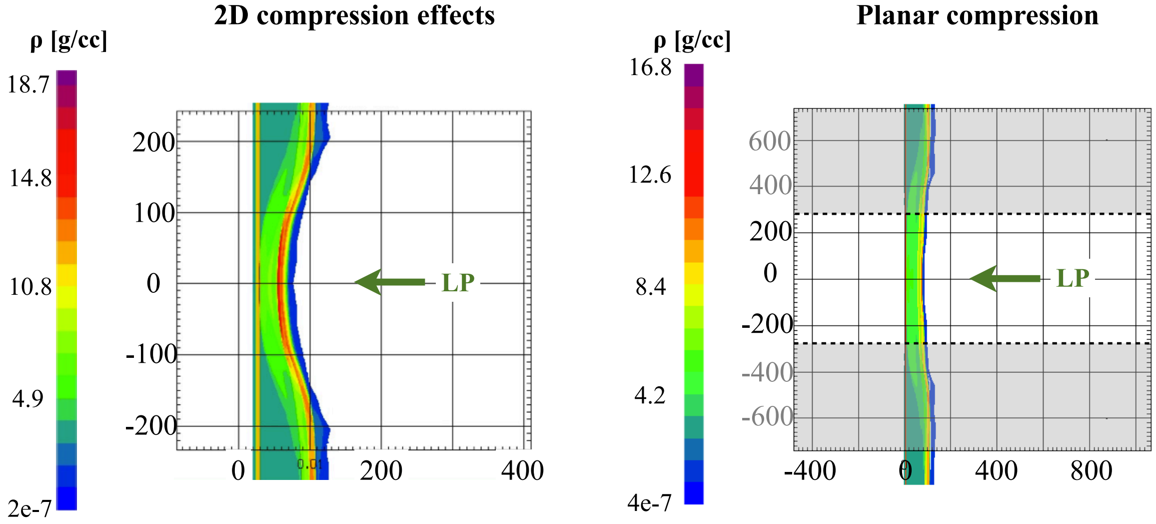

Figure 4.21: (Left) 2D density profile calculated considering a 200 μm FWHM LP beam focal spot incident on a target characterized by a 60 μm initial thickness central aluminum layer. (Right) 2D density profile calculated considering a 875 μm LP beam focal spot and a target characterized by a 60 μm initial thickness central aluminum layer. The grey area delimits the extension of the left plot. The comparison between those two plots demonstrate the presence of 2D density gradients in the smallest spot case.

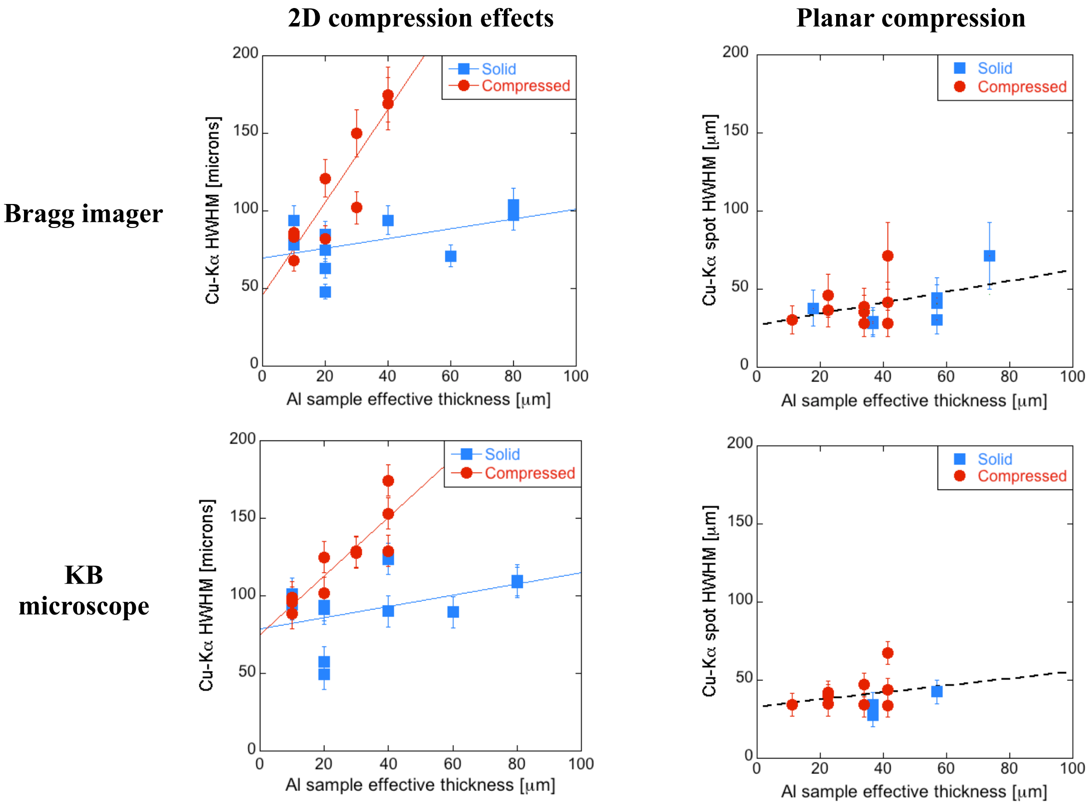

Figure 4.22: (Left) Dependence of the Cu-K$_\alpha$ spot size on the aluminum sample effective thickness measured with the Bragg imager (top) and the Kirkpatrick-Baez microscope (bottom). A significant difference between the solid and compressed cases disappears with a dramatically larger shock front radial extension producing a planar compression (right).

	Bragg imager [°]	**KB microscope [°]**
Solid	20 ± 3	18 ± 2
Compressed	77 ± 6	76 ± 5

Figure 4.23: Estimates of the electron beam divergence angles (half angles) in solid and compressed targets based on Bragg imager and Kirkpatrick-Baez microscopes results of Fig. 4.22.

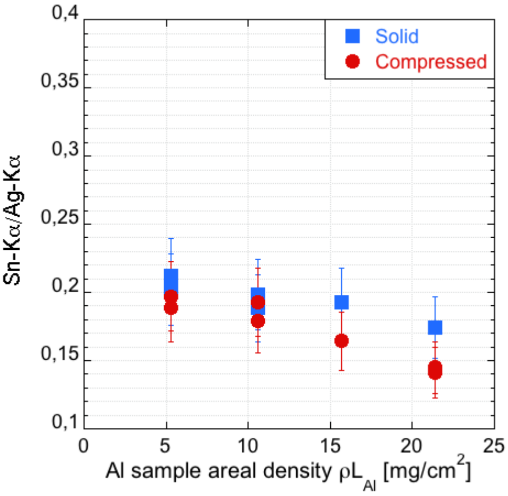

Figure 4.24: Dependence of the Sn-K_α/Ag-K_α ratio on the aluminum sample areal density with taking into account the 2D compression effects.

A large difference of beam divergence observed in the compressed targets never having been observed in any previous experiment constitutes an interesting effect to be investigated on. This phenomenon was numerically studied by Morace [2013] in his PhD thesis. We briefly summarize his results. Three hypothesis could possibly explain such a high divergence:

1. Density and temperature gradients could be responsible for the generation of defocusing magnetic fields. These fields should in addition be intense enough so that the main component of the fast electron distribution up to several hundred of eV is defocused.

2. Due to the lack of experimental measurements of the shock breakout time, the shock front could have breaked-out before fast electron injection, dramatically changing the laser-plasma interaction conditions between solid and compressed samples.

3. An important misalignment between the SP beam and the LP beam could be the reason for the interaction of the fast electron beam with an edge of the shocked region.

The first hypothesis relies on the following model. Let us assume that the fast electron beam with the current density $\mathbf{j} = j_r \mathbf{e_r} + j_z \mathbf{e_z}$ is propagating along the $z-$axis. By assuming a perfect neutralization of the incident current, the combination of Ohm's law, $\mathbf{E} = -\eta \mathbf{j_b}$, with Maxwell-Faraday's law neglecting current density gradients provides the time evolution of the magnetic field generated by resistivity gradients:

$$\frac{\partial \mathbf{B}}{\partial t} = \nabla \eta \times \mathbf{j} \tag{4.7}$$

which, written in cylindrical coordinates, yields:

$$\frac{\partial B_\theta}{\partial t} = j_r \frac{\partial \eta}{\partial z} - j_z \frac{\partial \eta}{\partial r} \tag{4.8}$$

This azimuthal component of the magnetic field could possibly be responsible for an important deviation and spreading of the fast electron beam in compressed targets. In order to check this assumption a set of transport simulations was performed with the LSP hybrid code [Welch et al., 2004]. The material resistivities were calculated with the LMD model. The ionization degree was calculated using the PROPACEOS equation of state tables [PROPACEOS, 2014]. The X-ray generation processes, including K$_\alpha$ emissions, were calculated using cross sections from the ITS Monte-Carlo code [Halbleib et al., 1992]. The fast electron source, presented in section 4.4.1, was obtained in 2D PIC simulations calibrated by experimental results. The 2D density and temperature profiles were calculated with the CHIC code, providing initial density and temperature maps of the simulated target. Spatial and temporal resolutions, $\Delta x = 0.5$ μm and $\Delta t = \Delta x/c$, respectively, were chosen, satisfying the CFL conditions[1]. The simulation was ran up to 3 ps, when the target temperature and resistivity reached there respective final values. The simulated Cu-K$_\alpha$ spot size in the case of the thickest targets with the aluminum layer of 80 μm initial thickness yielded 70 μm and 45 μm FWHM in solid and compressed samples, respectively, the two values being comparable to the experimental data obtained with the solid samples. As a consequence, no noticeable difference was observed between solid and compressed samples.

To further investigate the potential effects of a defocusing field generated by a non-planar shock front, a second set of transport simulations was performed considering a spherical shock generated by a 80 μm FWHM LP beam focal spot, leading to a small shock front radius. The unperturbed simplified target was initially made of 80 μm of aluminum, constituting the propagation layer, followed by a 10 μm copper tracer and by a 400 μm carbon layer acting as a lost layer (Fig. 4.25). The density profile follows an exponential decreasing trend behind the shock front. The shocked aluminum attains the four times compression peak value while the target temperatures was ranging from 0.03 eV in the unperturbed material to 3.1 eV at the shock front. The distribution of the target azimuthal magnetic field extracted 1 ps after injection of fast electrons is presented in Fig. 4.25. The de-collimating ∼ 3.5 MG magnetic fields can be observed at material interfaces, as well as on the solid-Al to compressed-Al interface.

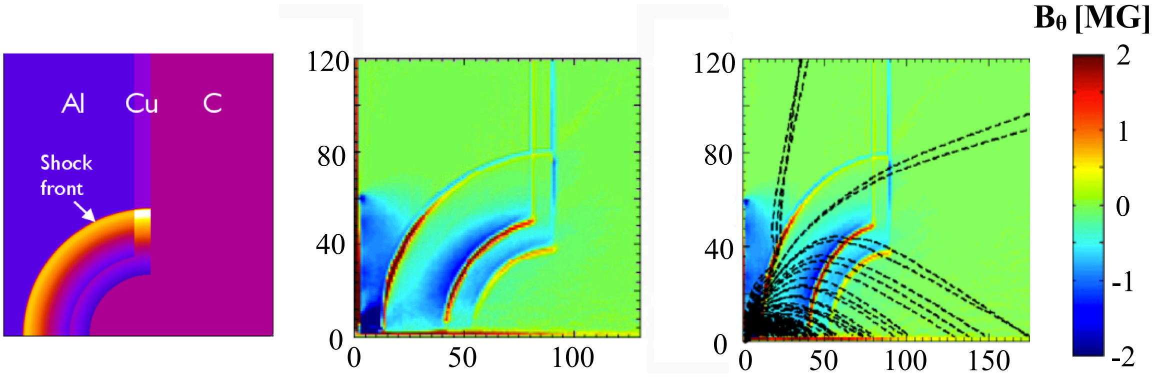

Figure 4.25: (Left) Illustration of the simulated target density. (Middle) 2D map of the azimuthal magnetic field extracted 1 ps after the beginning of the simulation. (Right) 500 keV electron trajectories super-imposed on the magnetic field map.

---

[1] The Courant-Friedrichs-Levy (CFL) conditions ensure that the information cannot propagate faster than a maximum speed, being the speed of light in this example, providing an essential stability criterion for simulations.

The collimating magnetic fields due to reversed resistivity gradients can also be observed in shocked regions. As a consequence, from the inspection of trajectories of 500 keV electrons (Fig. 4.25) injected into the target, one can conclude that particles are either deviated or focused depending of their initial injection angle into the simulation box. Therefore the de-focusing collimating effect plays a minor role in fast electron divergence, only adding a small correction to the Cu-K_α spot diameter.

A large electron divergence in compressed targets measured in the experiment remains unexplained. The most probable explanation would be given by the second hypothesis formulated further above. The breakout of the shock at the front side of the target before injection of fast electrons would indeed move the electron beam generation zone away from the target, artificially increasing the distance to the copper tracer and the measured divergence.

4.3 Comparison with lower current densities

As mentioned at the very beginning of this chapter, the Titan campaign builds upon the previous experiment performed on the pico2000 laser facility, at the LULI laboratory (France), using the same targets, and similar laser configuration and diagnostic tools, but with a lower short pulse intensity. The experiment, in which I was also involved, was dedicated to the fast electron transport study in cold-solid and warm-compressed aluminum, and to the characterization of collisional and resistive energy loss mechanisms. The data interpretation and the numerical simulation work presented in this section were performed by Vauzour [2012] during his PhD thesis. The interpretation of the Titan experimental result follows this previous work. We present in this section the main experimental and numerical results obtained by Vauzour. The reader may find more details in Vauzour's PhD thesis [Vauzour, 2012] and in the following articles [Vauzour et al., 2012, 2014].

4.3.1 Experimental results

The experiment was performed in 2010 on the pico2000 laser facility (LULI, France). This laser system offers, just like the JLF-Titan system, the combination of a LP beam and a SP beam. Their characteristics are the following. The $\lambda_L = 1.06$ μm, 1.5 ps FWHM short pulse laser beam used as a generator of fast electrons delivers 35 J on target in a 10 μm FWHM focal spot containing 25% of the pulse energy, yielding a peak intensity of $\sim 3.0 \times 10^{19}$ W.cm^{-2} on target. The frequency doubled ($\lambda_L = 0.53$ μm) LP laser beam used for target compression carries 250 J of laser energy into a 4.5 ns duration flat top profile focused into a 400 μm FWHM spot with a phase zone plate coupled to a lens, yielding a peak intensity of 3.0×10^{13} W.cm^{-2} on target. The detailed laser chain architecture is presented in chapter 5. The shock front is in this case fairly larger than the fast electron beam radius, avoiding any 2D compression effects.
Targets used in this experimental campaign follow the multi-foil design presented on Fig. 4.4, the only difference being the central aluminum thickness ranging from a minimum value of 10 μm to a maximum value of 60 μm, instead of 20 μm and 80 μm, respectively, in the Titan experiment. The delay between the two laser pulses is tuned by hydrodynamic CHIC simulations calibrated by shock breakout measurements, yielding to similar aluminum layer areal densities in solid and compressed cases, fairly close from the Titan experiment values (Table 4.4).

The Cu-K_α spot size is measured with the same HOPG spectrometer used in the Titan experiments, providing informations about the fast electron beam divergence. Its evolution as a function of the aluminum sample effective thickness is presented on Fig. 4.26. No striking

Al layer initial thickness [μm]		**10**	**20**	**40**	**60**
Solid	$\tau_{\mathrm{SP/LP}}$ [ns]	1.9	1.9	1.9	1.9
	L_{Al} [μm]	10	20	40	60
	ρL_{Al} [mg.cm^{-2}]	2.7	5.4	11.8	16.2
Compressed	$\tau_{\mathrm{SP/LP}}$ [ns]	2.5	3.1	4.4	5.7
	L_{Al} [μm]	6.3	12.2	23.6	35.1
	ρL_{Al} [mg.cm^{-2}]	2.6	5.3	10.6	15.9

Table 4.4: Summary of the different hydrodynamic parameters calculated for solid (top) and compressed (bottom) targets during the pico2000 campaign. The quantity $\tau_{\mathrm{SP/LP}}$ represents the delay between the two laser pulses adopted during the campaign. L_{Al} and ρL_{Al} stand for the actual thickness and for the areal density, respectively, of the central aluminum sample.

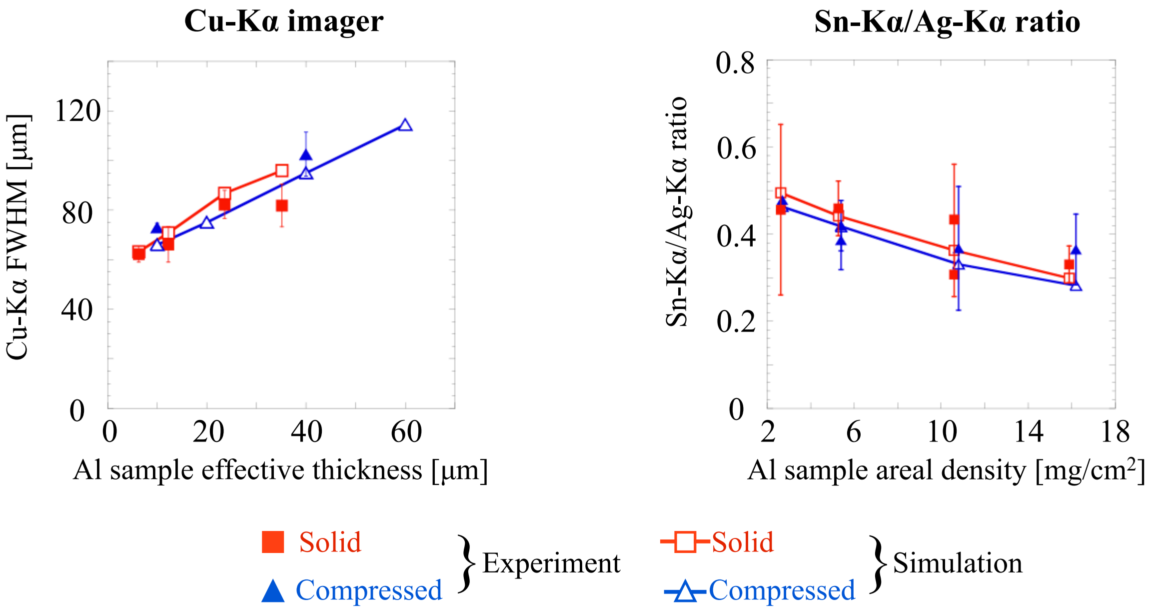

Figure 4.26: (Left) Evolution of the Cu-K$_\alpha$ spot size as a function of the aluminum layer effective thickness for solid (blue triangles) and compressed (red squares) targets. Experimental values are presented with full symbols. Hybrid transport simulation results are plotted with open symbols. (Right) Evolution of the Sn-K_α/Ag-K_α ratio as a function of the aluminum population layer areal density.

difference between solid and compressed samples can be seen, confirming the major influence of laser-plasma interaction mechanisms in the divergence of fast electrons. A mean divergence angle of $(22 \pm 6)^\circ$ can be estimated from this plot, which is in fair agreement with the value found in the Titan experiment. A similar Cauchois transmission spectrometer to the TCS used on Titan is set-up to measure the front side Ag-K_α and rear side Sn-K_α absolute yields. The evolution of the Sn-K_α/Ag-K_α ratio as a function of the aluminum layer areal density is plotted on Fig. 4.26. As already mentioned this ratio getting rid of any shot-to-shot laser energy fluctuation is directly related to the fraction of electron $>$ 70 keV having crossed the aluminum layer. Unlike in the Titan experiment, no noticeable difference can be seen between solid and compressed samples, which indicates that in this interaction regime, and considering that collisional losses should remain constant with target compression, resistive energy losses are possibly too weak to be experimentally evidenced. Energy deposition seems to be mainly dominated by collisional processes.

4.3.2 Theoretical interpretation: importance of resistive energy losses

In order to confirm these experimental results a series of numerical simulations are performed.

PIC simulations of the fast electron source

The pico2000 fast electron source is evaluated from 2D PIC simulations performed with the PICLS code, describing the interaction of a 3.0×10^{19} W.cm^{-2} short laser pulse with a $80 \times 100\ \mu\text{m}^2$ aluminum foil. The electron spectrum is extracted 15 μm from the interaction zone at each time step. The time-averaged fast electron energy distribution presented in Fig. 4.27 can be fitted by the following normalized function:

$$f(E) = \begin{cases} \left(\frac{E_0}{E}\right)^\alpha & \text{for } 0.01 \leq E \leq 5 \text{ MeV} \\ \xi \exp -\frac{E}{T_h} & \text{for } 5 \leq E \leq 20 \text{ MeV} \end{cases} \tag{4.9}$$

with $E_0 = 1.7$ keV, $\alpha = 1.6$, $T_h = 3$ MeV and $\xi = 10^{-5}$ the fitting parameters, yielding a mean electron energy of 190 keV. As already reported several times in the literature, the low energy

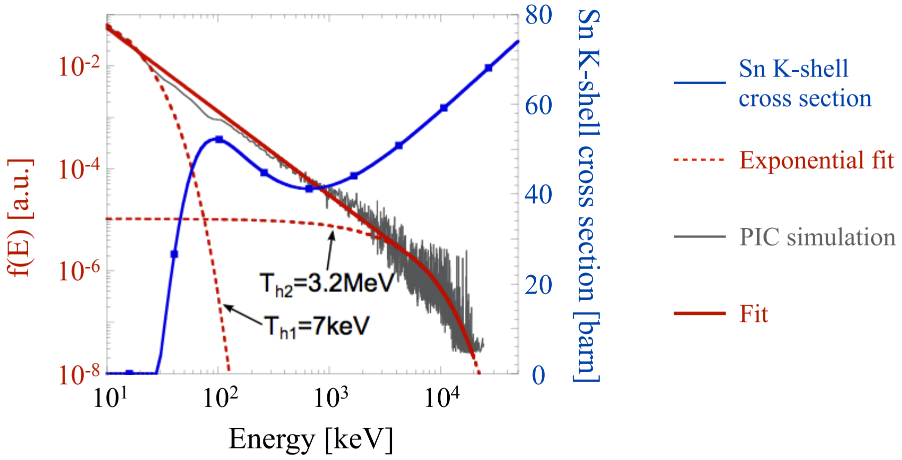

Figure 4.27: Fast electron distribution function calculated in PIC simulations (grey solid line) and the corresponding fitting function Eq. 4.9 (red solid line). The red dashed lines correspond to the double exponential sum fitting function. The tin layer K-shell ionization cross section is represented by the blue solid line.

part of the electron distribution is better described by a power law rather than by an exponential function [Micheau et al., 2010; Ren et al., 2004; Debayle et al., 2010]. As highlighted by the tin tracer K-shell ionization cross section, an accurate fit of this low energy part is essential in our study since it significantly impacts the restitution of absolute K$_\alpha$ yields (Fig. 4.27).
The angular distribution function is also extracted from the PIC simulation. The angle of divergence depends on both the energy and the initial transverse coordinate r with respect to the center of the laser focal spot, this latter condition being directly related to the Gaussian intensity distribution of the laser pulses. The angular distribution function is given by [Debayle et al., 2010]:

$$f(\theta, r) = \exp\left[-\left(\frac{\theta - \theta_r}{\Delta\theta_0}\right)^2\right] \tag{4.10}$$

Fast electrons propagate through the target within a cone characterized by an opening angle given by θ_r, with a dispersion of $\Delta\theta_0$ around this value, as illustrated in Fig. 4.28. The angle θ_r can be expressed as follows:

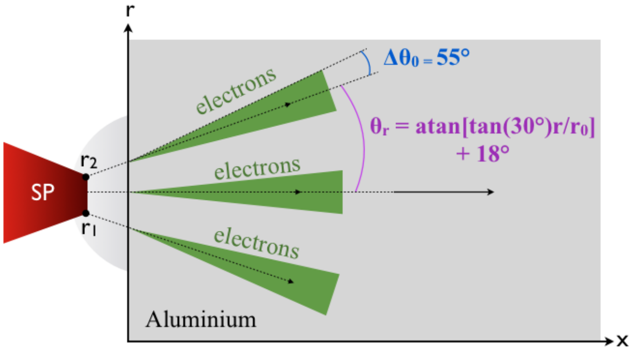

Figure 4.28: Illustration of the angular distribution function of fast electrons. Particles propagate in the direction given by $\theta_r(r)$ with a dispersion $\Delta\theta_0$ around this value.

$$\theta_r = \arctan\left[\tan\left(30^\circ\right)\frac{r}{r_0}\right] + 18^\circ \tag{4.11}$$

with $r_0 = 20$ μm the initial radius of the electron beam.

Hybrid transport simulations

Hybrid transport simulations were performed with the 2D axisymmetric code developed by Javier Honrubia from the University of Madrid [Honrubia et al., 2006]. This code allows to simulate the propagation of a fast electron beam in a background plasma, treated as an electron fluid, under the action of collisions and of self-generated electromagnetic fields. The plasma resistivity is calculated following the Eidmann-Chimier model presented in section 2.5.3. The hybrid code takes as initial conditions the fast electron energy distribution provided by PIC simulations, assuming a laser-to-electrons conversion efficiency of $\sim 30 \pm 10\%$. The injected initial 1D density and temperature profiles are extracted from the hydrodynamic simulations with the code CHIC along the fast electron propagation axis, at the injection time. This transport simulations resulted in a good reproduction of the experimental data concerning the Cu-K_α spot sizes as well as the Sn-K_α over Ag-K_α ratios, as presented in Fig. 4.26. This is confirming the absence of difference between solid and compressed targets. The distribution of the collisional and resistive energy deposition in the target volume extracted at the very end of the simulation, 1.5 ps after fast electron injection time, for the solid and compressed targets containing the 60 μm initial thickness aluminum sample is presented in Fig. 4.29. The collisional energy deposition per unit volume are higher in the compressed targets due to the rise of density up to $\sim 2\rho_0$. The deposition occurs in zone of the radius ≥ 35 μm and at the distance 90 μm at the front side and at the rear side of the target, respectively, but extends further away due to multiple scattering. In the solid targets the resistive energy losses are confined within a narrower radius, close to the fast electron beam propagation axis, where the current density is the highest. In the compressed targets the resistive energy losses extend further away due to the higher resistivity of the aluminum propagation layer. These additional resistive losses are however too small to be experimentally detected.

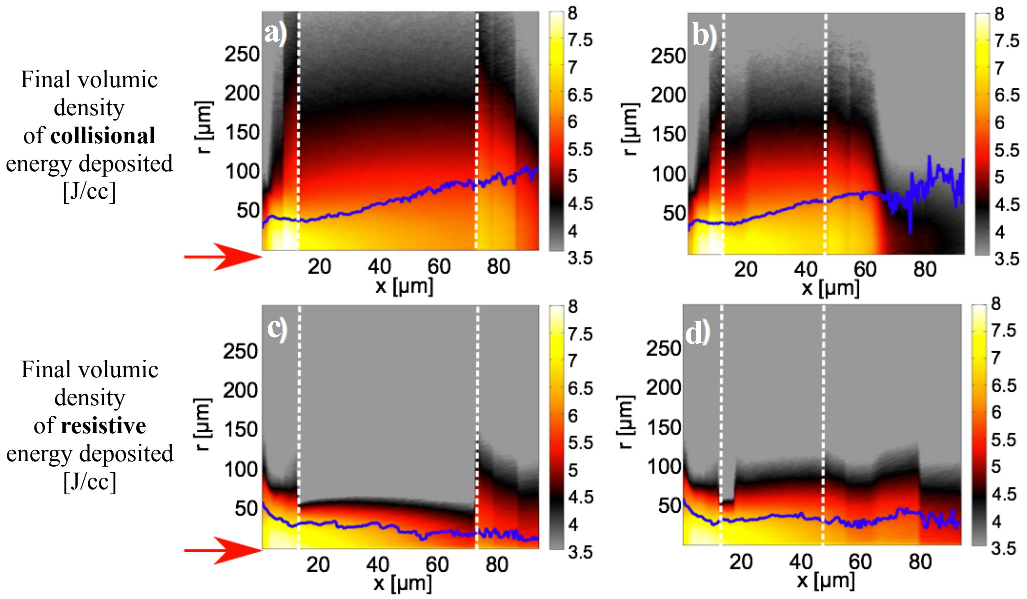

Figure 4.29: Volumic energy deposition due to the collisional (top) and resistive (bottom) processes extracted at the end of transport simulations for the solid (left) and compressed (right) targets. The values are given in the logarithmic scale. The blue solid lines represent the radius HWHM for each axial position. The white dashed lines delimit the aluminum sample position.

The role played by the current density in the fast electron energy losses in the aluminum sample is further detailed in Fig. 4.30. At $r = 5$ μm, where the current density is the highest, the resistive losses, scaling as $\langle j_b^2 \rangle$, are dominant over collisional losses, scaling as $\langle j_b \rangle$. The resistive losses are however similar in the solid and compressed aluminum samples. At the radius $r = 20$ μm the collisional losses become the dominant energy deposition mechanism at a target depth of ~ 30 μm. The current density averaged over time and over a $r \pm 5$ μm radius decreases from $\langle j_b \rangle \sim 2.6 \times 10^{11}$ A.cm^{-2} down to $\langle j_b \rangle \sim 1.6 \times 10^{11}$ A.cm^{-2}. At $r = 50$ μm, corresponding to an averaged current density $\langle j_b \rangle \sim 2.8 \times 10^{11}$ A.cm^{-2}, the collisional losses are much larger than the resistive losses. The difference between the solid and compressed samples is clearly visible.

The integrated values of both collisional and resistive energy losses as a function of the aluminum sample effective thickness are presented in Fig. 4.31. Even though the collisional energy losses are clearly dominant in this interaction regime, with $\langle j_b \rangle \sim 8.0 \times 10^{10}$ A.cm^{-2}, the resistive energy losses are responsible for about one third of total energy losses, playing an important role in the fast electron propagation. Both collisional and resistive losses are enhanced in the

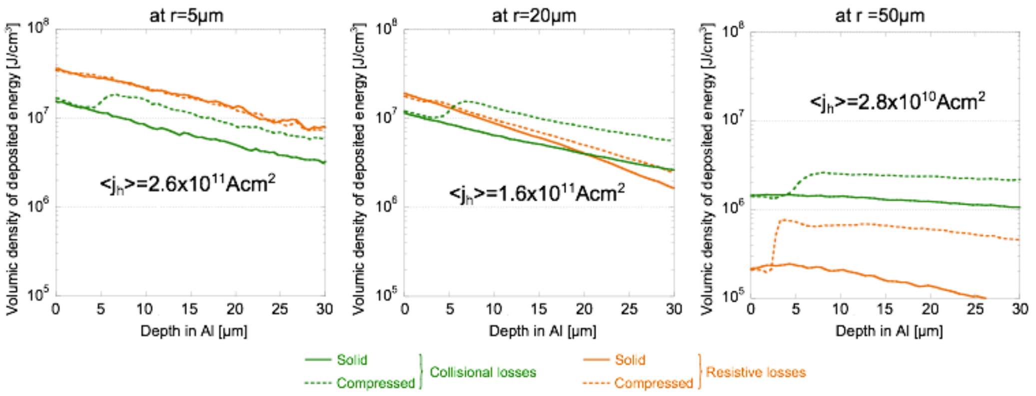

Figure 4.30: Volumic energy deposition due to the collisional (green) and resistive (orange) processes extracted at the end of transport simulations for the solid (solid line) and compressed (dashed line) targets averaged over 5 μm (left), 20 μm (middle) and 50 μm (right) around fast electron propagation axis. The labeled current densities correspond to time-averaged values at the very beginning of the target, corresponding to the 0 μm depth.

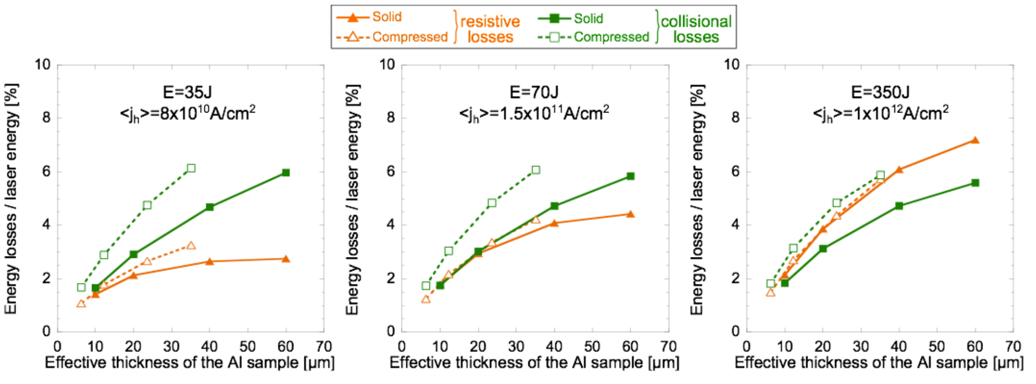

Figure 4.31: Integrated energy losses as a function of the aluminum sample thickness after compression (effective thickness) for three laser energies: 35 J, corresponding to the experimental conditions (left), 75 J (middle) and 350 J (right). The calculated energy losses are normalized to laser energies.

compressed targets due to higher initial density and resistivity values. The estimated collisional stopping powers are $1.1 - 1.5$ keV/μm ranging from cold-solid to warm-dense material, respectively, and the resistive ones are $0.6 - 0.8$ keV/μm.
This analysis allows an extrapolation of energy losses estimates to higher current density values. The easiest way to attain higher currents is to increase the SP beam energy, while assuming a conservation of the electron distribution shape and of the laser-to-electrons conversion efficiency. When considering a SP beam energy of 70 J (Fig. 4.31, middle) the current density averaged over time and over a radius of 30 μm around fast electron beam propagation axis increases up to $\langle j_b \rangle \sim 1.6 \times 10^{11}$ A.cm^{-2}. In this interaction regime the resistive losses seem to become comparable to the collisional losses. When increasing the current density to $\langle j_b \rangle \sim 1.0 \times 10^{12}$ A.cm^{-2} (Fig. 4.31, right) the difference between the energy deposition in the solid and compressed samples disappears. This result, illustrated in Fig. 4.32, can be explained as follows. The heating time of the transport layer up to the Fermi temperature T_F can be

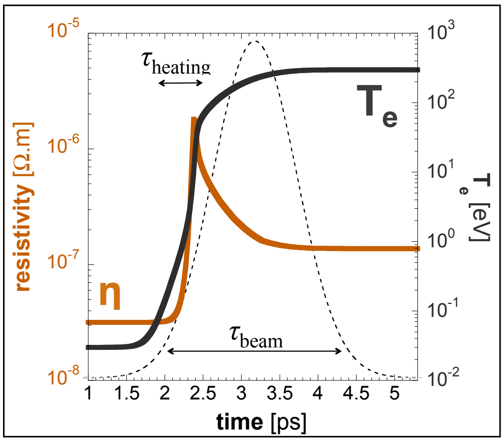

Figure 4.32: Evolution of the electron temperature (black solid line) and resistivity (orange solid line) with time in the aluminum propagation layer for the LULI experiment parameters. The heating time of the propagation medium up to several hundreds eV is shorter than the electron beam duration (black dashed line). This heating time becomes shorter with the increasing current density [Santos et al., 2013].

estimated as $\tau_F \sim 3n_e T_F / 2\eta j_b^2 \sim 0.3$ ps. It is rapidly decreasing when increasing j_b, and for high current densities it becomes shorter than the fast electron beam duration. The material resistivity quickly enters the Spitzer regime ($\eta \propto T_e^{-3/2}$) where it decreases with the electron temperature. Any initial difference in the electron temperature caused by the target compression is thus quickly erased.

In summary, this numerical study presented in [Vauzour et al., 2014] pointed out that the collisional energy losses are dominate over the resistive losses for $j_b < 10^{11}$ A.cm^{-2}. Above 10^{12} A.cm^{-2} any initial difference between the solid and compressed samples related to an initial higher resistivity rapidly disappears due to the extremely fast heating of the plasma. In between those two values, in the $10^{11} < j_b < 10^{12}$ A.cm^{-2} interaction regime, resistive energy losses become comparable to the collisional losses. The heating time of the background plasma in this regime is not too fast so that the difference between solid and compressed samples could be measured with our experimental setup. The main goal of the Titan experiment is to verify this theoretical prediction.

4.4 Fast electron generation and transport simulations

The interpretation of the experimental results requires the extended numerical simulations, allowing to precisely quantify the mechanisms responsible for fast electron energy losses in cold-solid and warm-compressed aluminum samples.

A PIC code is used to characterize the interaction of the SP laser beam with the front side aluminum generation layer. This simulation aims to determine the energy, angular and spatial distributions of the fast electrons beam injected into the target.

A hybrid code using as input PIC and hydrodynamic simulation results is used to simulate the fast electron transport in the target and to quantify the energy loss mechanisms. Results of hybrid simulations are compared with the experiment in terms of the absolute K_α yields emitted by the tracer layers buried into the target.

Finally, a Monte-Carlo code is used to simulate the bremsstrahlung emission generated by fast electron propagating into the target. It allows to interpret the bremsstrahlung cannon results and to determine the fast electron source spectrum, providing a link between the PIC simulation results.

4.4.1 PIC simulation of the fast electron source

The parameters of the fast electron source are evaluated with 2D PIC simulations performed by Anthony Link (LLNL, USA) with the LSP code. Those simulations, tuned by previous experimental measurements, allow to reproduce the interaction of the Titan short laser pulse with a 200 μm×200 μm aluminum layer. The temporal profile of the laser pulse is supposed to be Gaussian, with a 0.7 ps FWHM, carrying 150 J of energy, yielding a 1×10^{20} W.cm^{-2} peak intensity. The laser pulse polarized into the incident plane (P polarization) interacts at a normal incidence with a 100 μm×50 μm pre-plasma, as characterized by the experimental measurements described in section 4.1.1.

In order to characterize the fast electron distribution a probe is located at the position 5 μm into the aluminum target, far enough from the laser-plasma interaction region, the $Z = 0$ position corresponding to the target edge before the laser interaction. The position of the probe is illustrated in Fig. 4.33. The fast electron energy distribution function is measured by quantifying the number of electrons moving forward into the target (positive Z axis direction) through the probe layer. The electron spectrum temporally averaged over the entire simulation duration is presented in Fig. 4.33. It can be fitted over the 10 keV-142 MeV range by the following function:

$$f(E)^{\mathrm{PIC}} = \exp\left(-\frac{E}{T_{h_1}}\right) + \left(\frac{E_0}{E}\right)^{\alpha} \exp\left(-\frac{E}{T_{h_2}}\right) \tag{4.12}$$

with T_{h_1}, E_0, α and T_{h_2} the fitting parameters given by $T_{h_1} = 100$ keV, $E_0 = 20$ keV, $\alpha = 1$ and $T_{h_2} = 12.5$ MeV. The energy distribution function is thus well described by an exponential function at high energy whereas the low energy part of the spectrum is better fitted by a low temperature exponential function and a power law $\propto E^{-1.005}$. The temperature $T_h = 12.5$ MeV represents the mean energy of the high energy part of the fast electron population, which is significantly higher than Beg's and Wilks' laws predictions, being 1.04 MeV and 4.15 MeV, respectively.

The mean energy averaged over the $10 \leq E \leq 20$ MeV energy range, containing most of the electron population and injected into hybrid transport simulation described in section 4.4.2, given by $\int E.f(E)dE / \int f(E)dE$, yields $\langle E\rangle^{\mathrm{PIC}} \sim 1.0$ MeV. This energy is in a quite good agreement with the Beg's law. This Titan source is characterized by a more energetic population of electrons compared to the LULI source presented in section 4.3.2.

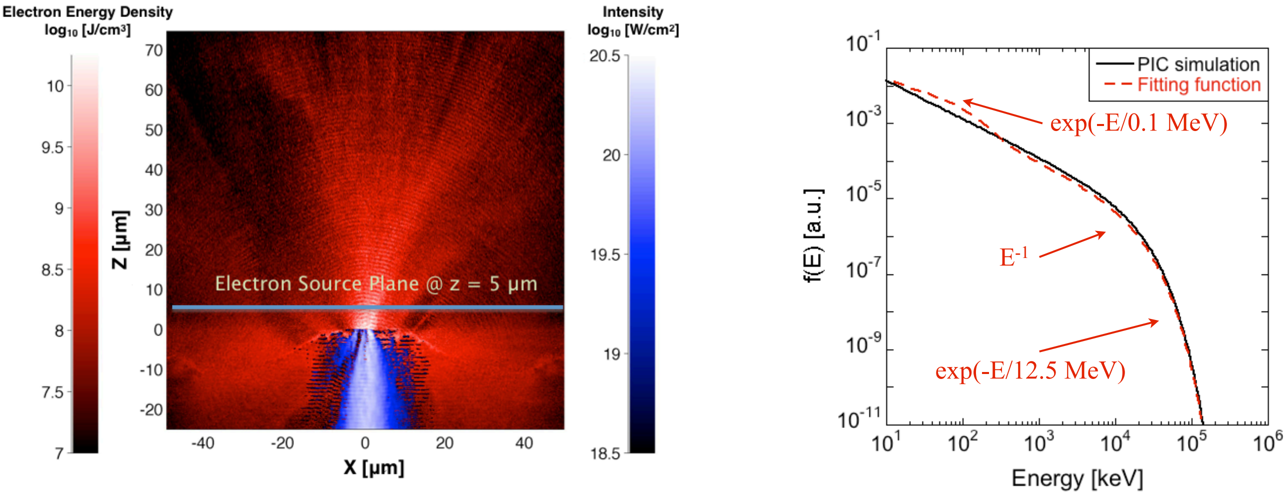

Figure 4.33: (Left) Electron (red) and laser (blue) intensity maps calculated with the LSP PIC code and extracted at maximum laser intensity. The position of the probe is illustrated by the horizontal blue line. (Right) Fast electron energy distribution function calculated by 2D PIC simulations (black solid line) and the corresponding fitting function (red dashed line).

Angular and spatial distributions

As previously mentioned the local direction of propagation of fast electrons depends on both their energy and their initial position in the perpendicular plane with respect to the center of the focal spot. The spatial distribution functions calculated with PIC simulations are plotted in Fig. 4.34 for different energy populations. One can note that the spatial distribution can be fitted by two Gaussian functions, with radii r_1 and r_2 depending on the fast electron population mean energy (Fig. 4.34). When averaging over all energies the mean radii are $\overline{r_1} \sim 4$ μm and $\overline{r_2} \sim 28$ μm. Most of the electrons with an energy $E > 10$ MeV are emitted from the $\overline{r_1}$-radius region, closely corresponding to the SP focal spot size.

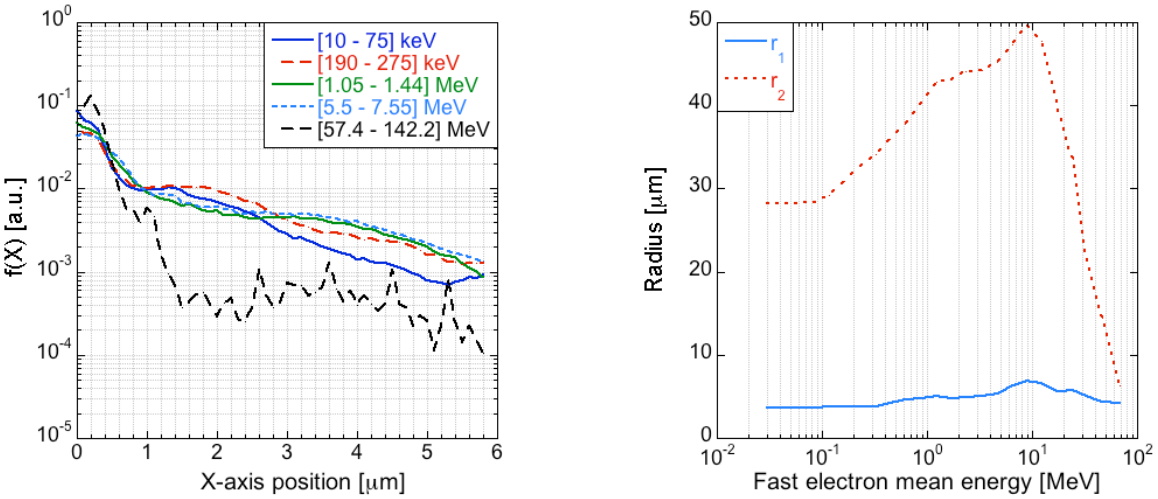

Figure 4.34: (Left) Fast electron radial distribution for different energy populations. (Right) Dependence of the two radii characterizing the radial distribution Gaussian fit on the fast electron energy.

The angular distribution functions calculated by the PIC code for different energy populations are presented in Fig. 4.35. One can note that the angular distribution can be fitted by a sum of two Gaussian functions, with the mean dispersion angle $\Delta\theta_0 = 55°$ over a large energy range (Fig. 4.35) and the mean propagation angles θ_{r_1} and θ_{r_2} given by:

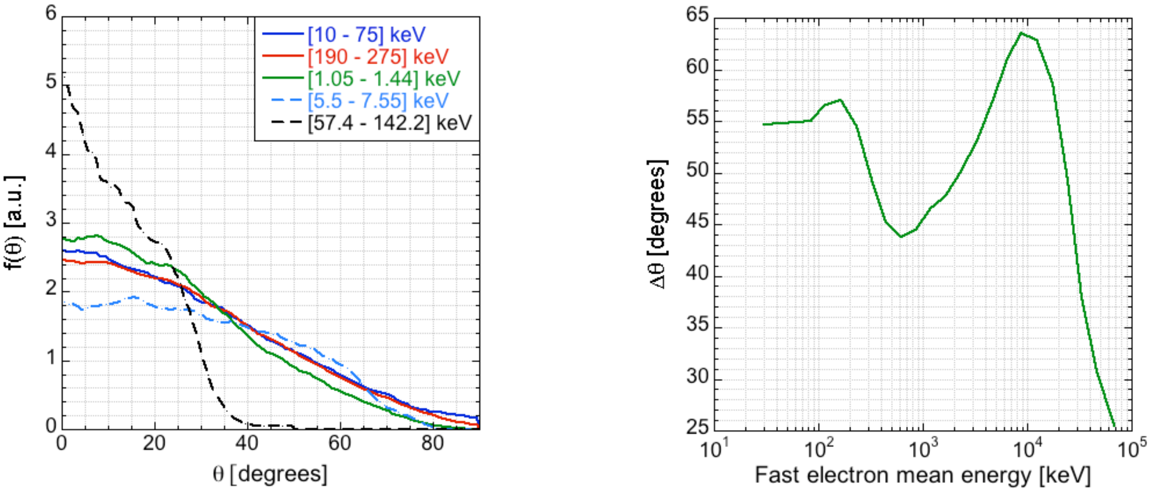

Figure 4.35: (Left) Fast electron angular distribution functions for different energy populations. (Right) Dependence of the mean dispersion angle $\Delta\theta$ on the fast electron energy.

$$\theta_{r_{1,2}} = \arctan\left[\tan(35°)\frac{r}{r_{1,2}}\right] \tag{4.13}$$

with $r_1 = 4$ μm and $r_2 = 28$ μm the initial radii of the electron beam. 80% of the fast electrons are described by the larger radius function.

4.4.2 Hybrid transport simulations

Knowing the characteristics of the fast electron source, we present here the results of simulation of the transport of fast electrons in the multi-layer targets. Transport simulations are performed using the hybrid code presented in the previous section, in close collaboration with Javier Honrubia, the designer of the code, and Arnaud Debayle from the University of Madrid.

Characteristics of the simulation

The characteristics of the simulations are the following:

- The hydrodynamic initial temperature and density profiles shown in Fig. 4.8 were calculated with the CHIC code and extracted from the 2D profiles in fast electron propagation axis at injection time. Eight cases were simulated equally divided between the cold-solid and warm-compressed aluminum targets with of the initial thickness of 20 μm, 40 μm, 60 μm and 80 μm.

- The fast electron energy and angular distributions are given by PIC simulation results presented in section 4.4.1.

- The laser-to-fast electrons conversion efficiency is set to $\eta_{\text{L}\rightarrow\text{e-}} = 25\%$.

- Simulations are ran during 8 ps into a 300 μm radius simulation box with 1 fs and 0.25 μm temporal and spatial resolutions, respectively. 5×10^6 macro-particles representing 3.3×10^{14} fast electrons are progressively injected into the simulation box.

- The evolution of the target hydrodynamic quantities are calculated with the equation of state SESAME [LANL, 1983].

- The electric resistivity η is calculated using the Drude model $\eta = m_e\nu/e^2n_e$, with ν the collision frequency calculated with the Eidmann-Chimier model presented in section 2.5.3.

- The absolute yield of K_α emissions from the tracer layers are computed using a module based on the Hombourger's cross section presented in section 3.1.1. A numerical mesh located right after the copper tracer layer also allows to generate the image of the Cu-K_α emission.

- Two probes are located at the front and the rear side of the central aluminum transport layer to measure fast electron energy flux and to characterize their propagation. The differences quantify the total energy losses over the sample thickness.

Comparison with experimental data

The simulated K_α yields were integrated and measured over the time of simulation. Fig. 4.36 presents a comparison between the experimental and calculated absolute yields. A fairly good agreement is found for the silver and tin K_α yields with the fast electron source defined in section 4.4.1. The simulated silver yields are as expected fairly constant which is explained by the similar hydrodynamic state of all targets. It is worth mentioning that the fluctuations of experimental data are not reproduced by simulations since they are performed considering a unique value of SP beam energy (115 J). This explains the discrepancy for the thinest targets. The apparent decreasing trend of Sn-K_α yield as a function of the aluminum layer thickness that could be guessed on experimental data can be clearly seen in numerical results. This is explained by the slowing down of fast electrons in a thicker transport layer. The simulated absolute Cu-K_α yield fails to reproduce experimental data. This difference by a factor 2 could be explained by the presence of re-circulating electrons in the lost layer. It is worth mentioning that this difference was already observed by Benjamin Vauzour (see section 4.3) using the same spectrometer and the same hybrid transport code.

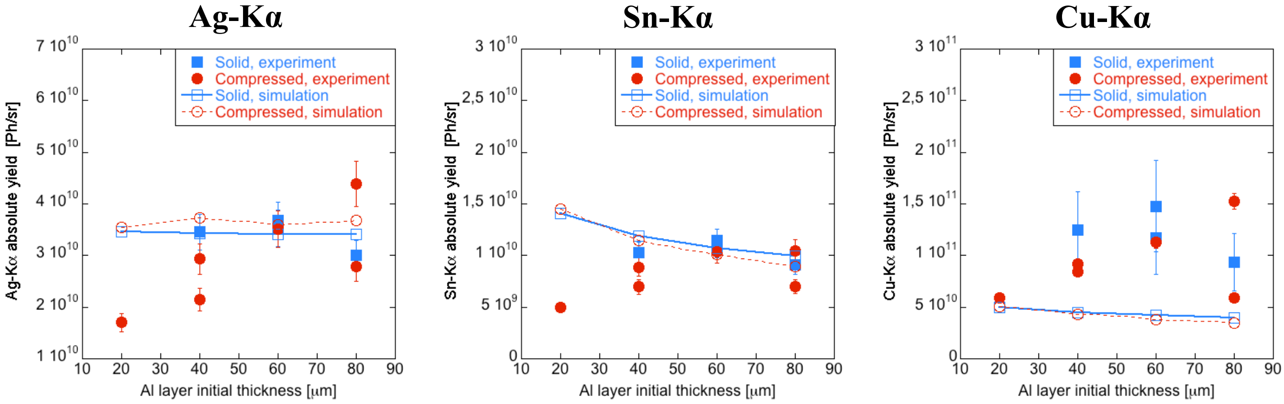

Figure 4.36: Comparison of the Ag-K_α (left), Sn-K_α (middle) and Cu-K_α (right) absolute yields obtained in the experiment (full symbols) and with hybrid transport simulations (open symbols) for cold-solid (blue symbols) and warm-compressed (red symbols) targets.

A line-out is extracted from the simulated Cu-K_α spot, measured right after the simulated copper layer, for each simulation case and convolved with a 10 μm FWHM Gaussian function, accounting for the resolution of the spherical Bragg imager. Numerical results are compared to the experimental results in Fig. 4.37. A fairly good agreement is found between the two sets of data, showing a similar trend for solid and compressed targets. The two experimental data showing a ∼ 70 μm HWHM spot, well above the general trend, are certainly due to experimental issues. The simulated angle of divergence is estimated to ∼ 19° by a linear fit, in good agreement with experimental data.

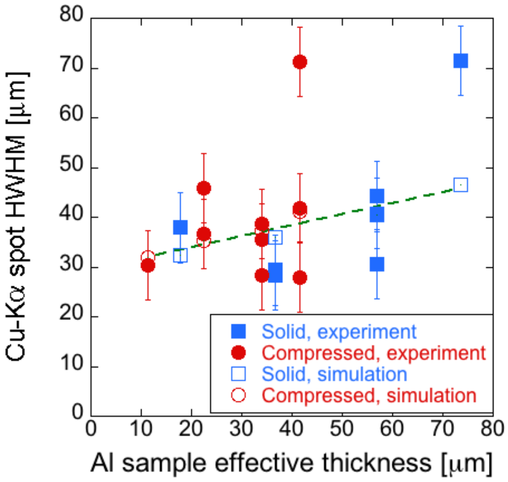

Figure 4.37: Comparison of Cu-K$_\alpha$ spot size obtained in the experiment (full symbols) and extracted from hybrid transport simulations (open symbols) for the cold-solid (blue symbols) and compressed (red symbols) targets as a function of the aluminum central layer actual thickness after compression (effective thickness). Numerical data are convolved with a 10 μm FWHM Gaussian function accounting for the spherical imager resolution.

The comparisons between experimental and simulated Sn-K$_\alpha$/Ag-K$_\alpha$ and Cu-K$_\alpha$/Ag-K$_\alpha$ ratios are presented in Fig. 4.38. As expected, the Cu-K$_\alpha$/Ag-K$_\alpha$ ratio is underestimated due to the discrepancy in the Cu-K$_\alpha$ absolute yield simulation. A small difference between solid and compressed targets that is not experimentally detected can be seen on numerical results. The

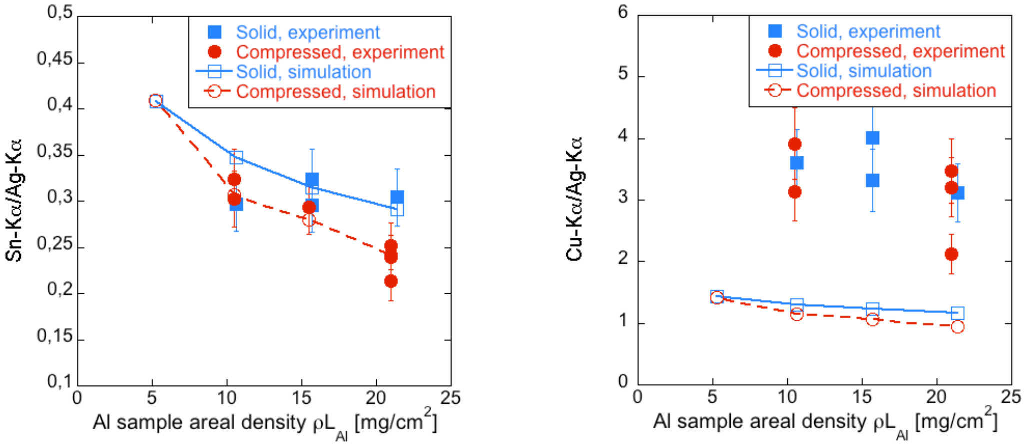

Figure 4.38: Comparison of the experimental (full symbols) and simulated (open symbols) Sn-K$_\alpha$/Ag-K$_\alpha$ (left) and Cu-K$_\alpha$/Ag-K$_\alpha$ ratios as a function of the aluminum sample areal density for the cold-solid (blue symbols) and warm-compressed (red symbols) targets.

decreasing trend of the ratio can however be clearly seen. The Sn-K$_\alpha$/Ag-K$_\alpha$ simulated ratio is in fairly good agreement with experimental data. The decreasing trend is also clearly seen. The most remarkable result is the good reproduction of the decreased signal observed for the thickest warm-dense aluminum samples. According to the simulations, such a weaker signal should also be present for thiner targets, with $\rho L \simeq 10$ mg.cm^{-2}, although this trend cannot been detected in experiment, probably due to the lack of statistics.

Interpretation of data

The transport simulations are in a reasonable agreement with the experimental results, taking into account the very limited number of shots and the detection errors. They are showing a clear reduction of the signal at the rear side of the sample which is explained by the transport inhibition in compressed targets. To understand this important result it is necessary to estimate the fast electron total current density in the aluminum propagation layer. This quantity is measured as follows. The input current density is measured at each time step with the probe located at the very beginning of the propagation layer. A Gaussian fit is then applied to extract both the mean and the peak value of the current density entering the aluminum propagation layer. These measurements are presented in Fig. 4.39. The estimated peak current density $j_b^{\text{peak}} = 5.6 \times 10^{11}$ A.cm^{-2} and the mean current density $\langle j_b \rangle = 2.4 \times 10^{11}$ A.cm^{-2} averaged over time and over a 30 μm radius across the fast electron propagation axis. Considering both the analytical of Eq. 2.149 on the ratio between the collisional and resistive energy losses, and the simulation presented in section 4.3, two conclusions can be drawn:

- The fast electron mean current density $\langle j_b \rangle = 2.4 \times 10^{11}$ A.cm^{-2} reached in the aluminum propagation layer is high enough so that the resistive energy losses attain the level of collisional energy losses in the compressed targets.
- The mean current density is not too high so that the heating time-scale of the plasma electrons does not erase too rapidly the initial resistivity difference between the solid and compressed samples.

Fig. 4.40 presents 2D maps of the collisional and resistive massic energy deposition by the fast electrons. They are calculated for the thickest targets of 80 μm, and time-integrated up to $t = 2.1$ ps after fast electron injection time. For the sake of clarity the presented plots are restrained over a 100 μm radius across the fast electron propagation axis. The collisional energy deposition (upper plots) takes mainly place inside the 100 μm radius. However some energy is deposited farther away due to the electron multiple scattering events. As illustrated by the contour lines (black solid lines) over-imposed on the energy loss maps, the collisional energy deposition is fairly similar in the compressed targets due to the conservation of the areal density with compression. It is worth noting that the main part of collisional energy deposition takes place at the very beginning of the target, close to the fast electron source region, where the lowest energy electrons are rapidly stopped. When considering the solid target, resistive energy deposition (middle plots) takes place in a narrower region than collisional losses, clearly delimited by a 60 μm radius across the electron propagation axis, where the current density is higher. The resistive energy deposition in the compressed target extends further away ($r \leq 100$ μm) due to the rise of resistivity in the shocked sample. Similarly to the collisional energy deposition, the resistive energy deposition is more important at the very beginning of the target, where the current density is the highest. The most remarkable result is that the increase of resistive energy deposition in the compressed sample can be clearly seen. It becomes comparable to the collisional energy deposition.

The energy deposited in the target leads to the increase of the electron temperature. As presented on the bottom plots in Fig. 4.40 the final averaged electron temperatures in the solid

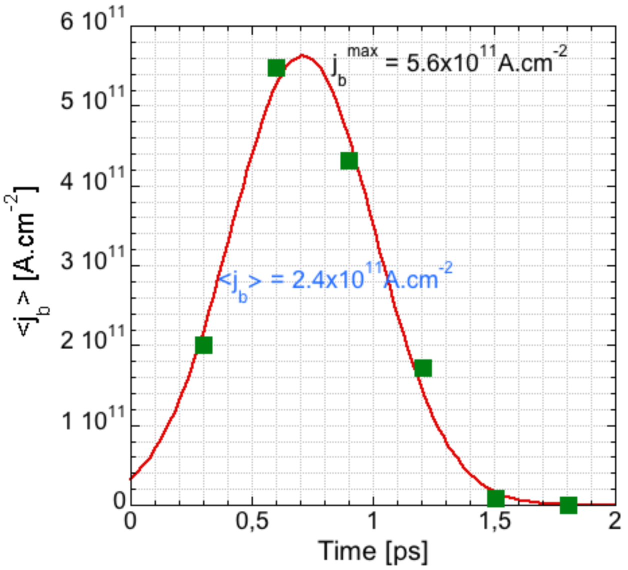

Figure 4.39: Evolution of the mean fast electron current density entering the aluminum propagation layer with time (green squares) extracted from the hybrid simulation and its Gaussian fit (red solid line). The hybrid simulation results are averaged over a 30 μm radius across the fast electron propagation axis.

and compressed aluminum samples is greater than 100 eV, making the aluminum resistivity goes to the Spitzer regime (Fig. 4.14).

In order to get a better idea of the relative importance of collisional and resistive energy losses, the dependence of the integrated losses by the two mechanisms on the aluminum areal density is presented in Fig. 4.41 (left). The error bars are relative to the laser-to-fast-electrons conversion efficiency incertainty of ±5%. The increase of both collisional and resistive losses with the target compression is clearly visible on the plot due to the rise of both density and resistivity of the aluminum sample. The most remarkable result is that in the explored fast electron current density $\langle j_b \rangle = 2.4 \times 10^{11}$ A.cm^{-2}, resistive losses become comparable to the collisional losses in compressed samples. Resistive losses seem to saturate beyond $L \sim 60$ μm, due to the decrease of current density j_b with target depth.

The Al resistivity in cold-solid (squares) and warm-compressed (circles) material, as well as the current, averaged over the first 25 μm of the Al sample, are plotted against time (and hence temperature) in Fig. 4.41 (right). The non-monotonic behavior of the resistivity is the signature of the transition between a regime ruled successively by electron-phonon, electron-electron and electron-ion collisions in the solid case, and successively by electron-electron and electron-ion collisions in the compressed case. For large target depths, the heating time required to reach the Spitzer regime in the solid case is comparable to the REB duration, and considerably shorter at shallow depths. As the solid resistivity is smaller than the compressed case, the energy losses in the compressed target increase for growing L. For thin targets, the current rapidly heats the Al sample to the Spitzer regime, therefore reducing the resistivity difference between solid and compressed Al.

A highly important physical quantity that can also be extracted from the hybrid simulation is the quantity of energy lost by fast electrons over a unit surface and per mass unit. It is calculated by normalizing the energy losses of Fig. 4.41 by the areal densities of 10.62 mg.cm^{-2} and 10.49 mg.cm^{-2} in the solid and compressed cases, respectively. This particular choice of areal density ensure that the quantity of crossed matter is sufficiently high, but that the resistive energy losses in the cold samples do not saturate. The results are presented in Table 4.4.2 for

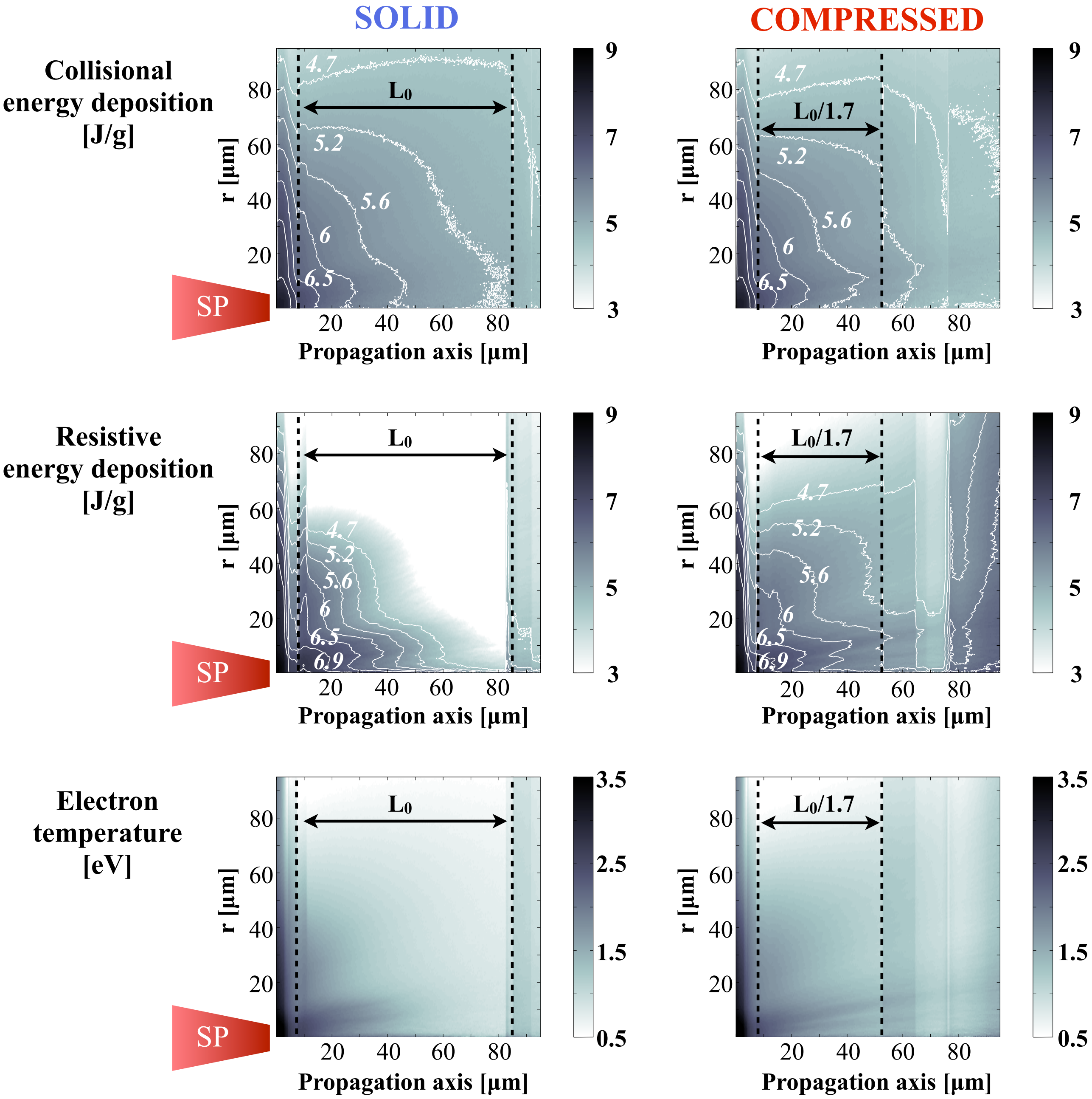

Figure 4.40: 2D maps of the time-integrated collisional (upper plots) and resistive (middle plots) massif energy densities, and the electron temperature (bottom plots), 2.1 ps after fast electron injection time in the solid (left) and compressed (right) targets of the initial thickness $L = 80\ \mu$m. The dashed lines delimit the compressed aluminum sample. All the color values are in logarithmic scales

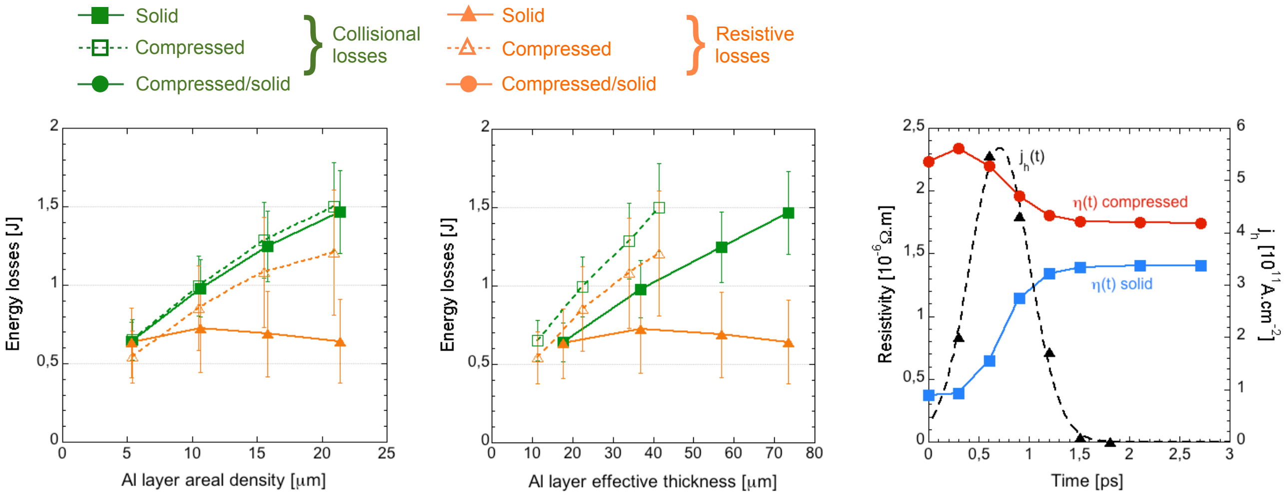

Figure 4.41: (Left) Time-integrated collisional (green squares) and resistive (orange triangles) energy losses calculated in the solid (full symbols) and compressed (open symbols) aluminum samples, as a function of the areal density. (Middle) Same quantities plotted as a function of the aluminum sample effective thickness. (Right) Time evolution of the resistivity of cold-solid (blue solid line) and of warm-compressed (red dashed line) Al samples averaged over $\rho L = 15.5$ mg.cm^{-2} and over 25 μm around REB propagation axis. The evolution of the current beam density (black triangle) averaged over 25 μm around REB propagation axis and its Gaussian fit (black solid line) are also presented.

	Solid	**Compressed**
Collisional [J.cm^2.g^{-1}]	92 ± 17	92 ± 17
Resistive [J.cm^2.g^{-1}]	67 ± 20	80 ± 20
Total [J.cm^2.g^{-1}]	159 ± 37	173 ± 37

Table 4.5: Summary of fast electron energy losses in cold-solid and warm-compressed materials for collisional and resistive energy loss mechanisms, and the corresponding total losses. Error bars correspond to a ±5% uncertainty in the laser-to-fast electrons conversion efficiency injected in hybrid transport simulations.

both the collisional and resistive losses. As expected, the difference observed for the collisional losses in the cold-solid and warm-compressed targets is fairly weak, and lower than the error bars. The most remarkable result is the 19% increase of the resistive energy losses calculated for the warm-compressed targets.

By multiplying these results by the respective density of the aluminum sample, and by normalizing by the number of electrons calculated by the hybrid transport simulations, we obtain the mean fast electron collisional and resistive stopping powers (Table 4.4.2). The density of the compressed sample, $\rho = 4.8$ g.cm^{-3}, is averaged over the entire aluminum length. The variation of the stopping power between the solid and compressed samples is slightly lower than the expected 50%. This difference is due to the imperfect target compression. An increase of the resistive stopping power of $\sim$ 53% is obtained with the aluminum sample heating, making its value comparable to the collisional stopping power. These results are in good agreement with the estimations given by the semi-analytical model of resistive energy losses developed by Arnaud Debayle, predicting a resistive stopping power of $\sim$ 4.5 keV/μm in warm-dense aluminum in the studied current density conditions [Vauzour et al., 2014].

	Solid	**Compressed**
Collisional [keV/μm]	3.5 ± 0.6	6.2 ± 1
Resistive [keV/μm]	2.5 ± 0.7	5.4 ± 1
Total [keV/μm]	6.0 ± 1	11.6 ± 2

Table 4.6: Summary of fast electron stopping powers in cold-solid and warm-compressed materials for collisional and resistive energy loss mechanisms, and the corresponding total stopping powers. Error bars correspond to a ±5% uncertainty in the laser-to-fast electrons conversion efficiency injected in hybrid transport simulations.

The experimental spectrum of fast electrons having escaped the target is compared to the distribution of electrons calculated at the rear side of simulated targets by hybrid simulations (Fig. 4.42). Considering the accessible bandwidth of the electron spectrometer ($E < 10$ MeV), one can see a fairly good agreement in term of slope between the two set of data. This results highlight the consistency of the injected fast electron source in hybrid simulations.

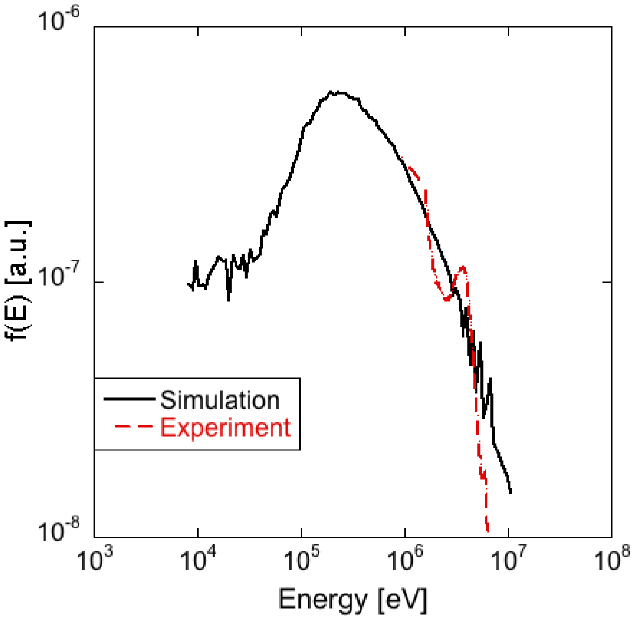

Figure 4.42: Comparison of the experimental spectrum of fast electrons which escaped the target (red dashed line) with the simulated distribution at the rear side of the target (black solid line). The two sets of data are normalized by their respective integral values.

4.4.3 Monte-Carlo simulations of the bremsstrahlung emission

The deconvolution of bremsstrahlung cannon results allows to characterize the electron energy distribution near the source. This was performed with Monte-Carlo simulations using the MCNPX code [Pelowitz, 2011]. Due to computational limitations the data analysis is subdivided into two steps for each laser shot, allowing to determine the generated bremsstrahlung emission energy distribution and the fast electron spectrum.

Determination of the bremsstrahlung emission spectrum

The first step of this numerical work consists in simulating the propagation of a given X-ray spectrum into the cannon, reduced to the stack of IPs and filters. The photon source is assumed to be confined into a 1.5 cm diameter disk, emitting a collimated photon spectrum. This bremsstrahlung spatial profile is justified by the presence of a 12.5 cm long lead collimator in front of the cannon, characterized by a 1/2 in entrance hole, located far enough from the target so that the photon spectrum is fully collimated when entering the cannon. As a consequence, the assumption of such a collimated bremsstrahlung spectrum allows to avoid to simulate the collimator. The energy deposition within the 15 IP sensitive phosphor layers is then compared to the cannon experimental results, assuming a linear relation of proportionality between the energy deposition and the number of PSL collected during the scanning process of IPs [Hidding et al., 2007; Bonnet et al., 2013]. The simulation process is illustrated on Fig. 4.43.

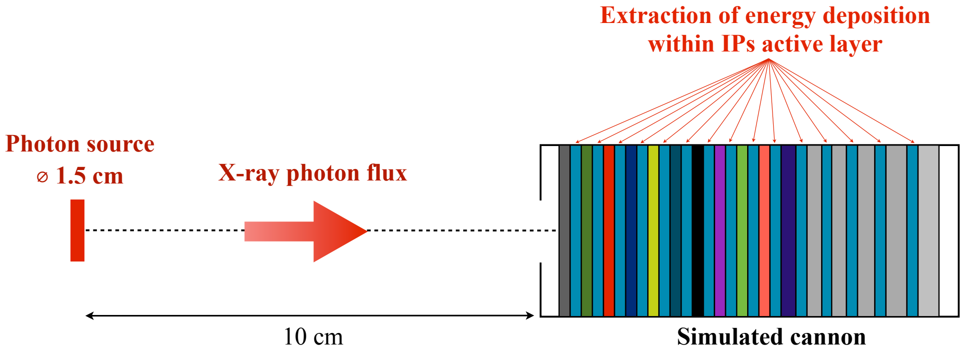

Figure 4.43: Illustration of the first step of the MCNPX deconvolution process of the bremsstrahlung cannons allowing to characterize the bremsstrahlung spectrum energy distribution.

As mentioned in a previous section, the user has to make an assumption on the injected photon energy distribution. Due to the largely shorter simulation time with the Matlab script described in section 4.2.3 compared to MCNPX simulations, the first energy distribution guess is taken as the best Matlab fit of experimental data. The parameters of the source are then modified until one finds the best MCNPX simulation fit. For the whole majority of shots, and for both cannons, the best Matlab fit parameters corresponds to the best MCNPX fit parameters, minimizing the chi-squared value:

$$\chi^2 = \sum_{i=1}^{15} \frac{(y_i - N_i)^2}{N_i} \tag{4.14}$$

with y_i the normalized energy deposition within the IP layer and N_i the normalized experimental value of the ith IP. An example of such a fit is presented in Fig. 4.44.

As already decried by Eq. 4.5, the bremsstrahlung photon source can be fitted by a double exponential sum:

$$I(E) = \alpha.\exp\left(-\frac{E}{T_1}\right) + \beta.\exp\left(-\frac{E}{T_2}\right) \tag{4.15}$$

with the different fitting parameters averaged over each laser shot given by $\alpha = (1.4 \pm 0.6) \times 10^4$, $\beta = (4 \pm 0.8) \times 10^3$, $T_1 = (22 \pm 2)$ MeV and $T_2 = (0.24 \pm 0.04)$ MeV, yielding a chi-squared value of $\chi = (1.34 \pm 0.3) \times 10^{-2}$. The weak dispersion of the fitting parameters characterizing the photon source over different laser shot illustrates the dependence of the bremsstrahlung spectrum on the fast electron distribution rather than on the electron propagation mechanisms

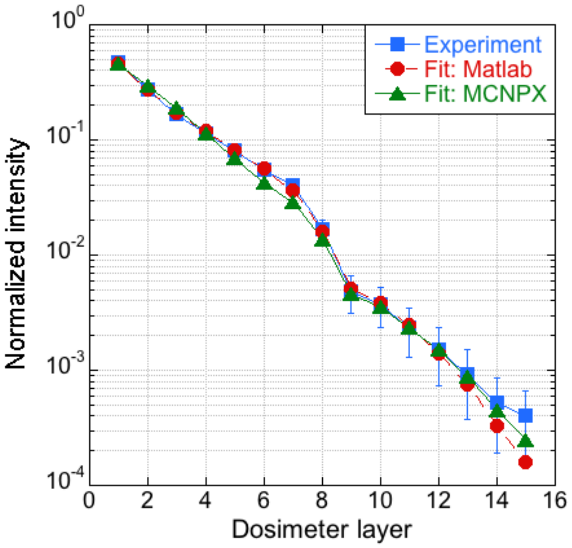

Figure 4.44: Number of PSL photons obtained in a representative laser shot (blue squares). The fitting values obtained with the Matlab script (red circles) and by MCNPX simulations (green triangles) are in fair agreement with experimental results. All quantities are normalized to the integral values.

themselves. It is worth noting that T_1 and T_2 are or the order of the temperature T_{h_1} characterizing the lower energy part of the REB spectrum. The accessible bandwidth of the spectrometer does not indeed allow to measure high photon temperatures.

To conclude this section, one can note that the simple Matlab script providing the results similar to the MCNPX simulations constitute a rather convenient tool to rapidly estimate the bremsstrahlung spectrum during an experimental campaign, after each laser shot.

Deconvolution of the fast electron spectrum

The second step of the simulation consists in the search for a relation between the photon spectrum and the fast electron spectrum. To do so, a chosen fast electron distribution is injected into the simulated target. The generated bremsstrahlung spectrum is then measured using two 1×1 mm^2 detectors of 10 μm thickness located 3 mm away from the target, at 45° and 70° from target normal, mimicking the direction of the two bremsstrahlung cannons set up during the experiment. An illustration of the simulation process is presented in Fig. 4.45. In order to get a good enough statistics, 3×10^8 particles representing the electron source are injected into the simulated target. It is worth mentioning that the goal of this second simulation step is to inject a fast electron distribution generating a bremsstrahlung spectrum that matches the photon spectrum obtained during step one.

In order to check the consistency of the fast electron distribution injected into hybrid simulations presented in the previous section, the following electron distribution is used as input in Monte-Carlo simulations:

1. the energy distribution is described by the function presented in Eq. 4.12 discretized over 5000 energy bins linearly spaced.

2. the initial radius of the fast electron beam is set at 28 μm, in agreement with the larger radius considered in hybrid simulations

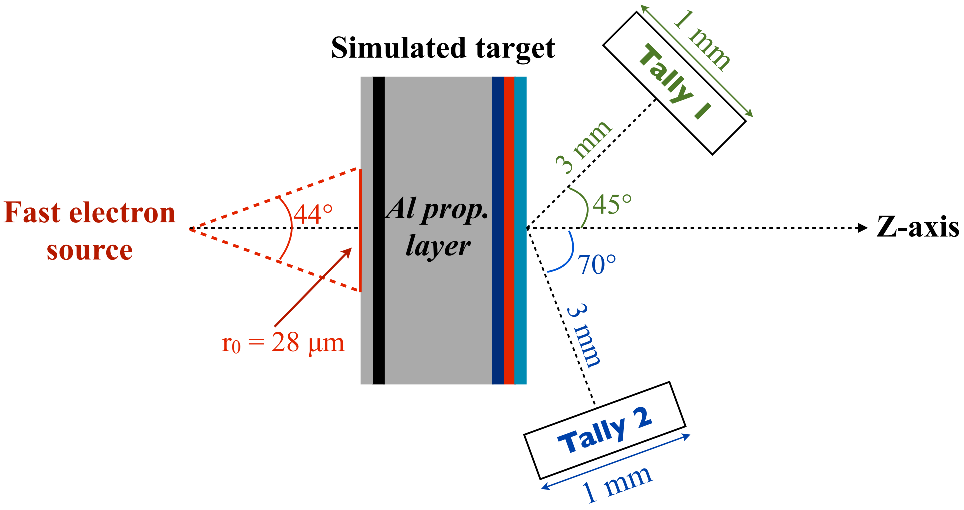

Figure 4.45: Illustration of the second step of the MCNPX deconvolution process of the bremsstrahlung cannons allowing to characterize the birth fast electron spectrum.

3. electrons are injected in a cone characterized by a 22° opening angle, in agreement with both experimental and hybrid simulation results. For the sake of simplicity, the divergence angle dependence on the initial transverse coordinate (X-axis) is also neglected.

A comparison of the photon spectrum found for each tally is presented in Fig. 4.46. As expected the number of photons measured at 70° from target normal is smaller than the same quantity measured at 45°. The oscillations in the spectra above 1 MeV are due to the lack of statistics which would necessitate to increase the number of injected electrons, dramatically increasing the simulation time. Since the most important part of the spectrum is located in the [20; 1000] keV energy range, this lack of precision at high energy does not constitute an important issue.

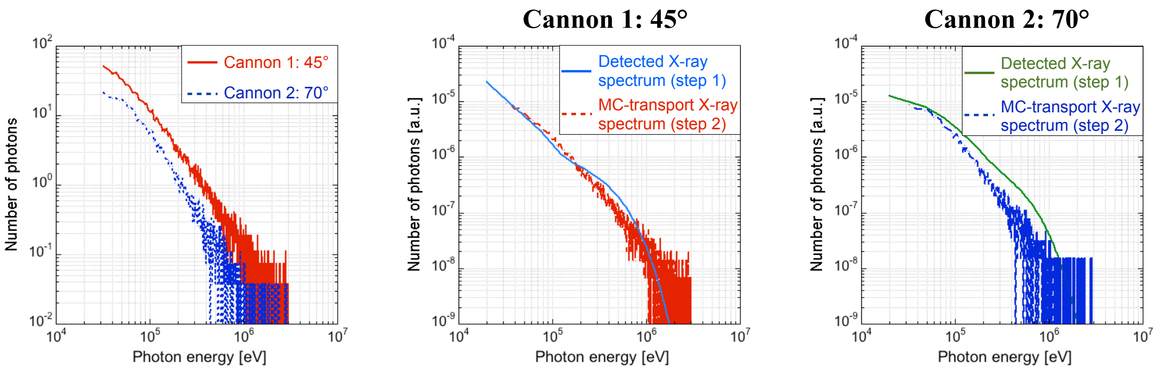

Figure 4.46: (Left) Comparison of the simulated spectra at 45° and at 70°, representing cannon 1 and cannon 2, respectively. (Middle and Right) Bremsstrahlung spectra results from MC simulations: experimental spectrum deduced from matching the X-ray detection simulation to the dosimeter layer data (first step: full line) compared to the spectrum generated by fast electron propagation into the simulated target (second step: dashed line) for cannon 1 (middle) and cannon 2 (right).

A comparison between the simulated bremsstrahlung spectra obtained when injecting the described fast electron source with the spectra obtained during the first step of the simulation is presented in Fig. 4.46 for the two cannons. All the presented spectra are normalized by their integral values to facilitate the comparison. One can see a good agreement between the two spectra for the cannon number 1, located 45° from target normal, with a chi-squared value $\chi^2 = 1.34 \times 10^{-2}$. To finally asses the consistency of this analysis, the photon spectrum obtained in step two is re-injected into the simulated cannon. A very good agreement is again found with experimental data, yielding $\chi^2 = 1.36 \times 10^{-2}$. These results allow to validate the fast electron spectrum used in hybrid simulations. For cannon number 2, the agreement between the two spectrum is not so obvious. The oscillations in the spectrum obtained during step 2 due to the lack of statistics begin earlier than for cannon 2 because of the larger angle of detection.

In conclusion, the deconvolution of bremsstrahlung cannons requires numerical simulations that cannot be completely performed during an experimental campaign. The deconvolution of the bremsstrahlung spectrum though can be rapidly performed using a simple Matlab script. A comparison of the Bremsstrahlung cannon data with the Monte-Carlo simulations provides a tool to check the consistency of PIC source simulations. They however fail to fully replace an hybrid transport code due to the total omission of collective effects. Moreover, the arbitrary choice of electron and photon energy distributions does not converge to a unique spectrum that fits experimental data.

4.5 Conclusion

The experiment presented in this chapter was dedicated to study the fast electron transport in a warm-dense plasma. Aluminum samples inserted into multilayer targets were used as propagation layers. The warm-dense state was generated by a counter-propagative laser-driven shock, heating the target up to a few eV, close to the Fermi temperature, where the resistivity is the highest, and compressing it by a factor ~ 2. A fast electron beam with a mean current density of $j_b = 2.4 \times 10^{11}$ A.cm^{-2} in the propagation layer (at 10 μm depth) was created by a 10^{20} W.cm^{-2} laser pulse. The large extent of the focus of the LP beam, used to generate the shock, ensured a planar compression, avoiding any transverse density and temperature gradients over the volume swept by the fast electron beam. For the first time, we experimentally detected an increase of resistive energy losses in warm aluminum samples by a factor of 19%, compared to solid samples of identical areal density. This demonstrates the importance of the resistive mechanisms in the fast electron transport.

The fast electron and target characteristics were calculated with the PIC and hydrodynamic codes. The target state (density and temperature) at the compression state are in a fairly good agreement with the experimental data. The resistive energy losses were calculated with the hybrid transport code. They are of the same order of the collisional losses in compressed targets, showing how important the former mechanism is for the fast electron transport. The temporal evolution of the resistivity was analyzed. For the explored regime and initially cold targets, the transition to the resistive regime, $T_e \geq T_F$, takes place in a few hundreds of femtoseconds. At higher current densities, this heating time would have been significantly reduced, leading to the reduction of the resistive losses. At lower current density $j_b < 10^{11}$ A.cm^{-2} the resistive effects are lower than the collisional effects, as it was demonstrated in the previous studies [Vauzour et al., 2012, 2014].

The achieved temperature and density of the compressed samples are relatively modest compared to a compressed DT core of ICF targets. However these results are relevant for the fast ignition because we succeed to characterize the transport in the high resistive regions such as the cone tip material and the plasma beyond it. The first hundreds of fs can indeed play a determinant role in the electron transport. The generation of resistive magnetic fields during this time is conditioning the subsequent beam profile characteristics [Scott et al., 2012; MacLellan et al., 2013]. Moreover, our results are useful for the benchmarking of the transport codes extendable to the full- scale FI conditions.

Chapter 5

Fast electron transport in planar compressed cone targets

In the improved design of the fast ignition scheme, a hollow cone is inserted into the D-T target. The fast electron source, generated by coupling an intense laser pulse with the cone tip, is thus located closer from the D-T core, potentially increasing the coupling efficiency. The introduction of such a cone, made of gold or of diamond, however rises a certain number of issues. The asymmetric compression of the target generates a plasma jet that propagates towards less dense regions, being in this case on the cone axis, pushing the fast electron source further from the D-T core. The cone must also survive the extremely high pressure generated during target compression. In addition to these hydrodynamic issues, the interaction of the laser pulse with both the cone tip and the cone walls, and the quality of generated fast electron beam with characteristics required for an efficient coupling with the D-T core, is still an open research field.

This chapter presents an experiment and its interpretation dedicated to the studies of fast electron transport in the cone compressed by a strong shock. The experimental campaign was performed on the LULI2000 laser facility. It was dedicated to a systematic study of the electron transport in a copper cone perturbed by a laser-driven planar shock. This campaign was subdivided into two distinct experiments. The first one was fully dedicated to the characterization of the shock propagation into the target, including its collision with the cone tip and its sliding along the cone walls. An X-ray point projection system was used to radiograph the target at different moments of compression. In a second step, a fast electron beam is generated by coupling a ps-scale intense laser pulse with the cone tip at different moments of compression. The diagnostics fielded into the experimental chamber allowed a precise visualization of the coupling between the intact cone tip, or with an expanding plasma into the cone, depending on the injection time.

5.1 Experimental setup

The experiments described in this chapter were performed on the LULI2000 laser facility (Laboratoire pour l'Utilisation des Lasers Intenses, France). The two campaigns were performed in collaboration with several laboratories around the world: the CELIA (France), the LULI (France), the University of Milan (Italy), the LLNL (USA), the University of California (USA), the University of Nevada (USA), General Atomics (USA), the University of Strathclyde (UK) and the University of Alberta (Canada).

5.1.1 The LULI-Pico2000 laser system

Overview of the laser system

The LULI2000 facility offers two Nd:glass laser chains, called North and South, delivering up to 1 kJ pulses at $\lambda_L = 1.053$ μm in a flat-top spatial profile. The square temporal pulse profile can be tuned in the $0.5-5$ ns duration range, with a rising front of 150 ps. The delay between the two pulses can be adjusted with a delay line, sending the South pulse 10 ps prior or after the North pulse. The repetition rate is limited to 1 shot every 90 min because of the required amplifier cooling, mandatory to avoid strong wavefront aberrations. A 10 Hz laser pulse is available for alignment operations. The laser pulses can be frequency doubled on request. Several other chains, of a moderate energy and intensity, are also available for diagnostic purposes. The so-called blue chain delivers ns laser pulses carrying 80 J of energy.

The South chain offers a CPA option, enabling the possibility to generated ultra-intense laser pulses of the order of $\sim 10^{19}$ W.cm^{-2}, delivered in 1 ps to 30 ps. The maximum laser energy is limited to $\sim$ 100 J to avoid any damage of the compressor gratings. The South chain is build as follows. A Ti:Sa oscillator generates an initial 250 mW, 100 fs laser pulse, which is then stretched up to a few ns duration through an Offner stretcher. The output laser pulse, carrying 700 pJ of energy, is then sent in a Nd:glass regenerative-amplifier. This optical device allows the incident pulse to achieve high gains by performing several passes (about 55 in this case) through the amplifying medium. The number of passes is controlled by a combination of a Pockels cell and a polarizer. The output beam, characterized by a 2 nm bandwidth, amplified by a factor $\sim 9 \times 10^6$, and carrying an energy of 7 mJ is then sent to the main amplifier, made of a combination of rods and disks, where it is amplified up to $\sim$ 150 J. The high-energy pulse is then compressed by a combination of two multi-layer dielectric (MLD) gratings. MLD's, composed of an alternance of low and high index layers, offer the advantage of increasing the achievable reflectivity while increasing the damage threshold compared to metallic gratings. The output pulse is then transported and focused at the target chamber center with an $f/4$, $f = 800$ mm off-axis parabola. A set of laser diagnostics, either set-up on every shot or on request, allows to precisely characterize the laser pulse (spectrum, energy at TCC, duration, ...).

Pre-pulse

The LULI2000 short pulse (SP) beam is characterized, similarly as the Titan short pulse, by an intense enough ASE-induced pedestal that created an expanding pre-plasma before the main pulse arrival. The pre-plasma density profile was characterized by Santos et al. [2009] using the following setup. A 8 ns, 10 mJ, 532 nm probe pulse was sent through the pre-plasma formed by the LULI short pulse beam pedestal at the surface of a multi-layer target, with a 10 μm front side plastic layer. The output pulse was then sent through a Wollaston prism located between two crossed linear polarizers, and finally recorded by a Gated Optical Imager (GOI), allowing to measure a 2D image of the pulse with a 90 ps gate width. This device allowed to obtain interferometric snapshots of the target at different delays relative to the ps beam. Fig. 5.1 presents two of such snapshots together with two reference images taken before each shot, allowing to obtain a reference for the initial target front side position. One can note that the effect of the pre-plasma is detected 1.1 ns before the main pulse.

An Abel inversion was applied to the interferogram, assuming a cylindrical symmetry around target normal. From that, the authors obtained the radial distribution of the refractive index, and thus of the electron density n_e (black solid line in Fig. 5.1). The pre-plasma extends 100 μm from the target front side initial position 250 ± 45 ps before the main pulse. A set

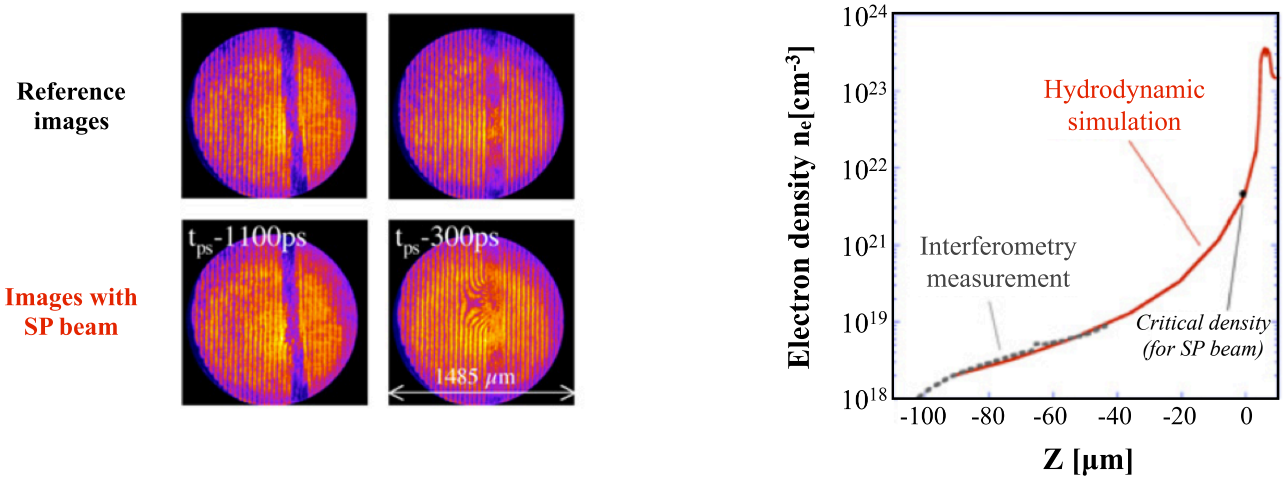

Figure 5.1: (Left) GOI interferometric images taken without (up) and with (down) SP laser beam 1.1 ns (left) and 0.3 ns (right) before arrival of the main pulse on the target. (Right) Comparison between the experimental (grey dashed line) and the simulated (red solid line) pre-plasma electron density profile. The SP beam critical density position is materialized by the black dot.

of 2D simulations performed with the CHIC code, and matching experimental data in the $10^{14} - 10^{20}$ cm^{-3} range, showed that the critical surface ($n_c = 4.56 \times 10^{21}$ W.cm^{-2}) moved by less than 1 μm compared to the unperturbed case. It is worth mentioning that the simulations in the 2D geometry were in this case mandatory compared to a 1D geometry because of a small extension ($\sim$ 10 μm) of the short pulse beam spot size.

In summary, the ASE pedestal intensity was estimated to be at the level of 10^{12} W.cm^{-2}, arriving 1.1 ns before the main pulse.

5.2 Step 1: Hydrodynamic characterization of the target

The first part of the experimental campaign is dedicated to a full hydrodynamic characterization of the compression of targets that are used in the second part to study fast electron generation and transport processes. This section presents the experimental results compared to the hydrodynamic simulations performed with the 1D MULTI and the 2D CHIC codes.

5.2.1 Laser pulse characteristics

During this first experimental campaign, both the LULI long pulse and short pulse beams are used. Their characteristics are the following.

The frequency doubled ($\lambda_L = 0.53$ μm) long pulse beam used to generate a planar compression shock, carries a mean energy of 475 ± 49 J, the error being related to the shot-to-shot energy variations. It is characterized by a 5 ns square temporal profile. The pulse is focused on the rear side of the targets by a combination of a lens with a random phase plate, generating an optically smooth 500 μm FWHM focal spot, carrying $\sim$ 70% of the laser energy, yielding a peak intensity of $(2.5 \pm 0.3) \times 10^{13}$ W.cm^{-2}.

The frequency doubled ($\lambda_L = 0.53$ μm) short pulse beam used for radiography purposes, as detailed in the next section, carried a mean energy of 10 J on target. It is characterized by a 1 ps FWHM Gaussian temporal profile. The SP beam is focused by a $f/4$ off-axis parabola into a 10 μm FWHM spot, yielding a peak intensity of 10^{19} W.cm^{-2}.

5.2.2 Experimental setup

The experimental setup is presented on Fig. 5.2. The targets are composed of a 10 μm thickness, 400 ± 10 μm long buried copper cone into a thick (500×1190 μm^2) carbon layer. A 10 μm silver tracer is located 100 μm away from the 50 μm diameter cone tip, followed by a 15 μm plastic layer acting as an ablator, and avoiding any direct irradiation of the silver layer. The LP beam is first focused on the plastic layer, generating a wide compression shock propagating towards the cone tip. The SP pulse beam is then focused either onto a 10 μm diameter copper wire, or onto a 10 μm thickness copper foil, both of them located 10 mm away from the cone tip, generating an intense X-ray emission, dominated by the Cu-K$_\alpha$ emission, used to radiograph the target. The X-ray signal, propagating through $\sim$ 1.2 mm of matter, is recorded on a MS-type imaging plate located 35 cm away from target chamber center, yielding a magnification $\gamma \sim 35$. The delay between the two laser pulses $\Delta\tau$ is variable, the long pulse beam being always fired before the short pulse beam, so that the target is radiographed at different moments of compression. Considering that the X-ray time of flight is negligible compared to the LP beam temporal jitter, estimated to $\sim$ 100 ps, the moment of target radiography is equal to the delay between the two laser pulses $\Delta\tau$.

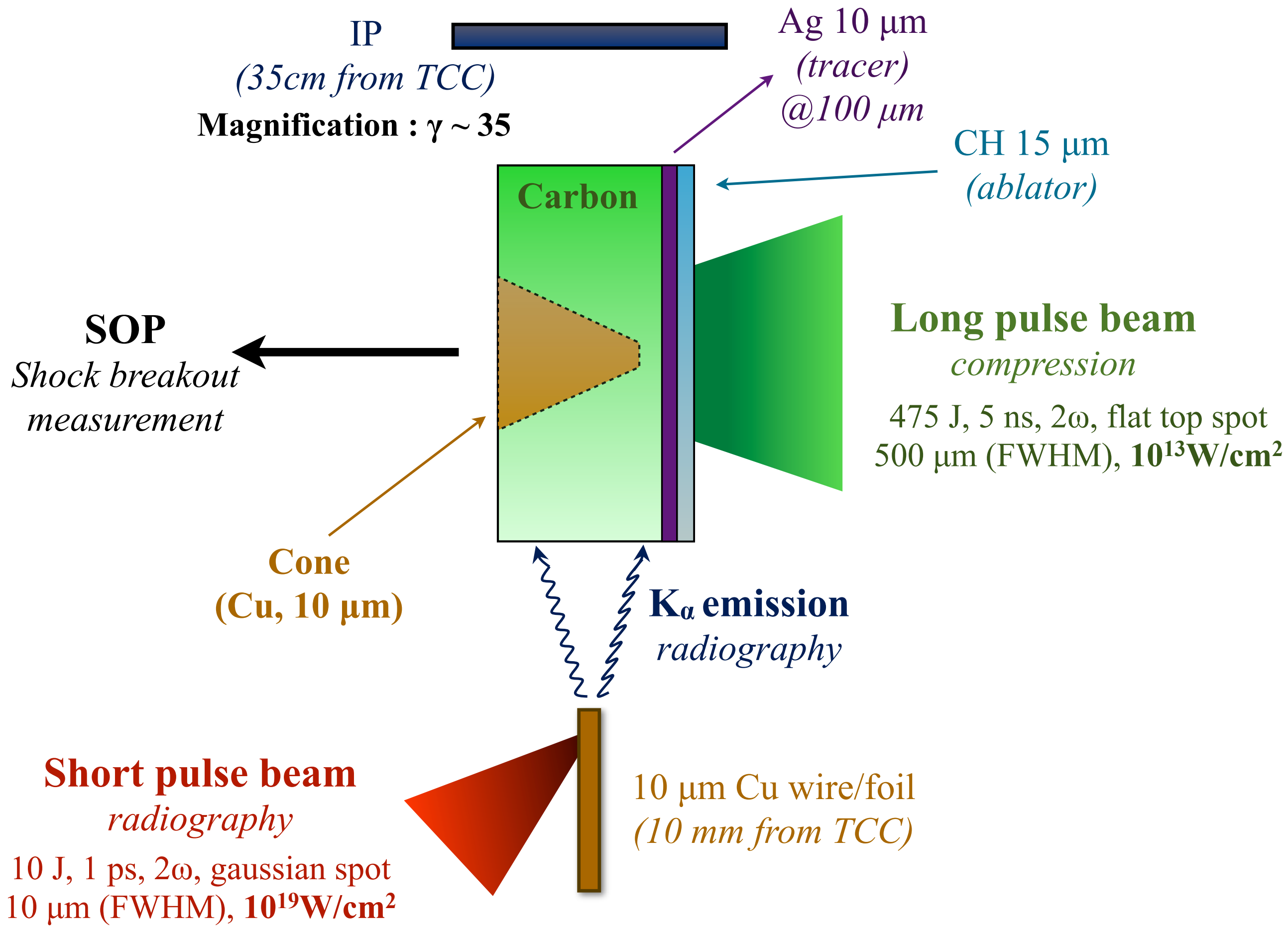

Figure 5.2: Experimental setup used on the first LULI campaign.

The silver tracer layer is used for two different purposes. First, it is a relatively dense material, absorbing much more the Cu-K$_\alpha$ emission compared to the copper cone or to the carbon block, allowing to monitor its deformation by the compression shock, and thus to estimate the fluid velocity. The second role of the silver tracer is to detect fast electrons in the second part of the experiment.

In addition to the radiography setup two other diagnostics are fielded:

- Streaked optical pyrometry measurements were performed to characterize the front-side thermal emission generated by the shock breaking-out from the inner cone tip. Similarly to the Titan experiment, these measurements allow a determination of the delays between the two laser pulses, and to characterize the target hydrodynamic state probed by the radiography. The synchronization process is detailed in section 5.2.3.

- A high speed visible sampling camera (HISAC) is used to obtain 2D images of the shock-induced emission zone in the cone tip. HISAC uses a bundle of optical fibers coupled to a streak camera [Kodama et al., 1999]. The two-dimensional image is transported by the fibers to the streak camera slit, to obtain a time resolution. The 2D time-resolved images are then reconstructed, the spatial resolution being limited by the size and the number of fibers, while the temporal resolution is limited by the characteristics of both the streak camera and the fibers, the latter being due to mode and spectral dispersions.

5.2.3 Synchronization of the laser pulses

One of the key issues in our experiment is the determination of the delay between the two laser pulses and the corresponding compression state of the target which is probed. This delay $\Delta\tau$ is inferred from shock breakout time measurements at the cone tip by the streaked optical pyrometry. The SOP setup is presented on Fig. 5.3. The thermal emission is first collected by a $f = 150$ mm lens. A beam splitter separates the incoming signal into the SOP and HISAC lines. A $f = 1000$ mm lens images the emission on a C 7700 Hamamatsu streak camera slit. The SOP line is also used for the LP beam alignment as illustrated in Fig. 5.3. A flip-flop mirror is used to chose either to send the incoming signal to the streak camera or to a CCD camera. The shock breakout signal generated by the LP beam, carrying 521 J of energy, on a cone target is presented in Fig. 5.2. It is compared to a reference signal obtained by directly sending the attenuated laser pulse to the streak camera. The experimental result is presented in Fig. 5.4. It is worth mentioning that when shooting on a cone target, a notch filter is located in front of the streak camera slit in order to avoid any 2ω laser light noise from entering the camera. The shock breakout time is estimated to 8.3 ± 0.6 ns, the error being due to a streak slit aperture of ~ 300 μm. The corresponding shock speed, averaged over the different layers of the target, is estimated to $v_{\text{shock}} = 17.5 \pm 1.8$ μm.ns^{-1}. A shock breakout time from a 40 μm aluminum foil compressed by the LP beam carrying 574 J of energy is also measured. It will be used in section 5.2.6 to calibrate hydrodynamic simulations of the cone target compression. The shock breakout image is compared to a reference image taken by sending the LP beam at a low flux directly in the streak camera (Fig. 5.5). The shock breakout time is estimated to 1.6 ± 0.3 ns. The corresponding shock speed averaged over the entire thickness of the aluminum foil is $v_{\text{alu}} = 25 \pm 5$ μm.ns^{-1}.

The HISAC line used a $f = 300$ mm lens in order to image the collimated thermal emission on the bundle of fibers. This diagnostic however did not provide data due to experimental issues, preventing any further characterization of the shock breakout.

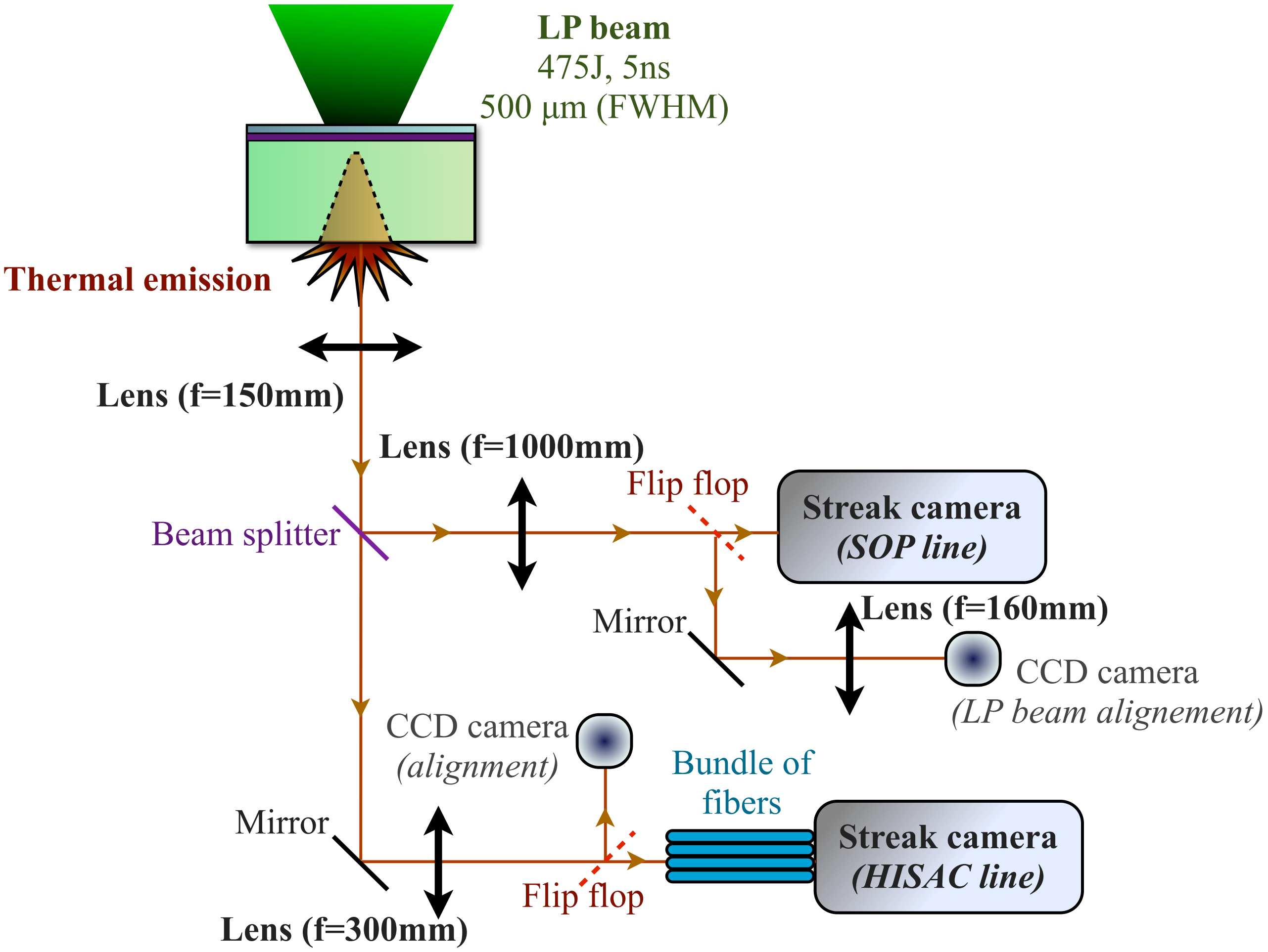

Figure 5.3: Design of the SOP (up) and HISAC (down) lines.

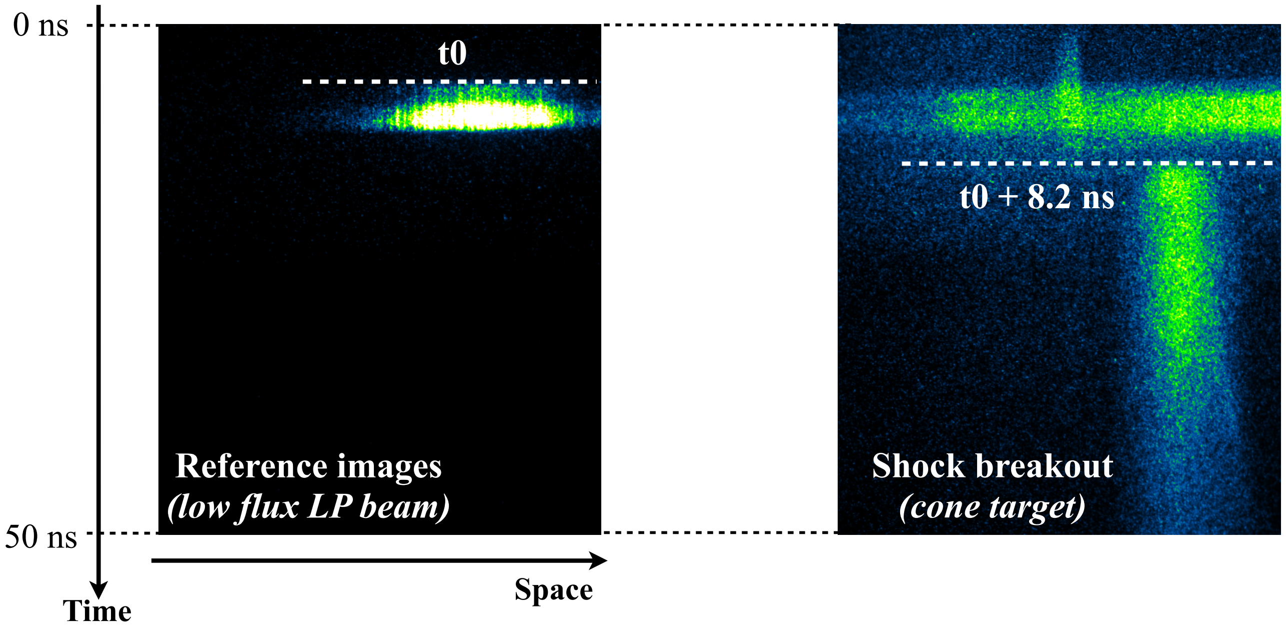

Figure 5.4: Determination of the shock breakout time. A reference image is taken by directly sending the LP beam at a low flux on the streak camera (left). The laser pulse is then fired on a cone target (right), and the resulting thermal emission due to the shock breakout from the cone tip is imaged on the streak camera. The determination of the shock breakout time, 8.2 ns, is obtained by comparing the two images. A sweep speed of 50 ns is used in the two cases.

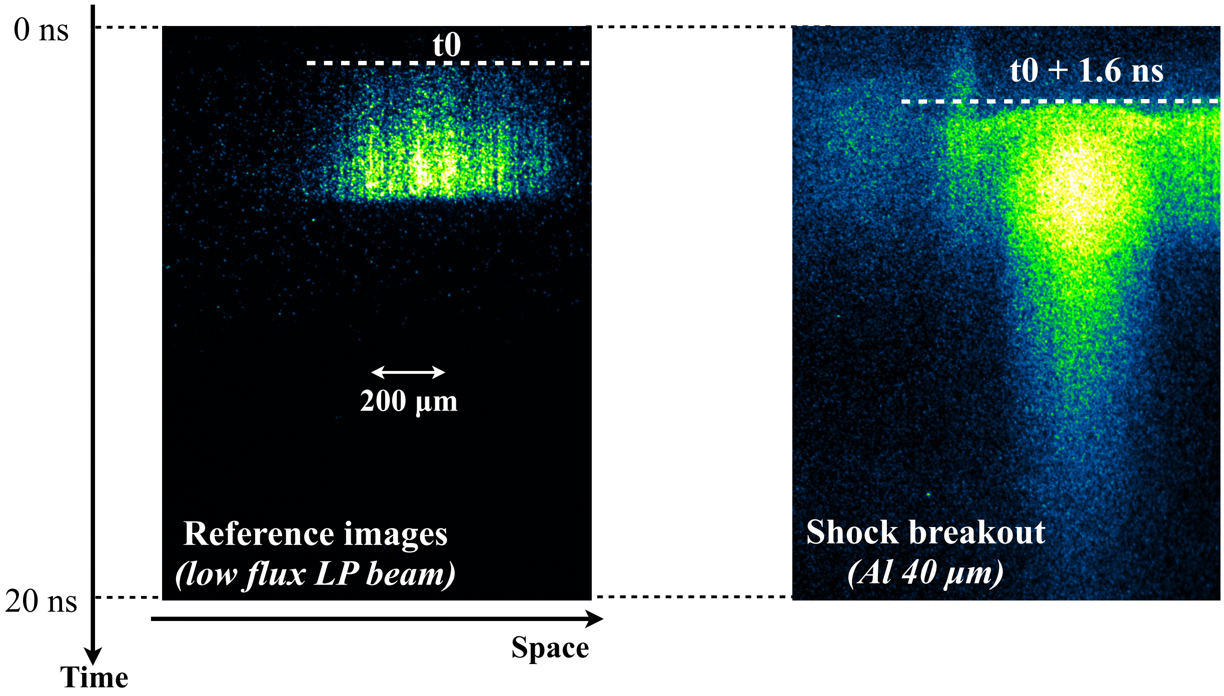

Figure 5.5: Determination of the shock breakout time from a 40 μm aluminum foil. The determination of the shock breakout time, 1.6 ns, is obtained by comparing the two images. A sweep speed of 20 ns is used in the two cases.

5.2.4 Characterization of the X-ray backlighter

The X-ray point projection technique set-up during the experiment uses an intense Cu-K_α line emission, obtained by shooting the LULI long pulse beam either on a copper wire or on a copper foil. As detailed in the next section, this technique provides informations about the cone hydrodynamic conditions at different moments of compression. Its main advantage consists in measuring simultaneously in the same shot the shock front position and the Ag/C interface position.

The first backlighting target chosen was a 10 μm diameter copper wire, its diameter being equivalent to the SP beam spot size. The use of copper was dictated by the good penetration of $\sim$ 8 keV photons through a millimeter thick target, while providing a good contrast to detect a shocked region compressed at nearly twice the solid density. The use of a wire is motivated by the resolution that is theoretically achievable both in the horizontal and vertical directions. Indeed, the resolution is in this case conditioned by the wire diameter rather than by the Cu-K_α spot size, a few times larger due to fast electron refluxing. The experimental spatial resolution is measured by radiographing a 20 μm thick gold mesh with a 60 μm spacing (Fig. 5.6). Two lineouts are extracted in the horizontal and vertical directions. The magnification is calculated by measuring the distance between 8 steps, each one measuring 80 μm, yielding $\gamma_{\text{exp}} = 34$, fairly close from the theoretical magnification ($\gamma = 35$). The horizontal and vertical resolution, given by the distance between two extrema, are 11 μm in both directions, fairly close from the wire diameter.

The choice of a wire as a backlighting target presents a major drawback due to its limited size. The spatial jitter of the SP beam focal spot was so important (> 10 μm) at the time of the experiment that it missed the wire, at least partially, at almost every shot. A possible solution was to replace the wire by a 10 μm thick copper foil oriented perpendicularly to the cone axis. In this position, the foil allows to conserve a fairly good resolution along the cone axis, which is mandatory in our experiment. Its major drawback is the dramatic loss of resolution along the vertical axis (> 50 μm). The source size in this case was dictated by the K_α spot size in the vertical direction, being wider than the SP beam spot size. This issue does not exist along the horizontal axis since the X-ray source size is limited by the target thickness. A comparison between a wire and a foil backlighting targets is presented on Fig. 5.7. Because of the conservation of the horizontal axis resolution, every shot presented in the next section is obtained using a 10 μm copper foil.

The X-ray emission used for the radiography was mainly dominated by the Cu-K_α line emission. A bremsstrahlung emission may however play a non negligible role. The spectral width of the emission was characterized by inserting stacks of aluminum layers of different thicknesses right in front of the imaging plate. The stacks were made of 2, 3, 5, 8 and 10 aluminum foils, a single layer being characterized by a 15.6 μm thickness. The evolution of the signal intensity as a function of the aluminum thickness is presented in Fig. 5.8. This experimental signal is compared to a theoretical spectrum given by the Cu-K_α line emission and a hard X-ray contribution coming from the bremsstrahlung. The parameters of this function are adjusted so that the theoretical spectrum, convolved with the MS-type IP sensitivity, matches the measured intensities. The contribution of the bremsstrahlung emission is found to be fairly low, at the level of 5.6 ± 0.6 mPSL, even if mandatory to reproduce experimental data.

5.2.5 Experimental results

We present in this section the experimental results obtained by X-ray point projection radiography. The backlighting targets that are used on the presented images are in all cases 10 μm thickness copper foils.

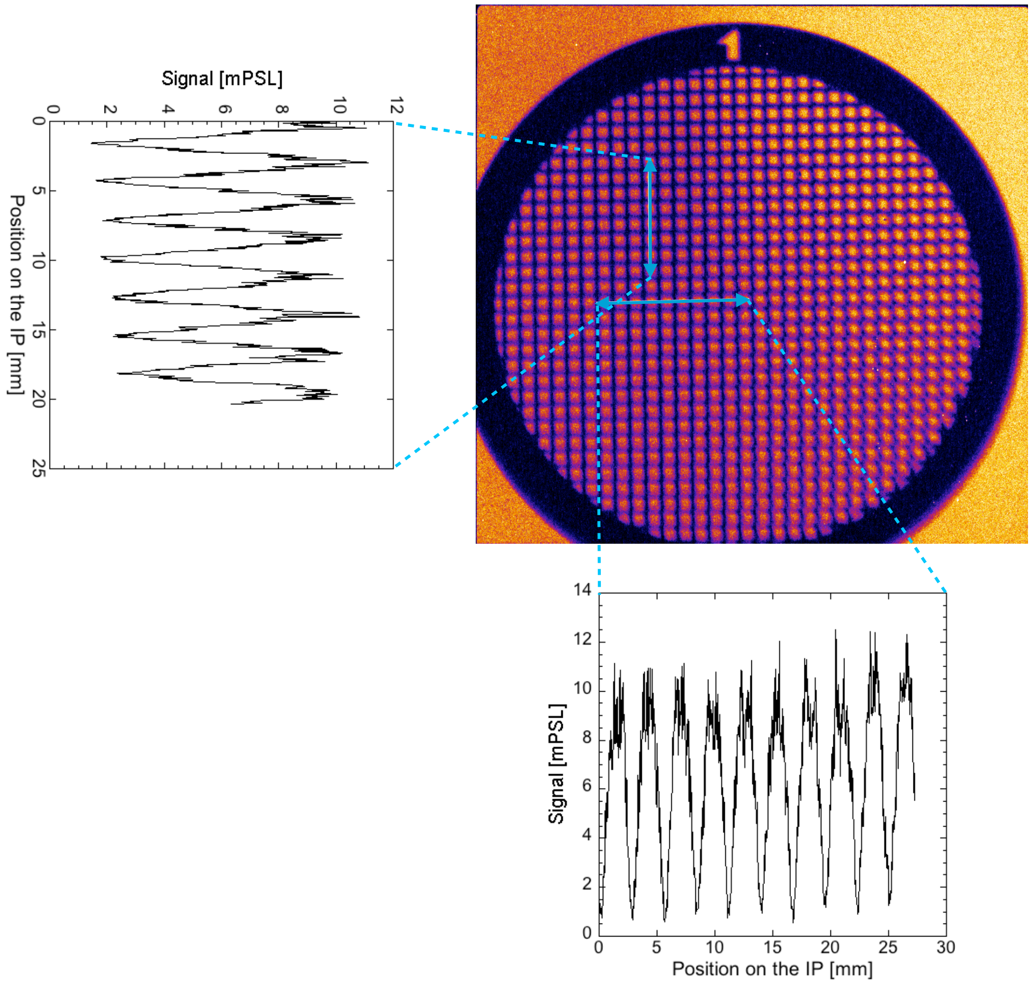

Figure 5.6: Radiographic image of a gold mesh obtained by focusing the 10 J SP beam on a 10 μm diameter copper wire. Horizontal and vertical lineouts are taken to determine the corresponding resolutions.

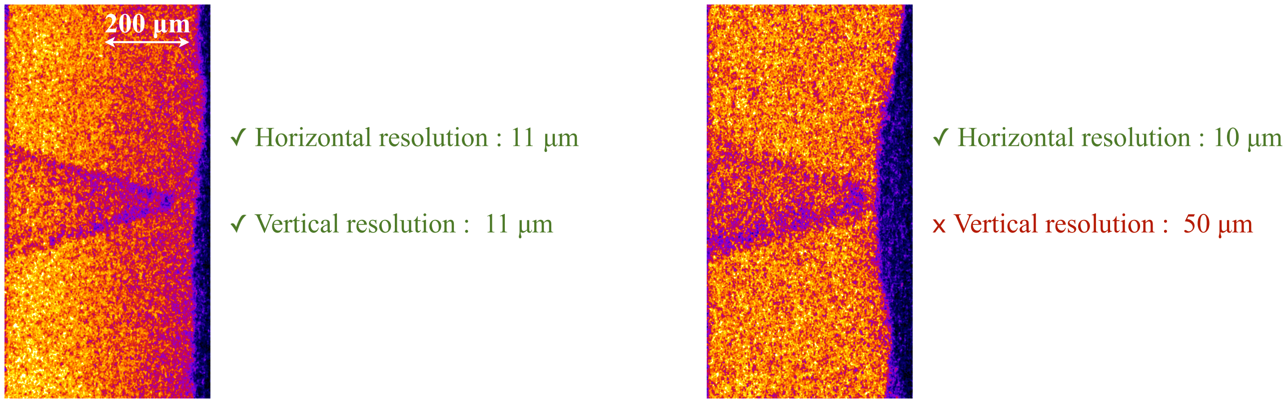

Wire

∅10 μm

Foil

10 μm thickness

Figure 5.7: Comparison between a 10 μm diameter copper wire (left) and a 10 μm thick copper foil (right) used as backlighting targets to radiograph a cone target. A loss of vertical resolution when using a foil can be clearly seen.

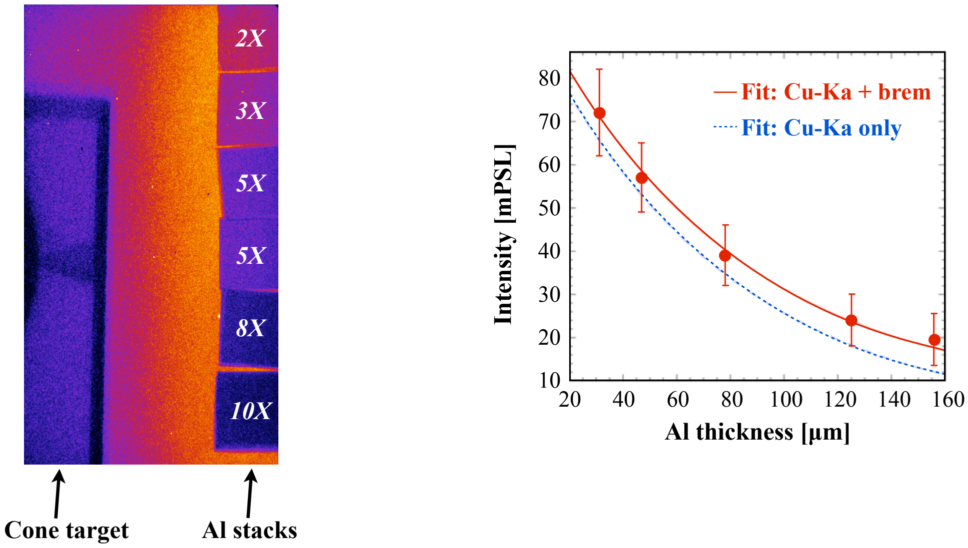

Figure 5.8: (Left) Illustration of the X-ray source monochromaticity characterization setup. Al stacks of different thicknesses, ranging from 31.2 μm to 156 μm, are located on the right-hand side of the imaging plate. The cone target is also clearly visible in this image. (Right) Measured IP signal as a function of the aluminum filter thickness (red circles). The intensity obtained for the 78 μm thickness is a mean value of the two experimental results. Data are fitted by a theoretical spectrum composed of an intense Cu-K$_\alpha$ line emission and a less intense bremsstrahlung spectrum (red solid line). The corresponding fit assuming a Cu-K$_\alpha$ emission only, and a mass attenuation coefficient of 50.33 cm^2.g^{-1} [Hubbel & Seltzer, 2014], is also represented (blue dashed line).

Fig. 5.9 (left) presents a typical radiographic image obtained without any compression of the target by the LP beam. The entire cone structure can be seen. The silver tracer, being the darker area at rear side of the target, and indicated by a white line, is also clearly detected. A radiographic image of the target under compression, acquired 9 ns after the beginning of the LP beam irradiation, is presented in Fig. 5.9 (right). At such a delay, the shock front, indicated by a green line, already compressed the cone tip, represented by a darker area. The deformation of the silver tracer/carbon layer interface, indicated by a white line at the beginning of the darker area at the rear side of the target, can be clearly seen. This Ag/C interface deformation is used further in this section to calculate the target fluid velocity. It is worth mentioning that the images are vertically cut in order to present clearer results, but they are actually fairly more extended.

Radiography results obtained at different times of compression are presented in Fig. 5.10. The image plotted in the left-hand side and labeled $\Delta\tau = 0$ ns corresponds to the radiography of the unperturbed target. One can clearly see the cone structure and the rear-side silver tracer, being the darker area, indicated by the two vertical white lines. For a delay between the two laser pulses of 9 ns, the shock is already propagating into the cone region. This result is consistent with the 8.3 ns shock breakout measurement on the cone tip presented above. The most striking result is that the deformation of the Ag/C interface due to the LP beam induced target compression is clearly visible in all images. The amplitude of this deformation increases when radiographing the target at later time of compression. One can also see that the overall structure of the cone is still visible at the latest time, showing that the cone survived the high shock pressure. The shock front position is more tricky to estimate due to a lack of contrast,

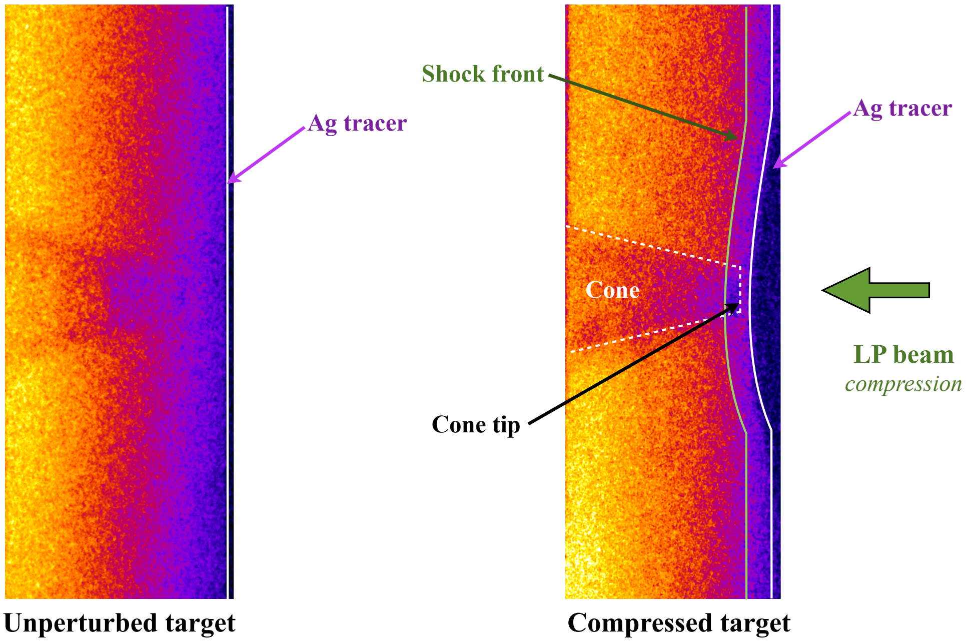

Figure 5.9: (Left) Radiographic image obtained without cone compression. (Right) Radiography of the compressed target 9 ns after the beginning of irradiation by the 507 J LP beam.

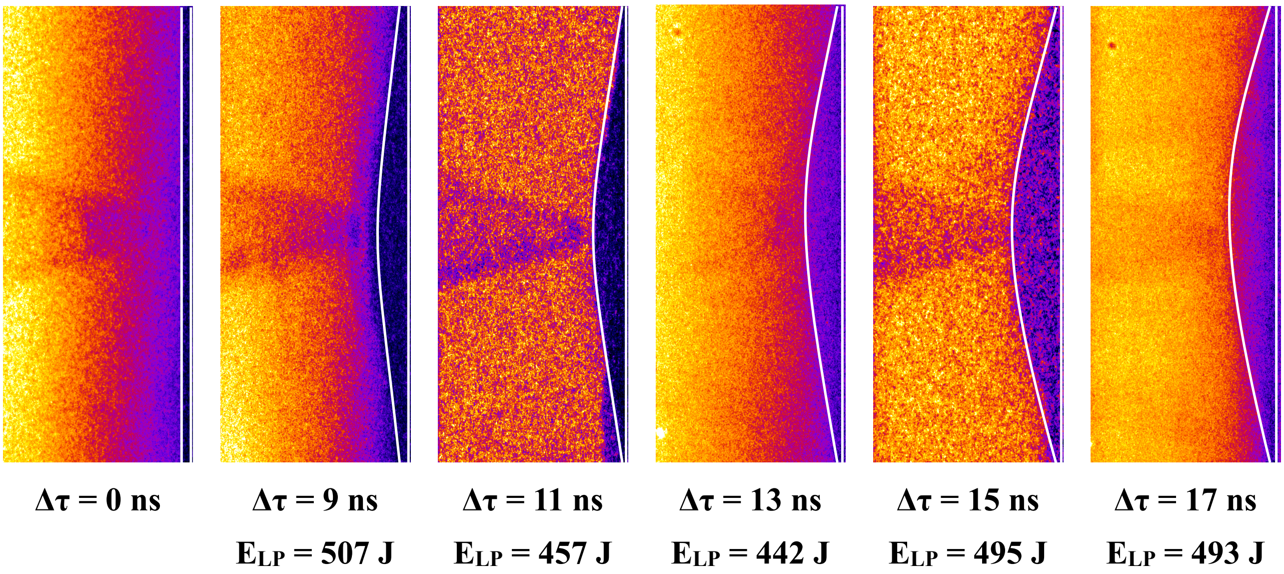

Figure 5.10: Radiographic images of the cone targets at different moments of compression. The delay between the laser pulses increasing when going from left to right. The LP beam irradiates the rear side of the target from the right side. The image on the left-hand side, labeled $\Delta\tau = 0$ ns, corresponds to a radiography of the unperturbed target. The silver tracer is indicated by two vertical white lines.

except of the image labelled $\Delta\tau = 9$ ns. However, a careful analysis of other images allows to determine the shock front position as a function of time, with a significantly larger error bars than for the Ag/C interface position. Fig. 5.11 presents the silver layer displacement and of the shock front position as a function of time. After an initial phase characterized by a constant velocity, the shock front velocity and the fluid velocity decrease with time. The green triangle,

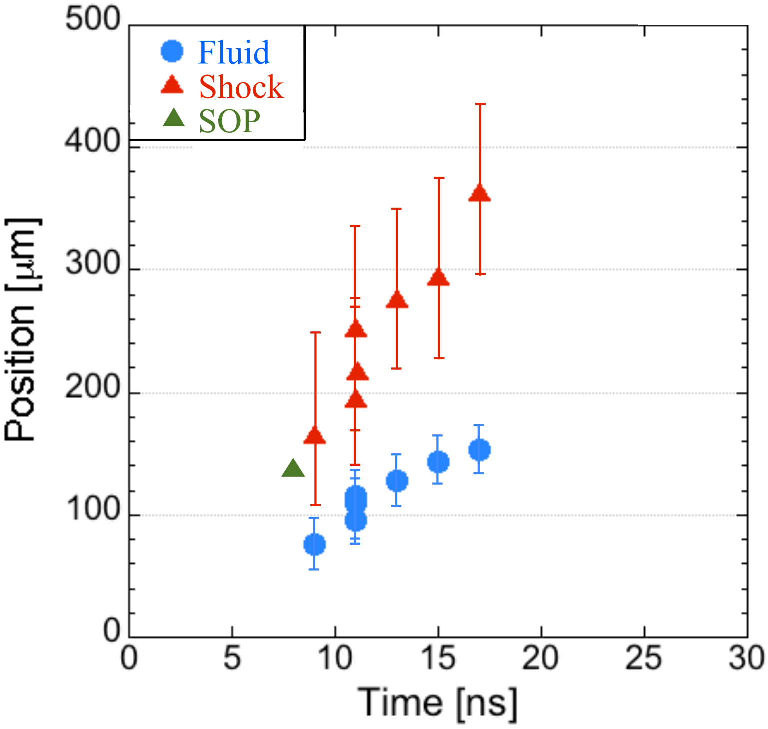

Figure 5.11: Positions of the shock front (red triangles) and of the Ag/C interface (blue circles) as a function of time. The 0 ns delay corresponds to the beginning of the irradiation of the target by the LP beam. The shock front position measured by SOP is represented by the green triangle.

labeled SOP, corresponds to the shock breakout measurement presented above. By considering only the initial phase, or, in other words, by taking the data points corresponding to early time delays ≤ 15 ns, one can estimate the fluid velocity D, being equal to the velocity of the Ag/C interface, and the shock velocity U, yielding:

$$D = 8.78 \pm 0.68\ \mu\text{m.ns}^{-1} \qquad U = 20.8 \pm 2.5\ \mu\text{m.ns}^{-1} \tag{5.1}$$

The early time delay restriction is justified by the slowing down of the shock and fluid at later time of compression. The density and pressure of the shocked regions of the carbon layer can be deduced from the Rankine-Hugoniot conditions. Let us consider a fluid at rest characterized by a pressure P_0, a density ρ_0 and a speed u_0 at the time $t = t_0$. At later time $t > t_0$, a piston is driven into the fluid at the constant speed U. The compressed fluid is characterized by a pressure P and density ρ. The discontinuity between the two fluids, called shock front, propagates with a speed D. This problem, schematically shown in Fig. 5.12, exhibits a discontinuous solution of the gas dynamic equations. The conservation equations across the discontinuity can be used to determine the jumps of P and ρ:

- Mass conservation: at the time $t > t_0$, a mass $\rho_0 D t$, contained into a unit section, is moved toward the positive $X-$axis direction. This mass occupies a volume $(D - U)t$,

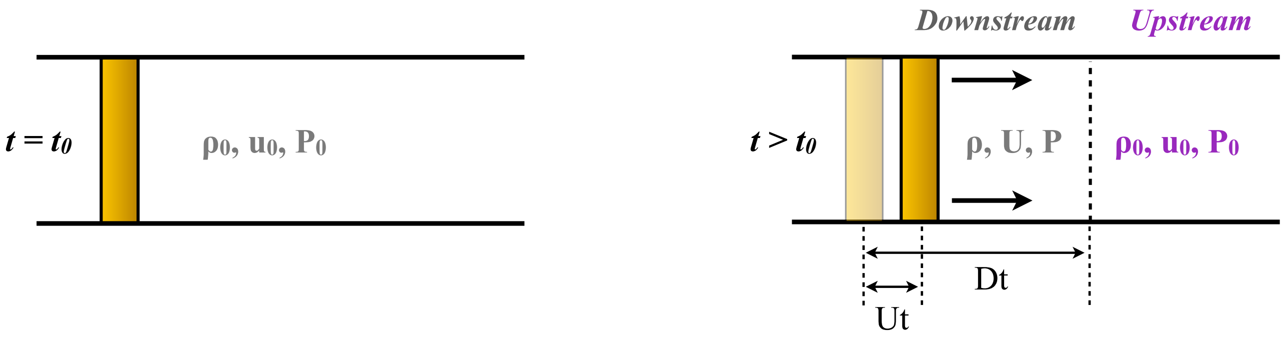

Figure 5.12: Illustration of a shock wave created by a piston propagating into a fluid.

yielding:

$$\rho_0 Dt = \rho(D - U)t \tag{5.2}$$

- Momentum conservation: the moving mass $\rho_0 Dt$ acquires a momentum $\rho_0 DtU$ that must be equal to the momentum induced by the pressure forces exerted by the piston, yielding:

$$\rho_0 DtU = (P - P_0)t \tag{5.3}$$

- Energy conservation: the work of pressure forces PUt exerted on the pistons responsible for a variation of the internal energy of the system, yielding:

$$\rho_0 Dt(\epsilon - \epsilon_0 + \frac{U^2}{2}) = PUt \Rightarrow \epsilon - \epsilon_0 = \frac{U^2}{2}(1 + \frac{2P_0}{P - P_0}) \tag{5.4}$$

  with $\epsilon - \epsilon_0$ the variation of internal energy. This latter equation illustrates the fact that for a strong shock, characterized by $P >> P_0$, the variation of internal energy corresponds to the kinetic energy gain.

From Eq. 5.2 and Eq. 5.3, one can deduce the values of the density and pressure of the shocked region:

$$\begin{aligned} \rho &= \rho_0 \frac{D}{D - U} \\ P &= \rho DU + P_0 \end{aligned} \tag{5.5}$$

By injecting the experimental values of ρ_0, D and U into these two equations, and by assuming a strong shock pressure so that $P >> P_0$, one finds:

$$\rho = 3.46 \pm 0.36 \text{ g.cm}^{-1} \qquad P = 3.65 \pm 0.52 \text{ Mbar} \tag{5.6}$$

5.2.6 Hydrodynamic simulations of the target compression

The cone target compression is simulated with the hydrodynamic code MULTI 1D [Ramis et al., 1988]. These simulations are calibrated using the shock breakout measurements from the 40 μm aluminum foil presented in section 5.2.3. The injected LP beam energy is 475 ± 49 J, corresponding to the experimental measurement. The simulation results are presented together with experimental data in Fig. 5.13. One can see a fairly good agreement between experiment and simulations (colored areas). The shock breakout time measurement, represented by the green triangle, is also fairly well reproduced. It is worth mentioning that the thickness of the

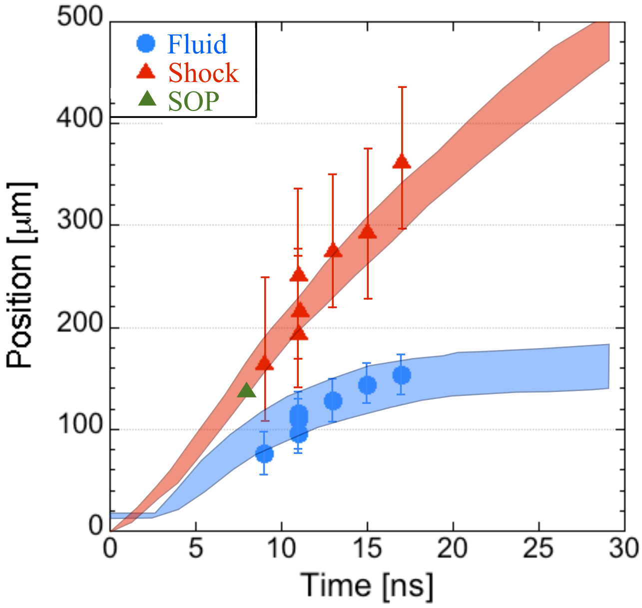

Figure 5.13: Positions of the shock front (red triangles) and of the Ag/C interface (blue circles) presented in Fig. 5.11 as a function of time. The 0 ns delay corresponds to the beginning of the irradiation of the target by the LP beam. The shock front position measured by the SOP is represented by the green triangle. Simulations performed with the MULTI code are represented by the red (shock front position) and blue (fluid position) colored areas.

two colored areas is directly linked to the error bar of the LP beam energy. The shock front and fluid deceleration with time can also be clearly seen.

5.2.7 Conclusion of the first experiment

The experiment described in this section was dedicated to the hydrodynamic characterization of copper coated cone targets inserted into thick carbon layers, compressed by a $\sim$ 500 J, $\sim 10^{13}$ W.cm^{-2} long laser pulse. The shock breakout measurement by streaked optical pyrometry allowed to infer a shock speed of $\sim$ 17.5 μm.ns^{-1} averaged over all the target layers (silver tracer, carbon layer and cone tip).

The target hydrodynamic evolution due to compression was characterized by X-ray point projection radiography, using a 10 μm thick copper foil irradiated by a $\sim 10^{19}$ W.cm^{-2} short pulse laser beam, generating intense X-rays dominated by Cu-K$_\alpha$ emission, probing the cone target at different times of the compression. This method, of primary interest to diagnose rapidly transient shock propagation phenomenon, allowed us to obtain in the same shot the position of the shock front and of the Ag/C interface. These data are fairly well reproduced by numerical simulations, allowing to infer the shock speed and the fluid velocity, and thus the pressure and density of the shocked region via the Rankine-Hugoniot relations. In addition, the cone tip structure could also be seen at late times of compression, showing the survival of the cone structure despite the $\sim$ 3.5 Mbar pressure exerted on it. The X-ray point projection technique used in this experiment is a valuable diagnostic for HEDP studies. This is especially important for shock ignition experiments where one widespread diagnostic, called VISAR (Velocity Interferometer System for Any Reflector) using visible light to measure shock speeds [Barker & Hollenbach, 1972] , is often blinded by the preheating caused by the laser pulse [Laffite et al., 2014]. The presented X-ray point projection technique is also an alternative to ns-scale backlighters that allow to measure on a single shot the shock and fluid velocities. This method allows to get around the energy fluctuation issue, but in return, it is more sensitive to misalignment issues and that does not allow checking of the planarity of the shock front in each laser shot.

5.3 Step 2: Fast electron transport in cone target

The second experiment is dedicated to study fast electron generation and transport in the shocked cone targets which was described in the previous section. The fast electrons generated by a high contrast short laser pulse interacting with the cone tip at different moments of target compression.

5.3.1 Experimental setup

The experimental setup is presented in Fig. 5.14. The targets used in this experiment were fairly similar to the design presented in section 5.2.2, with however slight changes in the target conception. The rear side tracer, used to characterize the fast electron beam energy transport inside the target, is in this case a copper tracer located 50 μm from the cone tip, instead of a silver tracer located 100 μm from the cone tip (Fig. 5.15). This modification indeed offers the possibility to image at the same time the K_α emission from both the copper coated cone and the tracer, as described further in this section. A dual laser beam configuration is used to generate fast electrons at different time moments of compression. The used long and short pulse characteristics are the following:

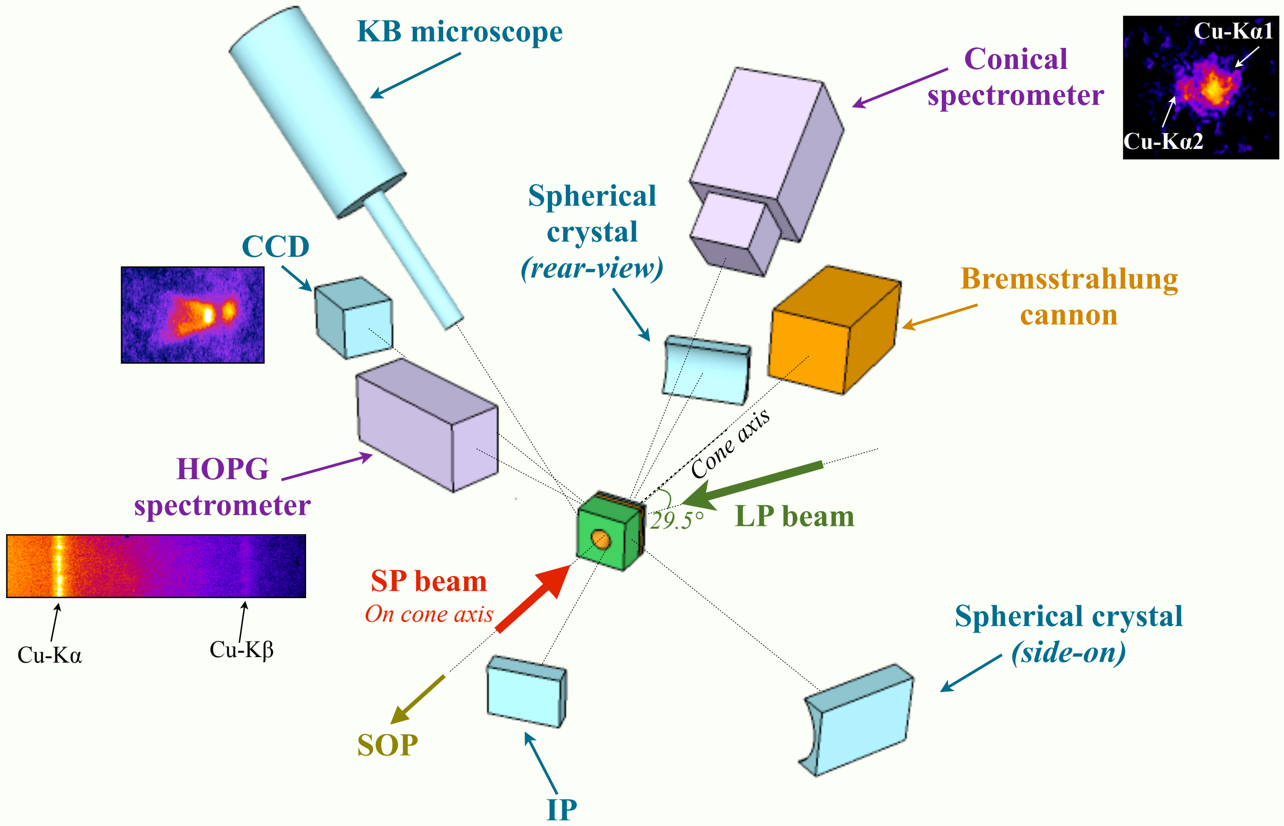

Figure 5.14: Illustration of the experimental setup used on the second LULI campaign.

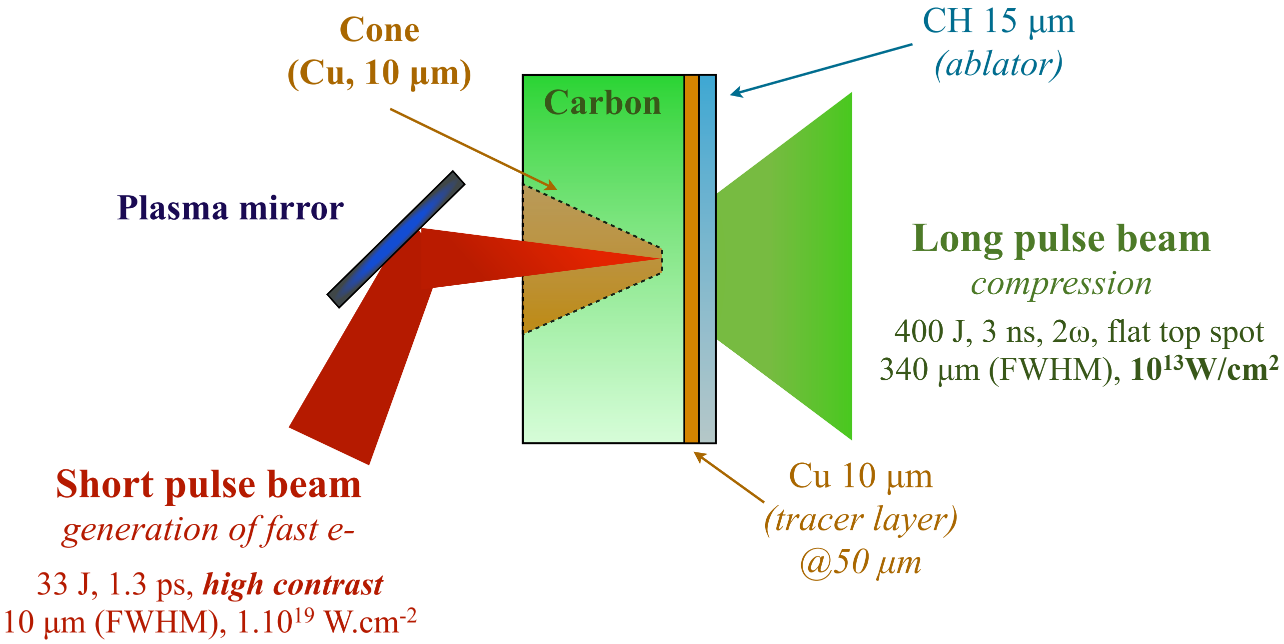

Figure 5.15: Target design used in the second LULI experiment. A 10 μm copper tracer is inserted at the rear side of the target 50 μm from the cone tip.

- The frequency doubled long pulse beam ($\lambda_L = 0.53$ μm), carrying 496 ± 50 J, is focused, at a 29.5° angle with respect to the target axis, on the 15 μm rear side plastic layer acting as an ablator, generating a planar compression shock. It is characterized by a 3 ns square temporal profile. The pulse is focused on the target by a combination of a random phase plate with a lens, resulting in an optically smoothed second order super-gaussian focal spot, with a 340 μm FWHM, and carrying 61% of the total laser energy, yielding an intensity of 10^{13} W.cm^{-2}.

- The LULI short pulse laser beam ($\lambda_L = 1.053$ μm), carrying 55 J of energy, and sent along the cone axis, creates a fast electron source. The pulse, characterized by a 1.3 ps FWHM gaussian temporal profile, is focused by a $f/4$ off-axis parabola. As mentioned in section 5.1.1, the LULI short pulse beam is characterized by a 1.1 ns pedestal generated by the ASE. This pedestal is highly detrimental is our study since it can ablate the cone tip, which hides any effect of the shock breakout inside the cone. A plasma mirror is mounted in the LULI chamber allowed us to suppress deleterious pre-plasma effect. The detailed set-up of the plasma mirror is presented in section 5.3.2. The energy on target measured after reflection from the plasma mirror is 33 J, with a plasma mirror efficiency of 60%, yielding an intensity on target of 1×10^{19} W.cm^{-2}.

The short pulse beam duration is determined using the third order cross-correlator "Sequoia" developed by Amplitude Technologies [Amplitude, 2014]. This instrument offers the possibility to measure temporal laser pulse shapes over a 270 ps range with the dynamic range $> 10^8$, and with a resolution of 20 fs. This features are sufficient to measure the ASE pedestal. However, considering that the LULI short pulse beam is characterized by a ∼ns scale pre-pulse, the sequoia instrument was only used to measure the pulse duration. The basic principle of such a measurement, illustrated in Fig. 5.16, can be explained by the following. The laser pulse is initially divided into two sub-pulses, one of them going through a fixed optical path while the second one going through a delay line, before being frequency doubled with a non-linear crystal. The two pulses then cross each other in a second non-linear crystal, generating a 3ω

signal along the bisecting line if the pulses are temporally over-imposed. The signal intensity, amplified by a photomultiplier (PtM), is proportional to the cross-correlation function of the incoming signal:

$$I_{3\omega}(\tau) = \int_{-\infty}^{+\infty} I_{\omega}(t).I_{2\omega}(t-\tau)dt \tag{5.7}$$

Assuming a Gaussian pulse shape (Fig. 5.16), the cross-correlation function is also a Gaussian function given by:

$$I(t) = a_0 \exp\left[-\frac{(t-a_1)^2}{2a_2^2}\right] + a_3 \tag{5.8}$$

with its FWHM given by $2\sqrt{2\ln 2}a_2$, and $a_2 = 0.78$ ps, related to the incident pulse FWHM by

$$\mathrm{FWHM_{pulse}} = \frac{\mathrm{FWHM_{cross\text{-}corr}}}{\sqrt{2}} = \frac{2\sqrt{2\ln 2}a_2}{\sqrt{2}} = 1.3 \text{ ps} \tag{5.9}$$

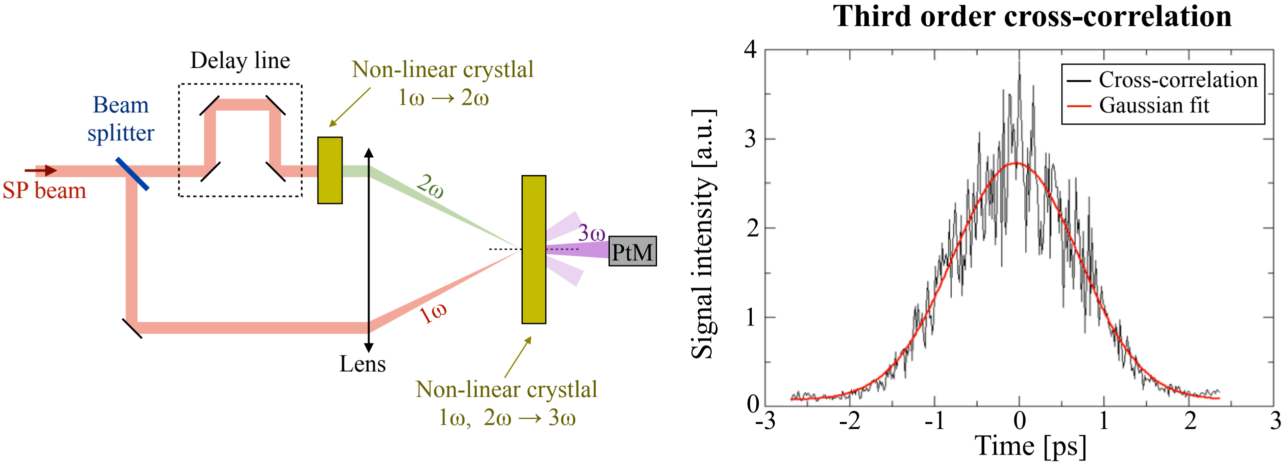

Figure 5.16: (Left) Scheme of a third order cross-correlator. (Right) Experimental cross correlation function (black solid line) and its Gaussian fit (red solid line) obtained for the LULI SP beam.

The delay between the SP and LP laser pulses is adjusted so that the electron beam is created at the desired times of compression, either in a solid or compressed cone tip, or in an expanding plasma at later times. The target compression, as well as the fast electron generation and transport are characterized by several diagnostics:

- Streaked optical pyrometry: the target composition, with a copper rear side tracer located closer to the cone tip, as well as the different characteristics of the LP laser pulse compared to the first campaign, implied to measure again the shock breakout time from the cone tip. This measurement allowed us to synchronize the two laser pulses and to calibrate hydrodynamic simulations. It is performed by detecting the shock-breakout induced thermal emission from the cone tip with a streak camera. The SOP line is represented in Fig. 5.17.

- Two HOPG and conical spectrometers are used to measure the copper K_α emission generated in the interaction of fast electrons with copper atoms in the cone and in the rear side tracer. The absolutely calibrated HOPG, from the university of San Diego (also used in the Titan experiment described in chapter 4), was located 5° from the target normal in the equatorial plane. The conical spectrometer, which was not absolutely calibrated, was located on the LP beam axis at 45° above the equatorial plane.

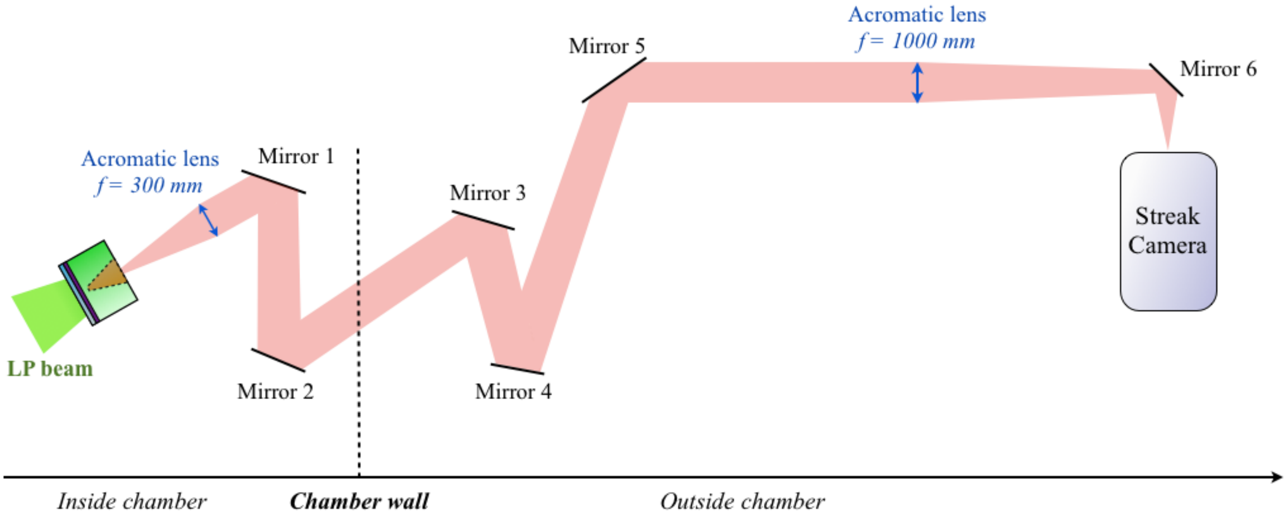

Figure 5.17: Illustration of the SOP line used to measure the shock breakout time from the cone tip.

- Three Cu-K$_\alpha$ imagers are fielded into the chamber. A first spherical crystal, imaging the emission of the cone and of the tracer from the side of the target (side-on imager), is located at 27.4° from the target normal. The required high magnification > 7.3 forced us to position the detector, an Andor CCD camera, at ~ 2.3 m from the target chamber center (TCC), well beyond the chamber walls, in a vacuum extension. A 0.5 T magnet is located at $\sim$ 0.8 m from the TCC in order to deviate fast electrons ejected from the target from the detector, and thus to decrease the background noise. In addition, a circular collimator located on the signal path and a lead block prevented any direct irradiation of the detector from the TCC and also decreased the background noise (Fig. 5.18). A second spherical crystal, located at 13.5° from the SP beam axis, is used to image the Cu-K$_\alpha$ emission from the rear side of the target. The detector, made of a MS-type imaging plate, was located $\sim$ 70 cm from the TCC, yielding a magnification of 3.9. It is worth mentioning that lead blocks were also set-up between the K$_\alpha$ source at TCC and the detector in order to avoid its direct irradiation and to consequently decrease the noise level signal. The optimization of the lead shielding, of primary importance in our experiment, is not a trivial issue and requires several shots in order to find to best configuration.
  A Kirkpatrick-Baez microscope is fielded at 15° from the target normal and 50° above the equatorial plane. This diagnostic, from the University of Alberta, is the same that was used in the Titan experiment described in the previous chapter.

- A bremsstrahlung cannon is fielded at the rear side of the target along the SP beam axis in order to characterize the fast electron spectrum.

5.3.2 Plasma mirror optimisation

The absolute necessity to remove the SP beam pedestal require to set a plasma mirror (PM). The optimization of such an optical switch is described in this section.

The plasma mirror is made of a thick silicate plate mounted in the chamber in order to reflect the LULI SP beam along the cone axis, at a 29.5° with respect to the LP beam axis. The plasma mirror optimization phase consists in finding the optimum position so that the SP

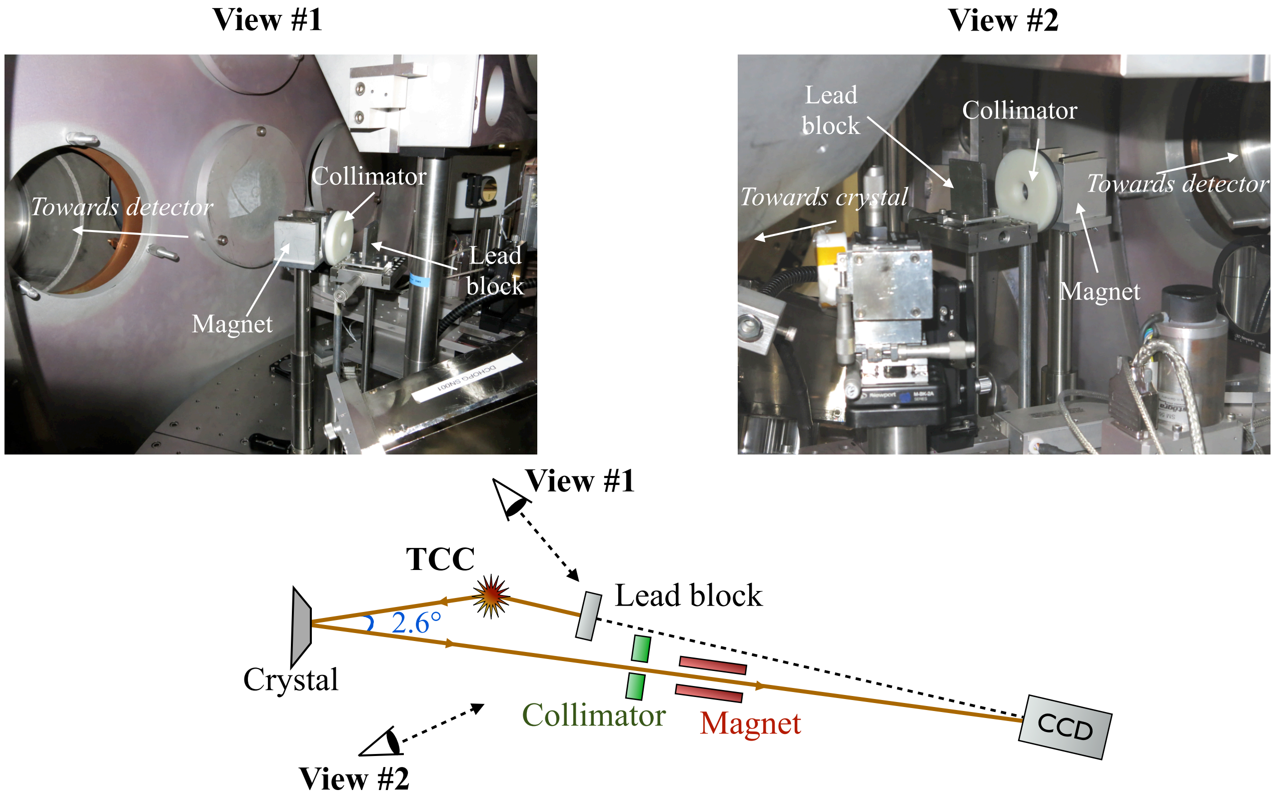

Figure 5.18: Images of the experimental setup showing the magnet, the collimator and the lead block used for the spherical imager with the higher magnification.

beam pedestal is cleaned enough, but also that the fraction of reflected energy is the highest possible. The fluence on the plasma mirror should be between 100 J.cm^{-2} and 300 J.cm^{-2}, the optimum value depending of the intrinsic SP initial contrast. The amount of pre-pulse after reflection of the plasma mirror is measured by recording and analyzing the homogeneity pattern of the SP beam using two different setups, labelled A and B, presented in Fig. 5.19. The reflectivity is measured by inserting a calorimeter after the TCC, and by comparing the measured energy value with the SP energy measured after the pulse compression (setup C in Fig. 5.19). A scheme of steps for the plasma mirror optimization is presented in Fig. 5.20. In the first setup A, the SP beam is focused on a thin cover glass that is normally designed for microscopy. The reflected pulse is then sent on a frosted glass located on the specular direction of the incident laser light, at a few tens cm distance, and recorded by a CCD camera. If the homogeneity pattern is judged insufficient, either the pre-pulse level or the fluence on the PM are too high, the setup B has been used. Fig. 5.21 presents a picture of the plasma mirror after 3 laser shots. Due to the 19° incidence angle of the SP beam, the pulse forms an ellipsoidal impact with a measured aspect ratio $a/b = 0.32$, with a and b the major and minor radii of the ellipse, respectively, yielding a laser fluence of $\sim$ 138 J.cm^{-2}. The experimental aspect ratio value is fairly close from the theoretical value given by $a/b = a/[a/\sin(19°)] = 0.33$. A protective aluminum foil located in front of the clean surface of the plasma mirror allowed us to avoid any plasma projection as seen in older laser impacts in Fig. 5.21.

When both the pattern uniformity and the mirror reflectivity are optimized, an ultimate test is performed in order to validate the pre-pulse level. The SP is focused after reflection on a 20 μm gold foil, generating an intense proton beam by the TNSA mechanism, the maximum ion energy achievable being much lower if the pre-pulse level is high. The accelerated proton beam then interacts with a stack of dosimetric radiocromic films located at 29 mm from TCC. RCFs

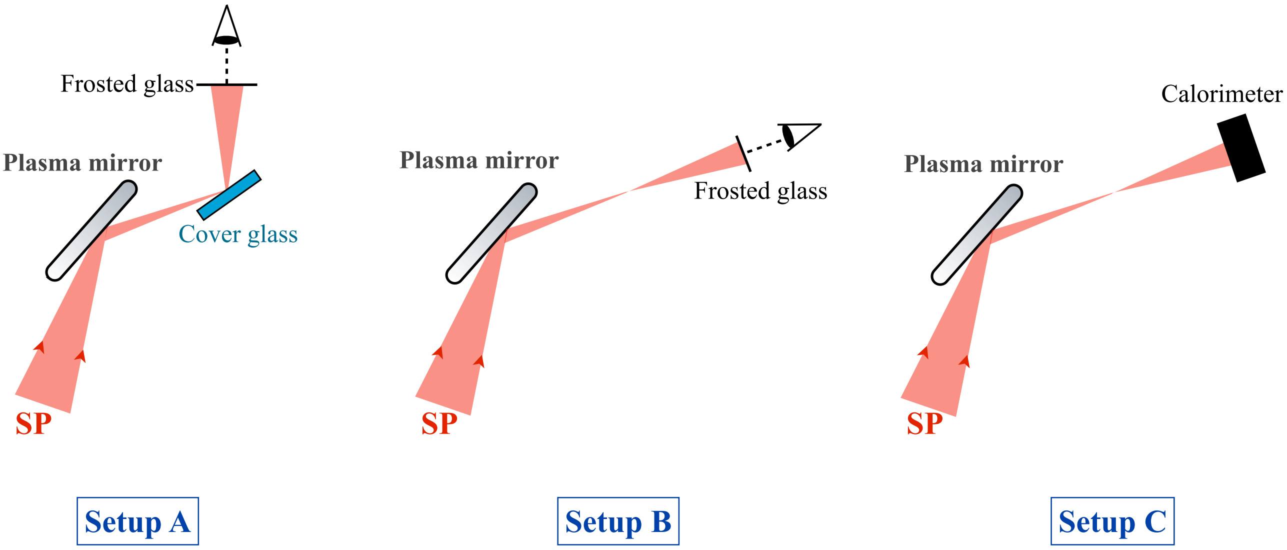

Figure 5.19: Illustration of the different setups, labeled A, B and C, used for plasma mirror optimization. The plasma mirror efficiency η_{PM} is measured with setup C.

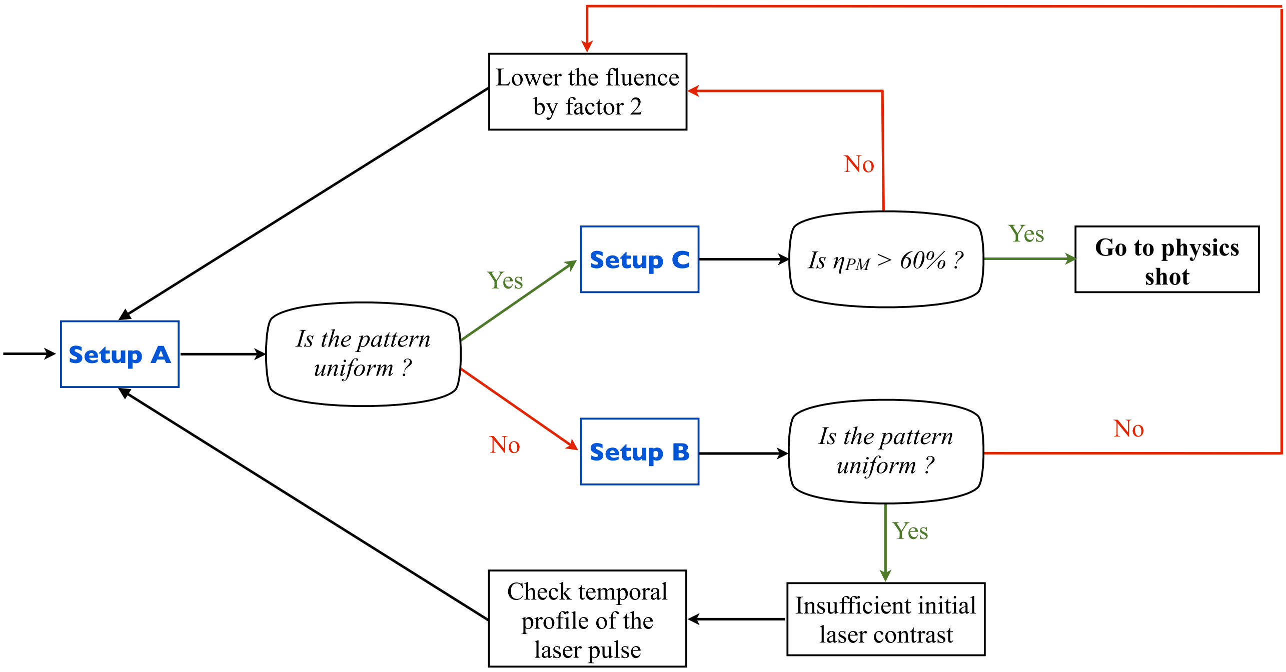

Figure 5.20: Illustration of the plasma mirror optimization process.

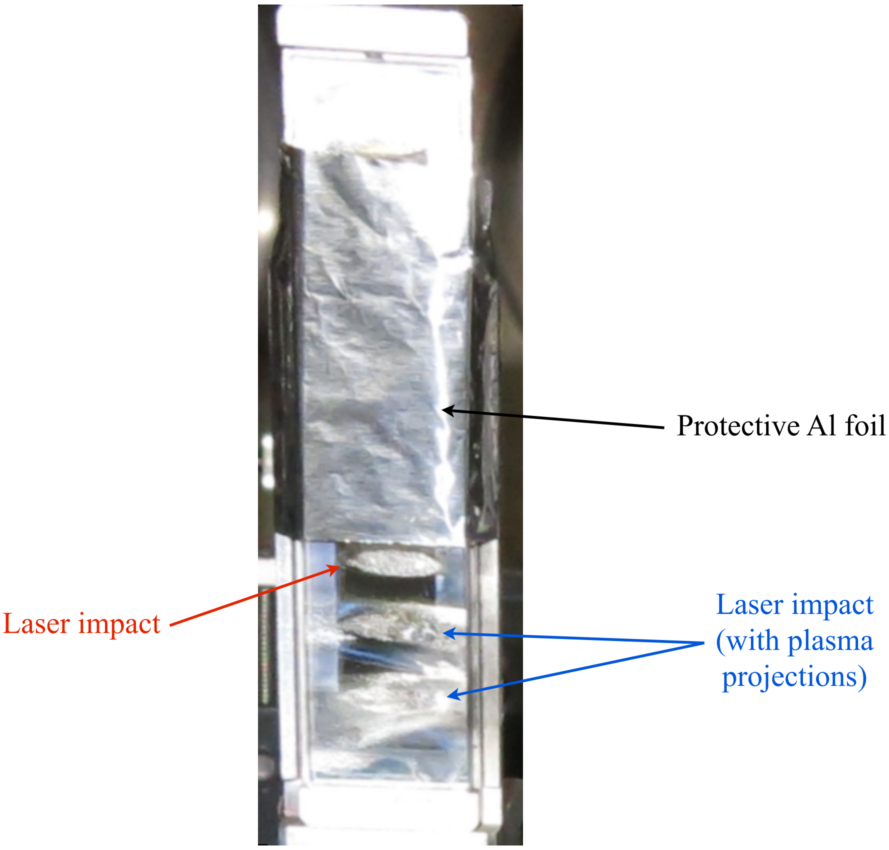

Figure 5.21: Picture of a plasma mirror with three ellipsoidal laser impacts.

are composed of a multilayer structure which includes an active layer that undergoes a chemical reaction when exposed to ionizing radiations. The active dye turns from white to blue, the optical density being directly related to the dose deposited into the film. RCF are commonly used in stacks to measure an accelerated proton spectrum, or the maximal ion energy, the latter being defined as the proton energy required to deposit a dose on the last marked film in the stack. We use in this experiment a stack of 5 HD-810 films followed by 10 MD-v2-55 films, the former being less sensitive and thinner than the latter. Experimental measurements are presented in Fig. 5.22. The presence of a dose up to the 10th MD film, showing that ~ 20 MeV protons are accelerated, and consequently confirming the very low level of pre-pulse.

The plasma mirror efficiency was measured with setup C by putting a calorimeter at 31 cm from the target chamber center. This particular distance was calculated so that the laser fluence did not exceed $F_{\text{max}} \sim 1$ J.cm^{-2} in order to avoid irreversible damage of the calorimeter. The plasma mirror efficiency is given by:

$$\eta_{PM} = \frac{E_{\text{TCC}}}{E_{BC} . \eta_{\text{comp}}} \tag{5.10}$$

with $E_{\text{TCC}} = 35.16$ J the energy measured at TCC after reflection on the plasma mirror, $E_{BC} = 94$ J the energy measured before SP compression and $\eta_{\text{comp}} = 59\%$ the compression efficiency, yielding a plasma efficiency $\eta_{PM} \sim 63\%$.

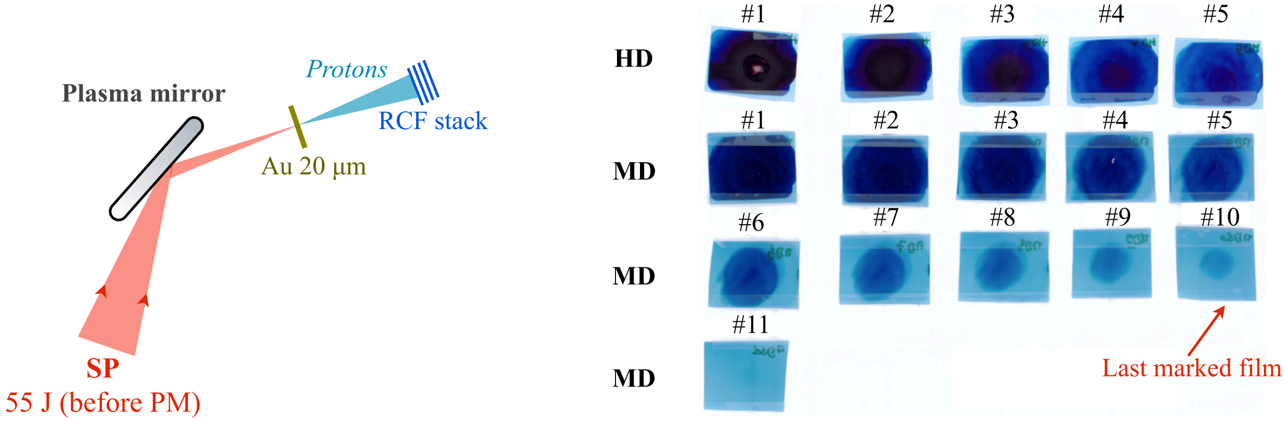

Figure 5.22: (Left) Illustration of the maximum proton energy measurement setup. The protons, accelerated in the interaction of the SP beam after reflection from the plasma mirror with a 20 μm Au foil is measured by a RCF stack (right) made of 5 HD films, followed by 11 MD films. The last marked film being the 10th MD film, the maximum proton energy is $\sim$ 20 MeV.

5.3.3 Synchronization of the laser pulses

One of the key issues in this study is the characterization of the delay between the two laser pulses. Since both the target design and the LP beam characteristics were changed compared to the first experimental campaign presented in section 5.2, the measurement of the shock breakout time from the cone tip was achieved by the streaked optical pyrometry using the setup presented in Fig. 5.17.

The shock breakout thermal emission from the cone tip was generated by focusing the LP beam, carrying 428 J of energy, on a cone target. Its design is presented on Fig. 5.15. It is compared to a reference signal obtained by sending the LP beam at a low flux in the streak camera. The SOP signal is presented in Fig. 5.23. A thick aluminum piece, much larger than the target size and with a central hole of 1 mm larger than the LP beam focal spot was attached to the front side of the target target in order to limit the background noise level on the streak camera. A notch filter cutting the 2ω light emission from the laser pulse is set-up right in front of the streak camera slit in order to suppress the noise level. The shock breakout time is estimated to 2.9 ± 0.2 ns. The estimated error is smaller than the one obtained in section 5.2 due to the smaller slit aperture of ~ 100 μm instead of ~ 300 μm.

The shock breakout time from two 20 μm aluminum foils was also measured. This is used in section 5.3.5 to calibrate hydrodynamic simulations of the target compression. The shock breakout images were compared to reference images obtained by sending the LP beam at a low flux in the streak camera. Two sweep time ranges of 5 ns and 20 ns are used (Fig. 5.24). Shock breakout times are 0.8 ± 0.2 ns and 0.6 ± 0.2 ns, respectively, yielding a mean shock breakout time of 0.7 ± 0.2 ns. The corresponding shock speed averaged over the thickness of the aluminum foil is $v_{\mathrm{alu}} = 28 \pm 8$ μm.ns^{-1}.

5.3.4 Experimental results

In all laser shots in this campaign implying the use of both the SP and LP beams, an additional shielding was attached to the target in order to decrease the noise level on the diagnostics. This shielding, presented in Fig. 5.25, is made of a 10 μm aluminum foil glued on a 100 μm thick mylar foil, the latter being directly glued to the target.

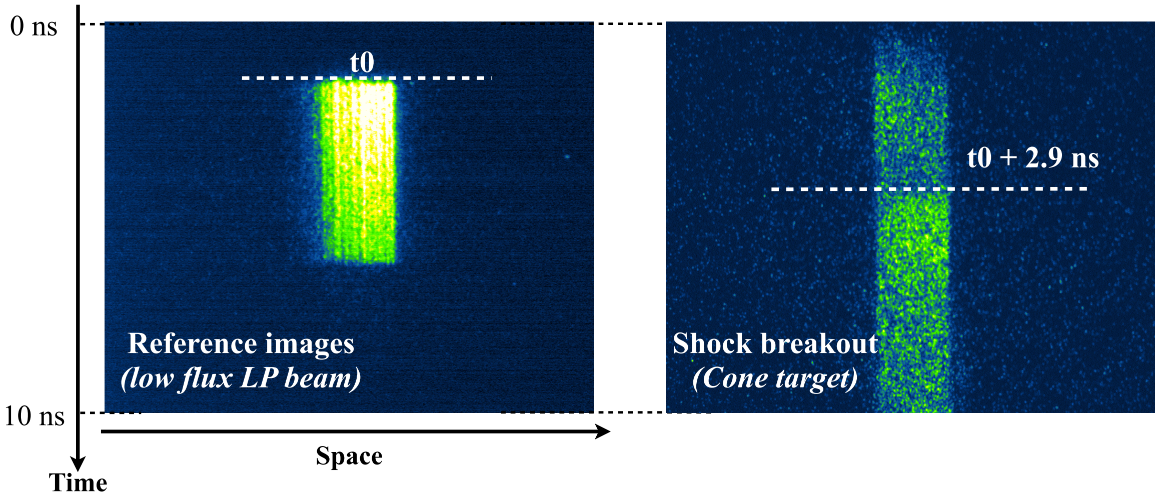

Figure 5.23: (Left) Reference signal obtained by sending the LP beam at low flux directly into the streak camera. (Right) Experimental shock breakout obtained by sending the 428 J LP beam on a cone target including a copper tracer located at 50 μm from the cone tip. The determination of the shock breakout time, 2.9 ns, is obtained by comparing the two images. A 10 ns sweep time range is chosen in the two cases.

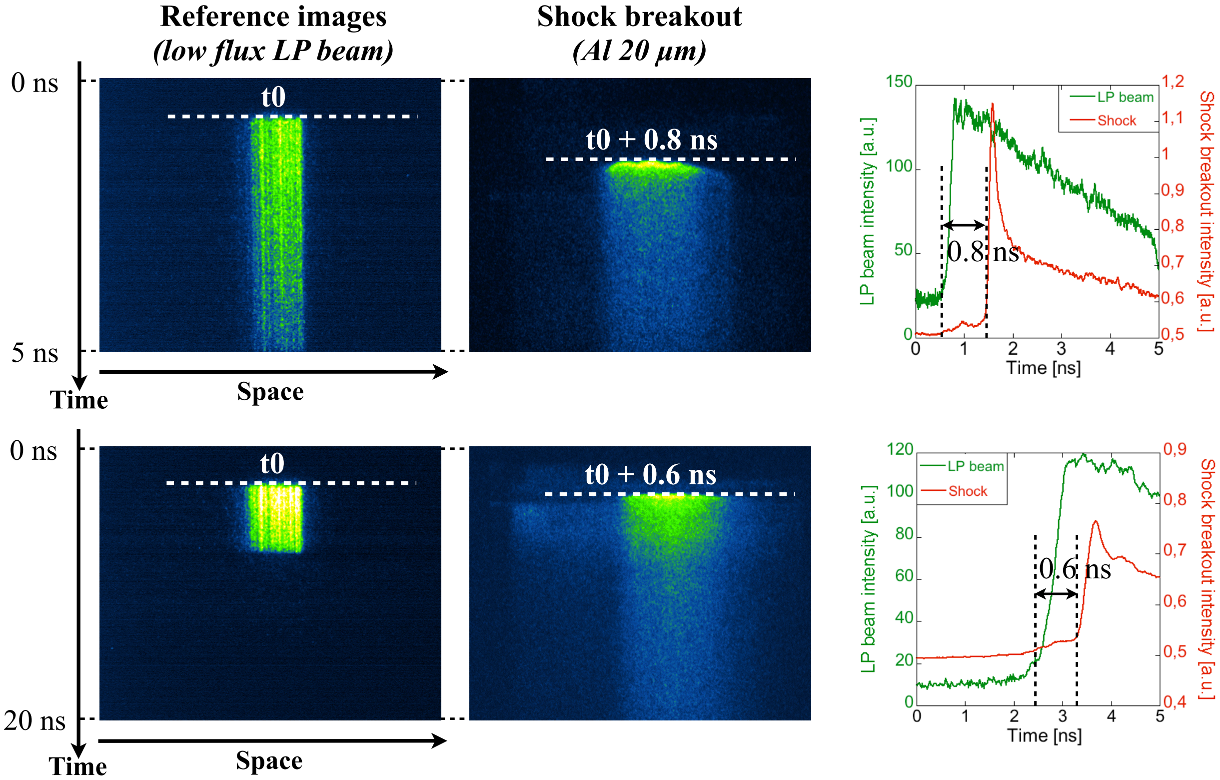

Figure 5.24: (Left) Reference signals obtained by sending the LP beam at a low flux to the streak camera. The sweep time ranges are 5 ns (up) and 20 ns (down). (Middle) Experimental shock breakout obtained by sending the 414 J (up) and the 517 J (down) LP beam on cone targets including a copper tracer located at 50 μm from the cone tip. The shock breakout time (right) is obtained by comparing two images with two reference signals, yielding 0.8 ns (up) and 0.6 ns (down).

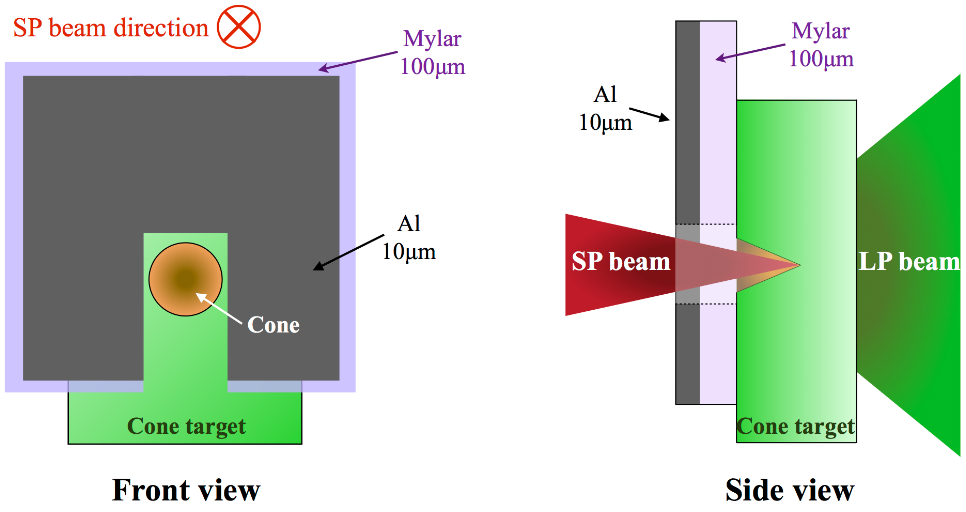

Figure 5.25: Front (left) and side (right) views of the additional shielding attached to the target in order to decrease the background noise level on the diagnostics. The shielding is made of a 10 μm thick aluminum foil glued to a 100 μm thick mylar foil.

Cu-K$_\alpha$ spectrometers

Two spectrometers, using a HOPG and a conical crystal, are fielded into the experimental chamber. Both of them are dedicated to measure the Cu-K$_\alpha$ emission generated in the interaction of fast electrons with copper atoms in the cone coating and in the rear side tracer. The HOPG spectrometer is absolutely calibrated.
The deconvolution process of the conical spectrometer is more straightforward since it was not absolutely calibrated. The background noise was firstly subtracted from the experimental image. An horizontal lineout is then taken on the image and integrated in order to measure the Cu-K$_\alpha$ yield. Experimental measurements obtained with the HOPG spectrometer and the conical spectrometer are presented in Fig. 5.26. A decreasing trend for late time of compression can be seen in the two diagnostics. It is clearly visible even considering the dispersion of experimental results due to the high background noise level generated in this experiment despite the crystal shielding. This noise level also affects other diagnostic results as detailed in the next section.

Cu-K$_\alpha$ imagers

Three imagers are fielded into the LULI chamber, using two quartz spherical crystals, looking at the side and at the rear of the target, and a Kirkpatrick Baez microscope. As mentioned in section 5.3.1, the side-on imaging system uses a CCD camera as a detector. However, during the optimization phase of this diagnostic, a MS-type imaging plate is used. Its main disadvantage compared to the CCD relies on the necessity to extract the IP after each shot, and to the subsequent possible repositioning error made by an user. Fig. 5.27 presents an image obtained using an IP as a detector in a shot with the SP beam only. One can clearly see the Cu-K$_\alpha$ emission from the cone tip and from the tracer located at 50 μm from the cone tip.

Experimental results obtained with the side-on imager and using the CCD camera as a detector are presented in Fig. 5.28 as a function of the delay between the two laser pulses, or in other words, as a function of the fast electron beam injection time. The color scale is the same in all panels. The second column, labeled "0 ps", is obtained by shooting the SP and LP beam at the same time.

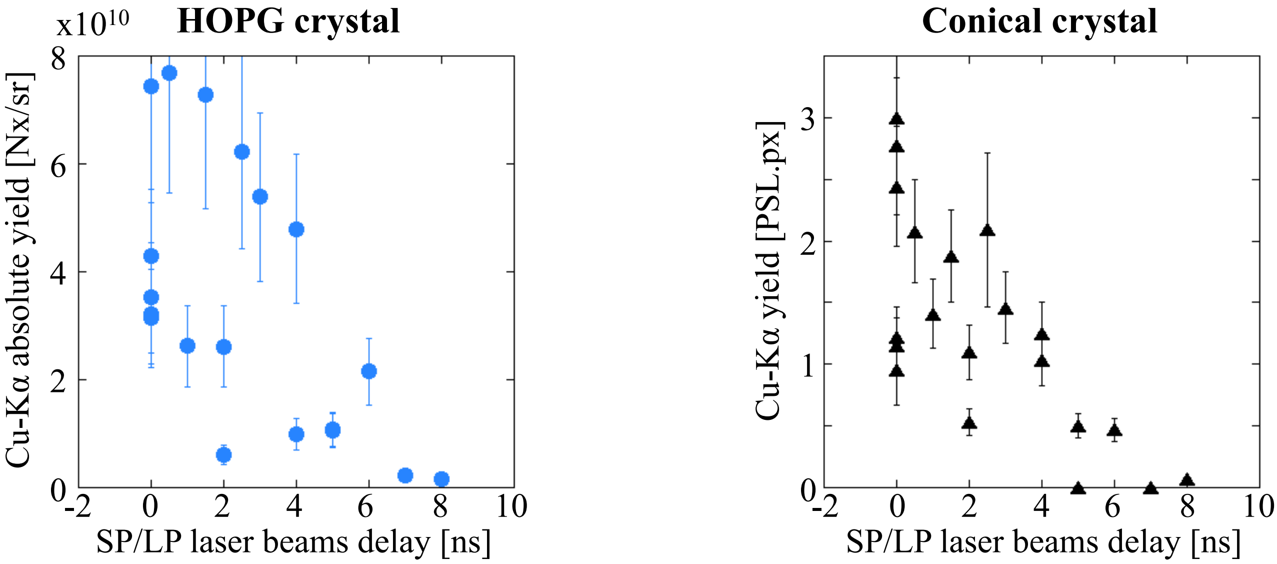

Figure 5.26: Experimental measurements of Cu-K_α yields with the HOPG spectrometer (left) and the conical spectrometer (right) as a function of the delay between the two laser pulses, the LP beam always being fired before the SP beam. The HOPG spectrometer is absolutely calibrated.

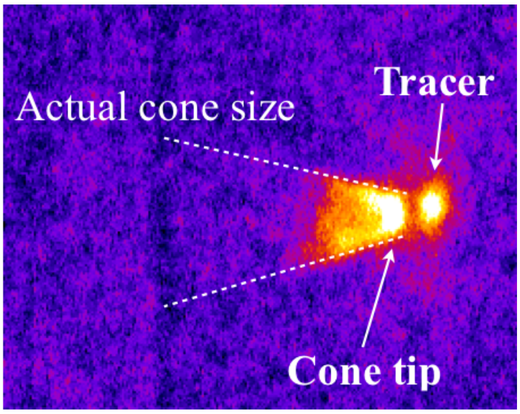

Figure 5.27: Experimental image obtained with the side-on spherical crystal. Only the SP beam is fired for this shot. The actual structure of the cone is indicated by the white dashed line.

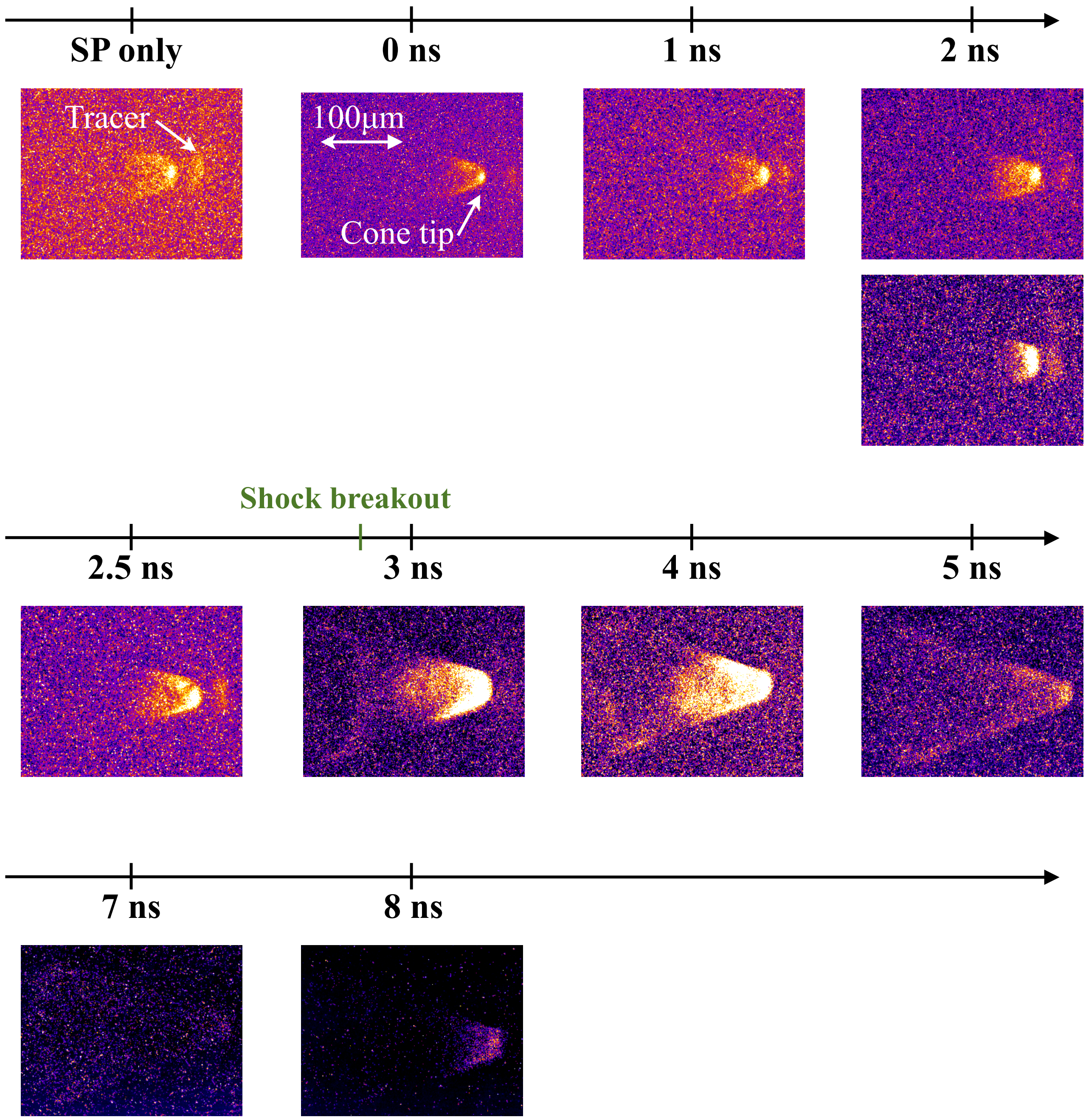

Figure 5.28: Experimental results obtained by side-on Cu-K_α imaging. The color scale is the same for all images. The delay between the two laser pulses increases from left to right and from top to bottom. The LP beam is always fired prior to the SP beam. The first column, labeled "SP only", is obtained without any LP beam. The second column, labeled "0 ns", is obtained by sending the two laser pulses at the same time. The 2.9 ns shock breakout time is labeled in green.

At early time of compression, one can see that the emission comes from the cone tip. The high-contrast SP beam was thus efficiently coupled to the cone tip, and the fast electrons were generated within this particular region. The emission from the rear side tracer is also clearly visible. This figure shows that a significant fraction of the fast electron energy is transported into the target depth, to the copper tracer layer. The tracer emission seems to be created closer to the cone tip when the delay between the two laser pulses increases. This can be explained assuming that the copper tracer is pushed towards the cone due to the shock-induced target compression. It was expected from the velocity of the Ag tracer on the above described first experimental run and will be confirmed by hydrodynamic simulations of the target compression presented in section 5.3.5.

When injecting the fast electron beam after 3 ns of compression, the image of emission completely changes. It comes not only from the cone tip, but also from the cone walls. The entire cone structure can clearly be seen at late time of compression. The K_α line emission comes from the entire volume of the cone. This can be explained by the fact that the shock breaks out from the cone tip at 2.9 ns, as demonstrated in section 5.3.3. Consequently, at 3 ns, the fast electrons are generated in an expanding copper plasma filling progressively the entire volume of the cone. This explanation will be checked with hydrodynamic simulations. The emission from the cone tracer disappeared. This could be explained by the fact that the copper tracer have been pushed so close to the cone tip that the experimental resolution of the imager ($\sim 10\ \mu$m) was not sufficient to separate its emission from the cone tip.

When injecting the fast electron beam 5 ns after the beginning of the target compression, the emission from the whole cone structure can be seen. At 7 ns, the spherical imager collects only a fairly faint signal, which however still shows the cone structure. At 8 ns, the only barely visible emission comes from the initial position of the cone tip.

It is necessary at this point to discuss the consistence of the side-on imager and the spectrometer results. The decreasing trend of the Cu-K_α signal is not so obvious in the images. However, the number of exploitable images obtained in the experiment is considerably smaller than the number of recorded spectra. The set-up of the side-on spherical imager is much more complex. Such a diagnostic is also sensitive to the background noise, which prevents the rear-view spherical imager from providing exploitable data despite an efficient shielding.

The obtained images allow to estimate the fast electron beam divergence in unperturbed targets, obtained by using the SP beam only. Two target designs were used for this purpose. The first one is presented in this section. The second one, referred as type B, is fairly similar, except that the copper tracer is located 100 μm from the cone tip instead of 50 μm. These targets were used in the experiment only for this the measurement of the electron beam divergence. Fig. 5.29 presents two images obtained with these two targets. The Cu-K_α emission is located further from the cone tip in the right image, obtained with the type B target. The divergence is calculated by measuring the extension of the Cu-K_α emission from the cone axis, yielding a value of $(30 \pm 5)^\circ$. This value, calculated using two shots only, can be only considered as a rough estimate of the fast electron beam divergence inside the target.

5.3.5 Hydrodynamic simulations of the target compression

A more careful analysis of the side-on images presented in the previous section requires a full characterization of the target compression. A set of 2D hydrodynamic simulations was

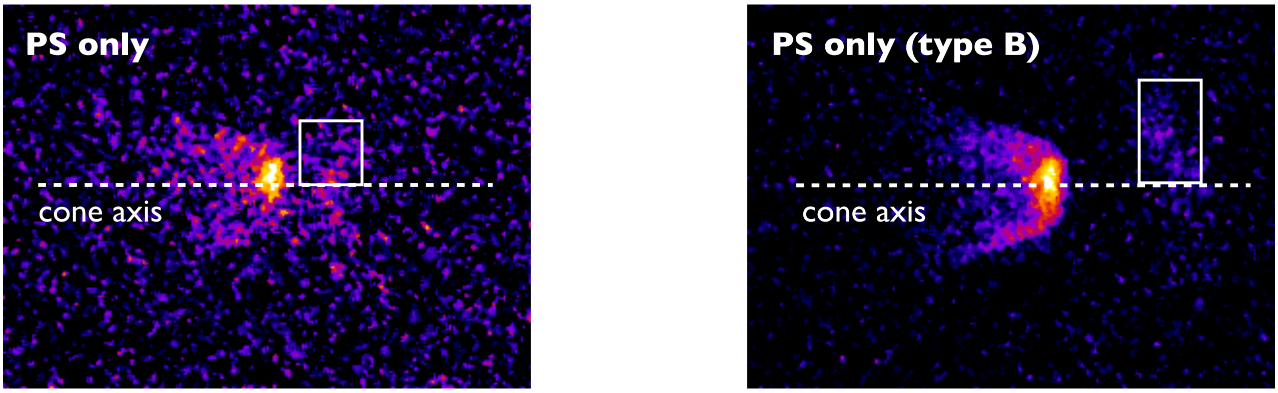

$d_{\text{cone-tracer}} = 50\ \mu\text{m}$

$d_{\text{cone-tracer}} = 100\ \mu\text{m}$

Figure 5.29: Experimental images obtained by sending only the SP beam on the target including a copper tracer at 50 μm from the cone tip (left) and at 100 μm (right). The extension of the Cu-K$_\alpha$ tracer emission is indicated by the white rectangle on the upper part of the two images.

performed with the Lagrangian CHIC code by Philippe Nicolaï and Jerôme Breil (CELIA laboratory, France). The 2D geometry of the simulation is in this particular case mandatory because of the presence of the cone structure.

Due to its complexity, the simulation was subdivided into three steps. The first one, used to calibrate the simulation, consists in simulating the compression of a 20 μm aluminum foil in order to reproduce the shock breakout time measured experimentally in section 5.3.3. At the second step, the compression of a simplified target without cone was simulated, which by itself presents serious numerical challenges. The cone was represented by a 7 μm copper layer imitating its tip (Fig. 5.30). The results of target compression are presented in Fig. 5.31 for two fast electron beam injection times of 2.4 ns and 3.0 ns after the beginning of LP beam irra-

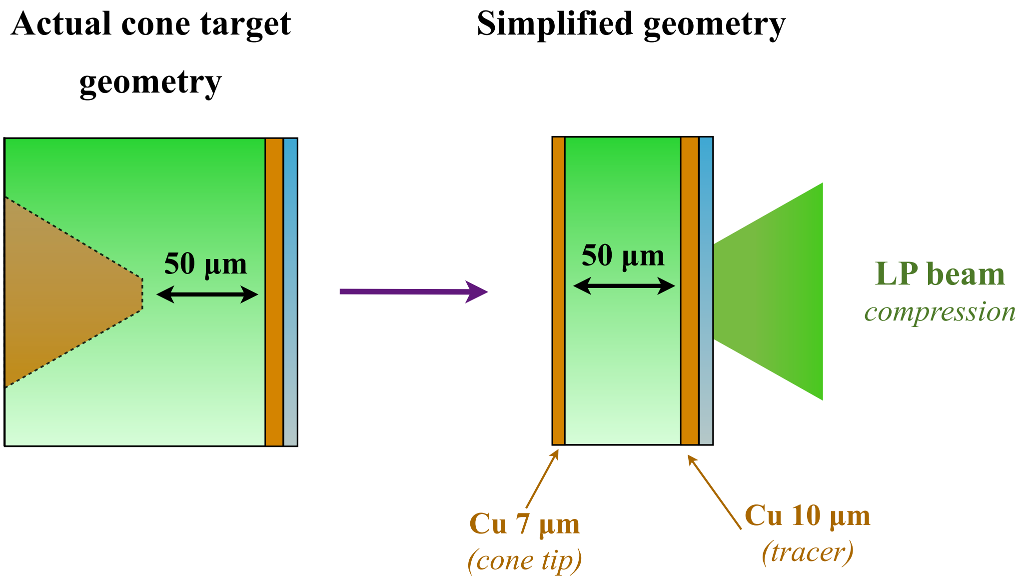

Figure 5.30: Illustration of the simplified cone target geometry (right) used in hydrodynamic simulations. The cone shape is not taken into account. The cone tip is imitated by a 7 μm copper layer extending over the whole target height.

diation. The LP beam strikes the target from the right-hand side. The lower parts of the plots represent the unperturbed target at the solid density. At 2.4 ns, the shock almost compressed the entire carbon layer, and it is close to the cone tip. At 3 ns, the cone tip is fully compressed and the shock approaches the rear target surface. The numerical shock breakout time of 3 ns is in good agreement with the time 2.9 ± 0.2 ns measured experimentally. 1D density and temperature profiles of the target compression at different delays were extracted from the 2D simulation. Fig. 5.32 presents such plots for different delays of compression. The unperturbed target plot (left) allows to see the structure of the target, with the cone tip, the carbon layer, the copper tracer and the plastic ablator. At 3 ns (middle), the entire target is compressed and the shock is about to breakout. The carbon layer is heated up to a few eV. At 4.6 ns (right), representing the target state 1.6 ns after shock breakout, the cone tip is expanding into vacuum.

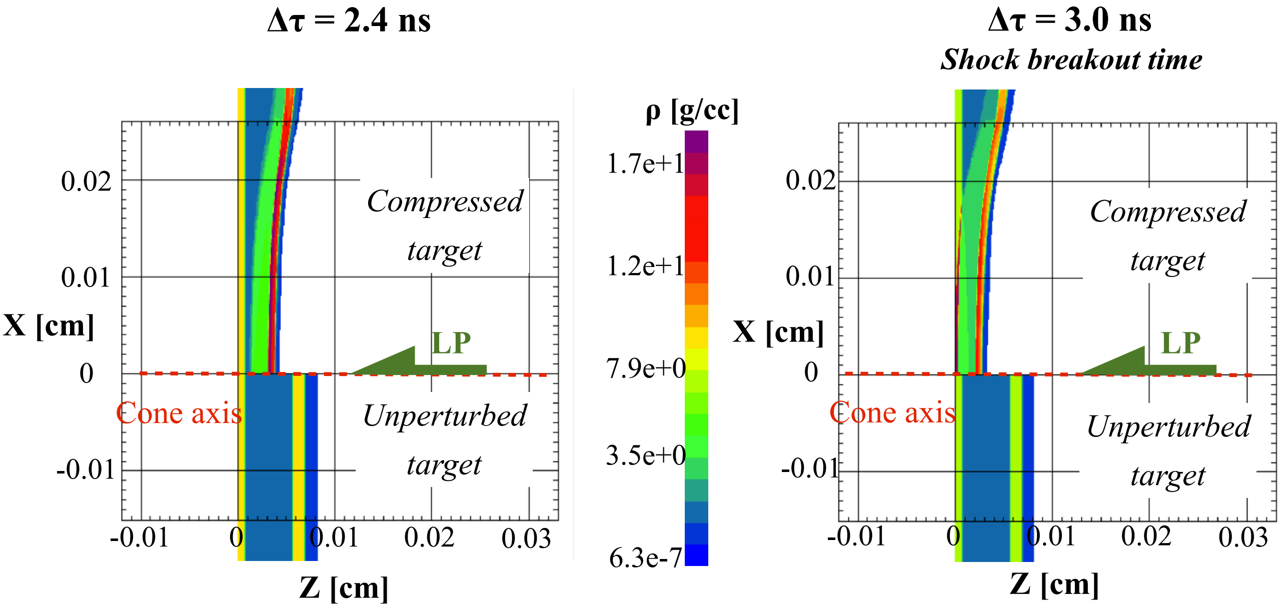

Figure 5.31: Density maps of the simplified target compression at 2.4 ns (left) and 3 ns (right) after the beginning of LP beam irradiation. The lower parts of maps represent the unperturbed target. The 3 ns delay is the simulated shock breakout time.

At the third step, the compression of the actual cone target was simulated. Fig. 5.33 presents 2D density and temperature profiles at different times of compression. In the first set of images labeled SP only, one can see the density and temperature of the unperturbed targets. The copper cone structure is clearly visible. The white dashed lines on the temperature profile indicate the inner part of the cone tip. The initial target temperature is set at 300 K. At 2.8 ns, the shock front has just reached the cone tip. The carbon layer is compressed at nearly twice the solid density. The copper tracer is pushed toward the cone tip. The rear side plastic layer is expanding into vacuum and heated from a few hundreds of eV up to a few keV. At 3.0 ns, the shock is about to breakout. The cone tip is fully compressed. At 3.8 ns, the cone tip is expanding into the cone. The shock front is sliding along the cone walls. On the edges of the cone tip, one can clearly see a vortex created by the shock compression. This vortex is responsible for the difficulty in running such simulations. As the CHIC code uses a Lagrangian scheme, the discrete cells are moving together with the fluid. For this reason the code cannot describe large distortions, such as the vortices created in our case, thus limiting the simulation time to 4.7 ns.

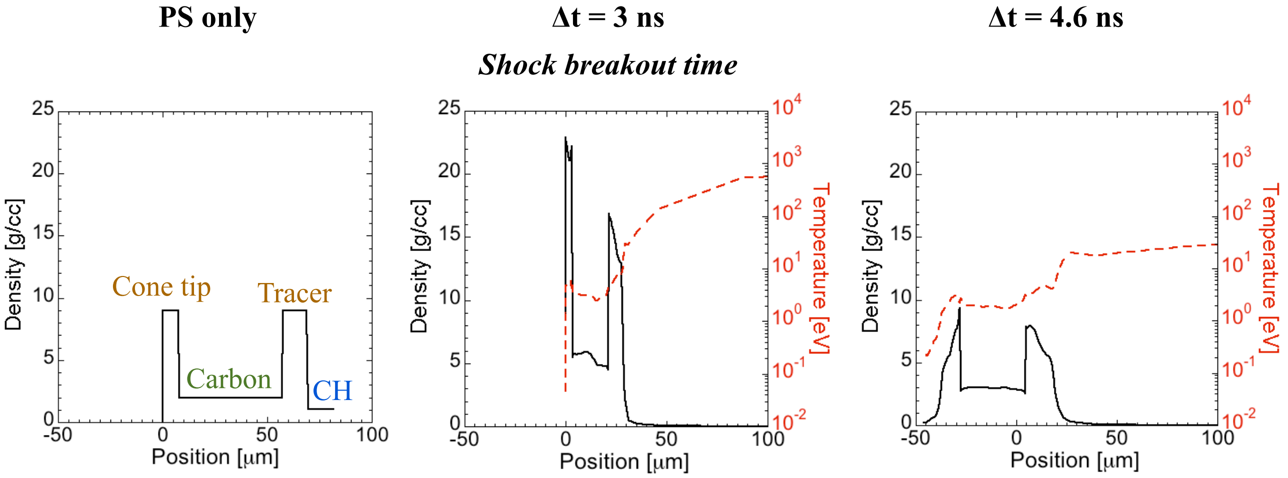

Figure 5.32: Density (black solid lines) and temperature (red dashed lines) 1D profiles extracted from 2D simulation on the cone axis for the unperturbed target (left), at 3 ns (middle) and 4.6 ns (right) after the beginning of LP beam irradiation.

The presented set of 2D hydrodynamic simulations allow to conclude on the Cu-K$_\alpha$ side-on images presented in section 5.3.4. At early time of compression, fast electrons are generated on the cone tip, which is characterized by a steep density gradient due the the absence of short pulse pedestal. The rear-side copper tracer is progressively pushed toward the cone tip. At later time of compression, after the shock breakout time, the emission from the tracer cannot be separated from the cone tip emission due to the lack of resolution. The cone is being filled with the copper plasma. Fast electrons are consequently generated on an expanding plasma in the entire volume of the cone. It is worth mentioning that the vortices are not experimentally observed due to the insufficient spherical crystal resolution close to 10 μm. These hydrodynamic conditions are used in the next sections as input of PIC and transport simulations.

5.3.6 PIC simulations of the fast electron source

In order to characterize the fast electron source in the experiment, the interaction of the high-contrast pico2000 short-laser pulse with the cone target was simulated with the OCEAN particle-in-cell code [Nuter & Tikhonchuk, 2013] in collaboration with Rachel Nuter at CELIA. In order to decrease the simulation time and to reduce the complexity of the simulation, we consider the 1D geometry of interaction, which does not allow to extract the fast electron angular distribution function. We present in this section the characterization of the fast electron source at different delays of injection.

PIC simulation parameters

The simulation box space-step is set at $\Delta x = 0.06\ c/\omega_L = 10$ nm. This value was chosen carefully as a compromise between the simulation precision and the simulation time. The time-step is calculated according to the so-called Courant-Freidrichs-Levy (CFL) condition, ensuring that the information does not propagate faster than the speed of light. The corresponding time-step is consequently given by $\Delta t = \Delta x/c = 0.06\ \omega_0 \simeq 3.3 \times 10^{-2}$ fs. The laser pulse is simulated by a $\tau = 5340/\omega_0 = 1.5$ ps FWHM Gaussian pulse, its maximum entering the simulation box at $\tau_{\max} = 8400/\omega_0 \sim 2.3$ ps, before half of the simulation is complete. The maximum intensity on the target is 1.0×10^{19} W.cm^{-2}, corresponding to a normalized intensity parameter $a_L = 2.85$. Collisions between particles are not yet taken into account in the OCEAN code. However this

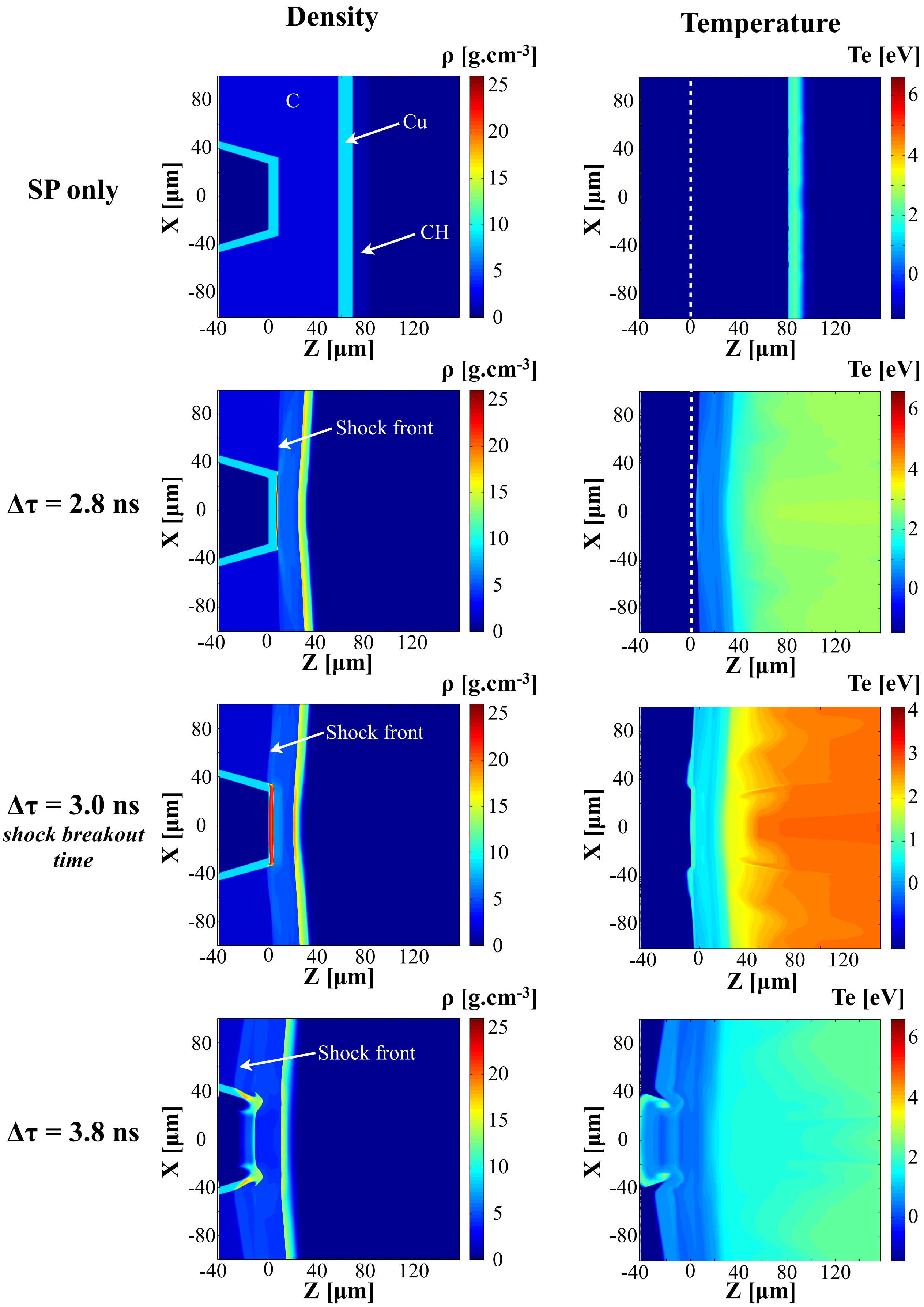

Figure 5.33: Density (left) and temperature (right) 2D maps extracted from hydrodynamic simulations for an unperturbed target, and 3.0 ns, 3.2 ns and 4.0 ns (from top to bottom) after the beginning of LP irradiation. Temperature maps are plotted in the common logarithmic scale. The inner part of the cone tip is indicated by the white dashed lines in the temperature maps.

is not a key issue since the goal of this step is to characterize the fast electron source at the very beginning of the target, and not to study any transport effect. The simulation is ran up to the final time $t_f = 1.6 \times 10^5$ c/$\omega_0 \simeq 5.3$ ps.

The initial density and temperature profiles were calculated with the CHIC code. The 1D profiles, taken on the cone axis, and presented in Fig. 5.32 correspond to the simplified target geometry, with a cone tip imitated by a homogenous copper layer extending over the whole height of the target. The unperturbed target, is made of a 7 μm cone tip followed by a 50 μm carbon layer and a 10 μm copper tracer. The plastic layer was not simulated in the presented PIC simulations. Four cases were considered, corresponding to the laser pulse injection time of 2.55 ns (cone tip at solid density, carbon layer almost fully compressed), 3.00 ns (cone tip fully compressed, shock breakout time), 4.00 ns (1 ns after shock breakout time) and 4.60 ns (1.6 ns after shock breakout time). For two later delays, the copper tip front side layers were modeled by an exponential function with a gradient length of 1.72 μm in the 4.00 ns case and 2.04 μm in the 4.60 ns case, followed by a fourth degree polynomial function. The minimum density is cut at $n_c/100$. Since the laser pulse is characterized by a fairly high contrast, the front side copper layer presents a steep density gradient for the two earlier injection times.
For the sake of simplicity, we start the PIC simulations with simplified hydrodynamic initial conditions. In all cases, the carbon layer is considered at a constant density, corresponding to the mean value averaged over the entire layer thickness.The rear-side copper tracer expansion was also not taken into account. Since the goal of this study is to characterize the fast electron sources at the cone tip, the simulation of the entire target is not necessary. The injected hydrodynamic profiles are presented on Fig. 5.34 (blue lines). The areal density of each layer is conserved in order to facilitate the comparison of the results between different cases. The temperature and the ionization degree were also kept constant within a specific material layer. Table 5.3.6 presents the initial ion temperatures, electron temperatures and ionization degrees used in the simulations for four fast electron beam injection times. The simulation box length

	Copper tip	**Carbon layer**	**Copper tracer**
2.55 ns	$T_e = 0.36$ eV $T_i = 0$ eV $Z^* = 4$	$T_e = 2.7$ eV $T_i = 0$ eV $Z^* = 3$	$T_e = 6.4$ eV $T_i = 0$ eV $Z^* = 6$
3.00 ns	$T_e = 4.4$ eV $T_i = 0$ eV $Z^* = 7$	$T_e = 3.2$ eV $T_i = 0$ eV $Z^* = 3$	$T_e = 6.4$ eV $T_i = 0$ eV $Z^* = 6$
4.00 ns	$T_e = 3$ eV $T_i = 0$ eV $Z^* = 3$	$T_e = 2$ eV $T_i = 0$ eV $Z^* = 3$	$T_e = 4$ eV $T_i = 0$ eV $Z^* = 4$
4.60 ns	$T_e = 3$ eV $T_i = 0$ eV $Z^* = 3$	$T_e = 2$ eV $T_i = 0$ eV $Z^* = 3$	$T_e = 4$ eV $T_i = 0$ eV $Z^* = 4$

Table 5.1: Initial electron temperatures (T_e), ion temperatures (T_i) and ionization degrees (Z^*) of the different layers set as input of PIC simulations as a function of the injection time.

ranges from 37.3 μm to 72.4 μm depending on the injection time. In the four cases, 1000 empty cells are set in the front of the cone tip, corresponding to 10 μm of vacuum. The rear side of the target is located at the right-side boundary of the simulation box. Absorbing conditions are chosen both for electromagnetic fields and particles. Such a choice of boundary conditions implies that particles exiting the simulation box are re-injected with their initial temperature.

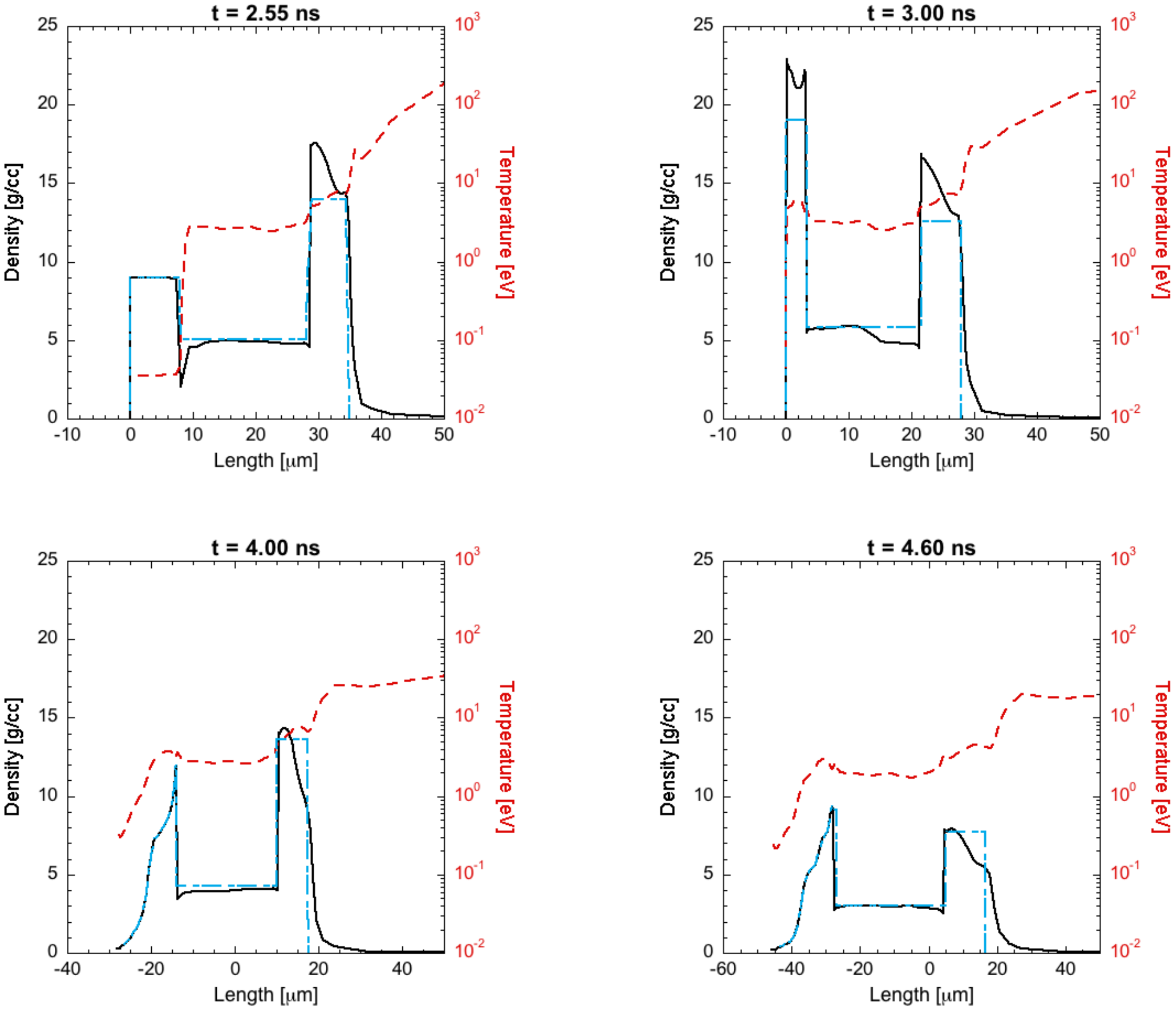

Figure 5.34: Density (black full-lines) and temperature (red dotted-lines) profiles from hydrodynamic simulations at different times of injection. The 2.55 ns case (top left) corresponds to a fully compressed carbon central layer but a copper tip still at the solid density. At 3.00 ns (top right) the shock is about to breakout. The two latter cases labeled 4.00 ns (bottom left) and 4.60 ns (bottom right) correspond to the laser injection time 1 ns and 1.6 ns, respectively, after the shock breakout. The density profiles considered in the PIC simulations are plotted with blue dash-dotted-lines.

In order to ensure a sufficient precision of the simulations, 500 particles per cell, both electron and ion species, are considered.

Characterization of the fast electron source

The electron source is characterized for each delay as follows. A probe is inserted 2 μm after the front side copper layer. This probe records the energy and the weight of macro-particles propagating from the cone tip towards the rear side copper tracer. A histogram with energy bins of 373 eV characterized the fast electron energy distribution. The corresponding distributions for 2.55 ns, 3.00 ns, 4.00 ns and 4.60 ns delays are presented in Fig. 5.35. The minimum energy is set at 10 keV since lower energy electrons are stopped into the generation layer. The 2.55 ns

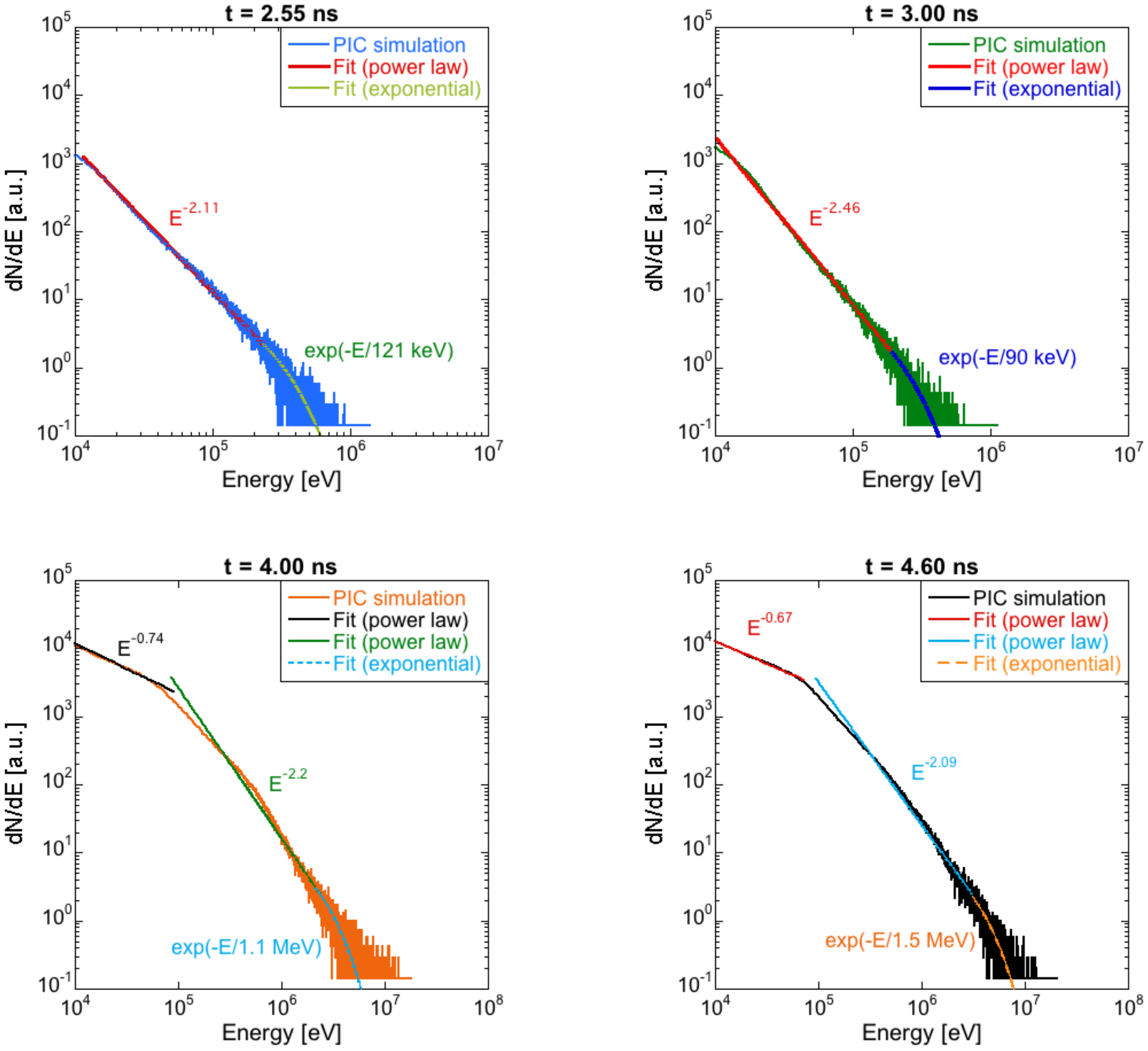

Figure 5.35: Comparison of the simulated fast electron energy distribution corresponding to an injection time of 2.55 ns (top left, blue solid line), 3.00 ns (top right, green solid line), 4.00 ns (bottom left, orange solid line) and 4.60 ns (bottom right, black solid line). The PIC results are fitted with combinations of power laws and exponential functions.

distribution function, corresponds to an interaction of the laser pulse with a steep gradient, the front side copper layer being still at solid density. This distribution function can be fitted with a decreasing power law characterized by a coefficient of 2.11 followed by an exponential function with a temperature of 121 keV. The 3.00 ns case, corresponding to a fully compressed cone tip, presents the same slope, with a power law coefficient of 2.46 and a temperature of 90 keV. The maximum electron energy is fairly low due to the absence of the pre-plasma in front of the target. The two latter cases exhibit similar shapes, except the low energy part < 100 keV. The power law coefficients are 2.2 and 2.09 for the 4.00 ns and 4.60 ns cases, respectively, while the temperatures characterizing the exponential shape of the high energy parts are 1.1 MeV and 1.5 MeV, respectively. The maximum energy of the accelerated electrons is close to 10 MeV. One can note that the number of accelerated fast electrons is higher in the later injection time case. The corresponding fast electron mean energies, given by $\langle E\rangle = \int_0^\infty f(E).EdE / \int_0^\infty f(E).dE$ and the conversion efficiency from laser energy to fast electrons are given in Tab. 5.2. The observed differences can again be explained by the absence of a pre-plasma in front of the target at early time of injection, before shock breakout time.

Case	$\langle \boldsymbol{E}\rangle$ **[keV]**	$\boldsymbol{\eta_{L\to e^-}}$
2.55 ns	20	5%
3.00 ns	15	5%
4.00 ns	210	45%
4.60 ns	190	45%

Table 5.2: Fast electron mean energy and laser to fast electron conversion efficiency for the different simulated case.

5.3.7 Hybrid transport simulations

2D transport simulations were performed for two different delays of compression in collaboration with Mickael Touati (CELIA, France) using a hybrid transport code M1 developed at CELIA [Dubroca et al., 2010; Touati et al., 2014]. The characteristics of the simulations are the following:

- Simulations were performed for two different delays of compression: 0 ps, corresponding to an unperturbed target and 2.8 ns, corresponding to the case where to cone tip starts to be compressed.
- The injected fast electron energy distributions are taken from the PIC simulations presented in section 5.3.6.
- The simulation box dimensions are 200 μm across the fast electron beam axis, and 67 μm and 30 μm along the cone axis for the 0 ps and 2.8 ps delays, respectively. The spatial resolution is 2 μm.
- The fast electron angular distribution is given by:

$$f(\theta, x, E) \propto \exp\left[-\left(\frac{\theta - \theta_0(x)}{\Delta\theta(E)}\right)^2\right] \tag{5.11}$$

  with x the transverse coordinate, $\theta_0 = 25°\tanh(x/\sigma_x)$ the mean propagation angle, $\sigma_x^2 = \Delta x^2/8\ln 2$, $\Delta x = 20$ μm and $\Delta\theta$ the mean dispersion angle depending on the fast electron energy. For the sake of simplicity, a mean value of 25° is chosen [Green et al., 2008].

- Hydrodynamic density and temperature profiles are taken from 2D hydrodynamic simulations presented in section 5.3.5.
- Simulations are run up to the final time $t_f = 4$ ps. The time evolution of the fast electron injection is described by a Gaussian function with the 1.5 ps FWHM corresponding to the laser pulse duration measured experimentally.
- For the two earlier delays of injection, the laser-to-fast electron conversion efficiency is risen from a few percent to 20% following the results of Davies [2009]. As discussed further below, this change allows to reproduce experimental K_α yield measurements.
- Fast electrons with an energy < 10 keV were considered as background electrons, they did not participate in the transport.
- The electrical conductivity of copper is based on the Drude model, with the Lee & More collision frequency presented in section 2.5.3. The electrical conductivity of the carbon layer, presented in Fig. 5.36, was taken from the quantum molecular dynamics calculations by McKenna et al. [2011] . One can note the monotonic rise of the carbon conductivity with the temperature.
- Absorbing conditions are chosen for particles.

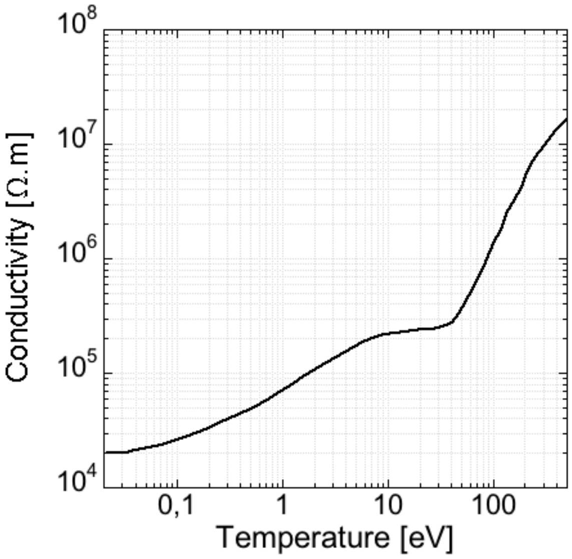

Figure 5.36: Dependence of the conductivity of vitreous carbon on the temperature.

Fig. 5.37 presents ion density and atomic number maps for the uncompressed target ($\Delta\tau = 0$ ps). One can see the copper coated cone tip in the left side of the image, and the copper tracer at the rear side of the target. Since the hybrid method assumes that the fast electron density n_b is much smaller than the background electron density, the hollow cone structure, containing vacuum inside, cannot be simulated. The evolution of the fast electron density with time is presented in Fig. 5.38. At 0.3 ps after the beginning of simulation, fast electrons just enter the carbon layer. At 1.9 ns, fast electrons already crossed the entire target. One can see a clear collimation of the fast electron beam inside the carbon layer. At the very end of the simulation, corresponding to a the time of 3.8 ps, the fast electron beam is significantly diluted and extends further across the cone axis.

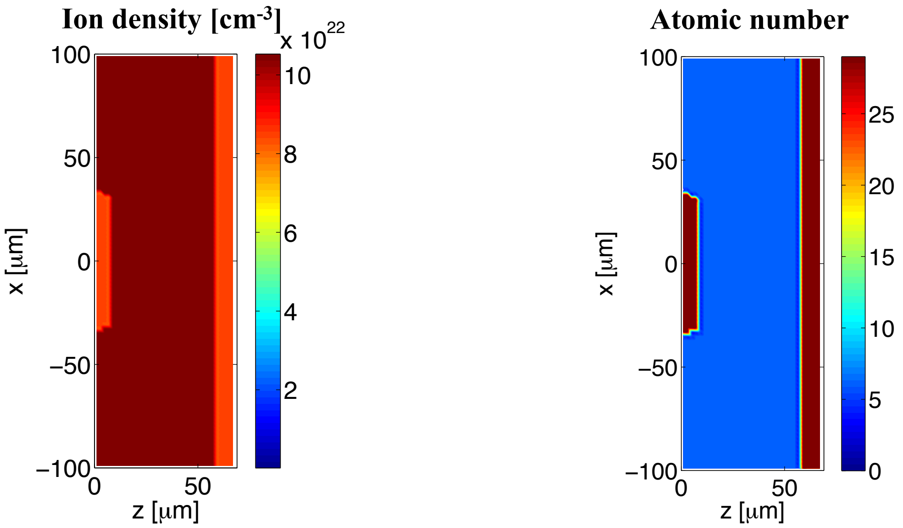

Figure 5.37: Ion density (left) and atomic number (right) of the unperturbed target injected into hybrid transport simulations.

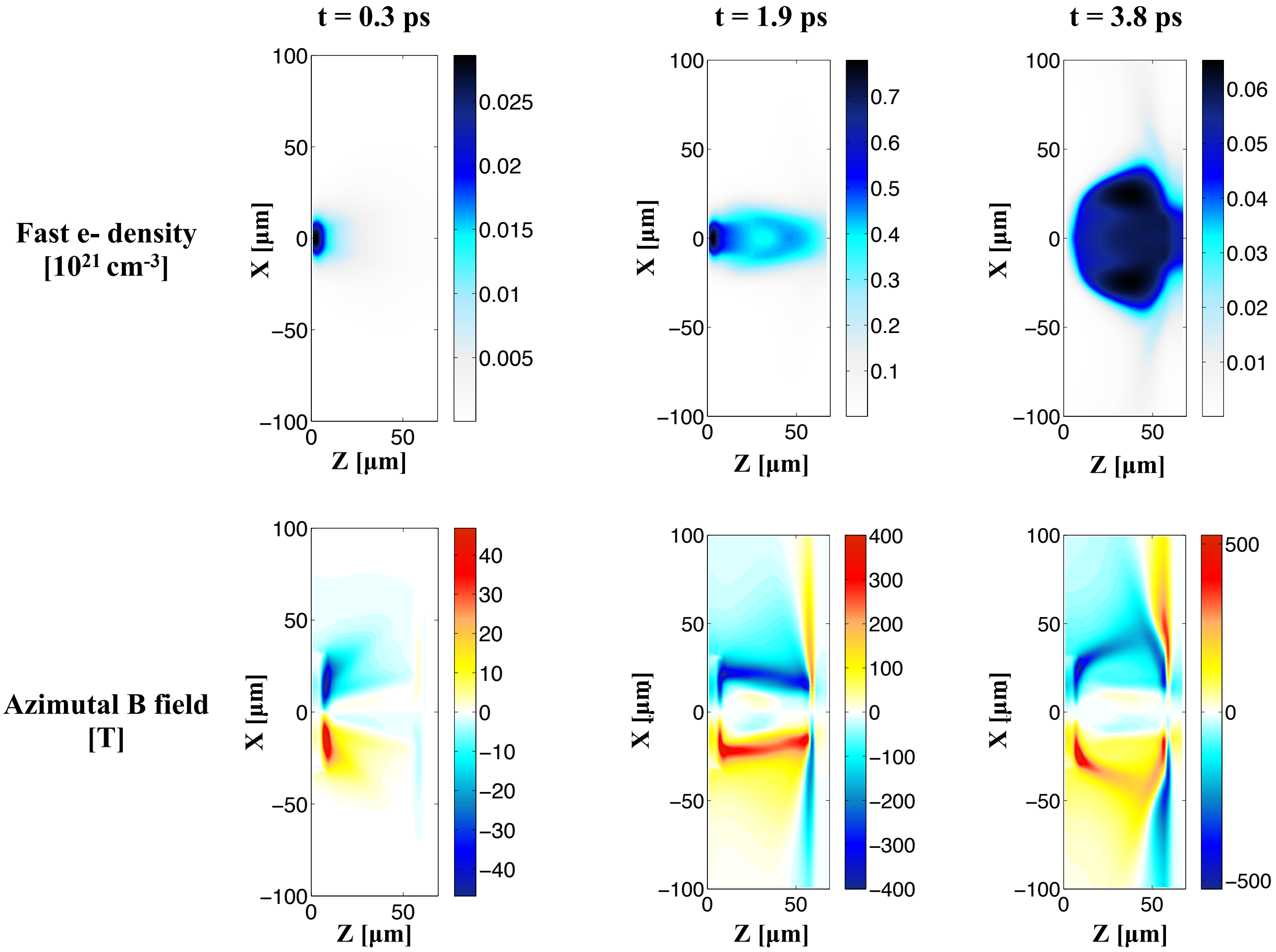

Figure 5.38: Evolution of the fast electron density (up) and of the total azimuthal magnetic field (down) for three different simulation times of 0.3 ps (left), 1.9 ps (middle) and 3.8 ps (right).

These observed features can be explained by analyzing the azimuthal magnetic field (Fig. 5.38). One can clearly see a collimating magnetic field at 1.9 ns. At 3.8 ps, this collimating magnetic field has diffused into the target. The field of the opposite sign appears at the interface between the carbon layer and the rear side tracer. The origin of this field can be understood from the Faraday equation for the self-generated magnetic field presented in section 2.5.2 (Eq. 2.123): The contribution of each term to the total magnetic field presented in Fig. 5.38 is shown in Fig. 5.39 for the simulation time of 2 ps, corresponding to the maximum of fast electron beam injection. The *current* term is responsible for the observed pinching of the fast electron beam.

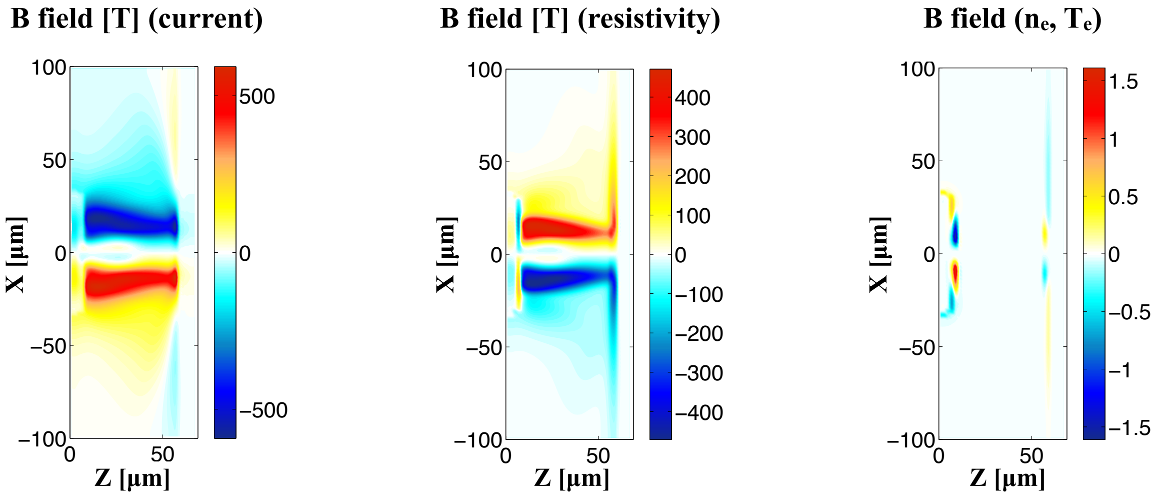

Figure 5.39: Contributions to the total azimuthal magnetic field of the *current* (left), *resistivity* (middle) and *crossed gradients* (right) terms detailed in Eq. 2.123.

This pinching effect is partially counter-balanced by the slightly less intense *resistivity* term, pushing electrons toward higher resistivity regions further away from the fast electron beam axis. The contribution of crossed density-temperature gradients, most important at the interface between the cone tip and the carbon layer, is negligible compared to the others.

As fast electrons propagate into the target, they loose a certain amount of energy both by collisional and collective mechanisms. Fig. 5.40 presents the time evolution of these two contributions. One can see that collisional energy losses are more important in the cone tip and in the tracer due to the high density of copper compared to carbon. At early time of the simulation, the resistive energy losses are more important in the carbon layer due its higher initial resistivity compared to the copper material (Fig. 5.41). The rapid heating of the central part of the carbon layer up to a few hundred eV due to fast electron beam energy losses however triggers a rapid decrease of the carbon resistivity, which becomes comparable to the copper resistivity. At 2 ps, resistive energy losses are more important on the cone tip than in the carbon layer due to the higher current density.

The time-integrated map of the simulated K_α emission from the copper coated cone tip, the copper tracer and the carbon layer is presented in Fig. 5.42 (left) at the end of the simulation. The emission from the cone tip is brighter but radially less extended than the emission from the rear side tracer. The 277 eV K_α emission from the carbon layer, which is not measured experimentally, is clearly less intense than the Cu-K_α emission. By taking a lineout of the emission inside the tracer layer, at Z= 65 μm from the cone tip, we measure the spatial extension of the emission $\sim$ 40 μm FWHM, which is comparable to the experimental measure presented in Fig. 5.29. The integrated Cu-K_α emission over the entire volume is $\sim 10^{11}$ sr^{-1}, which is in

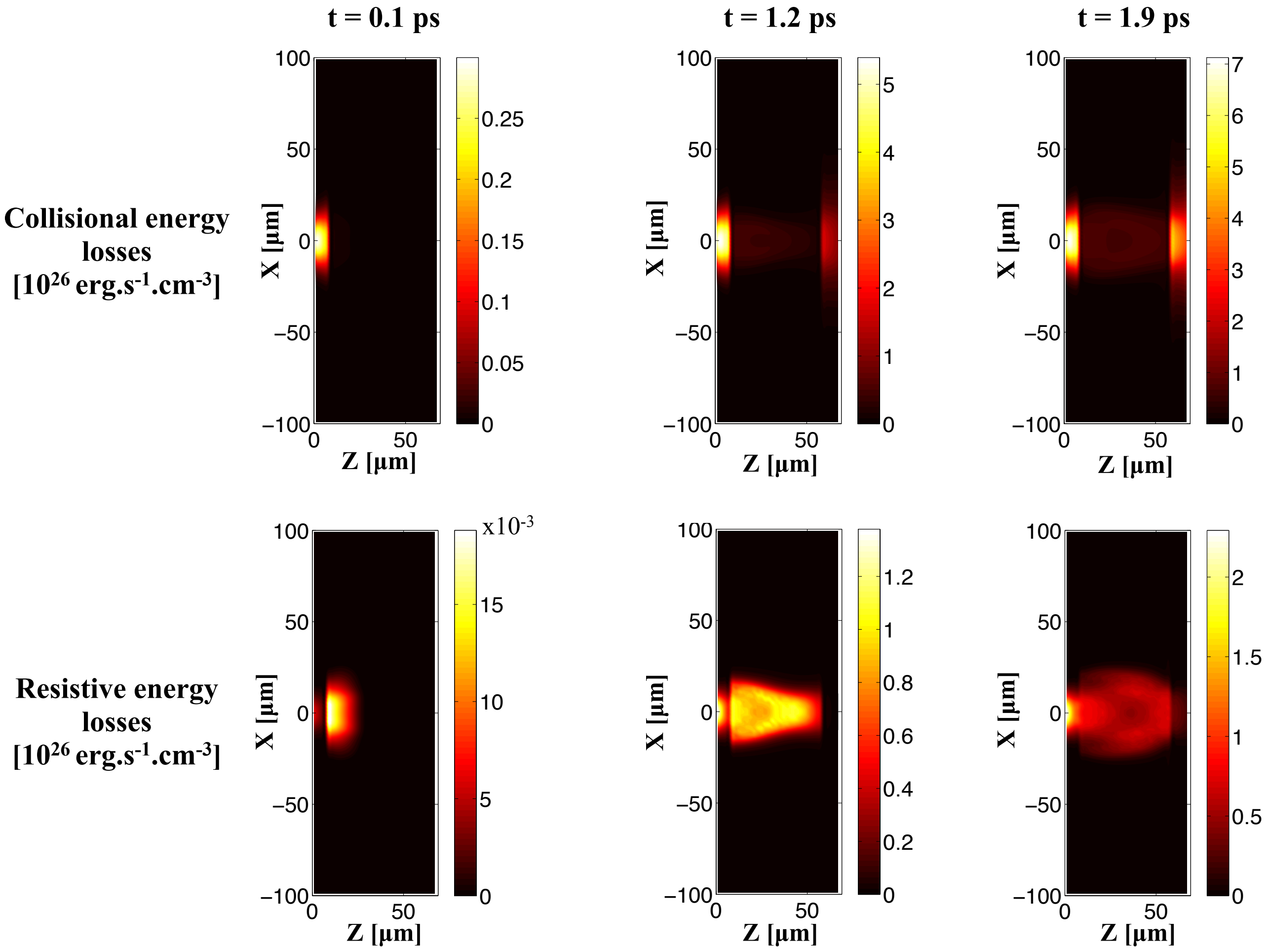

Figure 5.40: Collisional (up) and resistive (bottom) energy loss maps 0.1 ps (left), 1.2 ps (middle) and 1.9 ps after the beginning of the simulation.

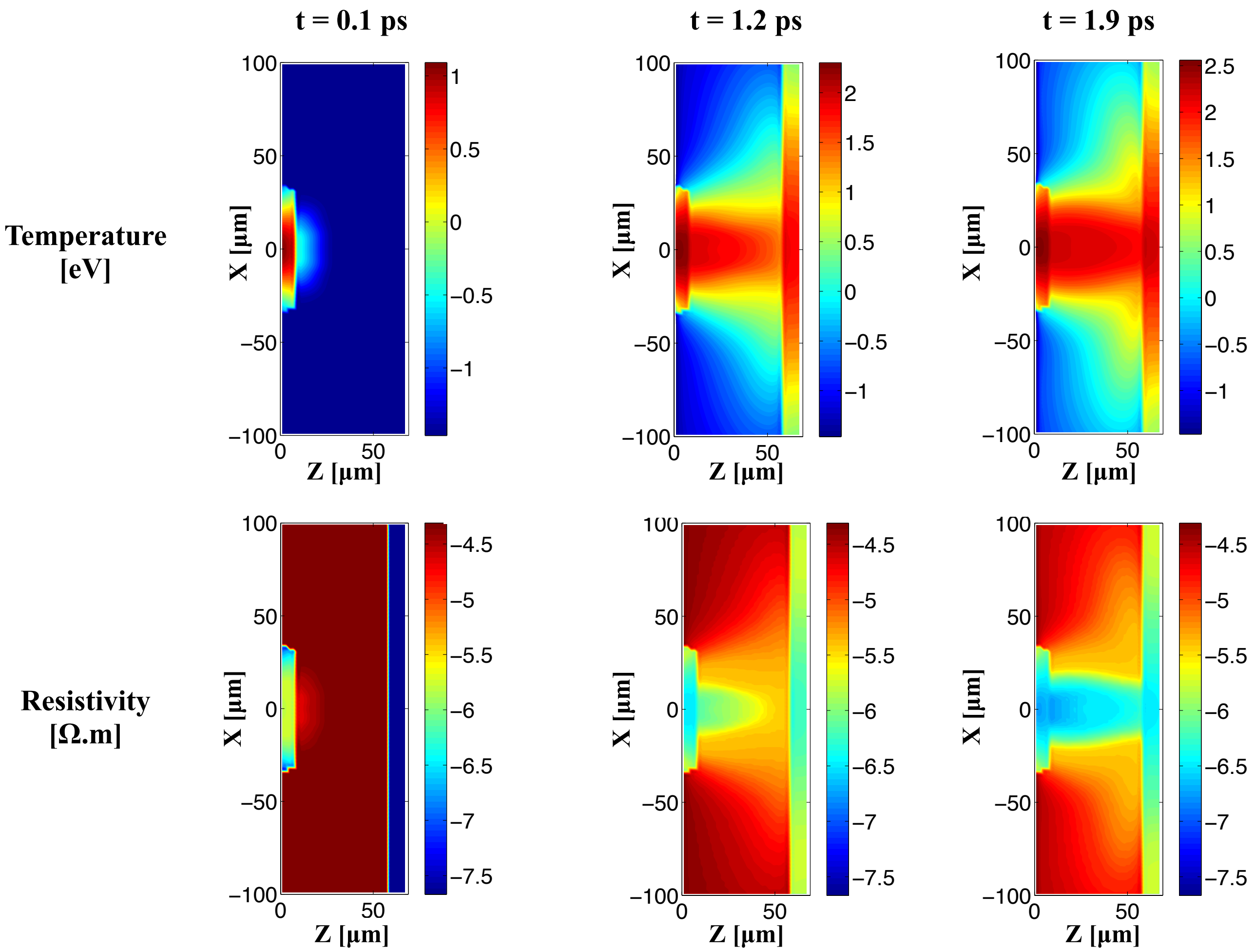

Figure 5.41: Target temperature (up) and resistivity (bottom) at 0.1 ps, 1.2 ps and 1.9 ps after the beginning of the simulation. The plots are presented in logarithmic scale.

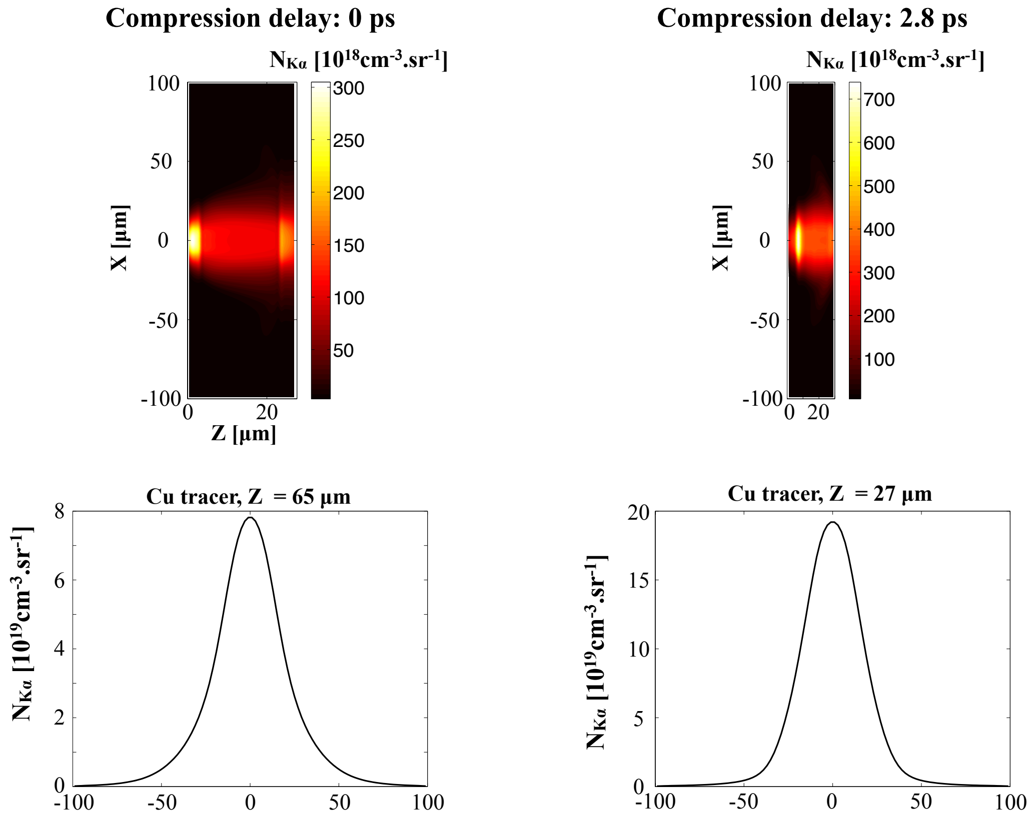
Compression delay: 0 ps

Compression delay: 2.8 ps

Cu tracer, Z = 65 µm

Cu tracer, Z = 27 µm

Figure 5.42: Integrated K_α maps at the end of the simulation (left) for the 0 ns (left) and 2.8 ns (right) compression delays. Transverse lineouts of the emission are also presented (bottom).

agreement with the measured yields presented in Fig. 5.26.

The similar analysis can be performed for the 2.8 ps injection time, where the shock has just reached the cone tip. The target ion density and atomic number are presented in Fig. 5.43. Fig. 5.44 presents the fast electron density 0.3 ps, 1.9 ps and 3.8 ps after the beginning of the simulation. The fast electron collimation in the carbon layer, already observed for the unperturbed target case, is still visible. In addition, the radial spread of the electron beam at the interface between the carbon layer and the copper tracer visible at the end of the simulation is more important in this case. These observed trends can be explained by analyzing the azimuthal magnetic field at the same time-steps (Fig. 5.44). The collimating magnetic field in the carbon layer is visible from 1.9 ps. The decollimating field at the carbon-tracer interface is more intense that what was observed for the unperturbed target case. The contributions to the azimuthal magnetic field are presented on Fig. 5.45. The *current* term is again responsible for the observed collimation. It is more intense than for the 0 ns case. The *resistivity* term, also more intense, partially counterbalances the previous contribution. In particular, it is responsible for the observed decollimation at the carbon-tracer interface due to the lower resistivity of the shocked copper tracer (Fig. 5.46). The contribution of the crossed density-temperature gradients at the interface between the shocked carbon layer and the cone tip is also more important than for the unperturbed target case, but still negligible compared to the *resistivity* and *current* terms.

A comparison of the energy balances for the 0 ns and 2.8 ns delays is presented in Fig. 5.47. The main contribution to the fast electron beam energy losses is due to collisional effects, mainly in the cone tip and in the copper tracer. Collisional energy losses are also slightly more

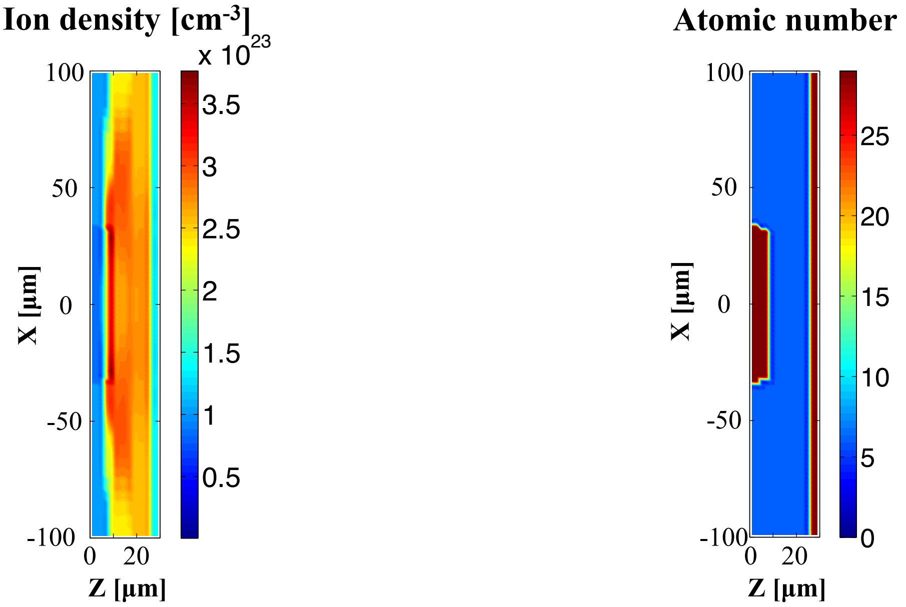

Figure 5.43: Ion density (left) and atomic number (right) of target 2.8 ps after the beginning of compression injected into hybrid transport simulations.

important in the 2.8 ns compression delay case, while resistive energy losses are slightly less important due to the drop of the resistivity with the target compression. The magnetic energy is also more important in the later case, which is consistent with higher azimuthal magnetic field amplitudes observed in Fig. 5.44.

A 2D map of integrated K_α emission at the end of the simulated is presented in Fig. 5.42 (right) together with a lineout taken in the copper tracer layer. The copper K_α emission is clearly brighter at the interface between the cone tip and the carbon layer, and slightly brighter in the copper tracer even if less extended, with a ~ 36 μm FWHM, than for the unperturbed target case.

5.4 Conclusion

The experiment presented in this chapter was dedicated to the study of fast electron transport in copper coated cone targets, compressed by a planar shock. It demonstrated the influence of a cone geometry on fast electron characteristics. Our results confirm previous studies that showed the deleterious effect of pre-plasmas, when confined in the cone, on the generation and the efficient transport of fast electron energy into the target depth [Baton et al., 2008; Norreys et al., 2014].

Our experimental setup allowed us to study the fast electron beam generation in a cone target at different moments of compression. Before the shock breakout time, the interaction of the intense laser takes place in the cone tip. A significant fraction of the laser energy is converted in the electron beam. Transport simulations and X-ray images show an efficient collimation of the beam (radial pinch) due to the self-generated magnetic fields. This was observed both in solid and compressed targets at twice the solid density, and heated at a few eV.

When injecting the short pulse after the shock breakout at the inner cone tip, fast electrons

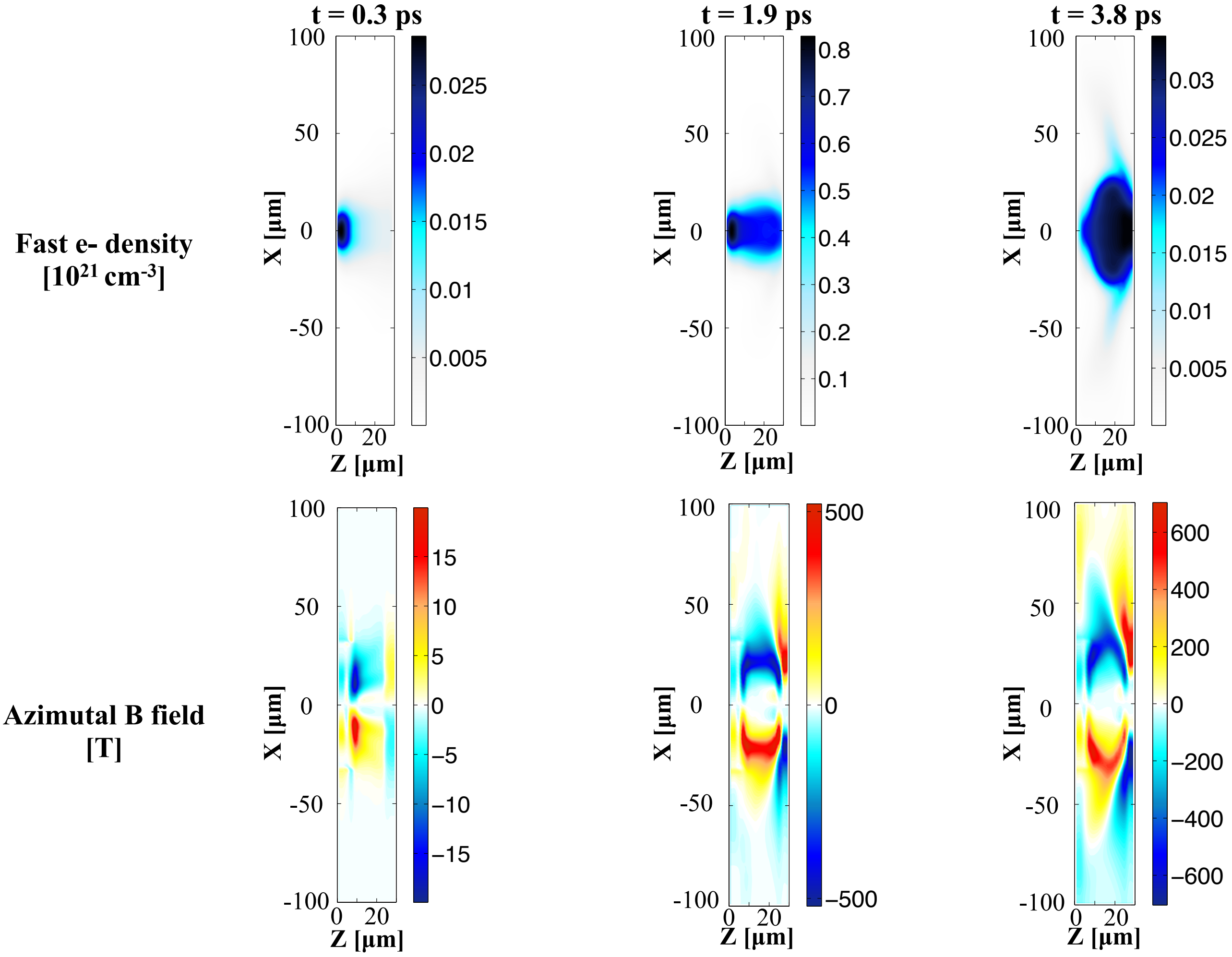

Figure 5.44: Fast electron density (up) and the azimuthal magnetic field (bottom) for the simulation times of 0.3 ps (left), 1.9 ps (middle) and 3.8 ps (right) for a compression time of 2.8 ns.

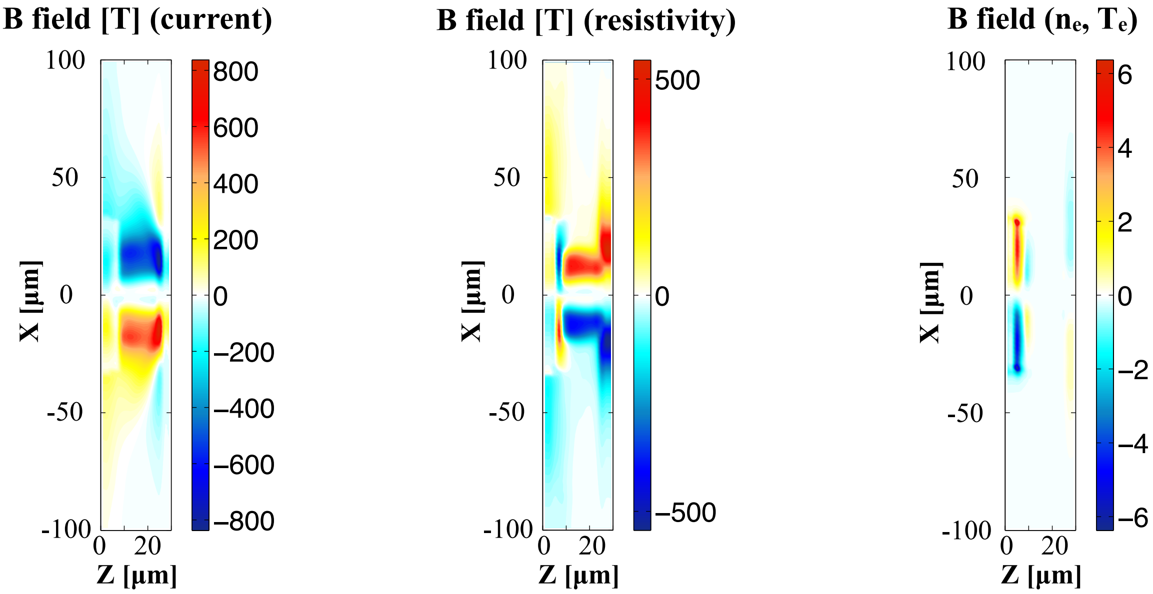

Figure 5.45: Contributions for the 2.8 ns compression delay to the total azimuthal magnetic field of the *current* (left), *resistivity* (middle) and *crossed gradients* (right) detailed in Eq. 2.123.

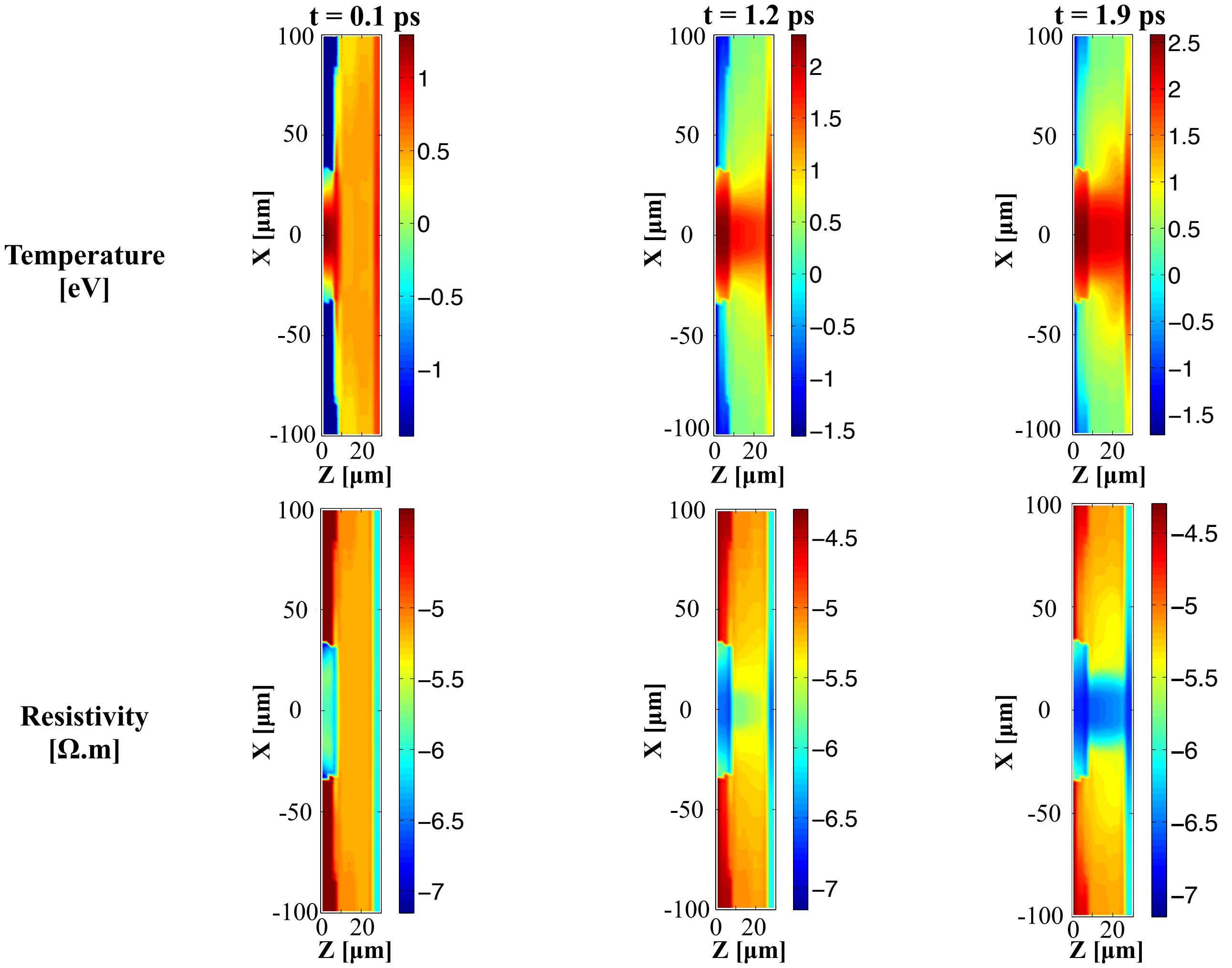

Figure 5.46: Target temperature (up) and resistivity (bottom) at 0.1 ps, 1.2 ps and 1.9 ps after the beginning of the simulation for the 2.8 ns compression delay. The plots are in the logarithmic scale.

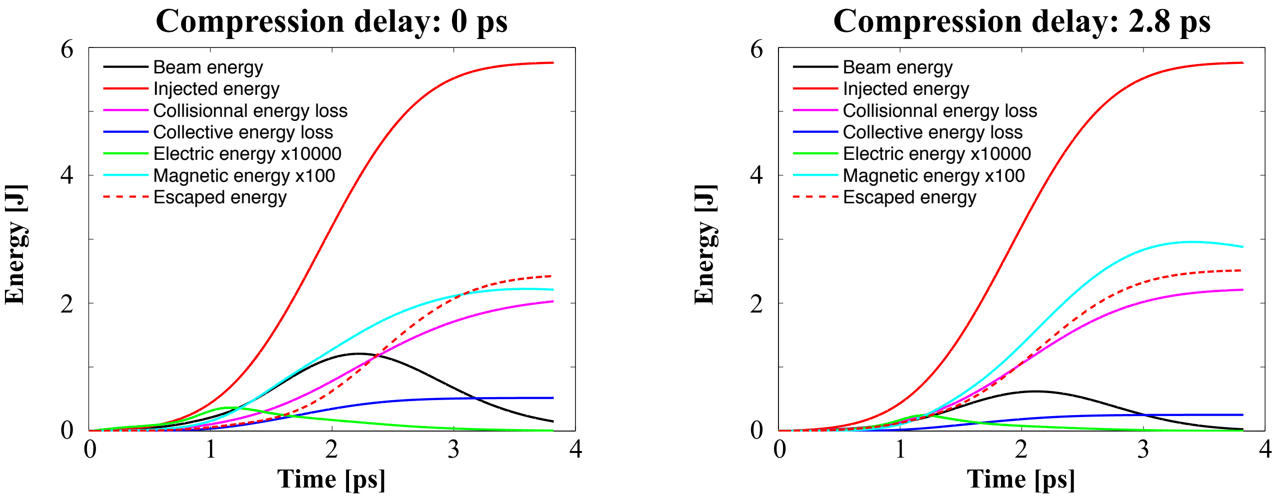

Figure 5.47: Energy balance for the 0 ns (left) and 2.8 ns (right) compression delays: fast electron beam energy (black solid line), total injected energy (red solid line), integrated collisional energy loss (purple solid line), integrated resistive energy loss (blue solid line), electric energy multiplied by a factor 10^4 (green solid line), magnetic energy multiplied by a factor 10^2 (blue solid line) and escaped energy carried by particle leaving the simulation box (red dashed line).

are generated and partially trapped in the plasma progressively filling the cone volume. At the latest tested time of compression (5 ns after shock breakout), the fast electron source is completely diluted, preventing any efficient injection into the target depth. This observation imposes a severe limit on the duration of the fast electron source in the cone geometry.

In terms of fast electron beam source spectra, the interaction of a short laser pulse with a steep or a long density gradient generates a significantly different electron source. PIC simulations showed that both the number of accelerated electrons and their mean energy were lower when injecting the fast electrons before the shock breakout time. Yet, they are more efficiently injected into the target depth.

The compression of the target was fully characterized by X-ray point projection radiography. This technique allowed us to measure in a single shot both the shock and fluid velocities. The cone structure is found to survive the ∼ 3 Mbar compression shock. The time evolution of the shock front and of the fluid velocity were reproduced by a set of hydrodynamic simulations, ensuring the good description of the target state for the fast electron transport shots.

Despite the modest pressure achieved in the experiment, we succeed to systematically study the effects of a shock on the cone survival. The use of a planar compression geometry offered an opportunity to observe the laser pulse coupling in a compressed, or blown-out cone targets, avoiding the constraints of a more complex spherical compression experiment. It also allows to demonstrate the key effects of pre-plasmas on the generation and the efficient transport of fast electron beams. The developed set of diagnostics and methodology will allow to repeat this experiment on a larger laser facility, as for example Orion (UK), Omega+EP (USA) or Gekko XII+Firex (Japan), enabling the study of stronger shocks with comparable or higher current densities, closer to fast ignition relevant conditions.

Chapter 6

Conclusion and perspectives

The work presented in this thesis is accomplished within the framework of the fast ignition scheme for inertially confined fusion targets. It is dedicated to studies of the transport of fast electrons, carrying high current densities ($j_b \sim 10^{11}$ A.cm^{-2}), and generated by intense laser pulses ($10^{19} - 10^{20}$ W.cm^{-2}) in planar compressed targets. The choice of a simpler compression geometry allowed us to reveal the contribution of the different physical mechanisms in the conditions relevant for the fast ignition scheme.

The experimental results were obtained in the framework of two experimental campaigns. Chapter 4 showed the results of a study dedicated to the quantification of both collisional and resistive energy losses of the fast electrons propagating in aluminum samples. We compared the results obtained in cold-solid and warm-compressed targets, initially heated to a few eV by shock compression, and representative of the cone regions in a fast ignition target. The 1D compression geometry allowed to generate a wide homogeneous plasma across the fast electron axis. It also conserved the areal density ρL during compression, allowing to clearly identify the contribution of resistive energy losses when comparing cold and warm samples of the same ρL. For the first time, the importance of resistive losses was directly demonstrated from experimental data. They peaked at the same level as collisional losses for the current density $10^{11} < j_b < 10^{12}$ A.cm^{-2} in a warm-dense aluminum. We confirmed the theoretical predictions of the transient behavior of the aluminum resistivity with the electron temperature. Our model, benchmarked by the experimental results, predicts a saturation of the resistive energy losses for $j_b > 10^{11}$ A.cm^{-2}, due to the rapid transition of the resistivity to the Spitzer regime.

The study presented in chapter 5 is based on an experimental campaign dedicated to the characterization of the generation and transport processes of a fast electron beam in a cone target, compressed by a planar shock front. The fast electrons were generated by coupling a high-contrast, $I_L \sim 10^{19}$ W.cm^{-2} short laser pulse with the cone tip at different moments of compression. We observed that the cone structure survives the ~ 3 Mbar shock pressure generated by the long pulse beam, using the X-ray diagnostics. We demonstrated the important role of the timing of fast electron injection with respect to the shock breakout time, and the subsequent plasma filling of the cone. Experimental measurements allowed to visualize the spatial extent of the fast electron source, and its transport into the target depth. At early time of compression, when the shock front has not reached the inner cone walls yet, the fast electrons are mainly generated in the cone tip and a significant fraction of them is injected into the depth, and propagates over tens of microns. In this case, transport simulations exhibited a collimation of the fast electrons due to self-generated magnetic fields. At later times, after the shock breakout, we observed the generation of fast electrons over larger volumes inside the cone, being filled by plasma. These results confirm the deleterious effects of pre-plasmas on the fast electron generation and transport into the cone. Even if the number and the average energy of the population generated in a long pre-plasma are higher than on a steep density gradient, a significant fraction is retained in the cone volume and is not injected into the target depth.

This thesis allowed a better understanding of the mechanisms associated with fast electron transport. The experimental studies were performed on modest laser facilities compared to what would be a fast ignition relevant laser system. However a comparison with the theoretical models and numerical simulations allowed us to identify the key physical processes and to evaluate their respective roles. The warm-dense state of matter reached in the experiments is representative of the cone region in a fast ignition target, although the characteristics of the generated electron source are much different from the fast ignition conditions. The physical effects addressed in this thesis, and the original setup configurations, are the following:

- Transport and resistive losses
- Use of buried cone targets
- Characterization of the fast electron source in the cone
- Cone tip survival
- X-ray point projection radiography

In the short-term perspective, these two experiments could be reproduced on already available bigger laser facilities, such as Orion (UK), Omega+EP (USA), Gekko XII+Firex (Japan), and soon LMJ+Petal. By increasing the current density to $j_b \sim 10^{12} - 10^{13}$ A.cm^{-2}, it would be possible to verify the predictions on the saturated contribution of resistive energy losses. Considering the cone target geometry, the use of a higher energy, and high contrast short laser pulse would allow to extend the study of fast electron generation on cone targets to higher energy conditions, and using 10 ps pulses duration.

An important effort has been done in the last years on the development of numerical codes, including hybrid models, that allow a good degree of realism of ignition-scale calculation. The PIC and hydrodynamic codes allow to simulate fast ignition relevant electron sources and target implosions, respectively. This numerical effort must be pursued to provide integrated capabilities, allowing to simulate self-consistently the generation and transport of fast electrons in a target under compression.

In the long-term perspective, the fast electron transport model benchmarking must be extended to fast-ignition relevant energies and pulse durations. Fast-ignition related experiments must take place on the LMJ+Petal, NIF+ARC and Gekko XII+Firex laser systems. The role of resistive energy losses using a 10 ps duration laser pulse, equivalent to the stagnation time, must be experimentally investigated. However, a 10 ps laser system presenting a ~ 100 kJ energy capability still does not exist. It would allow to explore an extreme but not yet accessible $j_b \sim 10^{14}$ A.cm^{-2} fast electron transport regime.

Finally, the main issue of the fast ignition scheme is the electron energy deposition in the DT core depth. The ignition with a reasonable short pulse beam energy is achievable only if one succeeds to confine the electron beam into a radius comparable to the DT core one.

Two main approaches are currently studied for this purpose: self-generated resistive magnetic fields, and external magnetic fields, both of them on the level of several kT. Resistive magnetic fields can be generated by resistivity gradients in engineered targets, such as with the magnetic switchyard. Magnetic pulsers can, on the other hand, generate magnetic fields on the level of few tens of T which could serve as seeds in magnetic field amplification by flow compression in a driven fast ignition target. Capacitor-coil targets driven by laser reach on their own the kT level, with typical duration of several ns. A first evidence of electron confinement in an external magnetic field has been obtained by our group in 2014 at the LULI facility, and more detailed tests are foreseen in 2015. The implementation of this technique on an integrated fast ignition geometry experiment is still to be done.

List of publications and communications

Publications

- X. Vaisseau, A. Debayle, J.J. Honrubia, S. Hulin, A. Morace, Ph. Nicolaï, H. Sawada, B. Vauzour, D. Batani, F.N. Beg, J.R. Davies, R. Fedosejevs, R.J. Gray, G.E. Kemp, S. Kerr, K. Li, A. Link, P. McKenna, H.S. McLean, M. Mo, P.K. Patel, J. Park, J. Peebles, Y.J. Rhee, A. Sorokovikova, V.T. Tikhonchuk, L. Volpe, M. Wei, and J.J. Santos, *Enhanced relativistic-electron beam energy loss in warm-dense aluminum*, Accepted in Physical Review Letters.

- A. Morace, L. Fedeli, D. Batani, S.D. Baton, F.N. Beg, L.C. Jarrot, S. Hulin, A. Margarit, M. Nakai, M. Nakatsutsumi, Ph. Nicolaï, N. Piovella, X. Vaisseau, L. Volpe, M. Wei and J.J. Santos, *Development of x-ray radiography for high energy density physics*, Physics of Plasmas, **21**, 102712, 2014.

- I. Thfoin, C. Reverdin, S. Hulin, C.I. Szabo, S. Bastiani-Ceccotti, D. Batani, E. Brambrink, M. Koenig, A. Duval, X. Leboeuf, L. Lecherbourg, B. Rossé, A. Morace, J.J. Santos, X. Vaisseau, C. Fourment, L. Giuffrida and M. Nakatsutsumi, *Monte-Carlo simulation of noise in hard X-ray Transmission Crystal Spectrometers: Identification of contributors to the background noise and shielding optimization*, Review of Scientific Instruments, **85**, 11D715, 2014.

- B. Vauzour, A. Debayle, X. Vaisseau, S. Hulin, H.-P. Schlenvoigt, D. Batani, S.D. Baton, J.J. Honrubia, Ph. Nicolaï, F.N. Beg, R. Benocci, S. Chawla, M. Coury, F. Dorchies, C. Fourment, E. d'Humières, L.C. Jarrot, P. McKenna, Y.J. Rhee, V.T. Tikhonchuk, L. Volpe, V. Yahia, and J.J. Santos, *Unraveling resistive versus collisional contributions to relativistic electron beam stopping power in cold-solid and in warm-dense plasmas*, Physics of Plasmas, **21**, 033101, 2014.

- X. Vaisseau, D. Batani, A. Debayle, J.J. Honrubia, A. Morace, Ph. Nicolaï, H. Sawada, V.T. Tikhonchuk, B. Vauzour, M. Wei and J.J. Santos, *Relativistic high-current electron beams in dense plasmas in the context of the fast ignition of inertially confined fusion targets*, IEEE, Energy (IYCE), 2013 4th International Youth Conference on, pp. 1-4, 2013 (best paper award).

- J.J. Santos, D. Batani, S.D. Baton, F.N. Beg, T. Ceccotti, A. Debayle, F. Dorchies, J.-L. Feugeas, C. Fourment, L. Gremillet, J.J. Honrubia, S. Hulin, A. Morace, Ph. Nicolaï, F. Pérez, H. Sawada, H.-P. Schlenvoigt, V.T. Tikhonchuk, X. Vaisseau, B. Vauzour and M.S. Wei, *Supra-thermal electron beam stopping power and guiding in dense plasmas*, Journal of Plasma Physics, **79**, 429, 2013.

- B. Vauzour, J.J. Santos, A. Debayle, S. Hulin, H.-P. Schlenvoigt, X. Vaisseau, D. Batani, S.D. Baton, J.J. Honrubia, Ph. Nicolaï, F.N. Beg, R. Benocci, S. Chawla, M. Coury, F. Dorchies, C. Fourment, E. d'Humières, L.C. Jarrot, P. McKenna, Y.J. Rhee, V.T. Tikhonchuk, L. Volpe, and V. Yahia, *Relativistic High-Current Electron-Beam Stopping-Power Characterization in Solids and Plasmas: Collisional Versus Resistive Effects*, Physical Review Letters **109**, 255002, 2012

Oral communications

- X. Vaisseau, A. Morace, S. Hulin, L. Fedeli, Ph. Nicolaï, D. Batani, S. Baton, F.N. Beg, J. Breil, R. Fedosejevs, P. Forestier-Colleoni, C. Fourment, L. Giuffrida, L.C. Jarrot, S. Kerr, A. Magerit, H.S. McLean, M. Nakatsutsumi, R. Nuter, N. Piovella, H. Powell, H. Sawada, V.T. Tikhonchuk, M. Touati, M.S. Wei and J.J. Santos, *Fast electron transport in planar-compressed cone targets*, 13th International Workshop on the Fast Ignition of Fusion Targets, Oxford, United-Kingdom, September 14-18, 2014.

- X. Vaisseau, A. Debayle, J.J. Honrubia, S. Hulin, A. Morace, Ph. Nicolaï, L. Fedeli, H. Sawada, D. Batani, S. Baton, F.N. Beg, J.R. Davies, R. Fedosejevs, R.J. Gray, G.E. Kemp, S. Kerr, K. Li, A. Link, P. McKenna, H.S. McLean, M. Mo, M. Nakatsutsumi, P.K. Patel, J. Park, J. Peebles, Y.J. Rhee, A. Sorokovikova, V.T. Tikhonchuk, L. Volpe, M. Wei, and J.J. Santos, *Etude expérimentale du transport d'électrons chauds dans les plasmas denses*, Forum Institut Lasers et Plasmas, Orcières, France, February 2-7, 2014.

- X. Vaisseau, A. Debayle, J.J. Honrubia, S. Hulin, A. Morace, Ph. Nicolaï, H. Sawada, D. Batani, S. Baton, F.N. Beg, J.R. Davies, R. Fedosejevs, R.J. Gray, G.E. Kemp, S. Kerr, K. Li, A. Link, P. McKenna, H.S. McLean, M. Mo, P.K. Patel, J. Park, J. Peebles, Y.J. Rhee, A. Sorokovikova, V.T. Tikhonchuk, L. Volpe, M. Wei, and J.J. Santos, *Experimental evidence of fast electron enhanced resistive energy losses in warm-dense plasmas*, Joint workshop on 'Alternative Ignition Scheme for Inertial Fusion Energy' and 'Theory and Simulation on Fast Ignition Target Design', Wakayama, Japan, September 16-18, 2013.

- X. Vaisseau, A. Debayle, J.J. Honrubia, S. Hulin, A. Morace, Ph. Nicolaï, H. Sawada, D. Batani, S. Baton, F.N. Beg, J.R. Davies, R. Fedosejevs, R.J. Gray, G.E. Kemp, S. Kerr, K. Li, A. Link, P. McKenna, H.S. McLean, M. Mo, P.K. Patel, J. Park, J. Peebles, Y.J. Rhee, A. Sorokovikova, V.T. Tikhonchuk, L. Volpe, M. Wei, and J.J. Santos, *Experimental evidence of fast electron enhanced resistive energy losses in warm-dense plasmas*, The Eighth International Conference on Inertial Fusion Sciences and Applications, Nara, Japan, September 8-13, 2013.

- X. Vaisseau, A. Debayle, J.J. Honrubia, S. Hulin, A. Morace, Ph. Nicolaï, H. Sawada, D. Batani, S. Baton, F.N. Beg, J.R. Davies, R. Fedosejevs, R.J. Gray, G.E. Kemp, S. Kerr, K. Li, A. Link, P. McKenna, H.S. McLean, M. Mo, P.K. Patel, J. Park, J. Peebles, Y.J. Rhee, A. Sorokovikova, V.T. Tikhonchuk, L. Volpe, M. Wei, and J.J. Santos, *Relativistic high-current electron beams in dense plasmas in the context of the fast ignition of inertially confined fusion targets*, 4th International Youth Conference on Energy (IYCE), Siófok, Hungary, June 6-8, 2013.

- X. Vaisseau, A. Debayle, J.J. Honrubia, S. Hulin, A. Morace, Ph. Nicolaï, H. Sawada, D. Batani, S. Baton, F.N. Beg, J.R. Davies, R. Fedosejevs, R.J. Gray, G.E. Kemp, S. Kerr,

K. Li, A. Link, P. McKenna, H.S. McLean, M. Mo, P.K. Patel, J. Park, J. Peebles, Y.J. Rhee, A. Sorokovikova, V.T. Tikhonchuk, L. Volpe, M. Wei, and J.J. Santos, *Experimental evidence of enhanced resistive stopping power of relativistic high-current electron beams in warm-dense compared to cold-solid aluminum*, Laser Energy Workshop, SPIE conference, Prague, Czech-Republic, April 15-18, 2013.

Contribution to poster sessions

- X. Vaisseau, A. Debayle, J.J. Honrubia, S. Hulin, A. Morace, Ph. Nicolaï, H. Sawada, B. Vauzour, D. Batani, F.N. Beg, J.R. Davies, R. Fedosejevs, R.J. Gray, G.E. Kemp, S. Kerr, K. Li, A. Link, P. McKenna, H.S. McLean, M. Mo, P.K. Patel, J. Park, J. Peebles, Y.J. Rhee, A. Sorokovikova, V.T. Tikhonchuk, L. Volpe, M. Wei, and J.J. Santos, *Relativistic high-current electron beam stopping power characterization in warm-dense compared to cold-solid aluminum*, NIF/JLF User Group Meeting, Livermore, United-States of America, February 10-13, 2013.

- X. Vaisseau, A. Debayle, J.J. Honrubia, S. Hulin, A. Morace, Ph. Nicolaï, H. Sawada, B. Vauzour, D. Batani, F.N. Beg, J.R. Davies, R. Fedosejevs, R.J. Gray, G.E. Kemp, S. Kerr, K. Li, A. Link, P. McKenna, H.S. McLean, M. Mo, P.K. Patel, J. Park, J. Peebles, Y.J. Rhee, A. Sorokovikova, V.T. Tikhonchuk, L. Volpe, M. Wei, and J.J. Santos, *Investigation of the stopping power of relativistic high-current electron beams in warm-dense compared to cold-solid aluminum*, Forum Institut Lasers et Plasmas, Île-de-Ré, France, September 23-29, 2012.

- X. Vaisseau, D. Batani, F.N. Beg, J. Bonlie, J.R. Davies, R. Fedosejevs, R.J. Gray, S. Hulin, G.E. Kemp, S. Kerr, K. Li, P. McKenna, H.S. McLean, A. Morace, Ph. Nicolaï, J. Peebles, Y.J. Rhee, H. Sawada, A. Sorokovikova, V.T. Tikhonchuk, M. Wei, and J.J. Santos , B. Vauzour, *Experimental study of fast electron propagation in warm and dense plasmas created by planar shock wave compression*, Joint ISTC-GSI Young Scientists School, Darmstadt, Germany October 10-15, 2011.

Résumé en français

1 Introduction

La fusion thermonucléaire contrôlée pourrait constituer à terme une source d'énergie quasi inépuisable, plus propre et plus sure que la production d'énergie d'origine nucléaire existant aujourd'hui à travers le monde. Ce processus, constituant le moteur des étoiles, est basé sur la quantité importante d'énergie dégagée lors de la fusion de deux noyaux plus légers que le noyau de fer. Parmi toutes les réactions envisagées pour reproduire ce schéma sur Terre, la réaction de fusion du deutérium et du tritium (D-T), actuellement à l'étude, présente la plus haute section efficace atteinte à la plus basse température, cette dernière étant de l'ordre de quelques dizaines de keV. Afin de garantir un bilan d'énergie positif il est nécessaire de confiner une quantité suffisante de plasma chauffé à plusieurs centaines de millions de degrés, et ce pendant un temps suffisamment long, suivant le critère de Lawson :

$$n.\tau_E \geq 10^{15}\ \text{cm}^{-3}.\text{s} \tag{6.1}$$

avec n la densité du plasma considéré et τ_E le temps de confinement. Cette inégalité est obtenue en supposant une température de 1 keV. Parmi les deux approches de confinement étant actuellement à l'étude, la fusion par confinement inertiel, constituant le cadre de cette thèse, consiste à confiner une capsule millimétrique de D-T, comprimée d'un facteur ~ 1000, par sa propre inertie. Le plasma de haute densité ainsi obtenu ($n \sim 10^{26}$ cm^{-3}) est confiné durant un laps de temps extrêmement bref, de l'ordre de quelque ps. Dans l'approche classique, cette compression importante est générée par une irradiation homogène de la cible par des faisceaux laser (attaque directe), ou par un rayonnement X intense (attaque indirecte), pendant quelques ns. Cette technique est cependant extrêmement sensible à la fois aux défauts de symétrie d'irradiation laser et aux défauts de surface de la cible qui peuvent être amplifiés de manière exponentielle en quelques centaines de ps par des instabilités hydrodynamiques, compromettant ainsi l'allumage des réactions de fusion.

Une alternative à ce schéma classique, appelée allumage rapide [Tabak et al., 1994], consiste à séparer les phases de compression et d'allumage des réactions de fusion, permettant ainsi de relâcher les contraintes sur la symétrie d'implosion. Dans un premier temps, la capsule de D-T est comprimée de manière la plus homogène possible par des impulsions laser d'intensité modérée ($I_L \sim 10^{15}$ W.cm^{-2}). A la fin de la compression une première impulsion laser intense ($I_L > 10^{18}$ W.cm^{-2}) est envoyée sur la cible afin de creuser dans le plasma un canal sous dense (*hole boring*). Ce dernier sert alors de guide à une deuxième impulsion laser intense ($I_L > 10^{19}$ W.cm^{-2}) qui est absorbée au niveau de la densité critique se trouvant proche du coeur de D-T afin d'accélérer un faisceau d'électrons relativistes, aussi appelés électrons rapides, sous l'influence d'un nombre important de mécanismes physiques. Ces électrons vont alors pénétrer dans le plasma dense et déposer leur énergie dans le coeur afin d'allumer les réactions de fusion. Ce schéma d'allumage rapide constitue la cadre principal de cette thèse.
Une alternative au creusement de canal consiste à insérer directement dans la cible un cône d'or

dont la pointe est située proche du coeur de D-T. L'introduction de ce cône soulève cependant un certain nombre de problèmes. La compression asymétrique de la cible va en effet générer un jet de plasma le long de l'axe du cône, repoussant la source d'électrons loin du coeur. De plus, la génération d'une source d'électrons suffisamment collimatée, et dont l'énergie est adaptée à un couplage efficace avec le D-T, est actuellement un sujet de recherche très actif.

Un certain nombre d'aspects concernant les processus de génération et de transport d'électrons rapides ont été étudiés au cours des 15 dernières années. Les différentes campagnes expérimentales ont bénéficié de l'augmentation des intensités laser accessibles ainsi que du développement des diagnostics plasmas. Les simulations numériques, bénéficiant de l'augmentation progressive des capacités calculatoires, ont permis une compréhension plus fine des processus de génération d'électrons rapides, des mécanismes de perte d'énergie ainsi que des phénomènes associés à la divergence des électrons, reproduisant alors avec un bon accord les résultats expérimentaux.

Un nombre important d'aspects liés au transport d'électrons restent cependant à caractériser, comme par exemple les modifications du pouvoir d'arrêt électronique dans des cibles tièdes et denses, par rapport à un milieu froid et solide. Le rôle particulier des pertes d'énergies d'origine résistive, modifiées de manière importante lors du chauffage changeant la résistivité du matériau, n'a jusqu'à présent qu'été très peu étudié de manière expérimentale. Comme le suggère un certain nombre d'études, les effets résistifs pourraient être responsables d'une fraction importante des pertes d'énergie près de la source d'électrons dans une cible de fusion, dans la zone oú la densité de courant est la plus forte. La génération d'un faisceau d'électrons lors du couplage d'une impulsion laser intense avec la pointe d'un cône doit aussi être caractérisée de manière systématique.

L'objectif de cette thèse est d'effectuer une caractérisation expérimentale du transport d'électrons dans les plasmas denses. Nous nous sommes principalement intéressés à l'étude des processus de physique fondamentale au cours de campagnes expérimentales se déroulant sur des installations modestes comparées aux conditions requises pour l'allumage rapide. Ce travail expérimental est indispensable afin de valider les codes numériques permettant de dimensionner une cible d'allumage rapide, et d'autre part d'évaluer la faisabilité de ce schéma. Toutes les expériences détaillées ont en commun l'utilisation d'une configuration à deux faisceaux laser, une impulsion longue ∼ns étant dédiée à la compression des cibles jusqu'à deux fois la densité du solide, et une impulsion courte ∼ps générant un faisceau d'électrons rapides. La géométrie de compression plane a été principalement choisie en raison de sa simplicité, comparée à la géométrie sphérique.

2 Etude du transport d'électrons rapides dans des cibles comprimées en géométrie plane

La mise en place du schéma d'allumage rapide nécessite une compréhension profonde des processus associés à la propagation de faisceaux d'électrons relativistes. La caractérisation des pouvoirs d'arrêts associés aux mécanismes collisionnels et résistifs est particulièrement indispensable.

Un nombre important d'expériences effectuées sur des installations laser modestes a été dédié à l'étude du transport d'électrons rapides dans des matériaux à l'état solide, loin des conditions hydrodynamiques de l'allumage rapide. La compression d'un matériau permet non seulement de modifier sa densité, mais aussi ses autres propriétés physiques comme sa résistivité. Cette dernière est directement impliquée dans la génération de champs magnétiques par

le faisceau d'électrons rapides lui-même, affectant à la fois ses pertes d'énergies et son confinement. Nous allons décrire dans cette partie les résultats d'une campagne expérimentale, et leur interprétation théorique, qui s'est déroulée sur l'installation laser JLF-Titan (Lawrence Livermore National Laboratory, Etats-Unis) et qui avait pour but l'étude de la propagation de faisceaux d'électrons rapides dans des cibles d'aluminium comprimées à deux fois la densité du solide. Nous avons adopté une géométrie de compression plane générée par une forte onde de choc laissant dans son sillage un matériau comprimé et chauffé de manière homogène. Cette configuration conservant la densité surfacique ρL de la couche d'étude d'aluminium permet de séparer les pertes d'énergies collisionnelle et résistive lors de la comparaison des résultats avec ceux obtenus en utilisant des cibles non comprimées d'épaisseur initiale identique. Par conséquent, cette géométrie expérimentale est adaptée à l'étude de la dépendance des pertes d'énergies résistives en fonction du chauffage de la cible associé à la compression.
Il est important de mentionner que ce travail expérimental est la suite directe du travail de thèse de Benjamin Vauzour [Vauzour, 2012], en augmentant cependant la densité de courant d'électrons chauds, permettant alors de valider de manière expérimentale les prévisions théoriques.

2.1 Dispositif expérimental

L'expérience décrite dans cette section à été réalisée en 2012 sur l'installation laser JLF-Titan. Le travail expérimental, ainsi que l'interprétation théorique et numérique, ont été conduits au sein d'une collaboration internationale entre le CELIA, l'Université Politécnica de Madrid (Espagne), UCSD (Etats-Unis), l'IST (Portugal), l'Université de Strathclyde (Royaume-Uni), l'Université de l'Ohio (OSU, Etats-Unis), le LLNL (Etat-Unis), l'institut KAERI (Corée du Sud) et General Atomics (Etat-Unis).

Nous avons utilisé dans le cadre de cette expérience les faisceaux lasers à impulsion courte et longue de l'installation. Leurs caractéristiques sont les suivantes :

- le faisceau laser court (SP), utilisé pour générer le faisceau d'électrons rapides, délivre des impulsions de $E_{\mathrm{SP}} = (115 \pm 30)$ J, l'incertitude sur l'énergie étant directement reliée aux importantes fluctuations tir à tir rencontrées. Ces impulsions, délivrées en $\tau_{\mathrm{SP}} = 0.7$ ps (FWHM), sont caractérisées par un piédestal arrivant 3 ns avant la composante principale, et par un contraste de $\sim 10^{-7}$ [MacPhee et al., 2008; Le Pape et al., 2009]. Le faisceau court est focalisé par une parabole hors axe d'ouverture $f/3$ en une tache focale de 7 μm (FWHM). L'intensité crête sur cible est de $I_{\mathrm{SP}} = (2 \pm 1) \times 10^{21}$ W.cm^{-2};

- le faisceau laser long (LP) doublé en fréquence ($\lambda_{LP} = 0.53$ μm) est utilisé pour comprimé la cible. Il délivre des impulsions de $E_{\mathrm{LP}} = (410 \pm 9)$ J en 5 ns et est caractérisé par un profil temporel carré. Ce faisceau est focalisé sur la cible par une combinaison d'une lentille de $f = 200$ mm avec une lame de phase (PZP) permettant de générer une tache focale de 875 μm (FWHM). Il est important de préciser que cette valeur est bien supérieure au diamètre du faisceau laser court. L'intensité crête est estimée à 1.4×10^{13} W.cm^{-2}.

La géométrie des cibles employées lors de l'expérience est présentée sur la Figure 6.1. Le but est ici d'étudier la propagation d'électrons rapides dans une couche d'aluminium d'épaisseur initiale $L_0 = \{20, 40, 60, 80\}$ μm. Le faisceau laser court, servant à générer le faisceau d'électrons,

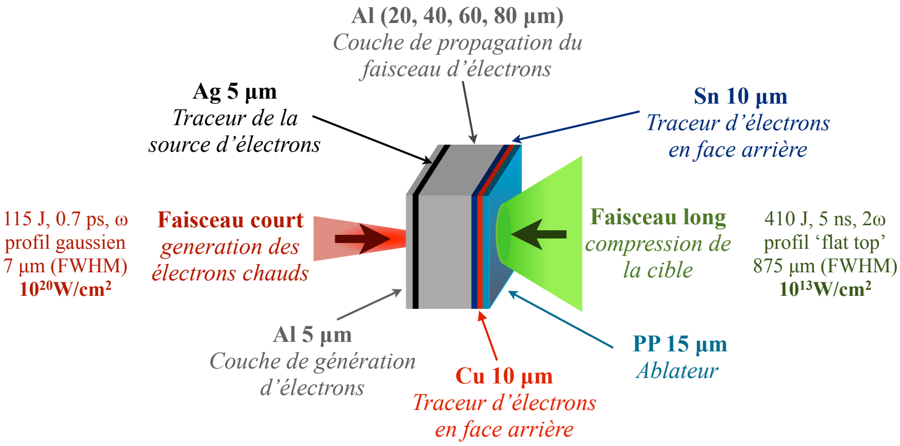

Figure 6.1: Géométrie des cibles utilisées lors de l'expérience sur l'installation laser Titan.

est focalisé en face avant avec un angle de 16.5° par rapport à la normale à la cible, sur une couche d'aluminium de génération de 5 μm d'épaisseur. Le faisceau laser long, utilisé pour comprimer la cible, est focalisé en face arrière avec un angle de 17° par rapport à la normale, sur une couche de polypropylène servant d'ablateur. L'expansion hydrodynamique de cette couche irradiée créé une onde de choc qui se propage dans la cible de manière contra-propagative par rapport au faisceau d'électrons. Les dimensions de la tache focale du faisceau long, bien supérieures à celles du faisceau court, permettent de générer des conditions hydrodynamiques uniformes tout autour de l'axe de propagation des électrons rapides, évitant ainsi tout effet 2D. Le retard entre les deux impulsions est variable, sa valeur dépendant directement de l'épaisseur de la couche d'aluminium. Il est en effet primordial lors de l'étude de la propagation d'électrons dans une cible comprimée que la couche d'aluminium soit presque totalement comprimée mais que le choc n'ait pas encore atteint la face avant de la cible. La propagation d'électrons rapides est caractérisée par l'émission K_α générée par les différentes couches de traceurs entourant la couche centrale d'aluminium : en face avant, une couche d'argent de 5 μm d'épaisseur placée juste après la couche de génération permet de caractériser la source d'électrons, tandis que deux couches consécutives de 10 μm d'étain et de cuivre placées juste après la couche de propagation permettent de caractériser la fraction d'électrons ayant franchi la couche centrale. Il est important de souligner qu'un deuxième avantage à l'utilisation du propylène en face arrière est de protéger le traceur de cuivre et d'éviter son irradiation directe avec le faisceau laser de compression.

Afin d'étudier la propagation du faisceaux d'électrons rapides, nous avons utilisé les diagnostics suivants, répartis tout autour de la cible :

- un spectromètre à rayonnement X dur de type Cauchois [Seely et al., 2008], appelé TCS, calibré de manière absolue et placé en face avant des cibles, est chargé de recueillir les émissions K_α des traceurs d'argent et d'étain. Le rapport de ces deux émissions est directement relié à la fraction d'électrons rapides ayant traversé la couche centrale d'aluminium. La mesure du nombre absolu de photons est aussi un paramètre clef de notre étude, celui-ci permettant de calibrer les simulations de transport présentées dans la section suivante;
- un spectromètre utilisant un cristal plan de type HOPG [Akli et al., 2010], placé en face avant des cibles et calibré de manière absolue, est utilisé pour mesurer l'émission K_α du traceur de cuivre;
- deux systèmes d'imagerie X constitués d'un cristal sphérique et d'un microscope de type

Kirkpatrick-Baez sont utilisés pour imager l'émission K_α du cuivre afin de caractériser la divergence du faisceau d'électrons chauds;

- enfin, un diagnostic de pyrométrie optique résolue en temps (SOP) est utilisé pour mesurer l'émission thermique générée lors du débouché de choc en face avant des cibles. Ces mesures ont une importance capitale pour le calcul du retard à adopter entre les deux faisceaux laser.

La propagation d'électrons rapides est étudiée dans deux cas, le premier correspondant aux conditions rencontrées dans une cible froide ($T_e = 0.03$ eV) et solide ($\rho_0 = 2.7$ g/cc) tandis que le deuxième correspond à une propagation dans un plasma d'aluminium tiède ($T_e \sim 3$ eV) et comprimé ($\rho \sim 2\rho_0 = 5.4$ g/cc).

2.2 Synchronisation des impulsions laser

La détermination expérimentale du retard à adopter entre les deux impulsions laser est un paramètre critique. Celui-ci dépend directement de l'épaisseur de la couche centrale d'aluminium. Deux cas sont à distinguer :

- dans le cas de cibles comprimées et chauffées, le faisceau d'électrons rapides doit être injecté juste avant que la couche centrale d'aluminium soit totalement comprimée, et avant que le choc n'ait débouché en face avant. Il est par conséquent nécessaire de déterminer en premier lieu la vitesse de propagation du front de choc. En utilisant le système de pyrométrie optique, nous avons pu mesurer une vitesse de choc $v_{\text{choc}} = 15.6$ μm/ns. Cette mesure est ensuite utilisée afin de calibrer des simulations hydrodynamiques 2D de la compression de la cible. Ces dernières, effectuées par Philippe Nicolaï avec le code Lagrangien CHIC [Maire et al., 2007], permettent alors de calculer les retards à adopter en fonction de l'épaisseur initiale d'aluminium. En extrayant des profils 1D de densité et de température sur l'axe de propagation des électrons, on note que l'épaisseur de la couche de propagation l'aluminium est effectivement divisée par un facteur ~ 2 tandis que sa température initiale atteint quelques eV (Fig. 6.2 [droite]).

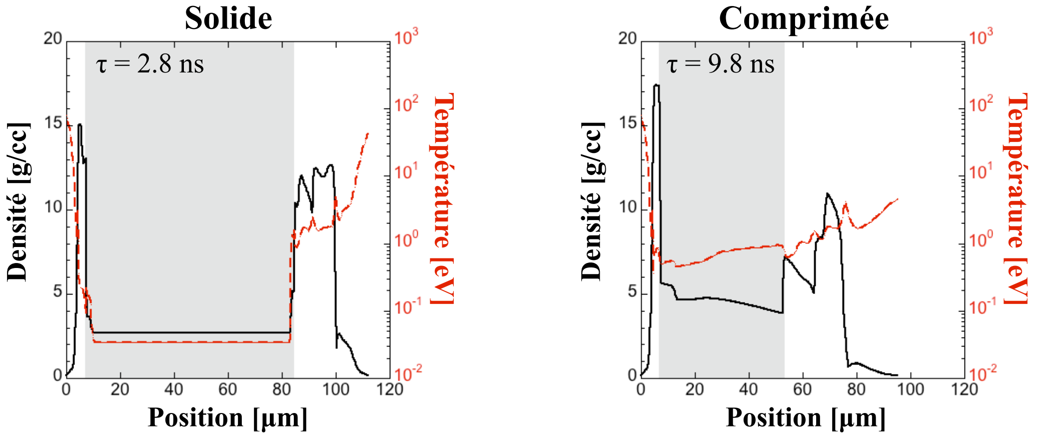

Figure 6.2: Profils de densité (noir) et de température (rouge) pour les cibles les plus épaisses ($L_0 = 80$ μm) extraits sur l'axe de propagation juste avant injection des électrons dans des cibles solides (gauche) et comprimées (droite). La couche de propagation d'aluminium est matérialisée par la zone grisée. Le retard choisi entre les deux faisceaux laser est indiqué sur chaque figure.

- Afin d'étudier la propagation d'électrons rapides dans des cibles à l'état solide et froide, il est tout de même nécessaire d'envoyer le faisceau laser court après le faisceau long, et ceci pour deux raisons. La première est qu'il est impératif de conserver des propriétés radiatives identiques des traceurs en face arrière afin de pouvoir comparer les résultats à ceux obtenus avec des cibles comprimées. La deuxième raison vient de la nécessité d'inhiber le phénomène de recirculation des électrons chauds dans la cible. Les électrons quittant la cible vont en effet créer un champ électrique de séparation particulièrement intense responsable de leur ré-injection. Ainsi, les électrons traversant la cible à de multiples reprises vont générer un rayonnement K_α supplémentaire responsable d'une augmentation artificielle du signal de fluorescence collecté, et par conséquent d'une estimation erronée des pertes d'énergie. Afin de pallier ce problème, le faisceau laser long est toujours envoyé en face arrière afin de créer un plasma en expansion, rejetant ainsi la zone de séparation de charges loin de la cible et piégeant les électrons dans ce plasma en détente. L'efficacité de cette inhibition a été montrée par une série de simulations de type Particle-In-Cell (PIC) en 1D [Vauzour, 2012]. Les électrons rapides sont ainsi injectés quand la face arrière de la cible, comprenant les couches de polypropylène, de cuivre et d'étain, est complètement comprimée. Le retard entre les deux impulsions laser calculé par les simulations hydrodynamiques 2D est $\tau = 2.8$ ns. Le profil hydrodynamique correspondant aux cibles solides les plus épaisses est présenté sur la Figure 6.2 (gauche).

2.3 Résultats expérimentaux

L'évolution du diamètre des taches d'émission K_α du cuivre en fonction de l'épaisseur de la couche centrale d'aluminium, permettant de quantifier la divergence du faisceau d'électrons rapides, est présentée sur la Figure 6.3 pour les deux imageurs. Ces derniers montrent des résultats similaires.

Aucune différence significative n'est visible sur ces résultats entre les cibles solides et comprimées, comme cela a été observé dans d'autres expériences [Vauzour et al., 2014]. Ce résultat suggère que dans cette gamme d'énergie et d'épaisseur de cible, la divergence du faisceau d'électrons est plus liée aux processus de génération qu'aux conditions hydrodynamiques rencontrées dans la cible.

Le nombre de photons K_α émis par les traceurs d'argent, d'étain et de cuivre mesuré par les deux spectromètres est présenté sur la Figure 6.4 en fonction de l'épaisseur réelle d'aluminium traversée. Etant donné la proximité du traceur d'argent avec la zone d'interaction laser-plasma, l'émission Ag-K_α est représentative du nombre d'électrons rapides générés en face avant des cibles. La dispersion des données due aux fluctuations du faisceau laser court entre chaque tir est inférieure à un facteur 3, indiquant une certaine stabilité de la source d'électrons. Les traceurs d'étain et de cuivre, placés juste après la couche de propagation d'aluminium, permettent de caractériser la fraction d'électrons ayant franchi cette couche centrale. Ces deux traceurs sont néanmoins sensibles à des énergies minimales d'électrons rapides différentes, de l'ordre de ~ 25 keV pour le cuivre et de ~ 70 keV pour l'étain. En traçant l'évolution des émissions Sn-K_α et Cu-K_α en fonction de l'épaisseur d'aluminium traversée, on pourrait s'attendre à une diminution du signal provoquée par un nombre de plus en plus important d'électrons arrêtés dans une couche d'aluminium de plus en plus épaisse. Cependant, cette tendance peut difficilement être observée sur les deux graphiques à cause des fluctuations du faisceau laser. Afin de s'en affranchir, une des possibilités consiste à normaliser les émissions Sn-K_α et Cu-K_α par l'émission Ag-K_α provenant de la face avant. Ces ratios, présentés sur la Figure 6.5 en fonction de la densité surfacique de la couche centrale d'aluminium, sont directement liés à la fraction d'électrons rapides ayant franchi la couche de propagation. Ces deux figures perme-

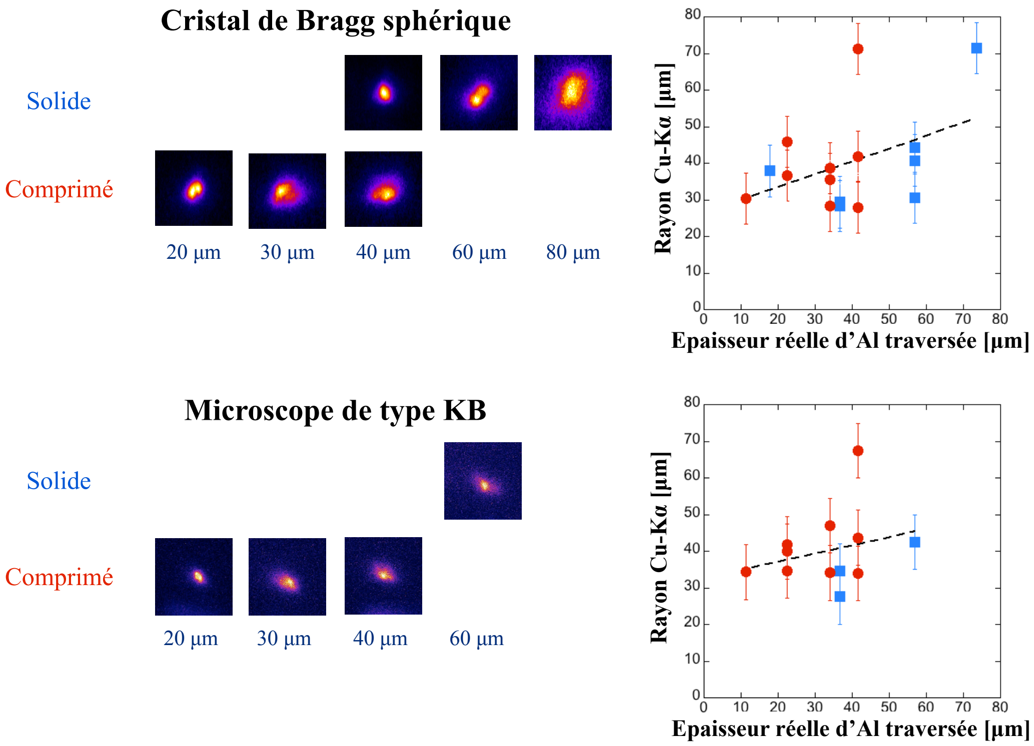

Figure 6.3: Evolution du rayon de la tache K_α du cuivre en fonction de l'épaisseur réelle d'aluminium traversée (droite). Ces données ont été extraites des images expérimentales (gauche) venant du cristal de Bragg sphérique (haut) et du microscope de type Kirkpatrick-Baez (bas).

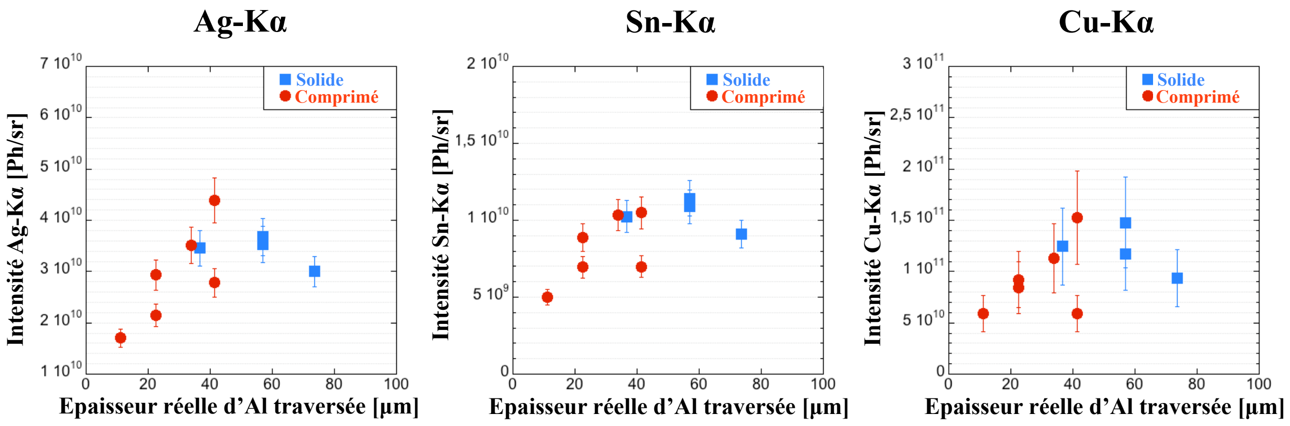

Figure 6.4: Evolution des émissions absolues des traceurs d'argent (gauche), d'étain (milieu) et de cuivre (droite) pour les cibles solides (carrés) et comprimées (disques) en fonction de l'épaisseur réelle d'aluminium traversée. Ces valeurs sont corrigées de la transmission des différents matériaux.

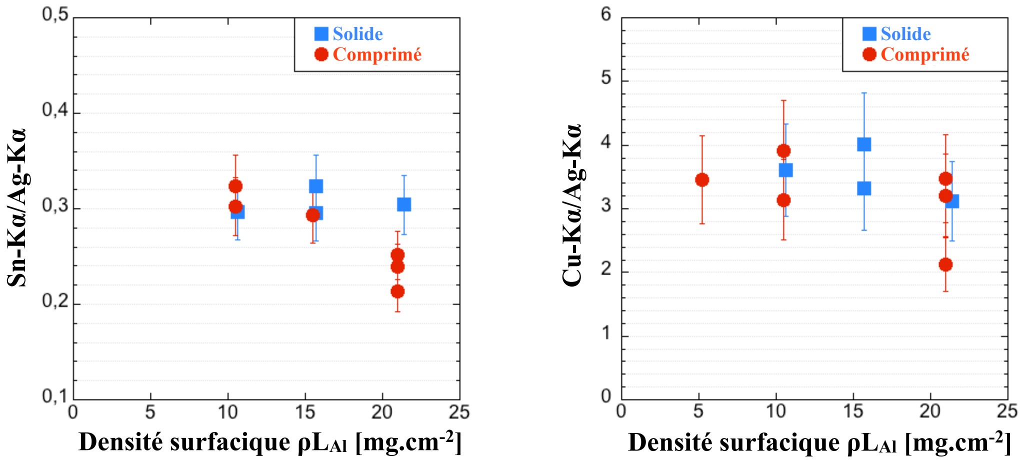

Figure 6.5: Evolutions des rapports Sn-K_α/Ag-K_α (gauche) et Cu-K_α/Ag-K_α (droite) en fonction de la densité surfacique de la couche centrale d'aluminium.

ttent de discriminer de manière graphique les pertes d'énergie collisionnelle et résistive. En effet, les pouvoirs d'arrêts liés à ces deux contributions et intégrés sur l'épaisseur d'aluminium s'écrivent :

$$\left.\frac{dE}{dz}\right|_{\text{coll}} \propto \rho \Rightarrow \Delta E_{\text{coll}} \propto \langle \rho \rangle L_{\text{Al}} \tag{6.2}$$

$$\left.\frac{dE}{dz}\right|_{\text{res}} \propto e\eta j_b \Rightarrow \Delta E_{\text{res}} \propto \langle \eta j_b \rangle L_{\text{Al}} \tag{6.3}$$

avec L_{Al} et η respectivement l'épaisseur d'aluminium traversée et sa résistivité, j_b la densité de courant d'électrons et les symboles $\langle\rangle$ signifiant une valeur moyennée sur l'épaisseur L_{Al}. Par conséquent, étant donné que la densité surfacique des cibles est conservée lors de la compression, les pertes d'énergies collisionnelles devraient rester similaires en comparant des cibles de même épaisseur initiale. Les pertes résistives, quant à elles, dépendent directement de la résistivité de l'aluminium. Comme le montre la Figure 6.6, la résistivité de l'aluminium comprimé et initialement chauffé à 3 eV, proche de la température de Fermi, est environ 20 fois supérieure à celle de l'aluminium froid. Les pertes d'énergies d'origine résistive devraient alors augmenter dans les cibles comprimées. Ce résultat est relativement visible en regardant le ratio Sn-K_α/Ag-K_α de la Figure 6.5. Celui-ci est en effet plus faible pour les cibles comprimées les plus épaisses, comparé au même résultat pour les cibles solides. Ce résultat constitue la première preuve expérimentale d'une augmentation des pertes d'énergie d'origine résistive dans les cibles comprimées, dans le régime d'interaction considéré ($I_L = 2 \times 10^{20}$ W.cm^{-2}). Cette différence n'est pas visible pour le ratio Cu-K_α/Ag-K_α. Ceci ne rentre cependant pas en contradiction avec le ratio Sn-K_α/Ag-K_α étant donné que les traceurs d'étain et de cuivre sont sensibles à des populations d'électrons rapides différentes.
Afin d'étudier en détail les mécanismes à l'origine de ces processus physiques et de quantifier la modification des pouvoirs d'arrêt collisionnel et résistif avec la compression, il est nécessaire d'effectuer une série de simulations de transport.

2.4 Simulations de la génération et du transport d'électrons rapides

Les paramètres de la source d'électrons sont calculés à l'aide de simulations de type PIC en 2D par Anthony Link (LLNL, Etats-Unis) en utilisant le code LSP [Welch et al., 2004]. Ces simulations permettent de reproduire de manière numérique l'interaction entre le faisceau

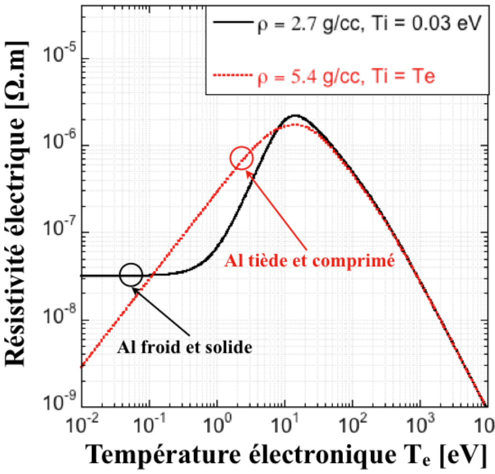

Figure 6.6: Evolution de la résistivité de la couche d'aluminium en fonction de la température électronique pour les cas froids et solides (courbe noire) et tièdes et comprimés (courbe rouge) en considérant dans ce dernier cas l'équilibre thermodynamique $T_i = T_e$.

laser court de Titan et une couche d'aluminium. Le spectre en énergie des électrons rapides moyenné sur toute la durée de la simulation peut être ajusté dans la gamme 10 keV-142 MeV par la fonction suivante :

$$f(E)^{\text{PIC}} = \exp\left(-\frac{E}{T_{h_1}}\right) + \left(\frac{E_0}{E}\right)^{\alpha} \exp\left(-\frac{E}{T_{h_2}}\right) \tag{6.4}$$

avec $T_{h_1} = 100$ keV, $E_0 = 20$ keV, $\alpha = 1$ et $T_{h_2} = 12.5$ MeV étant des paramètres d'ajustement. Tandis que la partie haute énergie est bien décrite par une fonction exponentielle, la partie basse énergie est quant à elle mieux décrite par une fonction exponentielle à basse température et une loi de puissance. L'énergie moyenne dans la gamme $10 \leqslant E \leqslant 20$ MeV, qui contient la majorité des électrons accélérés, est $\langle E \rangle^{\text{PIC}} \sim 1$ MeV.
La fonction de distribution angulaire moyennée sur toute les populations d'énergie peut être ajustée par une somme de deux fonctions gaussiennes :

$$f(\theta, r) \propto \exp\left[-\left(\frac{\theta - \theta_{r_1}}{\Delta\theta_0}\right)^2\right] + 0.2\exp\left[-\left(\frac{\theta - \theta_{r_2}}{\Delta\theta_0}\right)^2\right] \tag{6.5}$$

avec un angle de dispersion moyen $\Delta\theta_0 = 55°$ et des angles de propagation moyens θ_{r_1} et θ_{r_2} donné par :

$$\theta_{r_{1,2}} = \arctan\left[\tan(35°)\frac{r}{r_{1,2}}\right] \tag{6.6}$$

avec $r_1 = 4$ μm et $r_2 = 28$ μm les rayons initiaux du faisceau d'électron.

Les paramètres de la source d'électrons ainsi que les températures et densités initiales des cibles sont injectés dans un code de transport hybride. Le transport d'électrons est ainsi étudié en collaboration avec Javier Honrubia, le développeur du code, et Arnaud Debayle (Université de Madrid). Le coefficient de conversion de l'énergie laser en électrons rapides est pris égal à $\eta_{L\rightarrow e-} = 25\%$. L'énergie laser est prise égale à 115 J, ce qui correspond à l'énergie moyenne mesurée lors de l'expérience. La simulation est effectuée pendant 8 ps avec un pas temporel de 1 fs et un pas spatial de 0.25 μm. La résistivité de la cible est calculée en utilisant le modèle de Drude et la fréquence de collision provenant du modèle d'Eidmann-Chimier [Eidmann et al.,

2000; Chimier, 2008].
La figure 6.7 présente une comparaison des taux K_α des traceurs d'argent et d'étain mesurés lors de l'expérience et calculés par les simulations. Un bon accord est obtenu entre les deux jeux de données. L'émission Ag-K_α simulée est, comme attendu, relativement constante étant donné que les conditions hydrodynamiques de la face avant sont très semblables pour toutes les cibles. Les fluctuations expérimentales ne sont bien évidement pas reproduites étant donné qu'une seule énergie laser a été considérée. La décroissance du taux Sn-K_α due à un ralentissement des électrons rapides plus prononcé des les cibles épaisses est clairement visible sur les résultats de simulation.

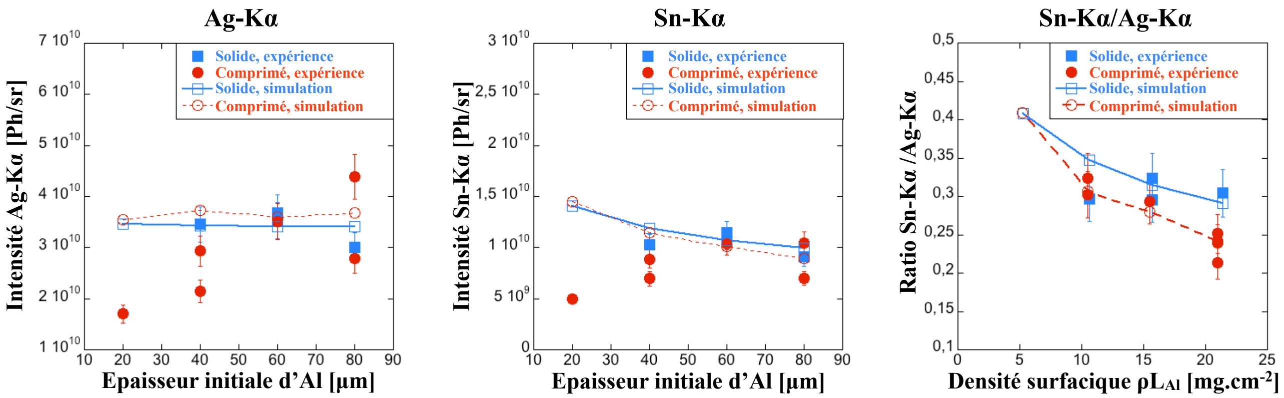

Figure 6.7: Comparaison des taux absolus Ag-K_α (gauche) et Sn-K_α (milieu) ainsi que du ratio Sn-K_α/Ag-K_α (droite) obtenus lors de l'expérience (symbole pleins) et calculés par les simulations de transport (symboles vides) pour les cibles solides (carrés) et comprimées (disques).

La figure 6.7 (droite) présente une comparaison du ratio Sn-K_α/Ag-K_α. Les ratios expérimentaux et simulés sont en très bon accord, les résultats numériques reproduisant particulièrement bien la décroissance du signal plus prononcée pour les cibles d'aluminium comprimées et chauffées les plus épaisses. Il est important de noter que les simulations prédisent aussi une décroissance du signal pour des cibles moins épaisses ($\rho L = 10$ mg.cm^{-2}) alors que cette tendance n'est pas détectée expérimentalement à cause du manque de statistique. Afin d'obtenir une quantification de l'importance relative des pertes résistives et collisionnelles, la quantité d'énergie perdue par ces deux mécanismes et intégrée sur l'épaisseur d'aluminium est représentée sur la Figure 6.8. Le résultat le plus marquant vient du fait que dans le régime de densité de courant étudié, caractérisé par une densité $\langle j_b \rangle = 2.4 \times 10^{11}$ A.cm^{-2}, les pertes d'énergie d'origine résistive deviennent comparables aux pertes d'énergie collisionnelle dans les cibles comprimées, le pouvoir d'arrêt résistif augmentant de $\sim 53\%$. Il est important de noter que cette augmentation est bien inférieure à celle de la résistivité dans l'aluminium comprimé. Ceci peut s'expliquer par le fait que le faisceau d'électrons rapides va chauffer en quelques centaines de fs la couche de propagation jusqu'à atteindre le régime de Spitzer, annihilant alors toute différence initiale entre matériau solide et comprimé [Vauzour et al., 2012, 2014].

3 Etude du transport d'électrons rapides dans des cibles coniques en géométrie de compression plane

Une amélioration du schéma d'allumage rapide conventionnel consiste à insérer un cône creux dans la cible de D-T. La source d'électrons rapides, générée lors du couplage d'un faisceau laser intense avec la pointe du cône, est alors située plus prés du coeur de la cible, pouvant ainsi

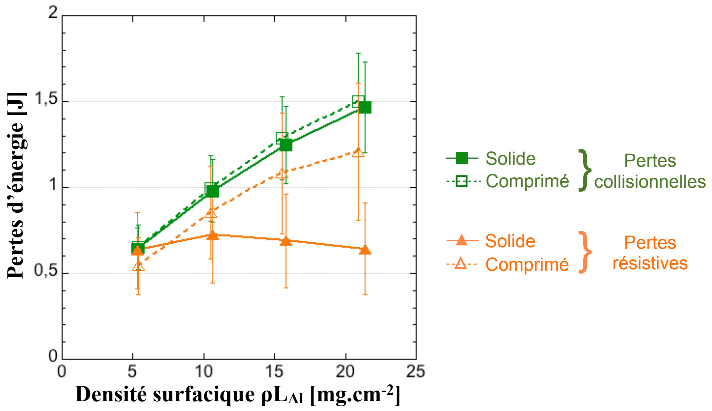

Figure 6.8: Pertes d'énergie collisionnelles (vert) et résistives (orange) intégrées sur la durée de la simulation et sur l'épaisseur d'aluminium en fonction de la densité surfacique pour les cibles solides (symboles pleins) et comprimées (symboles vides).

augmenter l'efficacité du couplage. L'utilisation d'un tel cône d'or ou de diamant est cependant à l'origine d'un certain nombre de problèmes. D'une part, la compression asymétrique de la capsule génère un jet de plasma le long de l'axe du cône, repoussant la source d'électrons loin du coeur. D'autre part, la génération d'une source d'électrons adaptée à un couplage efficace avec le coeur de D-T lors de l'interaction du faisceau laser avec le cône est actuellement un sujet de recherche très actif.

Cette section présente les résultats et l'interprétation théorique d'une campagne expérimentale effectuée sur l'installation LULI2000 (LULI, France). Cette expérience avait pour but d'effectuer une étude systématique du transport d'électrons dans des cibles coniques comprimées par un choc plan. Cette campagne expérimentale a été divisée en deux parties distinctes. La première a consisté à étudier la propagation du choc dans la cible, son interaction avec la pointe du cône et son glissement le long des parois. Un diagnostic de radiographie X a été utilisé à cet effet. Dans la deuxième partie, un faisceau d'électrons rapides a été généré en couplant un faisceau laser intense à haut contraste avec la pointe du cône à différents instants de la compression. Un diagnostic d'imagerie X nous a alors permis de visualiser le couplage avec la pointe du cône intacte ou avec un plasma en expansion, en fonction du moment d'injection. Le travail expérimental, ainsi que l'interprétation des données, sont le fruit d'une collaboration internationale entre le CELIA, le LULI, l'Université de Milan (Italie), le LLNL (Etats-Unis), UCSD (Etats-Unis), l'Université du Nevada (Etats-Unis), General Atomics (Etats-Unis), l'Université de Strathclyde (Royaume-Uni) et l'Université d'Alberta (Canada).

3.1 Caractérisation hydrodynamique de la cible

La première partie de cette expérience est dédiée à la caractérisation hydrodynamique des cibles coniques. Elle a été réalisée en 2011 sur l'installation laser LULI200.

Dispositif expérimental

Nous avons utilisé lors de cette campagne les faisceaux lasers court et long de l'installation. Leurs caractéristiques étaient les suivantes :

- le faisceau laser court (SP) doublé en fréquence ($\lambda_L = 0.53$ μm), utilisé afin de générer le rayonnement de radiographie, délivre des impulsions de 10 J sur cible. Il est caractérisé par un profil temporel gaussien de largeur à mi-hauteur égal à 1 ps. Ce faisceau est focalisé par une parabole hors axe d'ouverture f/4 en une tache de 10 μm (FWHM). L'intensité crête sur cible est de 10^{19} W.cm^{-2};

- le faisceau laser long (LP) doublé en fréquence ($\lambda_L = 0.53$ μm), utilisé afin de comprimer la cible, délivre des impulsions de 475 ± 49 J. Il est caractérisé par un profil temporel carré de 5 ns de largeur, et est focalisé en face arrière des cible par la combinaison d'une lentille est d'une lame de phase (RPP) en une tache focale homogène de 500 μm (FWHM) transportant $\sim 70\%$ de l'énergie. L'intensité crête est de $(2.5 \pm 0.3) \times 10^{13}$ W.cm^{-2}.

La géométrie des cibles utilisées est présentée sur la figure 6.9. Elles sont composées d'un cône de cuivre de 10 μm d'épaisseur et de 400 ± 10 μm de long, enchâssé dans un bloc épais de carbone de dimensions 500×1190 μm^2. Un traceur d'argent de 10 μm d'épaisseur est placé à 100 μm de la pointe du cône de 50 μm de diamètre. Un couche de polypropylène placée en face arrière des cibles sert à la fois d'ablateur et de protection permettant d'éviter toute irradiation directe du traceur d'argent par la faisceau laser long. Ce dernier est en effet focalisé sur la couche de plastique afin de générer un choc de compression transversalement étendu, se propageant vers la pointe du cône. Le faisceau laser court est ensuite focalisé sur une feuille de cuivre de 10 μm d'épaisseur placé à 10 mm de la cible afin de générer un rayonnement X intense, dominé par l'émission K$_\alpha$ du cuivre, utilisé pour radiographier la cible en cours de compression. Le retard entre les deux faisceaux peut être ajusté de manière à radiographier la cible à différents instants de la compression. Un diagnostique de pyrométrie optique résolu en temps (SOP) est ici encore utilisé afin de mesurer la vitesse de propagation du choc, cette dernière servant à calibrer des simulations hydrodynamiques 2D utilisées, comme dans l'expérience sur Titan, pour déterminer les retards à adopter entre les faisceaux laser.

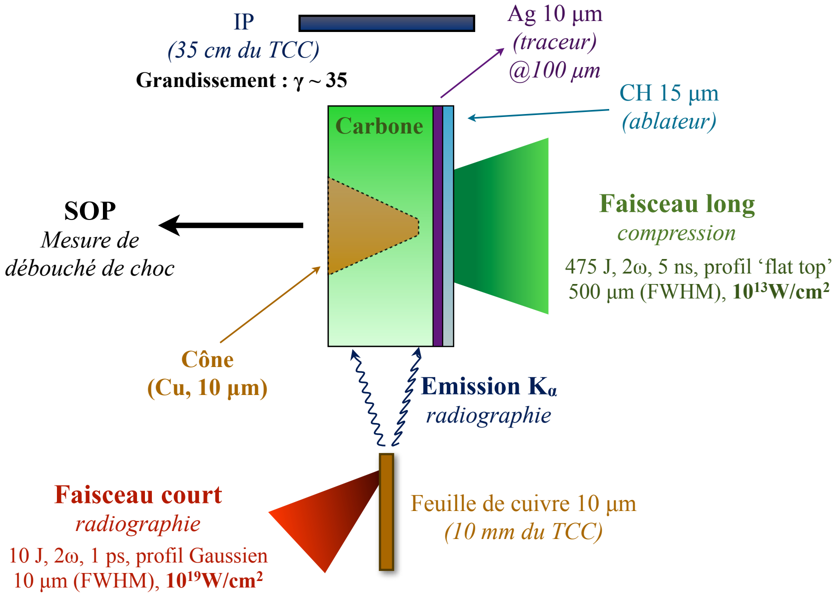

Figure 6.9: Dispositif expérimental utilisé sur la première campagne au LULI2000.

Résultats expérimentaux

Les images de radiographie obtenues à différents instants de compression sont présentées sur la Figure 6.10. La structure du cône est visible sur chaque image, montrant ainsi que ce dernier survit à la forte pression du choc. Pour un retard entre les deux faisceaux laser de 9 ns, le choc se propage déjà dans la région du cône, cette mesure étant consistante avec les mesures de débouché de choc de 8.3 ns obtenues avec le SOP. La déformation de l'interface entre la couche d'argent et celle de carbone est clairement visible sur chaque image, l'amplitude de sa déformation augmentant avec le retard. La position du front de choc, bien que plus difficile

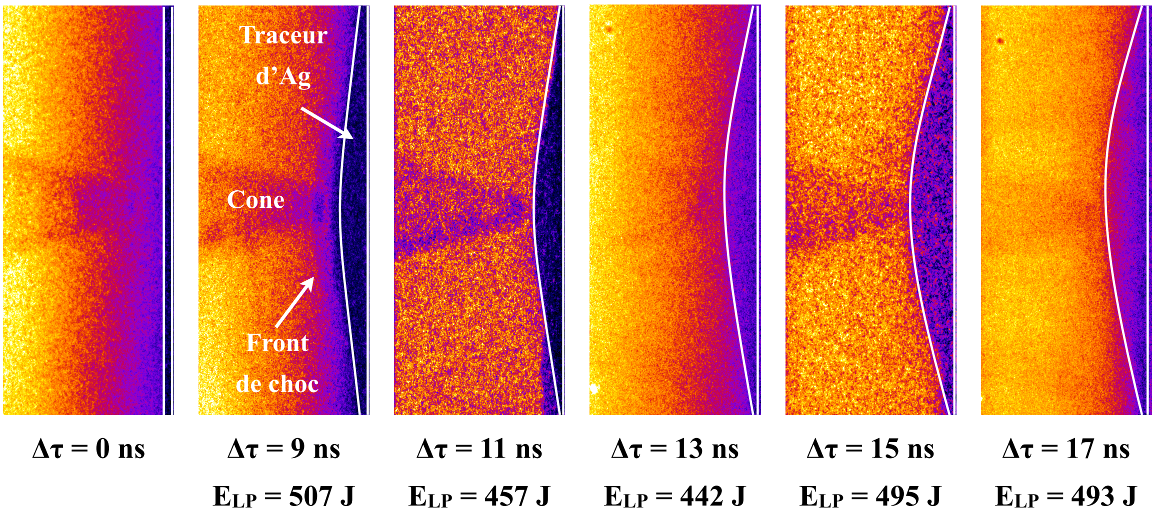

Figure 6.10: Images de radiographie de la cible obtenues à différents instants de la compression. Le retard entre les deux faisceaux laser croît en se déplaçant vers la droite. Le faisceau laser long irradie les cibles depuis le côté droit. L'image située tout à gauche, notée $\Delta\tau = 0$ ns, correspond à une radiographie de la cible non comprimée. Le traceur d'argent est matérialisé par deux lignes blanches verticales.

à déterminer, peut être mesurée par une étude attentive de chaque image avec cependant des barres d'erreur plus importantes que pour la position de l'interface Ag/C. La figure 6.11 présente l'évolution de ces positions en fonction du temps ainsi que leur comparaison à des simulations hydrodynamiques 1D effectuées avec le code MULTI [Ramis et al., 1988]. Après une phase à vitesse constante, les vitesses du front de choc et de l'interface Ag/C diminuent avec le temps. En ne considérant que cette première phase, il est possible d'estimer une vitesse de choc U et une vitesse fluide D égale à la vitesse de l'interface Ag/C :

$$U = 20.8 \pm 2.5\ \mu\text{m.ns}^{-1} \qquad D = 8.78 \pm 0.68\ \mu\text{m.ns}^{-1} \tag{6.7}$$

En injectant ces deux valeurs dans les équations de Rankine-Hugoniot, il est alors possible de remonter à la densité et à la pression moyennes de la couche de carbone :

$$\rho = 3.46 \pm 0.36\ \text{g.cm}^{-1} \qquad P = 3.65 \pm 0.52\ \text{Mbar} \tag{6.8}$$

3.2 Etude du transport d'électrons rapides dans la cible conique

La deuxième partie de l'expérience, réalisée en 2013, est dédiée à l'étude de la propagation d'électrons chauds dans la cible conique.

Dispositif expérimental

Nous avons utilisés ici encore les faisceaux lasers court et long de l'installation. Ceux-ci présentaient des caractéristiques et des fonctions légèrement différentes que celles rencontrées dans la première partie de l'expérience :

- le faisceau laser court doublé en fréquence, utilisé pour générer le faisceau d'électrons chauds, délivre des impulsions de 55 J. Il est caractérisé par un profil temporel gaussien de 1.3 ps (FWHM), et est focalisé sur la pointe du cône par la parabole hors axe. La mise en place pour la première fois sur cette installation d'un miroir plasma permet de s'affranchir du piédestal de l'impulsion. L'énergie sur cible et l'intensité crête sont respectivement de 33 J et de 1×10^{19} W.cm^{-2};

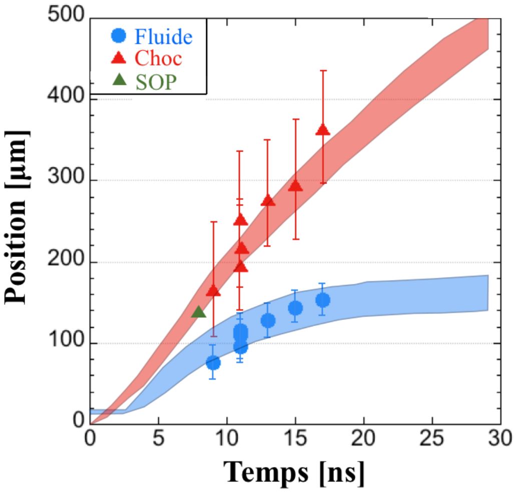

Figure 6.11: Positions du front de choc (triangles rouges), de l'interface Ag/C (disques bleus) et du débouché de choc mesuré par SOP (triangle vert) en fonction du temps. L'abscisse 0 ns correspond au début de l'irradiation de la cible par le faisceau laser long. Les simulations MULTI, en bon accord avec les résultats expérimentaux, sont représentées par les zones colorées en rouge et en bleu.

- le faisceau long doublé en fréquence, utilisé pour comprimer les cibles, délivre des impulsions de 496 ± 50 J. Il est caractérisé par un profil temporel carré de 3 ns de largeur. L'impulsion est focalisée sur la cible en une tache focale de 340 μm (FWHM) contenant 61% de l'énergie laser. L'intensité crête est d'environ 10^{13} W.cm^{-2}.

La géométrie des cibles utilisée est légèrement différente que lors de la première campagne. Le traceur d'argent est remplacé par un traceur de cuivre positionné à 50 μm de la pointe du cône. La modification majeure par rapport à la première campagne vient du faisceau laser court focalisé ici sur la pointe du cône à différents instants de la compression. Un imageur X regardant le côté de la cible et récoltant le signal K$_\alpha$ généré lors de l'interaction entre les électrons rapides et les atomes de cuivre constituant le cône et le traceur est le diagnostic principal de cette expérience. Des mesures de débouché de choc permettent une fois encore de déterminer les différents retards à adopter entre les deux faisceaux laser.

Résultats expérimentaux et simulations hydrodynamiques

La figure 6.12 présente les résultats obtenus avec l'imageur Cu-K$_\alpha$ en fonction du retard entre les deux impulsions laser. L'image de gauche, notée "PS seul", a été obtenue sans compression de la cible. Ces données sont comparées à des simulations hydrodynamiques 2D effectuées par Philippe Nicolaï et Jérôme Breil (CELIA) en utilisant le code CHIC. Au début de la compression, l'émission K$_\alpha$ provient principalement de la pointe du cône. Le faisceau laser court à haut contraste a par conséquent été couplé de manière efficace à la pointe du cône, et les électrons rapides ont été générés principalement dans cette région de la cible. L'émission du traceur en face arrière est aussi clairement visible. Quand le retard entre les deux faisceaux augmente, les résultats expérimentaux, ainsi que les simulations, montrent que le traceur est poussé vers la pointe du cône sous l'effet de la compression de la cible. Lorsque le faisceau d'électrons est injecté après 3 ns de compression, la carte d'émission change totalement : l'émission Cu-K$_\alpha$ provient de tout le volume du cône. Ceci peut-être expliqué par le fait qu'au delà de ce retard, le choc débouche dans le cône, entraînant ainsi son remplissage progressif par le plasma de

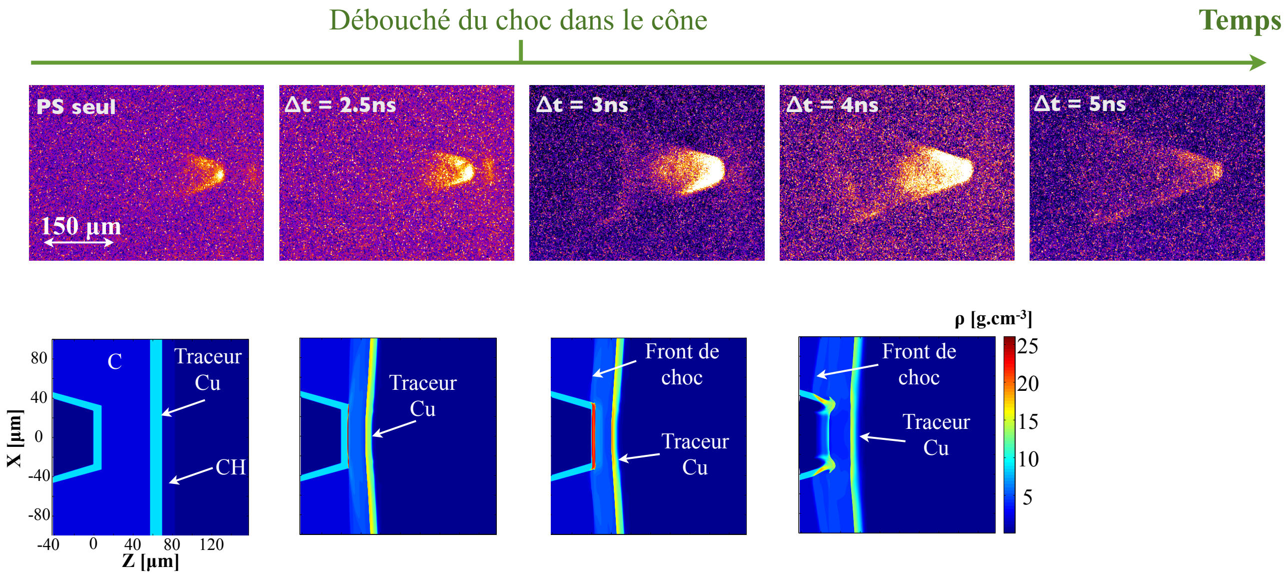

Figure 6.12: Résultats expérimentaux (haut) obtenus en imageant l'émission Cu-K_α de la cible. Le retard entre les deux faisceaux laser augmente en se déplaçant vers la droite. Ces images sont comparées à des résultats de simulations hydrodynamiques 2D (bas).

cuivre.

Simulations du transport d'électrons

Les paramètres de la source d'électrons ont été calculés avant et après le débouché de choc avec le code PIC OCEAN [Nuter & Tikhonchuk, 2013] en 1D en collaboration avec Rachel Nuter (CELIA). L'interaction du faisceau à haut contraste avec la cible présentant soit un gradient de densité raide, soit une face avant en expansion (retard de 4.6 ns entre les impulsions laser), a été simulée. Les fonctions de distribution en énergie extraites des simulations présentent des caractéristiques relativement différentes (Figure 6.13). Il existe en effet après débouché du choc une composante haute énergie, ajustée par une fonction exponentielle avec une température de 1.5 MeV, qui n'apparait pas avant le débouché de choc. De plus, l'énergie moyenne des électrons accélérés passe de ~ 15 keV à 190 keV après le débouché du choc.

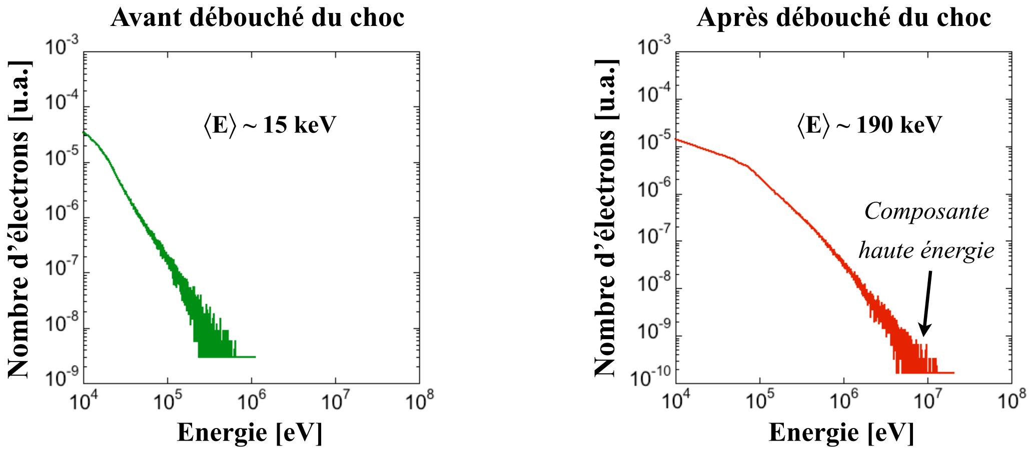

Figure 6.13: Comparaison des fonctions de distribution électroniques extraites des simulations PIC avant (gauche) et après (droite) débouché du choc.

Ces distributions en électrons, ainsi que les profils de densité et de température calculés par les simulations hydrodynamiques 2D, sont injectés dans le code de transport hybride M1 développé au CELIA [Dubroca et al., 2010; Touati et al., 2014]. La propagation des électrons dans la cible est simulée durant 4 ps avec une résolution spatiale de 2 μm, pour les cas correspondants à une propagation dans une cible non comprimée (0 ps) et à une cible où la couche de carbone est complètement comprimée mais où le choc n'a pas encore débouché dans la pointe du cône (2.8 ns). La résistivité du cuivre est calculée avec le modèle de Lee & More corrigé par Desjarlais [Lee, 1971; Desjarlais, 2001]. Celle du carbone est extraite de calculs de dynamique moléculaire [McKenna et al., 2011] (Figure 6.14).

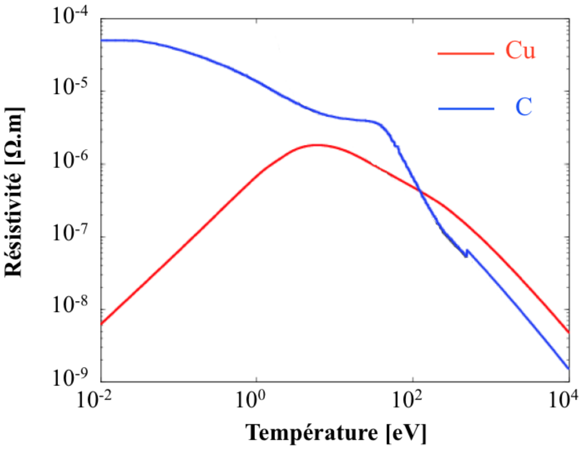

Figure 6.14: Evolution de la résistivé du cuivre (rouge) et du carbone (bleu) en fonction de la température.

La Figure 6.15 (gauche) présente la densité ionique de la cible non comprimée injectée dans la simulation de transport. La pointe du cône et le traceur de cuivre sont parfaitement visibles. Les électrons sont injectés sur la gauche. En regardant la densité électronique dans la cible 2.2 ps après injection des électrons rapides (Figure 6.15 [milieu]), il est possible de voir une collimation des électrons rapides dans la couche de carbone. Cette collimation est due à un champ magnétique azimuthal auto-généré d'origine résistive (Figure 6.15 [droite]) dont l'amplitude maximale importante, proche de 500 T, est liée à la haute résistivité de la couche

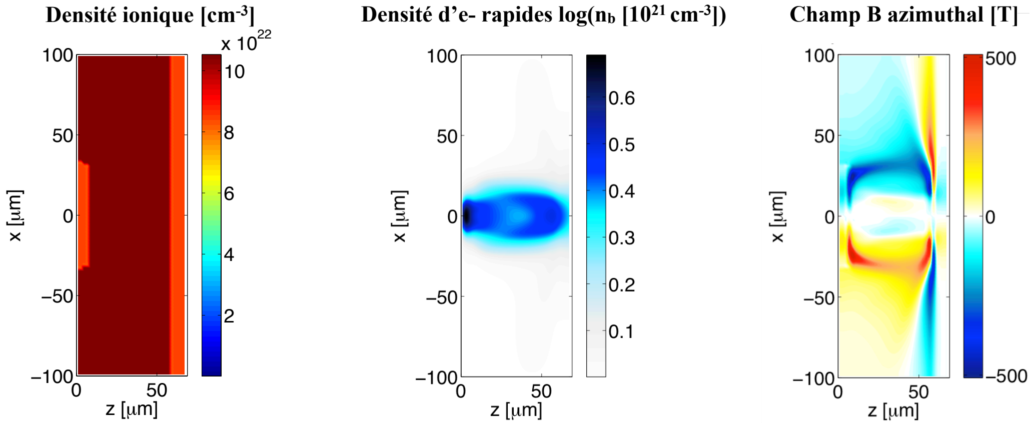

Figure 6.15: (Gauche) Densité ionique de la cible non comprimée injectée dans les simulations de transport. (Milieu) Densité d'électrons rapides dans la cible 2.2 ps après injection. (Droite) Champ magnétique azimuthal collimatant les électrons rapides.

de carbone traversée. Ce phénomène peut aussi être observé pour le cas à 2.8 ns (Figure 6.16). Le champ magnétique collimateur y est cependant légèrement plus fort du fait de la plus faible résistivité du carbone comprimé initialement chauffé à quelques eV diminuant l'effet du champ décollimateur lié aux gradients de résistivité.

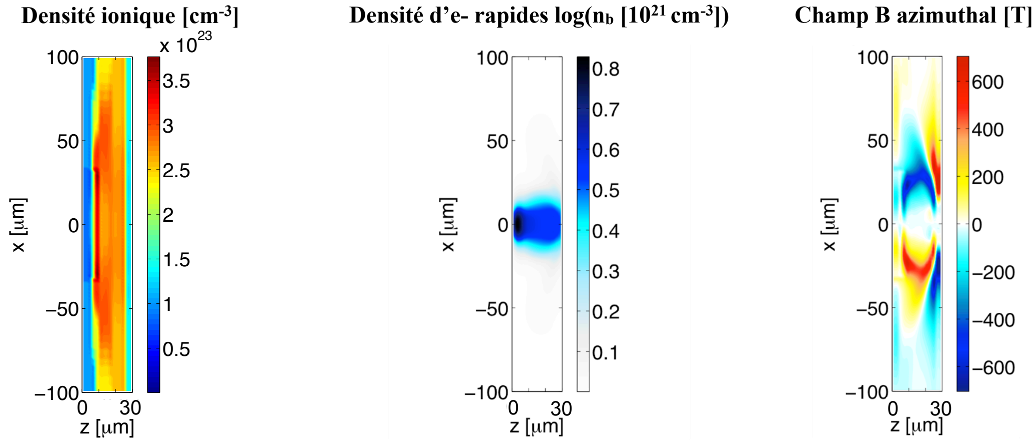
Densité ionique [cm^{-3}]

Densité d'e- rapides log(n_b [10^{21} cm^{-3}])

Champ B azimuthal [T]

Figure 6.16: (Gauche) Densité ionique de la cible après 2.8 ns de compression injectée dans les simulation de transport. (Milieu) Densité d'électrons rapides dans la cible 2.2 ps après injection. (Droite) Champ magnétique azimuthal collimatant les électrons rapides.

4 Conclusion et perspectives

Le travail présenté dans cette thèse a été accompli dans le contexte du schéma d'allumage rapide des cibles de fusion confinées de manière inertielle. Nous avons étudié la physique du transport d'électrons rapides, caractérisés par des hautes densités de courant ($j_b \sim 10^{11}$ A.cm^{-2}), et générés par des faisceaux lasers intenses ($10^{19} - 10^{20}$ W.cm^{-2}) dans des cibles comprimées de manière plane.

Les résultats expérimentaux ont été obtenus dans le contexte de deux campagnes expérimentales. La première présente les résultats d'une étude dédiée à la quantification des pertes d'énergie collisionnelle et résistive d'un faisceau d'électrons rapides se propageant dans des échantillons d'aluminium. Nous avons comparés les résultats obtenus dans des cibles solides et froides, et comprimées et initialement chauffées à quelques eV par choc laser. Les conditions rencontrées dans ces derniers types d'échantillons sont représentatives des régions hautement résistives que l'on peut trouver proche du cône dans une cible d'allumage rapide. La géométrie de compression 1D nous a permis de générer un plasma homogène étendu perpendiculairement à l'axe de propagation des électrons. La conservation de la densité surfacique avec la compression nous a aussi permis d'identifier de manière précise la contribution des pertes d'énergie résistive en comparant les cibles solides et tièdes de même épaisseur initiale. Nous avons pour la première fois démontré de manière expérimentale l'importance de ces mécanismes sur la propagation des électrons rapides. Ces pertes d'énergie résistive ont atteint, dans les échantillons d'aluminium comprimés, des valeurs comparables aux pertes collisionnelles dans la gamme de densité de courant étudié ($10^{11} < j_b < 10^{12}$ A.cm^{-2}). Nous avons aussi pu confirmer les prédictions théoriques du caractère transitoire de la résistivité de ce métal avec la température électronique. Notre modèle prédit ainsi une saturation des pertes d'énergie résistive pour $j_b > 10^{11}$ A.cm^{-2} à cause de la transition rapide de la résistivité vers le régime de Spitzer.

La deuxième étude présentée se base sur les résultats d'une campagne expérimentale dédiée à la caractérisation des processus de génération et de transport de faisceau d'électrons rapides dans une cible conique comprimée par un choc plan. Les électrons ont été générés lors du couplage d'un laser intense à haute contraste ($I_L \sim 10^{19}$ W.cm^{-2}) avec la pointe du cône à différents instants de la compression. Nous avons constaté la survie de la structure du cône, malgré la pression de 3 Mbar, en utilisant un système de radiographie X. Nous avons ainsi pu démontrer l'importance capitale du timing d'injection des électrons rapides par rapport au temps de débouché de choc provoquant le remplissage progressif du cône par le plasma. Nous avons pu observer l'extension spatiale de la source d'électrons ainsi que son transport dans les profondeurs de la cible. Au début de la compression, quand le choc n'a pas encore atteint la face interne des parois du cône, les électrons rapides sont principalement générés dans sa pointe. Une fraction importante d'entre eux est alors injectée à l'intérieur de la cible et se propage sur quelques dizaines de microns. Dans ce cas particulier, les simulations de transport ont clairement montré une collimation des électrons par des champs magnétiques résistifs auto-générés. Après le débouché du choc, nous avons constaté que les électrons étaient générés dans un volume important du cône, ce dernier étant en cours de remplissage progressif par le plasma. Ces résultats confirment l'effet délétère qu'a le pré-plasma sur la génération et les transport d'électrons dans la structure conique. Même si l'énergie moyenne de la population électronique générée sur un long gradient de densité est plus importante que sur un gradient raide, une partie importante d'entre eux est piégée dans le volume du cône et n'est par conséquent pas injectée dans les profondeurs de la cible.

Cette thèse a permis de mieux comprendre les mécanismes associés au transport d'électrons rapides. Les campagnes expérimentales se sont déroulées sur des installations laser bien plus modestes que celles qui seraient nécessaires pour atteindre les conditions d'allumage rapide. Cependant, la comparaison des données obtenues avec les différents modèles théoriques et les résultats de simulation nous ont permis d'identifier les processus physiques clefs et d'en évaluer leurs rôles respectifs. L'état de la matière tiède et dense atteint dans nos conditions expérimentales est représentatif de la région du cône dans une cible d'allumage rapide, bien que les caractéristiques de la source d'électrons générée sont relativement différentes de ces conditions. Les effets physiques abordés dans cette thèse, ainsi que les configurations expérimentales originales qui ont été testées, sont les suivants :

- transport et pertes résistives;
- utilisation de cônes enchâssés;
- caractérisation de la source d'électrons dans le cône;
- survie de la pointe du cône;
- technique de radiographie X.

A court terme, ces deux campagnes expérimentales pourraient être réitérées sur des installations plus puissantes déjà existantes comme Orion (Royaume-Uni), Omega+EP (Etats-Unis), Gekko XII+Firex (Japon) et bientôt le LMJ+Petal. L'augmentation de la densité de courant jusqu'à $10^{12} - 10^{13}$ A.cm^{-2} permettrait de vérifier les prédictions théoriques sur la saturation de la contribution des mécanismes de perte d'énergie résistive. Pour les cibles coniques, l'utilisation d'un faisceau laser à haut contraste, de plus haute énergie, et de 10 ps de durée, permettrait d'étendre cette étude.

Un effort important a été fourni durant les dernières années sur le développement de code numériques, incluant les modèles hybrides, permettant alors de simuler les conditions d'allumage rapide de manière relativement réaliste. Les codes PIC et hydrodynamiques permettent d'ores et déjà de simuler respectivement les sources d'électrons et la physique d'implosion des cibles dans le régime d'allumage rapide. Cet effort numérique doit être poursuivi de manière à fournir des possibilités de simulations intégrées, qui permettraient alors de simuler de manière consistante la génération et le transport des électrons chauds dans une cible en cours de compression.

Dans une perspective à plus long terme, la validation expérimentale du modèle de transport d'électrons doit être étendue aux conditions d'énergie et de durée d'impulsion du schéma d'allumage rapide. Des expériences d'intérêt pour l'allumage rapide doivent avoir lieu sur les installations LMJ+Petal, NIF+Arc et Gekko XII+Firex. Le rôle des pertes d'énergie résistive générées en utilisant un faisceau de 10 ps doit être étudié. Cependant, une installation laser présentant une telle durée d'impulsion et une capacité de génération d'impulsions de ~ 100 kJ n'existe pas pour le moment. Elle permettrait d'explorer le régime de densité de courant extrême $j_b \sim 10^{14}$ A.cm^{-2} qui reste pour le moment inaccessible.

Pour conclure, le problème principal du schéma d'allumage rapide réside dans le dépôt d'énergie des électrons dans le coeur de D-T. L'allumage des réactions de fusion avec une énergie laser raisonnable n'est possible que si l'on parvient à confiner le faisceau d'électrons dans un rayon comparable au rayon du coeur. Deux approches différentes sont pour cela actuellement en cours d'étude : la génération de champs magnétiques auto-générés et l'utilisation de champs magnétiques externes de l'orde de plusieurs kT. Les champs magnétiques résistifs peuvent être générés par des gradients de résistivité initialement implémentés dans les cibles, comme par exemple le système d'aiguillage magnétique. Les générateurs de champs magnétiques pulsés peuvent d'un autre côté créer des champs de quelques dizaines de T pouvant être alors amplifiés par compression de la cible. Les cibles de type *capacitor-coil* irradiées par laser permettent de leur côté de générer des champs de l'ordre du kT durant quelques ns. Une première preuve de la collimation de faisceaux d'électrons rapides dans un champ externe a été obtenue par notre groupe en 2014 au LULI, et d'autres tests sont planifiés pour 2015. L'implémentation de cette technique dans une expérience intégrée d'allumage rapide doit encore être réalisée.

Bibliography

2014, IAEA, http://www.iaea.org/pris/

2014, IPCC, http://www.ipcc.ch/

2014, ipp.mpg: http://www.ipp.mpg.de

Adam, J., Héron, A., & Laval, G. 2006, Physical Review Letters, 97, 205006

Akli, K., Patel, P., Maren, R. V., et al. 2010, Journal of Instrumentation, 5

Alfvén, H. 1939, Physical Review, 55, 425

Amplitude. 2014, http://www.amplitude-technologies.com/

Artep, I. 2014, Artep, Incorporated, http://artepinc.com

Atzeni, S. 1999, Physics of Plasmas, 6, 3316

Atzeni, S., Schiavi, A., & Davies, J. 2009, Plasma Physics and Controlled Fusion, 51, 015016

Atzeni, S., Temporal, M., & Honrubia, J. 2002, Nuclear Fusion, 42, L1

Azechi, H., Sakaiya, T., Watari, T., et al. 2009, Physical Review Letters, 102, 235002

Backus, S., Kapteyn, H., Murnane, M., et al. 1993, Optics Letters, 18, 134

Barker, L. & Hollenbach, R. 1972, Journal of Applied Physics, 43, 4669

Baton, S. D., Koenig, M., Fuchs, J., et al. 2008, Physics of Plasmas, 15, 042706

Beg, F. N., Bell, A. R., Dangor, A. E., et al. 1997, Physics of Plasmas, 4, 447

Bell, A., Davies, J., Guerin, S., & Ruhl, H. 1997, Plasma Physics and Controlled Fusion, 39, 653

Bellei, C., Divol, L., Kemp, A. J., et al. 2013, Physics of Plasmas, 20, 052704

Berger, M. & Seltzer, S. 1964, Tables of energy losses and ranges of electrons and positrons, Tech. Rep. NASA-SP-3012, National Aeronautics and Space Administration

Bethe, H. 1933, Handbuch für physik (Julius Springer)

Bethe, H. 1953, Physical Review, 89, 1256

Bethe, H. & Heitler, W. 1934, Proceedings of the Royal Society, A146, 83

Betti, R., Zhou, C. D., Anderson, K. S., et al. 2007, Physical Review Letters, 98, 155001

Bonnet, T., Comet, M., Denis-Petit, D., et al. 2013, Review of Scientific Instruments, 84, 103510

Bret, A., Firpo, M.-C., & Deutsch, C. 2004, Physical Review E, 70, 046401

Brookner, E. 1985, Scientific Amercian, 252, 2

Brunel, F. 1987, Physical Review Letters, 59, 52

Buneman, O. 1959, Physical Review, 115, 503

Cai, H.-b., Mima, K., Zhou, W.-m., et al. 2009, Physical Review Letters, 102, 245001

Campbell, R., DeGroot, J., Mehlhorn, T., Welch, D., & Oliver, B. 2003, Physics of Plasmas, 10, 4169

Casnati, E., Tartari, A., & Baraldi, C. 1982, Journal of Physics B: Atomic and Molecular Physics, 15, 155

Catto, P. & More, R. 1977, Physics of Fluids, 20, 704

Cauchois, Y. 1932, Journal de Physique et le Radium, 3, 320

Chang, P. Y., Fiksel, G., Hohenberger, M., et al. 2011, Physical Review Letters, 107, 035006

Chen, C. 2009, PhD thesis, Massachusetts Institue of Technology

Chen, C., King, J., Key, M., Akli, K., & Beg, F. 2008a, Review of Scientific Instruments, 79

Chen, C. D., Patel, P. K., Hey, D. S., et al. 2009a, Physics of Plasmas, 16

Chen, H., Fiksel, G., Barnak, D., et al. 2014, Physics of Plasmas, 21, 040703

Chen, H., Link, A., Maren, R. V., et al. 2008b, Review of Scientific Instruments

Chen, H., Patel, P., Price, D., Young, B., & Springer, P. 2003, Review of Scientific Instruments, 74, 1551

Chen, H., Wilks, S., Bonlie, J., et al. 2009b, Physical Review Letters, 102, 105001

Chen, H., Wilks, S., Patel, P., & Shepherd, R. 2006, Review of Scientific Instruments, 77

Chen, H., Wilks, S. C., Meyerhofer, D. D., et al. 2010, Physical Review Letters, 105, 015003

Chimier, B. 2008, PhD thesis, Universié Bordeaux 1

Chrisman, B., Sentoku, Y., & Kemp, A. 2007, Physics of Plasmas, 15, 056309

Cottrill, L., Kemp, A., Tabak, M., & Town, R. 2010, Nuclear Fusion, 50

Daido, H., Miki, F., Mima, K., et al. 1986, Physical Review Letters, 56, 846

Dasch, C. 1992, Applied Optics, 31, 1146

Davies, J. 2002, Laser and Particle Beams, 20, 243

Davies, J. 2003, Physical Review E, 68, 056404

Davies, J. 2004, Physical Review E, 69, 065402

Davies, J. 2009, Plasma Physics and Controlled Fusion, 51, 014006

Davies, J., Bell, A., Haines, M., & Guerin, S. 1997, Physical Review E, 56, 7193

Davies, J., Betti, R., Nislon, P., & Solodov, A. 2013, Physics of Plasmas, 20

Debayle, A. 2008, PhD thesis, Universié Bordeaux 1

Debayle, A., Honrubia, J., d'Humières, E., & Tikhonchuk, V. 2010, Physical Review E, 82, 036405

DeMaria, A. J., Gagosz, R., Heynau, H. A., Penney, A. W., & Wisner, G. 1967, Journal of Applied Physics, 38, 2693

Desjarlais, M. 2001, Contribution to Plasma Physics, 41, 267

d'Humières, E., Lefebvre, E., Gremillet, L., & Malka, V. 2005, Physics of Plasmas, 12, 062704

Dittrich, T. R., Hurricane, O. A., Callahan, D. A., et al. 2014, Physical Review Letters, 112, 055002

Dong, Q., Sheng, Z.-M., Yu, M., & Zhang, J. 2003, Physical Review E, 68, 026408

Doumy, G. 2006, PhD thesis, Ecole Polytechnique

Doumy, G., Quere, F., Gobert, O., Perdrix, M., & Martin, P. 2004, Physical Review E, 69, 026402

Drake, J. 1974, Physics of Fluids, 17, 778

Dubroca, B., Feugeas, J.-L., & Franck, M. 2010, The European Physical Journal D, 60, 301

efda. 2014, efda

Eidmann, K., ter Vehn, J. M., Schlegel, T., & Hüller, S. 2000, Physical Review E, 62, 1202

Estabrook, K. & Kruer, W. 1978, Physical Review Letters, 40, 42

Fermi, E. 1940, Physical Review, 57, 485

Fernandez, J., Albright, B., Beg, F., et al. 2014, Nuclear Fusion, 54, 054006

Fernandez, J., Albright, B., Flippo, K., et al. 2008, Journal of Physics: Conference Series, 112, 022051

Fork, R., Martinez, O., & Gordon, J. 1984, Optics Letters, 9, 150

Forslund, D., Kindel, J., & Lee, K. 1977, Physical Review Letters, 39, 284

Freidberg, J., Mitchell, R., Morese, R., & Rudsinski, L. 1972, Physical Review Letters, 28, 795

Friesen, H., Tiedje, H., Hey, D., Mo, M., & Beaudry, A. 2013, Review of Scientific Instruments, 84

Fujioka, S., Zhang, Z., Yamamoto, N., et al. 2012, Plasma Physics and Controlled Fusion, 54, 124042

Gahn, C., Taskiris, G., & Witte, K. 2000, Review of Scientific Instruments, 71, 1642

Gaillard, S. A., Kluge, T., Flippo, K. A., et al. 2011, Physics of Plasmas, 18, 056710

Garmire, E., Chiao, R., & Townes, C. 1966, Physical Review Letters, 16, 347

Gibbon, P. 2005, Short pulse laser interaction with matter: An introduction (World Scientific Publishing Company)

Gibbon, P. & Bell, A. 1992, Physical Review Letters, 68, 1535

Gibbon, P. & Forster, E. 1996, Plasma Physics and Controlled Fusion, 38, 769

Gitomer, S., Jones, R., Begay, F., et al. 1986, Physics of Fluids, 29, 2679

Glinec, Y., Faure, J., Dain, L. L., et al. 2005, Physics of Plasmas, 94, 025003

Gold, D. 1994, Optics Letters, 19, 2006

Goldstein, W. 2012, Science of Fusion Ignition on NIF, Report from the Science of Fusion Ignition Workshop LLNL-TR-570412, Lawrence Livermore National Laboratory

Goudsmit, S. & Saunderson, J. 1940, Physical Review, 57, 24

Green, J. S., Ovchinnikov, V. M., Evans, R. G., et al. 2008, Physical Review Letters, 100, 015003

Gremillet, L. 2001, PhD thesis, Ecole Polytechnique

Gryzinski, M. 1965, Physical Review, 138, A336

Haines, M. G., Wei, M. S., Beg, F. N., & Stephens, R. B. 2009, Phys. Rev. Lett., 102, 045008

Halbleib, J., Kensek, R., Valdez, G., Seltzer, S., & Berger, M. 1992, IEEE Transactions on, 39, 1025

Hall, T. 1984, Journal of Physics E: Scientific Instruments, 17, 110

Hammer, D. & Rostoker, N. 1970, Physics of Fluids, 13, 1831

Hamos, L. V. 1939, Zeitschrift für Kristallographie, 101, 17

Hargrove, L., Fork, R., & Pollack, M. 1964, Applied Physics Letters, 5, 4

Harrach, R. & Rogers, F. 1981, Journal of Applied Physics, 52, 5592

Hatchett, S., Brown, C., Cowan, T., et al. 2000, Physics of Plasmas, 7

Hauer, A., Kilkenny, J., & Landen, O. 1985, Review of Scientific Instruments, 56, 803

Hegelich, B., Jung, D., Albright, B., et al. 2011, Nuclear Fusion, 51, 083011

Henig, A., Kiefer, D., Markey, K., et al. 2009, Physical Review Letters, 103, 045002

Hidding, B., Pretzler, G., Clever, M., et al. 2007, Review of Scientific Instruments, 78, 083301

Hohenberger, M., Chang, P.-Y., Fiksel, G., et al. 2012, Physics of Plasmas, 19, 056306

Hombourger, C. 1998, Journal of Physics B: Atomic and Molecular Physics, 31, 3693

Honrubia, J., Alfonsìn, C., Alonso, L., Pérez, B., & Cerrada, J. 2006, Laser and Particle Beams, 24, 217

Honrubia, J. & ter Vehn, J. M. 2006, Nuclear Fusion, 46, L25

Hooper, M., ed. 1985, Plasma processes in non-ideal plasmas, Proceedings of the 29th Scottish Universities Summer School in Physics. Laser plasma interaction 3, ed. M. Hooper, NATO Advanced Study Institue, Scottish Universities Summer School in Physics

Huba, J. 2009, NRL plasma formulary, Naval Research Laboratory

Hubbel, J. & Seltzer, S. 2014, Tables of X-ray Mass Attenuation Coefficients and Mass Energy-Absorption Coefficients from 1 keV to 20 MeV for Elements Z = 1 to 92 and 48 Additional Substances of Dosimetric Interest, http://www.nist.gov/pml/data/xraycoef/

Hum, H. 1983, Physics of Fluids, 26, 3098

Hurricane, O. A., Callahan, D. A., Casey, D. T., et al. 2014, Nature, 506, 343

IEA. 2012, Energy Technology Perspectives

IEA. 2013, Key World Energy Statistics

Jackson, J. 1975, Classical Electrodynamics, 2nd Edition (John Wiley and Sons, Inc.)

Johzaki, T., Nagatomo, H., Sunahara, A., et al. 2011, Nuclear Fusion, 51, 073022

Jung, D., Yin, L., Albright, B., et al. 2013a, New Journal of Physics, 15, 023007

Jung, D., Yin, L., Gautier, D. C., et al. 2013b, Physics of Plasmas, 20, 083103

Kahoul, A., Abassi, A., Deghfel, B., & Nekkab, M. 2011, Radiation Physics and Chemistry, 80, 369

Kapteyn, H. & Murnane, M. 1991, Optics Letters, 16, 490

Kar, S., Robinson, A., Caroll, D., et al. 2009, Physical Review Letters, 102, 055001

Karasik, M., Weaver, J. L., Aglitskiy, Y., et al. 2010, Physics of Plasmas, 17, 056317

Katz, L. & Penfold, A. 1952, Review of Modern Physics, 24, 28

Kemp, A. & Divol, L. 2012, Physical Review Letters, 109, 195005

Key, M., Freeman, R., Hatchett, S., et al. 2006, Fusion Science and Technology, 49, 440

Key, M. H., Cable, M. D., Cowan, T. E., et al. 1998, Physics of Plasmas, 5, 1966

Kirkpatrick, P. & Baez, A. 1948, Journal of the Optical Society of America, 38, 766

Knauer, J. P., Gotchev, O. V., Chang, P. Y., et al. 2010, Physics of Plasmas, 17, 056318

Koch, H. & Motz, J. 1959, Review of Modern Physics, 51, 920

Kodama, R., Azechi, H., Fujita, F., et al. 2004, Nuclear Fusion, 44, S276

Kodama, R., Norreys, P. A., Mima, K., et al. 2001, Nature, 412, 798

Kodama, R., Okada, K., & Kato, Y. 1999, Review of Scientific Instruments, 70, 625

Kruer, W. & Estabrook, K. 1985, Physics of Fluids, 28, 430

Laffite, S., Baton, S., Combis, P., et al. 2014, Physics of Plasmas, 21, 082705

Lampe, M. 1970, Physics of Fluids, 13, 2578

Lancaster, K. L., Green, J. S., Hey, D. S., et al. 2007, Physical Review Letters, 98, 125002

Landau, L. 1936, Physikalische Zeitschrift der Sowjetunion

LANL, T. G. 1983, SESAME Report on the Los Alamos Equation-of-State Library, Tech. Rep. LALP-83-4, LANL

Le Pape, S., Tsui, Y., Macphee, A., et al. 2009, Optics Letters, 34, 2997

Lee, R. 1971, Physics of Fluids, 14, 1213

Lee, Y. & More, R. 1984, Physics of Fluids, 27, 1273

Lindl, J. 1995, Physics of Plasmas, 2, 3933

Liu, M., An, Z., Tang, C., et al. 2000, Atomic Data and Nuclear Bata Tables, 76, 213

Llovet, X., Merlet, C., & Salvat, F. 2000, Journal of Physics B: Atomic, Molecular and Optical Physics, 33, 3761

Lovelace, R. & Sudan, R. 1971, Physical Review Letters, 27, 1256

Mackinnon, A., Sentoku, Y., Patel, P., et al. 2002, Physical Review Letters, 88, 215006

MacLellan, D. A., Carroll, D. C., Gray, R. J., et al. 2013, Physical Review Letters, 111, 095001

MacPhee, A., Akli, K., Beg, F., et al. 2008, Review of Scientific Instruments, 79, 10F302

Maire, P.-H., Abgrall, R., Breil, J., & Ovadia, J. 2007, SIAM Journal on Scientific Computing, 29, 1781

Malka, G. & Miquel, J. 1996, Physical Review Letters, 77, 75

Malka, V., Faure, J., Glinec, Y., & Rechatin, C. 2008, Journal of Physics: Conference Series, 112, 042029

Martinez, O. 1987, IEEE Journal of Quantum Electronics, QE-23, 1385

Martinez, O., Gordon, J., & Fork, R. 1984, Journal of the Optical Society of America, 1, 1003

Martinolli, E. 2003, PhD thesis, Ecole Polytechnique

Martinolli, E., Koenig, M., Baton, S. D., et al. 2006, Physical Review E, 73, 046402

McClung, F. & Hellwarth, R. 1962, Journal of Applied Physics, 33, 828

McKenna, P., Robinson, A., Neely, D., et al. 2011, Physical Review Letters, 106, 185004

McKinstrie, C. & Dubois, D. 1988, Physics of Fluids, 31, 278

Micheau, S., Debayle, A., d'Humières, E., et al. 2010, Physics of Plasmas, 17, 122703

Michette, A. 1986, Soft X-ray interaction with matter (Plenum Press, New York)

Milchberg, H., Freeman, R., & Davey, S. 1988, Physical Review Letters, 61, 20

Moliere, G. 1948, Zeitschrift Naturforschung Teil A, 3a, 78

Möller, C. 1932, Annalen der Physik, 406, 531

Morace, A. 2013, PhD thesis, Università degli studi di Milano

More, R. 1981, Atomic physics in inertial confinement fusion, LLNL-report UCRL-84991, Academic Press

More, R. 1985, Advances in Atomic and Molecular Physics, 21, 305

Moseley, H. 1913, Philosophical Magazine, 26, 1024

Murakami, M. & Nagatomo, H. 2005, Nuclear Instruments and Methods in Physics Research A, 544, 67

Murakami, M., Nagatomo, H., Johzaki, T., et al. 2014, Nuclear Fusion, 54, 054007

Myatt, J., Theobald, W., Delettrez, J., et al. 2007, Physics of Plasmas, 14, 056301

Nardi, E. & Zinamon, Z. 1978, Physical Review A, 18, 1246

Nigam, B., Sundaresan, M., & Wu, T.-Y. 1959, Physical Review, 115, 491

Nilson, P. M., Theobald, W., Myatt, J., et al. 2008, Physics of Plasmas, 15, 056308

Nolte, R., Behrens, R., Schürer, M., Rousse, A., & Ambrosi, P. 1999, Radiation Protection Dosimetry, 84, 367

Norreys, P., Batani, D., Baton, S., et al. 2014, Nuclear Fusion, 54, 054004

Nuter, R., Gremillet, L., Combis, P., et al. 2008, Journal of Applied Physics, 104, 103307

Nuter, R. & Tikhonchuk, V. 2013, Physical Review E, 87, 043109

Pak, A., Gregori, G., Knight, J., et al. 2004, Review of Scientific Instruments, 75, 3747

Park, H.-S., Hurricane, O. A., Callahan, D. A., et al. 2014, Physical Review Letters, 112, 055001

Patel, P. 2013, Fast Ignition, HEDP Summer School

Pelowitz, D. 2011, MCNPX user's manual version 2.7.0

Pérez, F. 2010, PhD thesis, Ecole Polytechnique

Pérez, F., Debayle, A., Honrubia, J., et al. 2011, Physical Review Letters, 107, 065004

Perkins, L. J., Betti, R., LaFortune, K. N., & Williams, W. H. 2009, Physical Review Letters, 103, 045004

Pert, G. 1995, Physical Review E, 51, 4778

Pines, D. & Bohm, D. 1952, Physical Review, 85, 338

Pisani, F., Koenig, M., Batani, D., et al. 1999, Review of Scientific Instruments, 70, 3314

PROPACEOS. 2014, http://www.prism - cs.com/Software/PROPACEOS/PROPACEOS.htm

Quarles, C. 1976, Physical Review A, 13, 1278

Quesnel, B. & Mora, P. 1998, Physical Review E, 58, 3719

Quinn, M., Yuan, X., Lin, X., et al. 2011, Plasma Physics and Controlled Fusion, 53, 025007

Ramakrishna, B., Kar, S., Robinson, A. P. L., et al. 2010, Physical Review Letters, 105, 135001

Ramis, R., Schmalz, R., & ter Vehn, J. M. 1988, Computational Physics Communications, 49, 475

Ren, C., Tzoufras, M., Tsung, F. S., et al. 2004, Physical Review Letters, 93, 185004

Ribeyre, X., Guskov, S., Feugeas, J.-L., Nicolaï, P., & Tikhonchuk, V. T. 2013, Physics of Plasmas, 20, 062705

Robinson, A. & Schmitz, H. 2013, Physics of Plasmas, 20, 062704

Robinson, A., Strozzi, D., Davies, J., et al. 2014, Nuclear Fusion, 54, 054003

Rogers, F. 1981, Physical Review A, 24, 1531

Rohrlich, F. & Carlson, B. 1954, Physical Review, 93, 38

Roth, M., Cowan, T. E., Key, M. H., et al. 2001, Physical Review Letters, 86, 436

Roth, M., Jung, D., Falk, K., et al. 2013, Physical Review Letters, 110, 044802

Rozmus, W. & Tikhonchuk, V. 1990, Physical Review A, 42, 7401

Rozmus, W., Tikhonchuk, V., & Cauble, R. 1996, Physics of Plasmas, 3, 360

Salvat, F., Fernández-Varea, J., Sempau, J., & Llovet, X. 2006, Radiation Physics and Chemistry, 75, 1201

Santos, J., Batani, D., Baton, S., et al. 2013, Journal of Plasma Physics, 79, 429

Santos, J., Batani, D., McKenna, P., et al. 2009, Plasma Physics and Controlled Fusion, 51, 014005

Santos, J., Debayle, A., Nicolaï, P., et al. 2007, Physics of Plasmas, 14, 103107

Santos, J. J., Amiranoff, F., Baton, S. D., et al. 2002, Physical Review Letters, 89, 025001

Sawada, H., Wei, M. S., Chawla, S., et al. 2014, Physical Review E, 89, 033105

Schiff, L. 1951, Physical Review, 83, 252

Schmitz, H., Lloyd, R., & Evans, R. 2012, Plasma Physics and Controlled Fusion, 54, 085016

Scott, R., Clark, E., Pérez, F., et al. 2013, Review of Scientific Instruments, 84, 083505

Scott, R. H. H., Beaucourt, C., Schlenvoigt, H.-P., et al. 2012, Physical Review Letters, 109, 015001

Seely, J., Hudson, L., Holland, G., & Henins, A. 2008, Applied Optics, 47, 2767

Seltzer, S. 1974, Transmission of electrons through foils, Technical report COM-74-11792, National Bureau of Standards

Seltzer, S. & Berger, M. 1986, Atomic Data and Nuclear Bata Tables, 35, 345

Sentoku, Y., Cowan, T., Kemp, A., & Ruhl, H. 2003, Physics of Plasmas, 10, 2009

Sentoku, Y. & Kemp, A. 2008, Journal of Computational Physics, 227, 6846

Sinars, D., Bennet, G., Wenger, D., Cuneo, M., & Porter, J. 2003, Applied Optics, 42, 4059

Snavely, R., Key, M., Hatchett, S., et al. 2000, Physical Review Letters, 85, 2945

Solodov, A. & Betti, R. 2008, Physics of Plasmas, 15, 042707

Solodov, A., Betti, R., Anderson, K., et al. 2010, Bulletin of American Physical Society, 55, 69

Solodov, A. A., Betti, R., Delettrez, J. A., & Zhou, C. D. 2007, Physics of Plasmas, 14, 062701

Spitzer, L. 1956, Physics of fully ionized gases; 1st ed, Inter science Tracts on Physics and Astronomy (Interscience)

Stephens, R. B., Snavely, R. A., Aglitskiy, Y., et al. 2005, Physical Review E, 69, 066414

Sternheimer, R. 1966, Physical Review, 145, 247

Sternheimer, R., Seltzer, S., & Berger, M. 1982, Physical Review B, 26, 6067

Stoyer, M., Sangster, T., Henry, E., et al. 2001, Review of Scientific Instruments, 72, 767

Strickland, D. & Mourou, G. 1985, Optics Communications, 56, 219

Strozzi, D. J., Tabak, M., Larson, D. J., et al. 2012, Physics of Plasmas, 19, 072711

Tabak, M., Hammer, J., Glinsky, M., et al. 1994, Physics of Plasmas, 1, 1626

Theobald, W., Akli, K., Clarke, R., et al. 2006, Physics of Plasmas, 13, 043102

Theobald, W., Casner, A., Nora, R., et al. 2013, EPJ Web of Conferences, 59, 03001

Thfoin, I., Reverdin, C., Hulin, S., et al. 2014, Review of Scientific Instruments, 85, 11D615

Tikhonchuk, V. 2002, Physics of Plasmas, 9, 1416

Touati, M., Feugeas, J.-L., Nicolaï, P., et al. 2014, New Journal of Physics, 16, 073014

Vauzour, B. 2012, PhD thesis, Université Bordeaux 1

Vauzour, B., Debayle, A., Vaisseau, X., et al. 2014, Physics of Plasmas, 21, 033101

Vauzour, B., Santos, J. J., Debayle, A., et al. 2012, Physics of Plasmas, 109, 255002

Verner, D. & Yakovlev, D. 1995, Astronoy and Astrophysics, 109, 125

Weibel, E. 1959, Physical Review Letters, 2, 83

Weibel, E. 1967, Physics of Fluids, 10, 741

Welch, D., Rose, D., Clark, R., Genoni, T., & Hughes, T. 2004, Computer Physics Communication, 164, 183

Wentzel, G. 1927, Zeitschrift für Physik, 40, 590

Westover, B., Chen, C. D., Patel, P. K., et al. 2011, Physics of Plasmas, 18, 063101

Wharton, K. B., Hatchett, S. P., Wilks, S. C., et al. 1998, Physical Review Letters, 81, 822

Wilks, S. C., Kruer, W. L., Tabak, M., & Langdon, A. B. 1992, Physical Review Letters, 69, 1383

Wilks, S. C., Langdon, A. B., Cowan, T. E., et al. 2001, Physics of Plasmas, 8, 542

Williams, E. 58, Physical Review

Yakovlev, D. & Urpin, V. 1980, Soviet Astronomy, 24, 303

Yang, T.-Y., Kruer, W., More, R., & Langdon, A. 1995, Physics of Plasmas, 2, 3146

Yasuike, K., Key, M. H., Hatchett, S. P., Snavely, R. A., & Wharton, K. B. 2001, Review of Scientific Instruments, 72, 1236

Zhou, C.-G., An, Z., & Luo, Z.-M. 2000, Chinese Physics Letters, 18, 759